Disease Markers

The Discovery of Nucleotide and Nucleic Acid-Associated Biomarkers and Cancer Personalized Therapies 2022

Lead Guest Editor: Fu Wang
Guest Editors: Jian Song and Jingang Huang

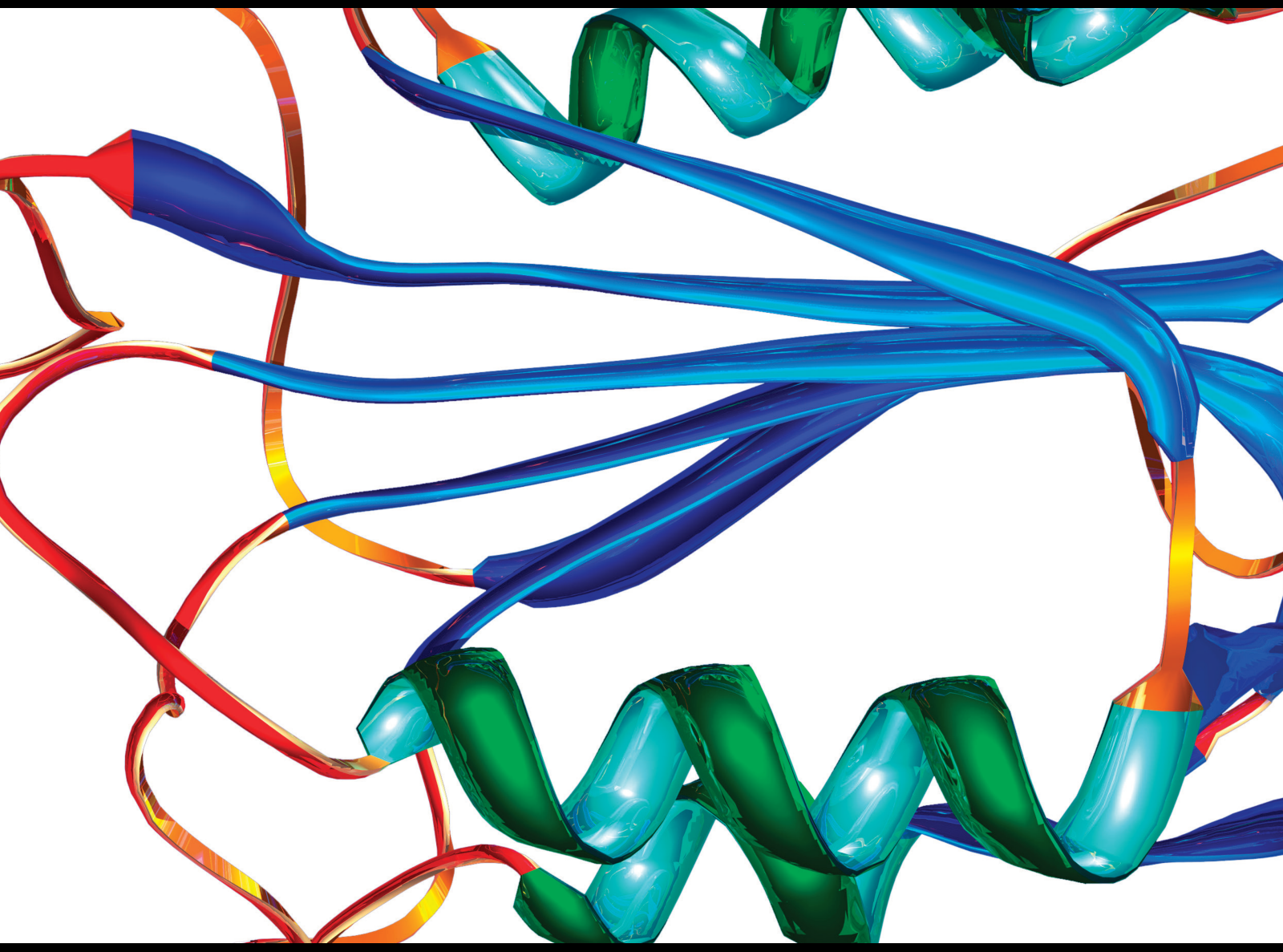

The Discovery of Nucleotide and Nucleic Acid-Associated Biomarkers and Cancer Personalized Therapies 2022

Disease Markers

The Discovery of Nucleotide and Nucleic Acid-Associated Biomarkers and Cancer Personalized Therapies 2022

Lead Guest Editor: Fu Wang
Guest Editors: Jian Song and Jingang Huang

Chief Editor

Paola Gazzaniga, Italy

Associate Editors

Donald H. Chace, USA
Mariann Harangi, Hungary
Hubertus Himmerich, United Kingdom
Yi-Chia Huang, Taiwan
Giuseppe Murdaca, Italy
Irene Rebelo, Portugal

Academic Editors

Muhammad Abdel Ghafar, Egypt
George Agrogiannis, Greece
Mojgan Alaeddini, Iran
Atif Ali Hashmi, Pakistan
Cornelia Amalinei, Romania
Pasquale Ambrosino, Italy
Paul Ashwood, USA
Faryal Mehwish Awan, Pakistan
Atif Baig, Malaysia
Valeria Barresi, Italy
Lalit Batra, USA
Francesca Belardinilli, Italy
Elisa Belluzzi, Italy
Laura Bergantini, Italy
Sourav Bhattacharya, USA
Anna Birková, Slovakia
Giulia Bivona, Italy
Luisella Bocchio-Chiavetto, Italy
Francesco Paolo Busardó, Italy
Andrea Cabrera-Pastor, Spain
Paolo Cameli, Italy
Chiara Caselli, Italy
Jin Chai, China
Qixing Chen, China
Shaoqiu Chen, USA
Xiangmei Chen, China
Carlo Chiarla, Italy
Marcello Ciaccio, Italy
Luciano Colangelo, Italy
Alexandru Corlateanu, Moldova
Miriana D'Alessandro, Saint Vincent and the Grenadines
Waaqo B. Daddacha, USA
Xi-jian Dai, China
Maria Dalamaga, Greece
Serena Del Turco, Italy
Jiang Du, USA
Xing Du, China
Benoit Dugue, France
Paulina Dumnicka, Poland
Nashwa El-Khazragy, Egypt
Zhe Fan, China
Rudy Foddis, Italy
Serena Fragiotta, Italy
Helge Frieling, Germany
Alain J. Gelibter, Italy
Matteo Giulietti, Italy
Damjan Glavač, Slovenia
Alvaro González, Spain
Rohit Gundamaraju, USA
Emilia Hadziyannis, Greece
Michael Hawkes, Canada
Shih-Ping Hsu, Taiwan
Menghao Huang, USA
Shu-Hong Huang, China
Xuan Huang, China
Ding-Sheng Jiang, China
Esteban Jorge Galarza, Mexico
Mohamed Gomaa Kamel, Japan
Michalis V. Karamouzis, Greece
Muhammad Babar Khawar, Pakistan
Young-Kug Kim, Republic of Korea
Mallikarjuna Korivi, China
Arun Kumar, India
Jinan Li, USA
Peng-fei Li, China
Yiping Li, China
Michael Lichtenauer, Austria
Daniela Ligi, Italy
Hui Liu, China
Jin-Hui Liu, China
Ying Liu, USA
Zhengwen Liu, China
César López-Camarillo, Mexico
Xin Luo, USA
Zhiwen Luo, China
Valentina Magri, Italy
Michele Malaguarnera, Italy
Erminia Manfrin, Italy
Upender Manne, USA

Contents

Contents

Hindawi
Disease Markers
Volume 2023, Article ID 9820901, 1 page
https://doi.org/10.1155/2023/9820901

Retraction

Retracted: Exogenous Hydrogen Sulfide Mitigates Oxidative Stress and Mitochondrial Damages Induced by Polystyrene Microplastics in Osteoblastic Cells of Mice

Disease Markers

Received 20 June 2023; Accepted 20 June 2023; Published 21 June 2023

This article has been retracted by Hindawi following an investigation undertaken by the publisher [1]. This investigation has uncovered evidence of one or more of the following indicators of systematic manipulation of the publication process:

(1) Discrepancies in scope

(2) Discrepancies in the description of the research reported

(3) Discrepancies between the availability of data and the research described

(4) Inappropriate citations

(5) Incoherent, meaningless and/or irrelevant content included in the article

(6) Peer-review manipulation

The presence of these indicators undermines our confidence in the integrity of the article's content and we cannot, therefore, vouch for its reliability. Please note that this notice is intended solely to alert readers that the content of this article is unreliable. We have not investigated whether authors were aware of or involved in the systematic manipulation of the publication process.

Wiley and Hindawi regrets that the usual quality checks did not identify these issues before publication and have since put additional measures in place to safeguard research integrity.

We wish to credit our own Research Integrity and Research Publishing teams and anonymous and named external researchers and research integrity experts for contributing to this investigation.

The corresponding author, as the representative of all authors, has been given the opportunity to register their agreement or disagreement to this retraction. We have kept a record of any response received.

References

[1] Q. Shi, F. Chen, Y. Feng, Y. Zheng, X. Zhi, and W. Wu, "Exogenous Hydrogen Sulfide Mitigates Oxidative Stress and Mitochondrial Damages Induced by Polystyrene Microplastics in Osteoblastic Cells of Mice," *Disease Markers*, vol. 2023, Article ID 2516472, 8 pages, 2023.

Hindawi
Disease Markers
Volume 2023, Article ID 5493415, 21 pages
https://doi.org/10.1155/2023/5493415

Research Article

Identification of Inflammatory Gene in the Congenital Heart Surgery Patients following Cardiopulmonary Bypass via the Way of WGCNA and Machine Learning Algorithms

Liang Cai and Bingdong Zhang

Department of Anesthesiology in Cardiovascular Institute, The First Affiliated Hospital of Guangxi Medical University, Nanning, Guangxi, China

Correspondence should be addressed to Bingdong Zhang; zbd2019@126.com

Received 27 September 2022; Revised 7 November 2022; Accepted 24 November 2022; Published 12 April 2023

Academic Editor: Jian Song

Performing cardiopulmonary bypass (CPB) to reduce ischemic injury during surgery is a common approach to cardiac surgery. However, this procedure can lead to systemic inflammation and multiorgan dysfunction. Therefore, elucidating the molecular mechanisms of CPB-induced inflammatory cytokine release is essential as a critical first step in identifying new targets for therapeutic intervention. The GSE143780 dataset which is mRNA sequencing from total circulating leukocytes of the neonatorum was downloaded from the Gene Expression Omnibus (GEO) database. A total of 21 key module genes were obtained by analyzing the intersection of differentially expressed gene (DEG) and gene coexpression network analysis (WGCNA), and then, 4 genes (TRAF3IP2-AS1, PPARGC1B, CD4, and PDLIM5) were further confirmed after the least absolute shrinkage and selection operator (LASSO) and support vector machine recursive feature elimination (SVM-RFE) screening and were used as hub genes for CPB-induced inflammatory cytokine release in patients with congenital heart defects. The enrichment analysis revealed 21 key module genes mainly related to the functions of developmental cell growth, regulation of monocyte differentiation, regulation of myeloid leukocyte differentiation, ERK1 and ERK2 cascade, volume-sensitive anion channel activity, and estrogen receptor binding. The result of gene set enrichment analysis (GSEA) showed that the hub genes were related to different physiological functions of cells. The ceRNA network established for hub genes includes 3 hub genes (PPARGC1B, CD4, and PDLIM5), 55 lncRNAs, and 34 miRNAs. In addition, 4 hub genes have 215 potential therapeutic agents. Finally, expression validation of the four hub genes revealed that they were all significantly low expressed in the surgical samples than before.

1. Introduction

Cardiopulmonary bypass (CPB) is a technique for maintaining survival, which is vital to the success of modern cardiac surgeries. The main reason for application is most sufferers undergoing cardiac surgery need CPB to reduce complications caused by the surgery itself. The blood will be exposed to high shear stress and plastic tubes during blood drawing by the artificial cardiopulmonary machine [1]. During the surgery, the temperature of patient is decreased to reduce metabolic needs, and the temperature rises rapidly after the procedure, which could induce a variety of complications. However, the current treatment methods, such as corticosteroids, CPB circuit coating, and modified ultrafiltration, fail to significantly reduce the complications secondary to CPB [2–5].

The way of CPB-induced inflammation involves a variety of mechanisms. Firstly, the coagulation cascade and complement system will be activated when blood flows through the foreign body surface of the extracorporeal circulation circuit, which causes the release of proinflammatory factors [6]. Secondly, aortic occlusion leads to ischemia-reperfusion injury in multiple organs, which makes these tissues and organs produce a series of inflammatory factors.

Table 1: Specific primer series for hub genes.

Genes	Forward primer	Reverse primer
CD4	5′-AACTGGAGAACAAGGAGGCAAAG-3′	5′-AAGAAGATGCCTAGCCCAATGAA-3′
PDLIM5	5′-GAGGATCCCAGGGTGACAGTAAA-3′	5′-CGCCAGTCTTCAGTATCCTCAAT-3′
TRAF3IP2-AS1	5′-TTCCTTCACGCCATCACAAG-3′	5′-CCTTTGTTGGTGCTCTGTCA-3′
PPARGC1B	5′-GAGCAGACCTTGACAGTGGA-3′	5′-GCTGAGAGCTATTTCTTTGCCT-3′
GAPDH	5′-TGTCAAGCTCATTTCCTGGTATG-3′	5′-TCTCTCTTCCTCTTGTGCTCTTG-3′

Thirdly, CPB results in endotoxemia, because CPB can lead to intestinal injury and bacterial translocation. Fourthly, gaseous microemboli in CPB lead to local thrombosis and activation of complement systems, such as C3a and C5a. Finally, iNOS or ROS produced during CPB, calcium metabolism disorder, and endothelial injury will further expand the inflammatory response [7–9] .

Systemic inflammation and multiorgan dysfunction are the most common and severe CPB-induced complications, especially in neonatal and pediatric patients. Cell infiltration, vasoconstriction, and glomerular fibrin deposition caused by inflammatory cytokines lead to renal injury [8]. Sasser et al. also found that inflammatory cytokines can increase vascular permeability, which will lead to multiple organ edema. For example, pulmonary edema can affect gas exchange [10]. The mechanism of CPB-induced inflammation is extremely complex, and there is no consensus on how to effectively reduce the inflammation. Considering inhibition of inflammation is expected to reduce incidence rate and mortality after surgery, it is important to clarify the pathological mechanism of inflammation during CPB.

In this study, we searched for the gene and signaling pathway between CPB and inflammation through comprehensive bioinformatics analysis [11]. Initially, we got the GSE143780 dataset from the Gene Expression Omnibus (GEO) database and performed gene coexpression network analysis (WGCNA) and differential analysis. Then, the least absolute shrinkage and selection operator (LASSO) and support vector machine recursive feature elimination (SVM-RFE) screening methods were performed on key module genes, and the results obtained were used as hub genes for CPB-induced inflammatory cytokine release in patients with congenital heart defects. The possible biological functions and involved signaling pathways were screened via immune and enrichment analysis of hub genes. The potential regulatory relationships of hub genes were explored by constructing endogenous RNA (ceRNA) networks. Ultimately, the expression levels of hub genes in tissues were examined by applying quantitative reverse transcription polymerase chain reaction (qRT-PCR).

2. Materials and Methods

2.1. Data Source. The GSE143780 dataset was obtained from the GEO database, including 5 CPB samples of 0 hour as control and 10 CPB-related samples of 1 hour or end as case [12].

2.2. WGCNA. The coexpression network was established by WGCNA [13]. First of all, we cluster samples according to the presence of obvious outliers. Second, automatic network construction function was used to construct the coexpression network. pickSoftThreshold in R was applied to compute the soft thresholding power, to which the proximity of coexpression was raised to compute adjacency. Then, detect modules by hierarchical clustering and the dynamic tree cut function. Finally, modules will be related to clinical traits according to gene significance (GS) and module membership (MM). The information on associated module genes was used for further analysis.

2.3. Differential Expression Analysis. So as to find out the DEGs between control and case samples and to do more in-depth functional mining, the limma package was used to identify genes with $P < 0.05$ and $|\log 2\,\mathrm{FC}| > 1$ as differentially expressed genes [14]. Then, the DEGs were intersected with the key module genes obtained by WGCNA to gain the key genes.

2.4. Functional Enrichment Analysis. For exploring the signaling pathways and characteristic biological attributes involved in key genes, Kyoto Encyclopedia of Genes and Genomes (KEGG) and Gene Ontology (GO) were analyzed by the function of clusterProfiler package in R. Significance was set at $P < 0.05$. In addition, to further search the potential biological functions of the signaling pathways involved and the selected hub genes, we carried out GSEA [15].

2.5. Ingenuity Pathway Analysis (IPA). To explore the interaction of key genes and the diseases or functional pathways involved, we performed IPA analysis on all genes [16]. Briefly, the expression matrix was entered into the software and screened for differential genes according to a threshold ($|\log 2\,(\text{fold change})| > 1$ and $P < 0.05$), after which the canonical pathways of the genes and the interaction network between genes and other substances, such as chemicals and drugs, could be obtained.

2.6. LASSO Regression and SVM-RFE Analyses. For further screening out the hub gene from the key genes, the R software glmnet package was used to set the parameter "family" to "binomial" to execute LASSO logistic regression [17]. The receiver operating characteristic curve (ROC) was used to validate the obtained LASSO model. Similarly, the SVM-RFE approach was applied to rank the features of the obtained key genes. Finally, take the intersection of the

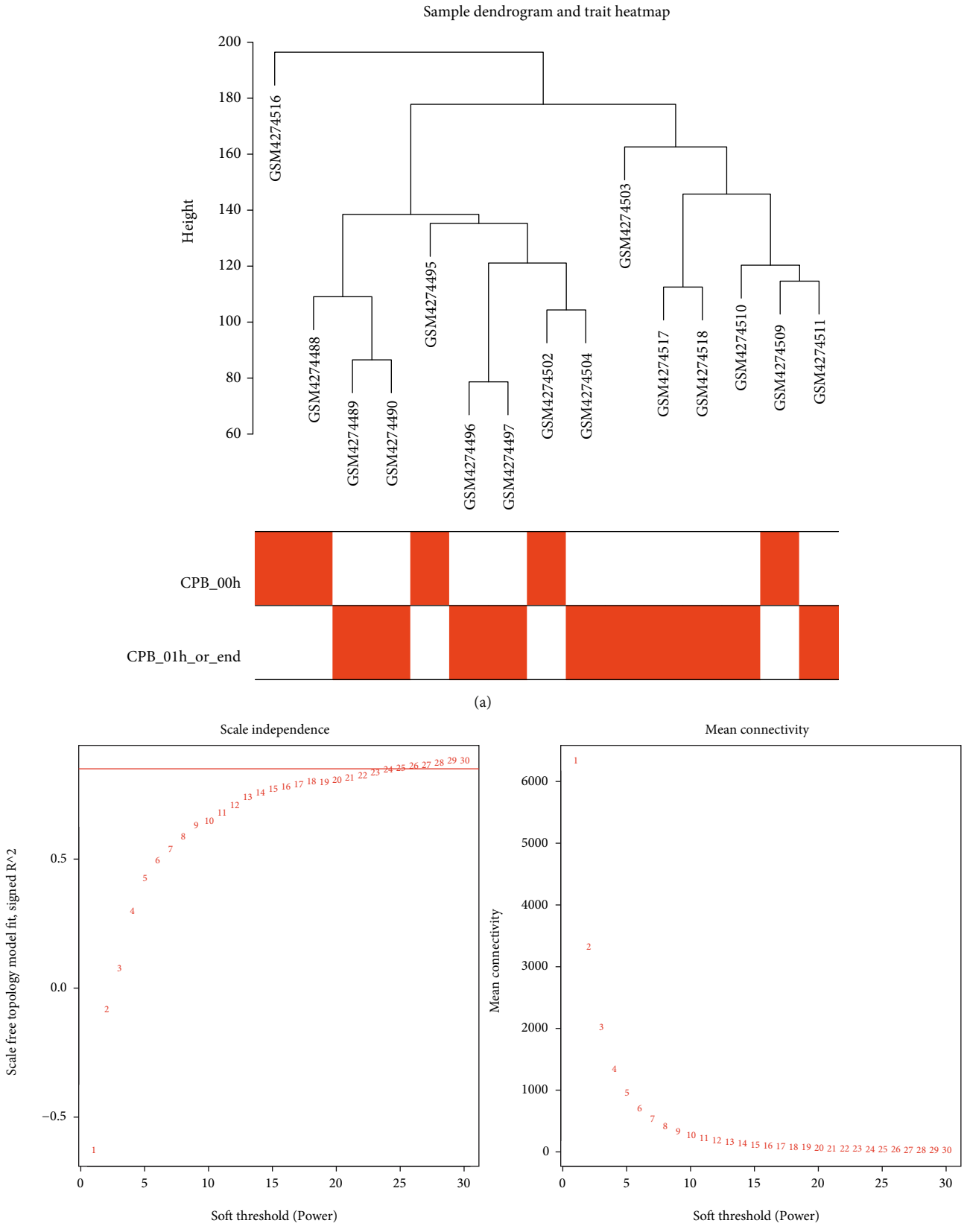

Figure 1: Continued.

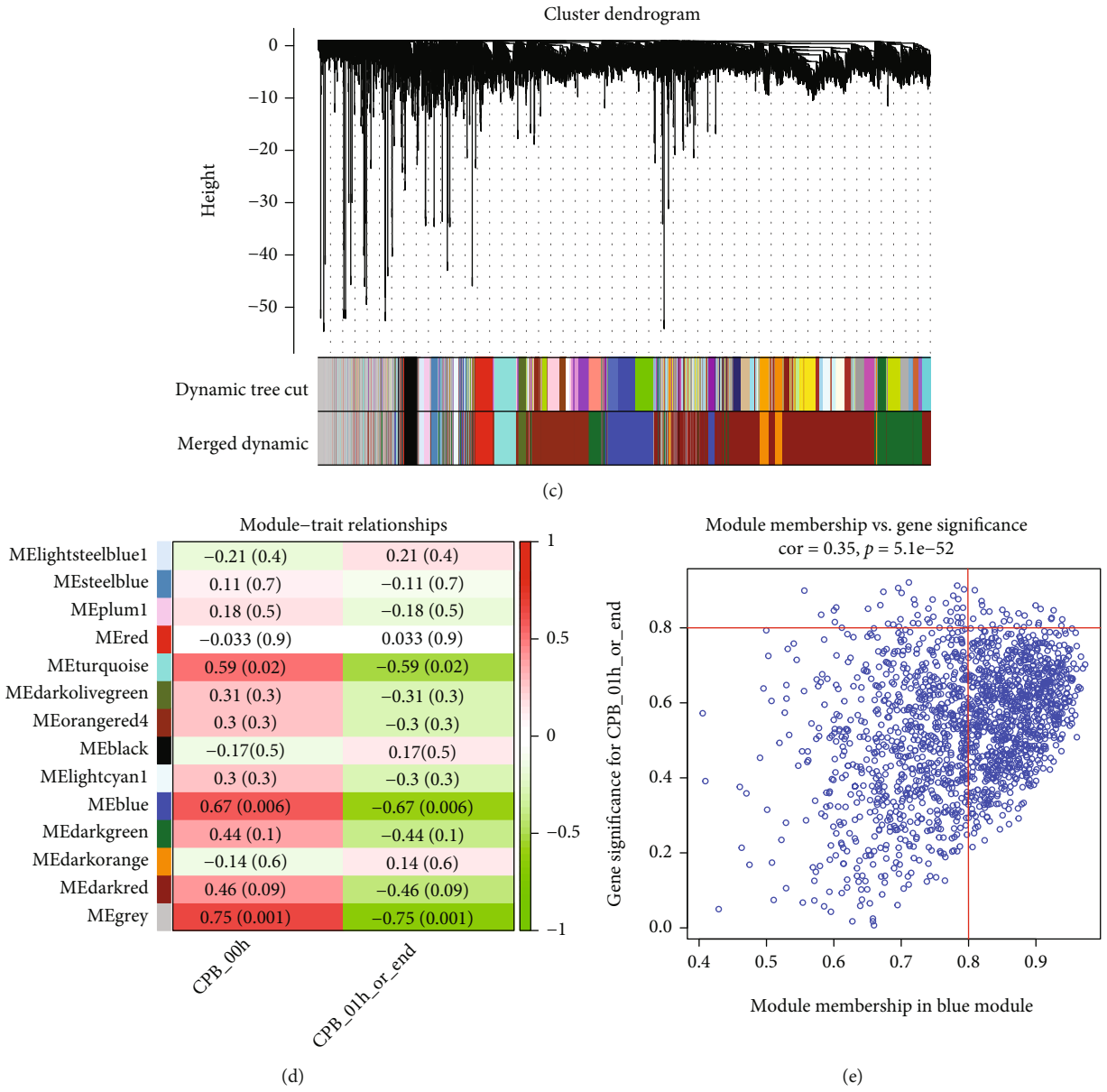

Figure 1: Screening of key modules and genes by WGCNA. (a) Clustering dendrogram of samples with trait heat map. (b) Analysis of network topology for various soft-thresholding powers. The left panel shows the scale-free fit index (y-axis) as a function of the soft-thresholding power (x-axis). The right panel displays the mean connectivity (degree, y-axis) as a function of the soft-thresholding power (x-axis). (c) Clustering dendrogram of genes, with dissimilarity based on topological overlap, together with assigned module colors. (d) Module-trait associations: each row corresponds to a module eigengene and each column to a trait. Each cell contains the corresponding correlation and P value. (e) MM and GS scatter plots for the key module blue. The vertical line is $|MM| = 0.8$, and the horizontal line is $|GS| = 0.8$. The key genes of the module are in the box in the upper right corner of the figure.

marker molecules obtained by the LASSO and SVM as the hub gene. To investigate the distinguishing ability of hub genes between control and case samples, we plotted the ROC curves of hub genes.

2.7. Immunoassay Based on Hub Genes. The ssGSEA algorithm was applied to compute the abundance of 28 kinds of immune cell infiltrates in all groups, and then, boxplots were drawn using R package ggplot2 and wilcox.test to screen immune cells with differences between case and control samples. Mcp_counter algorithm in immunedeconv package (version 2.0.4) was used to compute the proportion of 28 kinds of immune cells between the case and control groups, and the results were output as heat maps by pheatmap (version 1.0.12) [18, 19]. Then, the correlations between the proportions of 28 types of immune cells in the case and control groups were obtained through the Pearson correlation analysis and visualized. Finally, the Pearson analysis was further performed to analyze the intimacy between hub genes and the 28 kinds of immune cells.

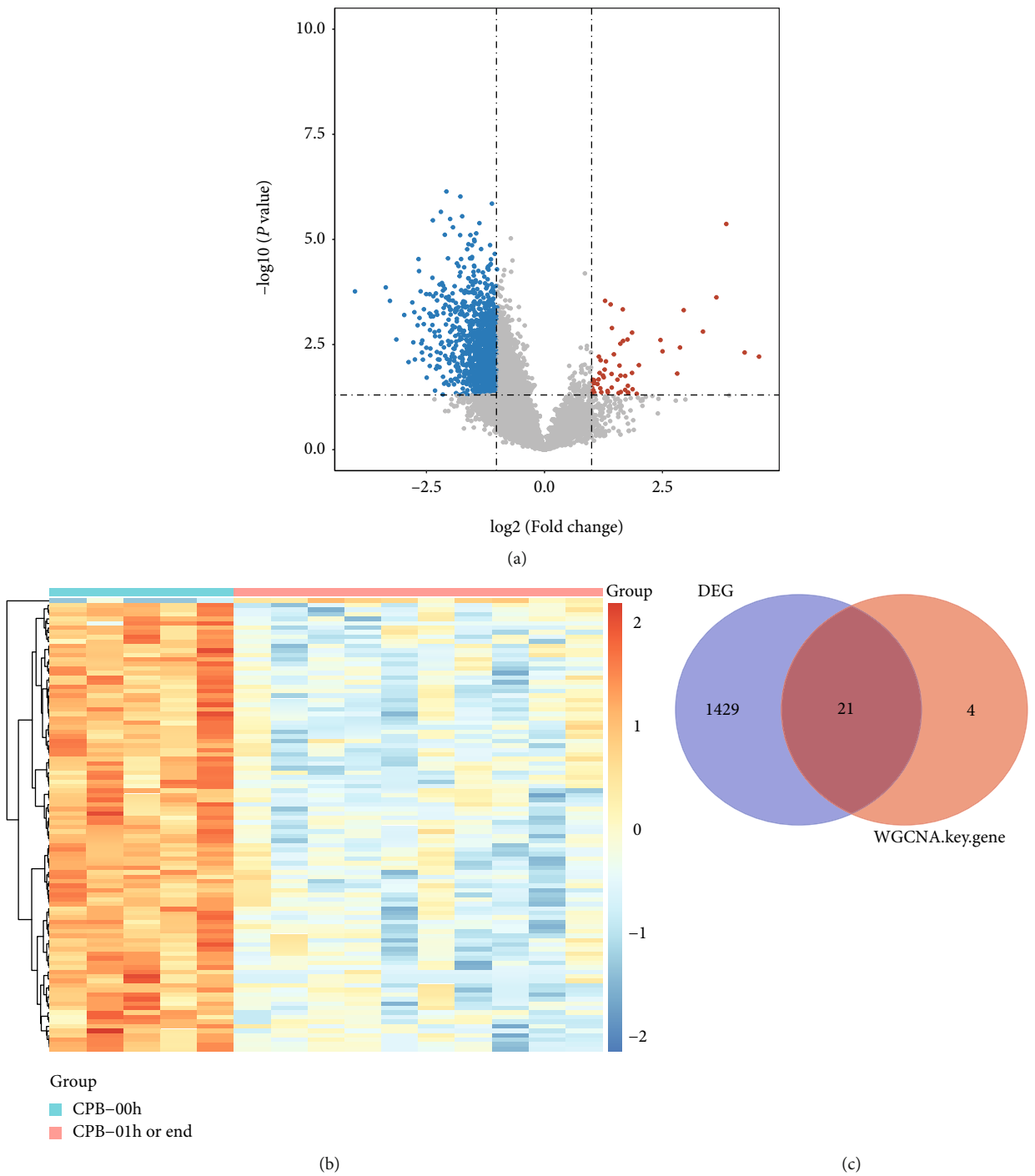

Figure 2: Continued.

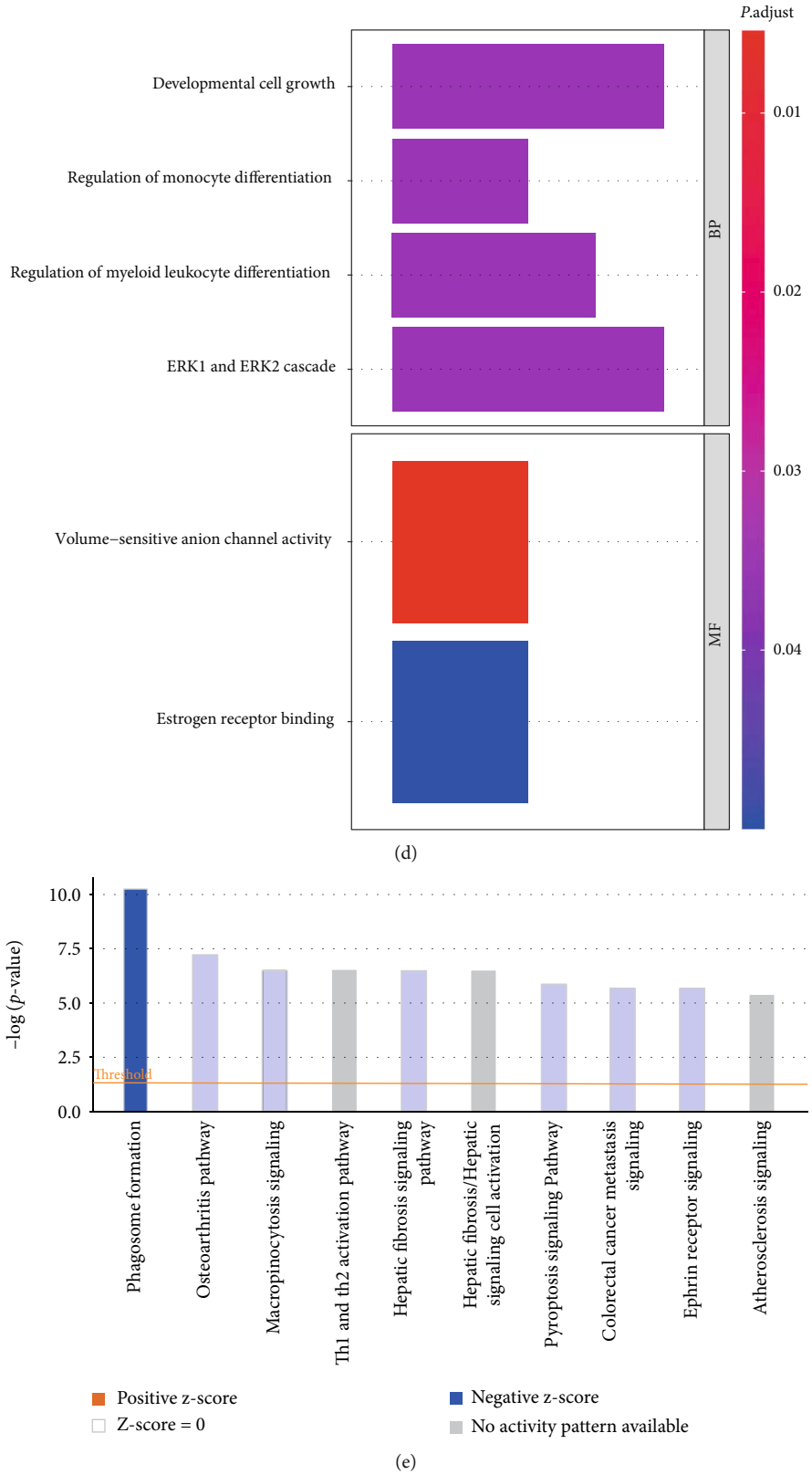

Figure 2: 21 differentially expressed key module gene identification and enrichment analysis in congenital heart defects following cardiopulmonary bypass. (a) Volcano plot of the DEGs between CPB samples and control samples. Downregulated genes are green and upregulated genes come as red. (b) Heat map of the DEGs. Red is high expression and blue is low expression. (c) Venn diagram of DEGs and key module genes. (d, e) Bar chart of GO enrichment results (TOP10) and canonical pathway analysis for 21 key genes.

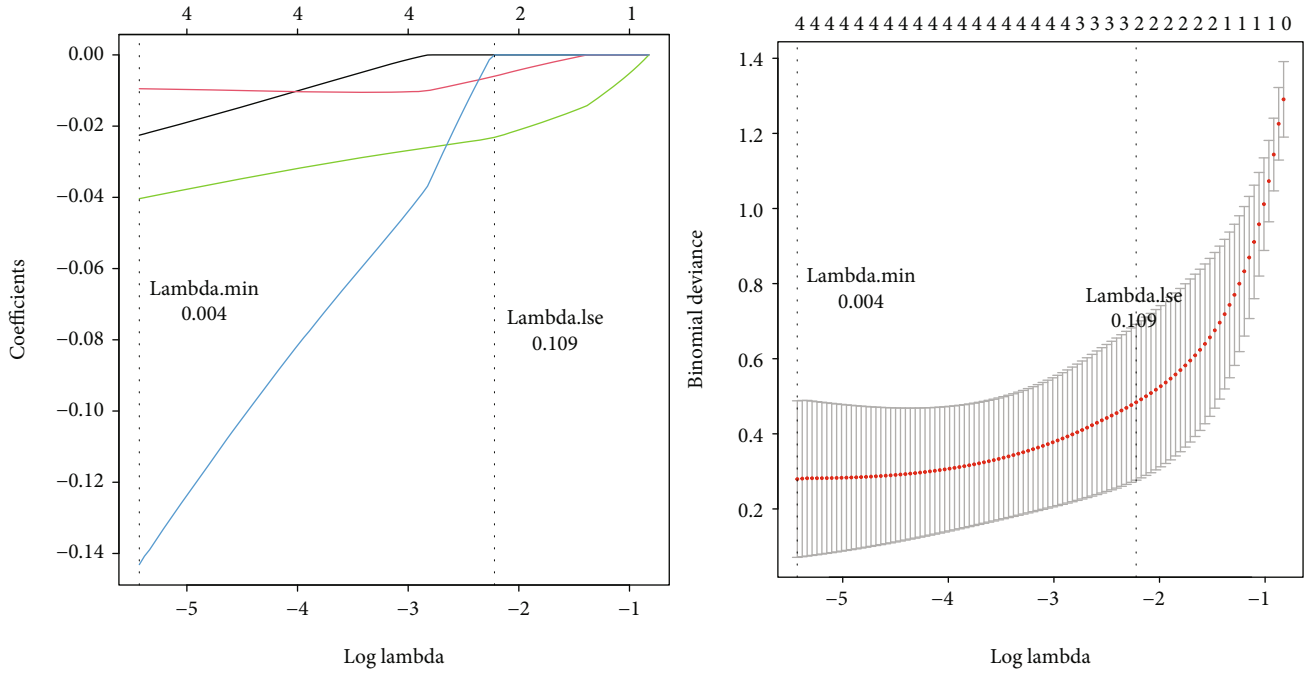

(a)

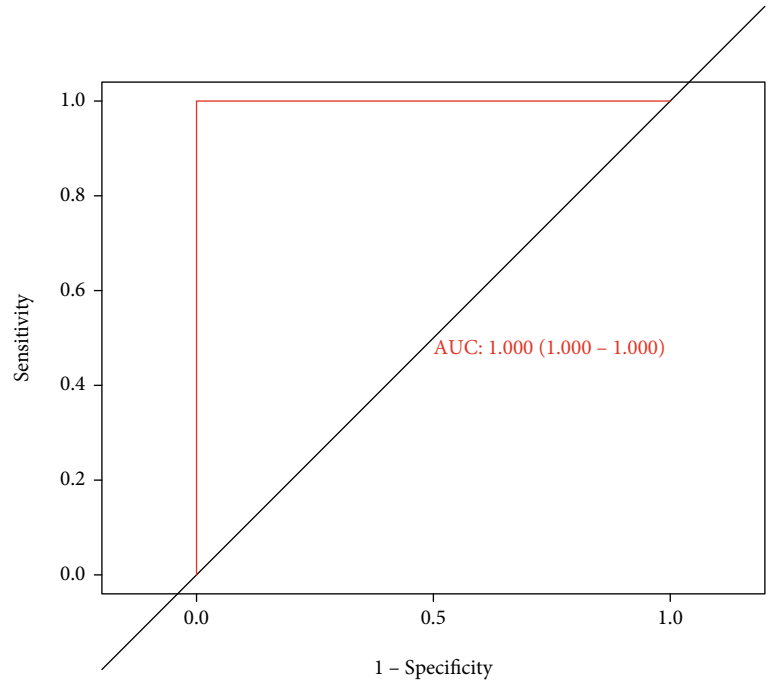

(b)

Figure 3: Continued.

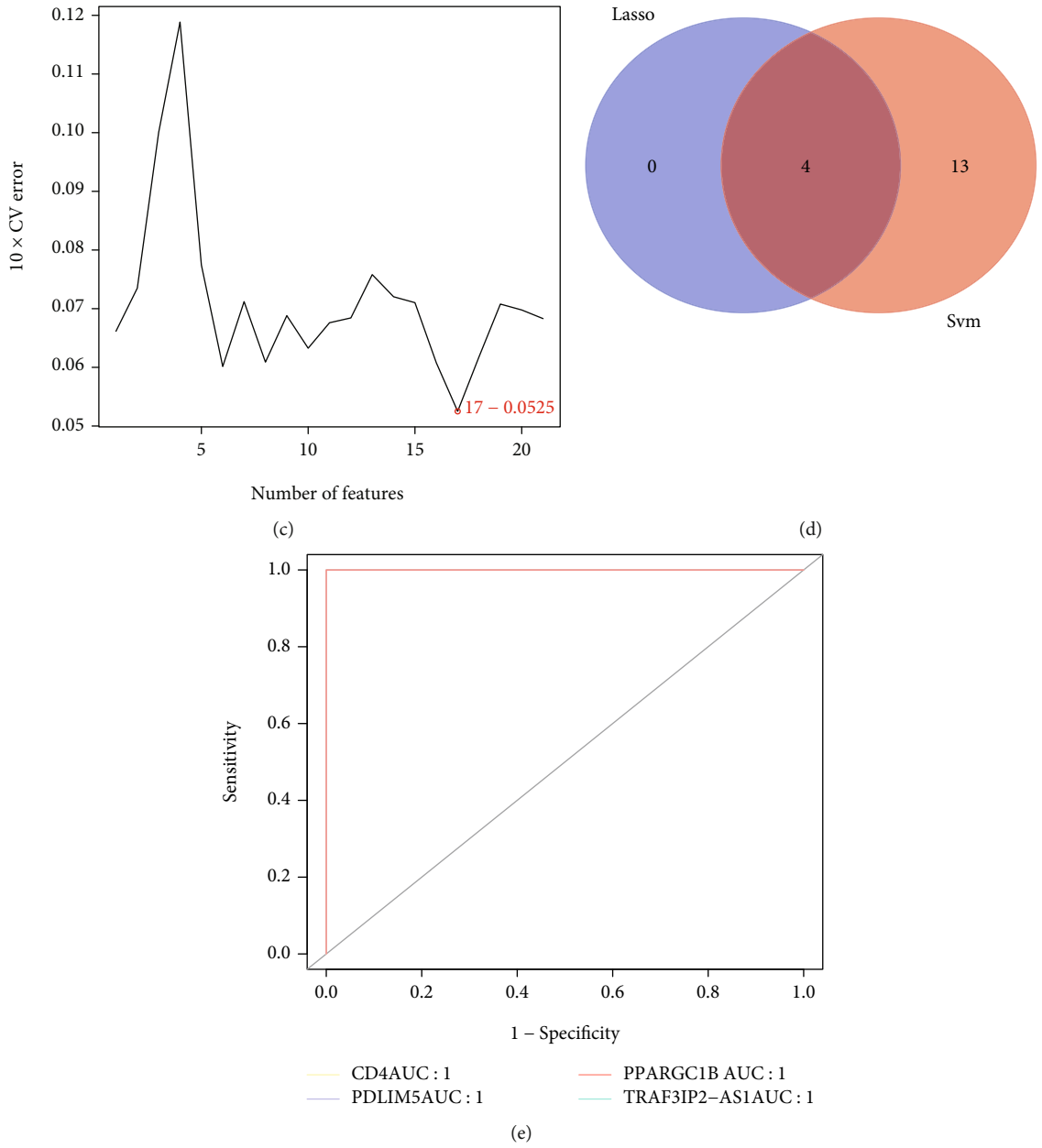

Figure 3: Identification of hub genes for CPB. (a) Log λ value of the differentially expressed CPB-related genes in the LASSO model (left). The most proper log λ value in the LASSO model (right). (b) The area under the ROC curve of LASSO model is 1.0. (c) Support vector machine-recursive feature elimination algorithm to screen 17 characteristic genes. (d) Venn diagram showed the 4 overlapped genes obtained by the LASSO algorithm and SVM-RFE algorithm. (e) The area under the ROC curve of all 4 hub genes is 1.0.

2.8. Competing Endogenous RNA (ceRNA) Network Construction. First, we used the miRWalk website (http://mirwalk.umm.uni-heidelberg.de/) to predict miRNAs for hub genes, and then, the starbase website (http://starbase.sysu.edu.cn/) was used to predict lncRNAs based on the predicted miRNAs [20]. The lncRNA-miRNA screening criteria were clipExpNum > 10. The ceRNA network maps were visualized by Cytoscape software [21].

2.9. Drug Prediction Analysis. To focus on which drugs affect the hub gene, we predicted drugs for the hub gene using the Comparative Toxicogenomics Database (CTD, http://ctdbase.org/) [22].

2.10. Verification of Gene Expression. The mRNA expression levels of hub genes were detected in 10 CPB-related blood samples including 5 cases at 1 hour or end and 5 control samples of 0 hour from the First Affiliated Hospital of Guangxi Medical University. This study was allowed by the Ethics Committee of the First Affiliated Hospital of Guangxi Medical University. All patients had approved for the use of clinical tissue for research purposes. Total RNA was isolated

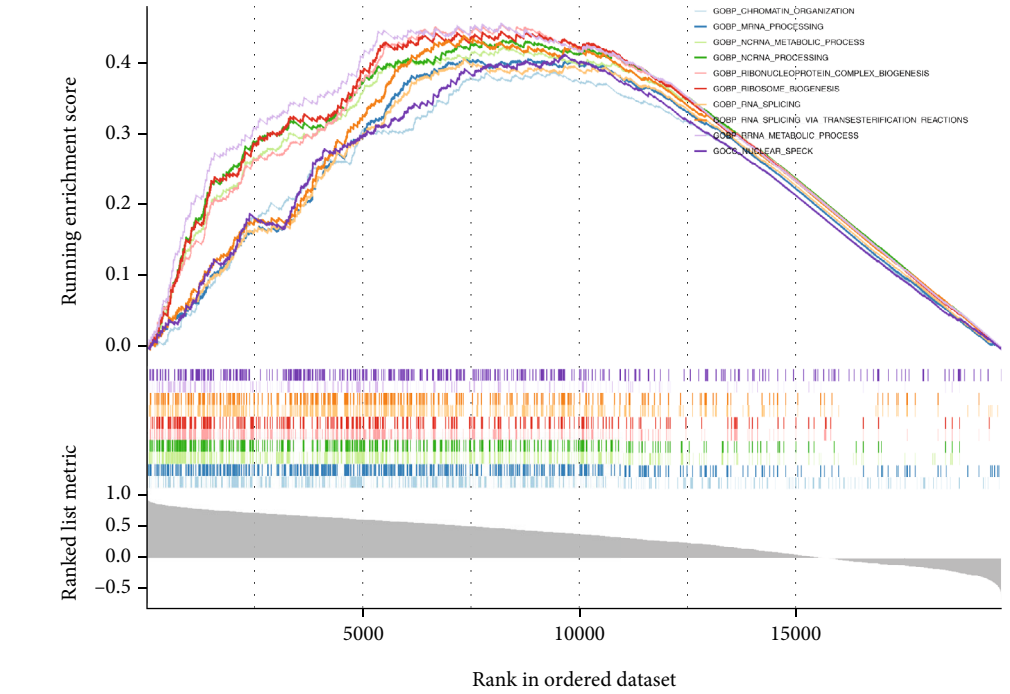

(a)

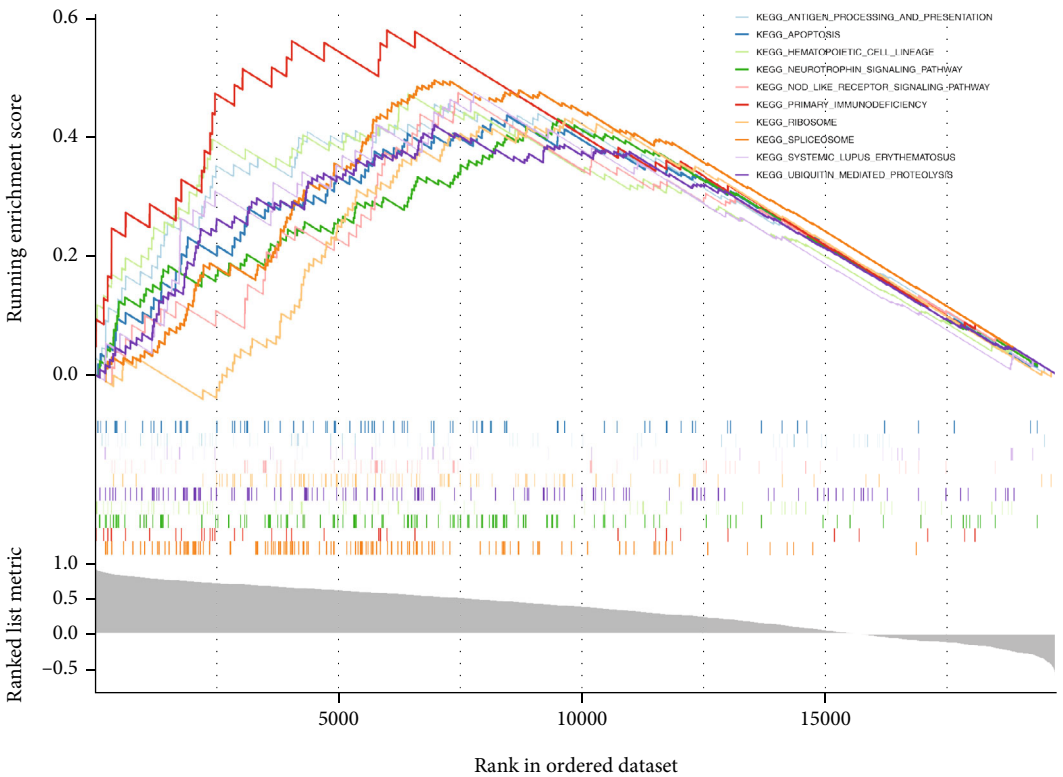

(b)

Figure 4: Continued.

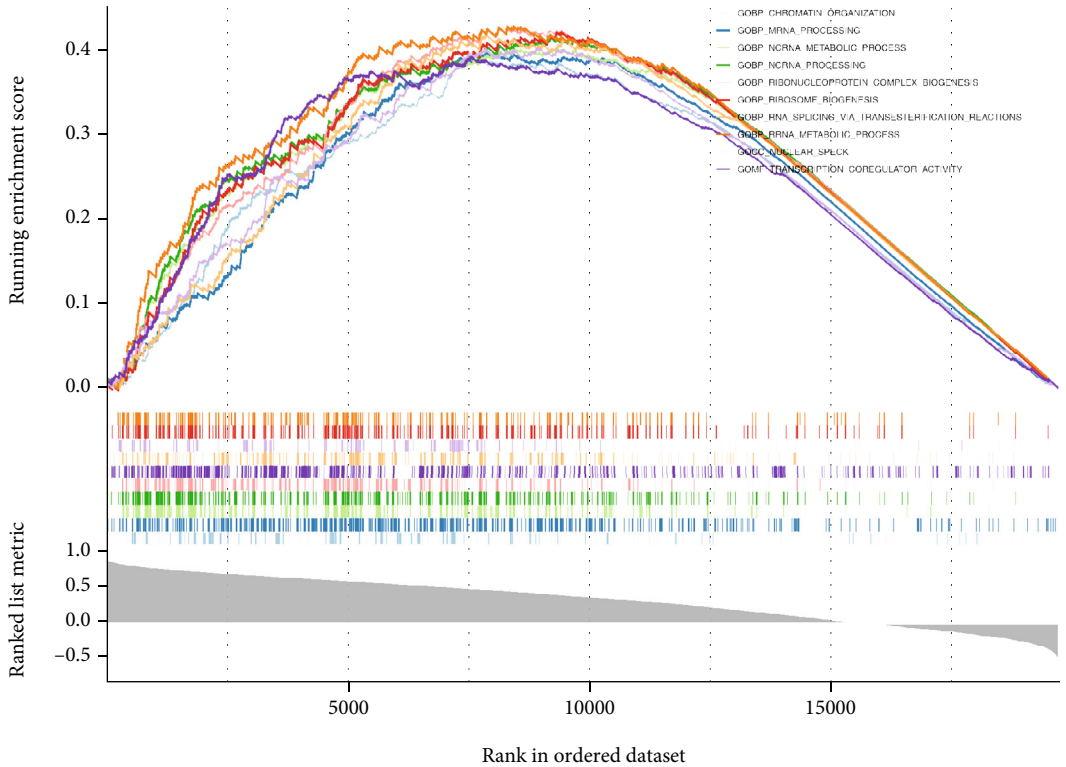

(c)

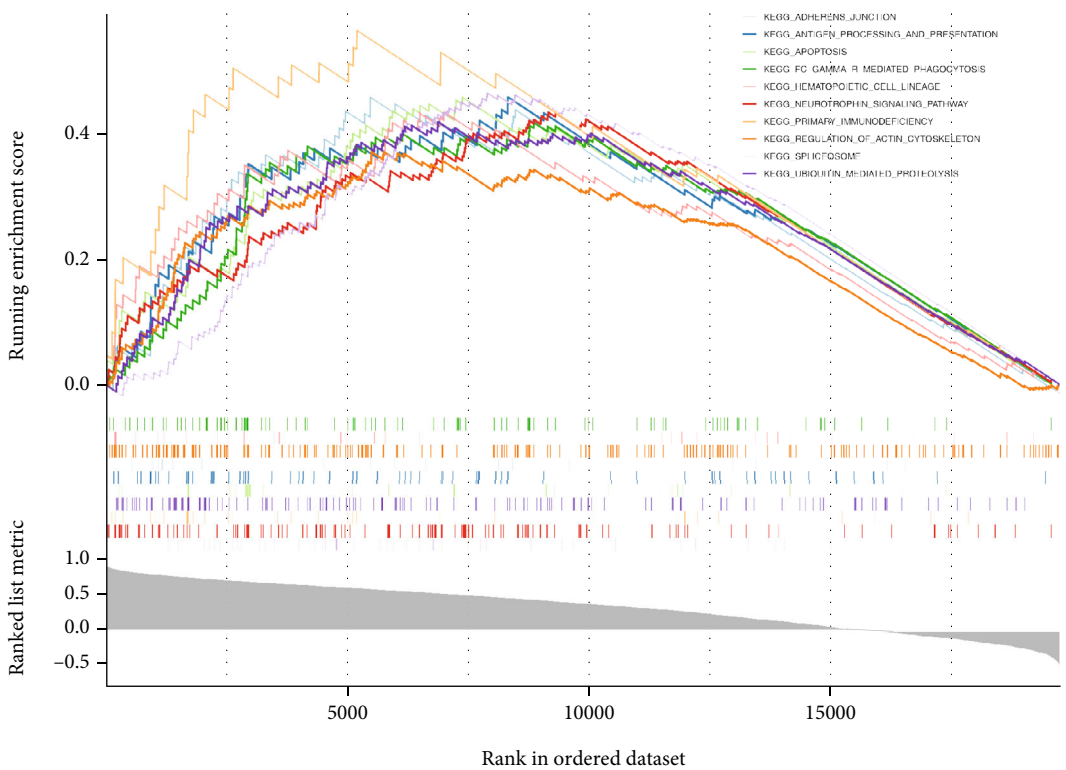

(d)

Figure 4: Continued.

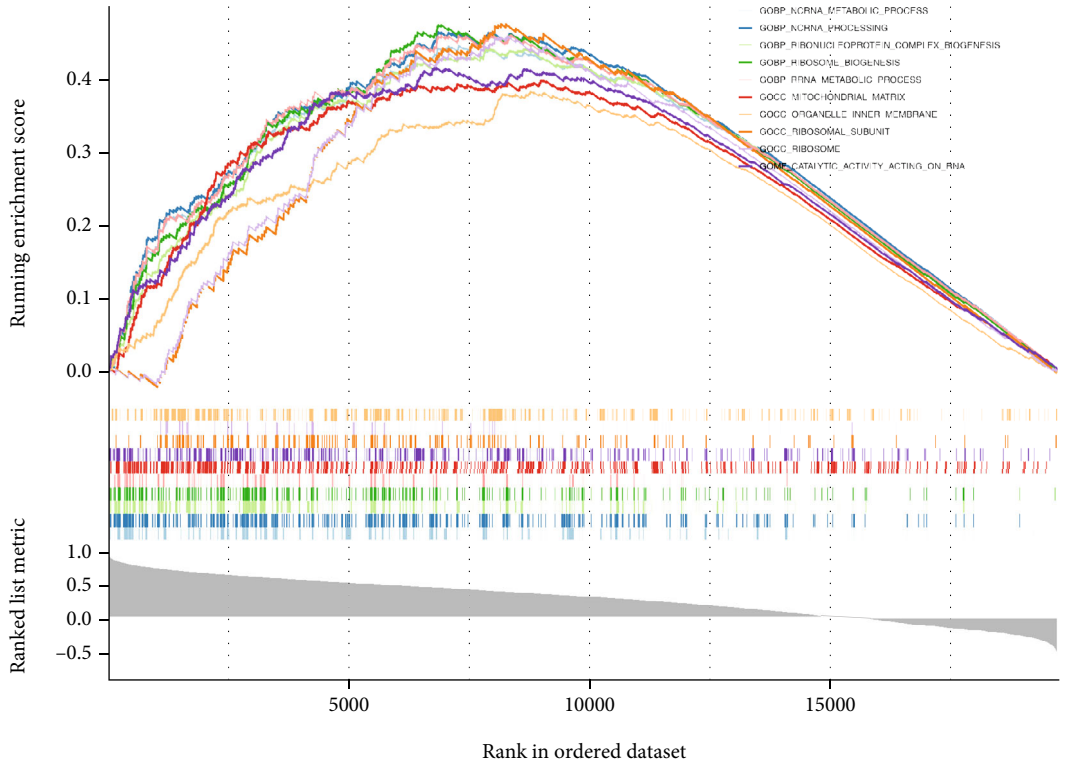

(e)

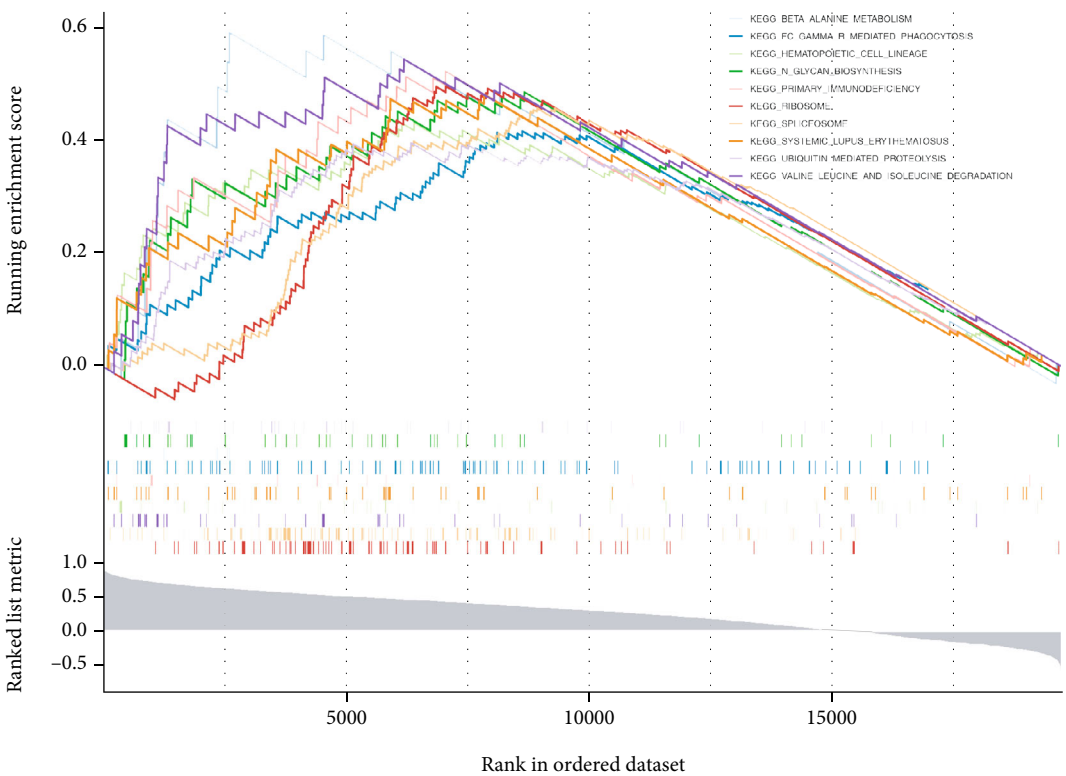

(f)

Figure 4: Continued.

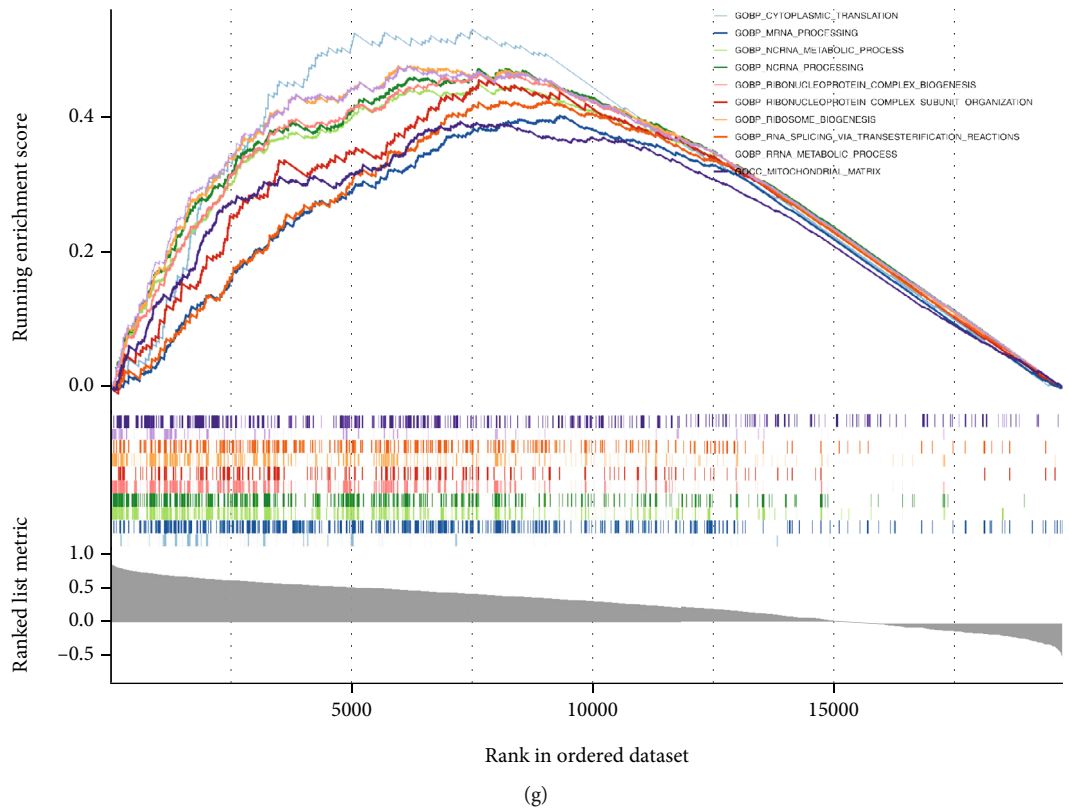

(g)

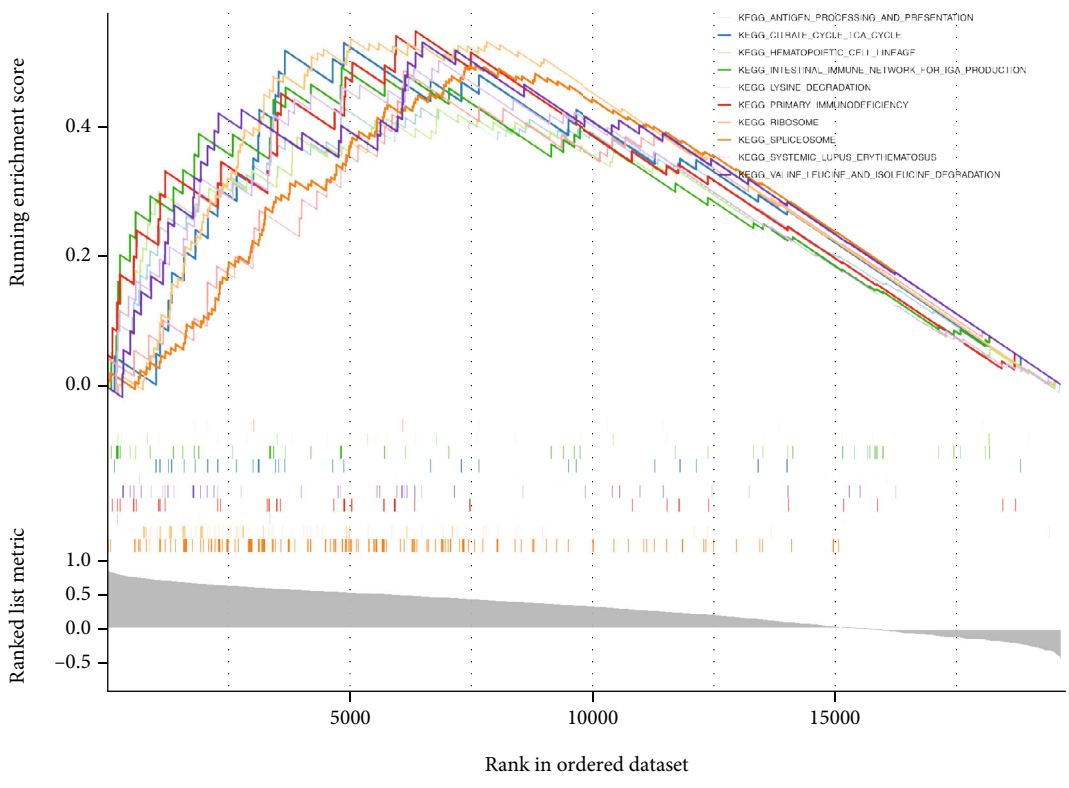

(h)

Figure 4: GSEA results for hub genes. (a) GO biological functions of CD4. (b) KEGG signaling pathways of CD4. (c) GO biological functions of PDLIM5A. (d) KEGG signaling pathways of PDLIM5A. (e) GO biological functions of PPARGC1B. (f) KEGG signaling pathways of PPARGC1B. (g) GO biological functions of TRAF3IP2-AS1. (h) KEGG signaling pathways of TRAF3IP2-AS1.

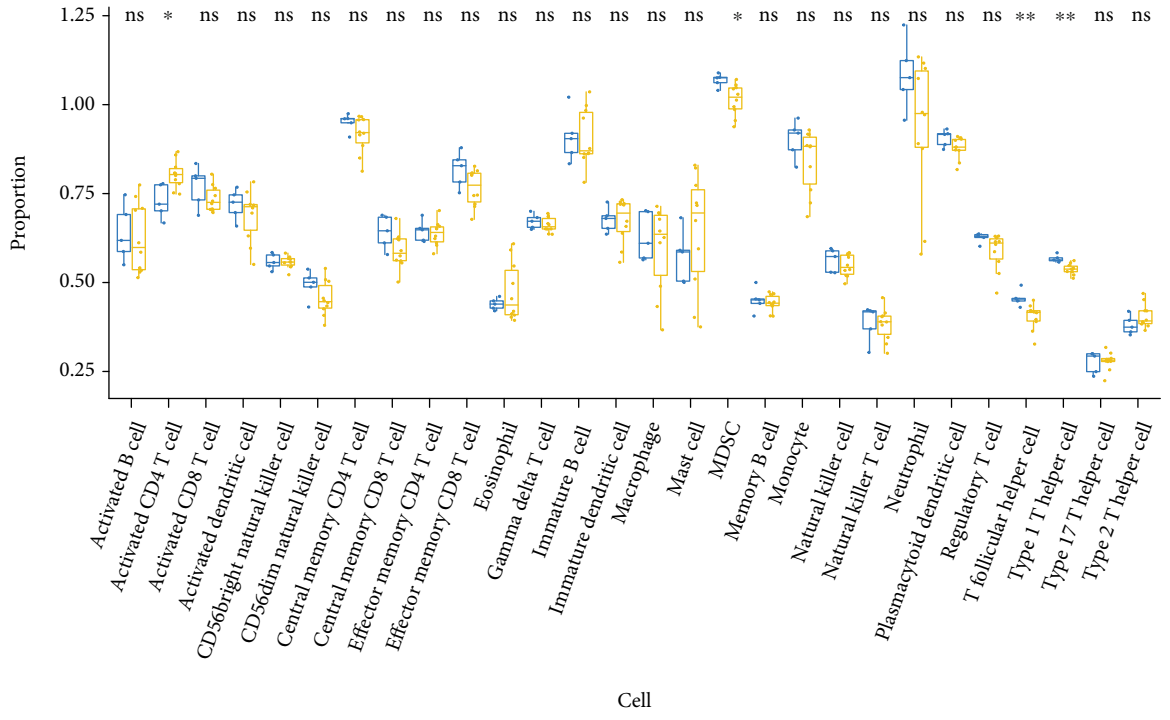

(a)

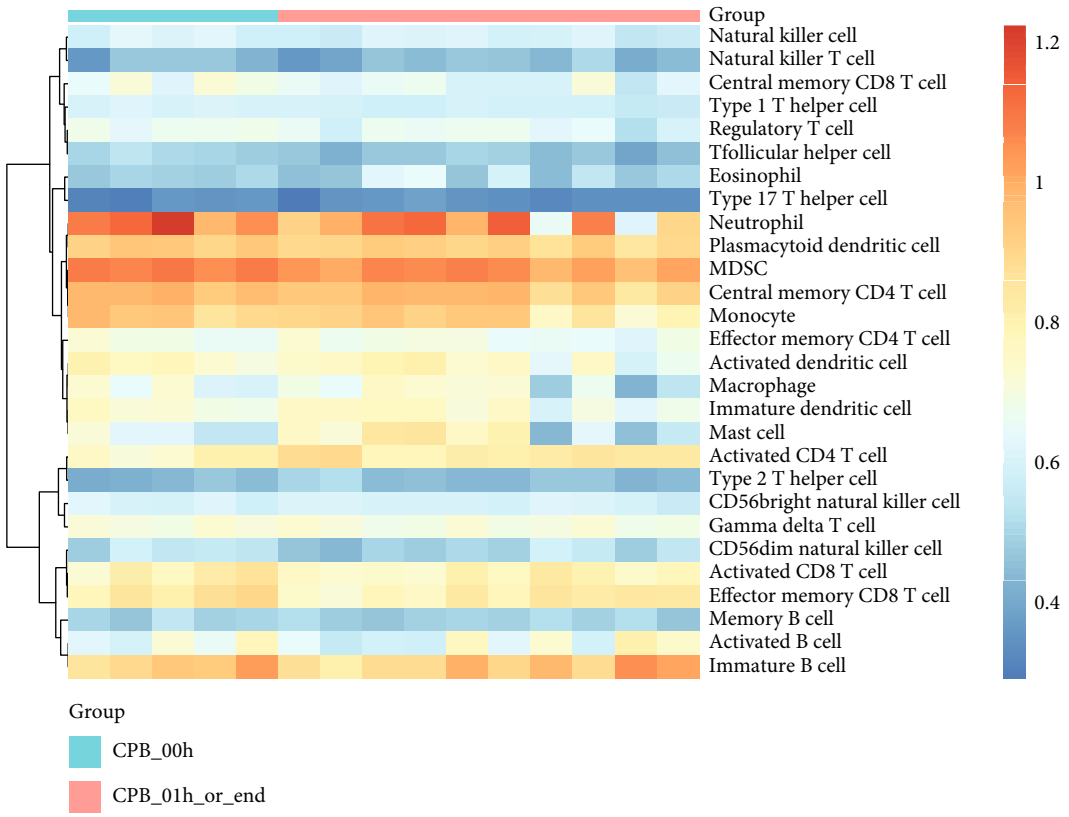

(b)

Figure 5: Continued.

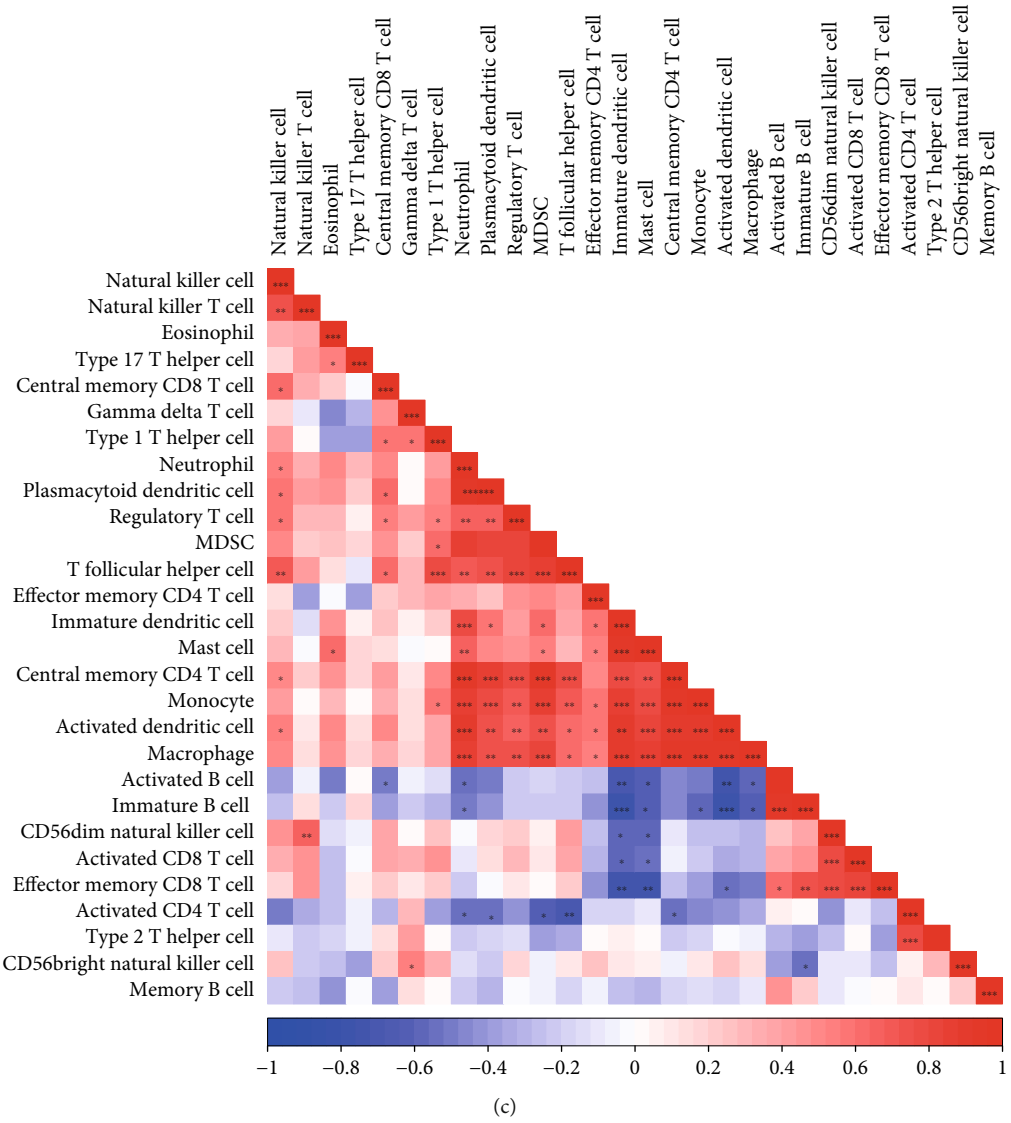

(c)

Figure 5: Continued.

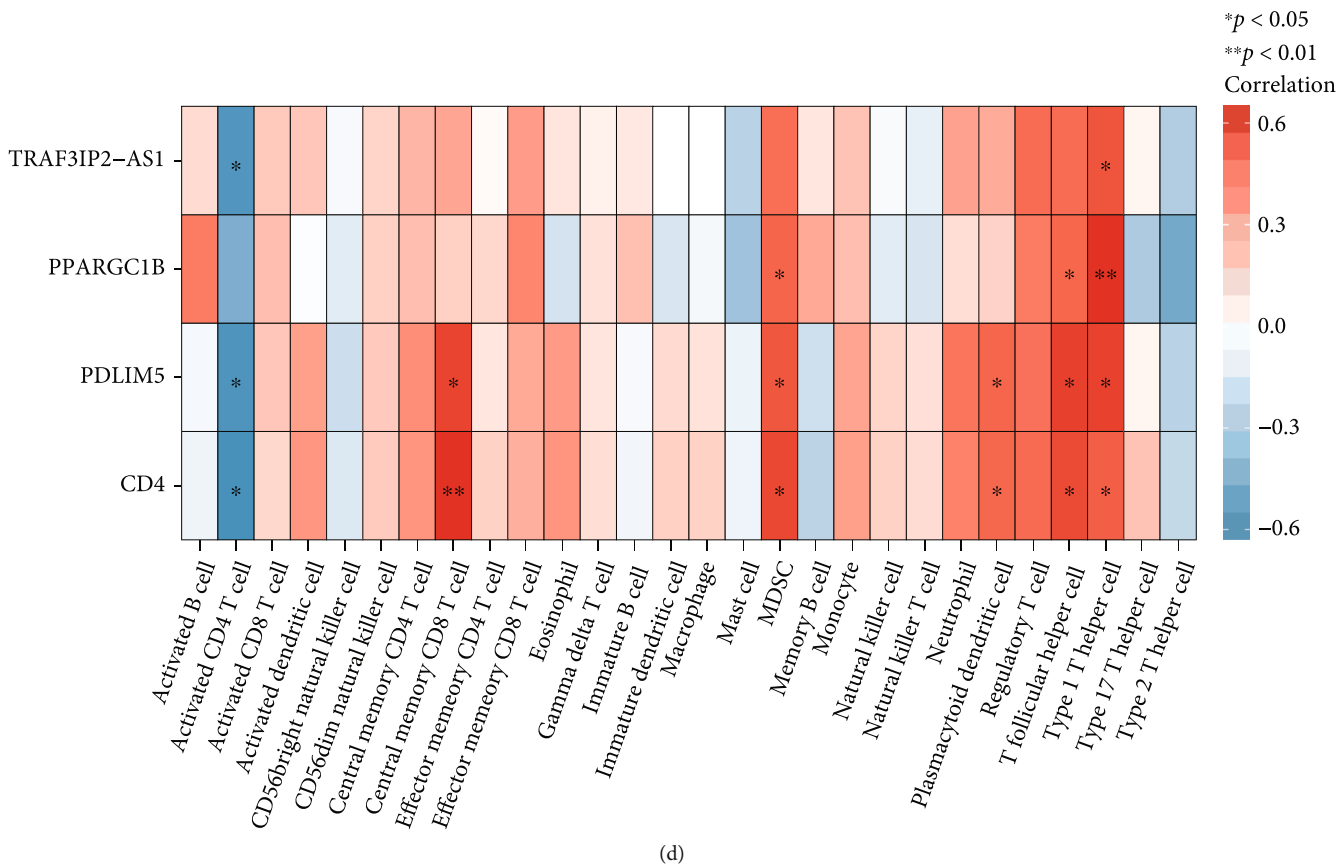

(d)

Figure 5: Evaluation and visualization of immune cell infiltration. (a) Boxplot of 28 types of immune cells proportions in the case and control groups. (b) Immunocyte proportional heat map of 28 immune cells between the case and control groups. (c) Correlations between immune cells in the case and control groups; the red represents the positive correlation and blue represents negative correlation. (d) Correlations between immune cells and hub genes. $^{*}P < 0.05$ and $^{**}P < 0.01$; ns represents no significant difference.

using RNAiso Blood (Takara No. 9113). PrimeScript RT reagent Kit with gDNA Eraser (Perfect Real Time) (Takara No. 047A) was used for first-strand cDNA synthesis. For the analysis of the target genes' mRNA levels, qPCR was performed using TB Green Premix Ex Taq II (Tli RNaseH Plus) (No. 820A) according to the manufacturer's instructions (Takara). The thermocycling protocol is predenaturation at 95°C for 30 seconds and 40 cycles of 5 seconds at 95°C and 34 seconds at 60°C, and melting were done at 95°C. The relative expression of mRNA was calculated by $2^{-\Delta\Delta Ct}$ method with the normalization to GAPDH [23]. The primers were synthesized by Tsingke Biotechnology, and the primer sequences are given in Table 1.

3. Results

3.1. Construction of Gene Coexpression Modules. To explore the overall correlation of all samples in the dataset, we first clustered the samples and removed outliers to ensure the accuracy of the analysis. Next, sample clustering and clinical trait heat maps were constructed (Figure 1(a)). A soft threshold was determined for the data to ensure that the gene interactions maximally conform to the scale-free distribution, and an optimal power value of 25 was determined (Figure 1(b)). Then, a total of 14 modules were aggregated on the basis of the criteria of dynamic tree cutting algorithm and MEDissThres set to 0.2 (Figure 1(c)). The correlation analysis between modules and traits found that the MEblue module had the highest correlation (Figure 1(d)), which contained 1765 genes, after excluding the gray modules that could not be classified. After screening according to the criteria of $|MM| > 0.8$ and $|GS| > 0.8$, a total of 25 key modular genes were obtained (Figure 1(e)).

3.2. Obtained Differentially Expressed Key Modular Genes and Enrichment Analysis. A total of 1450 DEGs were distinguished by comparing the control (0 h) with CPB (1 h or end) samples, of which 1390 were downregulated while the other 60 were upregulated (Figures 2(a) and 2(b)). Then, the overlap analysis between 1450 DEGs and the 25 key module genes from WGCNA analysis found 21 key genes (Figure 2(c)). Enrichment analysis identified 21 genes enriched to 6 GO entries, including developmental cell growth, regulation of monocyte differentiation, regulation of myeloid leukocyte differentiation, ERK1 and ERK2 cascade, volume-sensitive anion channel activity, and estrogen receptor binding (Figure 2(d)). Nevertheless, no KEGG pathway was found. Therefore, we performed ingenuity pathway analysis to explore potential signaling pathways, which resulted in a total of 514 significant pathways

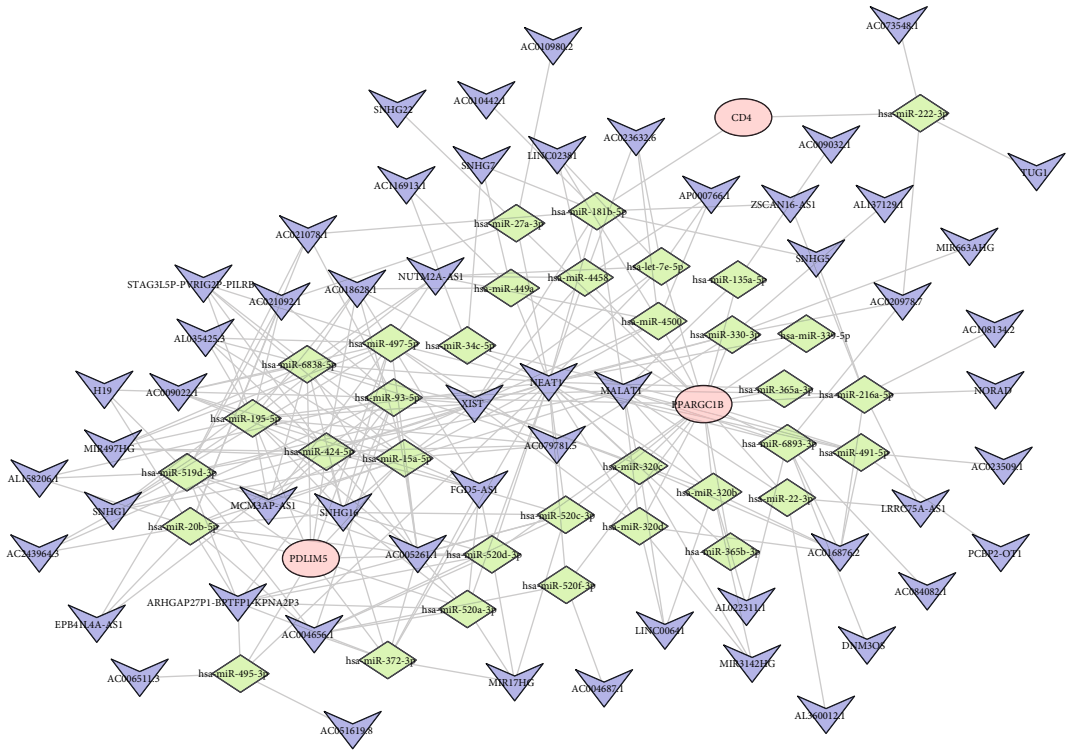

Figure 6: The ceRNA network based on 4 hub genes. Red ellipse indicate hub gene, purple quads indicate lncRNA, and green rhombus indicates miRNA.

(Figure 2(e)). Analysis of the interaction network between genes and other substances such as chemicals and drugs revealed that nine genes appeared in the network (Supplementary Figure 1A-G).

3.3. Acquisition of Four Hub Genes. The 21 obtained genes were deconstructed for LASSO regression, and four signature genes (TRAF3IP2-AS1, PPARGC1B, CD4, and PDLIM5) were screened out (Figure 3(a)). The ROC curve analysis of the LASSO model showed that the AUC value was 1 (Figure 3(b)), indicating that the model performed well. Meanwhile, 17 signature genes (TRAF3IP2-AS1, CD4, POLR1B, MYC, OXNAD1, GVINP1, PDLIM5, DPYSL2, FBXO32, SLC35B4, CA5B, PPARGC1B, LRRC8B, TIAM1, MINA, ARRB1, and NEK11) were obtained using the SVM-RFE method, and the model has withstood the test (Figure 3(c)). Finally, combining the two results, this study obtained four genes (TRAF3IP2-AS1, PPARGC1B, CD4, and PDLIM5) as the most final hub genes (Figure 3(d)). ROC curves were plotted for hub genes and found that all the AUC values were 1, indicating that hub genes can accurately differentiate between normal and patient samples (Figure 3(e)).

3.4. Hub Gene Functional Enrichment Results. By GSEA analysis of four hub genes, we discovered that CD4 is mainly related to chromatin organization, mRNA processing, noncoding RNA conversion process, noncoding RNA processing, biological functions of the ribosome, and other functions (Figure 4(a)). It can be found that CD4 was enriched in antigen processing and presentation, apoptosis, hematopoietic cell lineage, neurotrophin signaling pathway, NOD-like receptor signaling pathway, etc. (Figure 4(b)). Hub gene PDLIM5A is involved in biological functions such as chromatin organization, mRNA processing, and ribosome biogenesis (Figure 4(c)) and participates in adherens junction, antigen recognition, apoptosis, and Fc γ R-mediated phagocytosis (Figure 4(d)). The PPARGC1B gene was related to noncoding RNA conversion process, noncoding RNA processing, biological functions of the ribosome, etc. (Figure 4(e)), participating in β-alanine metabolism, Fc γ R-mediated phagocytosis, hematopoietic cell lineage, N glycan biosynthesis, and other signaling pathways (Figure 4(f)). TRAF3IP2-AS1 is associated with functions such as cytoplasmic translation, mRNA processing, and noncoding RNA metabolic process (Figure 4(g)). The signaling pathways involved include antigen processing and presentation, citrate cycle, TCA cycle, hematopoietic cell lineage, spliceosome, and ribosome (Figure 4(h)). Based on the functional analysis of the above hub genes, we found that the four key genes possessed many of the same biological functions and participate in the same signaling pathways.

3.5. Association between Hub Genes and Immune. It can be found from the boxplot of ssGSEA that the proportions of activated CD4 T cell, MDSC, T follicular helper cell, and type 1 T helper cell were significantly different between the two groups. In more detail, the proportions of MDSC, T

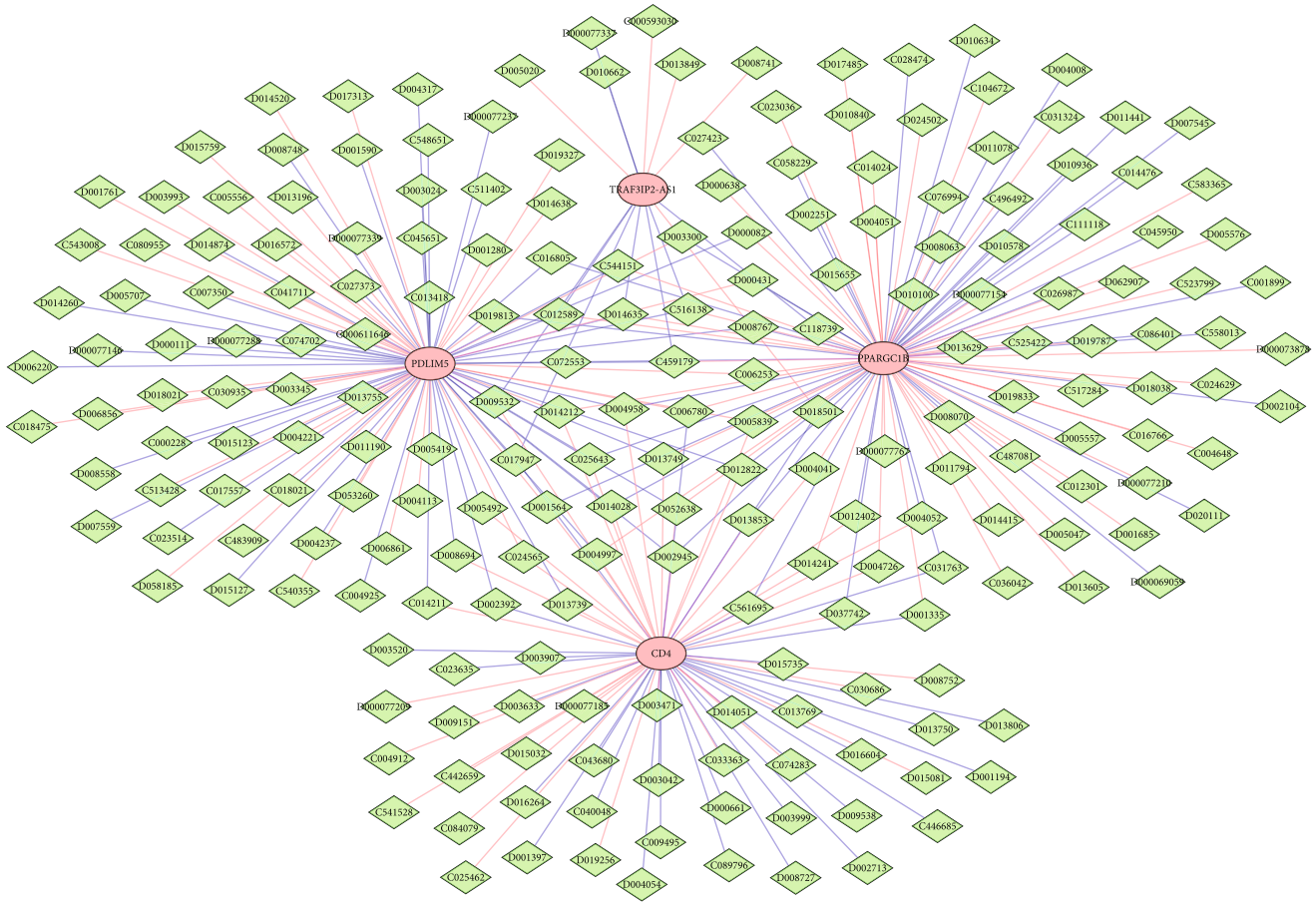

Figure 7: Drug hub gene network. The orange-red elliptic nodes represent hub genes. The green diamond nodes represent drugs. The orange-red line shows that the drug upregulates the expression of the target gene. The blue line shows that the drug downregulates the expression of the target gene.

follicular helper cell, and type 1 T helper cell were higher in the control group, but the proportion of activated CD4 T cell was higher in the case group (Figure 5(a)). Moreover, the immunocyte proportional heat map also showed the similar result (Figure 5(b)). In addition, most of the immune cells were positively correlated between the case and control groups, but some of them were negatively correlated such as immature B cell-immature dendritic cell, activated B cell-immature dendritic cell, and immature B cell-activated dendritic cell (Figure 5(c)). Finally, only activated CD4 T cell, central memory CD8 T cell, MDSC, plasmacytoid dendritic cell, T follicular helper cell, and type 1 T helper cell were significant with certain hub genes. For instance, type 1 T helper cell was positively interrelated to all hub genes, and MDSC and T follicular helper cell were positively bound up with CD4, PDLIM5, and PPARGC1B, but activated CD4 T cell was negatively bound up with CD4, PDLIM5, and TRAF3IP2-AS1 (Figure 5(d)).

3.6. Hub Gene ceRNA Regulatory Network. By predicting the miRNAs and lncRNAs associated with hub genes, a total of 92 nodes (including 3 hub genes PPARGC1B, CD4, PDLIM5, 55 lncRNAs, and 34 miRNAs) as well as 268 edges were found in the ceRNA network (Figure 6).

3.7. Hub Gene Targeted Drugs. A total number of 215 drugs that matched the relationships between increase-expression and decrease-expression were predicted by the 4 hub genes in the CTD database. Additionally, the drug network contains 219 nodes and 278 edges (Figure 7).

3.8. Hub Gene Expression Validation. Analysis of the amplification levels of the four hub genes in the GSE143780 dataset disclosed that the mRNA of these genes was significantly downregulated in CPB-related congenital heart defect patients compared with controls (Figure 8(a)). Similarly, assays in clinical blood samples revealed that the expression of TRAF3IP2-AS1, PPARGC1B, CD4, and PDLIM5 was lower in CPB-related samples than in control samples (Figure 8(b)).

4. Discussion

CPB can effectively reduce the mortality of patients undergoing cardiac surgery, especially children. However, despite the continuous improvement in CPB, the synthetic circuit in CPB is still considered a foreign body in the blood circulation, which eventually leads to inflammation [24]. However, the specific mechanism by which CPB induces inflammatory responses remains incompletely understood. To explore these molecular mechanisms, in this study, we

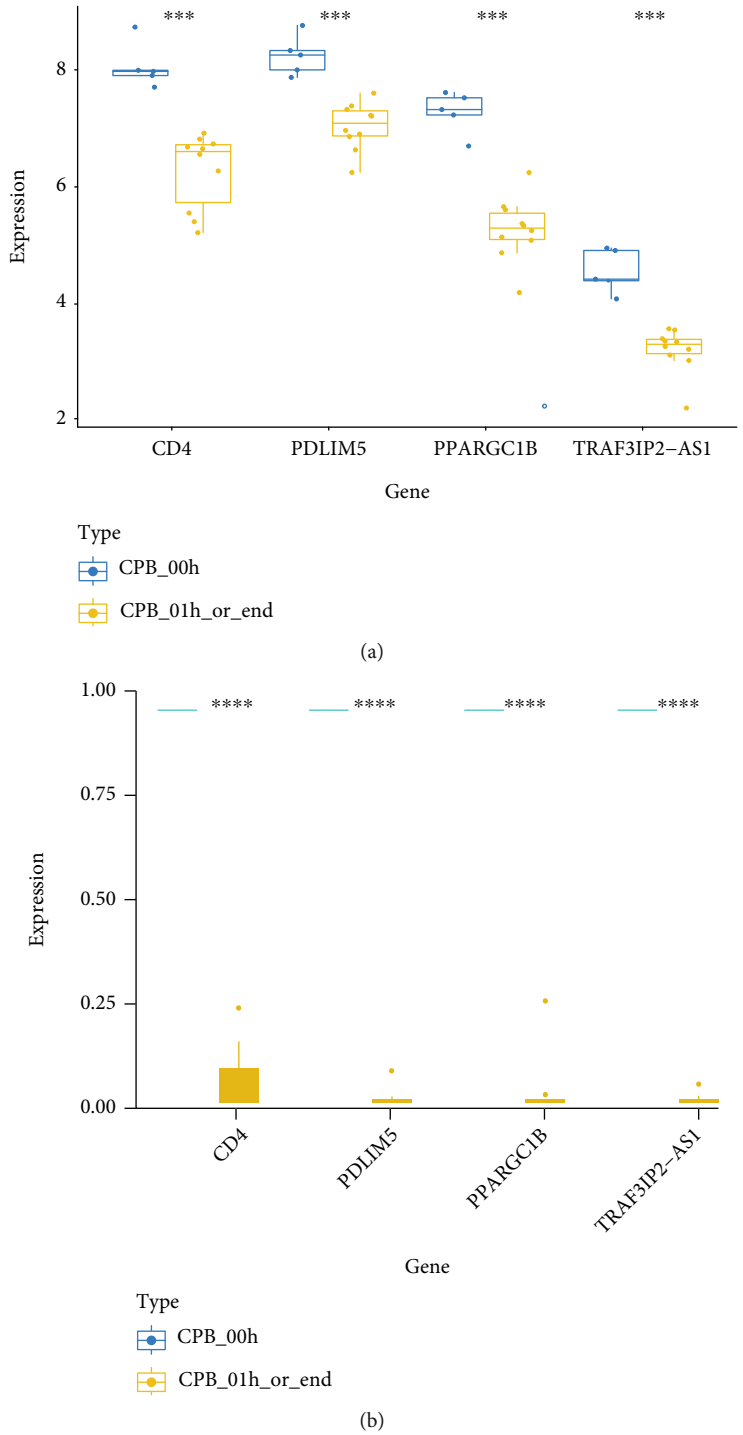

Figure 8: The expression levels of hub genes. (a) The expression levels of hub genes between CPB samples of 0 hour and CPB samples of 1 hour and end in the GSE143780 dataset. (b) The expression levels of hub genes in the between CPB samples of 0 hour and CPB samples of 1 hour and end in clinical samples. $^{***}P < 0.001$ and $^{****}P < 0.0001$.

conducted a differential analysis of the GSE143780 dataset and found a total of 1,450 significantly differentially expressed genes in CPB-related samples. Furthermore, 21 key genes were obtained by WGCNA.

GO analysis of 21 key genes identified six functional items, namely, developmental cell growth, regulation of monocyte differentiation, regulation of myeloid leucocyte differentiation, ERK1 and EEK2 cascade, volume-sensitive anion channel activity, and estrogen receptor binding. Furthermore, 514 significant pathways were found in ingenuity pathway analysis. Among these pathways, volume-sensitive anion channel activity affects neuroinflammation by regulating glial cells [25]. Estrogen receptor binding can participate in inflammatory responses by regulating

nuclear factor-κB, interferon, and toll-like receptor immune signaling pathways as well as immune cell differentiation; moreover, transcription factors such as SP1 and AP-1 also have mutual regulatory effects on estrogen receptors [26]. Additionally, the identification of regulation of monocyte differentiation, regulation of myeloid leukocyte differentiation, macropinocytosis signaling, and Th1 and Th2 pathways suggested that the 21 key genes directly affect the differentiation and secretion of immune cells [27, 28]. Moreover, it has been shown that the ERK1/2 signaling pathway and ephrin receptor signaling are involved in inflammatory responses in multiple organs and participate in processes such as development, activation, and migration of immune cells [28–33].

Furthermore, the 21 key module genes were obtained by WGCNA and differential expression analysis, and four genes (TRAF3IP2-AS1, PPARGC1B, CD4, and PDLIM5) were identified as the hub genes for CPB-induced inflammatory cytokine release in patients with congenital heart defects. The analysis of GSEA reveals that hub genes were involved in mRNA processing, noncoding RNA processing, apoptosis, and immune reaction. Among these, TRAF3IP2-AS1 mainly affects inflammatory responses by negatively regulating IL-17 signaling via the SRSF10-IRF1-Act1 axis. Several researches have found that IL-17 is an important factor in the pathogenesis of inflammatory and autoimmune diseases, for example, multiple sclerosis and rheumatoid arthritis [34].

PPPARGC1B and PPARGC1A are coactivators of immunomodulator PPARG. In addition, the product of the PPARGC1B gene, PGC1b, not only inhibits NLRP3 transcription but also indirectly or directly regulates the function of NLRP3. PPARGC1B suppresses IL-1β-induced inflammation by inhibiting the formation of NLRP3 inflammatory bodies [35, 36]. Moreover, CD4 is the key gene for the normal development of CD4 T lymphocytes. Some CD4 cells are regulatory T cells, which can produce TGF-β and IL-10 to inhibit inflammatory responses [37]. In the GSE143780 dataset and clinical samples, the expressions of TRAF3IP2-AS1, PPARGC1B, CD4, and PDLIM5 genes were lower in CPB-related samples, thereby supporting the possibility that the abovementioned four genes play important roles in CPB-induced inflammation.

By predicting the miRNAs and lncRNAs associated with hub genes, a total of 92 nodes (including 3 hub genes PPARGC1B, CD4, PDLIM5, 55 lncRNAs, and 34 miRNAs) as well as 268 edges were found in the ceRNA network. This could lay the foundation for the study of regulatory mechanisms of four key genes in diseases. In addition, Xu et al. found that PPARGC1B can alleviate IL-1β-mediated osteoarthritis [35]. If PDLIM5 is downregulated, some cancer progression rates will be suppressed [38]. More ceRNA-regulated mechanisms need to be further explored and validated. By prediction, the 4 hub genes were screened in the CTD database, resulting in a total of 215 drugs that matched the relationships between increase-expression and decrease-expression. The drug network contains 219 nodes and 278 edges. These analyses provide the basis for targeted therapy of key genes.

On the other hand, some shortcomings of the present study still exist. First, we only compared the gene expression between before and after CPB, but did not intensely investigate how these genes affect inflammation or the degree of the effect on inflammation. After that, the available dataset is lacking, and subsequent analysis in additional samples is required.

In conclusion, using CPB-associated cohort profile datasets and integrated bioinformatics analysis, 4 CPB-induced inflammatory cytokine release-associated hub genes, TRAF3IP2-AS1, PPARGC1B, CD4, and PDLIM5, were identified. These new potential targets may provide novel methods for preventing CPB-induced inflammation. Our future studies will aim at promulgating the potential diagnostic and prognostic value of these hub genes, which may ultimately support the translation of these targets into clinical practice.

5. Conclusion

We got four potential target genes (TRAF3IP2-AS1, PPARGC1B, CD4, and PDLIM5) about CPB-induced inflammation by analyzing the GSE143780 dataset and found that the expression of TRAF3IP2-AS1, PPARGC1B, CD4, and PDLIM5 was lower in CPB-related samples. Our research provides precious information on pathological mechanisms of CPB-induced inflammation.

Abbreviations

CPB: Cardiopulmonary bypass
GEO: Gene Expression Omnibus
lncRNA: Long noncoding RNA
miRNA: MicroRNA
iNOS: Inducible nitric oxide synthase
ROS: Reactive oxygen species
qRT-PCR: Quantitative real-time polymerase chain reaction
KEGG: Kyoto Encyclopedia of Genes and Genomes
GO: Gene Ontology
GSEA: Gene set enrichment analysis
IPA: Ingenuity pathway analysis
MDSCs: Myeloid-derived suppressor cells
NLRP3: NOD-like receptor thermal protein domain-associated protein 3
LASSO: Least absolute shrinkage and selection operator
SVM-RFE: Support vector machine recursive feature elimination
WGCNA: Gene coexpression network analysis
DEGs: Differentially expressed genes
ROC: Receiver operating characteristic curve
CTD: Comparative Toxicogenomics Database.

Data Availability

The data used to support the findings of this study are available from the corresponding author upon request.

Ethical Approval

The experiment was approved by the Medical Ethics Committee of First Affiliated Hospital of Guangxi Medical University.

Conflicts of Interest

The authors have no conflicts of interest to declare.

Authors' Contributions

Liang Cai and Bingdong Zhang performed the experiments and wrote the paper. Cai Liang performed data analysis. All the authors approved the manuscript for publication.

Supplementary Materials

Supplementary Figure 1: (A)–(G) show the representative networks of chemicals or drugs associated with LCRC8, LCRC8B, CA5B, FBXO32, OXNAD1, PDLIM5, SLC25A43, and SLC35B4, respectively. The right side of the image shows the representation of the geometric diagram of the network diagram. *(Supplementary Materials)*

References

[1] D. Whiting, K. Yuki, and J. A. DiNardo, "Cardiopulmonary bypass in the pediatric population," *Best Practice & Research. Clinical Anaesthesiology*, vol. 29, no. 2, pp. 241–256, 2015.

[2] K. A. Otto, "Therapeutic hypothermia applicable to cardiac surgery," *Veterinary Anaesthesia and Analgesia*, vol. 42, no. 6, pp. 559–569, 2015.

[3] E. M. Graham, A. M. Atz, K. E. McHugh et al., "Preoperative steroid treatment does not improve markers of inflammation after cardiac surgery in neonates: results from a randomized trial," *The Journal of Thoracic and Cardiovascular Surgery*, vol. 147, no. 3, pp. 902–908, 2014.

[4] S. B. Horton, W. W. Butt, R. J. Mullaly et al., "IL-6 and IL-8 levels after cardiopulmonary bypass are not affected by surface coating," *The Annals of Thoracic Surgery*, vol. 68, no. 5, pp. 1751–1755, 1999.

[5] M. S. Chew, V. Brix-Christensen, H. B. Ravn et al., "Effect of modified ultrafiltration on the inflammatory response in paediatric open-heart surgery: a prospective, randomized study," *Perfusion*, vol. 17, no. 5, pp. 327–333, 2002.

[6] M. Levi and T. van der Poll, "Inflammation and coagulation," *Critical Care Medicine*, vol. 38, 2 Supplement, pp. S26–S34, 2010.

[7] O. D. Aljure and M. N. Fabbro, "Cardiopulmonary bypass and inflammation: the hidden enemy," *Journal of Cardiothoracic and Vascular Anesthesia*, vol. 33, no. 2, pp. 346-347, 2019.

[8] D. Paparella, T. M. Yau, and E. Young, "Cardiopulmonary bypass induced inflammation: pathophysiology and treatment. An update," *European Journal of Cardio-Thoracic Surgery*, vol. 21, no. 2, pp. 232–244, 2002.

[9] O. Giacinto, U. Satriano, A. Nenna et al., "Inflammatory response and endothelial dysfunction following cardiopulmonary bypass: pathophysiology and pharmacological targets," *Recent Patents on Inflammation & Allergy Drug Discovery*, vol. 13, no. 2, pp. 158–173, 2019.

[10] W. C. Sasser, R. J. Dabal, D. J. Askenazi et al., "Prophylactic peritoneal dialysis following cardiopulmonary bypass in children is associated with decreased inflammation and improved clinical outcomes," *Congenital Heart Disease*, vol. 9, no. 2, pp. 106–115, 2014.

[11] C. Xie, Z. Yin, and Y. Liu, "Analysis of characteristic genes and ceRNA regulation mechanism of endometriosis based on full transcriptional sequencing," *Frontiers in Genetics*, vol. 13, article 902329, 2022.

[12] L. N. Tu, L. Hsieh, M. Kajimoto et al., "Shear stress associated with cardiopulmonary bypass induces expression of inflammatory cytokines and necroptosis in monocytes," *JCI Insight*, vol. 6, no. 1, 2021.

[13] P. Langfelder and S. Horvath, "WGCNA: an R package for weighted correlation network analysis," *BMC Bioinformatics*, vol. 9, no. 1, p. 559, 2008.

[14] G. J. Liu, L. Cimmino, J. G. Jude et al., "Pax5 loss imposes a reversible differentiation block in B progenitor acute lymphoblastic leukemia," *Genes & Development*, vol. 28, no. 12, pp. 1337–1350, 2014.

[15] A. Subramanian, P. Tamayo, V. K. Mootha et al., "Gene set enrichment analysis: a knowledge-based approach for interpreting genome-wide expression profiles," *Proceedings of the National Academy of Sciences of the United States of America*, vol. 102, no. 43, pp. 15545–15550, 2005.

[16] A. Krämer, J. Green, J. Pollard Jr., and S. Tugendreich, "Causal analysis approaches in ingenuity pathway analysis," *Bioinformatics*, vol. 30, no. 4, pp. 523–530, 2014.

[17] S. Engebretsen and J. Bohlin, "Statistical predictions with glmnet," *Clin Epigenetics*, vol. 11, no. 1, p. 123, 2019.

[18] G. Sturm, F. Finotello, and M. List, "Immunedeconv: an R package for unified access to computational methods for estimating immune cell fractions from bulk RNA-sequencing data," in *Bioinformatics for Cancer Immunotherapy*, S. Boegel, Ed., vol. 2120 of Methods in Molecular Biology, pp. 223–232, Humana, New York, NY, 2020.

[19] R. Kolde and M. R. Kolde, *Package 'pheatmap'*, vol. 1, R Package, 2018.

[20] C. Sticht, C. De La Torre, A. Parveen, and N. Gretz, "miRWalk: an online resource for prediction of microRNA binding sites," *PLoS One*, vol. 13, no. 10, article e0206239, 2018.

[21] P. Shannon, A. Markiel, O. Ozier et al., "Cytoscape: a software environment for integrated models of biomolecular interaction networks," *Genome Research*, vol. 13, no. 11, pp. 2498–2504, 2003.

[22] A. P. Davis, C. J. Grondin, R. J. Johnson et al., "Comparative toxicogenomics database (CTD): update 2021," *Nucleic Acids Research*, vol. 49, no. D1, pp. D1138–D1143, 2021.

[23] T. D. Schmittgen, B. A. Zakrajsek, A. G. Mills, V. Gorn, M. J. Singer, and M. W. Reed, "Quantitative reverse transcription-polymerase chain reaction to study mRNA decay: comparison of endpoint and real-time methods," *Analytical Biochemistry*, vol. 285, no. 2, pp. 194–204, 2000.

[24] Y. Hirata, "Cardiopulmonary bypass for pediatric cardiac surgery," *General Thoracic and Cardiovascular Surgery*, vol. 66, no. 2, pp. 65–70, 2018.

[25] M. Kittl, K. Helm, M. Beyreis et al., "Acid- and volume-sensitive chloride currents in microglial cells," *International Journal of Molecular Sciences*, vol. 20, no. 14, p. 3475, 2019.

[26] S. Kovats, "Estrogen receptors regulate innate immune cells and signaling pathways," *Cellular Immunology*, vol. 294, no. 2, pp. 63–69, 2015.

[27] X. Ji, M. Han, Y. Yun, G. Li, and N. Sang, "Acute nitrogen dioxide (NO_2) exposure enhances airway inflammation via modulating Th1/Th2 differentiation and activating JAK-STAT pathway," *Chemosphere*, vol. 120, pp. 722–728, 2015.

[28] S. Romagnani, "T-cell subsets (Th1 versus Th2)," *Annals of Allergy, Asthma & Immunology*, vol. 85, no. 1, pp. 9–18, 2000.

[29] T. K. Darling and T. J. Lamb, "Emerging roles for Eph receptors and ephrin ligands in immunity," *Frontiers in Immunology*, vol. 10, p. 1473, 2019.

[30] S. A. Theofanous, M. V. Florens, I. Appeltans et al., "Ephrin-B2 signaling in the spinal cord as a player in post-inflammatory and stress-induced visceral hypersensitivity," *Neurogastroenterology and Motility*, vol. 32, no. 4, article e13782, 2020.

[31] M. G. Coulthard, M. Morgan, T. M. Woodruff et al., "Eph/ephrin signaling in injury and inflammation," *The American Journal of Pathology*, vol. 181, no. 5, pp. 1493–1503, 2012.

[32] S. I. A. Abdel-dayem, M. N. A. Khalil, E. H. Abdelrahman, H. M. El-Gohary, and A. S. Kamel, "Sesquiterpene lactones; damsin and neoambrosin suppress cytokine-mediated inflammation in complete Freund's adjuvant rat model *via* shutting Akt/ERK1/2/STAT3 signaling," *Journal of Ethnopharmacology*, vol. 266, article 113407, 2021.

[33] T. Zhang, H. Ouyang, X. Mei et al., "Erianin alleviates diabetic retinopathy by reducing retinal inflammation initiated by microglial cells *via* inhibiting hyperglycemia-mediated ERK1/2–NF-κB signaling pathway," *The FASEB Journal*, vol. 33, no. 11, pp. 11776–11790, 2019.

[34] R. He, S. Wu, R. Gao et al., "Identification of a long noncoding RNA *TRAF3IP2-AS1* as key regulator of IL-17 signaling through the SRSF10-IRF1-Act1 axis in autoimmune diseases," *Journal of Immunology*, vol. 206, no. 10, pp. 2353–2365, 2021.

[35] J. Xu, Y. Pei, J. Lu et al., "lncRNA SNHG7 alleviates IL-1β-induced osteoarthritis by inhibiting miR-214-5p-mediated PPARGC1B signaling pathways," *International Immunopharmacology*, vol. 90, article 107150, 2021.

[36] T. Merriman and R. Terkeltaub, "*PPARGC1B*: insight into the expression of the gouty inflammation phenotype: *PPARGC1B* and gouty inflammation," *Rheumatology*, vol. 56, no. 3, pp. 323–325, 2017.

[37] A. Agita and M. T. Alsagaff, "Inflammation, immunity, and hypertension," *Acta Medica Indonesiana*, vol. 49, no. 2, pp. 158–165, 2017.

[38] P. Xie, M. Liu, F. Chen et al., "Long non-coding RNA AGAP2-AS1 silencing inhibits PDLIM5 expression impeding prostate cancer progression *via* up-regulation of microRNA-195-5p," *Frontiers in Genetics*, vol. 11, p. 1030, 2020.

Hindawi
Disease Markers
Volume 2023, Article ID 7620181, 16 pages
https://doi.org/10.1155/2023/7620181

Research Article

A Comprehensive and Systematic Analysis Revealed the Role of ADAR1 in Pan-Cancer Prognosis and Immune Implications

Jianlin Zhu,[1] Jianjian Zheng,[2] Jinjun Zhang,[3] Songyu Wang,[1] Lu Wang ,[4] and Yan Zhao [1]

[1]*Department of Dermatologic Surgery, The First Affiliated Hospital of Fujian Medical University, Fuzhou, Fujian, China*
[2]*Department of Urology, Xianyou County General Hospital, Putian, Fujian, China*
[3]*The First Department of Surgery, Xianyou County General Hospital, Putian, Fujian, China*
[4]*Institute of Precision Cancer Medicine and Pathology and Department of Pathology, School of Medicine, Jinan University, Guangzhou, Guangdong, China*

Correspondence should be addressed to Lu Wang; lullawind@163.com and Yan Zhao; minjiang98@163.com

Received 16 September 2022; Revised 9 October 2022; Accepted 25 November 2022; Published 21 February 2023

Academic Editor: Fu Wang

Adenosine deaminase RNA specific 1 (ADAR1) has been identified as an enzyme that deaminates adenosine within the dsRNA region to produce inosine, whose amplification reinforced the exhaustion of the immune system. Although there were currently cellular and animal assays supporting the relationship between ADAR1 and specific cancers, there was no correlation analysis that has been performed at the pan-cancer level. Therefore, we first analyzed the expression of ADAR1 in 33 cancers based on the TCGA (The Cancer Genome Atlas) database. ADAR1 was highly expressed in most cancers, and there was a closely association between ADAR1 expression and prognosis of patients. Furthermore, pathway enrichment analysis revealed that ADAR1 was involved in multiple antigens presenting and processing inflammatory and interferon pathways. Moreover, ADAR1 expression was positively correlated with $CD8^+$ T cell infiltration levels in renal papillary cell carcinoma, prostate cancer, and endometrial cancer and negatively correlated with Treg cell infiltration. In addition, we further found that ADAR1 expression was closely associated with various immune checkpoints and chemokines. Meanwhile, we observed that ADAR1 may be involved in the regulation of pan-cancer stemness. In conclusion, we provided a comprehensive understanding of the oncogenic role of ADAR1 in pan-cancer, and ADAR1 might serve as a new potential target for antitumor therapy.

1. Introduction

Despite advances in surgery, chemotherapy, and radiotherapy, the global morbidity and mortality of malignant tumors are on the rise [1]. Tumors remodel the tumor immune microenvironment (TIM) through various factors, such as dysfunction of immune checkpoints and secretion of chemokines [2]. Although there are advances in immunotherapy drugs targeting PD-1, PD-L1, and CTLA4, only a minority of patients benefit from immunotherapy [3]. The prognostic model constructed by combining multiple genes has been used to evaluate the efficacy of tumor immunotherapy, but there is no rigorous clinical proof [4]. Therefore, the exploration of appropriate immunotherapeutic targets is particularly urgent.

ADAR1, adenosine deaminase RNA specific 1, is the main RNA-editing enzyme responsible for the deamination of adenosine to produce inosine (A-to-I) [5]. ADAR1 also participates in a variety of biological processes in a non-RNA-editing manner, the most important of which is the creation of protein-protein interactions through the double-stranded RNA-binding domain (dsRBD) of ADAR1, which directly and systematically regulates protein-based immunity response [6]. As an enzyme, ADAR1 edits endogenous double-stranded RNA (dsRNA), making it unstable and unable to be recognized by nucleic acid sensors (NAS), thereby closing interferon-stimulated gene (ISG) expression and downregulating interferon (IFN) expression [7]. Previous research demonstrates that ISG-positive tumor cells are uniquely susceptible to ADAR1 deficiency, which

sensitises tumor cells to immunotherapy and overcomes resistance to checkpoint blockade [8]. The depletion of ADAR1 in cancer cells was susceptible to death by inflammation [9]. ADAR1 prevented the pathway to immune and translational catastrophe by blocking dsRNA activation.

In this study, we evaluated the expression and variation of ADAR1 and analyzed the relationship with the prognosis of patients. We investigated the relationship between ADAR1 and immune cell infiltration, immune suppressor genes, and chemokines. Our findings provided a new insight into the functional role of ADAR1 in pan-cancer and highlighted that ADAR1 may serve as a new potential target for cancer immunotherapy.

2. Methods

2.1. Data Collection and Handling. The TCGA Research Network (https://portal.gdc.cancer.gov/) has analyzed clinical and molecular data from over 10,000 oncology patients in 33 countries, covering 33 different tumor types and over 10,000 oncology patients. Transcriptomic RNA-seq data for 33 cancers were extracted from TCGA database. 33 cancer types were included: adrenocortical carcinoma (ACC), bladder urothelial carcinoma (BLCA), breast invasive carcinoma (BRCA), colon adenocarcinoma (COAD), lymphoid neoplasm diffuse large B cell lymphoma (DLBC), esophageal carcinoma (ESCA), glioblastoma multiforme (GBM), head and neck squamous cell carcinoma (HNSC), kidney chromophobe (KICH), kidney renal clear cell carcinoma (KIRC), kidney renal papillary cell carcinoma (KIRP), acute myeloid leukemia (LAML), brain lower grade glioma (LGG), liver hepatocellular carcinoma (LIHC), lung adenocarcinoma (LUAD), lung squamous cell carcinoma (LUSC), ovarian serous cystadenocarcinoma (OV), pancreatic adenocarcinoma (PAAD), prostate adenocarcinoma (PRAD), pheochromocytoma and paraganglioma (PCPG), rectum adenocarcinoma (READ), skin cutaneous melanoma (SKCM), stomach adenocarcinoma (STAD), testicular germ cell tumors (TGCT), thyroid carcinoma (THCA), thymoma (THYM), uterine corpus endometrial carcinoma (UCEC), cholangiocarcinoma (CHOL), cervical squamous cell carcinoma and endocervical adenocarcinoma (CESC), mesothelioma (MESO), sarcoma (SARC), uveal melanoma (UVM), and uterine carcinosarcoma (UCS).

2.2. Genomic Modifications of ADAR1 in Cancer Patients. Alterations in ADAR1 in cancer patients were obtained from the online cBioPortal database (http://www.cbioportal.org/). Cancer genomic alterations in ADAR1 include copy number amplification, profound deletions, missense mutations of unknown significance, and mRNA upregulation [10].

2.3. ADAR1 Protein Expression Analysis. The Human Protein Atlas (HPA: https://www.proteinatlas.org/) database was used to explore the protein levels of ADAR1 in human tumors and normal tissues [11]. The STRING (https://string-db.org/) database was used to construct a protein-protein interaction network (PPI) for ADAR1 [12].

2.4. Survival Analysis of the Prognostic Value of ADAR1. The Kaplan-Meier (KM) survival analysis was performed to identify different survival outcomes between the two group differences. The univariate Cox regression model was applied to determine the favourable or unfavourable prognosis of ADAR1. The KM analysis was performed by the R packages "survminer" and "survival" and by the R packages "survival" and "forestplot."

2.5. GSEA. GSEA is a method to analyze the function or pathway of target genes affecting tumor genetics. The Kyoto Encyclopedia of Genes and Genomes (KEGG) database and HALLMARK database were adopted in the R package "clusterProfiler" for GSEA [13, 14]. The significant enrichment results were demonstrated on the basis of net enrichment score (NES), gene ratio and p value. Gene sets with NES > 1, NOM $p < 0.05$, and FDR $q < 0.25$ were considered to be significantly enriched.

2.6. Correlation Analysis between ADAR1 Expression and Immune Function. TISIDB (http://cis.hku.hk/TISIDB/) is a web server that integrates multiple heterogeneous data types for tumor and immune system interactions [15]. We used the "Lymphocyte," "Immunomodulator," and "Chemokine" modules in TISIDB to analyze the correlation between ADAR1 expression and the level of immune infiltration, immune checkpoints, and chemokines for multiple cancer types in TCGA database.

2.7. Pan-Cancer Stemness Index Analysis. Sangerbox (http://vip.sangerbox.com/home.html) is a bioinformatics online analysis website; we used the tumor stemness and gene expression modules to analyze ADAR1 expression and tumor stemness index online; the results are presented in the form of barplot and column chart.

2.8. Statistical Analysis. Gene expression data from TCGA database were analyzed by Student's t-test. The expression of ADAR1 was correlated with the abundance scores of immune cells assessed using Spearman's correlation analysis. All analyses were performed with R software (version 4.1.1, http://www.r-project.org) loaded with R packages ("ggplot2," "ggpubr," "limma," "survival," "survminer," "clusterProfiler," "ESTIMATE," "enrichplot," and "forestplot"). $p < 0.05$ was considered statistically significant to provide confidence in the data analysis.

3. Results

3.1. The mRNA Expression Level and Copy Number Variation of ADAR1 in Pan-Cancer. We first evaluated the expression of ADAR1 in 33 cancers. Figure 1(a) shows the ranking of ADAR1 expression in cancer tissues from top to bottom. Subsequently, we observed the expression level of ADAR1 in different cancers. The results showed that ADAR1 was significantly upregulated in 14 cancers, including BRCA, LUAD, ESCA, LUSC, STAD, CHOL, CESC, HNSC, UCEC, PCPG, BLCA, COAD, THCA, and LIHC (Figure 1(b)). It is widely recognized that gene copy number affects the level of gene expression [16]. Therefore, we

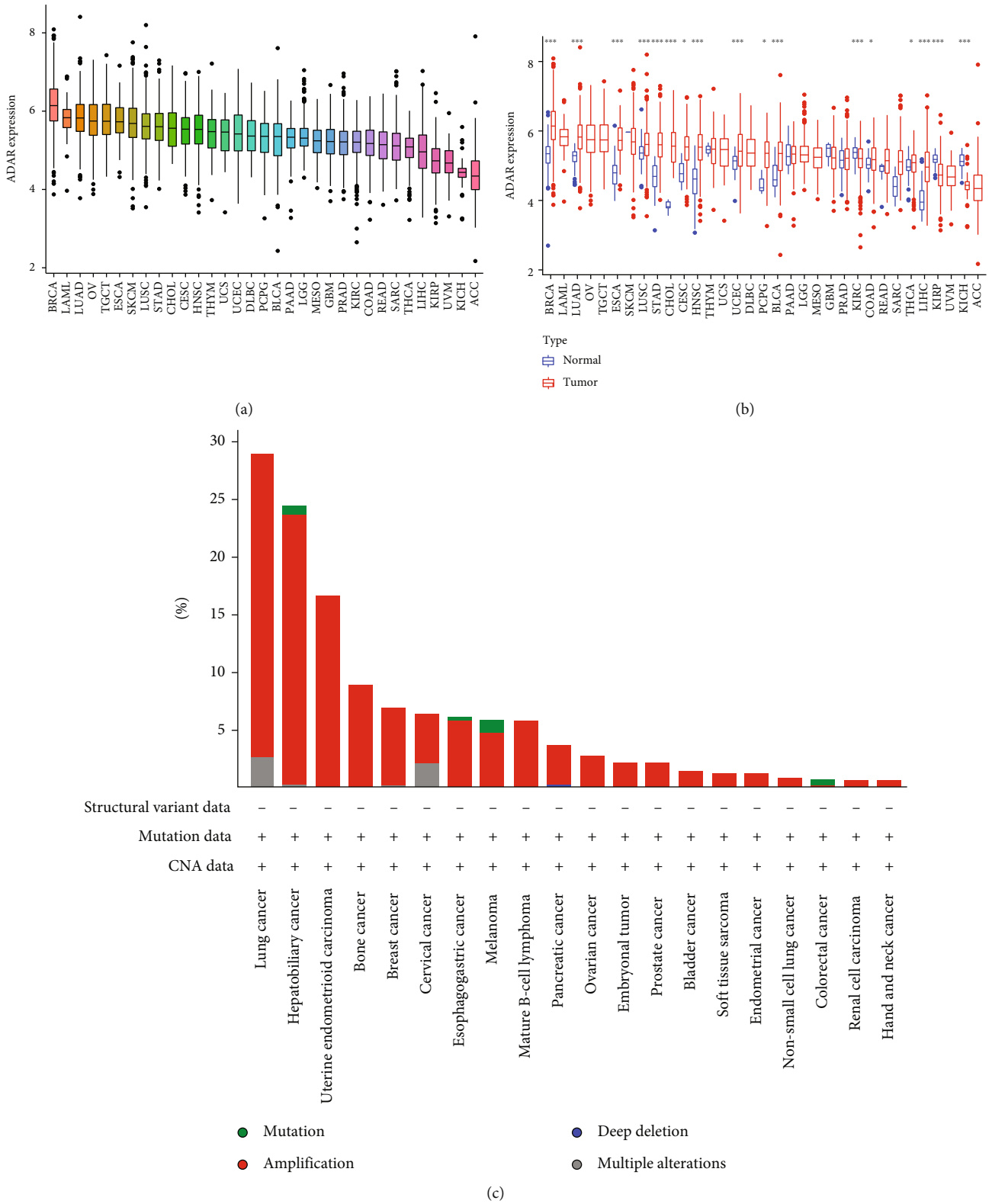

Figure 1: The transcription expression levels and copy number variation (CNV) of ADAR1 in pan-cancer. (a) Ranking of ADAR1 mRNA expression levels in pan-carcinoma tissues. (b) ADAR1 mRNA expression levels in pan-cancer tissues and paired normal tissues. (c) The CNV of ADAR1 in pan-cancer.

further analyzed ADAR1 copy number variation (CNV) by the cBioPortal database. We observed that most cancers with CNV exhibited copy number amplification (Figure 1(c)).

3.2. Protein Level and PPI Network Analysis of ADAR1 in Pan-Cancer. We previously analyzed mRNA expression level and the copy number of ADAR1 in pan-cancer. Next,

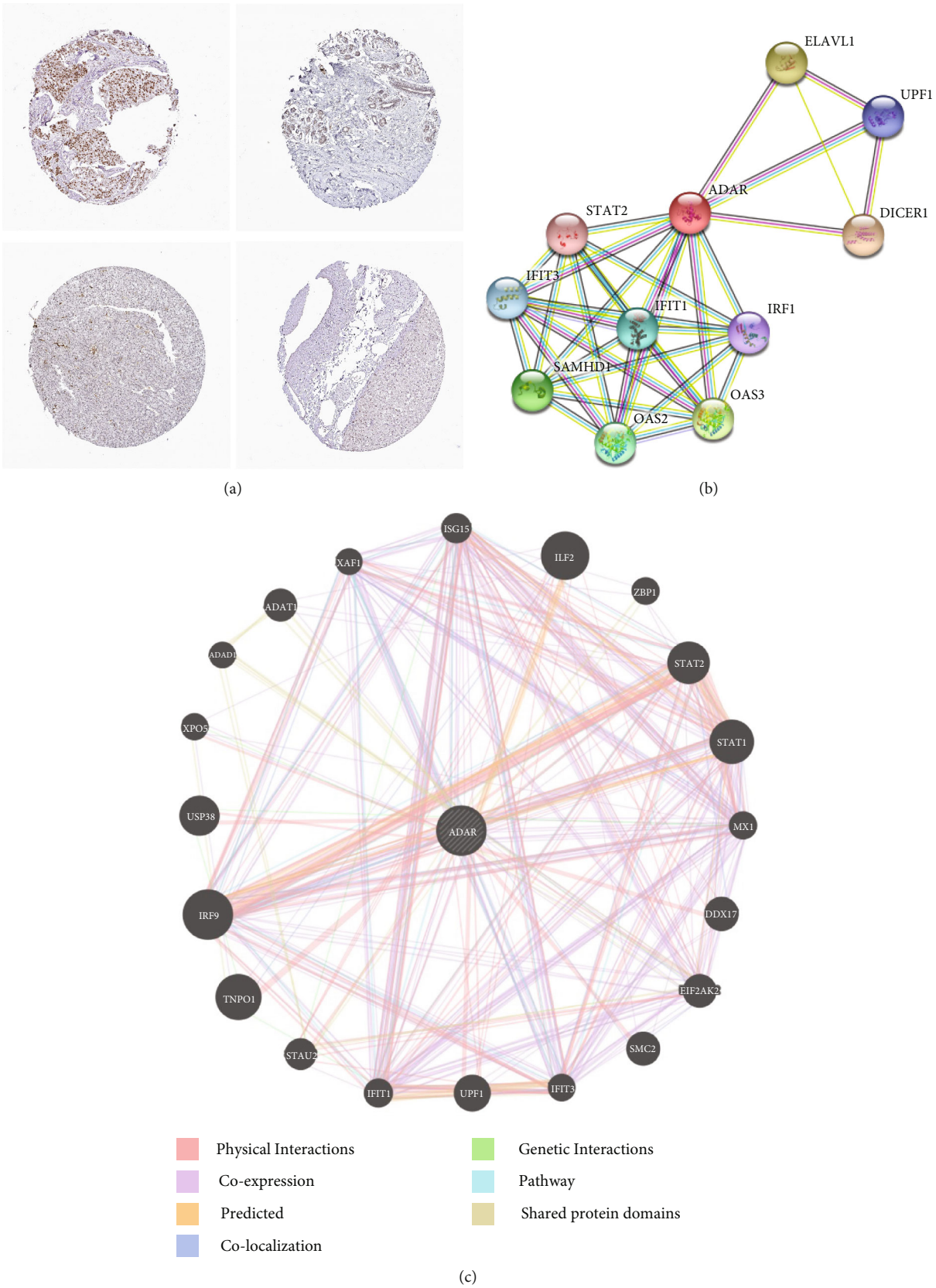

Figure 2: Immunohistochemical and protein-protein interactive modulation network of ADAR1. (a) Immunohistochemistry of ADAR1 in breast and liver cancer and their paired normal tissues. (b) The protein-protein interaction regulatory network of ADAR1 in STRING site. (c) The protein-protein interaction regulatory network of ADAR1 in the GeneMANIA site.

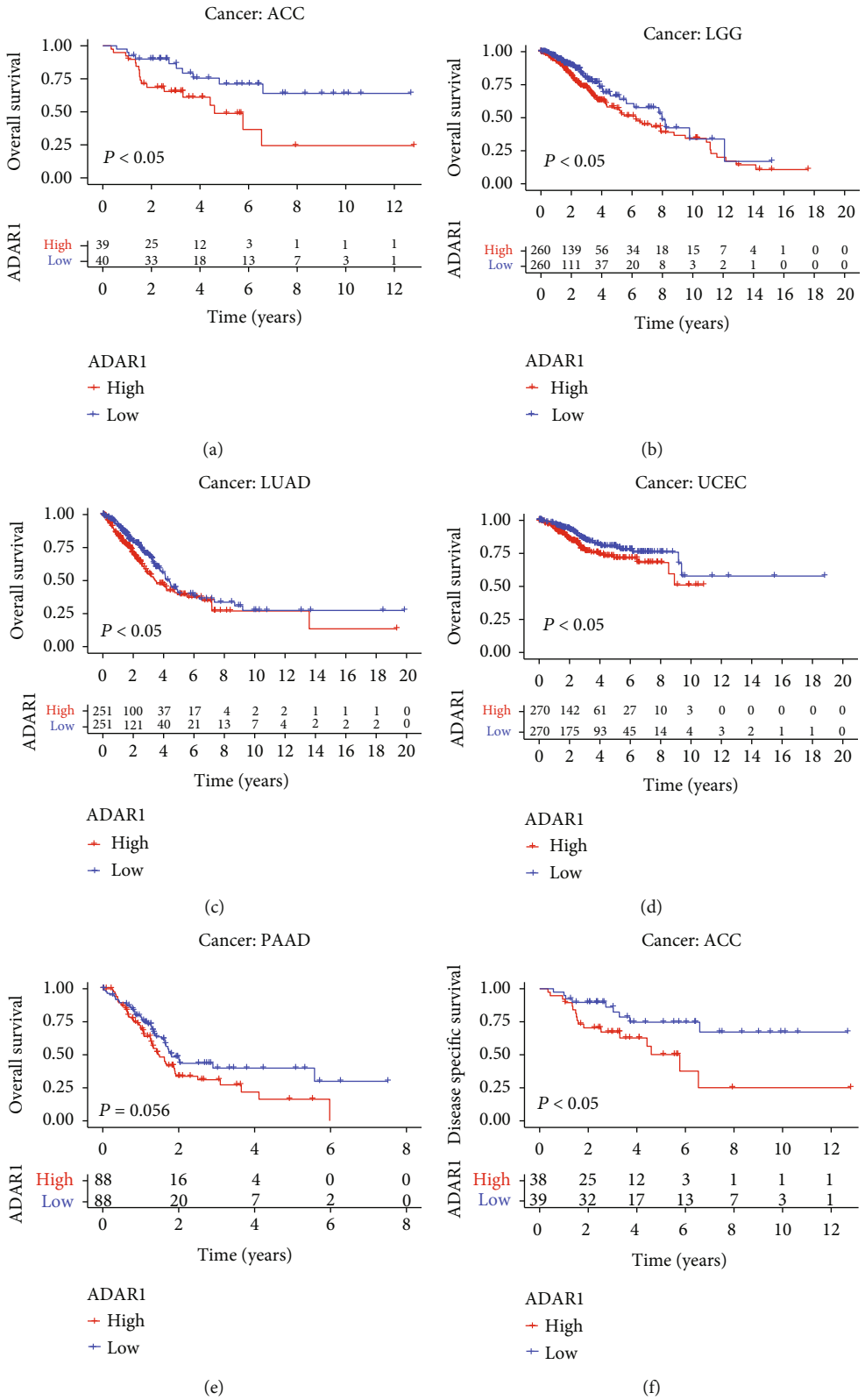

Figure 3: Continued.

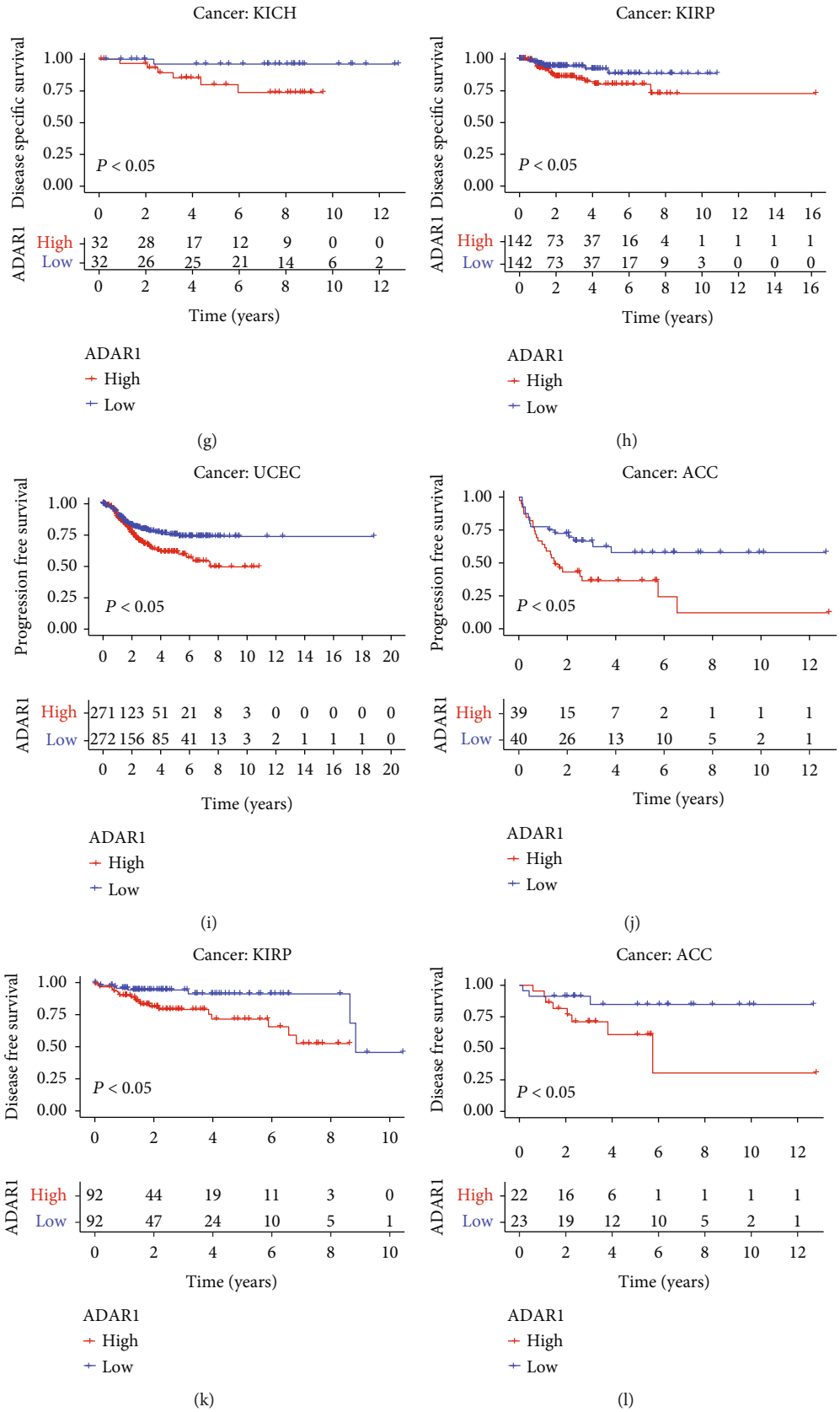

Figure 3: Prognostic analysis of OS and DSS of ADAR1 in different cancers. (a–e) OS analysis of high and low ADAR1 expression in different tumors. (f–h) DSS analysis of high and low ADAR1 expression in different tumors. (i and j) PFS analysis of high and low ADAR1 expression in different tumors. (k and l) DFS analysis of high and low ADAR1 expression in different tumors.

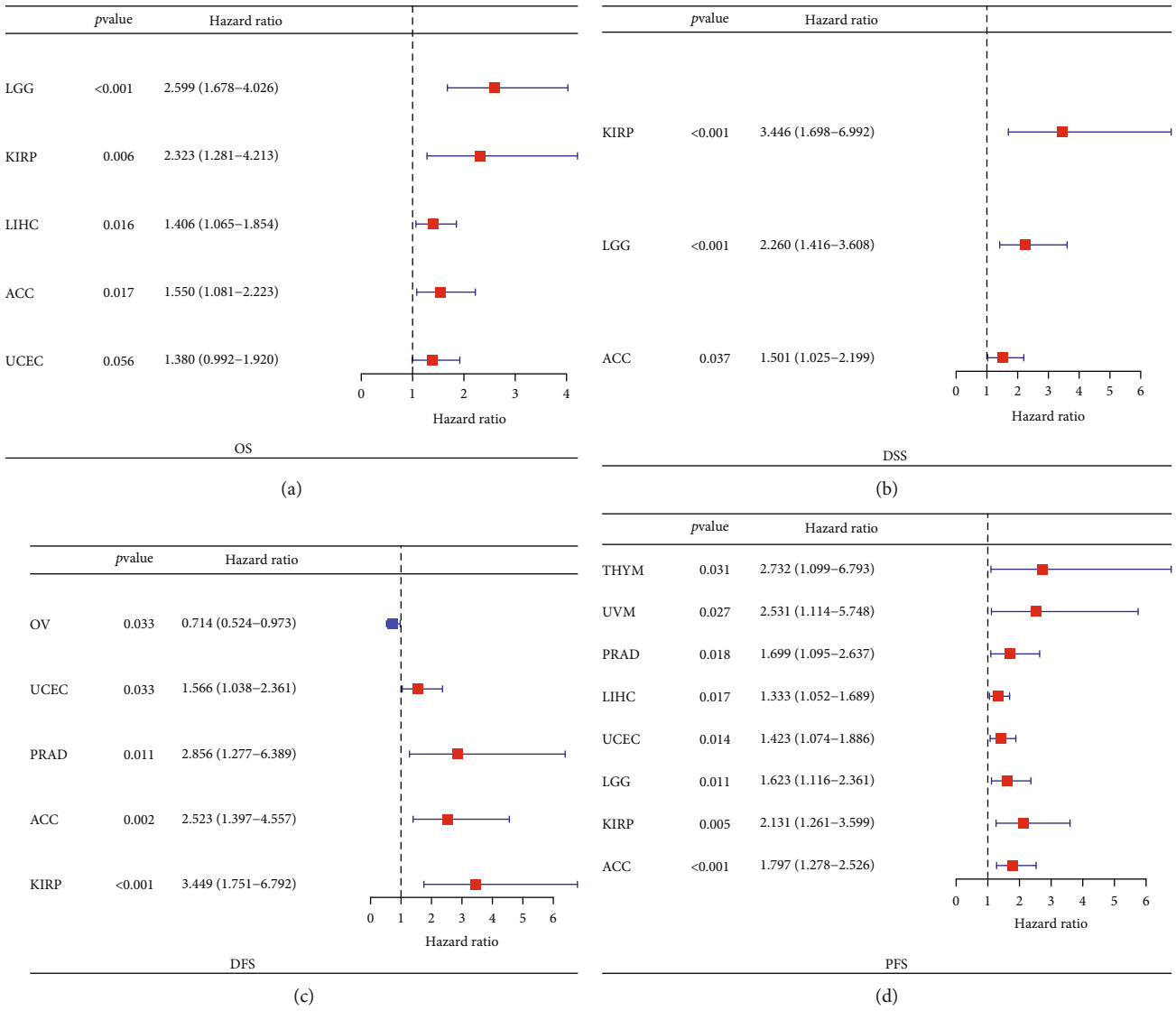

Figure 4: Univariate Cox regression analysis of OS, DSS, DFS, and PFS of ADAR1 in pan cancer. (a) OS, (b) DSS, (c) DFS, and (d) PFS.

we further investigated the protein level of ADAR1 in pan-cancer. The result showed that the protein levels of ADAR1 were highest in breast cancer and lung cancer by HPA database. (Figure 2(a) and Supplementary Figure 1). As a potential immunomodulatory gene, a location on the cell membrane is essential. To explore the potential role of ADAR1 in pan-cancer, we constructed a PPI network of ADAR1 via the GeneMANIA and STRING databases. Results from two databases showed that ADAR1 may interact with STAT2, IFIT1, and IFIT3 (Figures 2(b) and 2(c)). Given that STAT2, IFIT1, and IFIT3 play a role in regulating immune cell function, we firmly believed that ADAR1 may be involved in the regulation of the TIM [17, 18].

3.3. The Prognostic Significance of ADAR1 in Pan-Cancer. We further evaluated the prognostic value of ADAR1 in pan-cancer. We first plotted the KM curves by the median value of ADAR1 expression; the results showed that high expression of ADAR1 in ACC, LGG, LUAD, PAAD, and UCEC had poor overall survival (OS) (Figures 3(a)–3(e)). Interestingly, patients with high ADAR1 expression in ACC, KICH, and KIRP had poor disease-specific survival (DSS) (Figures 3(f)–3(h)). Likewise, UCEC and ACC patients with high ADAR1 expression had poor progression-free survival (PFS), and KIRP and ACC patients with high ADAR1 expression had poor disease-free survival (DFS) (Figures 3(i)–3(l)). In addition, we further analyzed the expression of ADAR1 in the four aspects of OS, DSS, DFS, and PFS by the univariate Cox analysis. The results showed that ADAR1was a risk factor for patients with LGG, KRIP, LIHC, ACC, and UCEC in terms of OS (Figure 4(a)). Meanwhile, DSS analysis revealed that ADAR1 served as a risk factor for patients with KIRP, LGG, and ACC (Figure 4(b)). The DFS analysis revealed that ADAR1 served as a risk factor for patients with UCEC, PRAD, ACC, and KIRP but may be a protective factor for OV (Figure 4(c)). The PFS analysis revealed that ADAR1 served as a risk factor for patients with ACC, KIRP, LGG, UCEC,

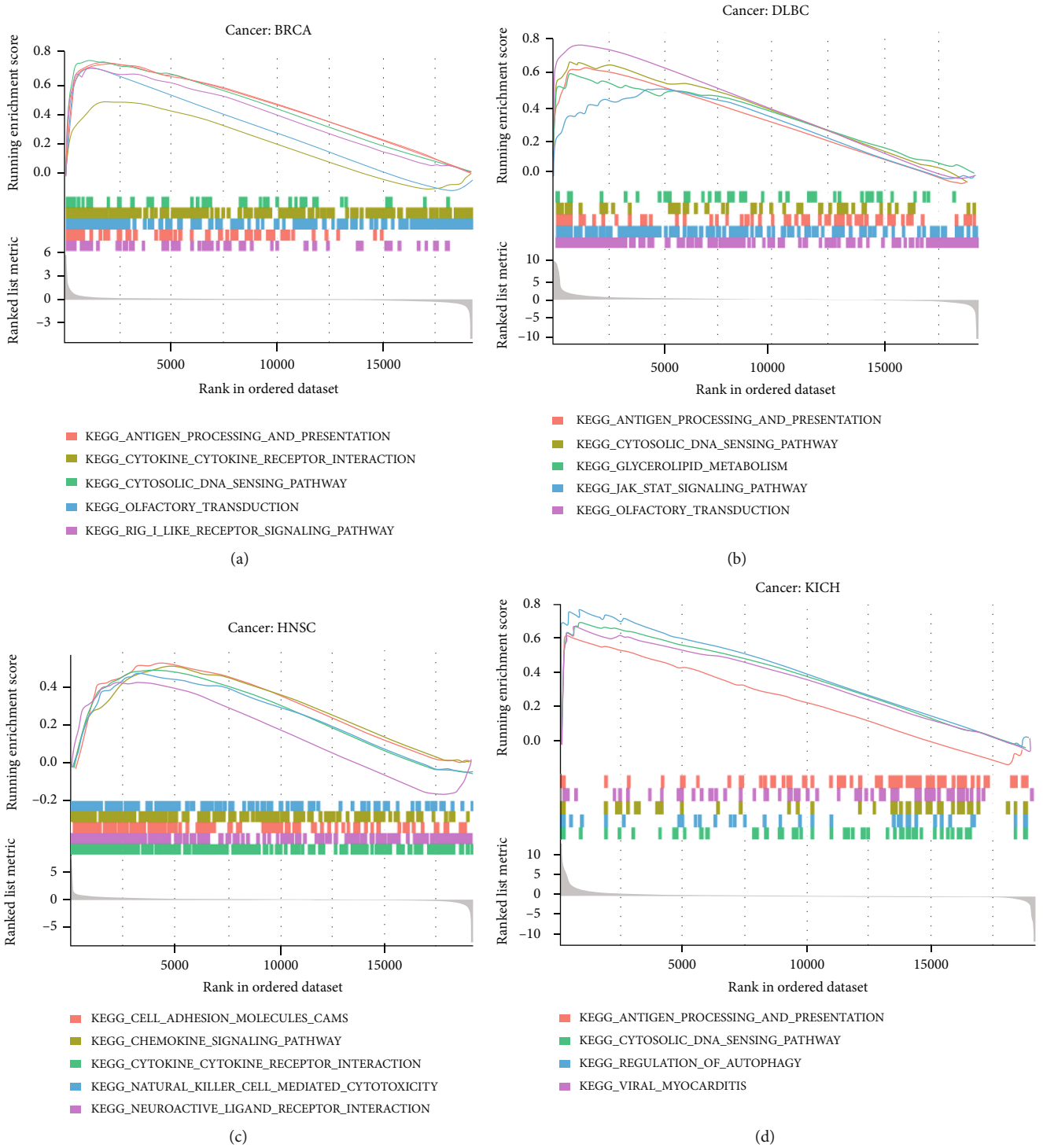

Figure 5: Continued.

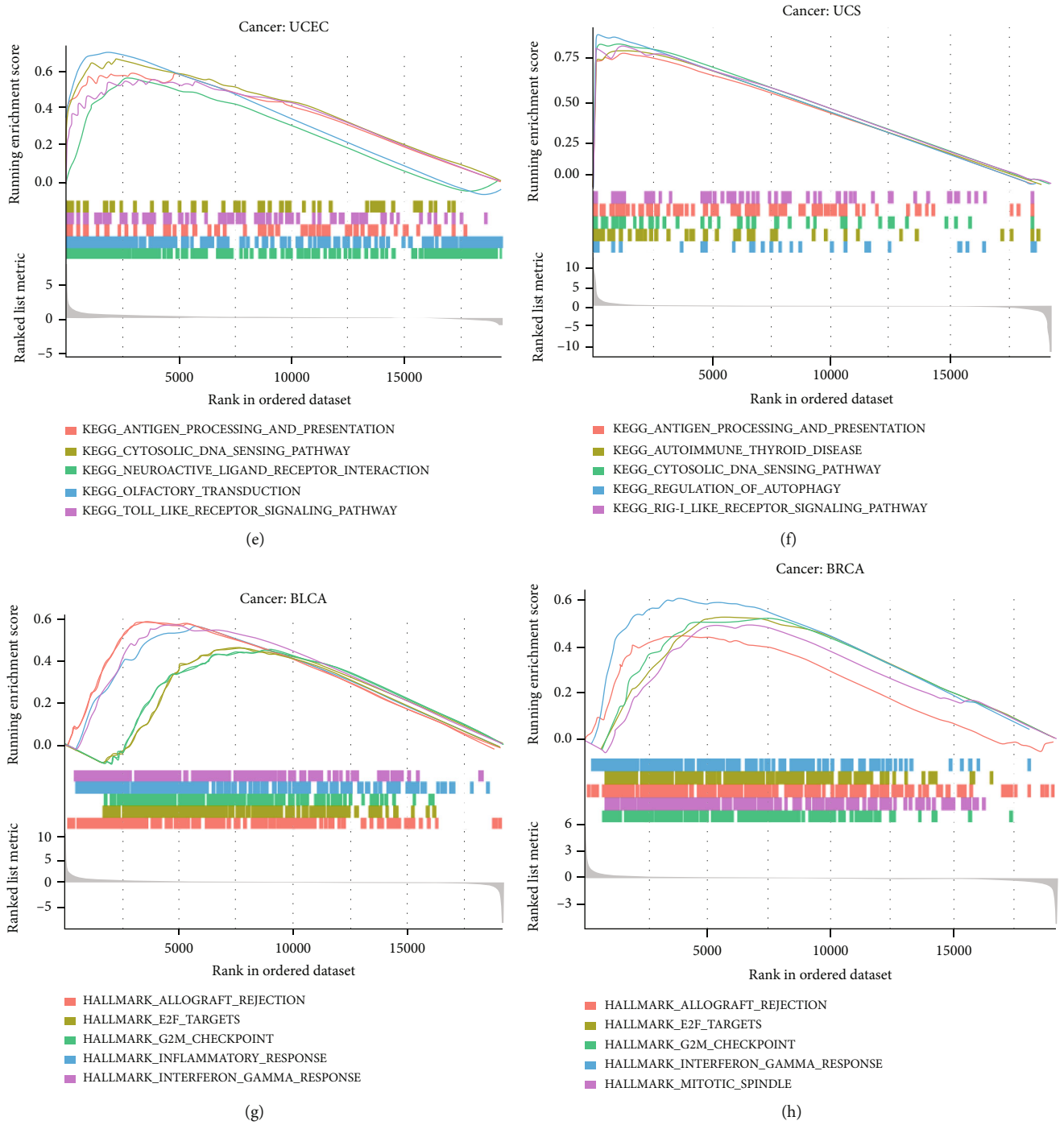

Figure 5: Continued.

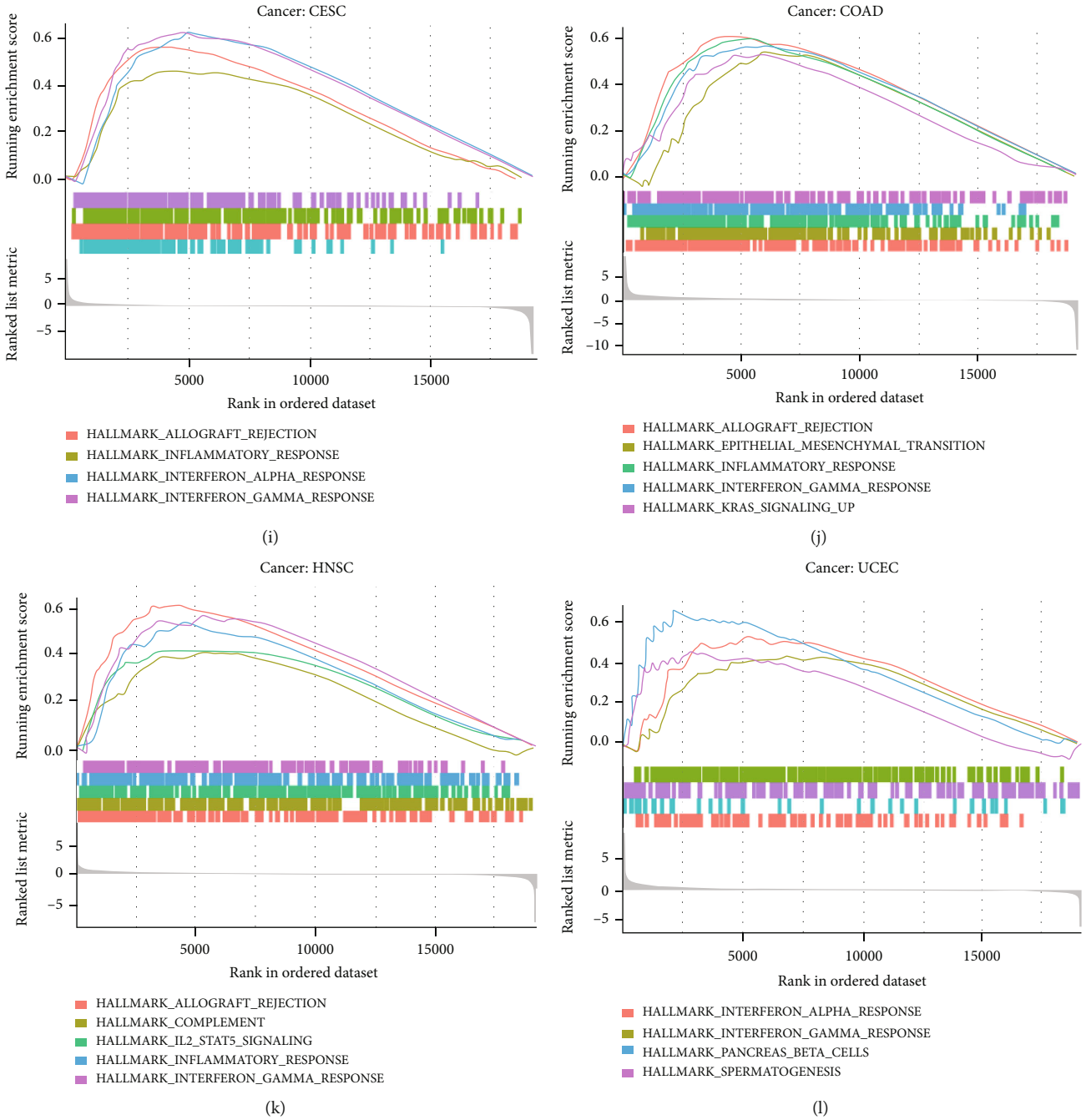

Figure 5: Gene set enrichment analysis of ADAR1 in the KEGG and HALLMARK gene sets. (a–f) KEGG and (g–l) HALLMARK.

LIHC, PRAD, UVM, and THYM (Figure 4(d)). These data strongly suggested that ADAR1 plays an important role in tumor prognosis.

3.4. Enrichment Analysis of ARDR1 Expression in Pan-Cancer. To preliminarily explore the mechanism of ADAR1 in pan-cancer, we performed GSEA analysis using KEGG, HALLMARKER, and immunologic signature gene sets, respectively. The results indicated that ADAR1 was involved in a variety of signaling pathways. In KEGG, ADAR1 is closely related to pathways of cell adhesion, antigen processing, and chemokine expression (Figures 5(a)–5(f)). In HALLMARK sets, ADAR1was involved in the inflammatory and interferon pathways (Figures 5(g)–5(l)). These results suggested that ADAR1 may play an important role in regulating the tumor immune microenvironment.

3.5. Association of ADAR1 Expression with Immune Cell Infiltration, Immune Checkpoints, and Chemokines in Pan-Cancer. Tumor-infiltrating immune cells are an important part of the complex microenvironment that regulates the development and progression of cancers [3]. Tumor-infiltrating immune cells are the main performers of tumor immune responses [19]. To explore whether ADAR1

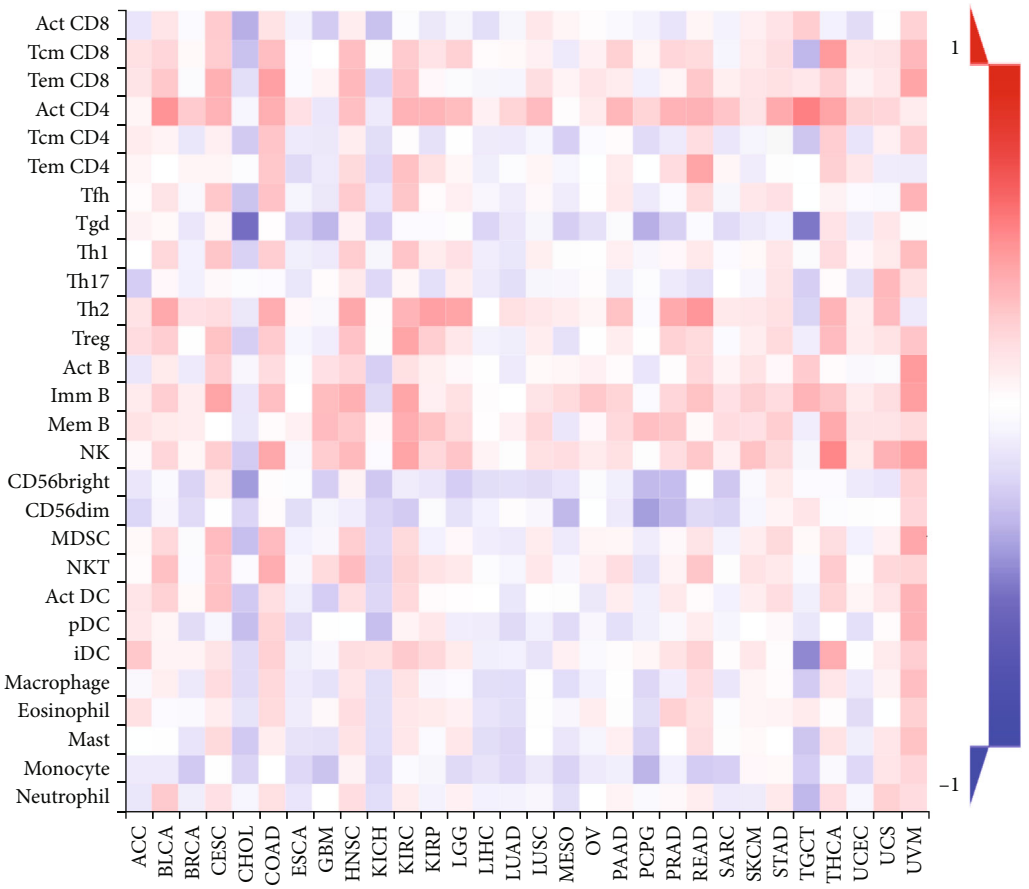

(a)

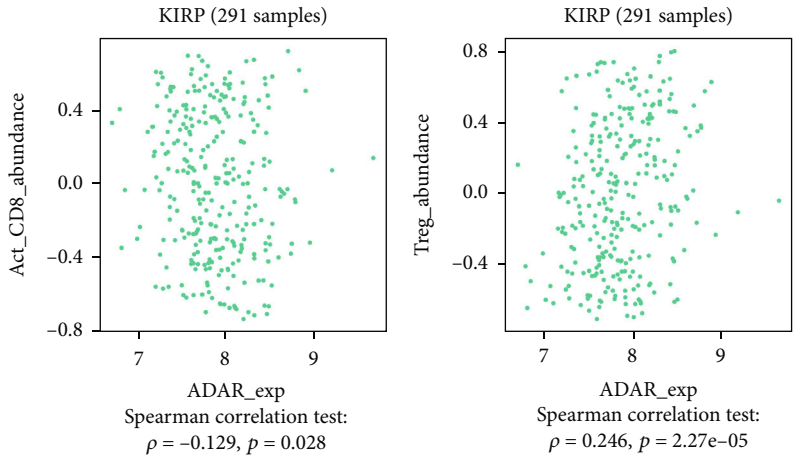

(b)

Figure 6: Continued.

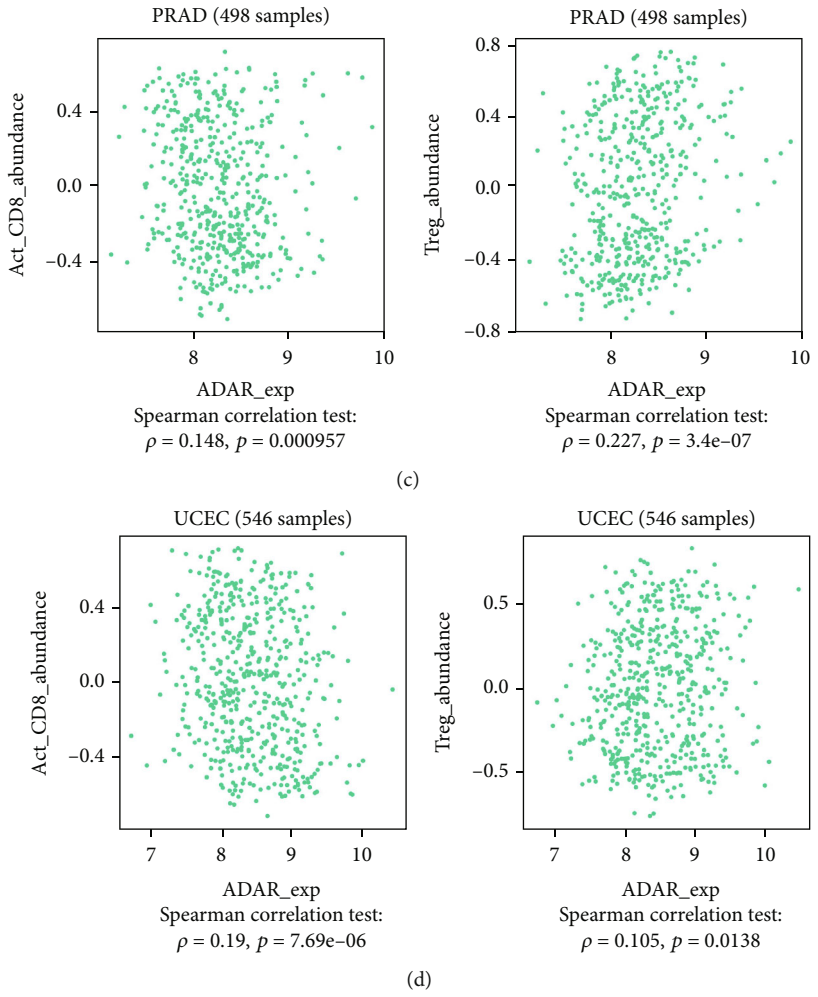

Figure 6: ADAR1 expression level and immune cell infiltration analysis. (a) Correlation between ADAR1 and the level of infiltration of indicator immune cells by TISDB database. (b) The association of ADAR1 with $CD8^+$ T cell and Treg cell infiltration in KIRP. (c) The association of ADAR1 with $CD8^+$ T cell and Treg cell infiltration in PRAD. (d) The association of ADAR1 with $CD8^+$ T cell and Treg cell infiltration in UCEC.

expression level modulates the level of immune cell infiltration, we analyzed it by the TISIDB database (Figure 6(a)). The results showed that ADAR1 was negatively correlated with activated $CD8^+$ T cells and positively correlated with Treg cells in KIRP, PRAD, and UCEC (Figures 6(b)–6(d)). Given that deficiencies in immune surveillance are an important cause of poor prognosis in various cancers. Tumors evade immune cell attack by exploiting multiple pathways, such as regulation of immune checkpoints and secretion of leukocyte chemokines. Therefore, we further investigated the relationship between ADAR1 and the above functions. The results showed that ADAR1 was positively correlated with the expression levels of immunosuppressive genes such as CD274, PDCD1, LAG3, CTLA4, TIGIT, CD96, and IDO1 in most tumors (Figure 7(a)). ADAR1 positively correlated with chemokines, such as CCL14 and CCL28 in most tumors (Figure 7(b)). These data suggested that ADAR1 may regulate the expression of immune checkpoints and chemokines to modulate the tumor immune microenvironment.

3.6. Correlation Analysis of ADAR1 and Tumor Stemness in Pan-Cancer. Stemness plays an important role in tumorigenesis and development [20]. We further analyzed the relationship between ADAR1 and tumor stemness. We further applied DNA stemness signature (DNAss) and RNA stemness signature (RNAss) to assess the role of ADAR1 on tumor stemness capacity. The results showed that ADAR1 expression levels were positively correlated with DNAss in STES, SKCM, STAD, GBM, PRAD, KIRP, KIPAN, THCA, LGG, UVM, CHOL, PCPG, ACC, TGCT, and THYM. In contrast, ADAR1 expression levels were negatively correlated with DNAss in CESC, KIRC, DLBC, LIHC, UCEC, SARC, LUAD, MESO, LUSC, LAML, READ, UCS, HNSC, KICH, PAAD, GBM, BRCA, COAD, BLCA, ESCA, and OV (Figure 8(a)). In addition, ADAR1 expression levels were positively correlated with RNAss in LAML, PRAD, OV, SARC, LUSC, UCEC, TGCT, LUAD, STAD, BRCA, LGG, STES, BLCA, ESCA, ACC, and PCPG. In contrast, ADAR1 expression levels were negatively correlated with RNAss in SKCM, KICH, GBM,

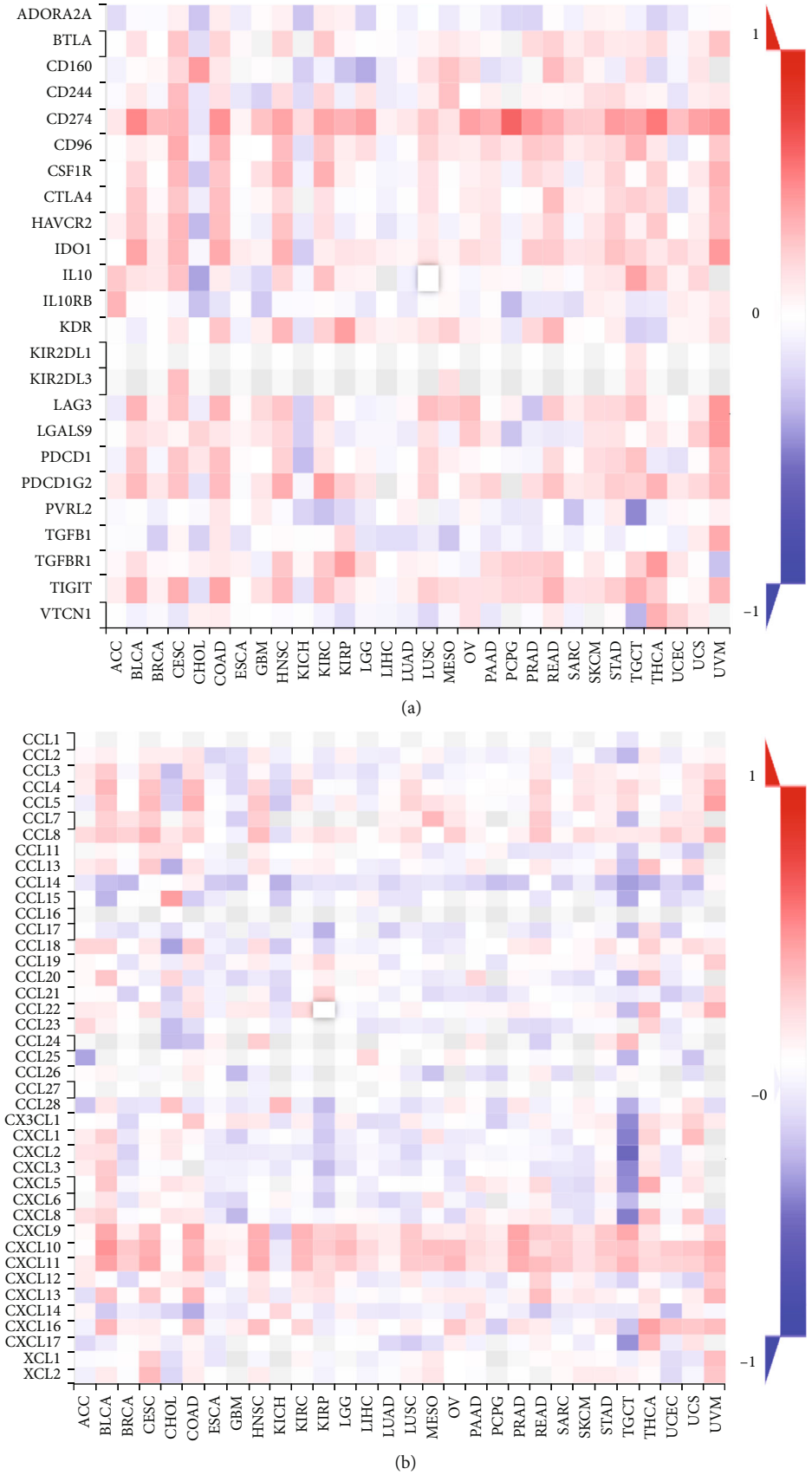

Figure 7: The relationship between ADAR1 and immunomodulatory molecules. (a) Association of ADAR1 with immune checkpoints in pan-cancer. (b) Association of ADAR1 with chemokines in pan-cancer.

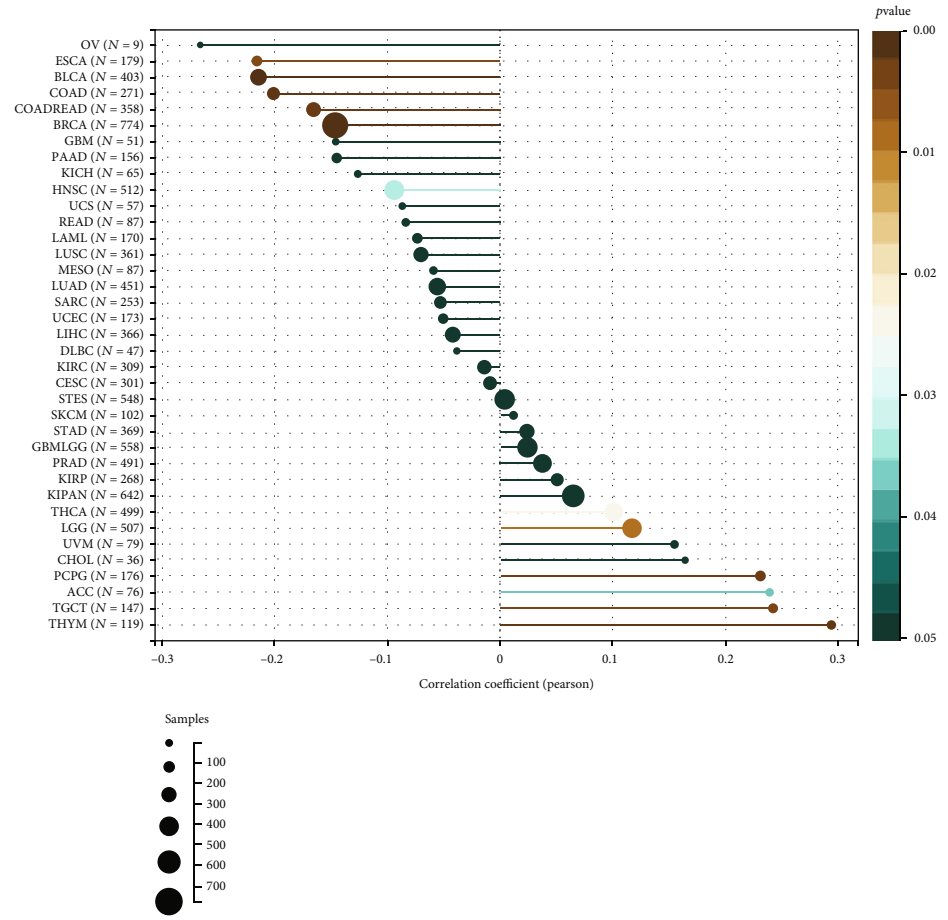

(a)

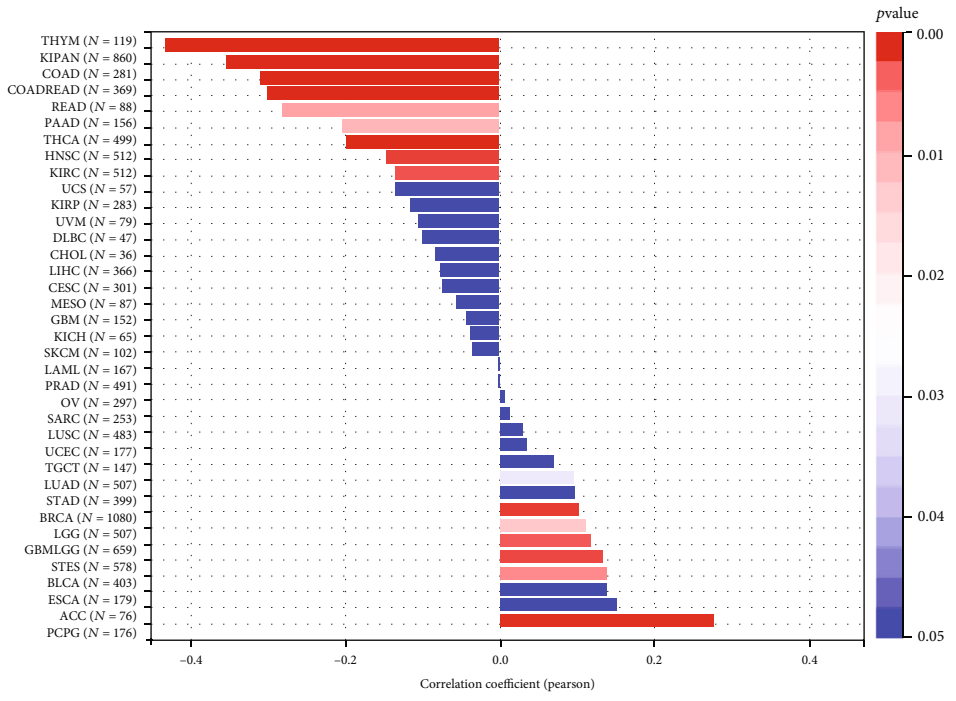

(b)

Figure 8: The correlation analysis of ADAR1 and tumor stem index in pan-cancer. (a) The relationship between ADAR1 and DNAss in pan-cancer. (b) The relationship between ADAR1 and RNAss in pan-cancer.

MESO, CESC, LIHC, CHOL, DLBC, UVM, KIRP, UCS, KIRC, HNSC, THCA, PAAD, READ, COAD, KIPAN, and THYM (Figure 8(b)).

4. Discussions

Immune evasion plays a crucial role in tumor progression and metastasis, which is the theoretical basis of immunotherapy [21]. In this study, we revealed that ADAR1 was highly expressed in most cancers, such as BRCA, LUAD, ESCA, LUSC, STAD, CHOL, CESC, HNSC, UCEC, PCPG, BLCA, COAD, THCA, and LIHC. In addition, GSEA analysis revealed that ADAR1 may be involved in immune processes such as antigen presentation, cell adhesion, and chemokine expression. Moreover, we also found that ADAR1 was significantly associated with patient prognosis in pan-cancer. In addition, we further found through public data that ADAR1 may be involved in the regulation of immune cell infiltration, immune checkpoints, and chemokine expression in pan-cancer. Finally, we revealed that ADAR1 is involved in the regulation of tumor stemness in pan-cancer.

The biological behavior of cells is regulated by gene networks [22]. A previous report revealed that loss of ADAR1 rendered tumors highly sensitive to immunotherapy and overcame resistance to immune checkpoint inhibitors [9]. In this study, we performed GSEA analysis at the pan-cancer level, and the results showed that the high expression of ADAR1 was mainly related to immune-related effects. This further corroborates the complex role of ADAR1 in regulating tumor immunity and provides a theoretical basis for the development of immune drugs targeting ADAR1.

At present, there are a variety of approaches for tumor immunotherapy, including monoclonal antibody-based immune checkpoint inhibitors, cancer vaccines, and therapeutic antibodies. Here, we collected more than 40 common immune checkpoint genes, extracted these immune checkpoint genes separately, and calculated the correlation with our target gene expression. The results showed that the upregulation of ADAR1 is closely related to the immune checkpoints of various cancers and also has a significant correlation with the infiltration of immune cells. Combining ADAR1 with prognostic and significant associations in a variety of tumors, our study thus elucidated the potential role of ADAR1 in tumor immunology and its use as a cancer prognostic biomarker.

Recent studies suggest that ADAR1 may also be involved in promoting tumorigenesis. Downregulation of ADAR1 in breast cancer cells reduced cell proliferation, which was not seen in other cell lines [23]. It is unclear why some cancer cells depend on ADAR1 or why other cells are not sensitive to the loss of ADAR1. Elevated expression of IFN and ADAR1 has been observed in many cancer types [8]. Kung et al. found that ADAR1-dependent TNBC cell lines also exhibited elevated IFN-stimulated gene expression and reduction of IFNAR1 apparently rescued the proliferation defect of ADAR1 deficiency [24]. Ramirez-Moya et al. have confirmed that ADAR1-mediated A-to-I editing was one of the important pathways that promote thyroid cancer progression, and blocking RNA editing is a potential therapeutic target for thyroid cancer [25]. In this study, our pathway enrichment results showed that ADAR1 is associated with multiple validated pathways in multiple cancers, which further supports these previous findings. This suggested that ADAR1 plays a diverse role in tumors, and targeting ADAR1 is a promising treatment option for tumor. The data and relevant clinical information of this study are all from public databases and lack of in vivo and in vitro verification. We will further confirm the role of ADAR1 in tumors in subsequent studies.

In conclusion, we conducted a comprehensive evaluation of ADAR1 in pan-cancer, revealing that ADAR1 is a prognostic indicator for a variety of tumors and further exploring its implications in tumor immunity. ADAR1 may be a potential target for immunotherapy in a variety of tumors.

Data Availability

The data in this study are available from the corresponding authors upon reasonable request.

Conflicts of Interest

All authors in this study declare no conflict of interest.

Authors' Contributions

Jianlin Zhu, Jianjian Zheng, and Jinjun Zhang contributed equally to this work.

Acknowledgments

The authors would like to express their sincere thanks for sharing the data from The Cancer Genome Atlas (TCGA) database. This research was supported by the following funding agency: Joint Funds for the Innovation of Science and Technology, Fujian Province (2021Y9120); National Natural Science Foundation of China (82002491); and Natural Science Foundation of Guangdong Province of China (2020A1515110049).

Supplementary Materials

Supplementary Figure 1: protein levels of ADAR1 in lung cancer. (A) Expression level of ADAR1 protein in lung cancer tissues. (B) Protein expression of ADAR1 in normal lung tissue. *(Supplementary Materials)*

References

[1] C. Santucci, G. Carioli, P. Bertuccio et al., "Progress in cancer mortality, incidence, and survival: a global overview," *European Journal of Cancer Prevention*, vol. 29, no. 5, pp. 367–381, 2020.

[2] K. Nakamura and M. J. Smyth, "Myeloid immunosuppression and immune checkpoints in the tumor microenvironment," *Cellular & Molecular Immunology*, vol. 17, no. 1, pp. 1–12, 2020.

[3] Y. Zhang and Z. Zhang, "The history and advances in cancer immunotherapy: understanding the characteristics of tumor-infiltrating immune cells and their therapeutic implications," *Cellular & Molecular Immunology*, vol. 17, no. 8, pp. 807–821, 2020.

[4] J. Yao, L. Duan, X. Huang et al., "Development and validation of a prognostic gene signature correlated with M2 macrophage infiltration in esophageal squamous cell carcinoma," *Frontiers in Oncology*, vol. 11, article 769727, 2021.

[5] A. O. Goncharov, A. A. Kliuchnikova, S. S. Nasaev, and S. A. Moshkovskii, "RNA editing by ADAR adenosine deaminases: from molecular plasticity of neural proteins to the mechanisms of human cancer," *Biochemistry*, vol. 84, no. 8, pp. 896–904, 2019.

[6] T. Nakahama and Y. Kawahara, "Deciphering the biological significance of ADAR1-Z-RNA interactions," *International Journal of Molecular Sciences*, vol. 22, no. 21, p. 11435, 2021.

[7] R. Radetskyy, A. Daher, and A. Gatignol, "ADAR1 and PKR, interferon stimulated genes with clashing effects on HIV-1 replication," *Cytokine & Growth Factor Reviews*, vol. 40, pp. 48–58, 2018.

[8] L. D. Xu and M. Ohman, "ADAR1 editing and its role in cancer," *Genes (Basel)*, vol. 10, no. 1, p. 12, 2019.

[9] J. J. Ishizuka, R. T. Manguso, C. K. Cheruiyot et al., "Loss of ADAR1 in tumours overcomes resistance to immune checkpoint blockade," *Nature*, vol. 565, no. 7737, pp. 43–48, 2019.

[10] J. Gao, B. A. Aksoy, U. Dogrusoz et al., "Integrative analysis of complex cancer genomics and clinical profiles using the cBioPortal," *Science Signaling*, vol. 6, no. 269, p. pl1, 2013.

[11] M. Uhlen, C. Zhang, S. Lee et al., "A pathology atlas of the human cancer transcriptome," *Science*, vol. 357, no. 6352, 2017.

[12] L. Zhang, L. Han, X. Wang et al., "Exploring the mechanisms underlying the therapeutic effect of Salvia miltiorrhiza in diabetic nephropathy using network pharmacology and molecular docking," *Bioscience Reports*, vol. 41, no. 6, 2021.

[13] W. Guo, F. Tan, Q. Huai et al., "Comprehensive analysis of PD-L1 expression, immune infiltrates, and m6A RNA methylation regulators in esophageal squamous cell carcinoma," *Frontiers in Immunology*, vol. 12, article 669750, 2021.

[14] Y. Fan, B. Liu, F. Chen et al., "Hepcidin upregulation in lung cancer: a potential therapeutic target associated with immune infiltration," *Frontiers in Immunology*, vol. 12, article 612144, 2021.

[15] T. Huang, J. Li, X. Liu, B. Shi, S. Li, and H. X. An, "An integrative pan-cancer analysis revealing the difference in small ring finger family of SCF E3 ubiquitin ligases," *Frontiers in Immunology*, vol. 13, article 968777, 2022.

[16] T. Ried, G. A. Meijer, D. J. Harrison et al., "The landscape of genomic copy number alterations in colorectal cancer and their consequences on gene expression levels and disease outcome," *Molecular Aspects of Medicine*, vol. 69, pp. 48–61, 2019.

[17] C. J. Lee, H. J. An, E. S. Cho et al., "Stat2 stability regulation: an intersection between immunity and carcinogenesis," *Experimental & Molecular Medicine*, vol. 52, no. 9, pp. 1526–1536, 2020.

[18] V. K. Pidugu, H. B. Pidugu, M. M. Wu, C. J. Liu, and T. C. Lee, "Emerging functions of human IFIT proteins in cancer," *Frontiers in Molecular Biosciences*, vol. 6, p. 148, 2019.

[19] F. Petitprez, M. Meylan, A. de Reynies, C. Sautes-Fridman, and W. H. Fridman, "The tumor microenvironment in the response to immune checkpoint blockade therapies," *Frontiers in Immunology*, vol. 11, p. 784, 2020.

[20] J. Xiong, L. Yan, C. Zou et al., "Integrins regulate stemness in solid tumor: an emerging therapeutic target," *Journal of Hematology & Oncology*, vol. 14, no. 1, p. 177, 2021.

[21] P. S. Hegde and D. S. Chen, "Top 10 challenges in cancer immunotherapy," *Immunity*, vol. 52, no. 1, pp. 17–35, 2020.

[22] F. Gomez-Vela and N. Diaz-Diaz, "Gene network biological validity based on gene-gene interaction relevance," *The Scientific World Journal*, vol. 2014, Article ID 540679, 11 pages, 2014.

[23] E. A. Sagredo, A. I. Sagredo, A. Blanco et al., "ADAR1 transcriptome editing promotes breast cancer progression through the regulation of cell cycle and DNA damage response," *Biochimica et Biophysica Acta (BBA)-Molecular Cell Research*, vol. 1867, no. 8, article 118716, 2020.

[24] C. P. Kung, K. A. Cottrell, S. Ryu et al., "Evaluating the therapeutic potential of ADAR1 inhibition for triple-negative breast cancer," *Oncogene*, vol. 40, no. 1, pp. 189–202, 2021.

[25] J. Ramirez-Moya, C. Miliotis, A. R. Baker, R. I. Gregory, F. J. Slack, and P. Santisteban, "An ADAR1-dependent RNA editing event in the cyclin-dependent kinase CDK13 promotes thyroid cancer hallmarks," *Molecular Cancer*, vol. 20, no. 1, p. 115, 2021.

Hindawi
Disease Markers
Volume 2023, Article ID 9820901, 1 page
https://doi.org/10.1155/2023/9820901

Retraction

Retracted: Exogenous Hydrogen Sulfide Mitigates Oxidative Stress and Mitochondrial Damages Induced by Polystyrene Microplastics in Osteoblastic Cells of Mice

Disease Markers

Received 20 June 2023; Accepted 20 June 2023; Published 21 June 2023

This article has been retracted by Hindawi following an investigation undertaken by the publisher [1]. This investigation has uncovered evidence of one or more of the following indicators of systematic manipulation of the publication process:

(1) Discrepancies in scope

(2) Discrepancies in the description of the research reported

(3) Discrepancies between the availability of data and the research described

(4) Inappropriate citations

(5) Incoherent, meaningless and/or irrelevant content included in the article

(6) Peer-review manipulation

The presence of these indicators undermines our confidence in the integrity of the article's content and we cannot, therefore, vouch for its reliability. Please note that this notice is intended solely to alert readers that the content of this article is unreliable. We have not investigated whether authors were aware of or involved in the systematic manipulation of the publication process.

Wiley and Hindawi regrets that the usual quality checks did not identify these issues before publication and have since put additional measures in place to safeguard research integrity.

We wish to credit our own Research Integrity and Research Publishing teams and anonymous and named external researchers and research integrity experts for contributing to this investigation.

The corresponding author, as the representative of all authors, has been given the opportunity to register their agreement or disagreement to this retraction. We have kept a record of any response received.

References

[1] Q. Shi, F. Chen, Y. Feng, Y. Zheng, X. Zhi, and W. Wu, "Exogenous Hydrogen Sulfide Mitigates Oxidative Stress and Mitochondrial Damages Induced by Polystyrene Microplastics in Osteoblastic Cells of Mice," *Disease Markers*, vol. 2023, Article ID 2516472, 8 pages, 2023.

Hindawi
Disease Markers
Volume 2023, Article ID 2516472, 8 pages
https://doi.org/10.1155/2023/2516472

Research Article

Exogenous Hydrogen Sulfide Mitigates Oxidative Stress and Mitochondrial Damages Induced by Polystyrene Microplastics in Osteoblastic Cells of Mice

Qingping Shi,[1,2,3] Feihong Chen,[4] Yuanyi Feng,[1,2] Yangxi Zheng,[2] Ximei Zhi,[2] and Wen Wu[1,2]

[1]*The Second School of Clinical Medicine, Southern Medical University, Guangzhou, Guangdong 510515, China*
[2]*Department of Endocrinology, Guangdong Geriatrics Institute, Guangdong Provincial People's Hospital, Guangdong Academy of Medical Sciences, Guangzhou, Guangdong 510080, China*
[3]*Department of Geriatric Medicine, People's Hospital of Shenzhen Baoan District, Affiliated Hospital of Shenzhen Bao'an of Southern Medical University, The Second Affiliated Hospital of Shenzhen University, Shenzhen, Guangdong 518000, China*
[4]*Department of Respiratory Medicine, People's Hospital of Shenzhen Baoan District, Affiliated Hospital of Shenzhen Bao'an of Southern Medical University, The Second Affiliated Hospital of Shenzhen University, Shenzhen, Guangdong 518000, China*

Correspondence should be addressed to Wen Wu; wuwen@gdph.org.cn

Received 8 September 2022; Revised 28 September 2022; Accepted 25 January 2023; Published 18 February 2023

Academic Editor: Fu Wang

Polystyrene microplastics (mic-PS) have become harmful pollutants that attracted substantial attention about their potential toxicity. Hydrogen sulfide (H_2S) is the third reported endogenous gas transmitter with protective functions on numerous physiologic responses. Nevertheless, the roles for mic-PS on skeletal systems in mammals and the protective effects of exogenous H_2S are still indistinct. Here, the proliferation of MC3T3-E1 cell was analyzed by CCK8. Gene changes between the control and mic-PS treatment groups were analyzed by RNA-seq. The mRNA expression of bone morphogenetic protein 4 (Bmp4), alpha cardiac muscle 1 (Actc1), and myosin heavy polypeptide 6 (Myh6) was analyzed by QPCR. ROS level was analyzed by 2′,7′-dichlorofluorescein (DCFH-DA). The mitochondrial membrane potential (MMP) was analyzed by Rh123. Our results indicated after exposure for 24 h, 100 mg/L mic-PS induced considerable cytotoxicity in the osteoblastic cells of mice. There were 147 differentially expressed genes (DEGs) including 103 downregulated genes and 44 upregulated genes in the mic-PS-treated group versus the control. The related signaling pathways were oxidative stress, energy metabolism, bone formation, and osteoblast differentiation. The results indicate that exogenous H_2S may relieve mic-PS toxicity by altering *Bmp4*, *Actc1*, and *Myh6* mRNA expressions associated with mitochondrial oxidative stress. Taken together, this study demonstrated that the bone toxicity effects of mic-PS along with exogenous H_2S have protective function in mic-PS-mediated oxidative damage and mitochondrial dysfunction in osteoblastic cells of mice.

1. Introduction

Polystyrene microplastics (mic-PS) are plastic particles with diameter < 5 mm [1], originating from industrial products and plastics demoted into pieces by UV radiation, physical, or biodegradation [2]. Mic-PS contain high-density and low-density polyethylene (HD/LD-PE), polyethylene terephthalate (PET), polypropylene (PP), and polyvinylchloride (PVC), together with polystyrene microplastic (PS-MP) [3]. More recently, these minor plastic products have been widely detected in freshwater organisms, ranging from algae to fish, even in mammals. Therefore, pollution by mic-PS was classified as the second most crucial threat in ecological environment at the United Nations Environmental Conference in 2015 [4].

Mic-PS less than 20 μm can easily access the mammalian tissues, while mic-PS with particle size of 0.1~10 μm can effectively pass through the cytomembrane, intestinal

mucosal barrier, and blood-brain barrier, even transmit through the placenta to the next generation [5, 6]. Further investigation substantiates the toxicity of mic-PS on index such as oxidative stress, enzymatic activity, quantity of egg laying, feeding rate, and growth rate [5–7]. Specific polystyrene mic-PS with size of 5 to 20 μm can accrue in the liver, lung, and kidney; additionally, they can evoke oxidative damage along with metabolic alterations [8, 9]. In contrast, it remains unknown the relationship among mic-PS intake and bone destruction of terrestrial mammals.

Hydrogen sulfide (H_2S), a colorless indispensable endogenous gas, can subsequently enhance catalytic activity by attaching hydropersulfide group (-SSH) to relevant cysteine residues into targeted protein. Exogenous H_2S has been reported to regulate numerous signaling pathways associated with biological processes, for instance, regulation of kinase, maintaining intracellular mitochondrial ATP generation, and scavenging reactive oxygen species (ROS). In osteoblastic cell, the scavenging ability to reduce oxidative stress and sustaining maintenance of mitochondrial membrane potential is a key signal for cells and is a crucial target of osteoporosis responsible for increased bone fracture threat. Further research on mic-PS stated that exogenous H_2S increases the expression of heme oxygenase-1 and NAD(P)H : quinone oxidoreductase 1, consequently decreasing microplastics producing hepatic apoptosis and inflammation [10]. Therefore, exogenous H_2S might be an innovative antioxidant medium under MP stress system. So far, the beneficial effect of exogenous H_2S in mic-PS-induced bone toxicity remains undiscovered.

In this study, we aimed to study the cytotoxic effects of mic-PS in MC3T3-E1 cells, then investigating the toxicity of mic-PS in osteoblastic cell through RNA sequencing (RNA-seq). Finally, we aimed to explore whether H_2S ameliorated mic-PS exposure induced damage by attenuating oxidative stress and mitochondrial damage.

2. Materials and Methods

2.1. Materials and Reagents. Mic-PS (100 nm) were purchased from the Tianjin DAE Scientific Co. Ltd (Tianjin, China). GYY4137 (as the donor of H_2S) and rhodamine 123 (Rh123) were bought from Sigma (St. Louis, MO, USA). 2′,7′-Dichlorofluorescein diacetate (DCFH-DA) was obtained from Nanjing Jiancheng Bioengineering Institute (Nanjing, China). Cell counting kit-8 (CCK-8) was obtained from Dojindo Laboratories (Kumamoto, Japan). Fetal bovine serum (FBS) and Gibco minimum essential medium α (α-MEM) were purchased from Thermo Fisher (Waltham, MA, USA).

2.2. Cell Culture and Treatment. The mouse calvaria-derived MC3T3-E1 osteoblasts were bought commercially from the National Collection of Authenticated Cell Cultures (Shanghai, China). Osteoblasts were seeded at 1×10^5 cells/mL into 75 cm^2 flasks, cultured in α-MEM supplemented with FBS (10%). The basic medium was replaced every three days. The growing conditions were at 37°C with 5% CO_2. There were four groups, including the control group, mic-PS group, mic-PS+H_2S group, and H_2S group. The concentration of H_2S released from GYY4137 was 100 μM.

Table 1: Sequences of primers used for the QPCR assay.

Gene	Primer sequences (5′ to 3′)
GAPDH	Forward: GAGAAACCTGCCAAGTATGATGAC
	Reverse: TAGCCGTATTCATTGTCATACCAG
Bmp4	Forward: CAACTCAACCAACCATGCCATTGTG
	Reverse: TTCAACACCACCTTGTCATACTCATCC
Myh6	Forward: TGGCACCGTGGACTACAACATTATG
	Reverse: CAGCAGAAGCATAGGTAGAGAAGAGTG
Actc1	Forward: GACTCTCTTCCAGCCCTCTTTCATTG
	Reverse: GGTGCCTCCAGATAGGACATTGTTG

2.3. Cell Viability Assay. MC3T3-E1 cells (1×10^4 cells/ml) were cultured in 96-well plates. Then they were incubated for 24 hours at 37°C. The cells were washed with phosphate-buffered saline (PBS), and the cell counting kit-8 (10 μl, at 10% dilution) was added in each well. After incubation, the absorbance was measured with the Multiskan MK3 microplate reader (Thermo Fisher). The mean optical density (OD) was conducted to count the cell viability (%) following the equation $(OD_{treatment}/OD_{control}) \times 100$. The cell viability assay in each group was repeated five times.

2.4. Measurement of Intracellular ROS Generation. MC3T3-E1 cells were incubated with 10 μM of 2′,7′-dichlorofluorescein (DCFH-DA) for 30 minutes at 37°C. Then, the cells were washed with PBS. The DCF fluorescence was visualized through a fluorescence microscope. The mean fluorescence intensity (MFI) indicated the amount of ROS in the intracellular environment. The measurements were performed by using the ImageJ software (version 1.8.0, Bethesda, Maryland, USA). The experiment was performed three times.

2.5. Examination of the Mitochondrial Membrane Potential (MMP). The MC3T3-E1 cells were incubated for 45 minutes at 37°C with Rh123 (2 μM). Then, the cells were washed with PBS. The fluorescence was then detected by a fluorescence microscope. The MFI of five random fields indicated the levels of MMP. The measurements were performed by using the ImageJ software (version 1.8.0).

2.6. mRNA Library Construction and Sequencing. The total RNA was isolated, purified, and next quantified by the NanoDrop ND-1000 spectrophotometer (Thermo Fisher Scientific, USA). The RNA integrity was assessed by Bioanalyzer 2100 (Agilent Technologies, CA) and later confirmed by gel electrophoresis. After purification from the total RNA (1 μg) with Dynabeads Oligo $(dT)_{25}$ (Thermo Fisher), the poly(A) RNA was fragmented through the Magnesium RNA Fragmentation Module (NEB, Ipswich, MA, USA). Then, the cleaved fragments were reverse transcribed through the SuperScript Reverse Transcriptase (Invitrogen, USA) and used to synthetize U-labeled, second-stranded

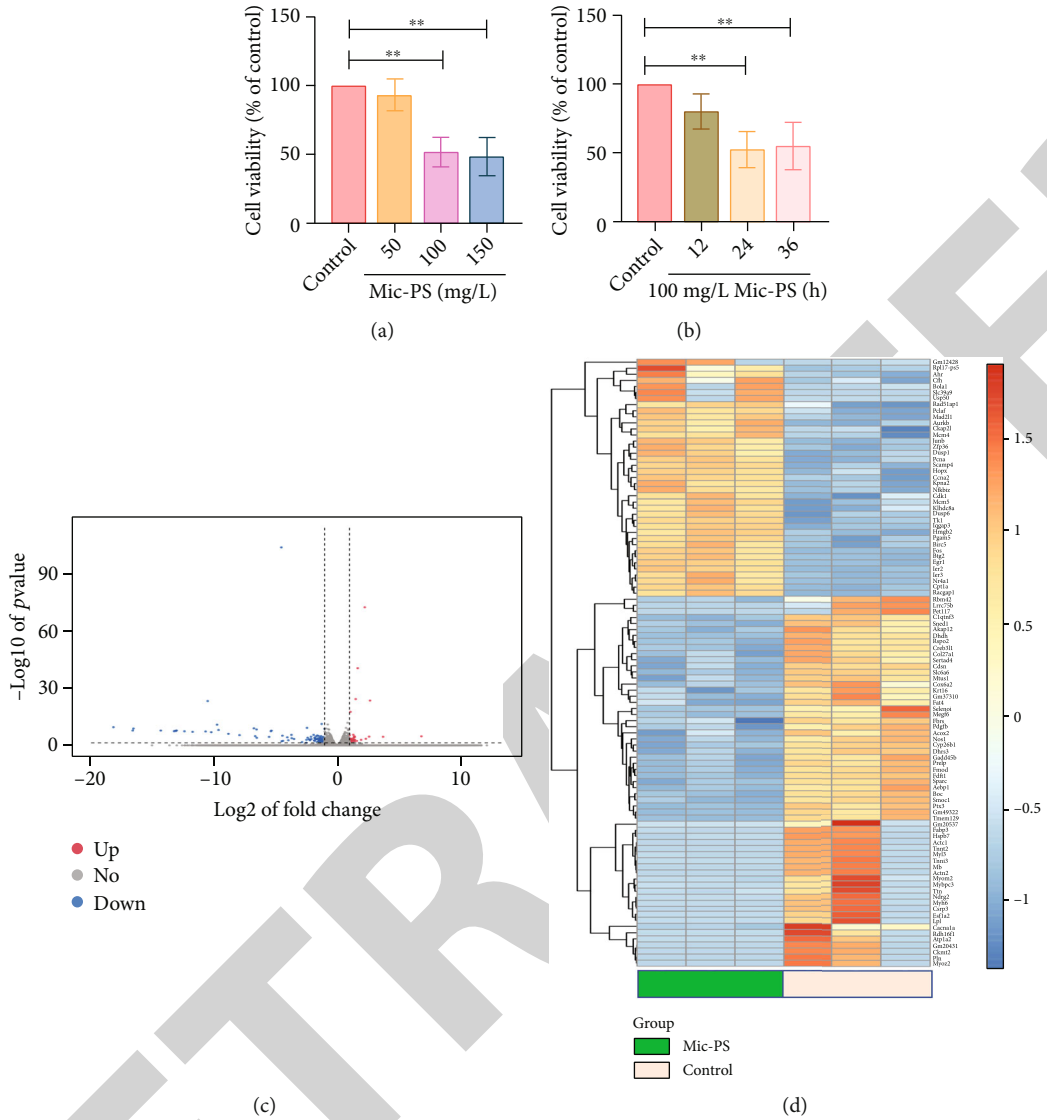

Figure 1: Cytotoxic effects of mic-PS in MC3T3-E1 cells. (a) Increasing concentrations (50, 100, and 150 mg/L) of mic-PS were added to MC3T3-E1 cells for 24 hours seeded in 96-well plate. (b) MC3T3-E1 cells were cultured with 100 mg/L mic-PS with different times. Continuous variables are displayed as mean ± standard error of the mean ($n = 5$) ($^{**}p < 0.01$ vs. control group). (c) Volcano plot visualizing the statistical difference of the DEGs. (d) Heatmap displaying the genes with the lowest p value.

DNA. The AMPure XP bead was used to perform the size selection. Later, the ligated products were expanded through the polymerase chain reaction (PCR). The denaturation was initially performed for 3 minutes at 95°C. Then, 8 cycles of denaturation were performed for 15 seconds at 98°C. The annealing was performed for 15 seconds at 60°C, with a following extension for 30 seconds at 72°C. The final extension was conducted at 72°C for 5 minutes. Regarding the final cDNA library, the average insert size was 300 ± 50 bp. The 2 × 150 bp paired-end sequencing (PE150) was done with the NovaSeq 6000 sequencing system (Illumina).

2.7. Quantitative Real-Time PCR (QPCR) Analysis. The total RNA of MC3T3-E1 cells was extracted and amplified using a SYBR Green based real-time PCR assay (Eppendorf, Germany). The PCR reaction was performed holding for 3 minutes at 95°C, then for 10 seconds at 95°C, for 30 seconds at 60°C, and for further 35 seconds at 72°C. The comparative cross threshold method was used to quantify the mRNA expression. The QPCR in each group was repeated three times. For primer sequences, see Table 1.

2.8. Statistical Analysis. Continuous variables are described as mean ± standard error of the mean (SEM). Comparisons were tested by one-way analysis of variance (ANOVA) followed by Dunnett's test using GraphPad Prism 8.0.2 software. A $p < 0.05$ was considered statistically significant.

3. Results

3.1. Cytotoxic Effects of Mic-PS in MC3T3-E1 Cells. To evaluate the cytotoxic effects of mic-PS in MC3T3-E1 cells, we treated the cells with different times and concentrations. As shown in Figure 1(a), MC3T3-E1 cells were exposed to

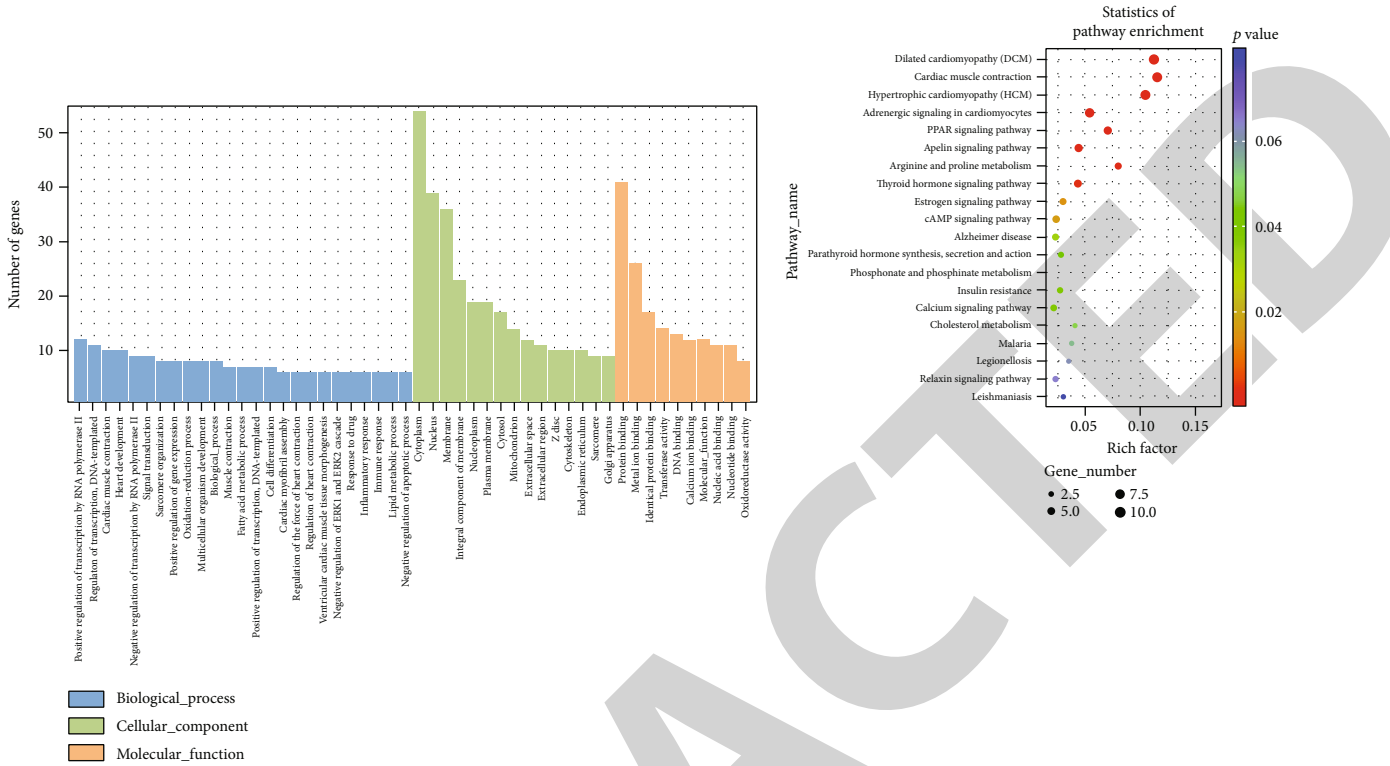

Figure 2: GO enrichment analysis and KEGG enrichment analysis. (a) GO terms significantly enriched in DGEs of mic-PS vs. control ($p < 0.05$). (b) KEGG analyses showed top twenty regulated pathways in MC3T3-E1 cells with 100 mg/L mic-PS compared to control group. p values were shown through different color. The sizes of the bubble indicate the gene count for each pathway.

increasing concentrations of mic-PS with the same 24 hours. Mic-PS at 50 mg/L showed no significant effects on cell viability ($p > 0.05$). Mic-PS at 100 and 150 mg/L displayed toxic effects on MC3T3-E1 cells ($p < 0.01$), with no statistical difference between the two concentrations ($p > 0.05$). Remarkably, both concentrations lead to a decline in cell viability to almost 50% compared to the control group ($p < 0.01$). Therefore, mic-PS at 100 mg/L was used in the following time-response experiment (Figure 1(b)). Exposed MC3T3-E1 cells to mic-PS for 24 hours and 36 hours induced considerable cytotoxicity; the maximum decrease in cell viability was observed at 24 h ($p < 0.01$). In accordance with the above results, the MC3T3-E1 cells were cultured with mic-PS at 100 mg/L for 24 h in the following experiments.

3.2. Mic-PS Treatment Induced Gene Expression Change in MC3T3-E1 Cells. Next, to further investigate the different gene expressions that occur between the mic-PS and control groups, RNA-seq was conducted. There were 147 differentially expressed genes (DEGs) (absolute Log2 fold change ≥ 1, $p \leq 0.05$). Among them, 103 genes were downregulated, while 44 genes were upregulated (Figure 1(c)). The top 100 genes with the lowest p value were further evaluated by hierarchical clustering analysis (Figure 1(d)). This analysis showed a clear distinction between the mic-PS and control groups.

3.3. The Gene Ontology (GO) Enrichment Analysis and Kyoto Encyclopedia of Genes and Genomes (KEGG) Enrichment Analysis. GO biological process (GO-BP), GO cellular component (GO-CC), and GO molecular function (GO-MF) were the three sections of the GO enrichment analysis (Figure 2(a)). According to the three parts of the GO analysis, the upregulated and downregulated DEGs were functionally categorized, especially regulation of transcription, inflammatory response, protein binding, oxidation-reduction process, and apoptotic. A biological pathway distribution was observed in KEGG enrichment analysis between the mic-PS and control groups (Figure 2(b)). There were several signaling pathways influenced by mic-PS, including peroxisome proliferator-activated receptors (PPAR), arginine and proline metabolism, thyroid hormone metabolism, estrogen metabolism, cyclic adenosine monophosphate (cAMP), phosphonate and phosphinate metabolism, and calcium signal transduction pathway. The signaling pathways are probably related to oxidative stress resistance, energy metabolism, osteoblast differentiation, and bone formation. Thus, the regulated oxidative stress resistance and mitochondrial ATP energy metabolism might be the determinative mechanism linking mic-PS to dysfunction in MC3T3-E1 cells.

3.4. Exogenous H_2S Reduced Mic-PS-Induced Cytotoxicity in MC3T3-E1 Cells. As described in Figure 3(a), exposure of MC3T3-E1 cells to 100 mg/L mic-PS for 24 hours induced

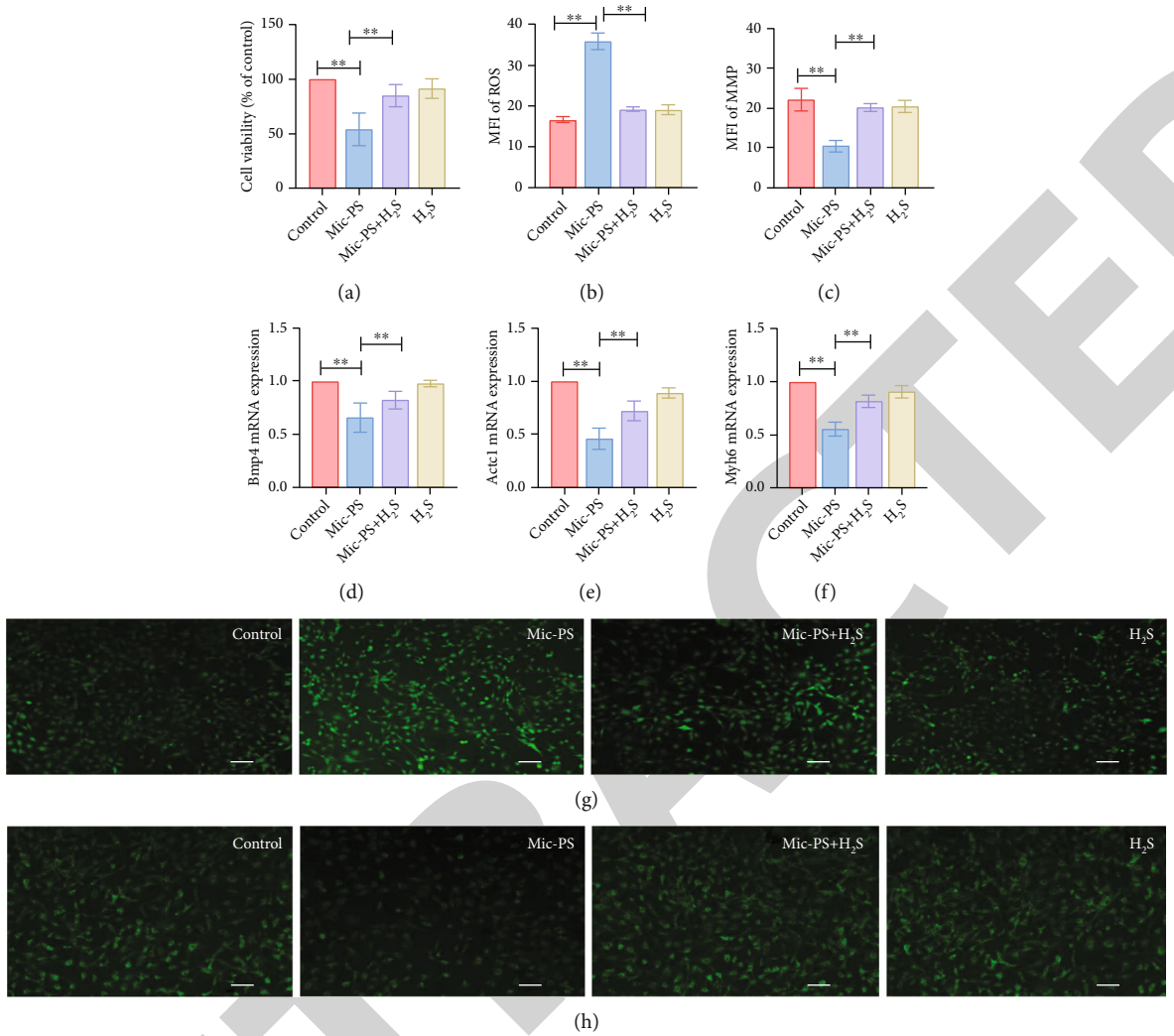

Figure 3: Exogenous 100 μM H_2S reduced 100 mg/L mic-PS-induced toxicity in MC3T3-E1 cells. (a) Cell viability evaluated through the CCK-8 assay. (b) Quantitative analysis for the MFI of DCFH-DA in different groups. (c) Quantitative analysis for the MFIs of Rh123 in different groups. (d–f) Expression of different mRNAs in different groups was tested by QPCR. (d) *Bmp*4, (e) Actc1, and (f) *Myh*6. (g, h) Representative fluorescent photographs of assessing the intracellular ROS/MMP level in different groups. (g) ROS and (h) MMP. Continuous variables are displayed as mean ± standard error of the mean ($n = 5$). $^{**}p < 0.01$. Scale bar: 100 μm.

considerable cytotoxicity ($p < 0.01$). When cells were treated with H_2S at 100 μM, 24 hours, they are markedly ameliorated from mic-PS injury ($p < 0.01$). We evaluated the effects of H_2S and mic-PS on ROS levels in MC3T3-E1 cells. As expected, mic-PS elevated ROS levels, but the effect was reversed by H_2S ($p < 0.01$) (Figures 3(b) and 3(g)). Similar findings were obtained with the MMP. The mic-PS exposure reduced MMP ($p < 0.01$). On the contrary, H_2S treatment alleviated ($p < 0.01$) the reduced MMP mediated by mic-PS (Figures 3(c) and 3(h)). The above results revealed that exogenous H_2S inhibits mic-PS-induced cytotoxicity, oxidative stress, and dissipation of MMP damage.

3.5. Exogenous H_2S Increased the Mitochondrial Damage-Related Gene Expression. According to the bioinformatic analysis and above results, we chose bone morphogenetic protein 4 (*Bmp4*), alpha cardiac muscle 1 (*Actc1*), and myosin heavy polypeptide 6 (*Myh6*) as the potential candidate genes. To verify whether these three genes are involved in H_2S signaling pathway, mRNA expression was tested by QPCR. Expression of these three gene expressions decreased in the mic-PS group, while exogenous H_2S increased a certain extent of these three genes ($p < 0.01$, Figures 3(d)–3(f)). Besides, we observed that mic-PS treatment most affected the Actc1 gene expression, while the effect of mic-PS on *Bmp4* expression was comparable minimal. These results suggested that H_2S increases *Bmp4*, *Actc1*, and *Myh6* expressions to mitigate mic-PS-induced oxidative stress and mitochondrial damage in osteoblastic cell.

4. Discussion

Since the durability and indecomposable features of plastics as discarded pollutants, the plastic contaminants have risen dramatically worldwide. 322 million tons were produced in

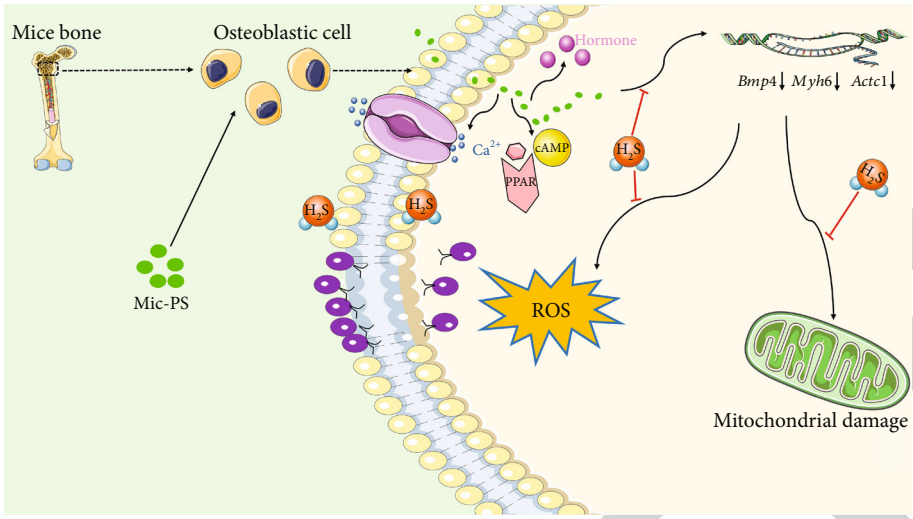

Figure 4: Proposed mechanistic schematic diagram of H_2S mitigates mic-PS-induced oxidative stress and mitochondrial damage in mouse osteoblastic cell.

2015 [11], while it will increase by 33 billion tons in 2050 as predicted [12]. Mic-PS can be detected everywhere, including human biological samples. Thus, it is meaningful to study the toxicity of mic-PS in mammals. Previous data have shown that mic-PS induces intestinal microbial growth, reproductive toxicity, metabolic disorders, and intestinal barrier dysfunction in mice [13, 14]. Nevertheless, little is known about mic-PS effects on mouse bone metabolism. In this study, we found that mouse osteoblastic cell activity declined after being exposed to mic-PS. RNA-seq analysis showed 147 differentially expressed genes between the mic-PS and control groups. Furthermore, we proved that exogenous H_2S could increase the related gene expression to reduce mic-PS-induced oxidative stress and mitochondrial injury (Figure 4).

The bioinformatic analysis was subsequently performed to evaluate the toxicity of mic-PS in mouse osteoblastic cell through GO and KEGG databases. GO analysis indicates that exposure to mic-PS significantly affected biological processes such as transcription, inflammatory response, protein binding, oxidation-reduction process, and apoptotic. Currently studies suggest that inducing oxidative stress was the relevant effect of mic-PS toxicity [15, 16]. Xu et al. researched on human lung epithelial cells; they proved that mic-PS significantly affect the cell viability via inducing significant upregulation of proinflammatory and proapoptotic proteins, including TNF-α, IL-8, caspase-3, caspase-8, and caspase-9 [17]. Based on the KEGG databases in our study, involving peroxisome proliferator-activated receptors (PPAR), arginine and proline metabolism, thyroid hormone, estrogen, cyclic adenosine monophosphate(cAMP), phosphonate and phosphinate metabolism, and calcium pathway were significantly enriched pathways for DEGs. PPAR signaling pathway was also observed in exposure to MPs on grass carp through KEGG enrichment analysis [18]. PPARs are transcription factors that regulate the expression of genes involved in energy and lipid metabolism; it is interesting that activation of PPARδ improves mitochondrial function [19]. Presently, Sun et al. reported that Jak/Stat pathway, nicotinamide metabolism, and unsaturated fatty acids are associated with mic-PS-mediated toxicity in the mouse hematological system; furthermore, they found that decreased Nnt is possibly correlated with reduced antioxidant power and mitochondrial damage after mic-PS exposure [20]. Oxidative stress and mitochondrial metabolic changes are closely related to osteogenic capacity. Mitochondrial dysfunction and ROS rise induced osteoblast senescence and osteoblast activity [21] and led to type 2 diabetic osteoporosis [22]. Proanthocyanidins and notoginsenoside R1 treatments reduced ROS level and weakened mitochondrial dysfunction to improve osteoblast activity [23, 24]. These studies suggest that oxidative stress and disturbances in mitochondrial metabolism are targets for improving osteogenic capacity. Hence, the change of oxidative stress and mitochondrial metabolism was selected for further toxicity mechanism caused by exposure to mic-PS in this research.

To validate of the potential of the change of oxidative stress and mitochondrial metabolism after mic-PS exposure, we then performed experiments in vitro. The mic-PS exposure significantly elevated oxidative stress, as well as dissipated MMP, while exogenous H_2S mitigated mic-PS-induced oxidative and mitochondrial injury. Presently, accumulating evidence has demonstrated that Bmp4, Actc1, and Myh6 are closely related to homeostasis of mitochondria and redox reactions [25–27]. Especially, BMP4 is a group of bone growth factors firstly identified because of their capability to enhance bone and cartilage formation. As a result, these three genes (*Bmp4*, *Actc1*, and *Myh6*) were selected. We next used QPCR to test our findings. We observed that the downward trend of QPCR results in the mic-PS group was essentially comparable with the sequencing analysis. A similar alteration of *Bmp4* and *Myh5* had also been observed in zebrafish exposed to mic-PS (100 μg/L) [28]. However, Bhagat et al. described upregulation of bmp4 in zebrafish embryos when exposed to polystyrene

nanoplastics (1 mg/L) and azole fungicides (ketoconazole and fluconazole) [29]. Different size and concentration of mic-PS should be considered in making the results. Meanwhile, experimental results of Umamaheswari et al. indicated that mic-PS exposure upregulated the gstp1, hsp70l, and ptgs2a gene expressions, while it downregulated cat, sod1, gpx1a, and ache genes, illustrating the potential of mic-PS to mediate different degrees of toxic effects in aquatic animals through changing ROS medicated oxidative stress altering its metabolic process, histological architecture, and gene regulatory modes [30].

Of note, in a range of biological mechanisms, exogenous H_2S has essential physiological and pathological impacts. According to a recent study, exogenous H_2S protects osteoblastic cells from H_2O_2-induced cell oxidative stress injury [31]. In this study, the findings supported the inhibitory effect of exogenous H_2S on mic-PS-induced mitochondrial damage and oxidative stress in mouse osteoblastic cells. In addition, exogenous H_2S considerably increases the alleviated expression of *Bmp4*, *Actc1*, and *Myh6* derived from mic-PS. The mechanisms underlying mic-PS-induced oxidative stress and mitochondrial damage could be complex and diverse. Mic-PS has been shown to reduce the activity of glutathione S-transferases, limiting detoxification and resulting in ROS generation [32]. Moreover, it is generally acknowledged that H_2S is associated with increasing glutathione S-transferase transcript level. Recently, a study has demonstrated that H_2S suppressed inflammation and oxidative stress induced by mic-PS in mouse liver via upregulated Keap1-Nrf2 pathway [10]. Notably, *Bmp4*, *Actc1*, and *Myh6* were reported to be associated with glutathione S-transferases. Reportedly, exogenous H_2S improved the *BMP4* expression in rat pulmonary arterial smooth muscle cells [33]. Thus, these results indicate that exogenous H_2S may relieve mic-PS toxicity by altering *Bmp4*, *Actc1*, and *Myh6* expressions associated with mitochondrial oxidative stress.

The study has two main limitations. First, the effect of exogenous H_2S and mic-PS needs to be explored in vivo. Second, the downstream signaling pathways regulated by H_2S in mic-PS-induced injury need to find in further exploration.

5. Conclusion

In conclusion, we used RNA-seq and validation experiment at molecular and cellular levels to demonstrate that mic-PS (100 mg/L) caused a significant toxicity in osteoblastic cells in mice (an advanced mammal), while exogenous H_2S may considerably mitigate mic-PS-induced oxidative stress and mitochondrial damage through increasing *Bmp4*, *Actc1*, and *Myh6* expressions. Our research unveiled the bone toxicity effects of mic-PS and provides novel insights in the mechanism of exogenous H_2S protective function in mic-PS-induced bone injury.

Data Availability

The research data are available upon request.

Conflicts of Interest

All authors declare they have no conflict of interest.

Authors' Contributions

Qingping Shi and Feihong Chen contributed equally to this work.

Acknowledgments

This research was supported by the Natural Science Foundation of Guangdong Province, China (No. 2015A030313872).

Supplementary Materials

Supplementary 1. Table S1: data used for CCK8 with different concentrations of mic-PS.

Supplementary 2. Table S2: data used for CCK8 with different times of mic-PS.

Supplementary 3. Table S3: data used for CCK8/ROS/MMP.

Supplementary 4. Table S4: data used for QPCR analysis.

References

[1] C. J. Moore, "Synthetic polymers in the marine environment: a rapidly increasing, long-term threat," *Environmental Research*, vol. 108, no. 2, pp. 131–139, 2008.

[2] K. L. Law and R. C. Thompson, "Microplastics in the seas," *Science*, vol. 345, no. 6193, pp. 144-145, 2014.

[3] J. Gigault, A. T. Halle, M. Baudrimont et al., "Current opinion: what is a nanoplastic?," *Environmental Pollution*, vol. 235, pp. 1030–1034, 2018.

[4] L. A. Amaral-Zettler, E. R. Zettler, B. Slikas et al., "The biogeography of the plastisphere: implications for policy," *Frontiers in Ecology and the Environment*, vol. 13, no. 10, pp. 541–546, 2015.

[5] M. A. Browne, A. Dissanayake, T. S. Galloway, D. M. Lowe, and R. C. Thompson, "Ingested microscopic plastic translocates to the circulatory system of the mussel, Mytilus edulis (L)," *Environmental Science & Technology*, vol. 42, no. 13, pp. 5026–5031, 2008.

[6] N. von Moos, P. Burkhardt-Holm, and A. Kohler, "Uptake and effects of microplastics on cells and tissue of the blue mussel *Mytilus edulis* L. after an experimental exposure," *Environmental Science & Technology*, vol. 46, no. 20, pp. 11327–11335, 2012.

[7] R. Sussarellu, M. Suquet, Y. Thomas et al., "Oyster reproduction is affected by exposure to polystyrene microplastics," *Proceedings of the National Academy of Sciences of the United States of America*, vol. 113, no. 9, pp. 2430–2435, 2016.

[8] Y. Deng, Y. Zhang, R. Qiao et al., "Evidence that microplastics aggravate the toxicity of organophosphorus flame retardants in mice (*Mus musculus*)," *Journal of Hazardous Materials*, vol. 357, pp. 348–354, 2018.

[9] Y. Deng, Y. Zhang, B. Lemos, and H. Ren, "Tissue accumulation of microplastics in mice and biomarker responses suggest widespread health risks of exposure," *Scientific Reports*, vol. 7, no. 1, article 46687, 2017.

Hindawi
Disease Markers
Volume 2023, Article ID 4397829, 21 pages
https://doi.org/10.1155/2023/4397829

Research Article

Endothelial Progenitor Cells Affect the Growth and Apoptosis of Renal Cells by Secreting Microvesicles Carrying Dysregulated miR-205 and miR-206

Yunbo Zhang,[1] Yanling Shen,[2] Yanling Song,[1] Yunyun Lin,[1] Ying Wang,[1] Minghui Chen,[1] Huade Mai,[1] and Shenhong Gu [1,3]

[1]*Department of General Practice, The First Affiliated Hospital of Hainan Medical University, Hainan 570102, China*
[2]*Hainan Medical University, Hainan 570000, China*
[3]*Key Laboratory of Tropical Cardiovascular Diseases Research of Hainan Province, Hainan 570102, China*

Correspondence should be addressed to Shenhong Gu; renee388@163.com

Received 19 September 2022; Revised 28 October 2022; Accepted 24 January 2023; Published 16 February 2023

Academic Editor: Fu Wang

Background. This study investigated the mechanism of microRNA (miRNA, miR) in microvesicles (MVs) secreted by endothelial progenitor cells (EPCs) involved in renal function in vivo and in vitro injury repair of rat primary kidney cells (PRKs). *Methods*. Gene Expression Omnibus analysis of potential target miRNAs in nephrotic rats. Real-time quantitative polymerase chain reaction verified the correlation of these miRNAs and screened the effective target miRNAs and their downstream putative target mRNAs. Western blot analyzes the protein levels of DEAD-box helicase 5 (DDX5) and the activation of the proapoptotic factor caspase-3/9 (cleaved). Dil-Ac-LDL staining, immunofluorescence, and a transmission electron microscope (TEM) were used to identify the successful isolation of EPCs and PRKs and the morphology of MVs. Cell Counting Kit-8 was used to detect the effect of miRNA-mRNA on the proliferation of PRKs. Standard biochemical kits were used to detect biochemical indicators in rat blood and urine. Dual-luciferase analysis of miRNA binding to mRNA was conducted. The effect of miRNA-mRNA interaction on the apoptosis level of PRKs was analyzed by flow cytometry. *Results*. A total of 13 rat-derived miRNAs were potential therapeutic targets, and miR-205 and miR-206 were screened as the targets of this study. We found that the EPC-MVs alleviated the increase of blood urea nitrogen and urinary albumin excretion and the decrease in creatinine clearance caused by hypertensive nephropathy in vivo. The effect of MVs in improving renal function indicators was promoted by miR-205 and miR-206 and inhibited by knockdown of expressed miR-205 and miR-206. In vitro, angiotensin II (Ang II) promoted growth inhibition and apoptosis of PRKs, and similarly, dysregulated miR-205 and miR-206 affected the induction of Ang II. We then observed that miR-205 and miR-206 cotargeted the downstream target DDX5 and regulated its transcriptional activity and translational levels, while also reducing the activation of proapoptotic factors caspase-3/9. Overexpressed DDX5 reversed the effects of miR-205 and miR-206. *Conclusion*. By upregulating the expression of miR-205 and miR-206 in MVs secreted by EPC, the transcriptional activity of DDX5 and the activation of caspase-3/9 can be inhibited, thereby promoting the growth of PRKs and protecting the injury caused by hypertensive nephropathy.

1. Introduction

The kidney is one of the major organs affected by hypertensive target organ damage [1, 2]. Hypertensive nephropathy (HN) is clinically characterized by progressive renal fibrosis and inflammation [3, 4], and prolonged hypertension can eventually lead to renal failure [4]. However, the current treatment of HN is still at the level of eliminating symptoms, and the research on the pathogenesis of HN is still unclear. It is generally believed that urinary albumin excretion (UAE) > 20 mg/24 h in Spontaneous Hypertension Rat (SHR) can be considered HN.

Endothelial progenitor cells (EPCs) are a type of stem cells with angiogenic and tissue repair capabilities [5].

Evidence shows that endothelial progenitor cells can improve renal function in patients with diabetic nephropathy [6], possibly because of the beneficial therapeutic effects of endothelial progenitor cell-derived microvesicles (MVs) in various diseases [7]. Many reports have confirmed that the protective effect of EPCs is closely related to the release of MVs [8]. The MVs secreted by EPCs can be absorbed by cells, thereby reducing damage [9] and repairing tissues [10]. The properties of EPC-MVs are similar to those of EPCs. However, the underlying molecular mechanism of EPC repairing renal injury through MVs is still unclear.

MicroRNAs (miRNA, miR) are small noncoding RNAs involved in the progression and treatment of various diseases including HN [11, 12]. Evidence suggests that MVs can ameliorate renal injury by delivering miRNAs [13, 14]. It is well known that dysregulated miRNAs can affect the occurrence and development of various diseases [15, 16], including HN [17]. miRNAs affect renal function by binding to the 3′-UTR of downstream mRNAs and regulating mRNA transcription and translation [18, 19]. The levels of angiotensin II (Ang II) and its receptors in the kidneys of hypertensive rats are much higher than those of Wistar-Kyoto (WKY) rats [20]. Ding et al. believed that angiotensin II-mediated urinary albumin, blood urea nitrogen (BUN), and creatinine clearance (Scr) can be improved by miR-101a by blocking nuclear factor kappa-B signaling [3]. Downregulated miR-205 was positively correlated with BUN and creatinine (Cr) levels in patients with renal injury [21]. After overexpression, miR-205 attenuated sepsis-induced acute kidney injury [22]. miR-206 binds to DEAD-box helicase 5 (DDX5) to inhibit the activation of NLR family pyrin domain containing 3 inflammasome and alleviate acute kidney injury [23].

These proteases, cysteinyl aspartate-specific proteinase (caspase) family of cysteine proteases, are key enzymes that cause apoptosis; once the caspase is activated, a cascade of caspase ensues, eventually leading to apoptosis. Evidence shows that, as important members of the caspase family, the activation of caspase-3 and caspase-9 is the key to affecting renal cell apoptosis [24, 25] and promotes the extent of damage to kidney cells in response to Ang II, chemotherapy drugs, or oxidative stress [26–28].

Studies have shown that renal injury caused by hypertension is related to the activation of the apoptosis pathway (caspase-3/9) [29]. Kidney tissue damage can be significantly alleviated and prevented by reducing the activity of apoptotic proteins such as cleaved caspase-9 and cleaved caspase-3 [30]. Proteins that promote apoptosis can exacerbate kidney damage caused by inflammation, oxidative stress, or high blood sugar and hypertension [31–33]. This study attempts to explore the mechanism by which miR-205 and miR-206 protect the kidneys from damage caused by hypertension from the perspective that EPC-MVs can carry dysregulated miRNAs to affect disease.

2. Methods

2.1. Animals. The study was conducted in accordance with the Declaration of Helsinki (as revised in 2013). Six Wistar-Kyoto- and SHR- (male, 10-week-old) specific pathogen-free rats weighing 300-330 g were obtained from the Beijing Vital River Laboratory Animal Technology Co. Ltd (Beijing, China). Wistar-Kyoto rats were used as the control group, and SHR rats as the model group. All rats were placed in a room with 12 h light/dark cycle, the temperature was maintained at 25°C, and the humidity was maintained at 55%; rats have ad libitum access to standard rat food and water in a polystyrene cage. At the end of the experiment, the rats were sacrificed by intraperitoneal injection of sodium pentobarbital (200 mg/kg body weight). Animal experiments were approved by the Animal Care and Use Committee of Hainan Medical University (Haikou, China, approval no. HYLL-2021-053) and were conducted according to the National Institutes of Health guidelines.

2.2. Biochemical Analysis of Blood and Urine. On the day before blood sample collection, urine samples were continuously collected from each animal for 24 hours. Blood urea nitrogen (BUN), serum creatinine (Scr), and UAE were measured by standard biochemical kits (BHKT Clinical Reagent Co., Ltd., Beijing, China). Creatinine clearance (CCr) was calculated according to the following formula: CCr = urinary creatinine (mg/ml) × urine output (ml/kg)/plasma creatinine (mg/ml) [34].

2.3. Gene Expression Omnibus (GEO) Analysis. The dataset GSE110231 was downloaded and analyzed from the GEO website (https://www.ncbi.nlm.nih.gov/geo/), which included 3 healthy SD rats (GSM2983040, GSM2983041, and GSM2983042) and 3 diabetic rats (GSM2983037, GSM2983038, and GSM2983039). Use Gene Expression Profiling Interactive Analysis 2 (http://gepia2.cancer-pku.cn/#index) to analyze the differential expression of miRNA, and the criteria for differential expression are as follows: $p < 0.05$ and $\log_2|fold\ change| \geq 2$.

2.4. Real-Time Quantitative Polymerase Chain Reaction (RT-qPCR). According to the manufacturer's instructions, PRKs, EPCs, and MVs were extracted using Trizol reagent (Invitrogen, Thermo Fisher Scientific, Inc.). After 10 minutes of centrifugation (13,000 × g, 4°C) using JIDI-17RS refrigerated centrifuge (Guangzhou JIDI Instrument Co., Ltd, Guangzhou, China), RNA was reverse-transcribed with PrimeScript RT kit (Takara Bio, Japan). SYBR® Premix Ex TaqTM II kit (Takara Bio) was used for RT-qPCR analysis using the Applied Biosystems®7500 Real-Time PCR system (CA, USA). PCR experiments were carried out under the following conditions: 50°C for 25 min, 94°C for 2 min, followed by 25 cycles of 94°C for 30 s, 60°C for 30 s, and 72°C for 2 min. The primer sequences of miR-205, miR-206, and DDX5 used for RT-qPCR are shown in Table 1. Target RNA levels were normalized to those of the housekeeping genes U6 or β-actin, and relative levels of miR-205, miR-206, and DDX5 expression were determined using the $2^{-\Delta\Delta Ct}$ method [35].

2.5. Culture and Identification of EPCs. After dissociation of rat femur and tibia, the mixture was rinsed with sterile PBS and collected. Following centrifugation at 4°C (1000 × g,

Table 1: Sequences of RT-qPCR primer.

Gene symbol	5′–3′
miR-1-3p forward	ACACTCCAGCTGGGTGGAATGTAAAGAAGT
miR-9a-5p forward	ACACTCCAGCTGGGTCTTTGGTTATCTAGCT
miR-98-5p forward	ACACTCCAGCTGGGTGAGGTAGTAAGTTGT
miR-205 forward	ACACTCCAGCTGGGTCCTTCATTCCACCGGA
miR-206 forward	ACACTCCAGCTGGGTGGAATGTAAGGAAGT
miR-216a-3p forward	ACACTCCAGCTGGGCACAGTGGTCTCTGGG
miR-451-5p forward	ACACTCCAGCTGGGAAACCGTTACCATTAC
miR-466b-5p forward	ACACTCCAGCTGGGTATGTGTGTGTGTATG
miR-490-3p forward	ACACTCCAGCTGGGCAACCTGGAGGACTCC
miR-743b-3p forward	ACACTCCAGCTGGGGAAAGACACCATACTG
miR-881-3p forward	ACACTCCAGCTGGGTAACTGTGGCATTTCT
miR-1949 forward	ACACTCCAGCTGGGTATACCAGGATGTCAGC
miR-219a-2-3p forward	ACACTCCAGCTGGGAGAATTGTGGCTGGAC
Universal reverse primer for miRNA	CTCAACTGGTGTCGTGGA
U6 forward	CTCGCTTCGGCAGCACA
U6 reverse	AACGCTTCACGAATTTGCGT
DDX5 forward	CGACCAAAACCCGTCAAAGG
DDX5 reverse	CCGAAGCTGCACTACGGAA
β-Actin forward	CACCCGCGAGTACAACCTTC
β-Actin reverse	CCCATACCCACCATCACACC

DDX5: DEAD-box helicase 5; RT-qPCR: real-time quantitative polymerase chain reaction; miR: microRNA.

5 min), EPCs were isolated by Ficoll (Sigma-Aldrich) density gradient centrifugation (1000 × g) and incubated at 37°C and 5% CO_2 with Endothelial Cell Growth Basal Medium-2 (EGM-2; Lonza, Basel, Switzerland), and the medium was changed after 24 hours. After 4 days, the medium was changed and the adherent cells were cultured for another 3 days [36]. Dil-Ac-LDL (SolarBio, Beijing, China) and PI (Solarbio) costaining were used to identify EPCs.

2.6. Preparation and Characterization of EPC-MVs. EPCs were cultured for 7 days as before, washed twice with PBS, and then serum starved for 12 h. Subsequently, EGM-2 medium containing cultured EPCs was centrifuged at 4°C (1000 × g, 15 min), and the supernatant was extracted at 4°C (100 000 × g, 60 min) for the collection of secreted EPC microvesicles. Transmission electron microscopy (TEM) was used to observe whether the collected MVs had double-membrane vesicle-like bodies. After centrifuging the collected medium supernatant at 4°C (1000 × g, 15 min), take the supernatant and extract the supernatant at 4°C (100 000 × g, 60 min) to collect MVs. Extraction of MVs was verified using transmission electron microscopy (TEM). In the coculture system, 50 μg/ml EPC-MVs were added to the top chamber of a transwell assay plate, and PRKs were added to the bottom chamber and incubated for 24 h [37].

2.7. Isolation and Culture of PRKs. As shown in our previous study, PRKs were successfully isolated and cultured [37]. Briefly, rat kidney tissue was isolated, a portion was used for RT-qPCR analysis, and a portion of the renal cortex was cut into tissue fragments of approximately ~1 mm^3. Tissue fragments were digested with collagenase type I (Gibco; Thermo Fisher Scientific, Inc.), and cells were isolated by Ficoll (Sigma-Aldrich; Merck KGaA) density gradient centrifugation, seeded in 6-well plates, and incubated at 37°C and 5% CO_2. After 24 h, the medium was removed and replaced with fresh medium. Immunofluorescence (IF) identification of PRKs was conducted. In short, PRKs were incubated for 3 passages with α-smooth muscle actin (α-SMA; 1 μg/ml; cat. no. ab7817; Abcam, Cambridge, England) and vimentin (1 : 250; cat. no. ab92547; Abcam) at 4°C overnight, then treated with Alexa Fluor® 488- (1 : 100; cat. no. ab150077; Abcam) or 647-labeled (1 : 200; cat. no. ab150075; Abcam) secondary antibodies for 1 hour at 37°C. Finally, cells were stained with DAPI (0.5 μg/ml; Solarbio) for 5 min at 25°C. Finally, images were captured using a fluorescence microscope (magnification, ×400; Leica Microsystems GmbH). PRK injury model was constructed by treating with Ang II (1 μM; Sigma-Aldrich) at 37°C for 24 h.

2.8. Cell Transfection. Transfect miR-205, miR-206 agomiR/antagomiR, overexpression (ov) DDX5 plasmid, and their negative control (NC) into PRKs or EPCs with Lipofectamine 3000 (Invitrogen) according to the manufacturer's instructions, and incubate in the dark for 4 hours (37°C, 5% CO_2). After changing the medium for 24 or 48 hours, collect the cells or supernatant for further processing. All RNAs were purchased from Sangon Biotech Co., Ltd (Shanghai, China), and their sequences are shown in Table 2.

Table 2: A list of miRNA's sequences.

Gene symbol	Sequences
agomiR-NC	UGCAUCACUCGUUGCGUCCUAUC
antagomiR-NC	GACTTAAGGAAGGTAGCCGGAAC
agomiR-205	UCCUUCAUUCCACCGGAGUCUGU
antagomiR-205	ACAGACTCCGGTGGAATGAAGGA
agomiR-206	UGGAAUGUAAGGAAGUGUGUGG
antagomiR-206	CCACACACTTCCTTACATTCCA

RT-qPCR: real-time quantitative polymerase chain reaction; miR: microRNA; NC: negative control.

2.9. EPC-MVs and PRK Fusion. EPC-MVs (50 g/ml) were combined with 2 ml PKH26 (2×10^{-6} M; Sigma-Aldrich) and incubated at 25°C for 5 min. After centrifugation (4°C, 120,000 × g, 60 min), the pellet was resuspended in EGM-2 medium, then added to PRK, and incubated at 37°C for 24 hours. Finally, add 1 μg/ml DAPI for nuclear staining at 25°C for 15 minutes. Cell images were acquired using a fluorescence microscope (magnification, ×400).

2.10. Cell Proliferation Assays. According to the manufacturer's instructions, 10 μl of Cell Counting Kit-8 reagent (CCK-8, Solarbio) was added to PRKs at 0 h and 24 h, respectively, and incubated for 1 h. The optical density at 490 nm was then measured with a microplate reader (Multiskan MK3, Thermo Fisher Scientific, Inc.) to assess the cell proliferation rate.

2.11. Western Blotting. After lysis of PRKs or MV with radio immunoprecipitation assay lysis buffer, the lysate protein concentration was determined using a bicinchoninic acid protein detection kit (Solarbio) and resolved using 10% SDS-polyacrylamide gel electrophoresis (Solarbio). Protein bands were transferred onto a polyvinylidene fluoride membrane, blocked with 5% BSA (Solarbio), and incubated with CD63 (1 : 1000; ab134045, Abcam), CD81 (1 : 1000; ab109201, Abcam), Tsg101 (1 : 1000; ab125011, Abcam), DDX5 (1 : 1000; ab128928, Abcam), cleaved caspase-3 (1 : 500; ab32042, Abcam), and cleaved caspase-9 (1 : 1000; 9505T, Cell Signaling Technology Co., LTD; Danvers, Massachusetts, USA) primary antibodies overnight (4°C). Then, they were rinsed with TBST buffer (Solarbio, contains 0.05% Tween-20) twice, for 10 min each time, and incubated with the secondary antibody for 90 min at 25°C. Subsequently, use ECL (enhanced chemiluminescence) reagent for chemiluminescence reaction. Finally, they were developed and fixed using Developer and Fixer Kit (Beyotime, Shanghai, China).

2.12. Dual Luciferase. The miRDB database (http://mirdb.org/) was used to predict binding sites between miR-205 or miR-206 and DDX5. PRKs were transfected with miR-205 or miR-206 and their negative controls, vector plasmid containing wild-type (WT) or mutant (mut) DDX5, and pRL-SV40 reporter vector plasmid. Transfected cells were incubated for 48 h, and luciferase activity was measured at 490 nm according to dual-luciferase reporter assay system (Promega, USA) instructions.

2.13. Detection of Cell Apoptosis Using Flow Cytometry (FCM). A dose of 5 μl of Annexin V-Fluorescein Isothiocyanate (FITC; BD Biosciences, CA, USA) and 10 μl of Propidium Iodide (PI; BD Biosciences) was incubated with PRKs (0.4×10^5 cells/ml) in the dark (25°C, 15 min), then rinsed twice with PBS (Gibco; Thermo Fisher Scientific, Inc.).

2.14. Statistical Analyses. All experiments were repeated three times. Data are expressed as the mean ± standard deviation (SD). Differences between multiple groups were assessed using one-way analysis of variance and Bonferroni post hoc test. Student's *t*-test was used for independent two-group analyses. Statistical significance was set at $p < 0.05$.

3. Results

3.1. Screening of Potential Therapeutic miRNAs. After continuous feeding of SHR rats for 4 weeks, the UAE of SHR rats was significantly higher than that of normal rats, and the UAE value was 39.27 ± 9.07 mg/24 h, which reached the standard of HN model (Figure 1(a)). Through GEO analysis of the GSE110231 dataset, it was found that there were 13 differentially expressed rat-derived miRNAs (Figure 1(b)), namely, miR-1-3p, miR-9a-5p, miR-98-5p, miR-205, miR-206, miR-216a-3p, miR-451-5p, miR-466b-5p, miR-490-3p, miR-743b-3p, miR-881-3p, miR-1949, and miR-219a-2-3p. The kidney tissues of normal rats and rats with HN were taken, and RT-qPCR analysis of these 13 miRNAs was performed, respectively. The results showed that compared with control, miR-1-3p, miR-9a-5p, miR-98-5p, miR-205, miR-206, miR-216a-3p, miR-219a-2-3p, miR-743b-3p downregulated, miR-451-5p, miR-1949 upregulated, miR-219a-2-3p, miR-490-3p, miR-466b-5p, miR-881-3p, and miR-219a-2-3p had no difference (Figures 1(c)–1(o)). We selected miR-205 and miR-206 as potential therapeutic targets and synthesized miR-205 and miR-206 agomiR/antagomiR.

3.2. EPC Isolation and Identification. Isolated EPCs were identified using Dil-Ac-LDL staining. The red fluorescence (Dil-Ac-LDL) coincided with blue fluorescence (DAPI nuclear staining) by more than 90% (Figure 2(a)), confirming the successful separation of EPCs. After the medium was collected, MVs were extracted and observed under TEM. TEM results observed double-membrane vesicle-like bodies (Figure 2(b)). After western blot analysis, the protein levels of CD63, CD81, and Tsg101 were all positive (Figure 2(c)), so we determined that MVs were successfully extracted. miR-205 and miR-206 construct agomiR/antagomiR transfected EPC and collected supernatant and secreted MVs. The results showed that miR-205 and miR-206 were upregulated in the agomiR-transfected group and downregulated in the antagomiR-transfected group regardless of EPCs, supernatant, or MVs (Figures 2(d)–2(i)). Therefore, we confirmed that the synthetic miR-205 and miR-206 agomiR/

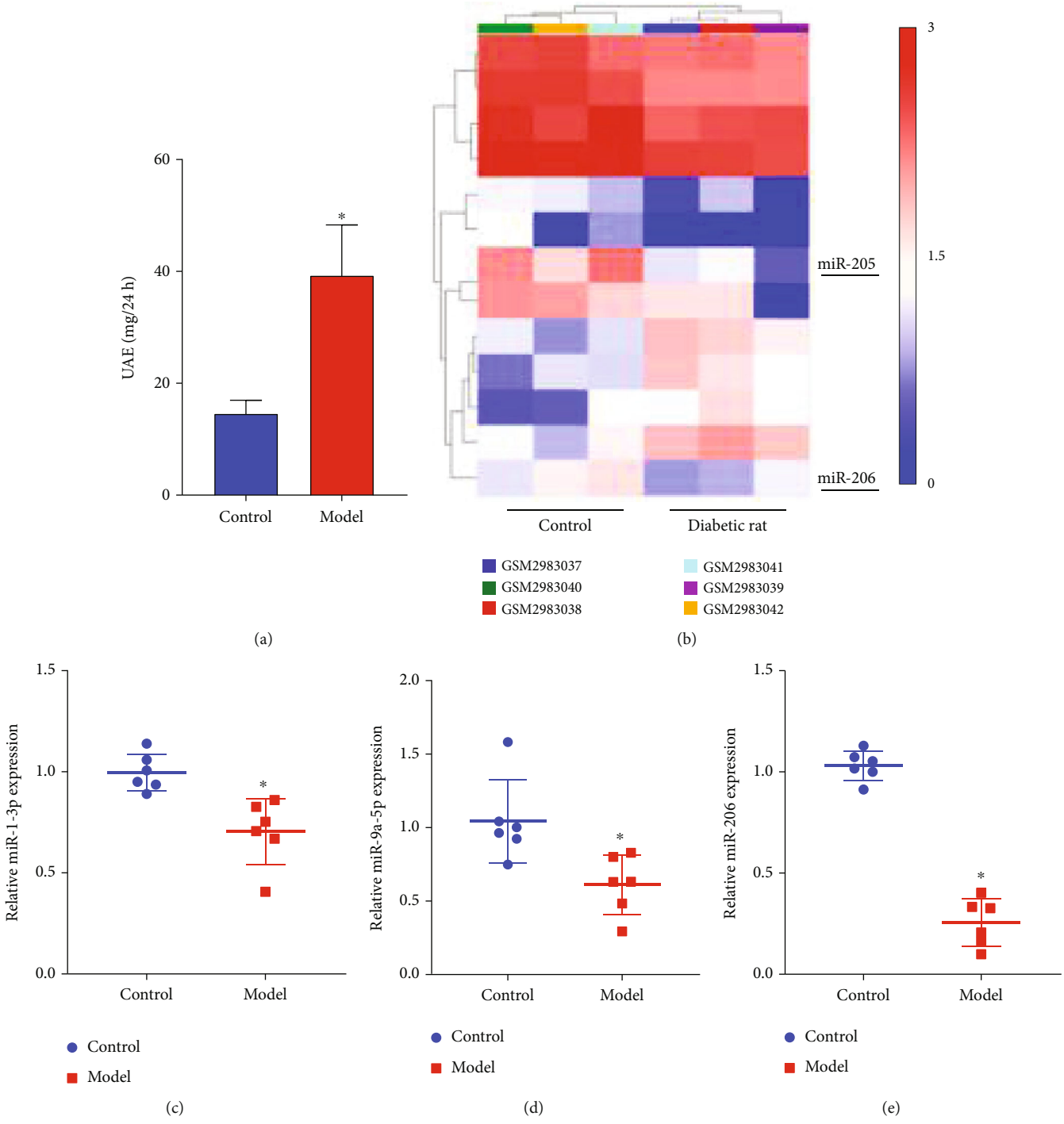

Figure 1: Continued.

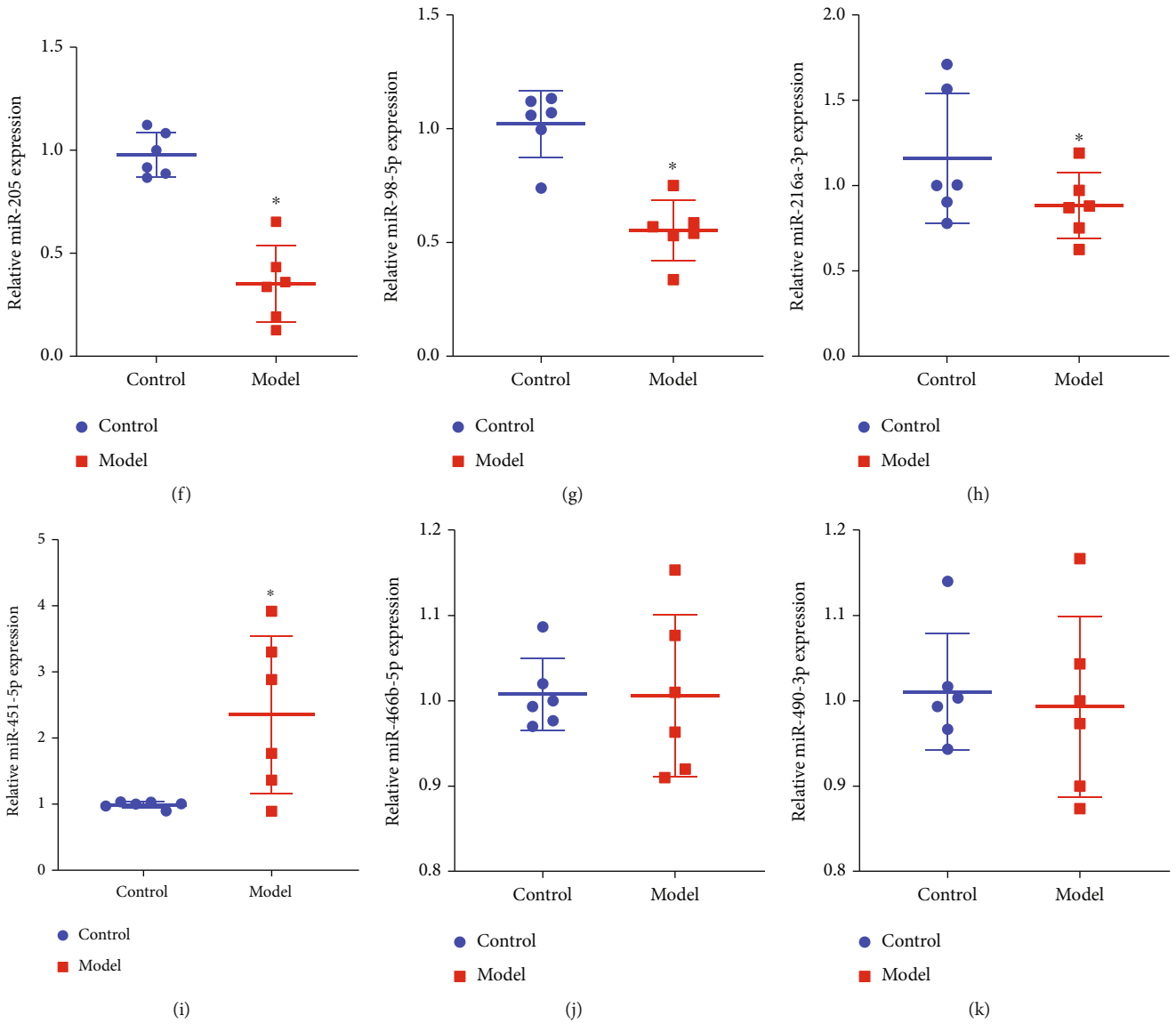

Figure 1: Continued.

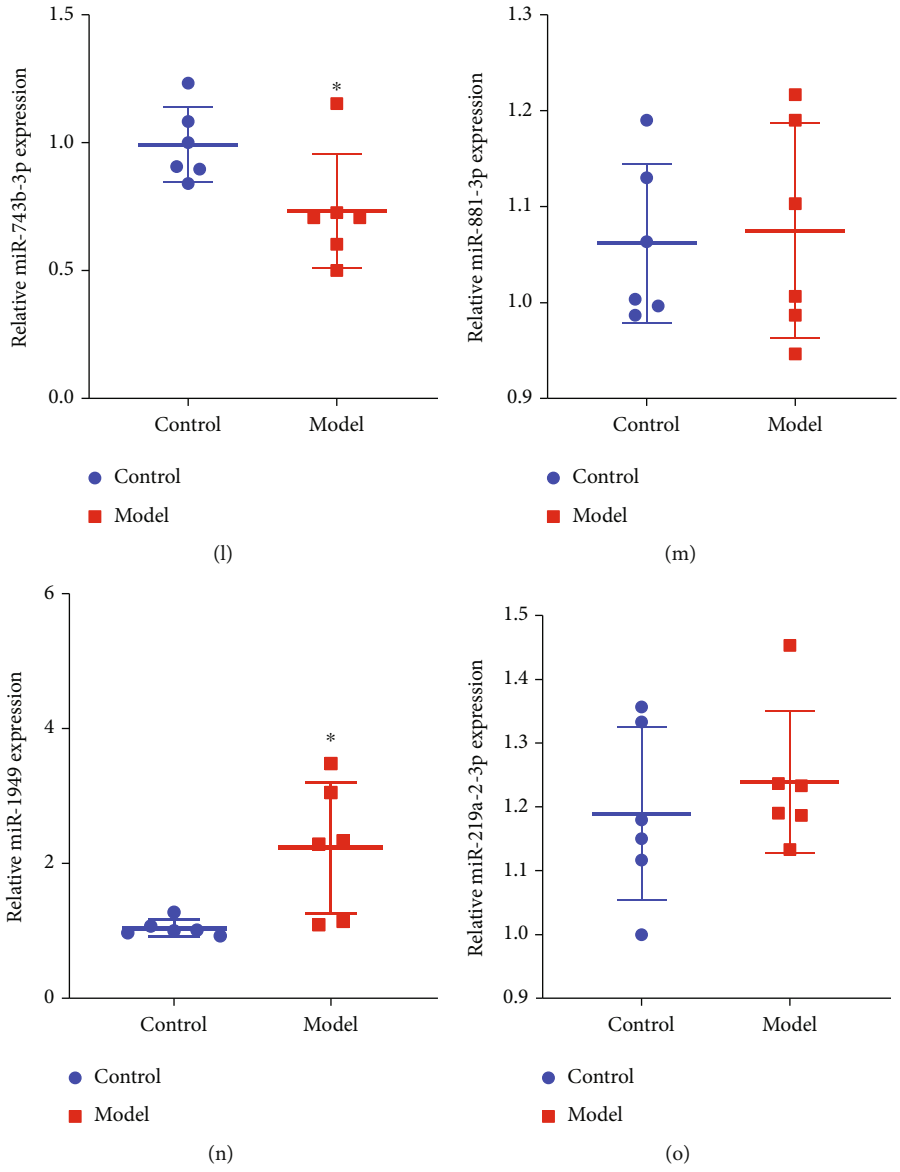

Figure 1: Screening of potential therapeutic miRNAs. (a) Determination of UAE in rats. (b) The sample GSE110231 was analyzed by GEO to screen miRNAs. Heat map shows differentially expressed miRNAs in diabetic rats compared with healthy rats. The blue band represents low expression, and the red band represents high expression. The blue part is low expression, and the red part is high expression. (c–o) RT-qPCR analysis of miR-1-3p (c), miR-9a-5p (d), miR-206 (e), miR-205 (f), miR-98-5p (g), miR-216a-3p (h), miR-451-5p (i), miR-466b-5p (j), miR-490-3p (k), miR-743b-3p (l), miR-881-3p (m), miR-1949 (n), and miR-219a-2-3p (o) expression in vivo. $^{*}p < 0.05$. GEO: Gene Expression Omnibus; RT-qPCR: real-time quantitative polymerase chain reaction; UAE: urinary albumin excretion; miR: microRNA.

antagomiR were effective, and the expression regulation of both was transmitted to MVs through EPCs.

3.3. Therapeutic Effects of miR-205 or miR-206-MVs on the Kidney In Vivo. The collected MVs were injected intravenously into rats. We observed that in rats injected with miR-205 and miR-206 MVs, the expressions of miR-205 and miR-206 were upregulated in the agomiR-injected group and downregulated in the antagomiR-injected group compared to the MV group (Figures 3(a) and 3(b)). UAE and BUN indicators were upregulated, and CCr decreased in HN. EPC-MVs significantly repaired the damage caused by HN, and this repair ability was amplified by miR-205 or miR-206 and was reduced by MVs that inhibited the expression of miR-205 or miR-206 (Figures 3(c)–3(h)). Therefore, we can confirm that miR-205 and miR-206 are therapeutic targets for HN, and EPCs regulate renal injury caused by HN in vivo by secreting MVs expressing miR-205 and miR-206. The molecular mechanism of action is still unclear.

3.4. MVs Protect PRKs from Ang II-Induced Damage. PRKs from normal rats were isolated, and the isolated PRKs were analyzed using IF staining (vimentin/α-SMA). The results showed that vimentin and α-SMA were highly expressed in

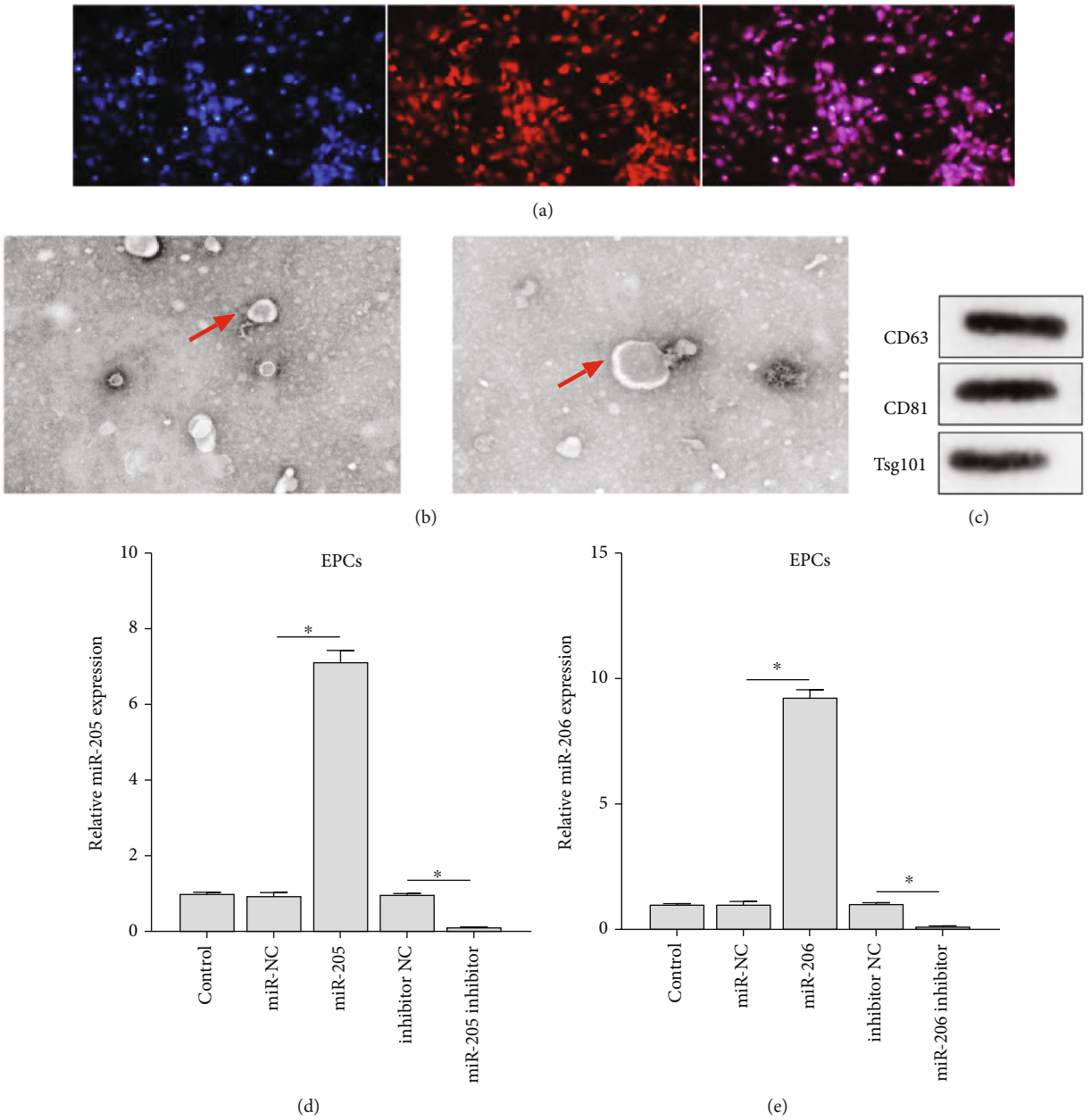

Figure 2: Continued.

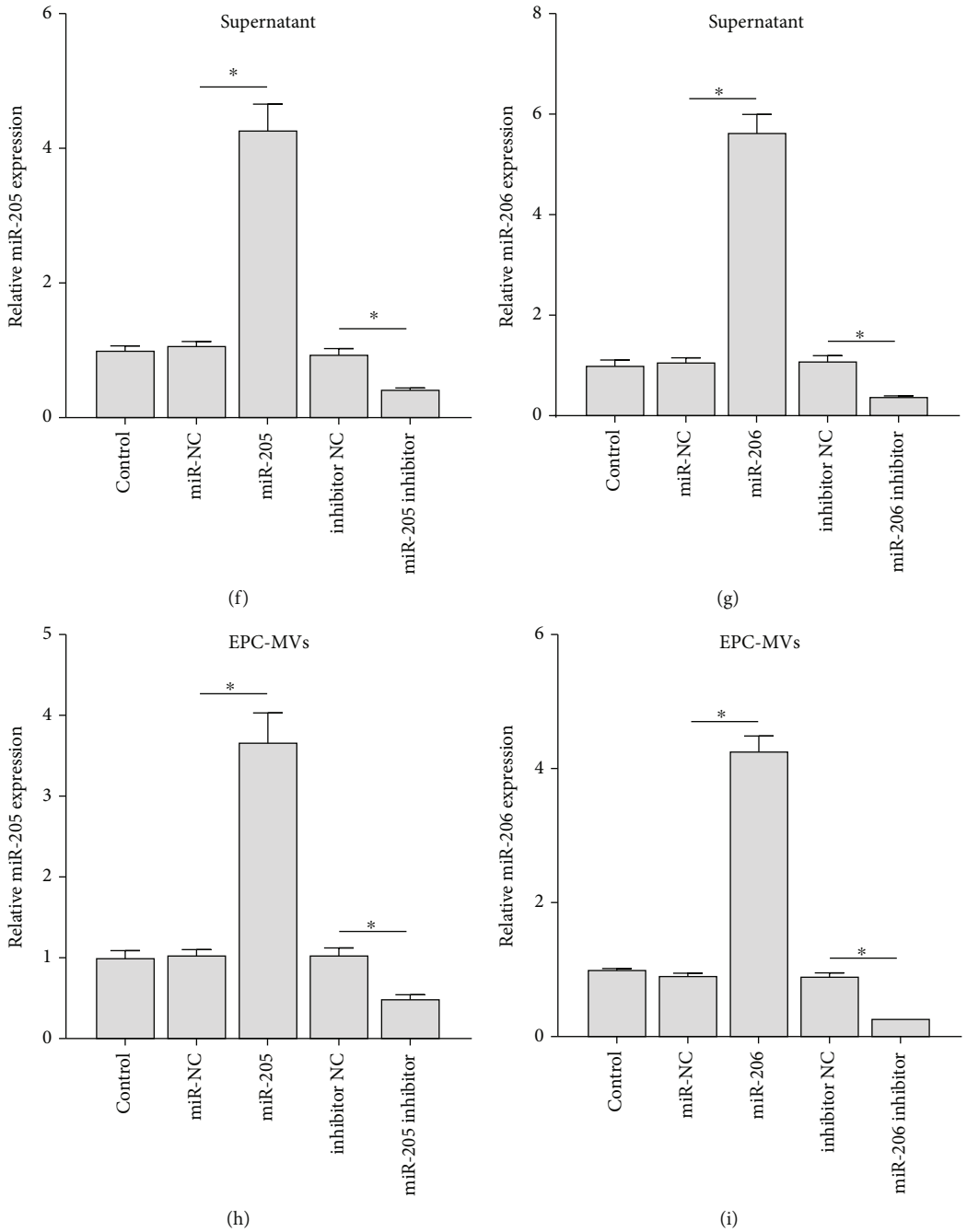

Figure 2: EPCs carry dysregulated miR-205 and miR-206 through the secreted MV pathway. (a) Dil-Ac-LDL staining was used to analyze the separation of EPCs. Blue is DAPI staining, and red is Dil-Ac-LDL staining. (b) TEM analysis of the extraction of MVs. Magnification: 40,000x. (c) Western blot analysis of the protein expression of CD63, CD81, and Tsg101 in the extracted MVs. (d–i) RT-qPCR analysis of the expression changes of miR-205 and miR-206 in EPCs (d, e), supernatants (f, g), and MVs (h, i). $^{*}p < 0.05$. Dil-Ac-LDL: Dil complex acetylated low-density lipoprotein; DAPI: 4′,6-diamidino-2-phenylindole; EPCs: endothelial progenitor cells; MVs: microvesicles; RT-qPCR: real-time quantitative polymerase chain reaction; TEM: transmission electron microscopy; IF: immunofluorescence; miR: microRNA.

PRKs, indicating that the isolation of PRKs was successful (Figure 4(a)). When MVs labeled with PKH26 were added to PRKs, we observed that red fluorescence of PKH26 was detected in the cytoplasm of PRKs, confirming that MVs could be incorporated into PRKs (Figure 4(b)). Ang II induction was added to mimic an in vitro HN model, and MVs carrying dysregulated miR-205 and miR-206 were fused to PRKs. Adding Ang II induction to mimic the HN model in vitro, Ang II mediated the expression inhibition of miR-205 and miR-206, and EPC-MVs reduced the effect of Ang II. The effect of EPC-MVs was enhanced by miR-205 and miR-206 agomiR and attenuated by miR-205 and miR-206 antagomiR (Figures 4(c) and 4(d)). Growth inhibition promoted by Ang II was suppressed by normal MVs.

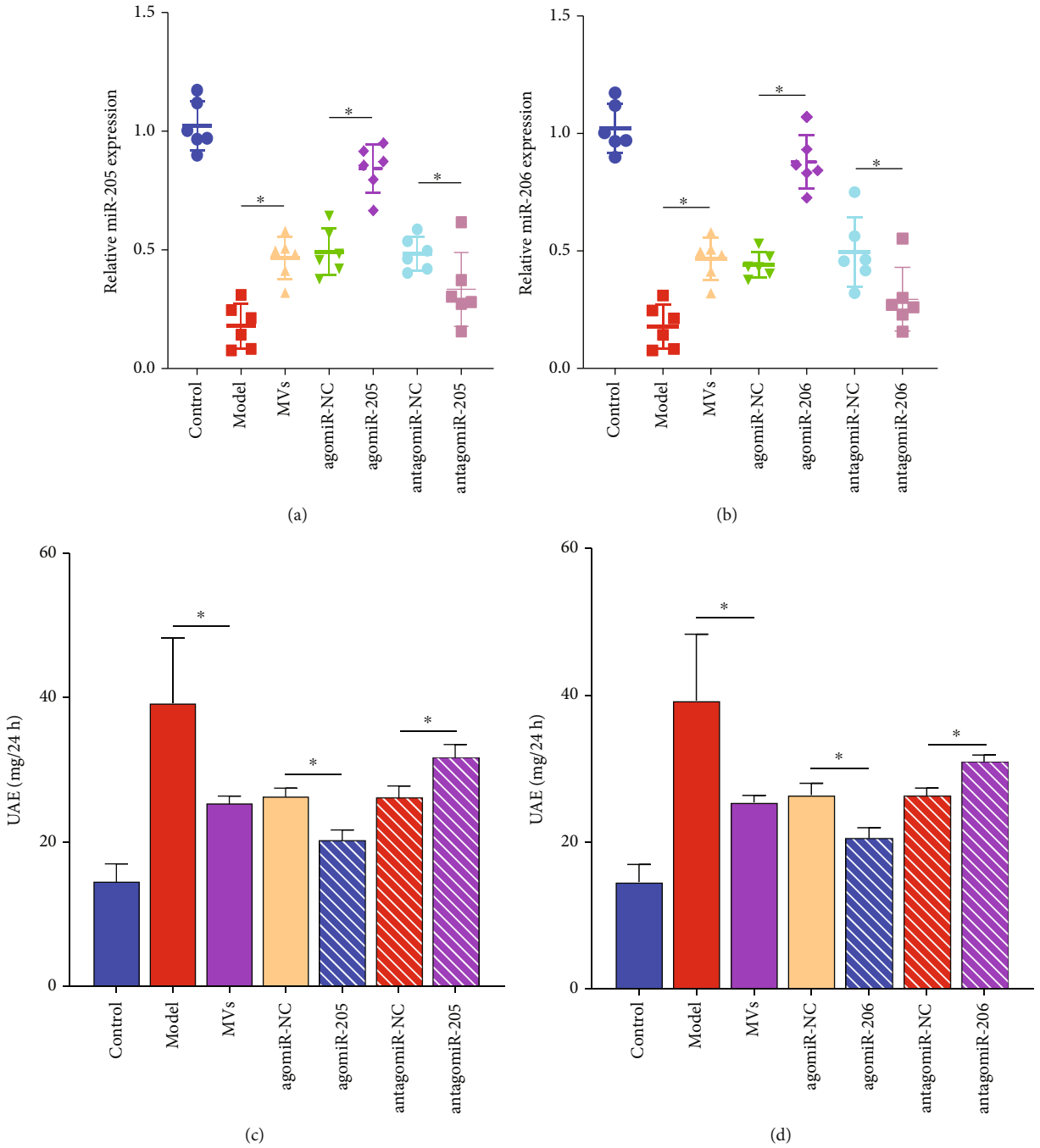

Figure 3: Continued.

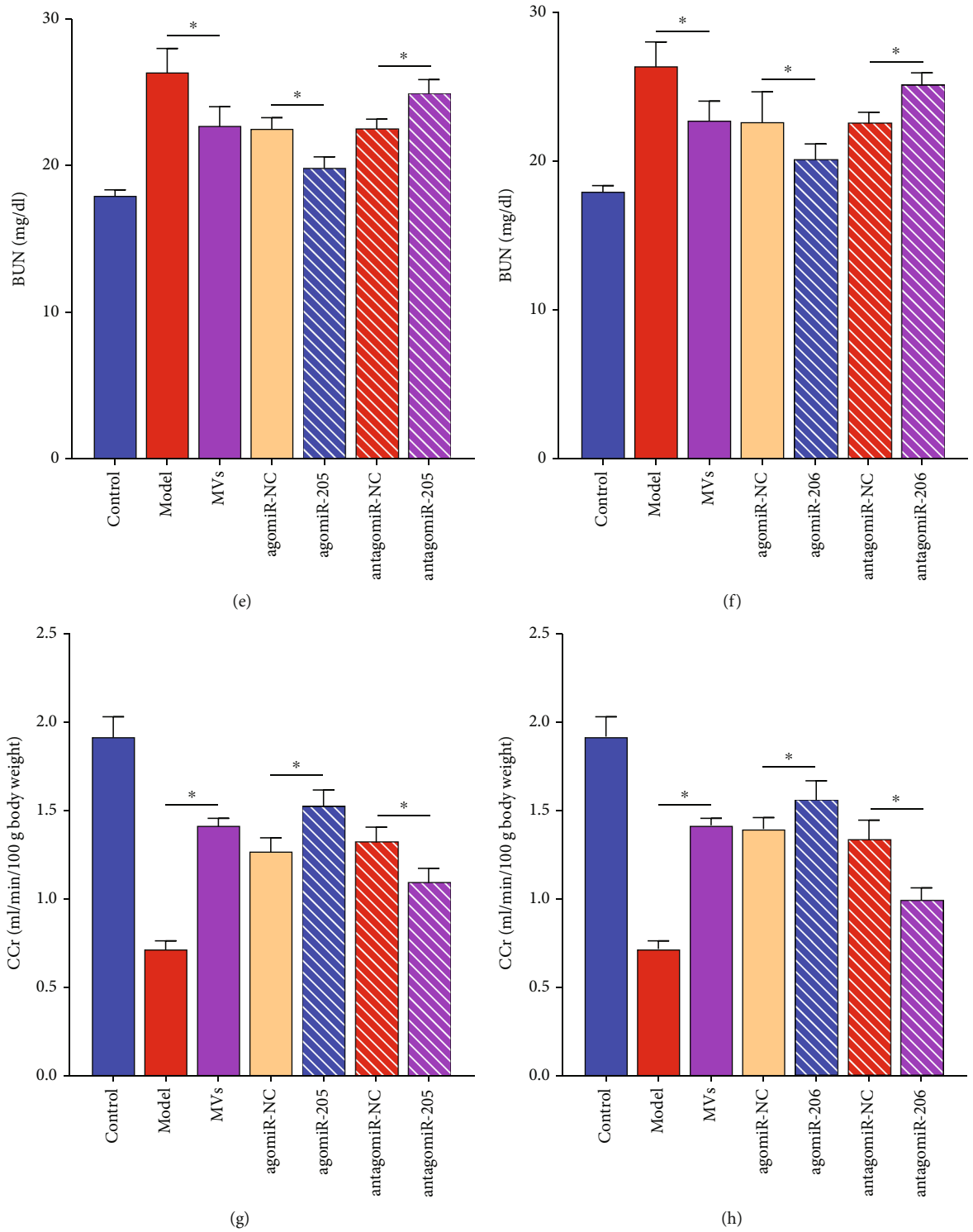

Figure 3: Kidney protection of miR-205 and miR-206-MVs in vivo. (a, b) RT-qPCR validated the effects of dysregulated miR-205 (a) and miR-206 (b) MVs on the expression of miR-205 and miR-206 in vivo. (c–h) Standard biochemical kits were used to analyze the effects of miR-205 and miR-206-MVs on UAE (c, d), BUN (e, f), and CCr (g, h) in vivo. $^*p < 0.05$. RT-qPCR: real-time quantitative polymerase chain reaction; miR: microRNA; UAE: urinary albumin excretion; BUN: blood urea nitrogen; CCr: creatinine clearance.

The action of normal MVs was promoted by MVs carrying miR-205 and miR-206 agomiR and suppressed by MVs carrying miR-205 and miR-206 antagomiR (Figures 4(e) and 4(f)).

3.5. miR-205 and miR-206 Were Negatively Correlated with DDX5. The miRDB database (http://mirdb.org/) screened putative targets and found that miR-205 and miR-206 share a common target, DDX5 (Figure 5(a)). Subsequent RT-

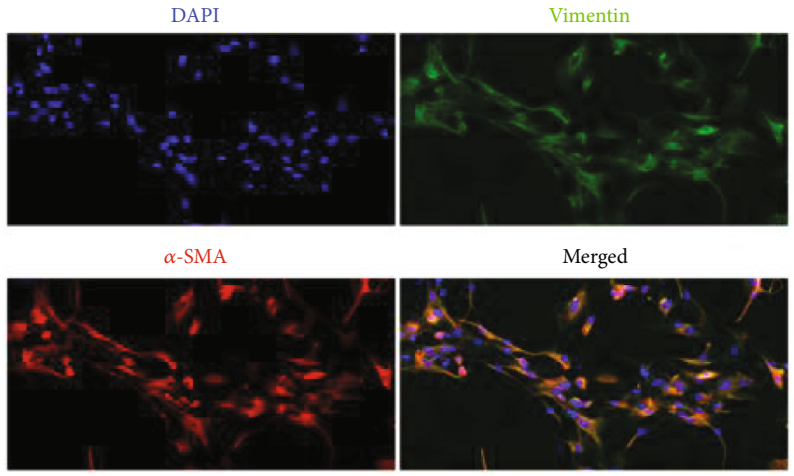

(a)

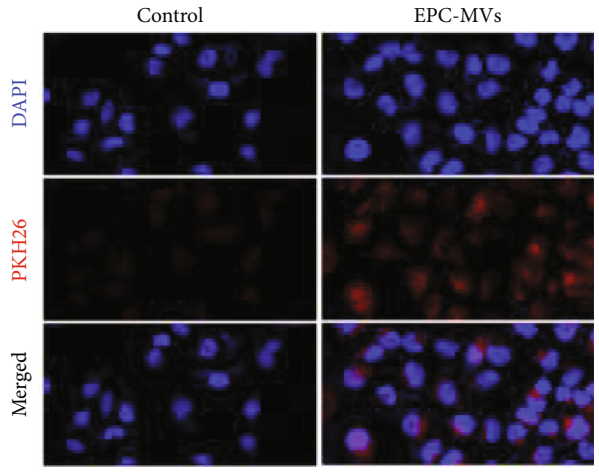

(b)

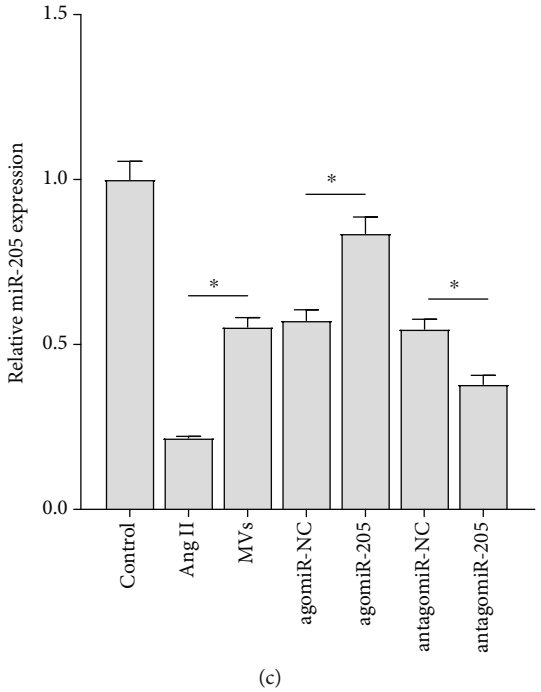

(c)

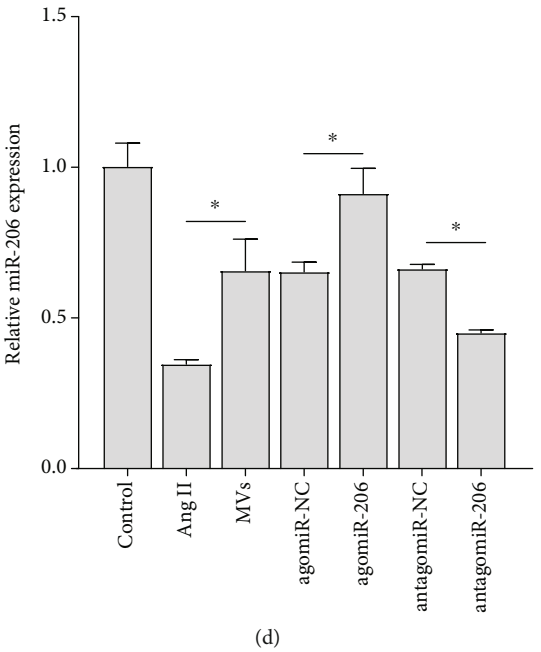

(d)

Figure 4: Continued.

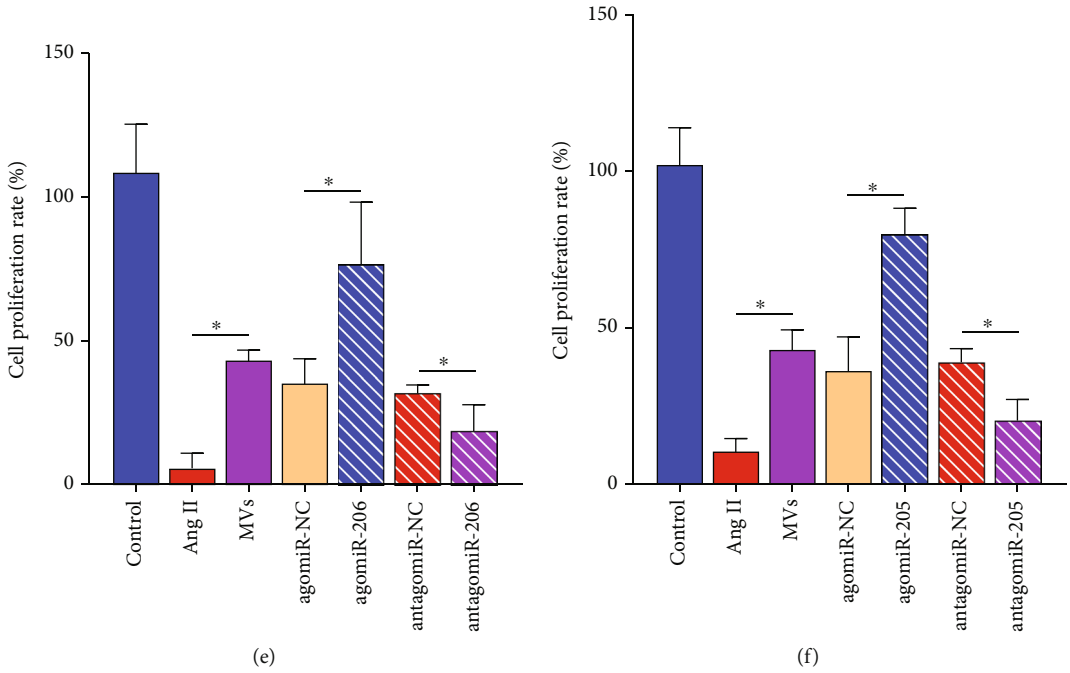

Figure 4: miR-205 and miR-206-MVs protect PRKs from Ang II damage in vivo. (a) IF analysis of the expression intensity of vimentin and α-SMA in the isolated PRKs. Blue is DAPI, green is anti-vimentin antibody, and red is anti-α-SMA antibody. (b) Fluorescence microscopy was used to observe the fusion of PKH26-labeled EPC-MVs and PRKs. Blue is DAPI, and red is MVs carrying PKH26-labeled. (c, d) RT-qPCR analysis in vitro miR-205 and miR-206-MVs regulate the expression of miR-205 and miR-206 in PRKs. (e, f) CCK8 analysis of the effects of miR-205 and miR-206-MVs on the proliferation of PRKs induced by Ang II in vitro. $^*p < 0.05$. RT-qPCR: real-time quantitative polymerase chain reaction; miR: microRNA; CCK-8: Cell Counting Kit-8; Ang II: angiotensin II; EPCs: endothelial progenitor cells; PRKs: primary rat kidney cells; MVs: microvesicles; IF: immunofluorescence; α-SMA: α-smooth muscle actin.

qPCR results showed that Ang II induced upregulation of DDX5 expression in PRKs, and the addition of EPC-MVs suppressed the effect of Ang II. The effect of EPC-MVs was enhanced by miR-205 and miR-206 agomiR and attenuated by miR-205 and miR-206 antagomiR (Figures 5(b) and 5(c)). Similar to the in vitro results, the expression of DDX5 was downregulated in the agomiR-transfected group and upregulated in the antagomiR group (Figures 5(d) and 5(e)). Therefore, miR-205 and miR-206 were negatively correlated with the expression of DDX5. We then constructed plasmids overexpressing DDX5 and transfected them into PRKs. The results showed that compared with the control group ov-NC, the gene and protein levels of overexpressing DDX5 were significantly upregulated (Figures 5(f) and 5(g)), so the construction of the plasmid overexpressing DDX5 was successful. We transfected ov-DDX5 in miR-205 and miR-206 mimic, and the results showed that the presence of miR-205 and miR-206 mimic suppressed the expression of DDX5 compared to ov-NC, but the addition of ov-DDX5 made this effect reversed (Figure 5(h)), while the expression of miR-205 and miR-206 did not change significantly (Figure 5(i)).

3.6. miR-205 and miR-206 Directly Target DDX5. Bioinformatics predicted binding sites of DDX5 to miR-205 or miR-206 (Figures 5(j) and 5(k)). The mechanism through which miR-205 and miR-206 modulate DDX5 expression was examined by introducing the 3′-UTR of DDX5 containing a joint binding site of miR-205 and miR-206 downstream of the luciferase reporter. Subsequently, the results of dual-luciferase analysis showed that the luciferase activity of WT DDX5 3′-UTR construct in cells transfected with miR-205 or miR-206 mimic was significantly lower compared with that in cells transfected with the mimic NC. A luciferase reporter containing the mut DDX5 3′-UTR binding site of miR-205 or miR-206 was also constructed. The luciferase activity of the mut DDX5 3′-UTR construct was not suppressed upon transfection with miR-205/miR-206 mimic or inhibitor (Figures 5(l) and 5(m)). These results show that miR-205 and miR-206 cotarget DDX5 and inhibit the transcriptional activity of DDX5 by binding to the 3′-UTR of DDX5.

3.7. Effects of the miR-205/miR-206-DDX5 Axis on Proapoptotic Proteins. By western blot analysis, we confirmed that Ang II promoted DDX5 protein level and the activation of proapoptotic protein caspase-3/9, and EPC-MVs had a significant inhibitory effect on this effect. The efficacy of EPC-MVs was enhanced in the overexpressed state of miR-205 or miR-206 and was attenuated by overexpression of DDX5 (Figure 6). Furthermore, EPC-MVs inhibited Ang II-mediated PRK growth inhibition and apoptosis promotion. miR-205 or miR-206 enhanced the utility of EPC-MVs, whereas overexpression of DDX5 inhibited the utility of miR-205 or miR-206 MVs (Figures 7(a)–7(d)).

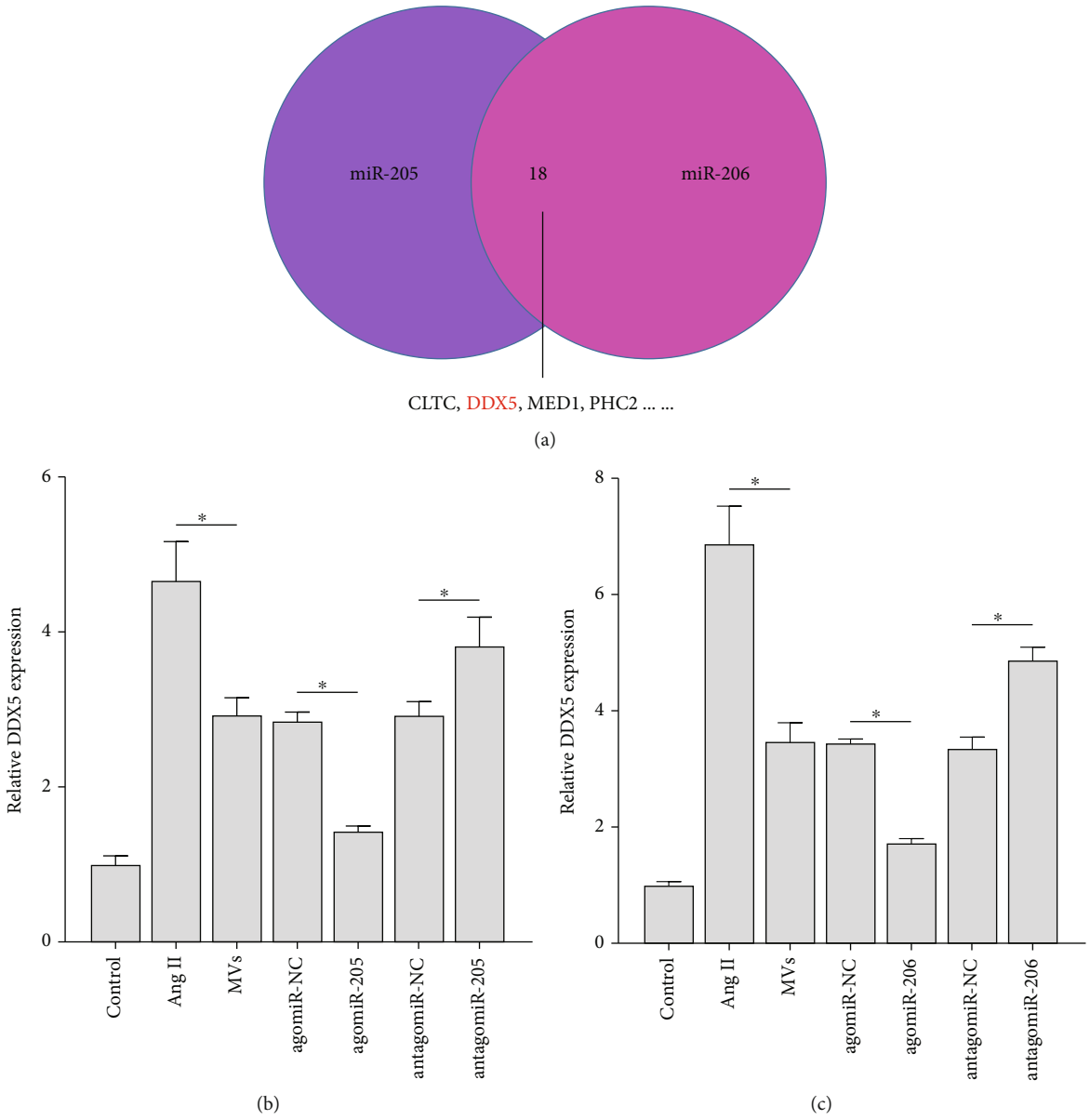

Figure 5: Continued.

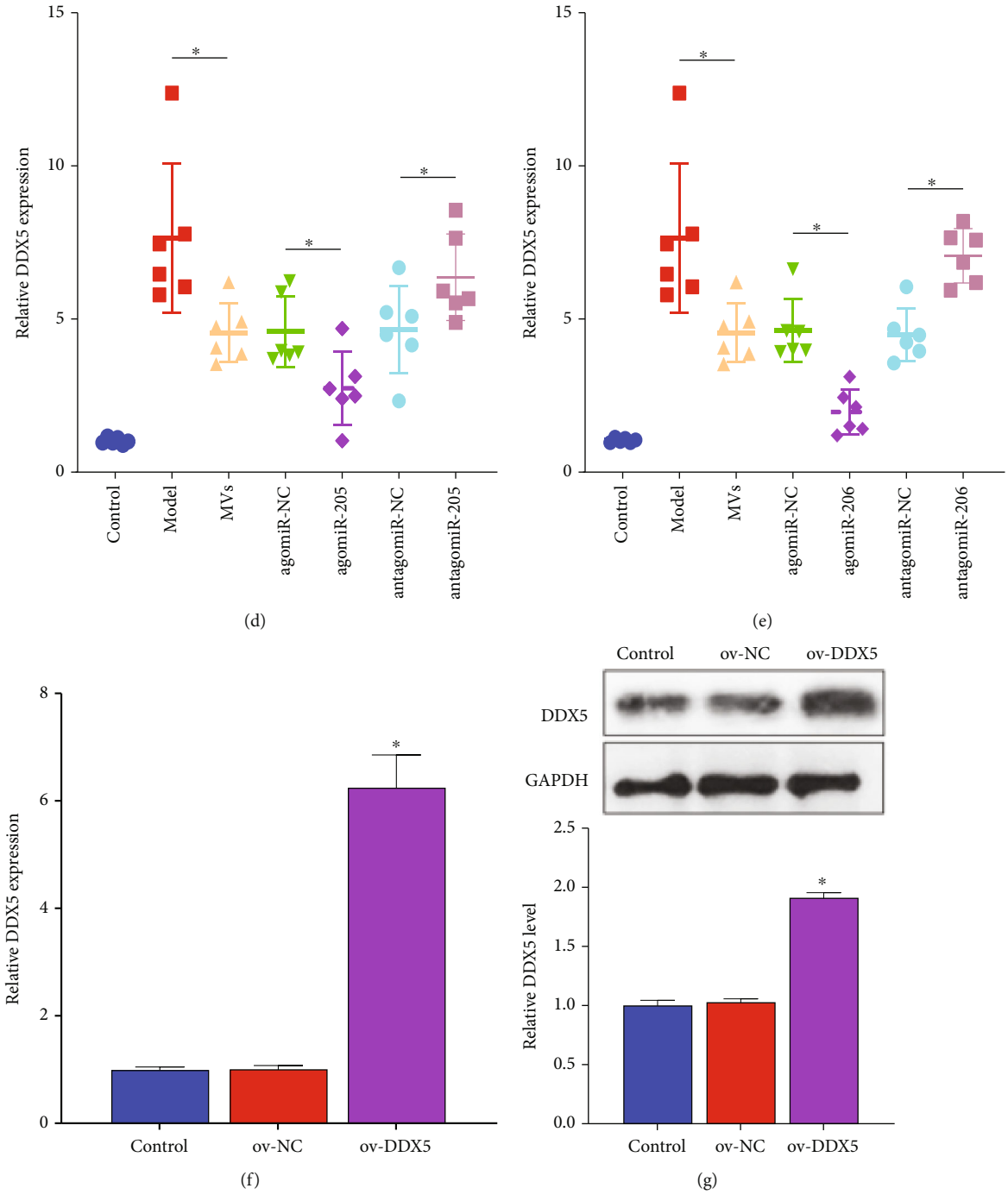

Figure 5: Continued.

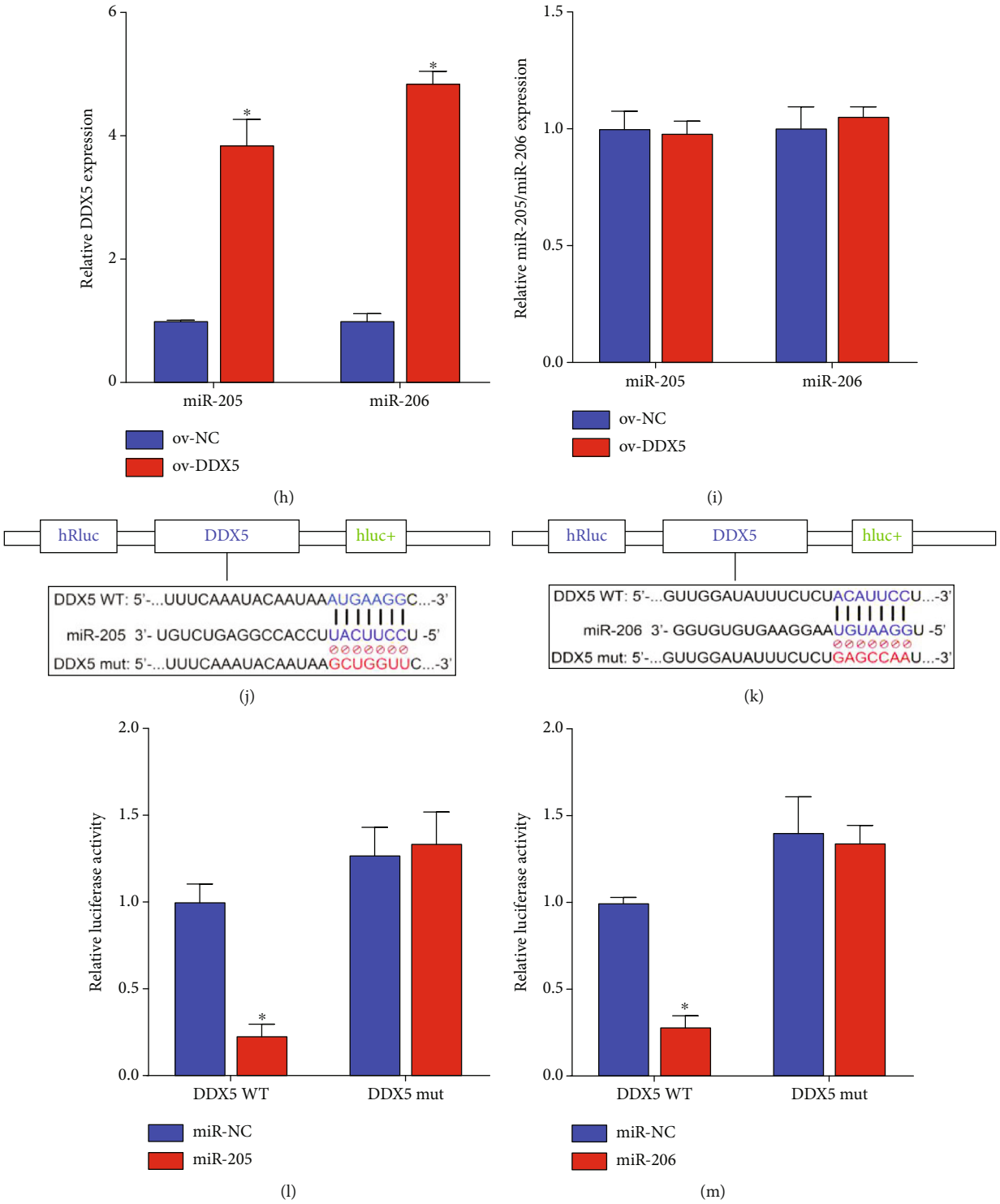

Figure 5: The mechanism by which miR-205 and miR-206 work is achieved by targeting downstream DDX5. (a) The miRDB database analyzed the common downstream targets of miR-205 and miR-206. (b, c) RT-qPCR analysis in vitro miR-205 (b) and miR-206 (c) MVs regulate DDX5 expression. (d, e) RT-qPCR analysis in vivo miR-205 (d) and miR-206 (e) MVs regulate DDX5 expression. (f) RT-qPCR verified the validity of the overexpressed DDX5 plasmid. (g) Western blot verified the effectiveness of overexpressing DDX5 plasmid. (h) RT-qPCR analysis of the effect of overexpressing DDX5 in the presence of miR-205 or miR-206 agomiR on DDX5 expression. (i) RT-qPCR analysis of the effect of overexpressing DDX5 in the presence of miR-205 or miR-206 agomiR on miR-205 or miR-206 expression. (j, k) The miRDB database analysis of the binding sites of miR-205 (j) or miR-206 (k) to DDX5. (l, m) Dual-luciferase assays for direct binding of miR-205 (l) or miR-206 (m) to DDX5. $^*p < 0.05$. RT-qPCR; real-time quantitative polymerase chain reaction; miR: microRNA; ov: overexpression; DDX5: DEAD-box helicase 5; EPCs: endothelial progenitor cells; PRKs: primary rat kidney cells; MVs: microvesicles; WT: wild type; mut: mutant.

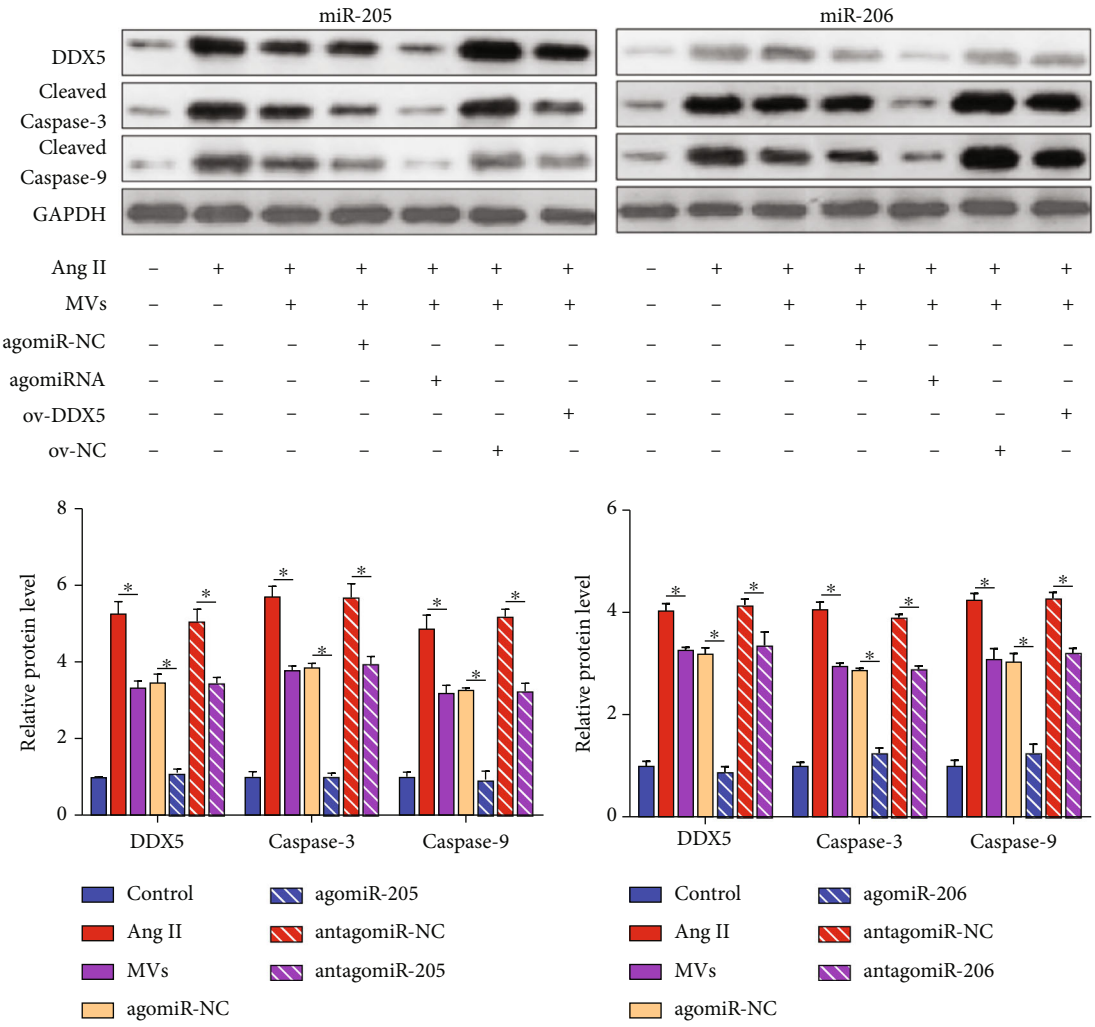

Figure 6: miR-205 and miR-206-MVs regulate the activation of apoptotic proteins. Western blot analysis of overexpression of DDX5 in the presence of miR-205 or miR-206 agomiR on the protein levels of DDX5, caspase-3/9. $^*p < 0.05$. miR: microRNA; ov: overexpression; DDX5: DEAD-box helicase 5; EPCs: endothelial progenitor cells; PRKs: primary rat kidney cells; MVs: microvesicles; Ang II: angiotensin II.

4. Discussion

In the present study, we demonstrated for the first time that EPC-MVs carrying high levels of miR-205 and miR-206 could protect kidneys or PRKs from cellular damage caused by hypertension or Ang II.

The proliferation and angiogenesis and anti-inflammatory abilities of EPCs can effectively protect the kidneys of patients with nephropathy [37, 38] and play an important role in maintaining vascular integrity and improving renal function [6]. Recent evidence suggests that EPCs play a role in protecting renal function through secreted MVs [7]. MVs are anti-inflammatory, improve endothelial function, and alleviate endothelial dysfunction caused by oxidative stress [39, 40]. Since the damaged kidneys cannot effectively filter the metabolic wastes in the blood, which eventually leads to the occurrence of kidney disease [41], this paper conducted a GEO analysis on the diabetic rats based on the possibility of kidney disease in the diabetic rats, and the data was used to analyze the same kidney damage caused by hypertension. One of the main conclusions of this study is that MVs secreted by EPCs reduced the rise in UAE and BUN and the decrease in CCr induced by HN in vivo. In vitro, MVs promoted the proliferation of PRKs and inhibited apoptosis; all these evidences confirmed that MVs can improve renal function. This is consistent with the conclusions reached by our previous study [37].

It has been reported that MVs can deliver miRNAs to cells, thereby affecting disease development. For example, MVs carrying miR-148a can regulate adipogenic and osteogenic differentiation by targeting the receptor tyrosine kinase-like orphan receptor 2 pathway [42]. miR-191 secreted by MVs induces renal tubular epithelial cell apoptosis by inhibiting cystathionine-β-synthase [43]. This study confirmed that both miR-205 and miR-206 secreted by MVs could promote the improvement of HN by MVs. The secreted low-expressed miR-205 and miR-206 inhibited the effect of MVs. The results in in vitro experiments were also similar; to be specific, MVs secreted miR-205 and miR-206 to promote MVs to ameliorate Ang II-induced PRK growth

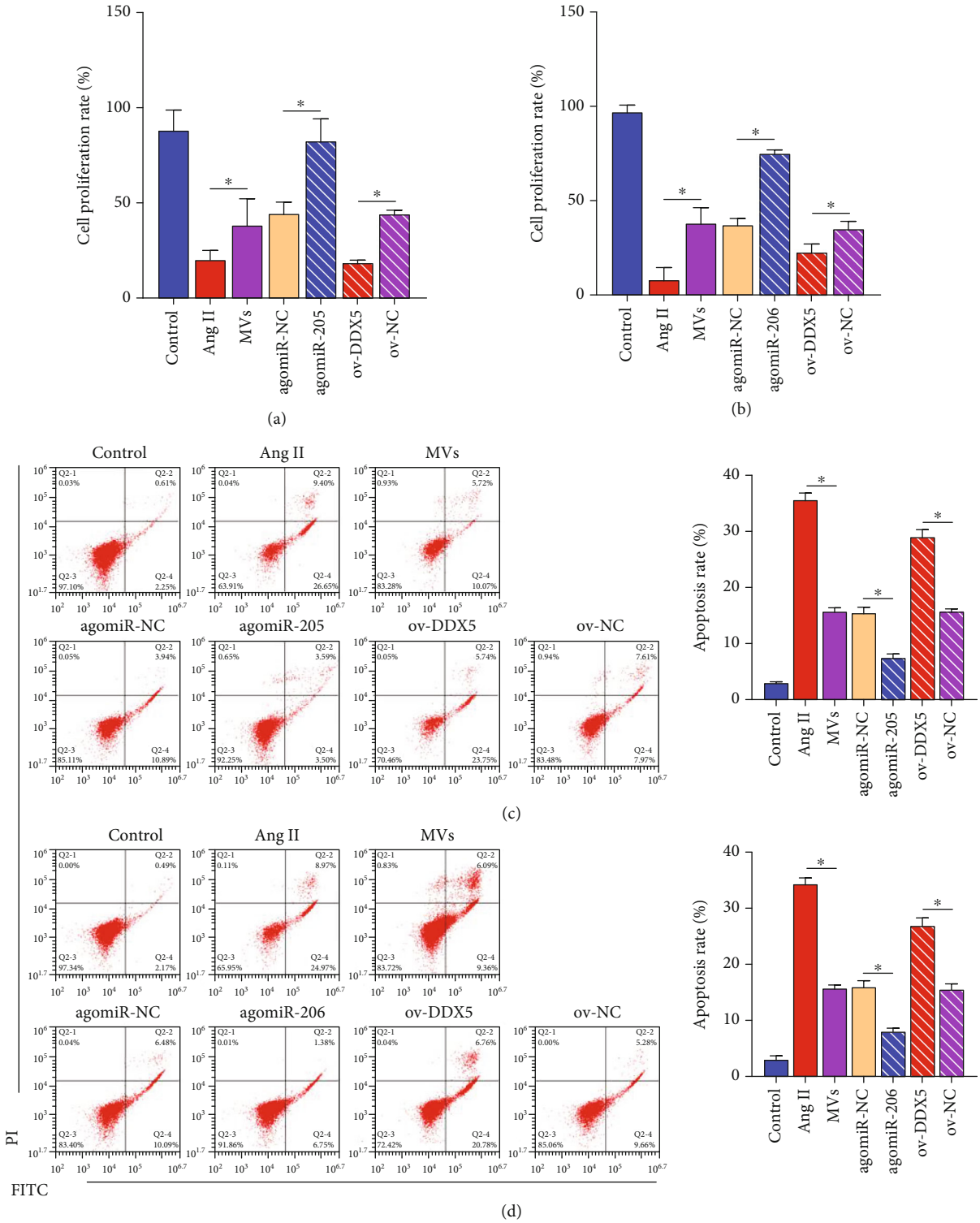

Figure 7: Effects of miR-205 and miR-206 interacting with DDX5 on the proliferation and apoptosis of PRKs. (a, b) CCK8 analysis of the effect of overexpressing DDX5 on the proliferation rate of PRKs in the presence of miR-205 (a) and miR-206 (b) agomiR. (c, d) FCM analysis of the effect of overexpressing DDX5 on the apoptosis of PRKs in the presence of miR-205 (c) and miR-206 (d) agomiR. $^{*}p < 0.05$. RT-qPCR: real-time quantitative polymerase chain reaction; miR: microRNA; ov: overexpression; DDX5: DEAD-box helicase 5; Ang II: angiotensin II; FCM: flow cytometry; EPCs: endothelial progenitor cells; PRKs: primary rat kidney cells; MVs: microvesicles; CCK-8: Cell Counting Kit-8.

inhibition and apoptosis, and low expression of miR-205 and miR-206 partially inhibited the effect of MVs. Furthermore, after transfection of miR-205 or miR-206 agomiR/antagomiR, deregulated expression of miR-205 or miR-206 was detected in EPCs, supernatants, and MVs, implying that MVs carried deregulated miR-205 or antagomiR miR-206 is produced by secretion from EPCs.

To further explore the mechanism by which miR-205 or miR-206 exert their effects, we analyzed their common downstream target DDX5 by bioinformatics. Studies have confirmed that miR-206 improves renal function by binding to DDX5 [23]. Here, we report that miR-205 and miR-206 together target DDX5. The growth promotion and inhibition of PRKs by miR-205 and miR-206 could be reversed by overexpressed DDX5, and the restriction of transcriptional activity and translational level of DDX5 by miR-205 and miR-206 was also alleviated by overexpressed DDX5. Therefore, DDX5 is negatively regulated with miR-205 and miR-206.

Increasing evidence suggests that abnormal activation of apoptotic proteins may be a major factor in causing kidney damage [31, 44]. Our study shows that MVs can reduce the activation of apoptotic protein caspase-3/9. Secretion of miR-205 and miR-206 enhanced the effect of MVs, while overexpression of DDX5 inhibited the enhancement of MVs by miR-205 and miR-206.

This study has some limitations. First, there are no clinical data on the treatment of EPC-MVs in HN. Second, changes in various signaling pathways, especially those related to inflammation or oxidative stress, have not been further explored. All of these will be the focus of our future research.

In conclusion, EPCs protect against hypertension-induced renal injury by secreting MVs carrying dysregulated miR-205 and miR-206 expression. The mechanism is related to miR-205 and miR-206 cotargeting DDX5 and promoting cell growth inhibition and apoptosis. This provides a new therapeutic strategy for HN.

Data Availability

The data used to support the findings of this study are included within the article.

Ethical Approval

The authors are accountable for all aspects of the work in ensuring that questions related to the accuracy or integrity of any part of the work are appropriately investigated and resolved. The study was conducted in accordance with the Declaration of Helsinki (as revised in 2013). The study was approved by the Animal Care and Use Committee of Hainan Medical University (Haikou, China, approval no. HYLL-2021-053).

Conflicts of Interest

The author(s) declare(s) that they have no conflicts of interest.

Authors' Contributions

Conception and design were performed by Y Zhang, Y Shen, and S Gu. Y Song was responsible for administrative support. Y Lin was responsible for the provision of study materials or patients. Collection and assembly of data were performed by Y Song, Y Lin, and Y Wang. Data analysis and interpretation were performed by M Chen and H Mai. Manuscript writing was performed by all authors. Final approval of the manuscript was performed by all authors. Yunbo Zhang and Yanling Shen contributed equally to this work.

Acknowledgments

This study was supported by the Finance Science and Technology Projects of Hainan Province (Grant No. ZDYF2022SHFZ101) and the National Natural Science Foundation of China (Grant No. 81560054).

References

[1] A. M. De Bhailis and P. A. Kalra, "Hypertension and the kidneys," *British Journal of Hospital Medicine*, vol. 83, no. 5, pp. 1–11, 2022.

[2] P. K. Whelton, R. M. Carey, W. S. Aronow et al., "2017 ACC/AHA/AAPA/ABC/ACPM/AGS/APhA/ASH/ASPC/NMA/PCNA guideline for the prevention, detection, evaluation, and management of high blood pressure in adults: a report of the American College of Cardiology/American Heart Association task force on clinical practice guidelines," *Journal of the American College of Cardiology*, vol. 71, no. 19, pp. e127–e248, 2018.

[3] H. Ding, Y. Zhou, and H. Huang, "MiR-101a ameliorates AngII-mediated hypertensive nephropathy by blockade of TGFβ/Smad3 and NF-κB signalling in a mouse model of hypertension," *Clinical and Experimental Pharmacology & Physiology*, vol. 46, no. 3, pp. 246–254, 2019.

[4] S. Mennuni, S. Rubattu, G. Pierelli, G. Tocci, C. Fofi, and M. Volpe, "Hypertension and kidneys: unraveling complex molecular mechanisms underlying hypertensive renal damage," *Journal of Human Hypertension*, vol. 28, no. 2, pp. 74–79, 2014.

[5] K. Chen, Y. Li, L. Xu et al., "Comprehensive insight into endothelial progenitor cell-derived extracellular vesicles as a promising candidate for disease treatment," *Stem Cell Research & Therapy*, vol. 13, no. 1, p. 238, 2022.

[6] N. Kundu, S. R. Nandula, L. D. Asico et al., "Transplantation of apoptosis-resistant endothelial progenitor cells improves renal function in diabetic kidney disease," *Journal of the American Heart Association*, vol. 10, no. 7, article e019365, 2021.

[7] A. A. Salybekov, A. D. Kunikeyev, S. Kobayashi, and T. Asahara, "Latest advances in endothelial progenitor cell-derived extracellular vesicles translation to the clinic," *Frontiers in Cardiovascular Medicine*, vol. 8, article 734562, 2021.

[8] Z. Xing, C. Zhao, H. Liu, and Y. Fan, "Endothelial progenitor cell-derived extracellular vesicles: a novel candidate for regenerative medicine and disease treatment," *Advanced Healthcare Materials*, vol. 9, no. 12, article e2000255, 2020.

[9] N. Sadanandan, J. Y. Lee, and S. Garbuzova-Davis, "Extracellular vesicle-based therapy for amyotrophic lateral sclerosis," *Brain Circulation*, vol. 7, no. 1, pp. 23–28, 2021.

[10] S. Terriaca, E. Fiorelli, M. G. Scioli et al., "Endothelial progenitor cell-derived extracellular vesicles: potential therapeutic application in tissue repair and regeneration," *International Journal of Molecular Sciences*, vol. 22, no. 12, p. 6375, 2021.

[11] C. Diener, A. Keller, and E. Meese, "Emerging concepts of miRNA therapeutics: from cells to clinic," *Trends in Genetics*, vol. 38, no. 6, pp. 613–626, 2022.

[12] Q. Lu, Z. Ma, Y. Ding et al., "Circulating miR-103a-3p contributes to angiotensin II-induced renal inflammation and fibrosis via a SNRK/NF-κB/p65 regulatory axis," *Nature Communications*, vol. 10, no. 1, p. 2145, 2019.

[13] L. Zhong, G. Liao, X. Wang et al., "Mesenchymal stem cells-microvesicle-miR-451a ameliorate early diabetic kidney injury by negative regulation of P15 and P19," *Experimental Biology and Medicine*, vol. 243, no. 15-16, pp. 1233–1242, 2018.

[14] Y. Wang, X. Lu, J. He, and W. Zhao, "Influence of erythropoietin on microvesicles derived from mesenchymal stem cells protecting renal function of chronic kidney disease," *Stem Cell Research & Therapy*, vol. 6, no. 1, p. 100, 2015.

[15] A. P. Ferragut Cardoso, M. Banerjee, A. N. Nail, A. Lykoudi, and J. C. States, "miRNA dysregulation is an emerging modulator of genomic instability," *Seminars in Cancer Biology*, vol. 76, pp. 120–131, 2021.

[16] M. Hill and N. Tran, "miRNA interplay: mechanisms and consequences in cancer," *Disease Models & Mechanisms*, vol. 14, no. 4, article dmm047662, 2021.

[17] M. Simeoni, S. Borrelli, C. Garofalo et al., "Atherosclerotic-nephropathy: an updated narrative review," *Journal of Nephrology*, vol. 34, no. 1, pp. 125–136, 2021.

[18] D. Guo, Y. Fan, J. R. Yue, and T. Lin, "A regulatory miRNA-mRNA network is associated with transplantation response in acute kidney injury," *Human Genomics*, vol. 15, no. 1, p. 69, 2021.

[19] Z. Wang, W. Bao, X. Zou et al., "Co-expression analysis reveals dysregulated miRNAs and miRNA-mRNA interactions in the development of contrast-induced acute kidney injury," *PLoS One*, vol. 14, no. 7, article e0218574, 2019.

[20] L. Zhang, J. Du, Z. Hu et al., "IL-6 and serum amyloid A synergy mediates angiotensin II-induced muscle wasting," *Journal of the American Society of Nephrology*, vol. 20, no. 3, pp. 604–612, 2009.

[21] Y. Lin, Y. Ding, S. Song, M. Li, T. Wang, and F. Guo, "Expression patterns and prognostic value of miR-210, miR-494, and miR-205 in middle-aged and old patients with sepsis-induced acute kidney injury," *Bosnian Journal of Basic Medical Sciences*, vol. 19, no. 3, pp. 249–256, 2019.

[22] B. Wang, Y. Wang, K. Xu et al., "Resveratrol alleviates sepsis-induced acute kidney injury by deactivating the lncRNA MALAT1/MiR-205 axis," *Central European Journal of Immunology*, vol. 46, no. 3, pp. 295–304, 2021.

[23] X. Zhang, Z. Huang, Y. Wang, T. Wang, J. Li, and P. Xi, "Long non-coding RNA RMRP contributes to sepsis-induced acute kidney injury," *Yonsei Medical Journal*, vol. 62, no. 3, pp. 262–273, 2021.

[24] Q. Ren, F. Guo, S. Tao, R. Huang, L. Ma, and P. Fu, "Flavonoid fisetin alleviates kidney inflammation and apoptosis via inhibiting Src-mediated NF-κB p65 and MAPK signaling pathways in septic AKI mice," *Biomedicine & Pharmacotherapy*, vol. 122, article 109772, 2020.

[25] Y. Chen, X. Feng, X. Hu et al., "Dexmedetomidine ameliorates acute stress-induced kidney injury by attenuating oxidative stress and apoptosis through inhibition of the ROS/JNK signaling pathway," *Oxidative Medicine and Cellular Longevity*, vol. 2018, Article ID 4035310, 12 pages, 2018.

[26] X. Shen, H. Wang, C. Weng, H. Jiang, and J. Chen, "Caspase 3/GSDME-dependent pyroptosis contributes to chemotherapy drug- induced nephrotoxicity," *Cell Death & Disease*, vol. 12, no. 2, p. 186, 2021.

[27] Y. Lu, H. Yuan, S. Deng et al., "Arsanilic acid causes apoptosis and oxidative stress in rat kidney epithelial cells (NRK-52e cells) by the activation of the caspase-9 and -3 signaling pathway," *Drug and Chemical Toxicology*, vol. 37, no. 1, pp. 55–62, 2014.

[28] L. Sun, L. Xiao, J. Nie et al., "p66Shc mediates high-glucose and angiotensin II-induced oxidative stress renal tubular injury via mitochondrial-dependent apoptotic pathway," *American Journal of Physiology. Renal Physiology*, vol. 299, no. 5, pp. F1014–F1025, 2010.

[29] A. Lazaro, J. Gallego-Delgado, P. Justo et al., "Long-term blood pressure control prevents oxidative renal injury," *Antioxidants & Redox Signaling*, vol. 7, no. 9-10, pp. 1285–1293, 2005.

[30] Y. Zhao, X. Feng, B. Li et al., "Dexmedetomidine protects against lipopolysaccharide-induced acute kidney injury by enhancing autophagy through inhibition of the PI3K/AKT/mTOR pathway," *Frontiers in Pharmacology*, vol. 11, p. 128, 2020.

[31] J. Gao, X. Tian, X. Yan et al., "Selenium exerts protective effects against fluoride-induced apoptosis and oxidative stress and altered the expression of Bcl-2/caspase family," *Biological Trace Element Research*, vol. 199, no. 2, pp. 682–692, 2021.

[32] U. Efe, S. Dede, V. Yuksek, and S. Cetin, "Apoptotic and oxidative mechanisms in liver and kidney tissues of sheep with fluorosis," *Biological Trace Element Research*, vol. 199, no. 1, pp. 136–141, 2021.

[33] A. Shopit, M. Niu, H. Wang et al., "Protection of diabetes-induced kidney injury by phosphocreatine _via_ the regulation of ERK/Nrf2/HO-1 signaling pathway," *Life Sciences*, vol. 242, article 117248, 2020.

[34] S. Zhang, H. Xin, Y. Li et al., "Skimmin, a coumarin from Hydrangea paniculata, slows down the progression of membranous glomerulonephritis by anti-inflammatory effects and inhibiting immune complex deposition," *Evidence-Based Complementary and Alternative Medicine*, vol. 2013, Article ID 819296, 10 pages, 2013.

[35] K. J. Livak and T. D. Schmittgen, "Analysis of relative gene expression data using real-time quantitative PCR and the $2^{-\Delta\Delta}{}_{-C}{}_{-}{}_{T}$ method," *Methods*, vol. 25, no. 4, pp. 402–408, 2001.

[36] E. M. Giles, C. Godbout, W. Chi et al., "Subtypes of endothelial progenitor cells affect healing of segmental bone defects differently," *International Orthopaedics*, vol. 41, no. 11, pp. 2337–2343, 2017.

[37] Y. Song, Z. Bai, Y. Zhang et al., "Protective effects of endothelial progenitor cell microvesicles on Ang II-induced rat kidney cell injury," *Molecular Medicine Reports*, vol. 25, no. 1, 2021.

[38] T. H. Huang, M. S. Lee, P. H. Sung et al., "Quality and quantity culture effectively restores functional and proliferative capacities of endothelial progenitor cell in end-stage renal disease patients," *Stem Cell Research*, vol. 53, no, article 102264, 2021.

[39] N. Yang, Y. Zhao, X. Wu et al., "Recent advances in extracellular vesicles and their involvements in vasculitis," *Free Radical Biology & Medicine*, vol. 171, pp. 203–218, 2021.

[40] W. Zeng, Q. Lei, J. Ma, and R. Ju, "Effects of hypoxic-ischemic pre-treatment on microvesicles derived from endothelial progenitor cells," *Experimental and Therapeutic Medicine*, vol. 19, no. 3, pp. 2171–2178, 2020.

[41] L. Tonneijck, M. H. Muskiet, M. M. Smits et al., "Glomerular hyperfiltration in diabetes: mechanisms, clinical significance, and treatment," *Journal of the American Society of Nephrology*, vol. 28, no. 4, pp. 1023–1039, 2017.

[42] D. Y. Duan, J. Tang, H. T. Tian, Y. Y. Shi, and J. Jia, "Adipocyte-secreted microvesicle-derived miR-148a regulates adipogenic and osteogenic differentiation by targeting Wnt5a/Ror2 pathway," *Life Sciences*, vol. 278, article 119548, 2021.

[43] X. Q. Wu, X. Y. Tian, Z. W. Wang, X. Wu, J. P. Wang, and T. Z. Yan, "miR-191 secreted by platelet-derived microvesicles induced apoptosis of renal tubular epithelial cells and participated in renal ischemia-reperfusion injury via inhibiting CBS," *Cell Cycle*, vol. 18, no. 2, pp. 119–129, 2019.

[44] X. Xu, L. Zhang, F. Hua et al., "FOXM1-activated SIRT4 inhibits NF-κB signaling and NLRP3 inflammasome to alleviate kidney injury and podocyte pyroptosis in diabetic nephropathy," *Experimental Cell Research*, vol. 408, no. 2, article 112863, 2021.

Hindawi
Disease Markers
Volume 2023, Article ID 9226712, 17 pages
https://doi.org/10.1155/2023/9226712

Research Article

NNMT Is an Immune-Related Prognostic Biomarker That Modulates the Tumor Microenvironment in Pan-Cancer

Wenxiu Liu,[1] **Meng Zhu**,[2] **Xiaoming Li**,[1] **Limian Er**,[3] **and Shengmian Li**[1]

[1]*Department of Gastroenterology and Hepatology, The Fourth Hospital of Hebei Medical University, Shijiazhuang, Hebei, China*
[2]*Hainan Yilai Telemedicine Center, Hainan, China*
[3]*Department of Endoscope room, The Fourth Hospital of Hebei Medical University, Shijiazhuang, Hebei, China*

Correspondence should be addressed to Shengmian Li; shengmianli2013@163.com

Received 15 August 2022; Revised 27 September 2022; Accepted 25 November 2022; Published 9 February 2023

Academic Editor: Fu Wang

Emerging evidence has revealed the significant roles of nicotinamide n-methyltransferase (NNMT) in cancer initiation, development, and progression; however, a pan-cancer analysis of NNMT has not been conducted. In this study, we first thoroughly investigated the expression and prognostic significance of NNMT and the relationship between NNMT and the tumor microenvironment using bioinformatic analysis. NNMT was significantly increased and associated with poor prognosis in many common cancers. NNMT expression correlated with the infiltration levels of cancer-associated fibroblasts and macrophages in pan-cancer. Function enrichment analysis discovered that NNMT related to cancer-promoting and immune pathways in various common cancers, such as colon adenocarcinoma, head and neck squamous cell carcinoma, ovarian serous cystadenocarcinoma, and stomach adenocarcinoma. NNMT expression was positively correlated with tumor-associated macrophages (TAMs), especially M2-like TAMs. The results suggest that NNMT might be a new biomarker for immune infiltration and poor prognosis in cancers, providing new direction on therapeutics of cancers.

1. Introduction

Cancer ranks as a leading cause of death, and the burden of cancer incidence and mortality is growing rapidly worldwide [1]. The Global Cancer Statistics 2020 estimates indicated that there were 19.3 million new cancer cases and almost 10 million cancer-related deaths in 2020 [2]. The etiology and tumorigenic process are extremely complicated and occur in concert with alterations in the surrounding stroma. The tumor microenvironment (TME) is an integral part of cancer, comprising various cell types (stromal cells, fibroblasts, endothelial cells, immune cells, etc.) and extracellular components (extracellular matrix, growth factors, hormones, cytokines, etc.) [3]. The TME not only plays a pivotal role during tumor progression and metastasis but also has profound effects on the therapeutic efficacy [4]. Innate or adaptive immune cells in TME have both anticancer and protumor activities, and accumulation of immune infiltrating cells in TME is involved in tumor development [5]. Former study has proved that oncogenes can rebuild TME and promote cancer development by directly or indirectly influencing immune cells or stromal cells. As an alternative to classic antitumor treatments, immunotherapy has verified efficacy in many different cancer types and been built up to reactivate adaptive and innate immune systems, which targets interactions between immune cells and cancer cells [6]. For example, programmed death ligand-1 (PD-L1) and programmed death-1 (PD-1) were found to have promising anticancer effects on some cancers. Unfortunately, present immunotherapies have been effective only in a few cancer patients with specific type but not in others. In consequence, it is urgent to identify new oncogenes that play key roles in TME and validate the new immune-related therapeutic targets for cancers.

Nicotinamide N-methyltransferase (NNMT) is a metabolic enzyme that catalyzes the methylation of nicotinamide using the universal methyl donor S-adenosyl methionine, directly linking one-carbon metabolism with the balance between the cell's methylation level and nicotinamide adenine dinucleotide levels [7]. Recent research showed that

NNMT promoted tumorigenesis in several ways, including facilitating cancer cell proliferation and migration, inhibiting autophagy, and regulating the differentiation of cancer-associated fibroblasts (CAFs) in the stroma [8–11].

However, most studies on the function of NNMT in cancers have been limited to a specific type of cancer. Its biological effects are not entirely known, and the role of NNMT in TME remains unclear. Whether NNMT can play a role in the pathogenesis of different tumors through certain common molecular mechanisms remains to be answered. Therefore, it is particularly important to conduct an in-depth examination of the regulatory functions of NNMT in a pan-cancer dataset to provide new directions and strategies for the clinical treatment of cancer.

The present study first consistently characterized the prevalence and prognostic value of NNMT expression in pan-cancer. Meanwhile, the molecular mechanism of NNMT in the cancer occurrence and progression and its function in TME and immune cell infiltration was also discussed. Generally, our first systematically pan-cancer analysis showed that NNMT expression was closely related with cancer patient prognosis and immune cell infiltration. NNMT played an oncogenic role in pan-cancer, and high NNMT expression had a bad effect on the survival time of cancer patients. NNMT expression remarkably correlated with the infiltration levels of CAFs and macrophages. These findings implied that NNMT influenced the clinical prognosis of cancer patients, probably by means of its interaction with tumor-infiltrating immune cells.

2. Materials and Methods

2.1. Analysis of NNMT Expression in Various Types of Tumors. NNMT mRNA expression levels in different cancer types were compared with their matched adjacent normal tissues by using web-based Oncomine analysis tools. Oncomine (https://www.oncomine.org/) is a major cancer microarray repository and web-based data mining platform [12], which contains 715 datasets and 86,733 samples. The thresholds were set at a P value of 0.001 and a fold change of 1.5 in our experiment. The NNMT expression profile and the abundance of immune infiltrates in pan-cancer were analyzed using the TIMER database (https://cistrome.shinyapps.io/timer). The gene expression levels are represented as log2 (TPM (transcripts per million) +1) values. The NNMT protein expression levels were analyzed using the Clinical Proteomic Tumor Analysis Consortium (CPTAC) database from UALCAN (http://ualcan.path.uab.edu/analysis).

Next, we used the "Expression analysis-Box Plots" module of the Gene Expression Profiling Interactive Analysis2 (GEPIA2) web server (http://gepia2.cancer-pku.cn/) to obtain the violin plots of NNMT expression at different pathological stages (stages I, II, III, and IV) of all cancers in The Cancer Genome Atlas (TCGA) [13]. The log2 TPM transformed expression data were applied to the violin plots.

2.2. Analysis of the Correlation between NNMT Expression and Patient Survival. The correlation between NNMT expression and survival in pan-cancer was analyzed using the Kaplan-Meier plotter (https://kmplot.com/analysis/) and GEPIA (http://gepia.cancer-pku.cn/). The Kaplan-Meier plotter is a powerful online tool that can be used to assess the effect of 54,675 genes on survival using 10,461 cancer samples in 21 cancer types [14]. We analyzed the relationship of NNMT expression with overall survival (OS) and relapse-free survival (RFS) in each available cancer type using the Kaplan-Meier plotter. The hazard ratio (HR) with 95% confidence intervals (CI) and logrank P value were computed. GEPIA is an interactive online platform with tumor sample information from TCGA and normal sample information from TCGA and Genotype-Tissue Expression project [15]. We explored the effect of NNMT expression on OS and disease-free survival (DFS) in 34 cancer types using GEPIA. A cut-off value of 50% was used as the expression threshold to distinguish the high expression and low expression cohorts. The logrank test was used in the hypothesis test, and the survival plots were obtained through the "Survival Analysis" module of GEPIA.

2.3. Correlation of NNMT Expression with the Tumor Microenvironment in Pan-Cancers. Using TCGA NNMT expression data, the stromal and immune cell scores were calculated after applying the ESTIMATE algorithm in R-package "estimate" and "limma" [16] for predicting the presence of infiltrating stromal/immune cells in pan-cancer tissues. The correlation analysis of NNMT expression with the tumor microenvironment (TME) and immune cell infiltration was pursued using the R-package "ggplot2," "ggpubr," and "ggExtra" ($P < 0.001$ as a cut-off value).

We used the "Immune-Gene" module of the TIMER2 web application to explore the association between NNMT expression and immune infiltrates across all TCGA tumors. The TIMER, CIBERSORT, CIBERSORT-ABS, QUANTISEQ, XCELL, MCPCOUNTER, and EPIC algorithms were applied for immune infiltration estimations. The P values and partial correlation values were obtained via the purity-adjusted Spearman rank correlation test. The data were visualized as a heatmap and a scatter plot.

Next, we confirmed the association between NNMT expression and immune infiltrates in pan-cancer using Immune Cell Abundance Identifier (ImmuCellAI; http://bioinfo.life.hust.edu.cn/ImmuCellAI). The ImmuCellAI is a tool to estimate the abundance of 24 immune cells from a gene expression dataset, including RNA sequencing and microarray data, wherein the 24 immune cells comprise 18 T cell subtypes and 6 other immune cells: B cell, dendritic cells (DCs), natural killer (NK) cell, neutrophils, monocytes, and macrophages. Cancer samples were divided into two groups according to the median NNMT expression (high versus low level), and their immune cell infiltration levels were compared.

The correlations between NNMT expression and gene markers of tumor-associated macrophages (TAMs) as well as M1 and M2 macrophages in colon adenocarcinoma (COAD), head and neck squamous cell carcinoma (HNSC), ovarian serous cystadenocarcinoma (OV), and stomach adenocarcinoma (STAD) were analyzed in the TIMER database.

Analysis type by cancer NNMT	Cancer vs. normal	
Bladder cancer		2
Brain and CNS cancer	8	
Breast cancer	2	
Cervical cancer	1	
Colorectal cancer	7	
Esophageal cancer	3	
Gastric cancer	5	
Head and neck cancer	4	
Kidney cancer	5	
Leukemia	1	2
Liver cancer		5
Lung cancer		1
Lymphoma	14	
Melanoma		
Myeloma		
Other cancer	3	
Ovarian cancer	1	
Pancreatic cancer	2	
Prostate cancer		
Sarcoma	1	1
Significant unique analyses	57	11
Total unique analyses	446	

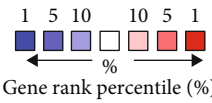

(a)

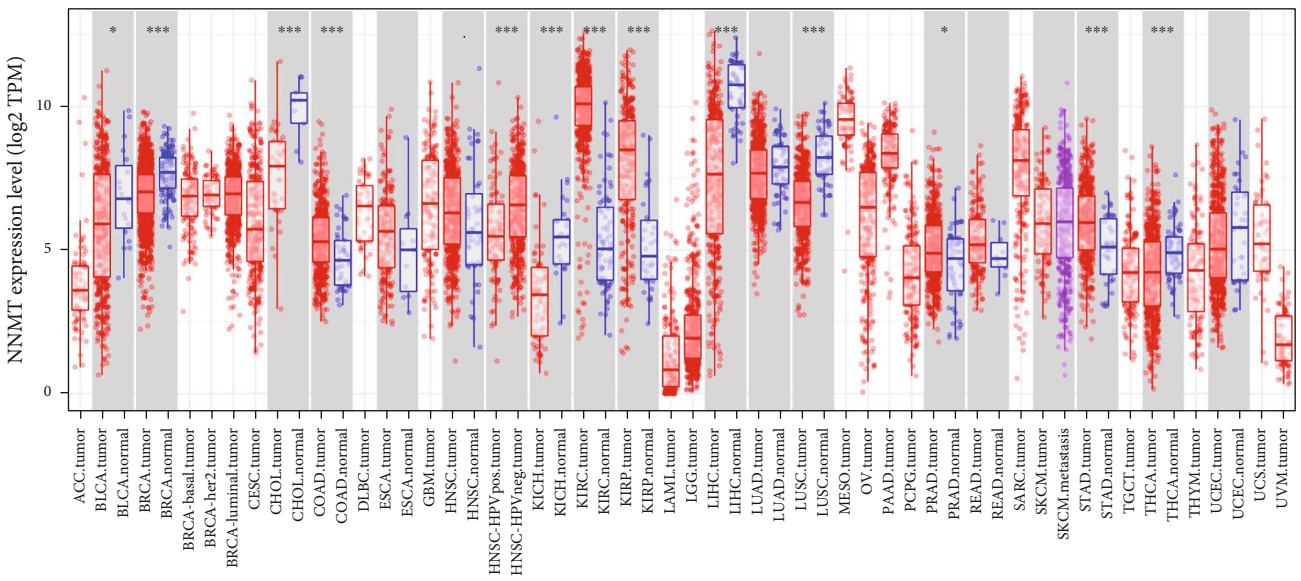

P-value significant codes: 0 ≤ *** < 0.001 ≤ ** < 0.01 ≤ * < 0.05

(b)

Figure 1: Continued.

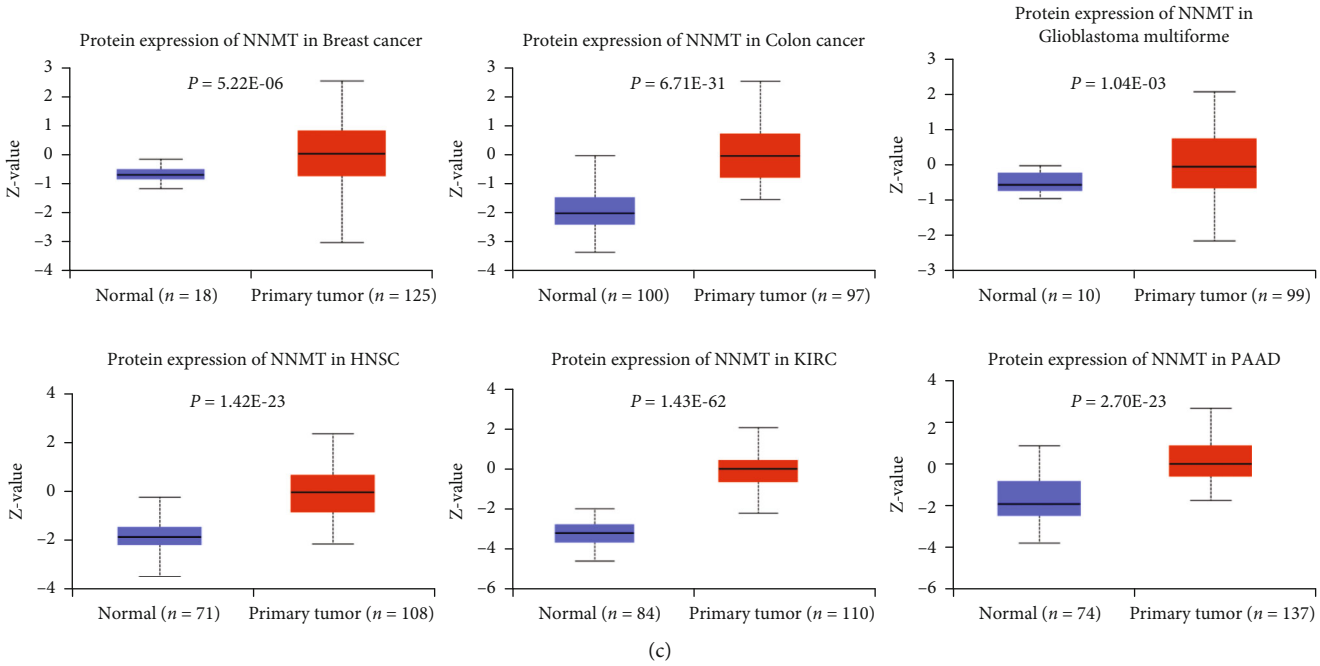

(c)

Figure 1: The NNMT mRNA expression levels in different human cancer types. (a) Increased or decreased expression of NNMT compared with normal tissues across different cancer types in the Oncomine database. (b) The NNMT mRNA expression levels in different cancer types from TCGA database in TIMER ($^{*}P < 0.05$, $^{**}P < 0.01$, and $^{***}P < 0.001$). (c) The NNMT protein expression levels in normal tissues and primary tissues of the breast cancer, colon cancer, glioblastoma multiforme, HNSC, KIRC, and PAAD were examined using the CPTAC dataset. CPTAC: Clinical Proteomic Tumor Analysis Consortium; HNSC: head and neck squamous cell carcinoma; KIRC: kidney renal clear cell carcinoma; NNMT: nicotinamide N-methyltransferase; PAAD: pancreatic adenocarcinoma.

2.4. Correlation and Enrichment Analyses. The Pearson correlation analysis of NNMT mRNA and other mRNAs was performed in the COAD, HNSC, OV, and STAD using TCGA data. The 300 genes most positively associated with NNMT were selected for an enrichment analysis to determine the function of NNMT. Gene set enrichment analysis (GSEA) was performed using the gseGO, gseKEGG, and gsePathway functions in the clusterProfiler R software package R with the following parameters: nPerm = 1,000, minGSSize = 10, maxGSSize = 1,000, and $P < 0.05$ as a cut-off value.

2.5. Statistical Analysis. Survival curves were generated by the Kaplan-Meier plots and GEPIA. The results generated in Oncomine were displayed with P values, fold changes, and ranks. The results of the GEPIA and Kaplan-Meier plots were displayed with HR and Por Cox P values from a logrank test. The correlations between NNMT expression and abundance scores of stromal/immune cells were evaluated by Spearman's correlation. The strength of the correlation was determined using the following guide for the absolute value: very weak, in between 0.00 and 0.19; weak, in between 0.20 and 0.39; moderate, in between 0.40 and 0.59; strong, in between 0.60 and 0.79; and very strong, in between 0.80 and 1.0. The results with $P < 0.05$ were considered as statistically significant.

3. Results

3.1. NNMT Expression in Different Cancer Types. First, we evaluated the NNMT mRNA levels in diverse cancers and their matched adjacent normal tissues over a cancer-wide range in Oncomine and TIMER databases. Compared with the normal tissues, in Oncomine database, the results revealed higher expression of NNMT in brain and central nervous system (CNS), breast, cervix, colon, esophagus, stomach, head and neck, kidney, lymphatic system, ovary, and pancreas cancers (Figure 1(a)). In contrast, decreased expression of NNMT was found in bladder, liver, and lung cancers.

To further verify the expression levels of NNMT in cancerous and normal tissues across all TCGA tumors, we profiled and compared them in TIMER platform. Specifically, NNMT expression levels were significantly elevated in colon adenocarcinoma (COAD), head and neck squamous cell carcinoma (HNSC), kidney renal clear cell carcinoma (KIRC), kidney renal papillary cell carcinoma (KIRP), and stomach adenocarcinoma (STAD); these results were consistent with those in the Oncomine database. In contrast, decreased expression of NNMT was found in bladder urothelial carcinoma (BLCA), breast invasive carcinoma (BRCA), cholangiocarcinoma (CHOL), kidney chromophobe (KICH), liver hepatocellular carcinoma (LIHC), lung squamous cell carcinoma (LUSC), and thyroid carcinoma (THCA) (Figure 1(b)).

Further comparison of NNMT protein expression according to the CPTAC database from UALCAN demonstrated that NNMT protein expression levels were significantly higher in advanced tumor tissues than in normal tissues; this was observed in breast cancer, colon cancer, glioblastoma multiforme, HNSC, KIRC, and pancreatic adenocarcinoma (PAAD) (Figure 1(c), all $P < 0.001$).

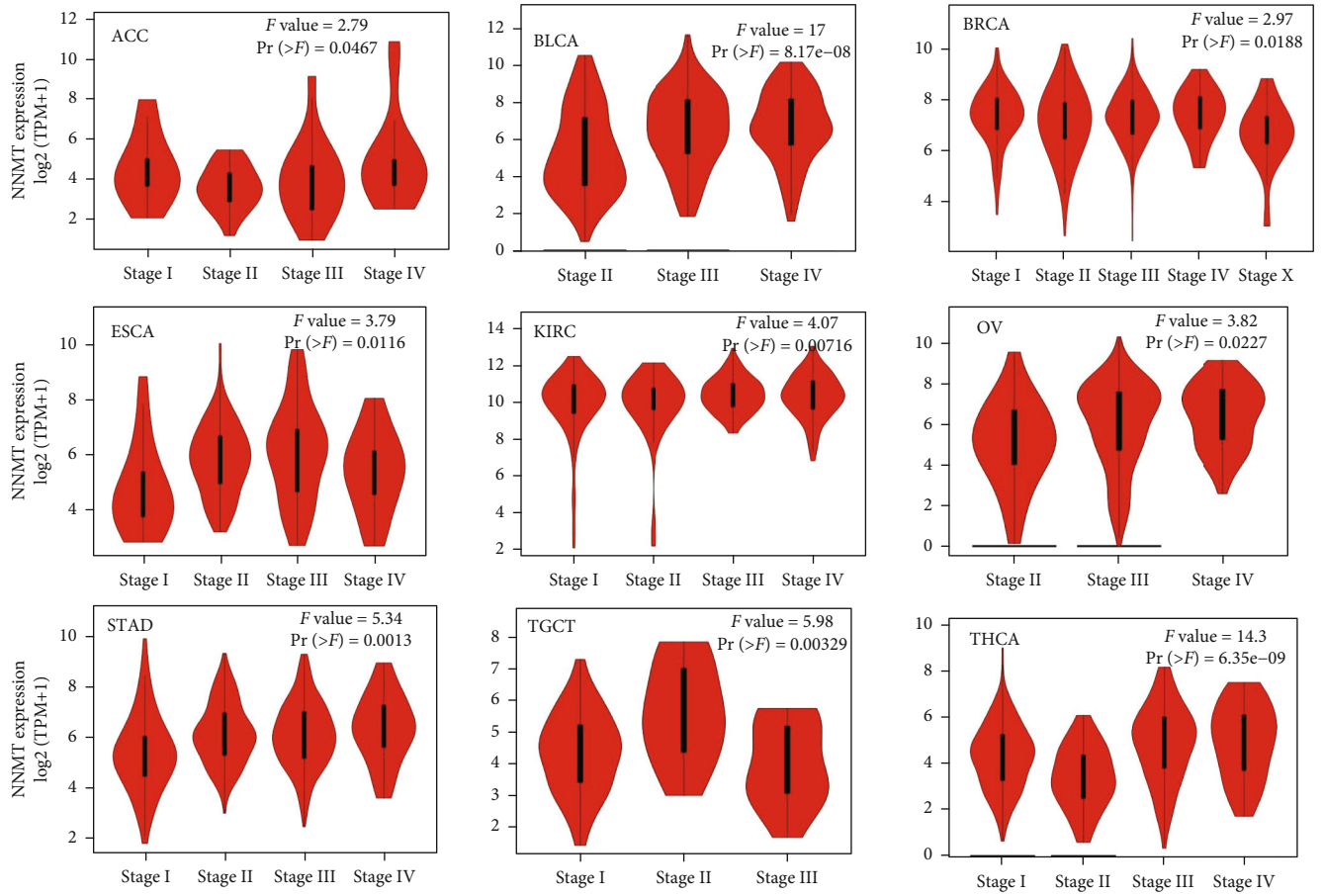

Figure 2: Association of NNMT expression level with different pathological stages. The expression levels of the NNMT were analyzed by the pathological stages (stages I, II, III, and IV) of ACC, BLCA, BRCA, ESCA, KIRC, OV, STAD, TGCT, and THCA from TCGA database in GEPIA. Log2 (TPM+1) was applied for log-scale. ACC: adrenocortical carcinoma; BLCA: bladder urothelial carcinoma; BRCA: breast invasive carcinoma; ESCA: esophageal carcinoma; GEPIA: Gene Expression Profiling Interactive Analysis; KIRC, kidney renal clear cell carcinoma; NNMT, nicotinamide N-methyltransferase; OV, ovarian serous cystadenocarcinoma; STAD, stomach adenocarcinoma; TGCT, testicular germ cell tumors; THCA, thyroid carcinoma; TPM, transcripts per million.

We also used the "Pathological Stage Plot" module of GEPIA2 to observe the correlation between NNMT expression and the pathological stages of cancers in all TCGA tumors. NNMT expression was significantly associated with the TNM stage in adrenocortical carcinoma (ACC), BLCA, BRCA, esophageal carcinoma (ESCA), KIRC, ovarian serous cystadenocarcinoma (OV), STAD, testicular germ cell tumors (TGCT), and THCA. As shown in Figure 2, NNMT expression level was significantly different from stage I to IV in ACC (F value = 2.79, Pr = 0.0467), BLCA (F value = 17, Pr = $8.17E-08$), BRCA (F value = 2.97, Pr = 0.0188), ESCA (F value = 3.79, Pr = 0.0116), KIRC (F value = 4.07, Pr = 0.00716), OV (F value = 3.82, Pr = 0.0227), STAD (F value = 5.34, Pr = 0.0013), TGCT (F value = 5.98, Pr = 0.00329), and THCA (F value = 14.3, Pr = $6.35E-09$). It seemed that NNMT expression was higher in the stage III-IV but lower in stage I-II patients in BLCA, OV, STAD, and THCA.

3.2. Prognostic Potential of NNMT in Cancers. Next, we analyzed the prognostic value of NNMT expression in pan-cancers using the Kaplan-Meier plotter and GEPIA data. The results in the Kaplan-Meier plotter database showed that 10 out of 21 cancer types displayed poorer prognosis, including bladder carcinoma (OS : HR = 1.53, 95%CI = 1.05 to 2.22, logrank $P = 0.026$), cervical squamous cell carcinoma and endocervical adenocarcinoma (CESC) (OS : HR = 1.71, 95%CI = 1.07 to 2.74, logrank $P = 0.023$; RFS : HR = 3.05, 95%CI = 1.4 to 6.68, logrank $P = 0.0032$), HNSC (OS : HR = 1.66, 95%CI = 1.27 to 2.19, logrank $P = 0.00021$; RFS : HR = 3.21, 95%CI = 1.51 to 6.81, logrank $P = 0.0014$), KIRC (OS : HR = 1.69, 95%CI = 1.23 to 2.31, logrank $P = 0.0011$), LUSC (OS : HR = 1.4, 95%CI = 1.07 to 1.85, logrank $P = 0.016$), OV (OS : HR = 1.35, 95% CI = 1.04 to 1.77, logrank $P = 0.025$; RFS : HR = 1.45, 95% CI = 1.0 to 2.1, logrank $P = 0.046$), STAD (OS : HR = 1.92, 95%CI = 1.37 to 2.69, logrank $P = 0.00012$; RFS : HR = 3.23, 95%CI = 1.68 to 6.19, logrank $P = 0.00019$), thymoma (THYM) (OS : HR = 3.95, 95%CI = 1.05 to 14.86, logrank $P = 0.028$), THCA (OS : HR = 3.05, 95%CI = 1.13 to 8.21, logrank $P = 0.02$), and ESCA (RFS : HR = 5.96, 95%CI = 0.82 to 43.3, logrank $P = 0.046$) (Figure 3(a)). Only in sarcoma (OS : HR = 0.63, 95%CI = 0.42 to 0.96, logrank $P = 0.03$) and uterine corpus endometrial carcinoma (UCEC)

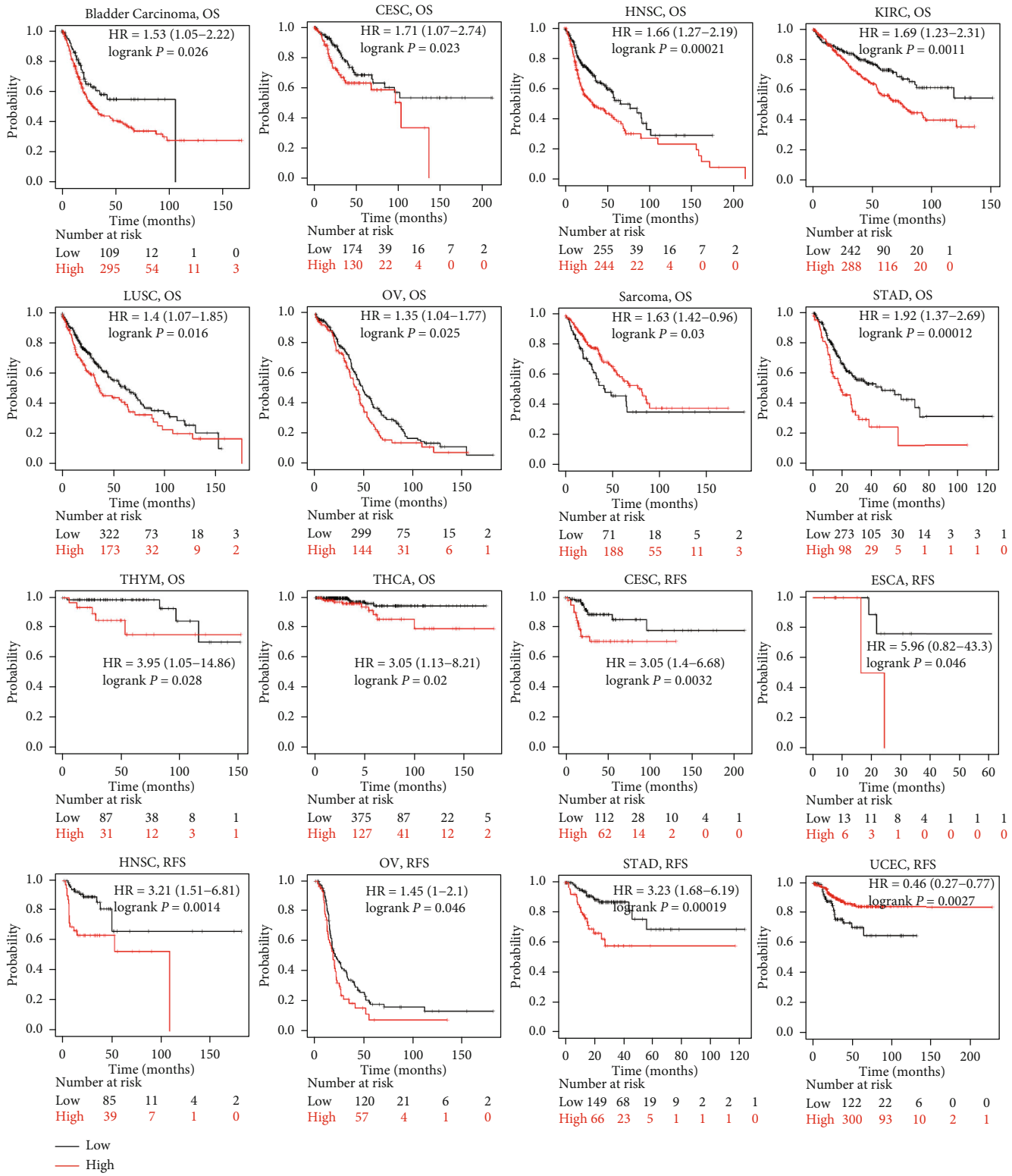

(a)

Figure 3: Continued.

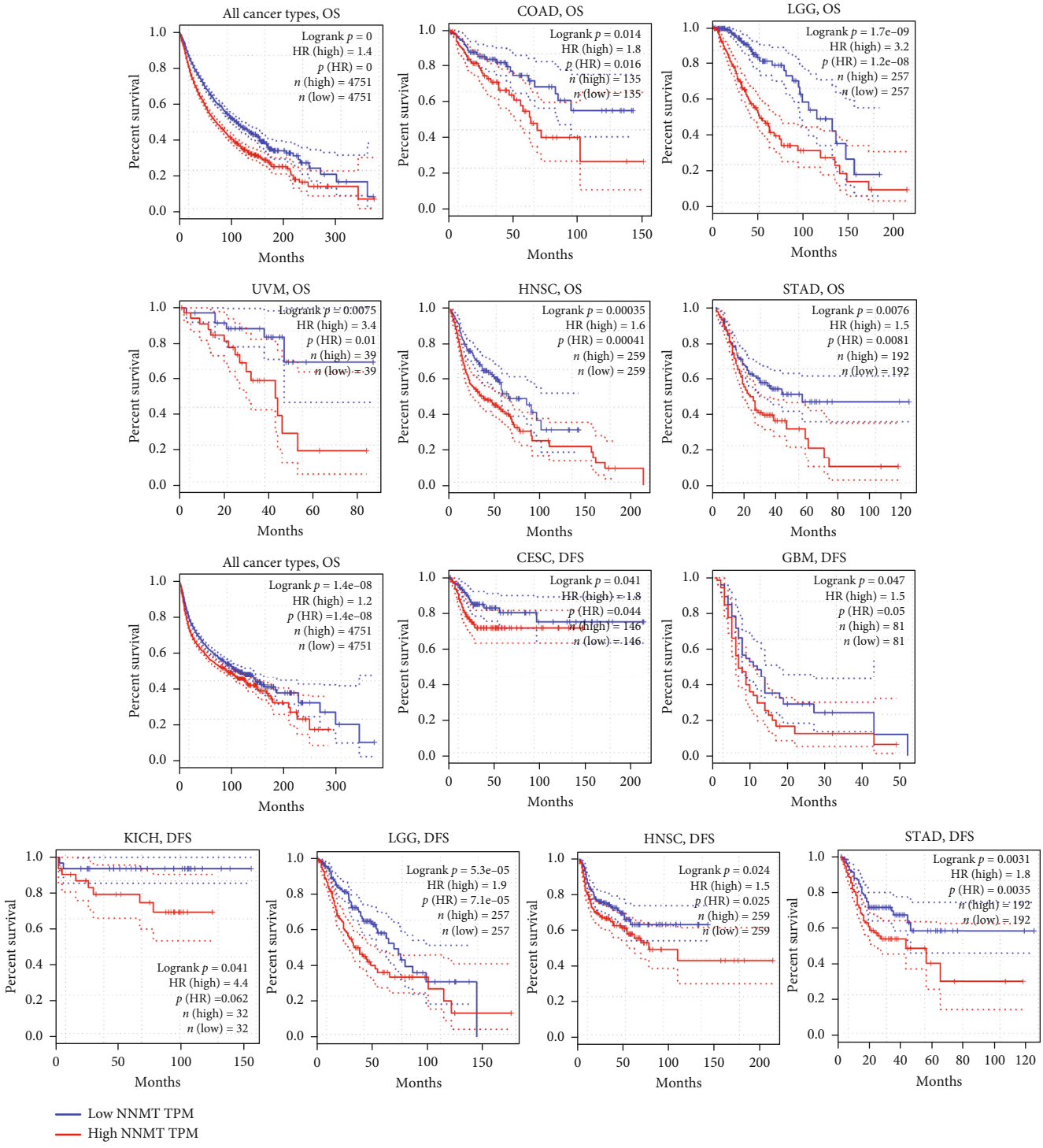

(b)

Figure 3: The Kaplan-Meier survival curves of NNMT expression in different cancer types. (a). Relationship between NNMT expression and the OS or RFS of cancer patients in the Kaplan-Meier Plotter. (b). Relationship between NNMT expression and the OS or DFS of cancer patients in the GEPIA. DFS, disease-free survival; GEPIA, Gene Expression Profiling Interactive Analysis; NNMT: nicotinamide N-methyltransferase; OS: overall survival; RFS: relapse-free survival.

(RFS : HR = 0.46, 95%CI = 0.27 to 0.77, logrank $P = 0.0027$), high NNMT expression was associated with better prognosis (Figure 3(a)).

To further clarify the function of NNMT in pan-cancer, the GEPIA database, which can provide more cancer types, was used. Equally, higher NNMT mRNA levels revealed a

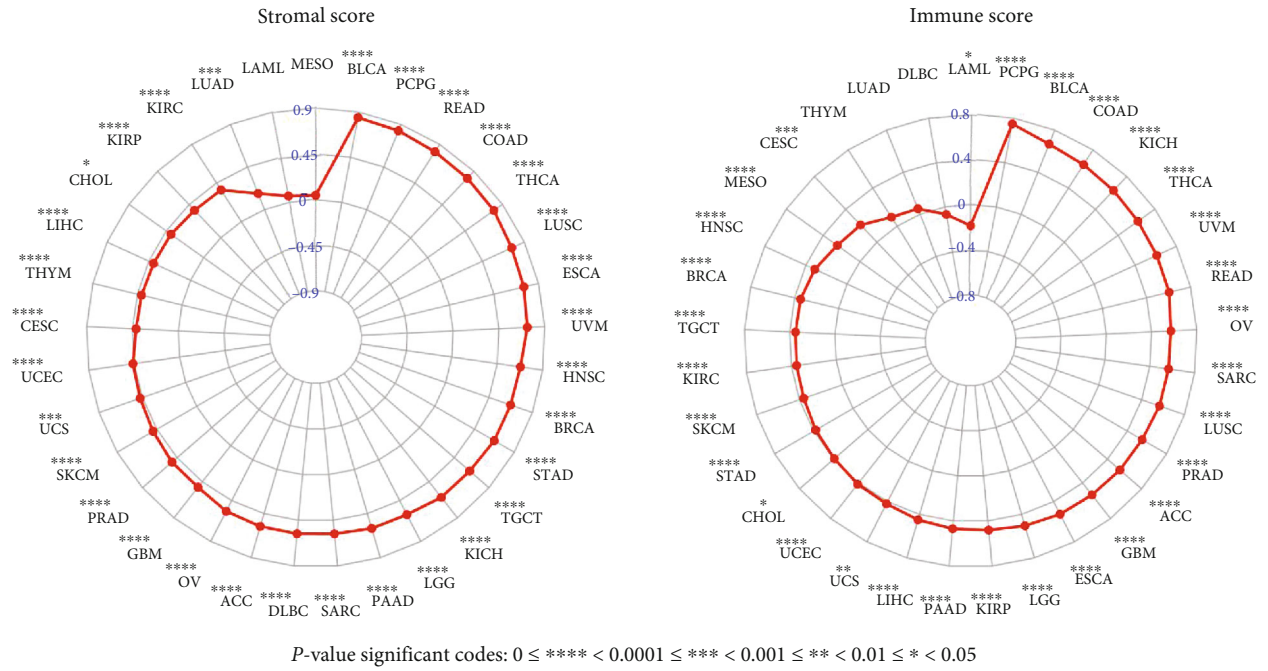

Figure 4: Correlation of NNMT gene expression with the stromal and immune scores in different cancers. (a) Correlation of NNMT gene expression with the stromal scores in pan-cancer. (b) Correlation of NNMT gene expression with the immune scores in pan-cancer. NNMT: nicotinamide N-methyltransferase.

worse prognostic prediction in all cancer types (OS : HR (high) = 1.4, logrank $P = 0$; disease − free survival (DFS): HR(high) = 1.2, logrank $P = 1.4E - 08$). NNMT high expression had a poorer prognosis in certain cancer types from GEPIA database, including COAD (OS : HR (high) = 1.8, logrank $P = 0.014$), HNSC (OS : HR (high) = 1.6, logrank $P = 0.00035$; DFS : HR (high) = 1.5, logrank $P = 0.024$), brain lower-grade glioma (LGG) (OS : HR (high) = 3.2, logrank $P = 1.7E - 09$; DFS : HR (high) = 1.9, logrank $P = 5.3E - 05$), STAD (OS : HR (high) = 1.5, logrank $P = 0.0076$; DFS : HR (high) = 1.8, logrank $P = 0.0031$), uveal melanoma (UVM) (OS : HR (high) = 3.4, logrank $P = 0.0075$), CESC (DFS : HR (high) = 1.8, logrank $P = 0.041$), glioblastoma multiforme (GBM) (DFS : HR (high) = 1.5, logrank $P = 0.047$), and KICH (DFS : HR (high) = 4.4, logrank $P = 0.041$) (Figure 3(b)). These results were consistent with the findings in the Kaplan-Meier plotter database.

Taking together, these integrated analyses revealed that NNMT played a detrimental role in cancer development and had prognostic value in pan-cancer.

3.3. Correlation between NNMT Expression and Tumor Microenvironment (TME) in Pan-Cancer. The TME is essential in stimulating heterogeneity among cancer cells, thus leading to cancer cell progression and metastasis [17]. Since our findings validated the prognostic role of NNMT in pan-cancer, it would be highly appropriate to further explore the relationship between TME and NNMT expressions in different types of cancers. We used the ESTIMATE algorithm to calculate the stromal and immune cell scores in pan-cancer. The results showed that NNMT expression had significant correlations with stromal scores in 30 types of cancer and significant correlations with immune scores in 29 types of cancers. As shown in Figure 4(a) and Table S1, NNMT expression had very strong correlation with stromal scores in BLCA, PCPG, READ, and COAD (all $r > 0.8$, $P < 0.0001$); had strong correlation with stromal scores in THCA, LUSC, ESCA, UVM, HNSC, BRCA, STAD, TGCT, KICH, LGG, and PAAD (all $r > 0.6$, $P < 0.0001$); and had moderate correlation with stromal scores in SARC, DLBC, ACC, OV, GBM, PRAD, SKCM, UCS, UCEC, CESC, and THYM (all $r > 0.4$, $P < 0.001$). NNMT expression had strong correlation with immune scores in PCPG, BLCA, COAD, KICH, THCA, UVM, and READ (all $r > 0.6$, $P < 0.0001$) and had moderate correlation with immune scores in OV, SARC, LUSC, PRAD, ACC, GBM, ESCA, LGG, KIRP, PAAD, LIHC, UCS, and UCEC (all $r > 0.4$, $P < 0.01$) (Figure 4(b) and Table S1). This results would particularly important for COAD, HNSC, OV, and STAD since NNMT expression was increased and associated with poor prognosis in these types of cancer (according to the Kaplan-Meier or GEPIA analyses). NNMT expression had a significantly positive correlation to both stromal and immune scores in these types of cancer (Table S1 and Figure S1). These results indicated that the infiltration of stromal or immune cells escalates accompanied with the increase of NNMT expression in COAD, HNSC, OV, and STAD.

3.4. Association between NNMT Expression and Immune Cell Infiltration in Pan-Cancer. Tumor-infiltrating immune cells in the TME play a key part in the initiation, progression,

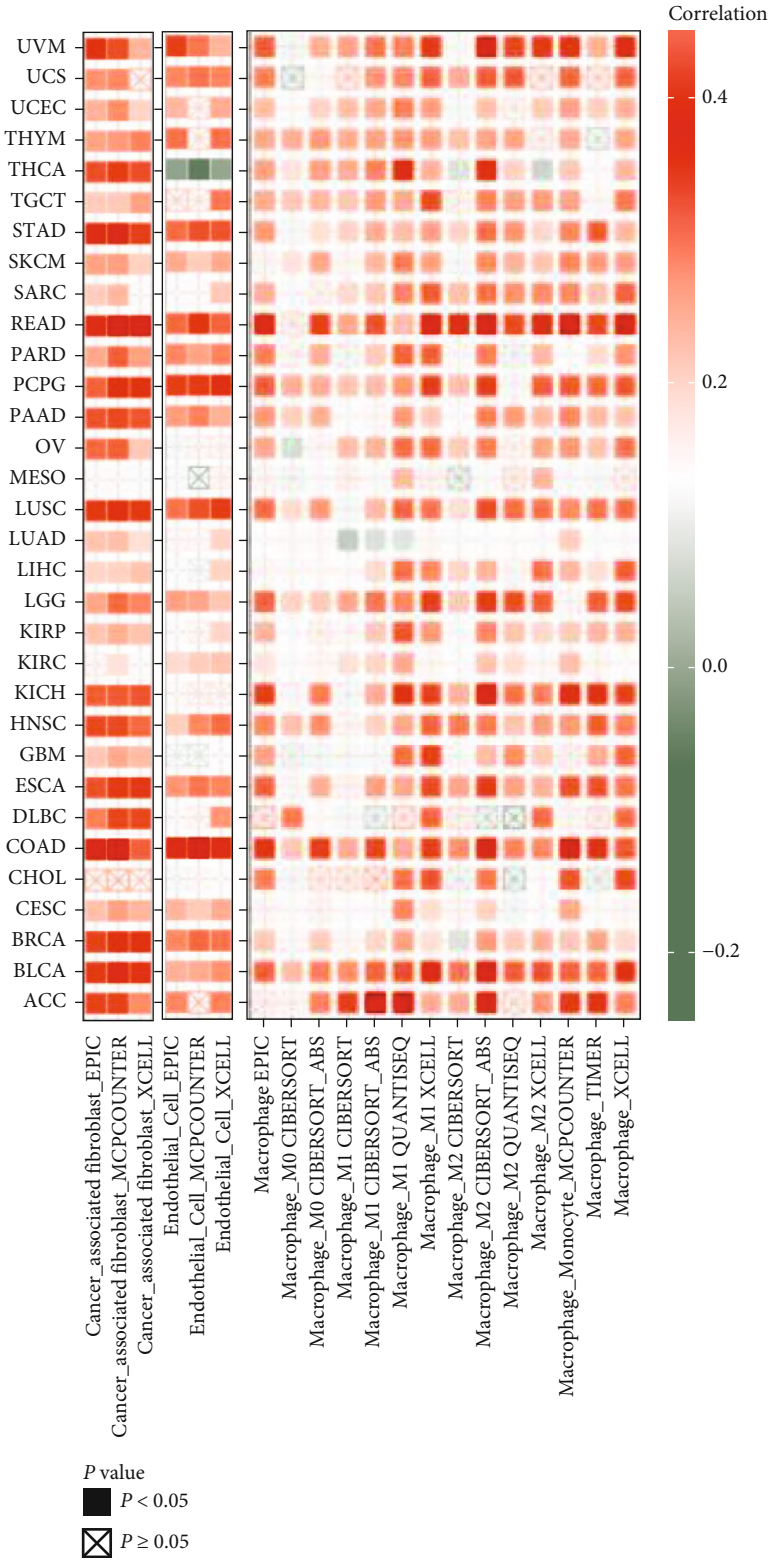

(a)

Figure 5: Continued.

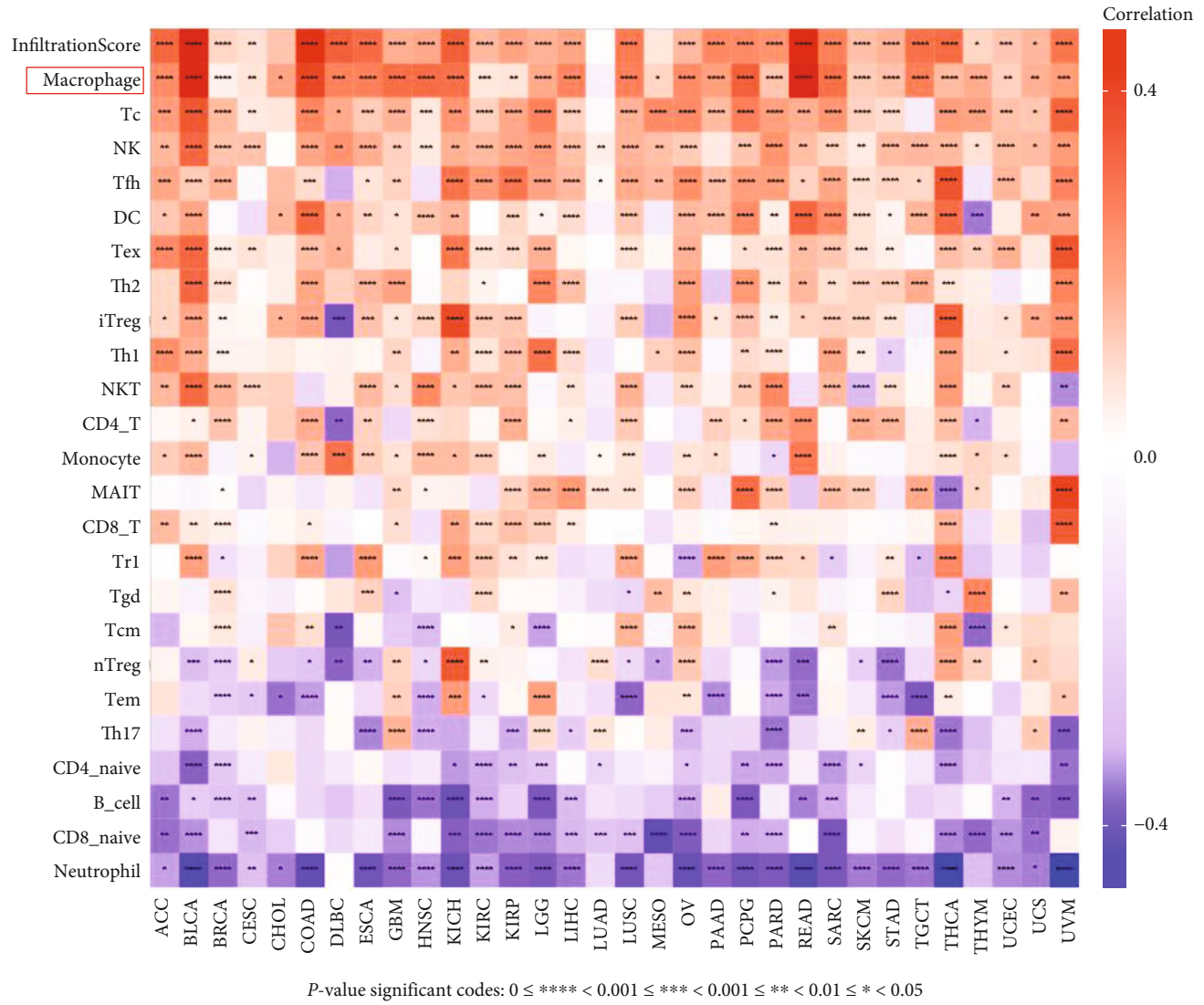

(b)

Figure 5: Correlation analysis between NNMT expression and immune cell infiltration. (a) NNMT expression significantly correlated with the infiltration levels of CAFs, endothelial cells, and macrophages in TCGA pan-cancer. (b) NNMT expression significantly correlated with the infiltration levels of various immune cells in the ImmuCellAI database. CAFs: cancer-associated fibroblasts; ImmuCellAI: Immune Cell Abundance Identifier; NNMT: nicotinamide N-methyltransferase; TCGA: The Cancer Genome Atlas.

recurrence, and metastasis of cancers. Here, we utilized some or all algorithms, including TIMER, EPIC algorithms, QUANTISEQ, CIBERSORT or CIBERSORT-ABS, MCPCOUNTER, and XCELL, to investigate the relationship between NNMT gene expression and the infiltration level of different immune cells in diverse cancers.

The results showed that NNMT expression was closely related to the abundance of immune cells infiltrating: cancer-associated fibroblasts (CAFs) in 30 types of tumor, endothelial cells in 27 types of tumor, macrophages in 28 types of tumor, $CD8^+$ T cells in 26 types of tumor, neutrophils in 25 types of tumor, $CD4^+$ T cells in 22 types of tumor, natural killer (NK) cells in 20 types of tumor, and B cells in 11 types of tumor (Table S2). Compared with other immune cells, we observed a stronger correlation between NNMT expression and the infiltration of CAFs and macrophages in TCGA pan-cancer. The expression of NNMT had a positively strong correlations with infiltration levels of CAFs in COAD, READ, STAD, and BLCA (all $r > 0.6$, $P < 0.0001$), had a positively strong correlation with macrophages in READ ($r = 0.63$, $P < 0.0001$), and had moderate correlation with macrophages in UVM, BLCA, KICH, CHOL, LGG, COAD, PCPG, LIHC, SARC, GBM, UCS, DLBC, and LUSC (all $r > 0.4$, $P < 0.001$) (Figure 5(a) and Table S2).

To verify the association between NNMT expression and immune cell infiltration, we perform the correlation analysis in pan-cancer using ImmuCellAI. Consistent with the results in TCGA pan-cancer, macrophages were the most positively relevant immune cells with NNMT expression (Figure 5(b)). In addition, in cancers which NNMT expression levels were correlated with poor prognosis, such as

Table 1: Analysis of the correlation between NNMT and gene markers of TAMs, M1 macrophages, and M2 macrophages in TIMER.

Cell type	Gene markers	COAD				HNSC				OV				STAD			
		None		Purity		None		Purity		None		Purity		None		Purity	
		Cor	*P*	Cor	*P*	Cor	*P*	Cor	*P*	Cor	*P*	Cor	*P*	Cor	*P*	Cor	*P*
TAM	CCL2	0.73	****	0.68	****	0.37	****	0.33	****	0.48	****	0.26	****	0.59	****	0.57	****
	CD68	0.47	****	0.40	****	0.25	****	0.19	****	0.42	****	0.14	*	0.23	****	0.19	****
	CD80	0.51	****	0.43	****	0.37	****	0.33	****	0.36	****	0.16	*	0.27	****	0.22	****
	IL10	0.52	****	0.46	****	0.35	****	0.30	****	0.47	****	0.27	****	0.45	****	0.42	****
M1 macrophage	INOS (NOS2)	-0.14	***	-0.21	****	-0.17	****	-0.13	***	0.02	0.73	-0.06	0.37	-0.05	0.27	-0.08	0.13
	IRF5	0.26	****	0.26	****	-0.03	0.54	-0.04	0.441	0.11	0.06	-0.03	0.63	0.23	****	0.24	****
	ARG2	0.02	0.65	-0.02	0.75	-0.24	****	-0.17	****	0.18	**	-0.14	*	0.13	*	-0.11	*
M2 macrophage	CD163	0.67	****	0.6	****	0.47	****	0.42	****	0.43	****	0.19	***	0.42	****	0.38	****
	VSIG4	0.68	****	0.61	****	0.50	****	0.45	****	0.52	****	0.292	****	0.49	****	0.47	****
	MRC1	0.55	****	0.47	****	0.45	****	0.38	****	0.36	****	0.11	0.08	0.38	****	0.35	****
	MS4A4A	0.64	****	0.57	****	0.50	****	0.45	****	0.49	****	0.252	****	0.46	****	0.42	****

None: correlation coefficient without adjustment; Purity: correlation adjusted by tumor purity; Cor: *R* value of Spearman's correlation. $^{*}P < 0.05$. $^{**}P < 0.01$. $^{***}P < 0.001$. $^{****}P < 0.0001$.

COAD, HNSC, OV, and STAD, macrophage levels were significantly upregulated in the NNMT high expression group (Figure S2). In COAD, NNMT expression had significantly positive correlation with infiltrating levels of macrophages ($r = 0.62$, $P = 1.35E-31$), dendritic cells (DCs) ($r = 0.54$, $P = 2.09E-22$), T cells ($r = 0.47$, $P = 4.80E-17$), induced regulatory T cells (iTregs) ($r = 0.38$, $P = 5.66E-11$), T-helper 2 (Th2) cells ($r = 0.38$, $P = 5.99E-11$), NK cells ($r = 0.38$, $P = 7.03E-11$), and $CD4^+$ T cells ($r = 0.36$, $P = 6.73E-10$). For HNSC, the results also displayed that NNMT expression significantly related to infiltrating levels of macrophages ($r = 0.53$, $P = 4.00E-39$), NKT cells ($r = 0.46$, $P = 5.94E-28$), monocyte ($r = 0.31$, $P = 3.78E-13$), and DCs ($r = 0.29$, $P = 2.34E-11$). As same as COAD and HNSC, the correlation between NNMT and infiltrating levels of immune cells in OV is as follows: macrophage ($r = 0.45$, $P = 6.49E-17$), T cells ($r = 0.46$, $P = 3.56E-17$), follicular helper T (Tfh) cells ($r = 0.44$, $P = 2.75E-16$), iTregs ($r = 0.43$, $P = 6.38E-15$), Th2 cells ($r = 0.40$, $P = 4.37E-13$), and DCs ($r = 0.32$, $P = 8.75E-09$). Moreover, NNMT expression was positively related to $CD4^+$ T cells ($r = 0.33$, $P = 1.20E-11$), NK cells ($r = 0.31$, $P = 9.07E-11$), and macrophages ($r = 0.29$, $P = 1.20E-09$) in STAD (Figure 5(b) and Table S3). These results reflected that NNMT might influence cancer patient survival by affecting immune cell infiltration in the TME.

3.5. NNMT Correlates with Polarization of M2 Macrophage. The results above showed that macrophages was the most positively relevant immune cells with NNMT expression in pan-cancer. Next, we analyzed the correlation of NNMT and the gene markers of macrophage subtypes including tumor-associated macrophages (TAMs) and M1 and M2 macrophages in COAD, HNSC, OV, and STAD. The results showed that gene markers of TAM such as CCL2, CD68, CD80, and IL10 had strong or moderate correlations with NNMT expression. M2 macrophage markers including CD163, VSIG4, MRC1, and MS4A4A also had strong or moderate correlations with NNMT expression. However, M1 macrophage markers including INOS, IRF5, and ARG2 had negatively or no apparent correlations with NNMT expression (Table 1). These results indicated that NNMT may regulate the differentiation of macrophages into TAMs by affecting the polarization of M2 macrophage, which contributes to tumorigenesis and development.

3.6. Functional Enrichment Analysis of NNMT in COAD, HNSC, OV, and STAD. We did Gene Set Enrichment Analysis (GSEA) of NNMT in COAD, HNSC, OV, and STAD to investigate the molecular mechanisms of NNMT in tumorigenesis and TME. Interestingly, we found the similar results in the selected cancers. NNMT was involved in a number of GO terms including MAPK cascade, regulation of cytokine production, and cytokine production in COAD, HNSC, OV, and STAD and angiogenesis in COAD, OV, and STAD (Figure 6(a)). GSEA results of KEGG analysis indicated that NNMT was associated with many cancer-promoting and immune-related pathways, such as the PI3K-Akt signaling pathways, cell adhesion molecules, and chemokine signaling pathways in COAD, HNSC, OV, and STAD; MAPK signaling pathways in HNSC, OV, and STAD; and cytokine-cytokine receptor interaction in COAD and OV (Figure 6(b)). The GSEA results for Reactome terms suggested that NNMT was positively regulated and provided several immune-related functions in COAD, HNSC, OV, and STAD. These activities included immunoregulatory interactions between a lymphoid and nonlymphoid cell, cytokine signalling in the immune system, adaptive and innate immune system, neutrophil degranulation, and interleukin-mediated signalling (Figure 6(c)). Generally, these results suggested that NNMT played a key role in carcinogenesis and tumor immune microenvironment.

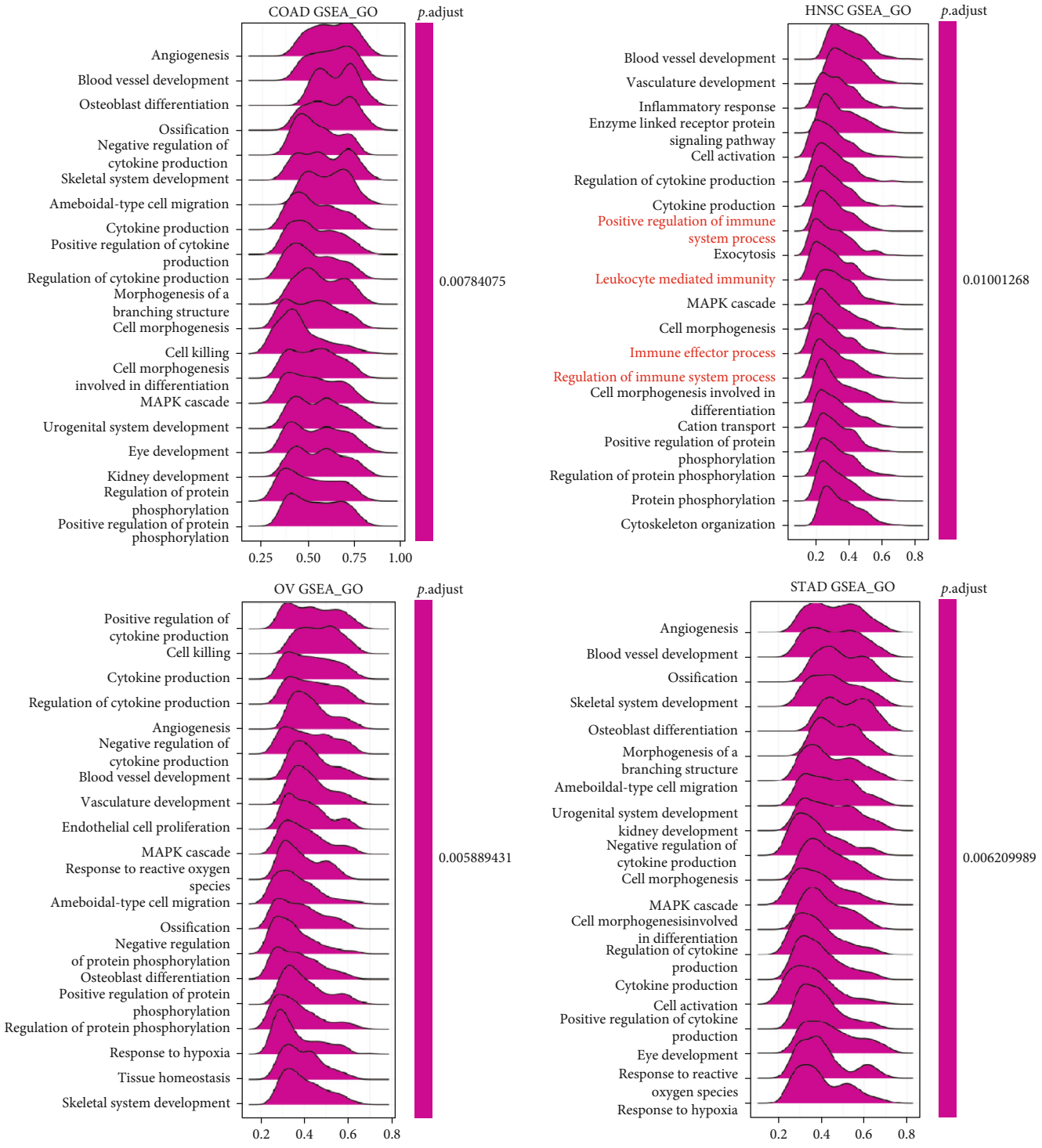

(a)

Figure 6: Continued.

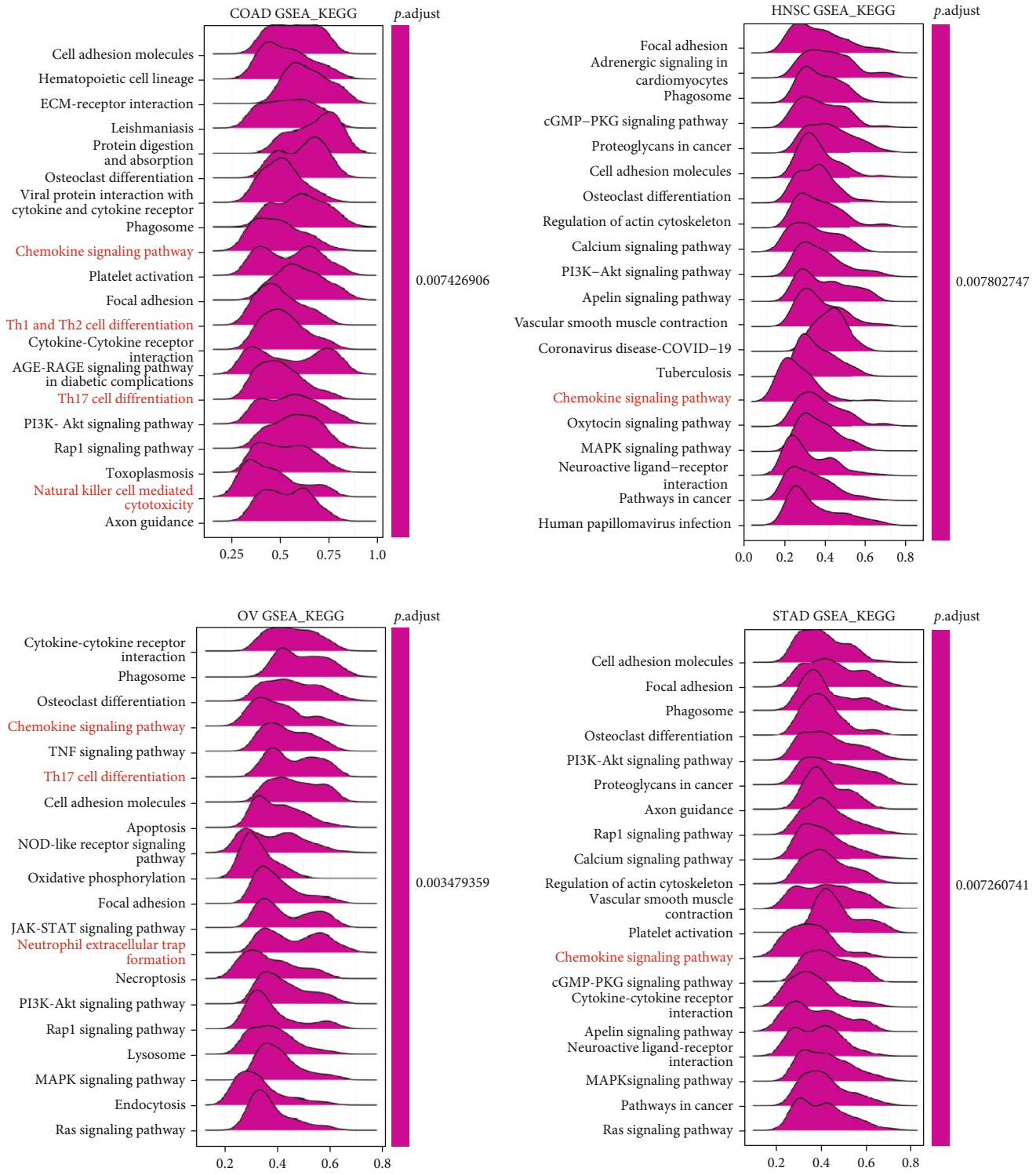

(b)

Figure 6: Continued.

Figure 6: Merged enrichment plots for NNMT obtained from GSEA. (a–c) Merged plots of GSEA indicating the top 20 significant pathways associated with NNMT expression according to GO (a), KEGG (b), and Reactome analyses (c) in COAD, HNSC, OV, and STAD. Red color represents immune-related pathways. COAD: colon adenocarcinoma; GO: Gene Ontology; GSEA: Gene Set Enrichment Analysis; HNSC: head and neck squamous cell carcinoma; KEGG: Kyoto Encyclopedia of Genes and Genome; NNMT: nicotinamide N-methyltransferase; OV: ovarian serous cystadenocarcinoma; STAD: stomach adenocarcinoma.

4. Discussion

Nicotinamide N-methyltransferase (NNMT) which was discovered 70 years ago methylates nicotinamide (NA) to generate 1-methyl nicotinamide. Its role in human health has evolved from serving only metabolic functions to being a driving force in a number of cancers. Although the increasing evidence showed NNMT was a feasible therapeutic

target, its primary functions and mechanisms in cancer development, especially in tumor immunology, are not fully understood. The present study first thoroughly investigated the expression and prognostic significance of NNMT and the correlation between NNMT expression and immune cell infiltration in tumor microenvironment (TME) using bioinformatic techniques.

By analyzing the differences expression of NNMT in diverse tumor tissues and adjacent normal tissues, we found that the expression level of NNMT in the tumor tissues of BRCA, COAD, HNSC, KIRC, PAAD, and STAD is higher, while low NNMT expression was observed in bladder, liver, and lung cancers. The difference levels of NNMT expression in various cancer types may reflect distinct underlying mechanisms and functions. NNMT overexpression increases the chemoresistance through SIRT1 stabilization and activity in breast cancer [18]. NNMT depletion contributes to liver cancer cell survival by enhancing autophagy under nutrient starvation [10].

We further found that NNMT expression in different pathological stages of cancers was significantly different, consistent with the previous study showing that increased expression of NNMT was associated with increased tumor stage in STAD and OV [19, 20]. In fact, increased NNMT expression was associated with primary tumor size, lymph node metastasis, distant metastasis, and TNM stage in gastric cancer [19] and with increased tumor stage, grade, and mesenchymal molecular subtype in ovarian cancer [20] which indicated that NNMT might promote the growth and progression of cancer.

Upon analysis of the Kaplan-Meier plotter, upregulated expression of NNMT correlated with poor OS, RFS, or DSS in several cancers including bladder carcinoma, CESC, COAD, HNSC, KIRC, LUSC, LGG, OV, STAD, and THCA while correlated with good OS in sarcoma and UCEC.

Similar results also indicated that NNMT expression was significantly higher and correlated with poor survival in breast cancer [18], colorectal cancer [21], gastric cancer [19], and OV [20]. In regard to endometrial cancer, NNMT expression was significantly higher in primary high-grade and metastatic tumors and NNMT overexpression in metastatic tissue was associated with decreased survival [22]. These data conflict with our current results, possibly because only primary uterine corpus types of endometrial carcinoma are present in our study. Interestingly, NNMT was identified as a poor prognostic factor in CESC, HNSC, KIRC, LUSC, and LGG which has not been reported in previous studies. These results confirmed that NNMT was a potential biomarker for predicting the prognosis of cancer patients.

The emerging tumor microenvironment (TME) is a complex and continuously evolving entity. Early in tumor growth, a dynamic and reciprocal relationship develops between cancer cells and components of the TME to support cancer cell survival, local invasion, and metastatic dissemination [23]. Here, we found that NNMT expression presents a significantly positive correlation with both stromal and immune components of TME in pan-cancer.

Cancer-associated fibroblasts (CAFs) are important ingredients of the microenvironment in most types of cancers, and CAFs in the stroma of the TME have been reported to participate in modulating the function of various tumor-infiltrating immune cells [24, 25]. CAFs contribute to cancer immune escape through multiple mechanisms, such as secretion of multiple cytokines and chemokines, mediating the recruitment and functional differentiation of innate and adaptive immune cells [25]. Previous work has reported that NNMT is a central, metabolic regulator of CAF differentiation, and cancer progression in the stroma and inhibition of NNMT activity led to a reversion of the CAF phenotype [11]. High stromal NNMT is a prognostic marker in colorectal cancer [21], and NNMT enhances resistance to 5-fluorouracil in colorectal cancer cells through inhibition of the ASK1-p38 MAPK pathway [26]. NNMT induces cellular invasion via activating PI3K/Akt/SP1/MMP-2 pathway in clear cell renal cell carcinoma (ccRCC) [27]. The decreased activation of p44/42 MAPK and Akt following NNMT silencing shows a similar trend under in vivo conditions [28]. Plenty of evidence has confirmed that PI3K/AKT pathway promotes the differentiation of diverse cells into CAFs. PI3K/AKT signaling pathways regulated CAF-mediated cancer cell proliferation in many cancers including STAD and COAD [29]. MAPK signal was found to be involved not only in the metabolism of fatty acids but also in glycolysis in CAFs. Compared with these studies, our results showed that NNMT expression level had a positively correlations with infiltration levels of CAFs in 30 types of cancer. Our KEGG analysis suggested that NNMT was significantly associated with many cancer-promoting and immune-related pathway including PI3K-Akt, chemokine, cytokine in the immune system, cytokine-cytokine receptor interaction, cell adhesion, JAK-STAT, and MAPK signaling pathways. Combined with the previous research, our results serve as a reminder that NNMT regulates the CAFs in various cancers.

Immunoscore is a routine parameter in predicting the response to immunotherapy and should be considered as a prognostic factor for patients' survival [30]. Recently, with the breakthrough of immune checkpoints, immune checkpoint inhibitors, such as PD-1/PD-L1 inhibitors, have been widely used in the treatment of diverse cancers. The dynamic characteristics of the TME, tumor infiltrating cells, and immune biomarkers are important for the immunotherapy response [31]. Our current results showed that NNMT had a wider tumor applicability and was more closely related with immune cells in pan-cancer. NNMT significantly correlated with the infiltration levels of B cells, $CD4^+$ T cells, $CD8^+$ T cells, macrophages, NK cells, and neutrophils in diverse cancers. Specifically, NNMT expression had a strongly positive correlation with macrophages.

Macrophage levels were remarkably increased in the NNMT high expression group compared with that in the NNMT low expression group in COAD, HNSC, OV, and STAD. Among these cancer types, tumor-associated macrophage (TAM) markers such as CCL2, CD68, CD80, and IL10 had strong or moderate correlations with NNMT expression. M2 macrophage markers, for example, CD163, VSIG4, MRC1, and MS4A4A, also had strong or moderate correlations with NNMT expression while M1 macrophage markers, including INOS, IRF5, and ARG2, had negatively

or no apparent correlations with NNMT expression. These findings indicated that NNMT may regulate the polarization of TAMs. TAMs in TME typically promote cancer cell proliferation, immunosuppression, and angiogenesis in support of tumor growth and metastasis. Oftentimes, the abundance of TAMs in tumor is correlated with poor disease prognosis. In colorectal cancer (CRC), TAMs induce EMT program to enhance CRC migration, invasion, and CTC-mediated metastasis by regulating the JAK2/STAT3/miR-506-3p/FoxQ1 axis, which in turn leads to the production of CCL2 that promote macrophage recruitment [32]. As for HNSC, HNSC cells drive TAMs towards M2 polarization. In turn, M2 TAMs contribute to migration and invasion of HNSC cells [33]. NNMT promotes epithelial-mesenchymal transition (EMT) in gastric cancer cells by activating transforming growth factor-β1 expression [34]. TAMs can also promote the invasiveness and migration properties of cancer cells by remodeling the extracellular matrix [35].

These above results indicate that NNMT may promote the differentiation of macrophages into TAMs involved in cancer progression resulting in poor prognosis. Together, our findings suggest that NNMT may play a key role in the regulation of cancer immune infiltrating, finally influencing prognosis of cancer patients.

5. Conclusions

In summary, we demonstrated that NNMT expression was related to clinicopathological characteristics and poor prognosis of pan-cancer. High expression of NNMT was closely related to CAF and immune cell infiltrations. High NNMT expression was predictive of macrophage infiltration and encouraged macrophage differentiation into TAMs in COAD, HNSC, OV, and STAD. These results displayed the prognostic value of NNMT and its potential role in tumor immunology.

Our study focused on the bioinformatic techniques of NNMT expression and patient survival utilizing multiple databases, without any verification experiments in vivo or in vitro. Future experimental studies of the NNMT expression and immune cell infiltration in different cancer populations may provide additional insights into the cancer mechanisms and the therapeutic strategies targeting NNMT to improve the therapeutic efficacy of immunotherapy.

Data Availability

The authors certify that all the original data in this research could be obtained from public database. NNMT gene expression in pan-cancer was verified in Oncomine (https://www.oncomine.org/), TIMER database (https://cistrome.shinyapps.io/timer), and UALCAN (http://ualcan.path.uab.edu/analysis). Survival data was verified in the Kaplan-Meier plotter (https://kmplot.com/analysis/) and PrognoScan (http://gepia.cancer-pku.cn/). Other data used to support the findings of this study are included within the supplementary information files. All the raw data of this study are available from the first author or corresponding author upon request.

Disclosure

This manuscript was submitted as a preprint in the link https://www.researchsquare.com/article/rs-1375958/v1 [36].

Conflicts of Interest

No potential conflicts of interest were disclosed.

Supplementary Materials

Figure S1: correlation of NNMT gene expression with stromal score and immune score in different cancers. NNMT gene expression has a significantly positive correlation with the stromal score (A) and immune score (B) in COAD, HNSC, OV, and STAD. COAD: colon adenocarcinoma; HNSC: head and neck squamous cell carcinoma; NNMT: nicotinamide N-methyltransferase; OV: ovarian serous cystadenocarcinoma; STAD: stomach adenocarcinoma. Figure S2: macrophage infiltration in the NNMT high and low expression groups in COAD, HNSC, OV, and STAD. Compared with the NNMT low expression group, macrophages were significantly upregulated in the NNMT high expression group in COAD, HNSC, OV, and STAD (all $P < 0.0001$). COAD: colon adenocarcinoma; HNSC: head and neck squamous cell carcinoma; NNMT: nicotinamide N-methyltransferase; OV: ovarian serous cystadenocarcinoma; STAD: stomach adenocarcinoma. Table S1: the correlation of NNMT with stromal and immune scores. Table S2: the correlation of NNMT with immune cell infiltration in TCGA pan-cancer. Table S3: the association between NNMT expression and different immune cells in COAD, HNSC, OV, and STAD from ImmuCellAI database. *(Supplementary Materials)*

References

[1] F. Bray, M. Laversanne, E. Weiderpass, and I. Soerjomataram, "The ever-increasing importance of cancer as a leading cause of premature death worldwide," *Cancer*, vol. 127, no. 16, pp. 3029-3030, 2021.

[2] H. Sung, J. Ferlay, R. L. Siegel et al., "Global cancer statistics 2020: GLOBOCAN estimates of incidence and mortality worldwide for 36 cancers in 185 countries," *CA: a Cancer Journal for Clinicians*, vol. 71, no. 3, pp. 209–249, 2021.

[3] E. Hirata and E. Sahai, "Tumor Microenvironment and Differential Responses to Therapy," *Cold Spring Harbor perspectives in medicine*, vol. 7, no. 7, article a026781, 2017.

[4] T. Wu and Y. Dai, "Tumor microenvironment and therapeutic response," *Cancer Letters*, vol. 387, pp. 61–68, 2017.

[5] TGS, "Innate and adaptive immune cells in tumor microenvironment," *The Gulf Journal of Oncology*, vol. 1, no. 35, pp. 77–81, 2021.

[6] E. Gangoso, B. Southgate, L. Bradley et al., "Glioblastomas acquire myeloid-affiliated transcriptional programs via epigenetic immunoediting to elicit immune evasion," *Cell*, vol. 184, no. 9, pp. 2454–2470.e26, 2021.

[7] A. Roberti, A. F. Fernandez, and M. F. Fraga, "Nicotinamide N-methyltransferase: at the crossroads between cellular

metabolism and epigenetic regulation," *Molecular Metabolism*, vol. 45, article 101165, 2021.

[8] Y. S. Hah, H. Y. Cho, S. Y. Jo, Y. S. Park, E. P. Heo, and T. J. Yoon, "Nicotinamide N-methyltransferase induces the proliferation and invasion of squamous cell carcinoma cells," *Oncology Reports*, vol. 42, no. 5, pp. 1805–1814, 2019.

[9] Y. Cui, L. Zhang, W. Wang et al., "Downregulation of nicotinamide N-methyltransferase inhibits migration and epithelial-mesenchymal transition of esophageal squamous cell carcinoma via Wnt/β-catenin pathway," *Molecular and Cellular Biochemistry*, vol. 460, no. 1-2, pp. 93–103, 2019.

[10] J. H. Shin, C. W. Park, G. Yoon, S. M. Hong, and K. Y. Choi, "NNMT depletion contributes to liver cancer cell survival by enhancing autophagy under nutrient starvation," *Oncogene*, vol. 7, no. 8, p. 58, 2018.

[11] M. A. Eckert, F. Coscia, A. Chryplewicz et al., "Proteomics reveals NNMT as a master metabolic regulator of cancer-associated fibroblasts," *Nature*, vol. 569, no. 7758, pp. 723–728, 2019.

[12] D. R. Rhodes, S. Kalyana-Sundaram, V. Mahavisno et al., "Oncomine 3.0: genes, pathways, and networks in a collection of 18,000 cancer gene expression profiles," *Neoplasia*, vol. 9, no. 2, pp. 166–180, 2007.

[13] Z. Tang, B. Kang, C. Li, T. Chen, and Z. Zhang, "GEPIA2: an enhanced web server for large-scale expression profiling and interactive analysis," *Nucleic Acids Research*, vol. 47, no. W1, pp. W556–W560, 2019.

[14] E. Cerami, J. Gao, U. Dogrusoz et al., "The cBio cancer genomics portal: an open platform for exploring multidimensional cancer genomics data," *Cancer Discovery*, vol. 2, no. 5, pp. 401–404, 2012.

[15] Z. Tang, C. Li, B. Kang, G. Gao, C. Li, and Z. Zhang, "GEPIA: a web server for cancer and normal gene expression profiling and interactive analyses," *Nucleic Acids Research*, vol. 45, no. W1, pp. W98–W102, 2017.

[16] I. Diboun, L. Wernisch, C. A. Orengo, and M. Koltzenburg, "Microarray analysis after RNA amplification can detect pronounced differences in gene expression using limma," *BMC Genomics*, vol. 7, no. 1, p. 252, 2006.

[17] R. Baghban, L. Roshangar, R. Jahanban-Esfahlan et al., "Tumor microenvironment complexity and therapeutic implications at a glance," *Cell Communication and Signaling: CCS*, vol. 18, no. 1, p. 59, 2020.

[18] Y. Wang, J. Zeng, W. Wu et al., "Nicotinamide N-methyltransferase enhances chemoresistance in breast cancer through SIRT1 protein stabilization," *Breast Cancer Research*, vol. 21, no. 1, p. 64, 2019.

[19] C. Chen, X. Wang, X. Huang et al., "Nicotinamide N-methyltransferase: a potential biomarker for worse prognosis in gastric carcinoma," *American Journal of Cancer Research*, vol. 6, no. 3, pp. 649–663, 2016.

[20] J. Li, H. Yue, H. Yu, X. Lu, and X. Xue, "Patients with low nicotinamide N-methyltransferase expression benefit significantly from bevacizumab treatment in ovarian cancer," *BMC Cancer*, vol. 21, no. 1, p. 67, 2021.

[21] M. Song, Y. Li, M. Miao et al., "High stromal nicotinamide N-methyltransferase (NNMT) indicates poor prognosis in colorectal cancer," *Cancer Medicine*, vol. 9, no. 6, pp. 2030–2038, 2020.

[22] S. Akar, I. Harmankaya, S. Ugras, and C. Celik, "Nicotinamide N-methyltransferase expression and its association with phospho-Akt, p53 expression, and survival in high-grade endometrial cancer," *Turkish journal of medical sciences*, vol. 49, no. 5, pp. 1547–1554, 2019.

[23] N. M. Anderson and M. C. Simon, "The tumor microenvironment," *Current Biology*, vol. 30, no. 16, pp. R921–R925, 2020.

[24] M. Q. Kwa, K. M. Herum, and C. Brakebusch, "Cancer-associated fibroblasts: how do they contribute to metastasis?," *Clinical & Experimental Metastasis*, vol. 36, no. 2, pp. 71–86, 2019.

[25] X. Chen and E. Song, "Turning foes to friends: targeting cancer-associated fibroblasts," *Nature Reviews. Drug Discovery*, vol. 18, no. 2, pp. 99–115, 2019.

[26] X. Xie, H. Liu, Y. Wang et al., "Nicotinamide N-methyltransferase enhances resistance to 5-fluorouracil in colorectal cancer cells through inhibition of the ASK1-p38 MAPK pathway," *Oncotarget*, vol. 7, no. 29, pp. 45837–45848, 2016.

[27] S. W. Tang, T. C. Yang, W. C. Lin et al., "Nicotinamide N-methyltransferase induces cellular invasion through activating matrix metalloproteinase-2 expression in clear cell renal cell carcinoma cells," *Carcinogenesis*, vol. 32, no. 2, pp. 138–145, 2011.

[28] K. Palanichamy, S. Kanji, N. Gordon et al., "NNMT silencing activates tumor suppressor PP2A, inactivates oncogenic STKs, and inhibits tumor forming ability," *Clinical Cancer Research*, vol. 23, no. 9, pp. 2325–2334, 2017.

[29] F. Wu, J. Yang, J. Liu et al., "Signaling pathways in cancer-associated fibroblasts and targeted therapy for cancer," *Signal Transduction and Targeted Therapy*, vol. 6, no. 1, p. 218, 2021.

[30] M. Xu, Y. Li, W. Li et al., "Immune and stroma related genes in breast cancer: a comprehensive analysis of tumor microenvironment based on The Cancer Genome Atlas (TCGA) database," *Frontiers in medicine*, vol. 7, no. 7, p. 64, 2020.

[31] C. Kaderbhaï, Z. Tharin, and F. Ghiringhelli, "The role of molecular profiling to predict the response to immune checkpoint inhibitors in lung cancer," *Cancers*, vol. 11, no. 2, p. 201, 2019.

[32] C. Wei, C. Yang, S. Wang et al., "Crosstalk between cancer cells and tumor associated macrophages is required for mesenchymal circulating tumor cell-mediated colorectal cancer metastasis," *Molecular Cancer*, vol. 18, no. 1, p. 64, 2019.

[33] B. Li, M. Ren, X. Zhou, Q. Han, and L. Cheng, "Targeting tumor-associated macrophages in head and neck squamous cell carcinoma," *Oral Oncology*, vol. 106, article 104723, 2020.

[34] L. Liang, M. Zeng, H. Pan, H. Liu, and Y. He, "Nicotinamide N-methyltransferase promotes epithelial-mesenchymal transition in gastric cancer cells by activating transforming growth factor-β1 expression," *Oncology Letters*, vol. 15, no. 4, pp. 4592–4598, 2018.

[35] K. Rihawi, A. D. Ricci, A. Rizzo et al., "Tumor-associated macrophages and inflammatory microenvironment in gastric cancer: novel translational implications," *International Journal of Molecular Sciences*, vol. 22, no. 8, p. 3805, 2021.

[36] W. Liu, M. Zhu, X. Li, L. Er, and S. Li, *NNMT is a immune-related prognostic biomarker that modulates the tumor microenvironment in pan-cancer*, 2022.

Hindawi
Disease Markers
Volume 2023, Article ID 5025868, 7 pages
https://doi.org/10.1155/2023/5025868

Research Article

lncRNA SSTR5-AS1 Predicts Poor Prognosis and Contributes to the Progression of Esophageal Cancer

Yuhao Hu, Ning Mao, Wei Zheng, Bin Hong, and Xiong Deng

Cardiothoracic Surgery, Yongchuan Hospital of Chongqing Medical University, Chongqing, China

Correspondence should be addressed to Xiong Deng; dengx@hospital.cqmu.edu.cn

Received 26 September 2022; Revised 19 October 2022; Accepted 24 November 2022; Published 23 January 2023

Academic Editor: Fu Wang

Esophageal cancer (ESCA), as a common cancer worldwide, is a main cause of cancer-related mortality. Long noncoding RNAs (lncRNAs) have been shown in an increasing number of studies to be capable of playing an important regulatory function in human malignancies. Our study is aimed at delving into the prognostic value and potential function of lncRNA SSTR5-AS1 (SSTR5-AS1) in ESCA. The gene expression data of 182 ESCA samples from TCGA and 653 nontumor specimens from GTEx. The expressions of SSTR5-AS1 were analyzed. We investigated whether there was a correlation between the expression of SSTR5-AS1 and the clinical aspects of ESCA. In order to compare survival curves, the Kaplan-Meier method together with the log-rank test was utilized. The univariate and multivariate Cox regression models were used to analyze the data in order to determine the SSTR5-AS1 expression's significance as a prognostic factor in ESCA patients. In order to investigate the level of SSTR5-AS1 expression in ESCA cells, RT-PCR was utilized. CCK-8 trials served as a model for the loss-of-function tests. In this study, we found that the expressions of SSTR5-AS1 were increased in ESCA specimens compared with nontumor specimens. According to the ROC assays, high SSTR5-AS1 expression had an AUC value of 0.7812 (95% CI: 0.7406 to 0.8217) for ESCA. Patients who had a high level of SSTR5-AS1 expression had a lower overall survival rate than those who had a low level of SSTR5-AS1 expression. In addition, multivariate analysis suggested that SSTR5-AS1 was an independent predictor of overall survival for ESCA patients. Moreover, RT-PCR experiments indicated that SSTR5-AS1 expression was distinctly increased in three ESCA cells compared with HET1A cells. CCK-8 experiments indicated that silence of SSTR5-AS1 distinctly inhibited the proliferation of ESCA cells. Overall, ESCA patients with elevated SSTR5-AS1 had a worse chance of survival, suggesting it could be used as a prognostic and diagnostic biomarker for ESCA.

1. Introduction

More than 300,000 people are diagnosed with esophageal cancer (ESCA) every year, making it one of the most common malignant tumors of the upper gastrointestinal tract and a serious threat to human health [1, 2]. Recent researches have indicated that a combination of factors, such as unhealthy lifestyle choices, exposure to carcinogens, underlying disorders, and genetics, has a role in the development of esophageal cancer [3, 4]. There are a number of risk factors that can enhance an individual's susceptibility to ESCA. These include an excessive consumption of mold, a genetic predisposition, an addiction to nicotine or alcohol, and a high intake of nitrosamines [5, 6]. At the present time, patients diagnosed with ECCA typically undergo one or more of the following standard treatment modalities: chemotherapy, radiation therapy, or surgery [7, 8]. Despite recent advancements in clinical interventions, the clinical outcomes for ESCA remain dismal, with <20% of patients surviving for five years after diagnosis [9, 10]. The late diagnosis, high frequency of metastases, and rapid progression of the tumor all contribute to the dismal survival rate of ESCA patients [11]. In addition, the specific genetics as well as the molecular pathways that are involved in ESCA are not well understood. The TNM stage is currently the most important factor in determining the prognosis of ESCA patients [12]. TNM stage is helpful; however, it can be different for different people even when the cancer is at the same stage [13]. In addition, clinicopathological characteristics include molecular comprehensive reflections, which include genes and

proteins [14]. Thus, it is of the utmost need to create a reliable predictive biomarker that can predict the clinical prognosis of ESCA patients as quickly as possible.

Only 3% of the human genome is transcribed into protein-coding mRNAs, but around 75% of the human genome is translated into RNA [15]. In the past, ncRNAs were considered to be "evolutionary garbage" because it was believed that they did not have any biological roles [16, 17]. However, as a result of advances in deep sequencing technology, there is mounting evidence to suggest that noncoding RNAs (ncRNAs) have a significant influence on the molecular mechanisms of animals and even humans. Long noncoding RNA (lncRNA) refers to a set of transcripts of the noncoding RNA class that are longer than 200 nucleotides but do not have the ability to translate proteins into other forms [18]. There is evidence that long noncoding RNAs, or lncRNAs, play regulatory functions in a variety of biological processes, such as the differentiation of cells, the maintenance of stem cells, and the regulation of epigenetics [19, 20]. An imbalance in the expression of lncRNAs has been linked to a variety of human diseases, including cancer, neurological disorders, and cardiovascular conditions [21–23]. For instance, Wu et al. reported that higher expressions of DLEU2 or low levels of miR-30a-5p expression were an independent predictive predictor of poor survivals and tumor recurrences in lung cancer, and both were observed in non-small-cell lung cancer specimens. DLEU2 knockdown inhibited carcinogenesis and lung cancer invasion via targeting miR-30a-5p [24]. Xu et al. showed that the level of KCNMB2-AS1 was dramatically increased in ESCA. Through the modulation of the miRNA-3194/PYGL axis, the downregulation of KCNMB2-AS1 was able to inhibit stemness as well as proliferation, invasion, and migration [25]. Although research on lncRNAs is fairly restricted at the moment, the roles that lncRNAs play are incredibly diverse and comprehensive.

In this study, we evaluated TCGA datasets and discovered a novel lncRNA connected to ESCA called SSTR5-AS1. Patients with ESCA showed a high level of SSTR5-AS1. After that, we conducted additional research to better investigate its diagnostic and prognostic usefulness in ESCA patients. In the end, we conducted functional trials to investigate the effect that it had on the development of ESCA. Based on these findings, we hypothesized that SSTR5-AS1 could serve as an innovative biomarker for ESCA patients.

2. Materials and Methods

2.1. Cell Culture and Cell Transfections. From the American Type Culture Collection (ATCC), we got human esophageal squamous epithelial cells HET1A as well as three ESCC cell lines: EC109, KYSE150, and KYSE450. At a temperature of 37 degrees Celsius, the cells were kept alive in a medium consisting of RPMI-1640 that had been supplemented with 10% fetal bovine serum (FBS; Thermo Fisher Scientific, Waltham, USA). The siRNAs for SSTR5-AS1 and scrambled siRNA were purchased from Ribobio (Guangzhou, China). Using the Lipofectamine 2000 reagent (Invitrogen, Carlsbad, USA), siRNAs were introduced into the cells to be transfected.

2.2. RNA Extraction and Quantitative Real-Time PCR. The total RNA from the cultivated cells was extracted with Trizol reagent (Invitrogen, California, USA) in accordance with the instructions provided by the manufacturer. In the second step, 2 μg of total RNA was subjected to reverse transcription utilizing a PrimeScript™ RT reagent kit with gDNA Eraser (Takara, Dalian, Niaoning, China) in an overall volume of 20 L in accordance with the procedure provided by the manufacturer. After that, a real-time quantitative polymerase chain reaction (qRT-PCR) was performed with the SYBR Premix Ex TaqTM II PCR Kit (Takara, Otsu, Shiga, Japan) by carefully adhering to the instrument that was provided by the manufacturer. Results were normalized to the content of GAPDH. The results of each experiment were recorded three times. The $2^{-\Delta\Delta Ct}$ method was used to represent the fold-change values of lncRNA expression. Primers used for RT-RCR are presented as follows: SSTR5-AS1-F: 5′-ACTA CAGGTGCCATCAGACC-3′, SSTR5-AS1-R: 5′-AGCCTG CCATCCTAACACTT-3′; GAPDH-F: F: 5′-AGGTGAAGG TCGGAGTCAACG-3′, GAPDH-R: R: 5′-AGGGGTCAT TGATGGCAACA-3′.

2.3. Cell Proliferation. For the purpose of analyzing cell proliferation, a Cell Counting Kit-8 (CCK-8, Beyotime in Shanghai, China) was applied. In a nutshell, following transfection for a period of 48 hours, various types of cells were seeded into 96-well plates. Incubation of the cells in CCK-8 solution took place for one hour on days 1, 2, and 3. After that, the optical density (OD) was measured using a microplate reader set to 450 nm. The experiments were repeated three times.

2.4. Patients and Datasets. The gene expression data of 182 ESCA samples from TCGA and 653 normal specimens from GTEx were derived from UCSC Xena (https://xena.ucsc.edu/). In order to provide a more accurate depiction, the expression levels of lncRNAs that were used in TCGA and GTEx were normalized to log2 (TPM+0.001).

2.5. Statistical Analysis. Data analysis was performed by using GraphPad Prism 6.0 (GraphPad Software, La Jolla, USA). Student's paired two-tailed t-test was utilized in order to analyze the statistical differences that existed between the groups. The chi-squared test was utilized in order to investigate and analyze the relationships that existed between clinical features and SSTR5-AS1 expression. The Kaplan-Meier methods were applied to plot survival curves. The Cox regression model was utilized in order to investigate the relevance of each variable's prognostic impact on overall survival. A statistically significant difference was determined to exist when p was less than 0.05.

3. Results

3.1. SSTR5-AS1 Was Upregulated in ESCA Patients. The observation that numerous malignancies exhibited aberrant expressions of lncRNAs has led researchers to hypothesize that these molecules are crucial regulators in the progression of tumors [26, 27]. RT-PCR was utilized to investigate the

levels of SSTR5-AS1 in a total of 182 ESCA samples and 653 nontumor samples. SSTR5-AS1 exhibited a significantly increased expression in ESCA specimens vs. corresponding normal specimens ($p < 0.01$, Figure 1).

3.2. SSTR5-AS1 Has a Diagnostic Value for ESCA Patients. Subsequently, the diagnostic values of SSTR5-AS1 for ESCA patients were explored. According to the ROC assays, high SSTR5-AS1 expression had an AUC value of 0.7812 (95% CI: 0.7406 to 0.8217) for ESCA (Figure 2). Our findings revealed that SSTR5-AS1 may be an indicator of the diagnosis of ESCA patients.

3.3. The Association between SSTR5-AS1 Expression and Clinicopathologic Features of ESCA. After that, an investigation into the connection between the amount of SSTR5-AS1 expression and the clinicopathological aspects was carried out. The average expression levels of SSTR5-AS1 were taken into consideration in order to classify ESCA patients into two distinct groups: the group of patients whose expression levels were high and the group of patients whose expression levels were low. The relations are outlined in Table 1. There was no clear connection between the expression of SSTR5-AS1 and a number of clinicopathological features (all $p > 0.05$).

3.4. Survival Analysis and Prognostic Significance of SSTR5-AS1 Expression in ESCA Patients. To further investigate the correlations of SSTR5-AS1 expression level with survivals of patients with ESCA, Kaplan-Meier analyses were performed. We found that, for ESCA patients whose SSTR5-AS1 expression level was higher, the overall survival was obviously shorter than those with low SSTR5-AS1 expression level (Figure 3). For further exploring the prognostic value exhibited by SSTR5-AS1 expression in ESCA patients, a univariate Cox model was performed. As presented in Table 2, we observed that pathologic stage and SSTR5-AS1 expression were prognostic predictors for ESCA patients (all $p < 0.05$). In multivariate assays, SSTR5-AS1 expression could independently predict the clinical outcomes of SSTR5-AS1 regarding the overall survival (HR = 2.286, 95% CI: 1.268-4.122; $p = 0.006$) of ESCA patients.

3.5. SSTR5-AS1 Promoted ESCA Cell Proliferation. In order to provide evidence of the presence of SSTR5-AS1 in ESCA samples, we carried out RT-PCR and discovered that the levels of SSTR5-AS1 were noticeably higher in three ESCA cells when compared with HET1A cells (Figure 4(a)). RNA interference was used to successfully knock down the expression of SSTR5-AS1 in the KYSE150 and KYSE450 cells. Figure 4(b) shows that SSTR5-AS1 was successfully knocked down in KYSE150 and KYSE450 cells by using the si-SSTR5-AS1 reagent (Figure 4(b)). We undertook CCK-8 tests to further investigate whether SSTR5-AS1 could play a functional role in the evolution of ESCA. The data revealed that silence of SSTR5-AS1 markedly inhibited the proliferation of ESCA cells (Figures 4(c) and 4(d)).

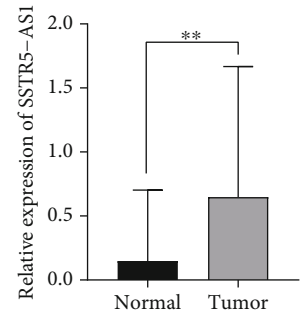

Figure 1: SSTR5-AS1 expression in ESCA samples and nontumor samples from TCGA and GTEx datasets was analyzed. $^{**}p < 0.01$.

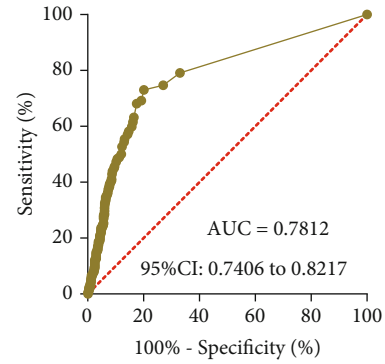

Figure 2: The receiver operating characteristic (ROC) curve was used to assess the diagnostic value of SSTR5-AS1 in ESCA patients.

4. Discussion

The overall mortality rate for ESCA can reach as high as 88%, making it one of the most deadly forms of cancers [28]. Despite the fact that there have been some improvements made to clinical outcomes as a result of developments in treatments, the survival rate is still very low [29, 30]. There are a great number of biomarkers that have been discovered to have a correlation with survival, and there is mounting evidence to suggest that gene markers are the most accurate technique to forecast clinical outcomes [31, 32]. Thus, there is an immediate need to examine the gene expression profile of ESCA for the better examination of the outcomes of ESCA patients. This progress can be accomplished by conducting research on ESCA patients. It is possible that in the not-too-distant future, the development and validation of prognostic gene biomarkers will result in improved clinical outcomes for these individuals.

Over the course of the last few years, a significant portion of the repertoire of nonprotein-coding transcripts found in the genome, including lncRNAs, has been regarded as irrelevant "junk" associated with transcription [33, 34]. lncRNAs have recently come to the forefront of attention as a result of the completion of ENCODE and the launch of the TCGA program, which have brought to light the significant roles that they play in the development and progression of cancer [22, 35]. In individuals suffering from ESCA, the diagnostic and prognostic usefulness of lncRNAs has been the subject of a number of researches in recent years.

Table 1: The association between SSTR5-AS1 expression and characteristics of patients suffering from ESCA.

Clinicopathological features	No. of cases	SSTR5-AS1 expression		p value
		High	Low	
Gender				0.653
Male	23	10	13	
Female	139	71	68	
Age				0.209
≤60	93	46	37	
>60	79	35	44	
Histologic grade				0.061
G1	16	13	3	
G2	66	32	34	
G3	44	24	20	
Pathologic stage				0.321
Stage I	16	6	10	
Stage II	69	40	29	
Stage III	49	23	26	
Stage IV	8	3	5	

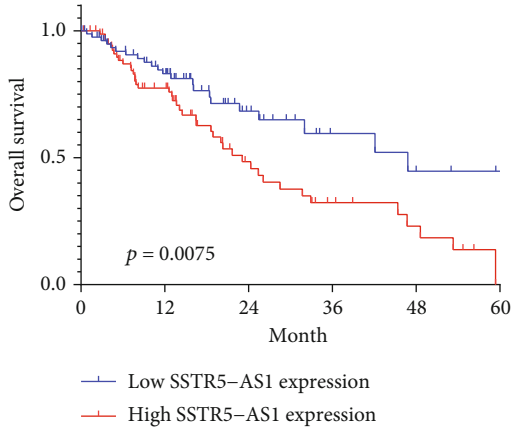

Figure 3: Kaplan-Meier survival curves of patients with ESCA based on SSTR5-AS1 expression.

For instance, Liu et al. showed that the expressions of LINC00963 were dramatically elevated in ESCC tissues, and its elevation was found to be linked with advanced TNM stage, metastasis, and a poor prognosis. Through the targeting of the miR-214-5p/RAB14 axis, the suppression of LINC00963 expression was able to inhibit the proliferation and invasion of ESCC cells in vitro, as well as the formation of tumors in vivo [36]. Xie et al. found that lncRNA RMRP showed considerable upregulation in ESCC, which was related with the presence or absence of lymph node metastases, the TNM stage of patients, and a poor prognosis for ESCC patients. In addition to this, RMRP regulated miR-613/NRP2, which in turn led to the promotion of ESCC cell proliferation, migration, and invasion. Through its role in the regulation of the miR-613/NRP2 axis, RMRP played a role in the progression of ESCC [37]. This finding identifies RMRP as a possible therapeutic target in the treatment of ESCC. These findings brought to light the possibility of using lncRNAs as new biomarkers for patients with ESCA.

In this study, we identified a novel ESCA-related lncRNA SSTR5-AS1 which was highly expressed in ESCA patients. In the past, a number of researches came to the conclusion that SSTR5-AS1 played a role in the development of a number of cancers. For instance, Xue et al. reported that higher SSTR5-AS1 expression was connected with a lower overall survival rate in gallbladder carcinoma patients. SSTR5-AS1 was dramatically enhanced in both gallbladder carcinoma samples and cell lines, particularly in gemcitabine-resistant cell lines. In terms of their functionality, knockdowns of SSTR5-AS1 made drug-resistant gallbladder cancer cells more sensitive to gemcitabine in vitro, and they greatly reduced the formation of xenografts in vivo by drug-resistant gallbladder carcinoma cells by stabilizing NONO [38]. Xu et al. showed that the role of SSTR5-AS1 as a ceRNA is to regulate CA2 expression by sponging miR-15b-5p, which is important for the progression and prognosis of hepatocellular carcinoma caused by HBV [39]. In addition, it was found that high expression of SSTR5-AS1 was connected to the clinical outcome of both laryngeal squamous cell carcinoma and gastric cancer [40, 41]. The clinical importance of SSTR5-AS1 in ESCA, on the other hand, has not been studied. In this study, we confirmed the diagnostic value based on the results of the ROC assays with an AUC value of 0.7812 for ESCA. Moreover, we found that patients with high SSTR5-AS1 expressions were related to poor outcomes of ESCA patients. In a multivariate Cox model, SSTR5-AS1 expression could independently predict the outcomes of SSTR5-AS1 regarding the overall survival of ESCA patients. Our findings firstly provided evidences that SSTR5-AS1 may be a functional regulator in ESCA patients and may be used as a novel biomarker. In order to provide more evidence of our findings, we performed an RT-PCR experiment. The data showed that the level

Table 2: Univariate and multivariate analyses of prognostic variables of overall survival in ESCA patients.

Characteristics	Total (*N*)	Univariate analysis		Multivariate analysis	
		HR (95% CI)	*p* value	HR (95% CI)	*p* value
Age	162				
≤60	83	Reference			
>60	79	0.831 (0.506-1.365)	0.466		
Gender	162				
Female	23	Reference			
Male	139	2.306 (0.922-5.770)	0.074	1.571 (0.543-4.543)	0.405
Pathologic stage	142				
Stage I & Stage II	85	Reference			
Stage III & Stage IV	57	3.223 (1.807-5.747)	<0.001	2.961 (1.623-5.402)	<0.001
SSTR5-AS1	162				
Low	81	Reference			
High	81	2.002 (1.192-3.361)	0.009	2.286 (1.268-4.122)	0.006

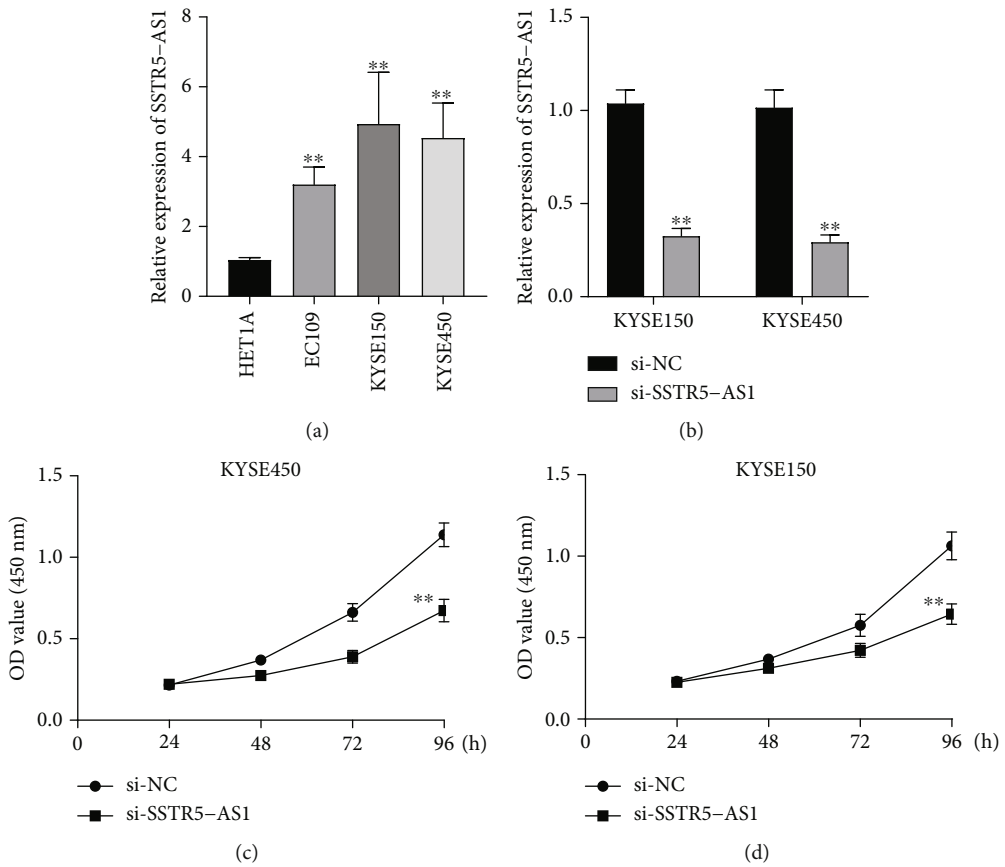

Figure 4: Knockdown of SSTR5-AS1 suppressed the proliferation of ESCA cells. (a) RT-PCR of SSTR5-AS1 expressions in HET1A, KYSE450, KYSE150 and EC109 cells. (b) qRT-PCR evaluation of SSTR5-AS1 expressions in KYSE450 and KYSE150 cells after the transfection. (c, d) CCK-8 assays examined cell proliferative abilities of KYSE450 and KYSE150 cells.

of expression of SSTR5-AS1 was noticeably elevated in ESCA cells in contrast to HET1A cells. We were able to show that inhibiting SSTR5-AS1 functioned to limit the proliferation of ESCA cells, which led us to hypothesize that it may play a role as a tumor promotor in the advancement of ESCA.

There are some limitations in our study. Firstly, the sample size is relatively small, large clinical trials are needed to conduct. Secondly, the specific function of SSTR5-AS1 was not explored in vivo. In the future, we will design more complex experiments to further understand the function of SSTR5-AS1 in ESCA progression.

5. Conclusion

To our knowledge, this is the first study to demonstrate a close association between high SSTR5-AS1 expression and a bad prognosis in ESCA patients, suggesting that SSTR5-AS1 may serve as a useful novel molecular marker for predicting ESCA prognosis.

Data Availability

The analyzed datasets generated during the study are available from the corresponding author on reasonable request.

Conflicts of Interest

The authors declare that they have no competing interests.

Acknowledgments

This work was supported by the Natural Science Foundation Project of Yongchuan District of Chongqing (Grant No. 2022yc-jckx20050).

References

[1] M. Watanabe, R. Otake, R. Kozuki et al., "Recent progress in multidisciplinary treatment for patients with esophageal cancer," *Surgery Today*, vol. 50, no. 1, pp. 12–20, 2020.

[2] Y. M. Yang, P. Hong, W. W. Xu, Q. Y. He, and B. Li, "Advances in targeted therapy for esophageal cancer," *Signal Transduction and Targeted Therapy*, vol. 5, no. 1, p. 229, 2020.

[3] E. Marabotto, G. Pellegatta, A. D. Sheijani et al., "Prevention Strategies for Esophageal Cancer-An Expert Review," *Cancers*, vol. 13, no. 9, p. 2183, 2021.

[4] R. Chen, R. Zheng, J. Zhou et al., "Risk prediction model for esophageal cancer among general population: a systematic review," *Frontiers in Public Health*, vol. 9, article 680967, 2021.

[5] T. X. Huang and L. Fu, "The immune landscape of esophageal cancer," *Cancer Communications*, vol. 39, no. 1, p. 79, 2019.

[6] A. Fatehi Hassanabad, R. Chehade, D. Breadner, and J. Raphael, "Esophageal carcinoma: towards targeted therapies," *Cellular Oncology*, vol. 43, no. 2, pp. 195–209, 2020.

[7] Y. Zhang, Y. Zhang, and L. Zhang, "Expression of cancer-testis antigens in esophageal cancer and their progress in immunotherapy," *Journal of Cancer Research and Clinical Oncology*, vol. 145, no. 2, pp. 281–291, 2019.

[8] O. Ahmed, J. A. Ajani, and J. H. Lee, "Endoscopic management of esophageal cancer," *World journal of Gastrointestinal Oncology*, vol. 11, no. 10, pp. 830–841, 2019.

[9] S. Kwiecien, M. Magierowski, J. Majka et al., "Curcumin: a potent protectant against esophageal and gastric disorders," *International Journal of Molecular Sciences*, vol. 20, no. 6, p. 1477, 2019.

[10] E. Pinto, F. Cavallin, and M. Scarpa, "Psychological support of esophageal cancer patient?," *Journal of Thoracic Disease*, vol. 11, Suppl 5, pp. S654–s662, 2019.

[11] Q. Wu, Z. Wu, C. Bao et al., "Cancer stem cells in esophageal squamous cell cancer," *Oncology Letters*, vol. 18, no. 5, pp. 5022–5032, 2019.

[12] S. L. Betancourt-Cuellar, M. F. K. Benveniste, D. P. Palacio, and W. L. Hofstetter, "Esophageal cancer: tumor-node-metastasis staging," *Radiologic Clinics of North America*, vol. 59, no. 2, pp. 219–229, 2021.

[13] S. J. Hong, T. J. Kim, K. B. Nam et al., "New TNM staging system for esophageal cancer: what chest radiologists need to know," *Radiographics*, vol. 34, no. 6, pp. 1722–1740, 2014.

[14] F. L. Huang and S. J. Yu, "Esophageal cancer: risk factors, genetic association, and treatment," *Asian Journal of Surgery*, vol. 41, no. 3, pp. 210–215, 2018.

[15] F. Kanwal and C. Lu, "A review on native and denaturing purification methods for non-coding RNA (ncRNA)," *Journal of Chromatography B, Analytical Technologies in the Biomedical and Life Sciences*, vol. 1120, pp. 71–79, 2019.

[16] V. A. Erdmann, M. Z. Barciszewska, A. Hochberg, N. de Groot, and J. Barciszewski, "Regulatory RNAs," *Cellular and Molecular Life Sciences: CMLS*, vol. 58, no. 7, pp. 960–977, 2001.

[17] N. Laham-Karam, P. Laitinen, T. A. Turunen, and S. Ylä-Herttuala, "Activating the chromatin by noncoding RNAs," *Antioxidants & Redox Signaling*, vol. 29, no. 9, pp. 813–831, 2018.

[18] P. K. Puvvula, "LncRNAs regulatory networks in cellular senescence," *International Journal of Molecular Sciences*, vol. 20, no. 11, p. 2615, 2019.

[19] P. Han and C. P. Chang, "Long non-coding RNA and chromatin remodeling," *RNA Biology*, vol. 12, no. 10, pp. 1094–1098, 2015.

[20] P. McDonel and M. Guttman, "Approaches for understanding the mechanisms of long noncoding RNA regulation of gene expression," *Cold Spring Harbor Perspectives in Biology*, vol. 11, no. 12, 2019.

[21] F. Chu, L. Xue, and H. Miao, "Long noncoding RNA TP73-AS1 in human cancers," *Clinica Chimica Acta; International Journal of Clinical Chemistry*, vol. 500, pp. 104–108, 2020.

[22] T. Wu and Y. Du, "LncRNAs: from basic research to medical application," *International Journal of Biological Sciences*, vol. 13, no. 3, pp. 295–307, 2017.

[23] W. X. Peng, P. Koirala, and Y. Y. Mo, "LncRNA-mediated regulation of cell signaling in cancer," *Oncogene*, vol. 36, no. 41, pp. 5661–5667, 2017.

[24] W. Wu, Y. Zhao, E. Gao et al., "LncRNA DLEU2 accelerates the tumorigenesis and invasion of non–small cell lung cancer by sponging miR-30a-5p," *Journal of Cellular and Molecular Medicine*, vol. 24, no. 1, pp. 441–450, 2020.

[25] J. Xu, X. Liu, X. Liu, and Y. Zhi, "Long noncoding RNA KCNMB2-AS1 promotes the development of esophageal cancer by modulating the miR-3194-3p/PYGL axis," *Bioengineered*, vol. 12, no. 1, pp. 6687–6702, 2021.

[26] W. Huang, H. Li, Q. Yu, W. Xiao, and D. O. Wang, "LncRNA-mediated DNA methylation: an emerging mechanism in cancer and beyond," *Journal of Experimental & Clinical Cancer Research: CR*, vol. 41, no. 1, p. 100, 2022.

[27] S. Ghafouri-Fard, T. Khoshbakht, M. Taheri, and K. Ebrahimzadeh, "A review on the role of PCAT6 lncRNA in tumorigenesis," *Biomedicine & Pharmacotherapy*, vol. 142, article 112010, 2021.

[28] H. Kato and M. Nakajima, "Treatments for esophageal cancer: a review," *General Thoracic and Cardiovascular Surgery*, vol. 61, no. 6, pp. 330–335, 2013.

[29] E. Bollschweiler, P. Plum, S. P. Mönig, and A. H. Hölscher, "Current and future treatment options for esophageal cancer in the elderly," *Expert Opinion on Pharmacotherapy*, vol. 18, no. 10, pp. 1001–1010, 2017.

[30] M. Yamasaki, H. Miyata, Y. Miyazaki et al., "Perioperative therapy for esophageal cancer," *General Thoracic and Cardiovascular Surgery*, vol. 62, no. 9, pp. 531–540, 2014.

[31] M. J. Krasna, "Multimodality therapy for esophageal cancer," *Oncology*, vol. 24, no. 12, pp. 1134–1138, 2010.

[32] M. Ikebe, M. Morita, M. Yamamoto, and Y. Toh, "Neoadjuvant therapy for advanced esophageal cancer: the impact on surgical management," *General Thoracic and Cardiovascular Surgery*, vol. 64, no. 7, pp. 386–394, 2016.

[33] K. Liao, J. Xu, W. Yang, X. You, Q. Zhong, and X. Wang, "The research progress of LncRNA involved in the regulation of inflammatory diseases," *Molecular Immunology*, vol. 101, pp. 182–188, 2018.

[34] J. Liu, L. Z. Yang, and L. L. Chen, "Understanding lncRNA-protein assemblies with imaging and single-molecule approaches," *Current Opinion in Genetics & Development*, vol. 72, pp. 128–137, 2022.

[35] W. Lin, Q. Zhou, C. Q. Wang et al., "LncRNAs regulate metabolism in cancer," *International Journal of Biological Sciences*, vol. 16, no. 7, pp. 1194–1206, 2020.

[36] H. F. Liu, Q. Zhen, and Y. K. Fan, "LINC00963 predicts poor prognosis and promotes esophageal cancer cells invasion via targeting miR-214-5p/RAB14 axis," *European Review for Medical and Pharmacological Sciences*, vol. 24, no. 1, pp. 164–173, 2020.

[37] Z. Xie, S. Liu, S. Chu, Y. Liu, B. Huang, and Q. Zhang, "lncRNA RMRP predicts poor prognosis and mediates tumor progression of esophageal squamous cell carcinoma by regulating miR-613/neuropilin 2 (NRP2) axis," *Bioengineered*, vol. 12, no. 1, pp. 6913–6922, 2021.

[38] Z. Xue, B. Yang, Q. Xu, X. Zhu, and G. Qin, "Long non-coding RNA SSTR5-AS1 facilitates gemcitabine resistance via stabilizing NONO in gallbladder carcinoma," *Biochemical and Biophysical Research Communications*, vol. 522, no. 4, pp. 952–959, 2020.

[39] J. Xu, J. Zhang, F. Shan, J. Wen, and Y. Wang, "SSTR5-AS1 functions as a ceRNA to regulate CA2 by sponging miR-15b-5p for the development and prognosis of HBV-related hepatocellular carcinoma," *Molecular Medicine Reports*, vol. 20, no. 6, pp. 5021–5031, 2019.

[40] B. Wang, L. Zhao, W. Chi, H. Cao, W. Cui, and W. Meng, "Aberrant methylation-mediated downregulation of lncRNA SSTR5-AS1 promotes progression and metastasis of laryngeal squamous cell carcinoma," *Epigenetics & Chromatin*, vol. 12, no. 1, p. 35, 2019.

[41] Y. Cheng, J. Di, J. Wu et al., "Diagnostic and prognostic significance of long noncoding RNA SSTR5-AS1 in patients with gastric cancer," *European Review for Medical and Pharmacological Sciences*, vol. 24, no. 10, pp. 5385–5390, 2020.

Hindawi
Disease Markers
Volume 2022, Article ID 6832680, 17 pages
https://doi.org/10.1155/2022/6832680

Research Article

Study on the Mechanism of miR-125b-5p Affecting Melanocyte Biological Behavior and Melanogenesis in Vitiligo through Regulation of MITF

Xiaochuan Wang, Yifei Wu, Peng Du, Liangheng Xu, Yuan Chen, Jingzi Li, Xuying Pan, and Zhiqiong Wang

Department of Dermatology, The First People's Hospital of Yunnan Province, Kunming, 650032 Yunnan, China

Correspondence should be addressed to Zhiqiong Wang; huadt@163.com

Received 26 July 2022; Revised 18 August 2022; Accepted 23 August 2022; Published 16 November 2022

Academic Editor: Fu Wang

Objective. The goal was to confirm the mechanism by which miR-125b-5p influences melanocyte biological behavior and melanogenesis in vitiligo by regulating MITF. *Methods*. oe-MITF, sh-MITF, miR-125b-5p mimic, NC-mimic, NC-inhibitor, and miR-125b-5p inhibitor were transfected into cells by cell transfection. Western blotting was used to detect the related protein expression, qRT–PCR was used to detect miR-125b-5p and MITF expression, immunohistochemistry was used to detect the MITF-positive cells in vitiligo patients tissues, and a dual-luciferase reporter system was used to detect the target of miR-125b-5p and MITF. PIG1 and PIG3V cell proliferation by the CCK-8 method, cell cycle progression and apoptosis by flow cytometry, apoptosis was detected by TUNEL, Tyr activity and melanin content were measured using Tyr and melanin content assay kits. *Results*. Compared with the healthy control group, the expression of miR-125b-5p in the tissues and serum of vitiligo patients was upregulated, and the expression of MITF was downregulated; compared with PIG1 cells, the expression of miR-125b-5p and MITF in the PIG3V group was consistent with the above. Compared with the NC-minic group, the cell proliferation activity of the miR-125b-5p mimic group decreased, apoptosis increased, and the expression levels of melanogenesis-related proteins Tyr, Tyrp1, Tyrp2, and DCT were downregulated. Compared with the NC-inhibitor group, the above indices in the miR-125b-5p inhibitor group were all opposite to those in the miR-125b-5p mimic group. Transfection of oe-MITF into the miR-125b-5p mimic group reversed the effect of the miR-125b-5p mimic, while transfection of sh-MITF enhanced the effect of the miR-125b-5p mimic. *Conclusion*. miR-125b-5p affects vitiligo melanocyte biological behavior and melanogenesis by downregulating MITF expression.

1. Introduction

Vitiligo characterized by melanocyte destruction is an acquired and idiopathic disease resulting in dilution of pigment in affected areas [1]. Its lesion sites are characterized by white patches and colorless, nonscaly, and distinct edges. With research advances, great progress has been made in the understanding of the pathogenesis of vitiligo, which is associated with the destruction of melanocyte function leading to impaired melanin deposition as an autoimmune disease [2]. Nonetheless, the mechanism of melanin deposition disorder is not clear in the current study; therefore, there is an urgent need to study the specific mechanism of melanin deposition and find effective therapeutic targets.

As an evolutionarily conserved noncoding RNA molecule, microRNA (miRNA) is approximately 22 nucleotides. miRNA bind to their target mRNA to regulate gene expression, resulting in their translation inhibition or degradation. Each miRNA has multiple targets, and each miRNA is regulated by multiple miRNAs simultaneously [3]. Previous studies have shown that miRNAs play a key role in all kinds of life activities, including the immune response, cell proliferation, differentiation, and apoptosis [4]. There are four kinds of miRNAs with abnormal expression in the

Table 1: Primer sequence.

Genes	Primers	Sequence (5′-3′)
miR-125b-5p	forward	5′-TCCCTGAGACCCTAACTTGTGA-3′
	reverse	5′-AGTCTCAGGGTCCGAGGTATTC-3′
U6	forward	5′-CTCGCTTCGGCAGCACA-3′
	reverse	5′-AACGCTTCACGAATTTGCGT-3′
MITF	forward	5′-TCTGCCTGGTGCTGTACAAG-3′
	reverse	5′-CCAGGCCTTACCATCAGCAA-3′
GAPDH	forward	5′-AGTGATGGCATGGACTGTGG-3′
	reverse	5′-GATTTGGTCGTATTGGGCGC-3′

peripheral blood of vitiligo patients: miR-1238-3p, miR-202-3p, miR-630, and miR-766-3p [5]. Upregulation of miR-21-5p and downregulation of SOX5 lead to upregulation of melanogenesis [6]. miR-211 can regulate mitochondrial energy metabolism in vitiligo patients [7]. The relationship between miR-125b-5p, melanocyte biological behavior, and melanogenesis was investigated. As a member of the miR-125b family, miR-125b-5p is a new regulator of homeostatic melanogenesis [8]. However, the specific mechanism by which miR-125b-5p regulates melanocyte biological behavior and melanogenesis is not clear.

As a key regulator of melanocyte development, MITF (small eye transcription factor) is necessary in many stages of the melanocyte life cycle and is required for the survival of melanocyte precursors or melanoblasts [9]. In a study by Steingrímsson et al. [10], deletion of MITF resulted in the entire absence of mouse embryonic adult melanocytes, and mice were born with all-white hair follicles. Biological information indicates that miR-125b-5p interacts with MITF, but whether miR-125b-5p influences the biological behavior of melanocytes and melanin production by regulating MITF is not known. Therefore, this study was aimed at confirming the relationship between miR-125b-5p, MITF, melanocyte biological behavior, and melanogenesis to explore the potential mechanism and provide a new way to treat vitiligo.

2. Methods

2.1. Clinical Data and Patient Samples. In this study, serum and skin tissue were collected from patients with vitiligo ($n = 17$) and normal healthy individuals ($n = 17$). Patients who had other serious diseases or started treatment within 3 months prior to admission were excluded. Healthy controls were shown to have normal physiological functions in a whole-body physiological examination performed at the abovementioned hospital. All the experiments in this study were approved by the ethics committee. Before participating in this study, the included patients and healthy volunteers signed informed consent forms.

2.2. Cell Culture. Normal human skin melanocytes (PIG1) and vitiligo melanocytes (PIG3V) (BeNa Culture Collection, Beijing, China) were cultured in 90% RPMI1640 containing fetal bovine serum (10% USA), penicillin (100 U/mL), and streptomycin (100 mg/mL). The cells were placed in a standard incubator with 5% CO_2 and incubated at a cell density of 80% for subsequent experiments.

2.3. Cell Transfection. In 6-well plates, PIG1 and PIG3V cells were inoculated at a density of 1×10^5 cells/well. miR-125b-5p mimic, sh-MITF, oe-MITF, NC-mimic, NC-inhibitor, and miR-125b-5p inhibitor were synthesized by Sangon (Shanghai, China) and transfected into cells by Lipofectamine™ 3000 reagent. The control group was transfected into cells as a control group, and the cells were subsequently placed in saturated humidity and CO_2 for 48 h. The transfection efficiency was detected using qRT–PCR and WB for subsequent experiments.

2.4. qRT–PCR. A total RNA extractor (Sangon Biotech) was used to extract the total RNA from 17 serum samples (tissues and cells). A 1 μL RNA sample was taken, and RNA integrity was detected by 1% agarose gel electrophoresis. A 1 μL RNA sample was taken after dilution to measure the OD value through the ratio of OD_{260}/OD_{280} to identify the total RNA purity. A cDNA synthesis kit (Vazyme, Nanjing, China) was used to reverse transcribe 2 μg of mRNA into cDNA, which was then diluted 10 times. One microliter of the prepared cDNA was used for qPCR. U6 and GAPDH were used as the reference genes for expression detection on an ABI7500 real-time PCR system, followed by PCR analysis of cDNA using SYBR qPCR Master Mix (Vazyme, Nanjing, China) to quantify miR-125b-5p and MITF expression. qRT–PCR conditions are as follows: 95°C for 30 s, 3 s at 95°C, followed by annealing at 60°C for 30 s for 40 cycles. All primers (Table 1) used in this study were designed with Premier 5.0. The results were calculated by the 2-$\Delta\Delta$Ct method after repetition at least 3 times.

2.5. Cell Proliferation Assay (CCK-8). In this study, PIG1 and PIG3V cells (1×10^5 cells/well) were placed in 96-well plates. In a 37°C incubator, 100 μL of medium was added to every plate and cultured in a cell incubator for 36 h until the cell density was 70-80%. After transfection or dosing and incubation for 0, 24, 48, and 72 h, ten microliters of CCK-8

reagent (Biotrans, Shanghai, China) was added to detect the influence of miR-125b-5p and MITF on cells. Subsequently, the 96-well plates were subjected to an enzyme marker (Bio-Rad, CA, USA) at 450 nm to detect the absorbance values.

2.6. Cell Clone Formation Experiments. To prepare the cell suspensions, we used trypsin (0.25%) to digest the PIG1 and PIG3V cells at the logarithmic growth stage. After gradient dilution, the cell suspension was inoculated into a 37°C plate containing 10 mL of preheated culture medium at gradient densities of 50, 100, and 200 cells. Then, the plate was gently rotated to evenly distribute the cells, and the cells were cultured in a cell incubator. They were observed frequently, and when clones visible to the naked eye appeared in the dishes, the culture was terminated, the supernatant was discarded, the cells were washed twice with PBS, 15 mL of 4% paraformaldehyde was added to fix the cells, the fixation was discarded, GIMSA application staining solution (Jinglai Biological, China) was added to the dye for 10-30 min, and they were then washed with water, air-dried, and counted under a microscope.

2.7. Protein Blotting. In this study, the proteins were extracted utilizing RIPA lysis buffer (Sangon Biotech, Shanghai), and a lysate containing benzoyl fluoride (PMSF) was added. A BCA assay (Sangon Biotech, Shanghai) was used to determine the total protein content. The target bands were transferred to a nitrocellulose membrane (PVDF) by taking 50 μg for 10% SDS–PAGE and using skim milk powder (5%) to block the PVDF membrane for 2 h. PVDF membranes were cultured with Abcam antibodies: MITF (1/1000; cat. no. ab140606, Abcam, UK), CDK2 (1 : 5000; cat. no. ab32147, Abcam, UK), CDK4 (1/1000; cat. no. ab108357, Abcam, UK), CyclinA2 (1/20000; cat. no. ab181591, Abcam, UK), CyclinD1 (1/200; cat. no. ab16663, Abcam, UK), BcL-2 (1/1000; cat. no. ab32124, Abcam, UK), Bax (1/1000; cat. no. ab32503, Abcam, UK), Caspase-3 (1/5000; cat. no. ab32351, Abcam, UK), Tyr (1/100000; cat. no. ab137869, Abcam, UK), Tyrp1 (1/1000; cat. no. ab235447, Abcam, UK), Tyrp2 (1/1000; cat. no. ab221144, Abcam, UK), DCT (1/1000; cat. no. ab221144, Abcam, UK), and GAPDH (1/1000; cat. no. ab9485, Abcam, UK) overnight at 4°C. TBST buffer was used to wash the PVDF membranes, which were then incubated with secondary antibodies (1/2000, cat. no. ab205718, Abcam) at 25°C for 1 h. Subsequently, ECL color development, gel imaging system analysis, semiquantitative determination of expression, and ImageJ analysis of the grayscale values of the bands were performed.

2.8. Immunohistochemistry (IHC). IHC experiments were carried out by 3,3′-diaminobenzidine (DAB) analysis. First, paraffin sections were routinely dewaxed and incubated with 3% H_2O_2 for 10 min at 37°C (to inactivate endogenous peroxides), rinsed with distilled water, immersed in citrate buffer in a boiling water bath for antigen repair, rinsed, and then immersed three times with PBS for 5 min each. After the glass slide was baked at 65°C for 2 h, it was placed in xylene for 10 min and then treated with xylene for 10 min. The sections were incubated in the following ethanol gradient (5 min for each solution): 90%, 80%, 70%, and distilled water. In a wet room, citric acid buffer was used to treat the slices, and hydrogen peroxide (3%) was used to remove endogenous peroxidase (25°C, 10 min). Sections were blocked with 5% bovine serum at 37°C for 30 min and then incubated with the primary antibody for 12 h at 4°C. They were incubated with the second antibody for 30 min at 37°C after washing the slices with PBS buffer. 3,3′-Diaminobenzidine (DAB) was used to observe the sections, and a light microscope was used to acquire the images.

2.9. Flow Cytometry Detects the Cell Cycle and Apoptosis. PIG1 and PIG3V cells at the logarithmic growth stage from each group of treatments were inoculated in 6 cm culture dishes and cultured for 12 h. Subsequently, PBS was used to wash the cells three times, and the cells were resuspended in 100 μL of buffer. At 25°C, the cells were coincubated with 5 μL of PI (BD Biosciences) for 10 min. Finally, after adding termination buffer, flow cytometry was performed to determine the apoptosis rate. Images were processed and analyzed using FlowJo X software. The experiment was performed 3 times independently.

2.10. Dual-Luciferase Reporter Assay. Dual-luciferase reporter analysis was used to detect the relationship between miR-125b-5p and MITF. The StarBase (http://starbase.sysu.edu.cn/) database was used to confirm the targeting of miR-125b-5p with MITF. The 3′-UTR of MITF was ligated into the pmir-GLO vector to construct the MITF wild-type vector (MITF-WT). In addition, it was ligated into the pmir-GLO vector by changing the target binding site of miR-125b-5p and MITF using a gene mutation technique to construct an MITF mutant vector (MITF-MUT). With the miR-125b-5p mimic, the generated reporter plasmid was transfected into HEK293T cells, and a dual-luciferase reporter assay kit was used to measure the luciferase activity after 48 h of incubation.

2.11. Terminal deoxynucleotidyl transferase dUTP nick end labeling (TUNEL) Assay. According to the TUNEL kit (Beyotime, Shanghai, China), PIG1 and PIG3V cells at the logarithmic growth stage were taken, prepared in cell suspension by trypsin digestion, centrifuged, supernatant discarded, washed with PBS, and fixed with 4% paraformaldehyde solution at 25°C for 30 min. Subsequently, a 0.3% H_2O_2 methanol solution was used to block the cells. Of note, care should be taken to keep the surrounding area moist with sufficient water-soaked paper or cotton pads to minimize evaporation of the TUNEL assay solution during incubation. The TUNEL assay solution was washed off with PBS. The slices were sealed with antifluorescence quenching blocking solution, and the tissue and cells were photographed under a fluorescence microscope at 450-500 nm (400857, Nikon, Japan). PI/DAPI can stain both apoptotic and nonapoptotic cells red/blue, with green fluorescence localized by FITC-12-dUTP doping only in the nuclei of apoptotic cells.

2.12. Statistics and Analysis. In this study, GraphPad Prism 8 software was used to analyze and prepare graphs, and the means and standard deviations (SD) are shown. Unpaired one-way analysis and Student's *t* test were used to analyze the multiple groups and two groups of data, respectively. The *P* value for statistical significance was 0.05.

3. Results

3.1. Differential Expression of miR-125b-5p and MITF in the Serum, Melanocytes, and Tissues of Vitiligo Patients. This study used qRT–PCR to confirm the levels of miR-125b-5p and MITF in serum and tissues from 17 vitiligo patients and 17 healthy individuals. It was shown that in either serum or tissues in the vitiligo patient group, miR-125b-5p expression was increased compared to the healthy controls (Figure 1(a)). Western blotting was used to detect MITF expression. MITF expression was significantly downregulated in vitiligo patients (Figure 1(b)). Immunohistochemical results indicated a significant decrease in MITF expressions from vitiligo patient tissues (Figure 1(c)). In melanocytes by qRT–PCR compared to normal human skin melanocytes (PIG1) and in vitiligo melanocytes (PIG3V), the level of miR-125b-5p was increased, and MITF was decreased (Figure 1(d)). At the same time, the level of MITF was significantly reduced in PIG3V cells according to Western blotting (Figure 1(e)). miR-125b-5p and MITF are abnormally expressed in vitiligo and may play a key role in the development of vitiligo.

3.2. The Influence of miR-125b-5p on Apoptosis, Melanogenesis, and the Proliferation of Melanocytes and Cycle and Pigment PIG1 and PIG3V Cells. To confirm the biological function of miR-125b-5p in vitiligo development, we altered the level of miR-125b-5p in cells by transfecting miR-125b-5p mimic and miR-125b-5p inhibitor. CCK-8 was used to evaluate the proliferation of PIG1 and PIG3V cells, as shown in Figure 2(a). Compared with the NC-minic group, the cell proliferation activity of the miR-125b-5p mimic group decreased, while the cell proliferation activity of the NC-inhibitor group showed no significant change. However, compared with the NC-inhibitor group, the cell proliferation activity of the miR-125b-5p inhibitor group was significantly increased. In addition, the influence of miR-125b-5p on PIG3V cells was found to be stronger than that on PIG1 cells during the assay. The cell clone formation assay was performed again, and the assay results were consistent with the CCK-8 results, as shown in Figure 2(b).

The cell cycle and apoptosis were detected by flow cytometry, and the miR-125b-5p mimic group showed G0/G1 phase ; the levels of cycle regulation-related proteins CDK2, CDK4, and CyclinA2 protein were decreased, and CyclinD1 expression was increased. Meanwhile, apoptosis was increased and apoptosis-related protein BcL-2 expression was decreased, the expressions of Bax and Caspase-3 were increased, and the above indicators in the NC-inhibitor group did not change significantly. However, compared with the NC-inhibitor group, the changing trend of the miR-125b-5p inhibitor group was completely opposite to that of the miR-125b-5p group. The duration of the G0/G1 and S phase was reduced, the levels of cycle regulation-related CDK2, CDK4, and CyclinA2 proteins were increased, and CyclinD1 expression was decreased; meanwhile, apoptosis was attenuated, the BcL-2 level was increased, and Bax and Caspase-3 expressions were decreased (Figures 2(c)–2(f)).

The levels of melanogenesis-related proteins were detected by Western blotting. Tyr, Tyrp1, Tyrp2, and DCT were downregulated after treatment with the miR-125b-5p mimic, while all of them were upregulated in the miR-125b-5p inhibitor group (Figure 2(g)).

3.3. miR-125b-5p Targets and Negatively Regulates MITF Expression. miRNAs can specifically bind to the 3′-untranslated region (3′-UTR) of target mRNAs to regulate gene expression. Therefore, we used a bioinformatics database to identify the target sites of miR-125b-5p with MITF and showed that there are MITF binding sites in miR-125b-5p (Figure 3(a)). Subsequently, a dual-luciferase reporter was used to analyze the miR-125b-5p and MITF targeting relationship. Overexpression of miR-125b-5p inhibited theluciferase activity of MITF-WT, while it had no significant effect on the luciferase activity of MITF-MUT (Figure 3(b)). Western blotting was used to examine the regulatory relationship between miR-125b-5p and MITF, and the results showed that the miR-125b-5p mimic decreased the levels of MITF, while the inhibitor increased the level of MITF (Figure 3(c)).

3.4. miR-125b-5p Affects PIG1 and PIG3V Proliferation and Apoptosis by Regulating MITF. To confirm whether miR-125b-5p affects PIG1 and PIG3V proliferation and apoptosis by targeting regulating MITF, miR-125b-5p with MITF overexpression and a low expression vector were constructed to alter the level of miR-125b-5p with MITF. A CCK-8 assay was used to examine the proliferation of cells after 72 h of growth. Compared with the NC-mimic group, the proliferation activity of the miR-125b-5p mimic group was decreased. After cotransfection of oe-MITF with miR-125b-5p mimic, compared with the miR-125b-5p mimic +NE-oe group, the miR-125b-5p mimic+oe-MITF group can effectively reverse the inhibitory effect of miR-125b-5p mimic on cell proliferation. After the expression of MITF was inhibited, the inhibitory effect of miR-125b-5p mimic on the proliferation of PIG1 and PIG3V cells was further enhanced (Figure 4(a)). The results of the cell clone formation assay were consistent with those of the CCK-8 assay of cell proliferation (Figure 4(b)).

Flow cytometry was used to detect PIG1 and PIG3V apoptosis in this study. The level of apoptosis was increased under the treatment of miR-125b-5p mimic, Caspase-3 and Bax expression was increased, but BcL-2 protein was decreased. After overexpression of MITF, the effect of miR-125b-5p alone was reversed, and apoptosis was attenuated, but BcL-2 was upregulated, and Bax and Caspase-3 were downregulated. If the expression of MITF was decreased while overexpressing miR-125b-5p, it promoted the effect

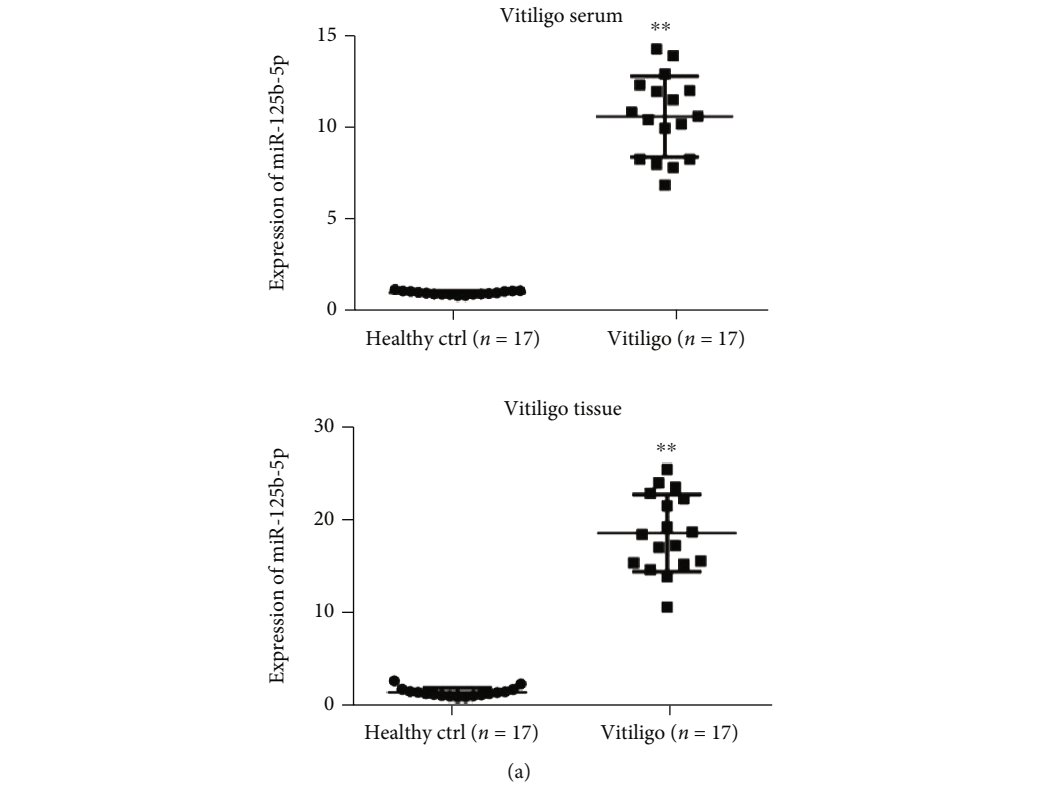

(a)

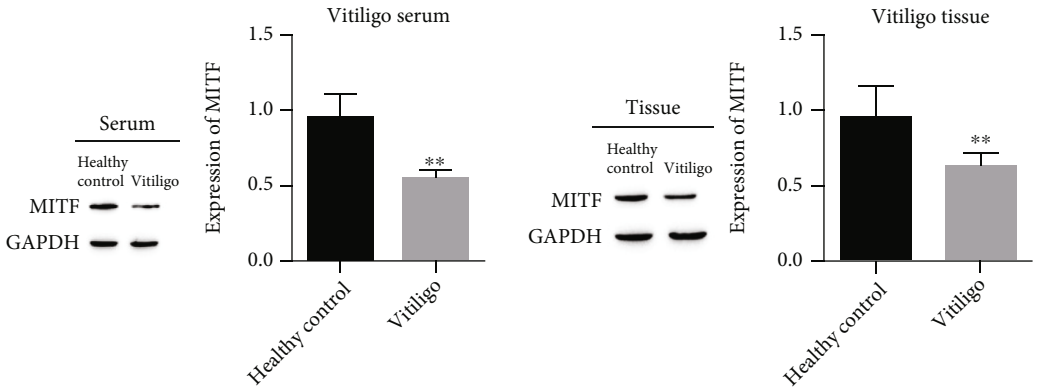

(b)

Figure 1: Continued.

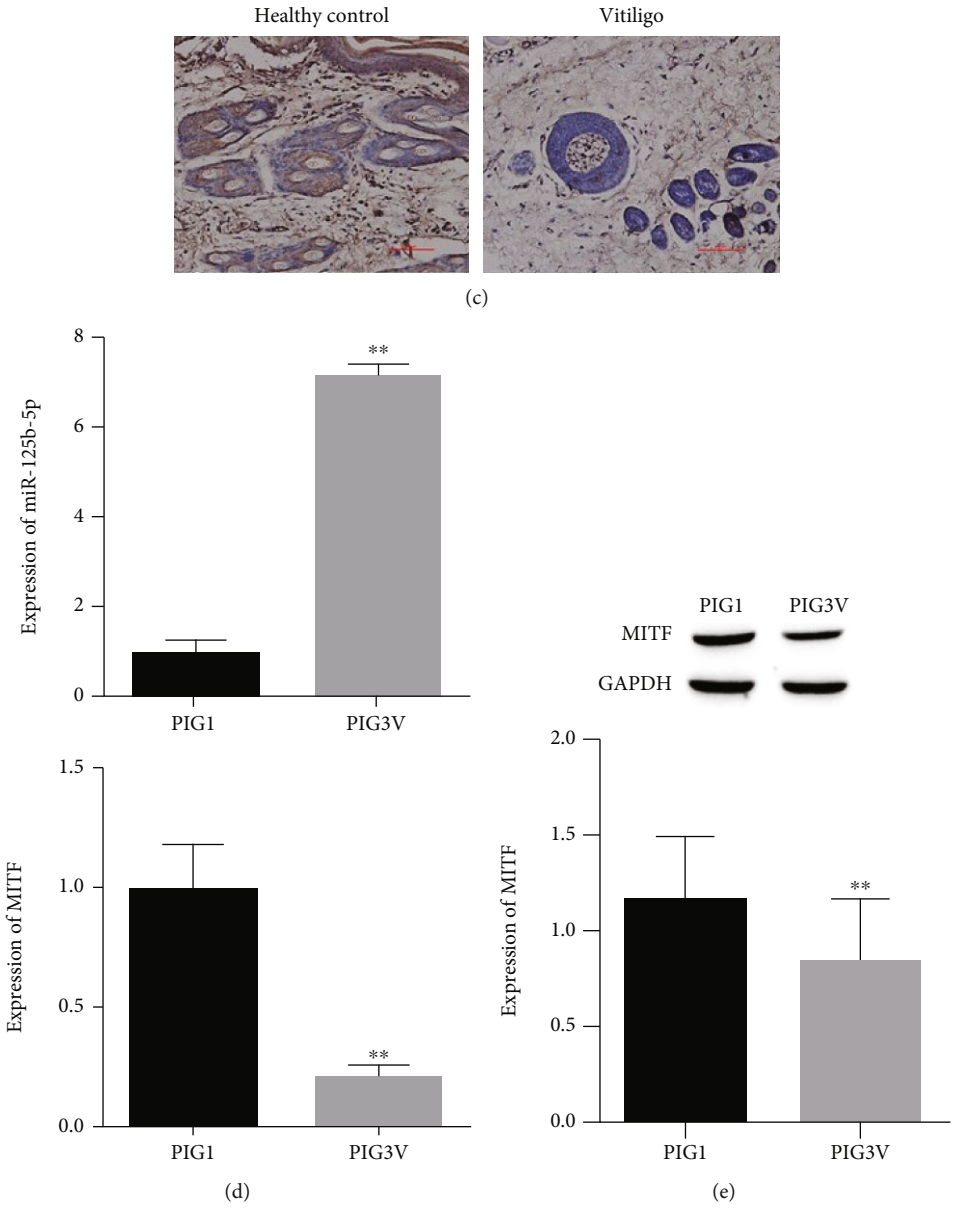

Figure 1: Differential levels of miR-125b-5p and MITF in the serum, tissues, and melanocytes of vitiligo patients. (a) RT-qPCR for differential expression of miR-125b-5p and MITF; (b) Western blot for MITF expression; (c) immunohistochemical detection of vitiligo patients' tissues; (d) RT–qPCR for differential levels of miR-125b-5p and MITF in PIG1 and PIG; (e) Western blot for differential levels of miR-125b-5p and MITF in PIG1 and PIG3V. $^{**}P < 0.01$.

of overexpressing miR-125b-5p alone, apoptosis was increased again, and the expression of apoptosis-related protein BcL-2 was decreased again, but Bax and Caspase-3 were increased again (Figures 4(c) and 4(d)).

TUNEL assay of apoptosis in PIG1 and PIG3V cells showed an increase in apoptosis under the treatment of the miR-125b-5p mimic, cotransfection of oe-MITF with it partially reversed the influence of miR-125b-5p mimic transfection alone, and apoptosis was attenuated. However, cotransfection of sh-MITF with it promoted the effect of transfection of the miR-125b-5p mimic alone and apoptosis was diminished, while cotransfection of sh-MITF with it promoted the influence of the treatment of miR-125b-5p mimic alone, and apoptosis was increased again (Figure 4(e)). In summary, miR-125b-5p influences the proliferation and apoptosis of PIG1 and PIG3V cells by targeting the negative regulation of MITF expression and has a greater effect on PIG3V.

3.5. miR-125b-5p Affects the PIG1 and PIG3V Cycles by Targeting Regulating MITF. Using flow cytometry to detect cell PIG1 and PIG3V cycles, the results showed that, under the treatment of the miR-125b-5p mimic, cells had G0/G1 and S phase block; downregulated CDK2, CDK4, and CyclinA2 protein expression; and upregulated CyclinD1 expression. After cooverexpressing MITF, cell G0/G1 phase and S phase block was relieved; CDK2, CDK4, and CyclinA2 protein expressions were upregulated; and CyclinD1

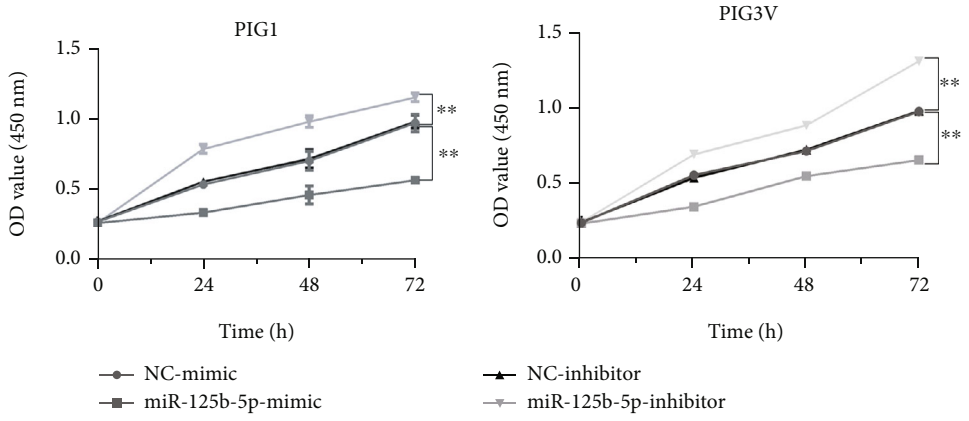

(a)

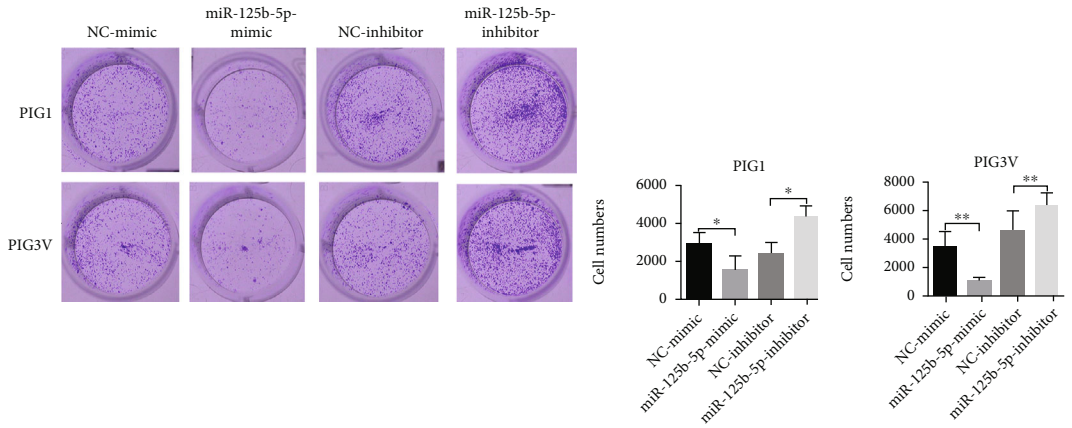

(b)

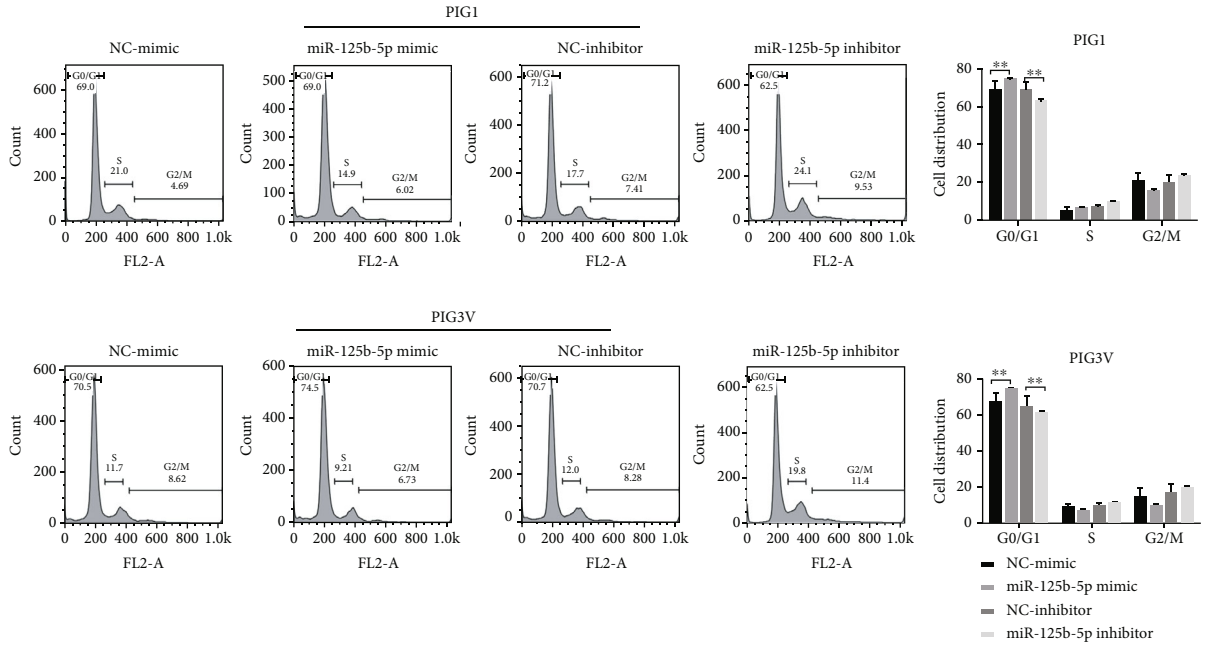

(c)

Figure 2: Continued.

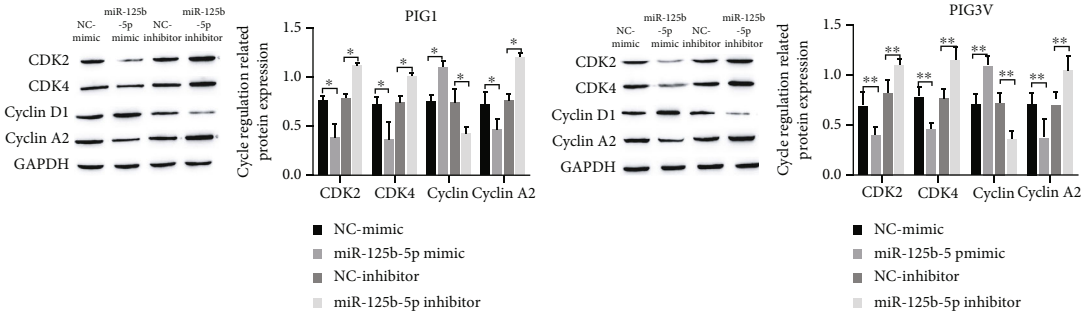

(d)

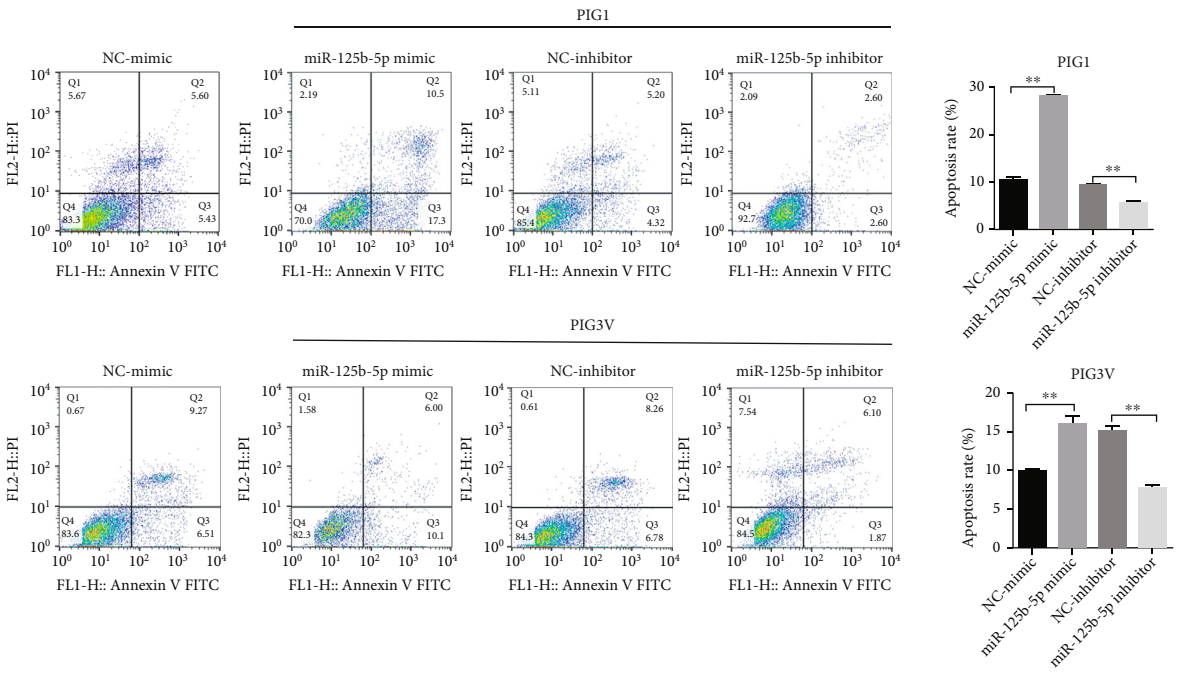

(e)

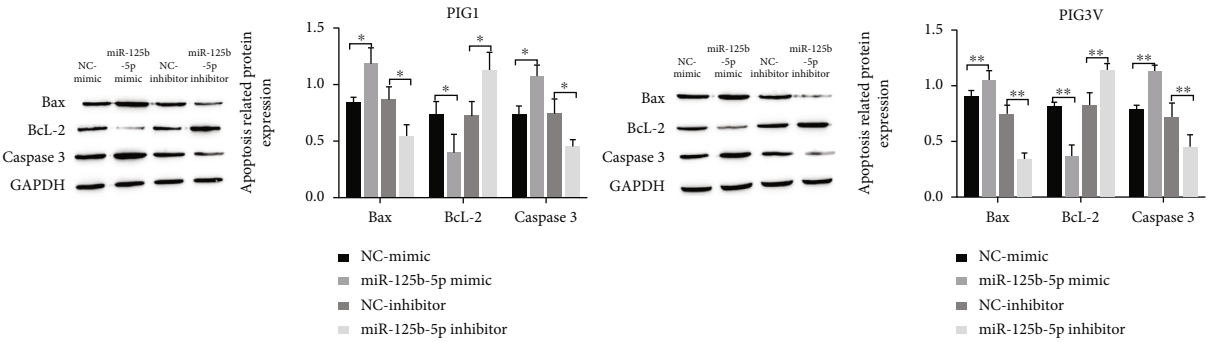

(f)

FIGURE 2: Continued.

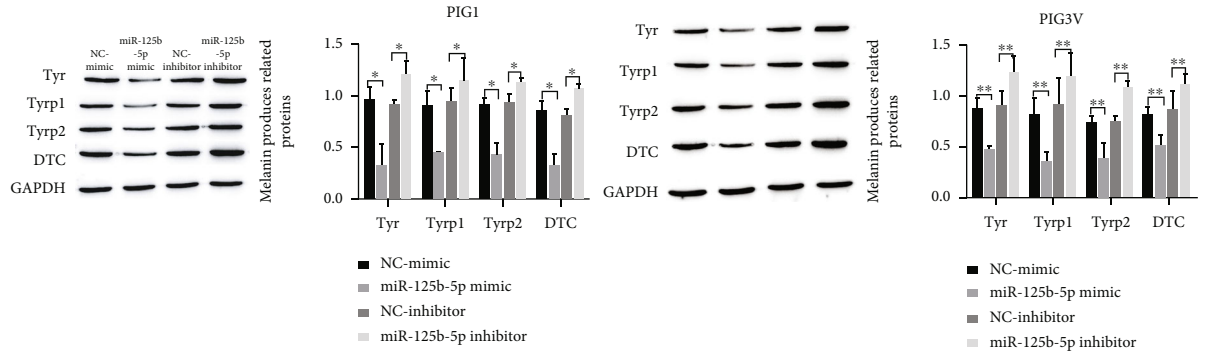

(g)

Figure 2: The influence of miR-125b-5p on the apoptosis, cycle, proliferation, and melanogenesis of melanocytes PIG1 and PIG3V. (a, b) CCK-8 and cell cloning experiments to evaluate the proliferation of PIG1 and PIG3V cells; (c, d) evaluation of the cell cycle of PIG1 and PIG3V by Western blot and flow cytometry; (e, f) detection of the apoptosis of PIG1 and PIG3V cells by Western blot and flow cytometry; (g) Western blot detection of melanogenesis-related protein expression. $^{*}P < 0.05$; $^{**}P < 0.01$.

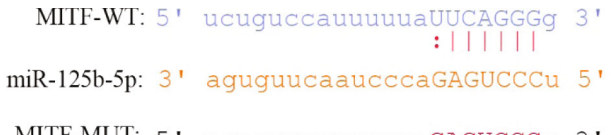

(a)

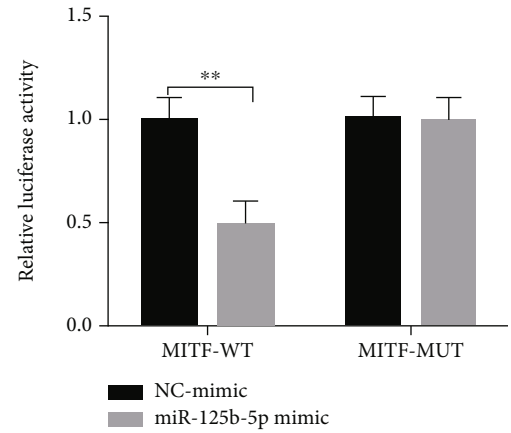

(b)

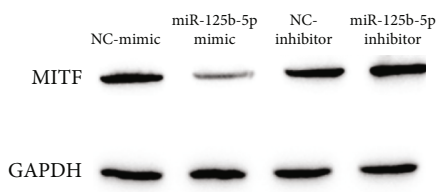

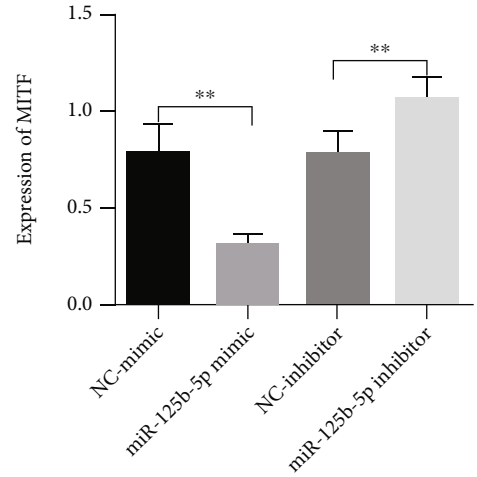

(c)

Figure 3: miR-125b-5p targets and negatively regulates MITF expression. (a) miR-125b-5p and MITF binding sequence; (b) dual-luciferase detection of miR-125b-5p in regard to MITF targeting; (c) Western blot detection of miR-125b-5p in regard to MITF regulation, $^{**}P < 0.01$.

expression was downregulated. However, when knocking down MITF, under the treatment of miR-125b-5p mimic +NE-sh, cells in the miR-125b-5p mimic+sh-MITF group had G0/G1 and S phase block; CDK2, CDK4, and CyclinA2 protein expressions were decreased; and CyclinD1 expression was increased (Figures 5(a) and 5(b)).

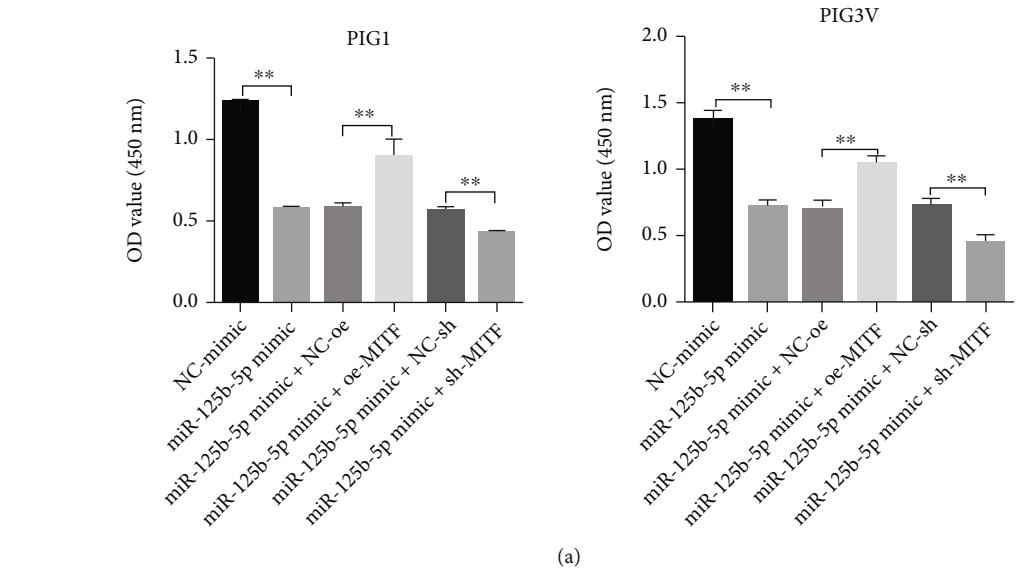

(a)

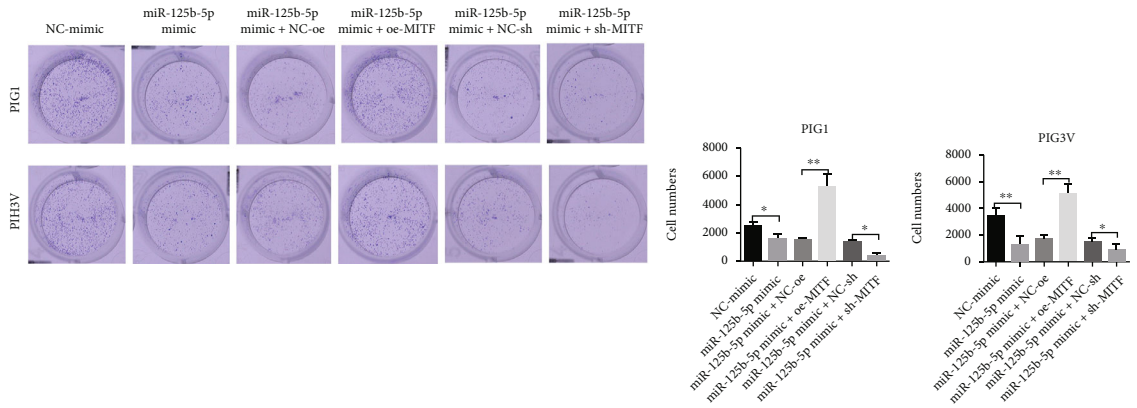

(b)

Figure 4: Continued.

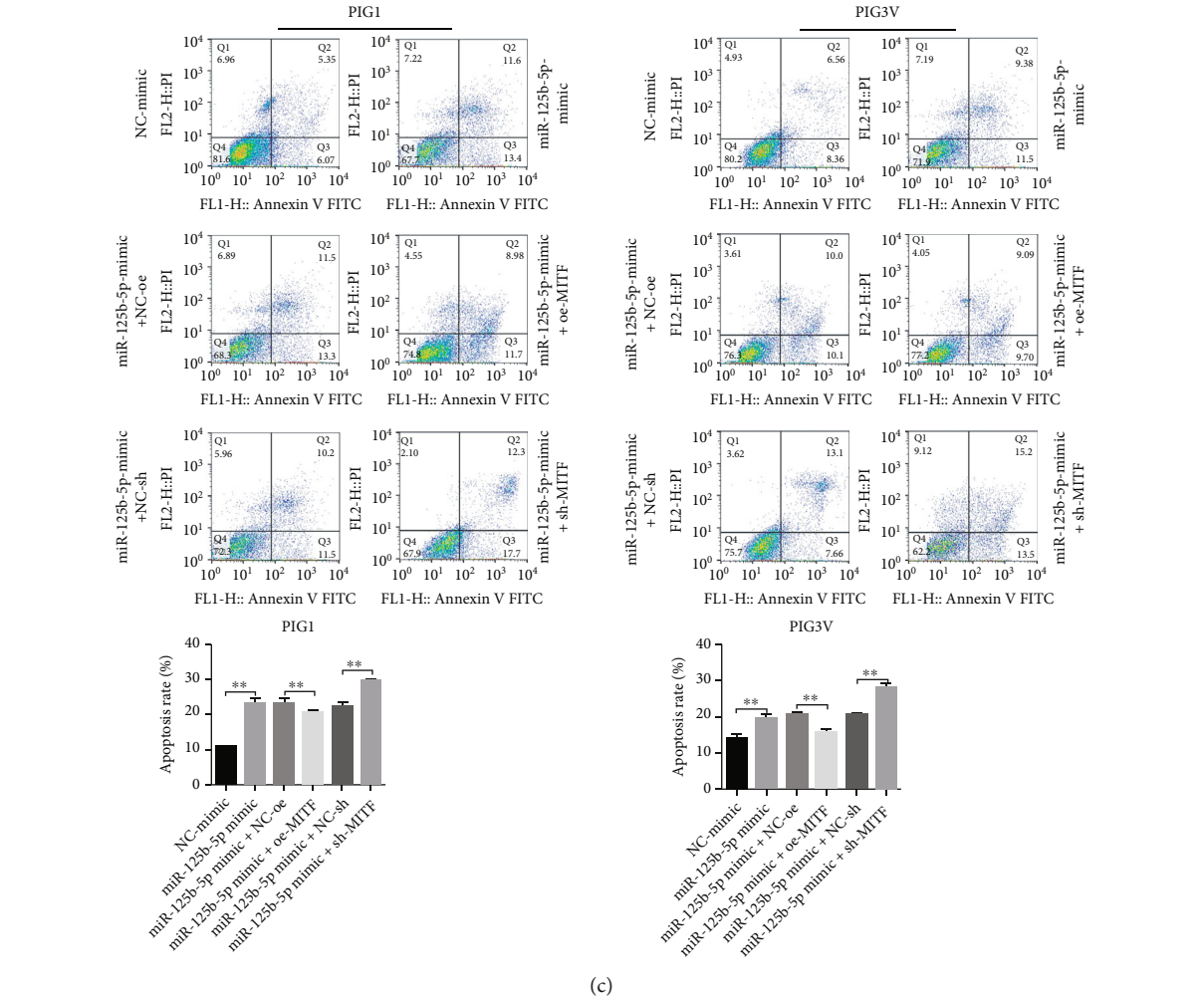

(c)

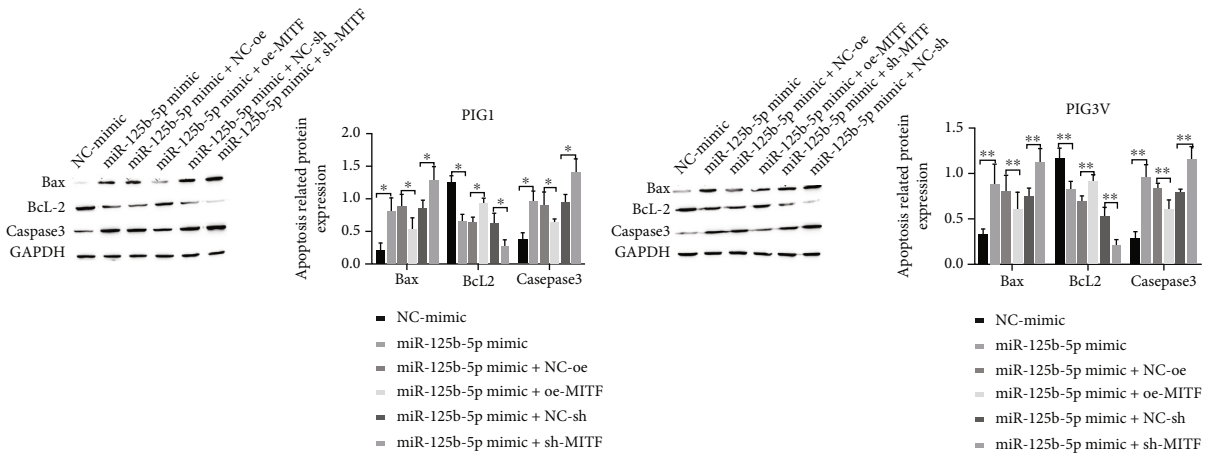

(d)

Figure 4: Continued.

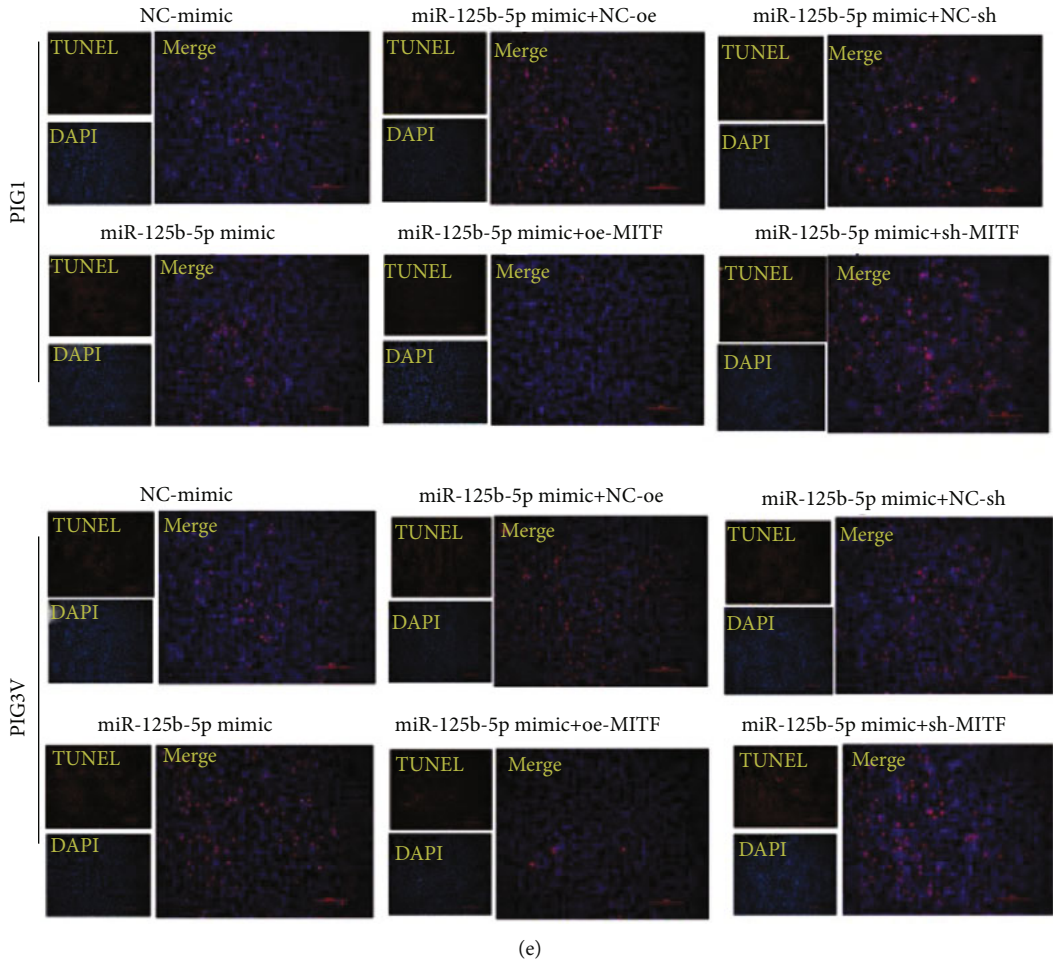

(e)

Figure 4: miR-125b-5p influences PIG1 and PIG3V apoptosis and proliferation through targeted regulation of MITF. (a, b) CCK-8 and cell cloning experiments to evaluate the proliferation of PIG1 and PIG3V cells, $^{**}P < 0.01$; (c, d) PIG1 and PIG3V apoptosis, $^{*}P < 0.05$ and $^{**}P < 0.01$; (e) detection of PIG1 and PIG3V cell apoptosis by TUNEL.

3.6. miR-125b-5p Affects Melanogenesis of PIG1 and PIG3V through Target Regulation of MITF. To confirm whether miR-125b-5p can affect PIG1 and PIG3V melanin production by regulating MITF expression, we examined the activity of Tyr, the melanin content, and melanogenesis-related protein expression. The results showed that, compared with the miR-125b-5p mimic+NE-oe group, Tyr activity was enhanced under the treatment of with cotransfection of oe-MITF with the miR-125b-5p mimic. Tyr activity was reduced when MITF was knocked down because it reduced the inhibitory effect of the miR-125b-5p mimic on Tyr activity (Figure 6(a)).

Melanin production was reduced under the treatment of the miR-125b-5p mimic, and the expressions of melanin production-related proteins MITF, Tyr, Tyrp1, Tyrp2, and DCT were downregulated according to western blotting; meanwhile, overexpression of MITF reversed the above phenomenon, and the cellular melanin content increased. Compared with the treatment of miR-125b-5p mimic+NE-sh, the expressions of melanin-related proteins Tyr, Tyrp1, Tyrp2, MITF, and DCT were upregulated, and the suppression of MITF expression further enhanced the inhibitory influence of the miR-125b-5p mimic on melanogenesis, but the treatment of the miR-125b-5p mimic+sh MITF showed reduced cellular melanin content and downregulated expression of melanogenesis-related proteins MITF, Tyr, Tyrp1, Tyrp2, and DCT (Figures 6(b) and 6(c)).

4. Discussion

Vitiligo is an acquired pigmented skin disease resulting in a lack of pigment cells in the epidermis, which clinically manifests as white patches on the body that are symmetrically distributed, well-defined, and varying in size; it has a worldwide incidence of 0.5-1%. Segmental vitiligo (SV) and nonsegmental vitiligo (NSV) are the main types of vitiligo [11]. The development of vitiligo is a result of many factors. In the epidermis, vitiligo is caused by a variety of factors, but its main feature is damage to melanocytes between the hair follicles [12]. The unique biological function of melanocytes is melanin synthesis and plays a key role in the photoprotection of the skin; however, abnormal melanin reduction can

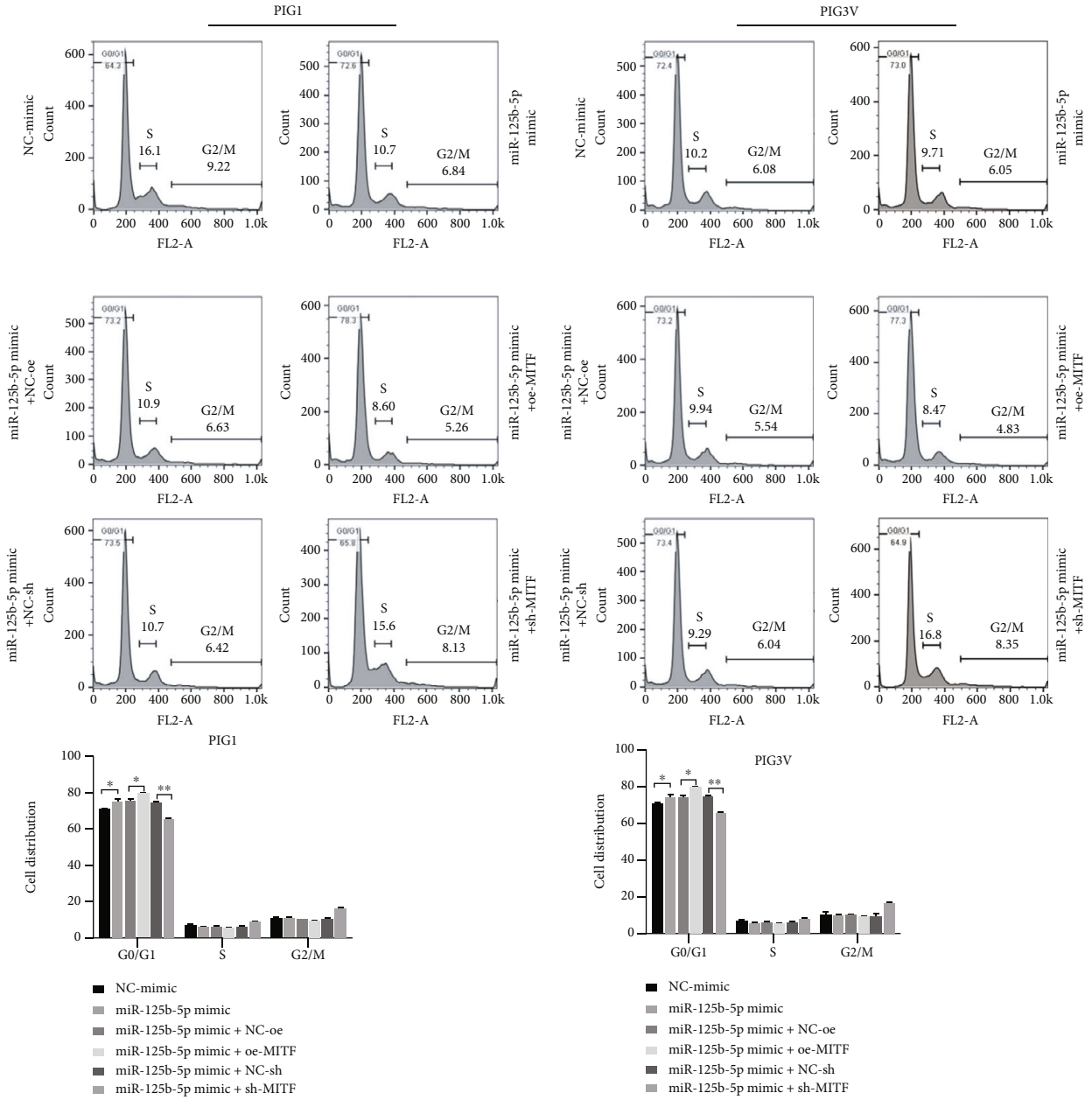

(a)

Figure 5: Continued.

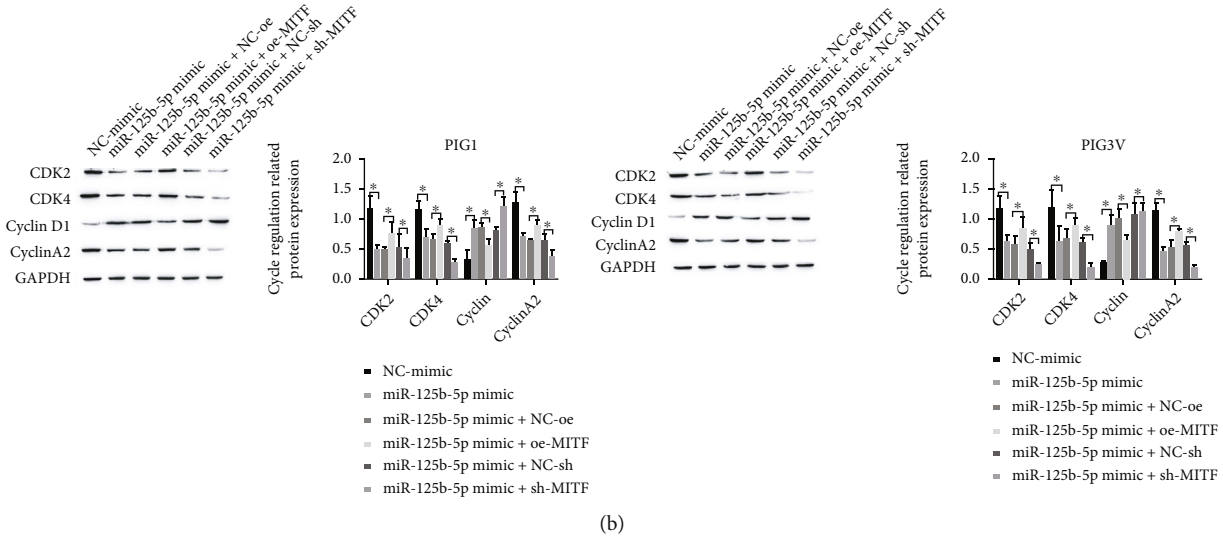

(b)

Figure 5: miR-125b-5p influences the cycle of PIG1 and PIG3V by targeting and regulating MITF. (a) Flow cytometry detection of cellular PIG1 and PIG3V cycles; (b) detection of cycle-regulated related proteins by Western blot, $^{*}P < 0.05$ and $^{**}P < 0.01$.

have an obvious influence on the appearance and health of the individual. The study of melanin synthesis is of great importance for the treatment of vitiligo. Therefore, it is crucial to investigate new targets that can effectively promote melanin synthesis in melanocytes. miRNAs and some noncoding RNAs may play a key role in individual susceptibility to vitiligo [13]. In the present study, qRT–PCR assays revealed that miR-125b-5p expression was increased in the serum and tissues of vitiligo patients and was aberrantly expressed in the development of vitiligo. It has also been shown that altered gene expression is involved in melanogenic dysfunction, and the role of miRNAs in melanogenesis has been extensively studied. In melanoma, some miRNAs regulating melanogenesis have been found to play a key role [14]. miR-340 and miR-218 inhibit melanogenesis by negatively regulating MITF expression and thus play an inhibitory role in melanoma production [15, 16]. For example, miR-21a-5p, miR-25, and miR-27a-3p play a carcinogenic role in melanoma, and the levels are increased in metastatic melanoma [17, 18]. In this research, miR-125b-5p showed elevated expression in PIG3V compared to in PIG1 according to assay. The proliferative activity of melanocytes can be decreased by the overexpression of miR-125b-5p, blocking the cell cycle, increasing apoptosis, and decreasing the levels of melanogenesis-related proteins Tyr, Tyrp1, Tyrp2, and DCT, while reversing the inhibition of miR-125b-5p, such as shortening the G0/G1 and S phases, decreasing apoptosis, and upregulating melanogenesis-related protein expression. The results suggest that miR-125b-5p has a key role in melanogenesis in melanocytes.

miRNAs can regulate the level of related genes by binding to the 3′-UTR sequence of target gene mRNAs. MITF is a key developmental and differentiation program master transcriptional regulator that coordinates the melanocyte lineage [19, 20]. Several studies have shown a potential effect of MITF expression controlled by miRNAs and further regulate melanogenic enzymes at the mRNA level [21, 22]. For example, miR-508-3p overexpression led to decreased expression of MITF, Tyr, TyrP-2, and melanogenesis [23]. miR-137 also decreased MITF protein expression in transgenic mice [24]. In this study, the target binding between miR-125b-5p and MITF was predicted by a bioinformatics website, and the negative expression level of MITF was influenced by miR-125b-5p. Overexpression of miR-125b-5p resulted in weak proliferative viability, G0/G1 cell cycle arrest, and S phase arrest in melanocytes and increased apoptosis, while coexpression of MITF with miR-125b-5p significantly reversed the effect of miR-125b-5p overexpression. Moreover, knockdown of MITF increased the level of miR-125b-5p. The results indicate that miR-125b-5p affects the apoptosis and cycle of PIG1, proliferation, and PIG3V by targeting and regulating MITF. It is also a master regulator of three major pigmentation enzymes required for melanin synthesis: Tyr, TyrP1, and TyrP [25]. As a membrane-bound glycoprotein, Tyr plays a key role in melanin synthesis and is considered to be the rate-limiting enzyme for melanin synthesis, while TyrP1 and TyrP2, also known as dobutamine isomerase (DCT), act mainly in the later stages of melanin synthesis [26, 27]. In this study, after the level of miR-125b-5p was increased, the activity of Tyr in PIG1 and PIG2 cells was weakened, cellular melanin content was reduced, and the levels of MITF, Tyr, Tyrp1, Tyrp2, and DCT, which are proteins related to melanogenesis, were decreased. This phenomenon was obviously reversed after simultaneous overexpression of MITF, and if MITF was knocked down at the same time, the level of miR-125b-5 was enhanced, which affects melanogenesis of PIG1 and PIG3V through target regulation of MITF.

In summary, the level of miR-125b-5p was upregulated, and MITF was downregulated in vitiligo tissues and serum. miR-125b-5p regulates MITF expression, thereby affecting PIG1 and PIG3V cell proliferation, cell cycle progression, apoptosis, and melanogenesis, and it has a greater effect on PIG3V cells.

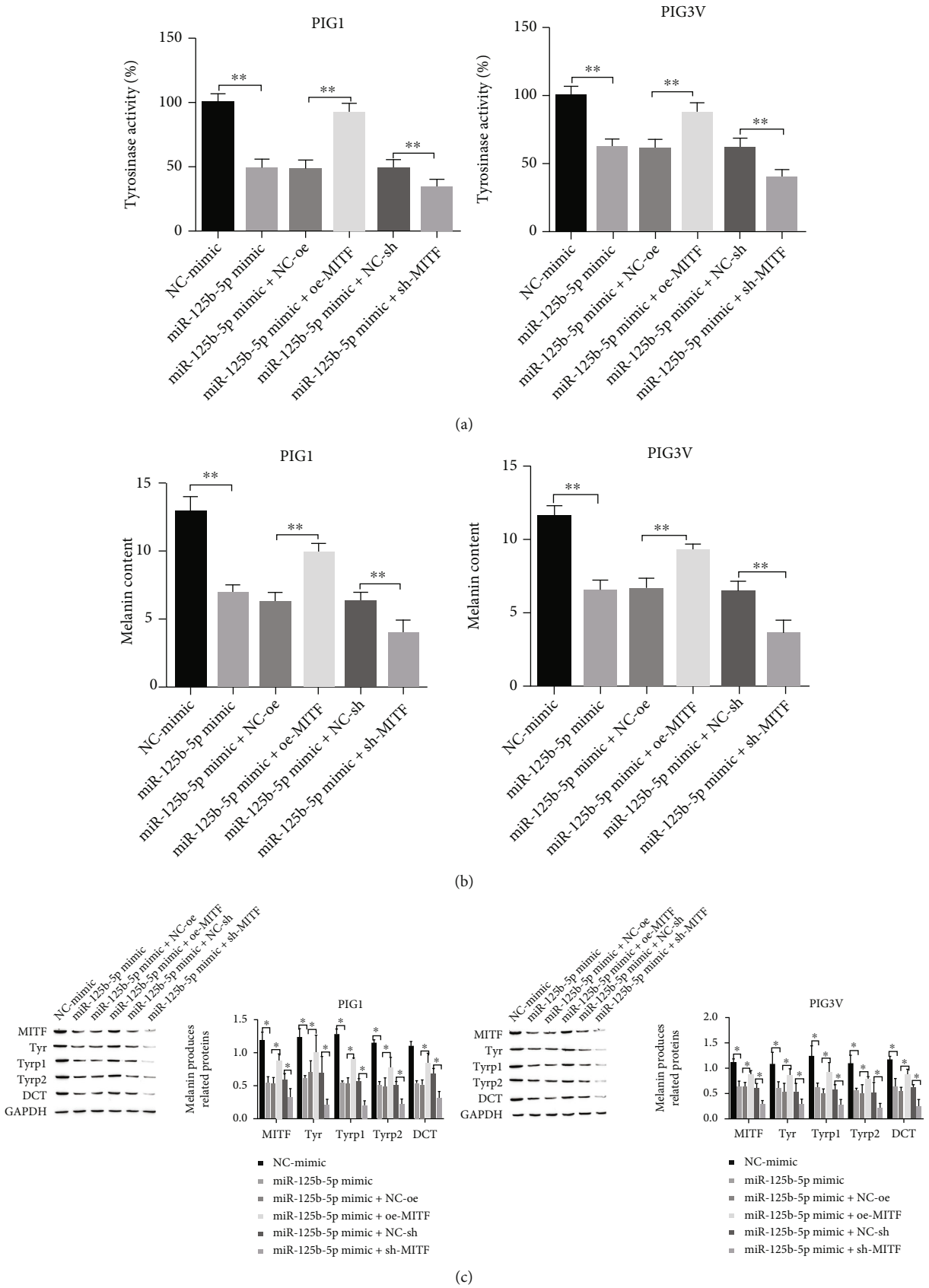

Figure 6: miR-125b-5p influences melanogenesis of PIG1 and PIG3V through target regulation of MITF. (a) Try activity assay; (b) melanin content measurement; (c) Western blot for the level of melanin production-related protein. $^{*}P < 0.05$ and $^{**}P < 0.01$.

Data Availability

The datasets used and/or analyzed during the current study are available from the corresponding author upon reasonable request.

Ethical Approval

The study involving human beings was approved by the Ethics Committee of the First Affiliated Hospital of Kunming Medical University (Approval No. 2020KYS11S) and was in line with the Declaration of Helsinki.

Conflicts of Interest

The authors have no conflicts of interest to declare.

Authors' Contributions

Xiaochuan Wang and Yifei Wu were responsible for conceptualization; Peng Du, Liangheng Xu, and Xiaochuan Wang were responsible for the methodology; Yuan Chen and Jingzi Li were responsible for the software; Xiaochuan Wang and Peng Du were responsible for validation; Zhiqiong Wang, Liangheng Xu, and Yuan Chen were responsible for formal analysis; Xiaochuan Wang, Zhiqiong Wang, and Yifei Wu were responsible for investigation, writing, review, and editing; Yifei Wu was responsible for the resources; Xiaochuan Wang, Zhiqiong Wang, Peng Du, and Liangheng Xu were responsible for data curation; Xiaochuan Wang, Zhiqiong Wang, Yuan Chen, and Jingzi Li were responsible for writing the original draft preparation; Zhiqiong Wang and Xuying Pan were responsible for visualization; Yifei Wu was responsible for supervision; Yifei Wu was responsible for funding acquisition. All authors have read and agreed to the published version of the manuscript. Xiaochuan Wang and Yifei Wu contributed equally to this work.

Acknowledgments

This research was supported by Provincial Basic Research Program, Kunming Medical University Joint Project 2019FE001(-122).

References

[1] K. Ezzedine, V. Eleftheriadou, M. Whitton, and N. van Geel, "Vitiligo," *Lancet*, vol. 386, no. 9988, pp. 74–84, 2015.

[2] M. Rodrigues, K. Ezzedine, I. Hamzavi, A. G. Pandya, J. E. Harris, and Vitiligo Working Group, "New discoveries in the pathogenesis and classification of vitiligo," *Journal of the American Academy of Dermatology*, vol. 77, no. 1, pp. 1–13, 2017.

[3] S. Jonas and E. Izaurralde, "Towards a molecular understanding of microRNA-mediated gene silencing," *Nature Reviews Genetics*, vol. 16, no. 7, pp. 421–433, 2015.

[4] A. Rebane and C. A. Akdis, "MicroRNAs: essential players in the regulation of inflammation," *Journal of Allergy and Clinical Immunology*, vol. 132, no. 1, pp. 15–26, 2013.

[5] Z. Shang and H. Li, "Altered expression of four miRNA (miR-1238-3p, miR-202-3p, miR-630 and miR-766-3p) and their potential targets in peripheral blood from vitiligo patients," *The Journal of Dermatology*, vol. 44, no. 10, pp. 1138–1144, 2017.

[6] M. H. Aguennouz, F. Guarneri, R. Oteri, F. Polito, R. Giuffrida, and S. P. Cannavò, "Serum levels of miRNA-21-5p in vitiligo patients and effects of miRNA-21-5p on SOX5, beta-catenin, CDK2 and MITF protein expression in normal human melanocytes," *Journal of Dermatological Science*, vol. 101, no. 1, pp. 22–29, 2021.

[7] V. S. Spiegelman and I. A. Elcheva, "Metabo-miR: miR-211 regulates mitochondrial energy metabolism in vitiligo," *Journal of Investigative Dermatology*, vol. 137, no. 9, pp. 1828–1830, 2017.

[8] K. H. Kim, B. H. Bin, J. Kim et al., "Novel inhibitory function of miR-125b in melanogenesis," *Pigment Cell & Melanoma Research*, vol. 27, no. 1, pp. 140–144, 2014.

[9] J. Yang, J. Wang, L. Pan et al., "BMP4 is required for the initial expression of MITF in melanocyte precursor differentiation from embryonic stem cells," *Experimental Cell Research*, vol. 320, no. 1, pp. 54–61, 2014.

[10] E. Steingrímsson, H. Arnheiter, J. H. Hallsson, M. L. Lamoreux, N. G. Copeland, and N. A. Jenkins, "Interallelic complementation at the mouseMitf locus," *Genetics*, vol. 163, no. 1, pp. 267–276, 2003.

[11] K. Ezzedine, H. W. Lim, T. Suzuki et al., "Revised classification/nomenclature of vitiligo and related issues: the Vitiligo Global Issues Consensus Conference," *Pigment Cell & Melanoma Research*, vol. 25, no. 3, pp. E1–E13, 2012.

[12] M. L. Frisoli, K. Essien, and J. E. Harris, "Vitiligo: mechanisms of pathogenesis and treatment," *Annual Review of Immunology*, vol. 38, no. 1, pp. 621–648, 2020.

[13] M. S. Mansuri, M. Singh, M. Dwivedi, N. C. Laddha, Y. S. Marfatia, and R. Begum, "MicroRNAprofiling reveals differentially expressed microRNAsignatures from the skin of patients with nonsegmental vitiligo," *British Journal of Dermatology*, vol. 171, no. 5, pp. 1263–1267, 2014.

[14] S. Sabarimurugan, M. Madurantakam Royam, A. Das, S. Das, K. M. Gothandam, and R. Jayaraj, "Systematic review and meta-analysis of the prognostic significance of miRNAs in melanoma patients," *Molecular Diagnosis & Therapy*, vol. 22, no. 6, pp. 653–669, 2018.

[15] J. Guo, J. F. Zhang, W. M. Wang et al., "MicroRNA-218 inhibits melanogenesis by directly suppressing microphthalmia-associated transcription factor expression," *RNA Biology*, vol. 11, no. 6, pp. 732–741, 2014.

[16] S. Goswami, R. S. Tarapore, A. M. Poenitzsch Strong et al., "MicroRNA-340-mediated Degradation of Microphthalmia-associated Transcription Factor (MITF) mRNA Is Inhibited by Coding Region Determinant-binding Protein (CRD-BP)," *Journal of Biological Chemistry*, vol. 290, no. 1, pp. 384–395, 2015.

[17] F. Varrone and E. Caputo, "The miRNAs role in melanoma and in its resistance to therapy," *International Journal of Molecular Sciences*, vol. 21, no. 3, p. 878, 2020.

[18] K. Takano, A. Hachiya, D. Murase et al., "Quantitative changes in the secretion of exosomes from keratinocytes homeostatically regulate skin pigmentation in a paracrine manner," *The Journal of Dermatology*, vol. 47, no. 3, pp. 265–276, 2020.

[19] N. T. Nguyen and D. E. Fisher, "MITF and UV responses in skin: from pigmentation to addiction," *Pigment Cell & Melanoma Research*, vol. 32, no. 2, pp. 224–236, 2019.

[20] C. Levy, M. Khaled, and D. E. Fisher, "MITF: master regulator of melanocyte development and melanoma oncogene," *Trends in Molecular Medicine*, vol. 12, no. 9, pp. 406–414, 2006.

[21] J. Vachtenheim and J. Borovanský, ""Transcription physiology" of pigment formation in melanocytes: central role of MITF," *Experimental Dermatology*, vol. 19, no. 7, pp. 617–627, 2010.

[22] T. Chen, B. Zhao, Y. Liu et al., "MITF-M regulates melanogenesis in mouse melanocytes," *Journal of Dermatological Science*, vol. 90, no. 3, pp. 253–262, 2018.

[23] X. Liu, B. Du, P. Zhang et al., "miR-380-3p regulates melanogenesis by targeting SOX6 in melanocytes from alpacas (*Vicugna pacos*)," *BMC Genomics*, vol. 20, no. 1, p. 962, 2019.

[24] L. T. Bemis, R. Chen, C. M. Amato et al., "MicroRNA-137 targets microphthalmia-associated transcription factor in melanoma cell lines," *Cancer Research*, vol. 68, no. 5, pp. 1362–1368, 2008.

[25] C. Bertolotto, R. Buscà, P. Abbe et al., "Different *cis*-acting elements are involved in the regulation of TRP1 and TRP2 promoter activities by cyclic AMP: pivotal role of M boxes (GTCATGTGCT) and of microphthalmia," *Molecular and Cellular Biology*, vol. 18, no. 2, pp. 694–702, 1998.

[26] T. Hida, T. Kamiya, A. Kawakami et al., "Elucidation of melanogenesis cascade for identifying pathophysiology and therapeutic approach of pigmentary disorders and melanoma," *International Journal of Molecular Sciences*, vol. 21, no. 17, p. 6129, 2020.

[27] K. U. Schallreuter, S. Kothari, B. Chavan, and J. D. Spencer, "Regulation of melanogenesis – controversies and new concepts," *Experimental Dermatology*, vol. 17, no. 5, pp. 395–404, 2008.

Hindawi
Disease Markers
Volume 2022, Article ID 3153362, 15 pages
https://doi.org/10.1155/2022/3153362

Research Article

YTHDF2 Regulates Macrophage Polarization through NF-κB and MAPK Signaling Pathway Inhibition or p53 Degradation

Luhui Cai, Di Li, Zhihui Feng, Xiaofei Gu, Qiong Xu, and Qimeng Li

Hospital of Stomatology, Guangdong Provincial Key Laboratory of Stomatology, Guanghua School of Stomatology, Sun Yat-sen University, Guangzhou 510055, China

Correspondence should be addressed to Qiong Xu; xqiong@mail.sysu.edu.cn and Qimeng Li; liqm29@mail.sysu.edu.cn

Received 12 August 2022; Accepted 19 September 2022; Published 12 October 2022

Academic Editor: Fu Wang

Macrophages are heterogeneous cells that can be polarized into M1 or M2 phenotype. m^6A "reader" YTH domain family protein 2 (YTHDF2) has been the m^6A binding protein with the highest activity, which can recognize and disturb m^6A-containing mRNA in processing bodies to reduce mRNA stability. YTHDF2 is recently identified as an effective RNA binding protein that modulates inflammatory gene levels within inflammatory responses. However, the role of YTHDF2 in M1/M2 macrophage polarization has not been reported. We established a M1/M2 macrophage polarization model using bone-marrow-derived macrophages and found that the expression levels of YTHDF2 in M1/M2 macrophages were both elevated. YTHDF2-knockdown macrophage polarization model was then established, and through qPCR, ELISA, and FACS, we discovered that suppressing YTHDF2 encouraged M1 polarization but restrained M2 polarization. In M1 macrophages, YTHDF2 silencing had no significant effect on p53 expression; however, in YTHDF2 knockdown, M2 macrophage p53 expression was remarkably upregulated. p53 inhibitor PFT-α was then applied and revealed that suppressing p53 simultaneously promoted YTHDF2-silenced M1 polarization and facilitated M2 macrophage polarization. Actinomycin D assays were further utilized to examine the mRNA degradation level of different cytokines, and p53 mRNA degradation in YTHDF2-depleted M2 cells was discovered impeded. Western Blot analysis also implied that a deficit in YTHDF2 expression may activate MAPK and NF-κB pathways. In this study, YTHDF2 induces M2 macrophage polarization by promoting the degradation of p53 mRNA. YTHDF2 suppresses M1 macrophage polarization by inhibiting NF-κB, p38, and JNK signaling pathways, yet p53 remains unaffected in YTHDF2-silenced M1 macrophages.

1. Introduction

Macrophages are important innate immune cells that can trigger antimicrobial responses by identifying infection through pattern-recognition receptors [1, 2]. Their heterogeneity and malleability enable macrophages to polarize into M1 or M2 phenotypes in response to different infections [3, 4]. M1 macrophages, called the classically-activated macrophages as well, are usually induced via lipopolysaccharide (LPS) and interferon-γ (IFN-γ) and are featured by producing higher levels of surface markers CD86 and CD16/32 and excessive pro-inflammatory factors such as Interferon (IL)-1β, IL-6, inducible nitric oxide synthase (iNOS), and tumor necrosis factor-α (TNF-α) [5]. Upon LPS and IFN-γ stimulation, MAPK and NF-κB pathways can be triggered to modulate the expression of many pro-inflammatory gene related to M1 polarization, which are indispensable for alleviating infections from bacteria, virus or fungus [5, 6]. M2 macrophages, also named alternatively activated macrophages, are generally featured by their upregulation of IL-10, arginase1 (Arg1), found in inflammatory zone-1 (Fizz1), transforming growth factor-β (TGF-β), dendritic cell–associated C-type lectin 1 (dectin-1), and mannose receptor (MR that encodes Mrc1, called CD206 as well) [7]. M2 cells are well known for their essential role in regulating infection, remodeling tissue, angiogenesis, and tumor progression [8–11].

N6-methyladenosine (m^6A), methylated in adenosin's N6 position, shows the highest prevalence among internal RNA modifications in eukaryotes [8]. It has been reported and actively involved in many critical stages during the post-transcriptional course of RNA and regulates gene expression by modifying RNA processing, including

localization, translation, and eventual decay [9, 10]. m^6A deposition functions co-transcriptionally through its methyltransferases ("m^6A writers"), comprising the catalytic subunit methyltransferase-like 3 (METTL3) and METTL14, as well as its demethylases ("erasers") like ALKB homolog 5 (ALKBH5) and fat mass and obesity-associated protein (FTO) [11]. m^6A modification can be "interpreted" through the binding of m^6A "reader" proteins, like YTH-domain containing protein (YTHDC1, 2) and YTH-domain family proteins (YTHDF1-3) [12]. m^6A is correlated with numerous biological activities, such as stem cell differentiation and pluripotency, embryogenesis, DNA damage response, and tumorigenesis [12–15]. Researches have been recently carried out to reveal the significant role of m^6A in inflammatory responses, such as microglia inflammation, renal inflammation, and endothelial inflammation [16–18].

The m^6A binding protein YTHDF2, belonging to the YTH domain family (YTHDF), can selectively bind m^6A-methylated mRNA to destabilize or degrade mRNA [19]. YTHDF2 has been reported to have indispensable effect on various physiological courses, for example, neural development, cancer progression, and hematopoietic stem cell expansion [20–22]. Until recently, YTHDF2 has also been found to relate to inflammatory response progress [23]. YTHDF2 depletion within human hepatic cell carcinoma (HCC) cells or knockdown within mouse hepatocytes prompts metastasis, vascular reconstruction, and inflammation by mediating mRNA decay in cytokines that contain m^6A [23]. Our previous study indicated that YTHDF2 regulated LPS-induced inflammatory response of macrophages through specifically mediating target mRNAs degradation [24]. As revealed by our RNA sequence results, differentially expressed genes within YTHDF2-silenced macrophages were predominantly enriched in the p53 signaling pathway (unpublished data). The transcription factor p53 is a well-known tumor suppressor and is recently reported to participate in the regulation of macrophage polarization [25–27]. In p53 deficient mice, LPS stimulation prompts pro-inflammatory cytokine production in macrophages by regulating NF-κB activity [25]. Another study on p53-deficient mice revealed that in IL-4-stimulated peritoneal macrophages, M2 markers Arg1, interferon regulatory factor 4 (Irf4), Fizz1, and c-Myc were highly expressed [27]. In addition, through the mRNA analysis of p53 in the m^6A modification database SRAMP (sequence-based RNA adenosine methylation site predictor) (http://www.cuilab.cn/sramp/), our team found that the mRNA of p53 has m^6A modification sites (unpublished data), so it is speculated that p53 may be regulated by m^6A and participate in the regulation of YTHDF2 on macrophage polarization. This present study focused on investigating YTHDF2 expression within M1/M2 polarization model as well as how YTHDF2 knockdown affects macrophage polarization. We further present evidence that YTHDF2 inhibited M1 polarization through the activation of MAPK and NF-κB pathways while promoted M2 polarization by destabilizing *p53* mRNA.

Table 1: siYTHDF2 sequences for transcription (5′-3′).

siRNA	Sequences (5′-3′)
#1 siRNA	CCAUGAUUGAUGGACAGUCAGCUUU
#2 siRNA	CCCAGUGGGAUUGACUUCUCAGCAU
#3 siRNA	GGGUGGAUGGUAAUGGAGUAGGACA

2. Materials and Methods

2.1. Ethical Statement. This work gained approval from Ethical Review Board of Guanghua School of Stomatology of Sun Yat-sen University. Each animal experimental procedure was conducted in line with "Guide for the Care and Use of Laboratory Animals" formulated via the US National Institutes of Health. In addition, animal number adopted in this study was minimized.

2.2. Cell Culture and Macrophage Polarization. In this work, C57BL/6 mouse (6-8-weeks-old) were sacrificed (Animal Center of Sun Yat-sen University) and immersed them in 75% ethanol. Dissect the tibias and femurs from the body, and wash them with 90% alpha-minimal complete medium (α-MEM; Gibco, New York, NY, USA) including the concentration of 10% fetal bovine serum (FBS; Gibco, Carlsbad, CA, USA) with supplementation of penicillin/streptomycin. Expel the bone marrow cells with a 0.5 ml syringe containing α-MEM complete medium. Thereafter, cells were isolated by 24-h cultivation within α-MEM and 10% FBS. Besides, this work collected the suspended cells for resuspension within the α-MEM that contained 10% FBS and 30 ng/ml M-CSF (Sino Biological, Beijing, China). At day 6 of post-incubation under 37°C, 95% air, and 5% CO_2 conditions, bone-marrow-derived macrophages (BMDMs) were harvested. Logarithmic growth phase cells were utilized. After reaching 80% cell density, 0.25% trypsin/EDTA (Gibco; Thermo Fisher Scientific, Inc.) was utilized for detaching macrophages. Then, inoculation was performed (1×10^6/well) into the 6-well plates. Thereafter, cells were exposed to 6-h treatment using IFNγ (10 ng/mL, R&D Systems, Minneapolis, MN, USA) as well as *Escherichia coli* LPS (1 μg/mL, Sigma-Aldrich, St. Louis, MO, USA) or 24-h exposure to 20 ng/mL murine interleukin-4 (IL-4, Sino Biological Inc.), for the generation of M1 or M2 macrophages, separately. The untreated cells were used to be negative control.

2.3. YTHDF2 Small Interfering RNA (siRNA) Transfection. YTHDF2 was knocked down by siRNA transfection in macrophages. Cells (6×10^5/well) were later inoculated before transfection into the 6-well plates that contained 2 ml α-MEM for a 24-h period. By adopting Lipofectamine ® 3000 transfection reagent (7 μL, Invitrogen; Thermo Fisher Scientific, Inc.), cells reaching 70% density were exposed to transfection with 50 nM siRNA against YTHDF2 or a nontargeting siRNA control (siYTHDF2 and the negative control NC; Invitrogen, Carlsbad, CA, USA). Macrophages were subject to 24-h incubation under 5% CO_2 and 37°C conditions following specific protocols. The present study

Table 2: Primers used for the analysis of mRNA levels by qRT-PCR.

Gene	Forward primer (5′-3′)	Reverse primer (5′-3′)
YTHDF2	ATAGGAAAAGCCAATGGAGGG	CCAAAAGGTCAAGGAAACAAAG
IL-6	CTGCAAGAGACTTCCATCCAG	AGTGGTATAGACAGGTCTGTTGG
IL-10	AGCCTTATCGGAAATGATCCAGT	GGCCTTGTAGACACCTTGGT
IL-1β	CTTTGAAGTTGACGGACCCC	GCTTCTCCACAGCCACAATG
Arg-1	GCTGGGAAGGAAGAAAAAGGC	TGCCGTGTTCACAGTACTCT
TNF-α	CCACCACGCTCTTCTGTCTA	GGTCTGGGCCATAGAACTGA
TGF-β	TACATGCTCTAACTGAAGGGGA	TTGGATTTCTTCGCAAATGGTTC
Fizz	CAGAAGGCACAGCAGTCTTG	GGGTATTAGCTCCTGTCCCC
p53	GGCGTAAACGCTTCGAGATG	AAGGCTTGGAAGGCTCTAGG
iNOS	CGGGTTGAAGTGGTATGCAC	CACAGCCACATTGATCTCCG
GAPDH	GCAAAGTGGAGATTGTTGCC	TGGAAGATGGTGATGGGCTT

prepared 3 siRNA sequences for targeting mouse YTHDF2 gene. Table 1 presents these sequences. Cells at the 70-85% transfection rate were adopted in later analysis.

2.4. Quantitative Real-Time PCR (qRT-PCR). In this work, we applied TRIzol ® reagent (Invitrogen; Thermo Fisher Scientific, Inc.) in cell lysis. After extraction, Revert Aid First Strand cDNA Synthesis Kit (Takara, Tokyo, Japan) was used to synthesize cDNA from total RNA through the reverse transcription in line with specific instructions. The complementary DNA served as the template to perform PCR. Results were then detected by a LightCycler ® 480 thermal cycler. Conditions for thermal cycling included, 5-min initial denaturation under 95 °C; 10 s under 95 °C, 20 s under 65 °C, and 30 s under 72 °C for altogether 45 cycles. Table 2 displays sequences of all primers prepared with the Primer Express Software v3.0.1 (Thermo Fisher Scientific, Inc.). *Gapdh* served as the reference for normalizing gene expression.

2.5. Enzyme-Linked Immunosorbent Assay (ELISA). To analyze mouse IL-6, IL-10, TNF-α, and TGF-β contents within supernatants in line with specific protocol, the ELISA kits (R&D, Minneapolis, MN, USA) were employed. Moreover, a microplate reader was utilized for examining absorbance (OD) values at 450 nm. Sample contents were later determined based on OD values as well as standard solution concentration.

2.6. Flow Cytometry (FCM). Samples were incubated with Fc receptor blocker according to the instructions for 20 minutes in dark under ambient temperature. Cells were then proceeded by antibody staining on ice for 30 min; rinse twice before resuspend them in PBS. Later, these samples were conducted FCM (Beckman, San Francisco, Calif., USA) using different antibodies to analyze samples. FITC-labeled anti-mouse CD16/32 and CD86, PE-labeled anti-mouse CD206 and F4/80 (BD Biosciences, San Jose, USA) were used to perform the analysis. At the same time, PE-labeled anti-mouse DECTIN-1 (Sino Biological Inc.) was utilized for analysis.

2.7. Western-Blot (WB) Assay. This work applied RIPA lysis buffer (Beyotime, Haimen, China) in combination with protease as well as phosphatase inhibitor cocktails (Cwbiotech, Beijing, China) for sample collection within a 30-min period on ice. Later, BCA protein assay (Beyotime) was conducted for measuring protein content. Subsequently, 8% SDS-PAGE was applied in separating 30 μg proteins. Then, transfer on PVDF membrane was performed (Millipore, Billerica, MA, USA). After being blocked by 5% BSA for an 80-min under ambient temperature for eliminating nonspecific protein binding, the membrane was subject to overnight incubation with primary antibodies (1 : 1000) under 4 °C, including YTHDF2, p53 (Abcam, Cambridge, UK), IκBα, p-IκBα, IKKα, IKKβ, p-IKKα/β, p38, p-p38, p65, p-p65, JNK, p-JNK, ERK, p-ERK, β-actin, VINCULIN, and GAPDH (Cell Signaling Technologies, Danvers, MA, USA). Membrane was rinsed TBST and further probed for a 1-h period using the 1 : 2000 diluted HRP-labeled secondary antibody (Cell Signaling Technology, Boston, MA, USA). This work employed enhanced chemiluminescence system (Millipore, Billerica, MA, USA) for protein band visualization by adopting ImageJ v1.47 software (National Institutes of Health, Bethesda, MD, USA), with GAPDH or VINCULIN being the endogenous reference.

2.8. RNA Stability Test and Determination of mRNA Half-Life. mRNA transcription in M1 and M2 macrophages was suppressed through exposure to 5 μg/ml actinomycin D (Sigma, St. Louis, MO, USA). In addition, after being exposed to transcription suppression for 3 and 6 h, RNA samples were harvested for measuring the respective mRNA degradation. Finally, the half-life of corresponding mRNA was determined by degradation rate and level of obtained mRNA.

2.9. Statistical Analysis. Every assay was carried out in triplicate for 3 or more replicates. Results were shown by mean ± SD. In addition, this work utilized SPSS20.0 (SPSS Inc., Chicago, IL, USA) for One-way ANOVA and student's t -test in carrying out statistical analyses. Obviously, $P < 0.05$ stood for statistical significance.

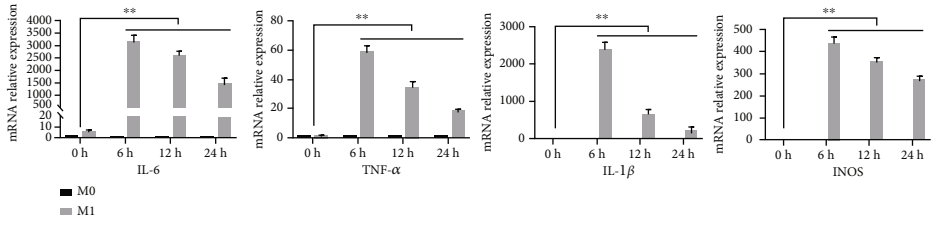

(a)

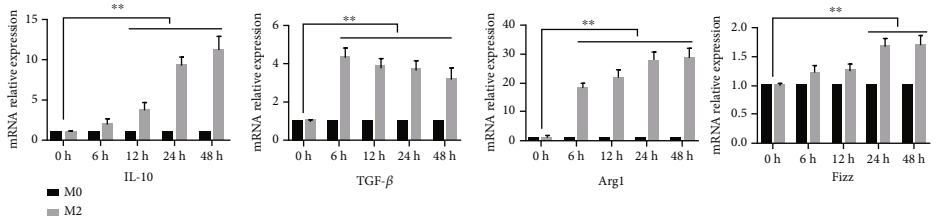

(b)

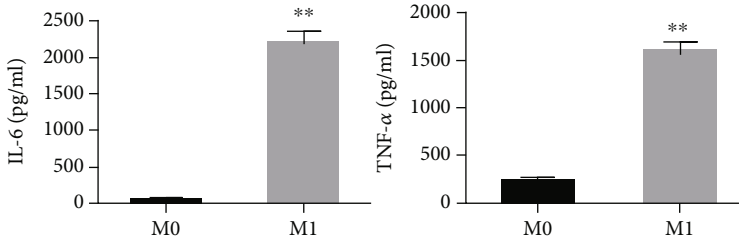

(c)

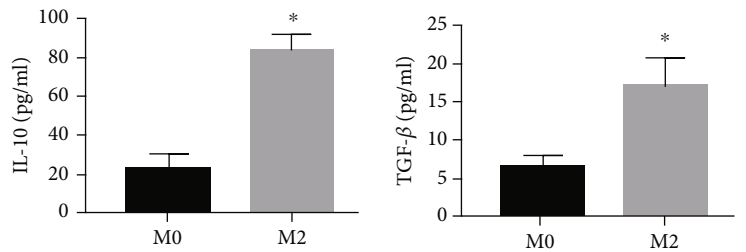

(d)

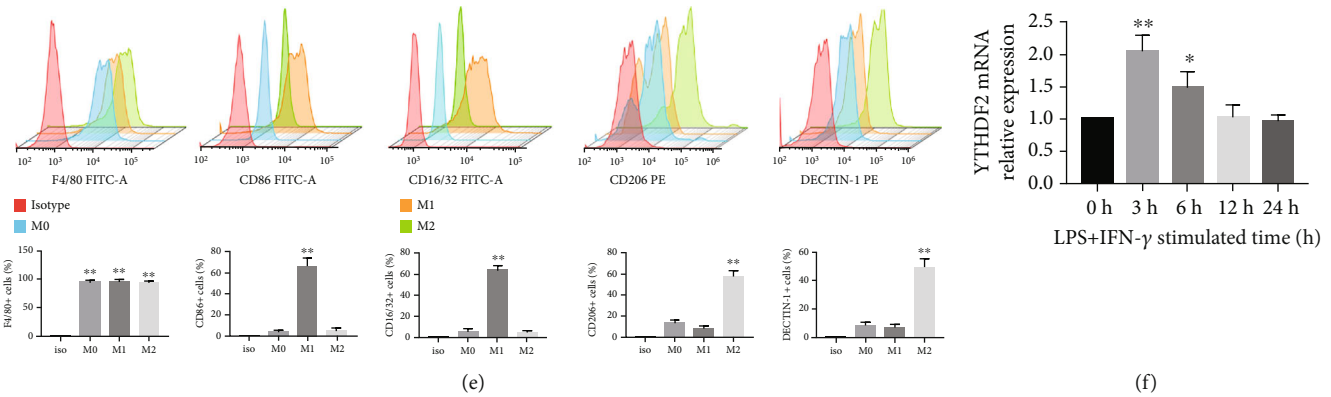

(e) (f)

Figure 1: Continued.

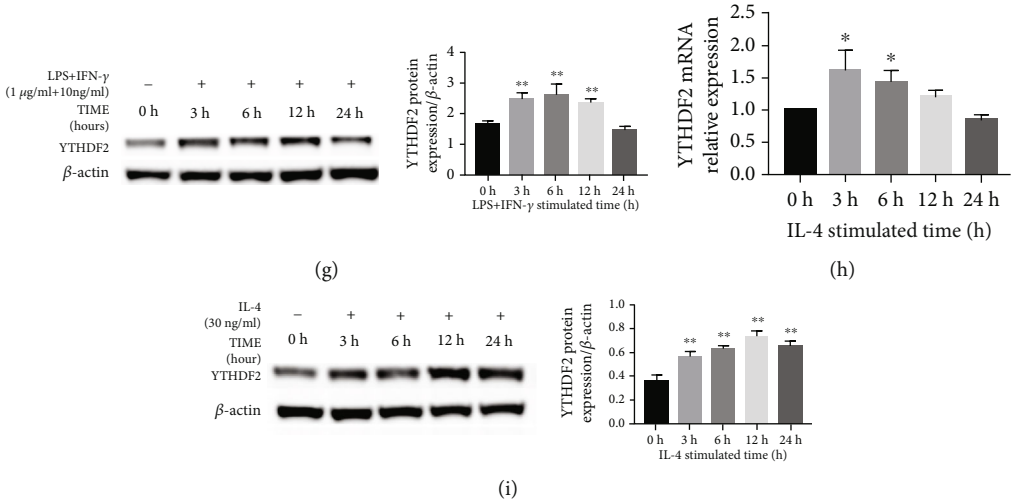

Figure 1: Polarization and YTHDF2 levels in M1/M2 macrophages. (a) LPS+ INF-γ and (b) IL-4 were utilized to treat M0 macrophages for 0, 6, 12, and 24 h, separately. *IL-1β*, *IL-6*, *IL-10*, *TNF-α*, *TGF-β*, *iNOS*, *ARG1*, and *FIZZ* levels were analyzed through qRT-PCR, with *GAPDH* being the endogenous reference. (c, d) IL-6 and TNF-α production in M1 cells, together with IL-10 and TGF-β levels within M2 cells, were detected through ELISA. (e) CD16/32, CD86, CD206, F4/80, and DECTIN-1 expression were determined through FCM in M0/M1/M2 cells. (f) *YTHDF2* mRNA level was measured through qRT-PCR following treatment of M0 cells with LPS + INF-γ, with *GAPDH* being the endogenous reference. (g) YTHDF2 protein expression detected through western blotting after treated M0 cells with LPS+ INF-γ, with β-actin being the endogenous reference. (h) *YTHDF2* mRNA expression quantified through qRT-PCR after treated M0 cells with IL-4, with *GAPDH* being the endogenous reference. (i) YTHDF2 protein expression measured through western blotting after treated M0 cells with IL-4, with β-actin being the endogenous reference. Results are demonstrated by mean ± S.E.M. ($n = 3$). $^*P < 0.05$; $^{**}P < 0.01$.

3. Results

3.1. YTHDF2 Expression Increases within M1 and M2 Macrophages. To uncover m^{6}A binding protein YTHDF2's role in regulating macrophage polarization, we first used bone-marrow-derived macrophages (BMDMs) to establish a M1/M2 polarization model. M0 macrophages were cells without any treatment. M0 macrophages were treated by PBS (1 μg/ml) plus INF-γ (10 ng/ml) for 0/6/12/24 h to induce M1 macrophages and 20 ng/ml IL-4 for 0/6/12/24/48 h) to produce M2 macrophages.

According to M1 marker mRNA levels displayed in Figures 1(a) and 1(b), *IL-1β*, *IL-6*, *iNOS*, and *TNF-α* expression elevated significantly after LPS/INF-γ stimulation at all time points, while M2 marker *ARG-1*, *TGF-β*, *IL-10*, and *FIZZ* increased with IL-4 stimulation at 12 to 48 h. The augmentation peaked at 6 h when inducing M1 polarization and at 24 h when inducing M2 polarization, which was used for further experiments. In response to 6-h LPS/INF-γ stimulation, IL-6 and TNF-α secretion significantly enhanced (Figure 1(c)), while IL-4 stimulation for 24 h prompted IL-10 and TGF-β secretion with significant increase (Figure 1(d)).

For further verification, this work detected cell surface markers for macrophages. After M1 stimulation, the cells presented obvious M1 phenotype with a notable growth in CD86+ cells and CD16/32+ cells, while M2 stimulation increased M2 features with an increase in DECTIN-1+ and CD206+ cells (Figure 1(e)). We further used qRT-PCR and WB assays for assessing YTHDF2 level during polarization for confirmation. The level of YTHDF2 showed a noteworthy increase after M1 (Figures 1(f) and 1(g)) and M2 stimulation (Figures 1(h) and 1(i)).

3.2. YTHDF2 Knockdown Promotes M1 but Inhibits M2 Polarization. To find out YTHDF2's effect on polarization in M1/M2 macrophages, siRNAs were designed for suppressing YTHDF2 expression in M0 cells. According to Figures 2(a) and 2(b), YTHDF2 mRNA and protein expression were notably decreased after siRNA treatment. The knockdown efficiency of siYTHDF2 #1 was the highest, so we selected it to continue the following experiments.

To study the effect of YTHDF2 knockdown during polarization, YTHDF2-silienced M0 macrophages were exposed to 6-h LPS/INF-γ treatment to induce polarization of M1 cells or 24-h IL-4 treatment to induce polarization of M2 cells. Then, M1 and M2 markers were examined, respectively. As the result presented, *IL-1β*, *IL-6*, *iNOS*, and *TNF-α* mRNA levels elevated within siYTHDF2 M1 group (Figure 2(c)). Similarly, IL-6, TNF-α, CD86, and CD16/32 protein expression also increased in YTHDF2-knockdown macrophages (Figures 2(e) and 2(g)). Different from M1 cells, M2 markers *IL-10*, *TGF-β*, *ARG-1*, and *FIZZ* showed a significant decrease at mRNA level after IL-4 stimulation in YTHDF2-knockdown cells (Figure 2(d)). The protein levels of IL-10, TGF-β, CD206, and DECTIN-1 were also reduced in cells after YTHDF2 knockdown (Figures 2(f) and 2(h)). Thus, these results prompted us that YTHDF2 can inhibit M1 but encourage M2 polarization.

3.3. YTHDF2 Knockdown Modulates M2 Macrophage Polarization through Upregulating p53. p53 has recently

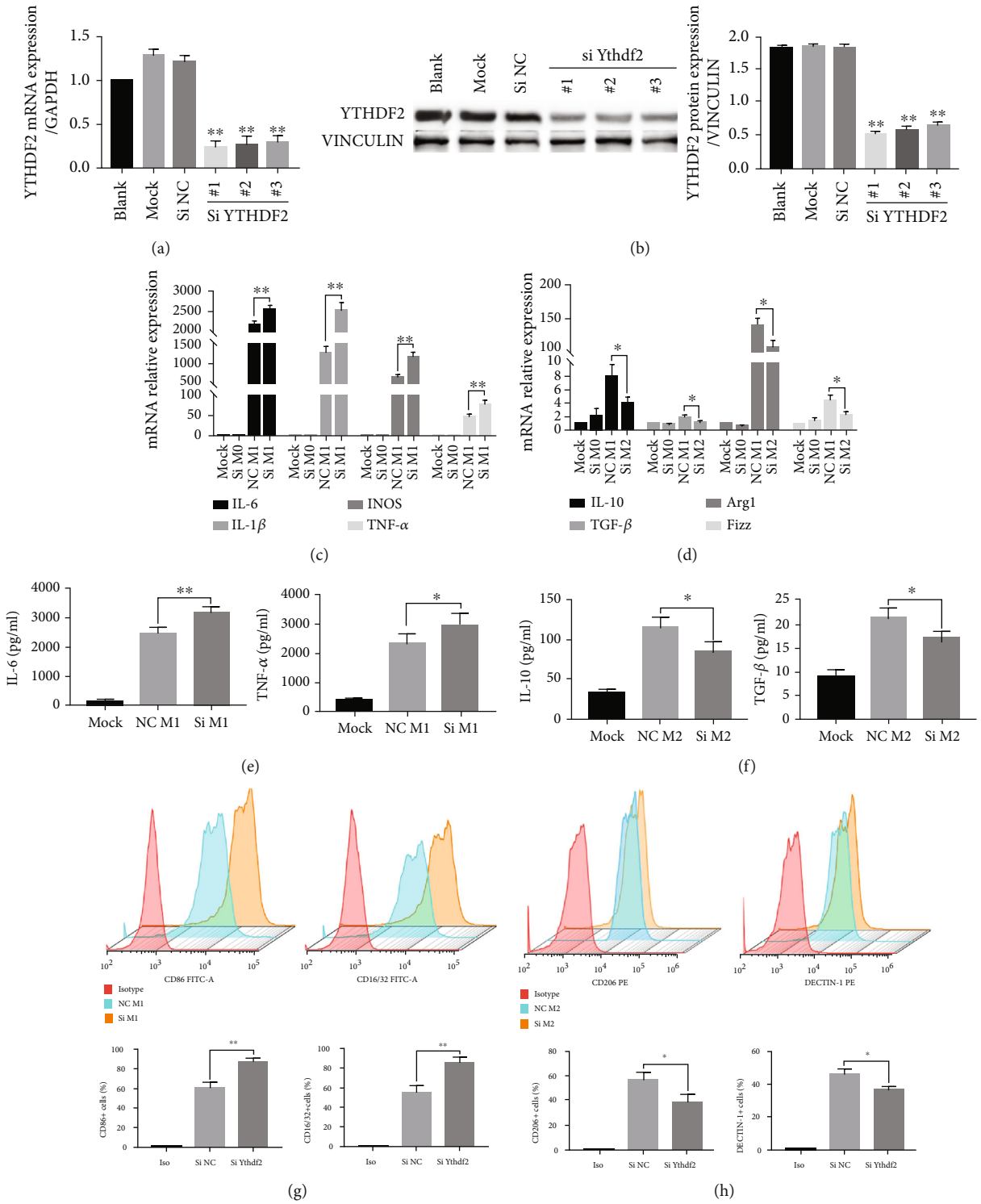

Figure 2: Role of YTHDF2 silencing in M1/M2 macrophage polarization. (a, b) YTHDF2 silencing efficiency in M0 macrophages was determined through qRT-PCR as well as WB. Mock: transfection reagent-transfected cells; siNC: NC-siRNA-treated cells; $^{\#}n$ ($n = 1/2/3$) siRNA: YTHDF2 siRNA-treated cells. (c, d) M0 macrophages were subject to transfection using YTHDF2 siRNA (Si) or NC-siRNA (NC), followed by activation using LPS+ INF-γ or IL-4, *IL-1β*, *IL-6*, *TNF-α*, and *iNOS* levels within M1 cells, together with *IL-10*, *TGF-β*, *ARG-1*, and *FIZZ* within M2 macrophages were determined through qRT-PCR, with *GAPDH* being the endogenous reference. (e) IL-6 and TNF-α production in M1 macrophages were determined by ELISA before (NC) or after YTHDF2 knockdown (Si). (f) IL-10 and TGF-β levels within M2 cells were determined by ELISA before (NC) or after YTHDF2 knockdown (Si). (g) CD86 and CD16/32 protein levels within M1 macrophages were detected through FACS before (NC) or after YTHDF2 knockdown (Si). (h) CD206 and DECTIN-1 levels within M2 macrophages were determined through FACS before (NC) or after YTHDF2 knockdown (Si). Data are demonstrated by mean ± S.E.M. ($n = 3$). $^{*}P < 0.05$; $^{**}P < 0.01$.

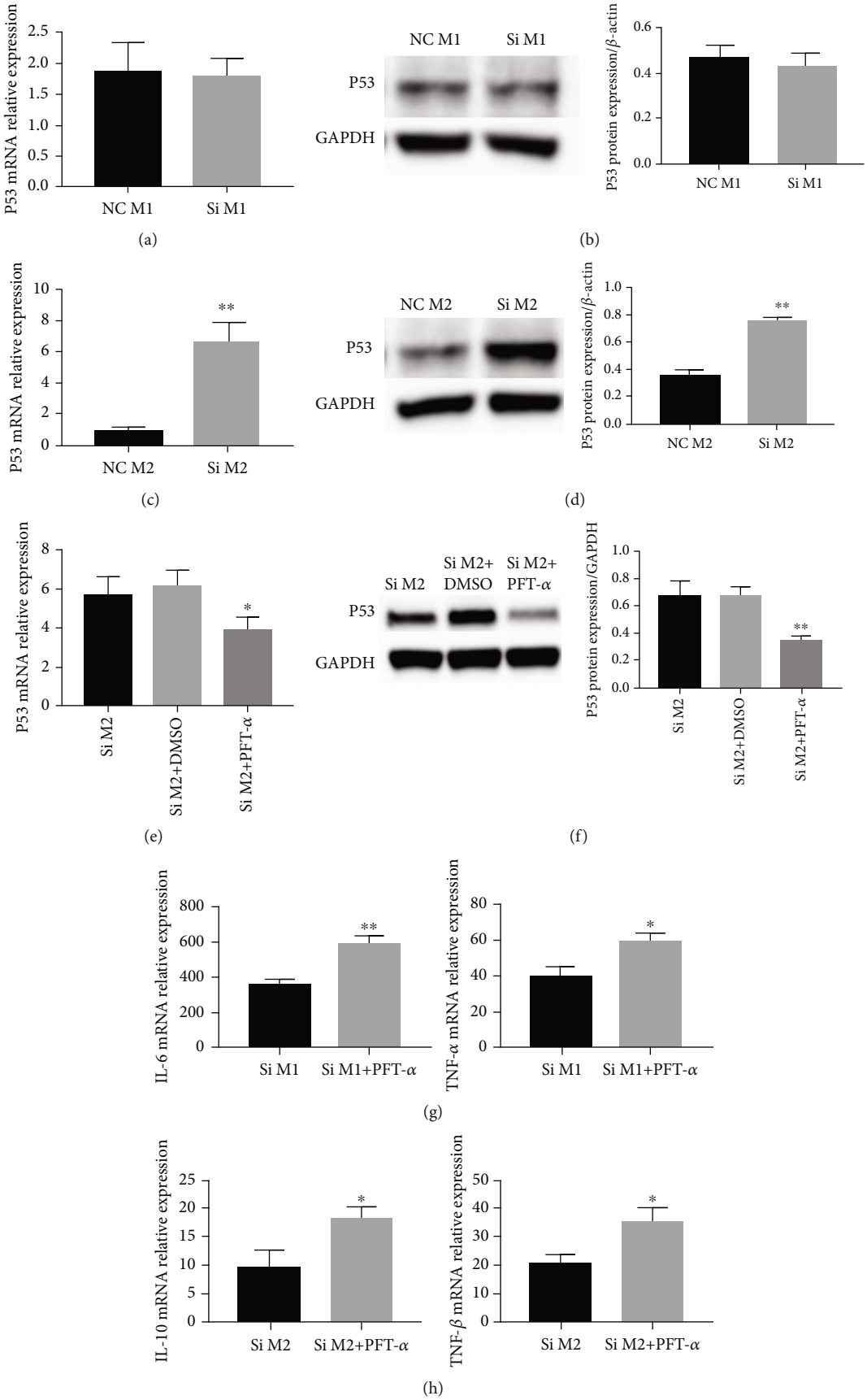

Figure 3: Continued.

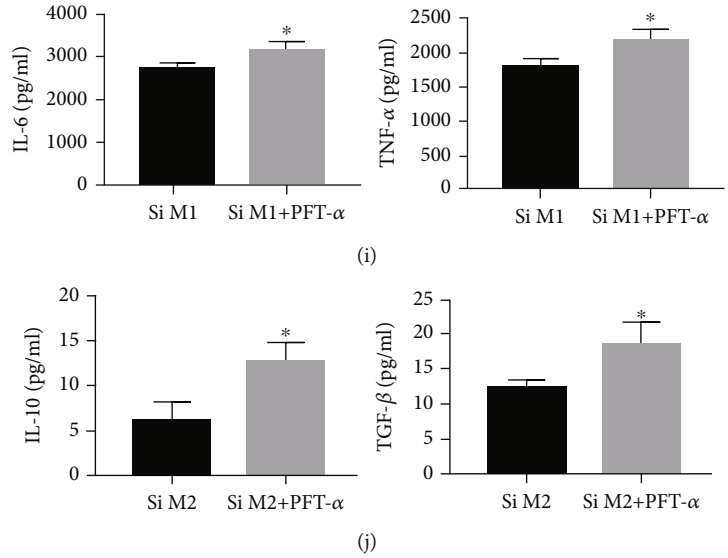

Figure 3: The role of p53 in YTHDF2 regulating M1/M2 macrophage polarization. (a, b) p53 mRNA and protein expression were explored through qRT-PCR as well as western blotting within M1 macrophages before and after YTHDF2 knockdown, with GAPDH being the endogenous reference. (c, d) p53 mRNA and protein expression were decided through qRT-PCR as well as western blotting within M2 macrophages before and after YTHDF2 knockdown, with GAPDH being the endogenous reference. (e, f) p53 mRNA and protein expression were detected via qRT-PCR together with WB after stimulation with PFT-α in YTHDF2-silenced M2 macrophages. (g, h) *IL-6*, *IL-10*, *TNF-α*, and *ARG1* mRNA levels in YTHDF2-silenced M1/M2 macrophages with or without PFT-α were determined through qRT-PCR, with *GAPDH* being the endogenous reference. (i, j) IL-6, IL-10, TNF-α, and TGF-β protein levels within YTHDF2-silenced M1/M2 macrophages with or without PFT-α were evaluated through ELISA. Results are revealed by mean ± S.E.M. ($n = 3$). $^{*}P < 0.05$; $^{**}P < 0.01$.

been uncovered as a regulator in macrophage polarization. To determine whether p53 has a modulating effect on macrophage polarization role in regulating M1/M2 polarization in YTHDF2-knockdown macrophages, we tested the expression of p53 in M1/M2-polarized cells, and p53 inhibitor Pifithrin-α (PFT-α) was used to inhibit p53 expression. As revealed in Figures 3(a) to 3(d), p53 mRNA and protein were increased in M2 macrophages, but remain unchanged in M1 polarization after YTHDF2 knockdown. After verifying the inhibitory effect of PFT-α on p53 (Figures 3(e) and 3(f)), we found that PFT-α promoted TNF-α and IL-6 mRNA levels within YTHDF2-silenced M1 macrophages, suggesting that PFT-α has little effect on YTHDF2-silenced M1 cells (Figure 3(g)). Meanwhile, PFT-α upregulated TGF-β and IL-10 within YTHDF2-knockdown M2 cells, indicating that PFT-α reversed the inhibitory effect of YTHDF2 knockdown in M2 cells (Figure 3(h)). The ELISA results were consistent with those of the qRT-PCR (Figures 3(i) and 3(j)), suggesting that the inhibition of p53 only encouraged the polarization of M2 cells after YTHDF2 knockdown. Our results suggest that YTHDF2 knockdown might impede M2 polarization by upregulating the expression of p53.

3.4. YTHDF2 Knockdown Increases p53 mRNA Stability but Does Not Significantly Affect Pro-Inflammatory Cytokines mRNA Stability. For exploring the role of YTHDF2 in regulating macrophage polarization through modulating the mRNA degradation of p53 or pro-inflammatory factors, *IL-6*, *IL-10*, *TNF-α*, *p53*, and *TGF-β* mRNA stability were measured with actinomycin D. As indicated in Figure 4, YTHDF2 knockdown promoted the stability of p53 mRNA transcript in M2 macrophages, but no significant difference was detected among the mRNA stability of the cytokines. These results indicate that YTHDF2 has no notable influence on IL-6, p53, and TNF-α mRNA stability of M1 cells or TGF-β and IL-10 of M2 macrophages; YTHDF2 silencing upregulated the expression of p53 through stabilizing its mRNA, thereby inhibiting the polarization of M2 macrophages.

3.5. YTHDF2 Knockdown Activates the Activity of MAPK and NF-κB Pathways in M1 Macrophages. MAPK and NF-κB pathways have been known to be key pathways for inflammation and macrophage polarization. To discover whether YTHDF2 depletion affects these pathways within M1 macrophages, we performed WB assay for measuring p38, p65, JNK, ERK, IKKα/β, and IκBα phosphorylation levels. As shown in our results, YTHDF2 silencing evidently induced p-p38, p-JNK, p-IKKα/β, p-p65, and p-IκBα expression but reduced JNK phosphorylation level (Figures 5(a)-5(d)). Therefore, YTHDF2 knockdown activates NF-κB pathway, as well as JNK and p38 within MAPK pathway.

For further validating how both signaling pathways affected M1 macrophage polarization in YTHDF2-silenced cells, the inhibitors NF-κB (BAY 11-7082), p38 (SB203580) and JNK (SP600125) were applied sepaparately to impede the signaling. *IL-6* and *TNF-α* mRNA expression were then evaluated. According to the results, the inhibitors of NF-

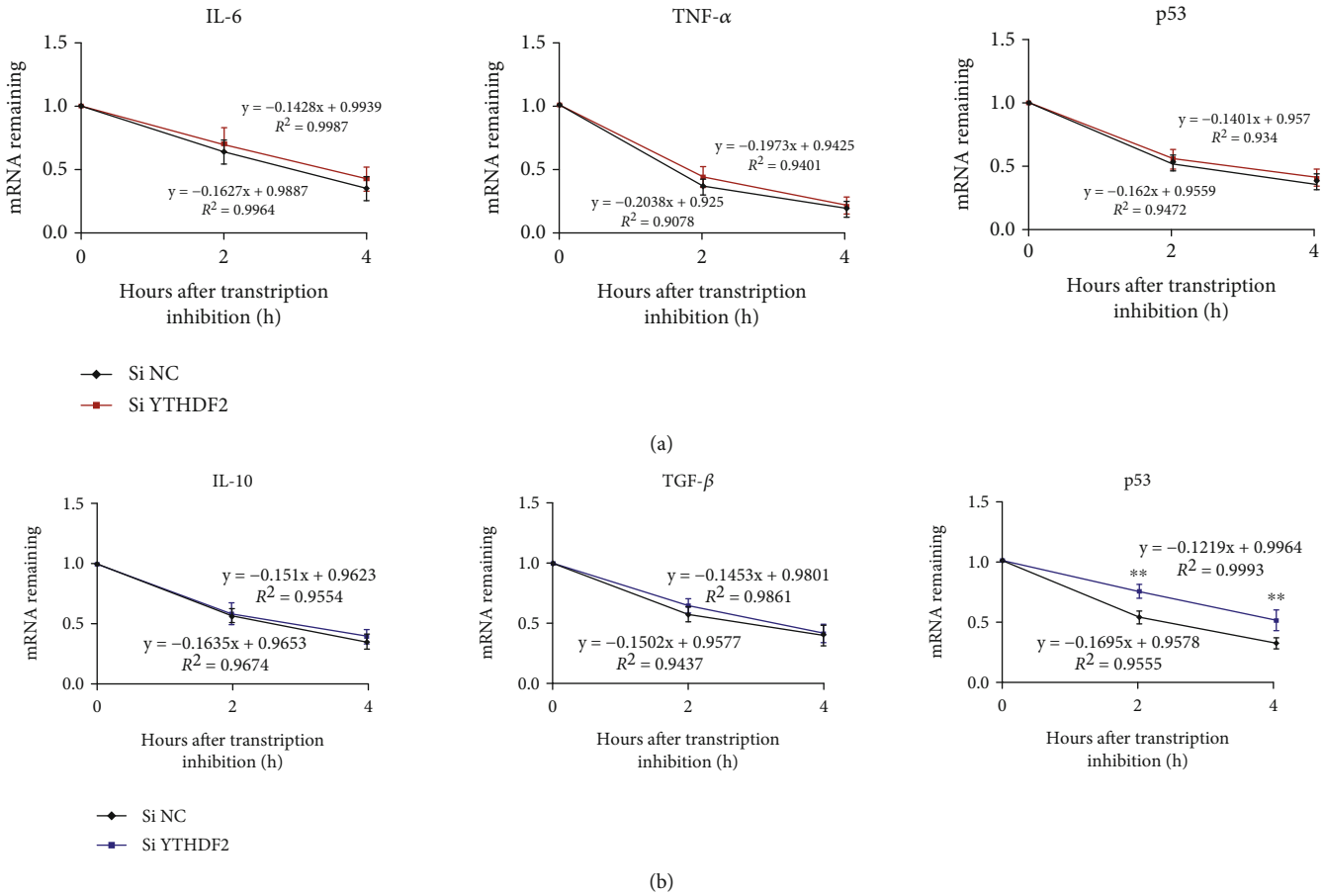

Figure 4: Role of YTHDF2 silencing in inflammatory cytokines and p53 mRNA stability in M1/M2 macrophages. M0 macrophages were subject to 24-h transfection using YTHDF2 siRNA (si YTHDF2) or si-NC before M1 (a) or M2 (b) stimulation. Actinomycin D (5 μg/mL) was then applied for inhibiting mRNA transcription for a 0-, 2-, and 4-h period. mRNA levels of *IL-6*, *IL-10*, *TNF-α*, *TGF-β*, and *P53* were determined through qRT-PCR, with *GAPDH* being the endogenous reference. Results are indicated by mean ± S.E.M. ($n = 3$). $^{*}P < 0.05$; $^{**}P < 0.01$. The red and blue lines stand for M1 and M2-stimulated cells, respectively.

κB, p38, and JNK reversed the increased *TNF-α* and *IL-6* mRNA levels within YTHDF2-silenced M1 cells (Figures 5(e) and 5(f)). Taken together, these results suggest that YTHDF2 suppression enhanced M1polarization by triggering the NF-κB, p38, and JNK signalings.

4. Discussion

N6 position of adenosine (m^6A) shows the highest prevalence among internal epigenetic modifications in mRNA [28]. Methyltransferase serves as a "writer" of m^6A modification, demethylases work as the "eraser," and m^6A-selective-binding proteins act as the "reader" by selective recognizing methylated RNA to perform regulations [13, 14]. YTHDF2 is a well-known "reader" protein that targets and facilitates the degradation of m^6A-containing RNAs [29]. Recent discoveries on YTHDF2 highlighted that YTHDF2 has a critical effect on regulating neural development, hematopoietic stem cell proliferation, cancer development, viral infection, and other physiological and pathological processes [23, 29–31].

Macrophages are heterogeneous cells endowed with great plasticity [32]. Upon exposure to different stimuli, recruited macrophages can be polarized into M1 or M2 phenotypes [3, 4, 33]. While M1 macrophages mediate innate immune responses against pathogens and activate adaptive responses through antigen processing and presentation, M2 macrophages are important in eliminating inflammation, tissue repairing, and maintaining homeostasis [34, 35]. Recently, studies in inflammatory and autoimmune diseases implicated that m^6A modifications have regulatory roles in the activation of macrophages [36, 37]. m^6A methyltransferase promotes M1 polarization through methylating the mRNA of *STAT1* [36]. Knockdown of demethylase FTO inhibits M1 polarization and restrains M2 activation at the same time [37]. However, the effect of m^6A reader on macrophage activation still lingers to be elucidated.

To investigate the role of m^6A reader YTHDF2 during macrophage polarization, BMDMs was used to establish the M1/M2 polarization system and investigated the expression of YTHDF2 after macrophage polarized. In our study, IL-4 increased the mRNA expressions of IL-10, TGF-β, Arg1, and Fizz in M2 cells, suggesting that M2 polarization model was established successfully. However, the changing expression levels of each inflammatory factor were not consistent at different time points. Secreted cytokines can bind to different receptors to induce activation of an intracellular

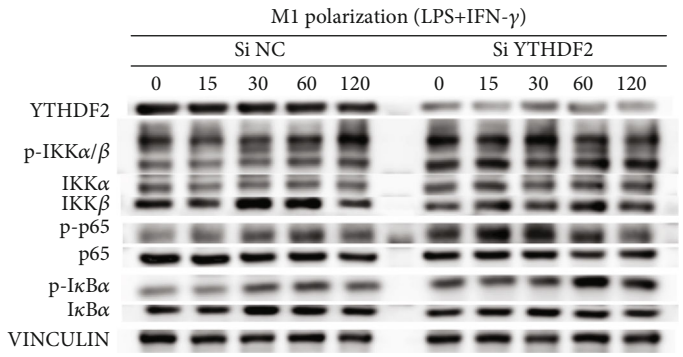

(a)

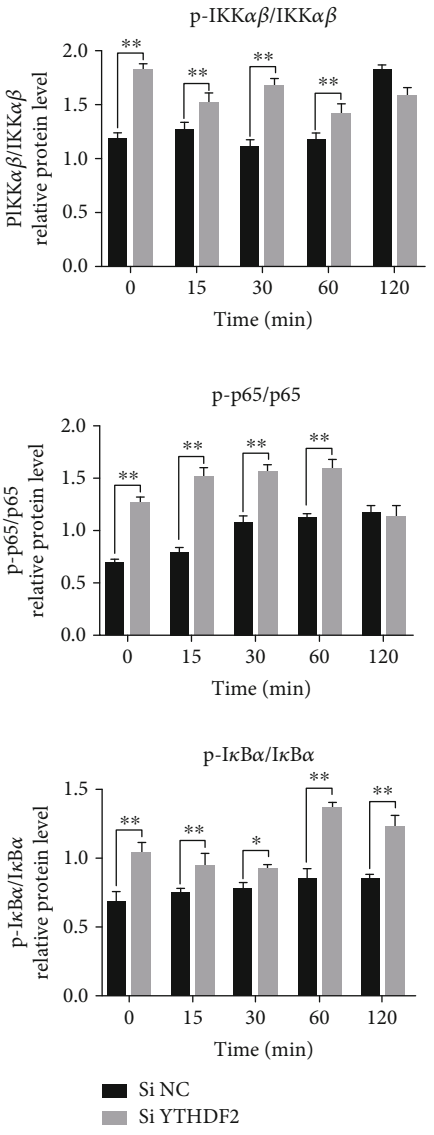

(b)

Figure 5: Continued.

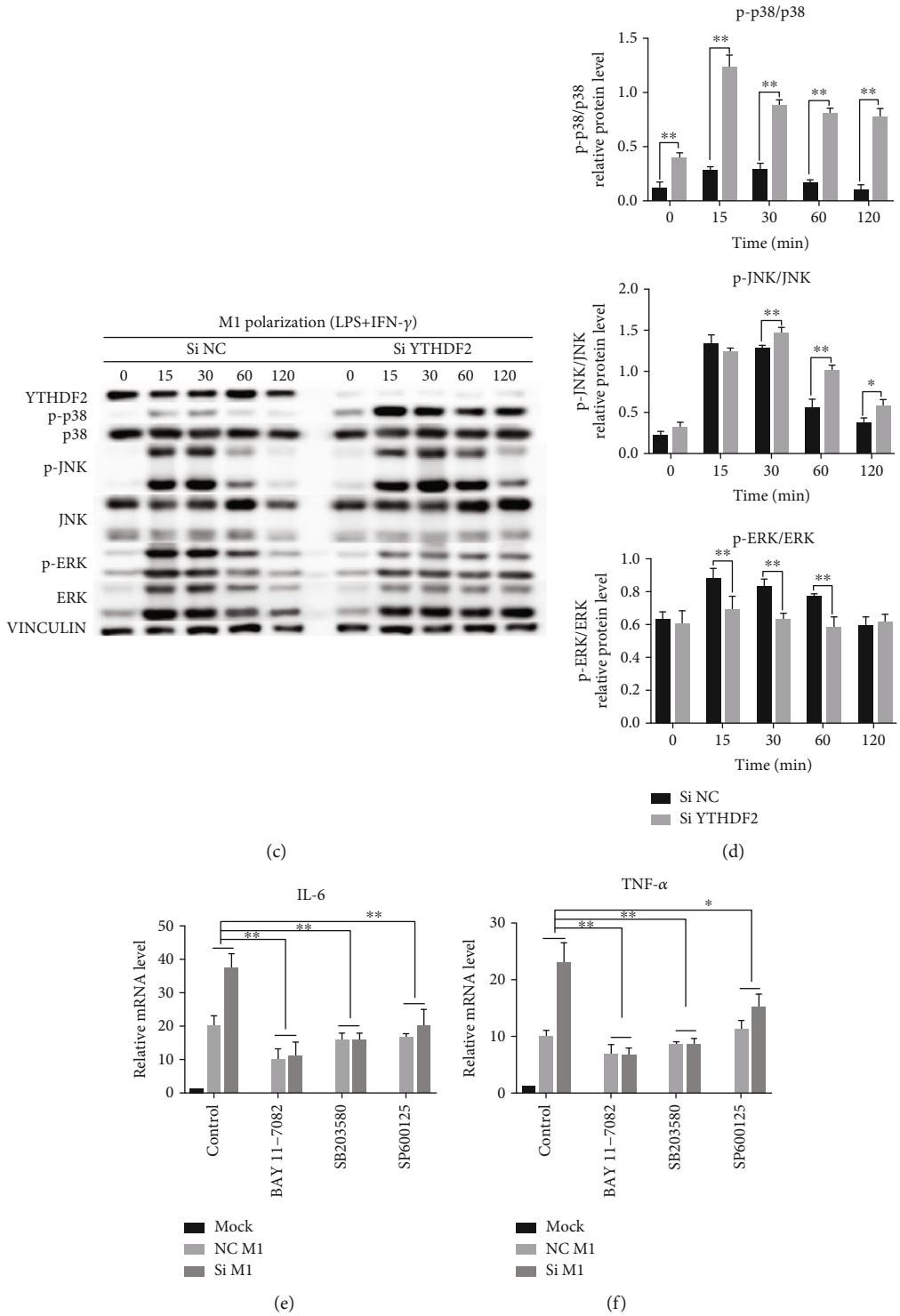

Figure 5: Role of YTHDF2 silencing in activation of NF-κB and MAPK signalings within M1 macrophages. M0 macrophages were subject to transfection using YTHDF2 siRNAs or NC-siRNA for 24 h before 0-, 15-, 30-, 60-, and 120-min LPS+ INF-γ treatment. (a) p65, IκBα, and IKKα/β phosphorylation expression within NF-κB pathway were analyzed through WB, with VINCULIN being the endogenous reference. (b) Quantification of p65, IκBα, and IKKα/β phosphorylation levels in comparison with control. (c) p38, ERK, and JNK phosphorylation levels within MAPK pathway were analyzed through western blotting. (d) Quantification of p38, JNK, and ERK phosphorylation levels in comparison with control. (e, f) M0 macrophages subject to transfection using YTHDF2 siRNA or NC-siRNA were further exposed to BAY 11-7082, SB203580, or SP600125 (inhibitors for NF-κB, p38, and JNK pathways, separately) for a 2-h period, while non-treated cells served as blank control. Thereafter, LPS/IFN-γ was added to stimulate cells for a 6-h period. *IL-6* and *TNF-α* mRNA expression were determined through qRT-PCR, with GAPDH being an endogenous reference. Data are denoted by mean ± S.E.M. ($n = 3$). $^{*}P < 0.05$; $^{**}P < 0.01$.

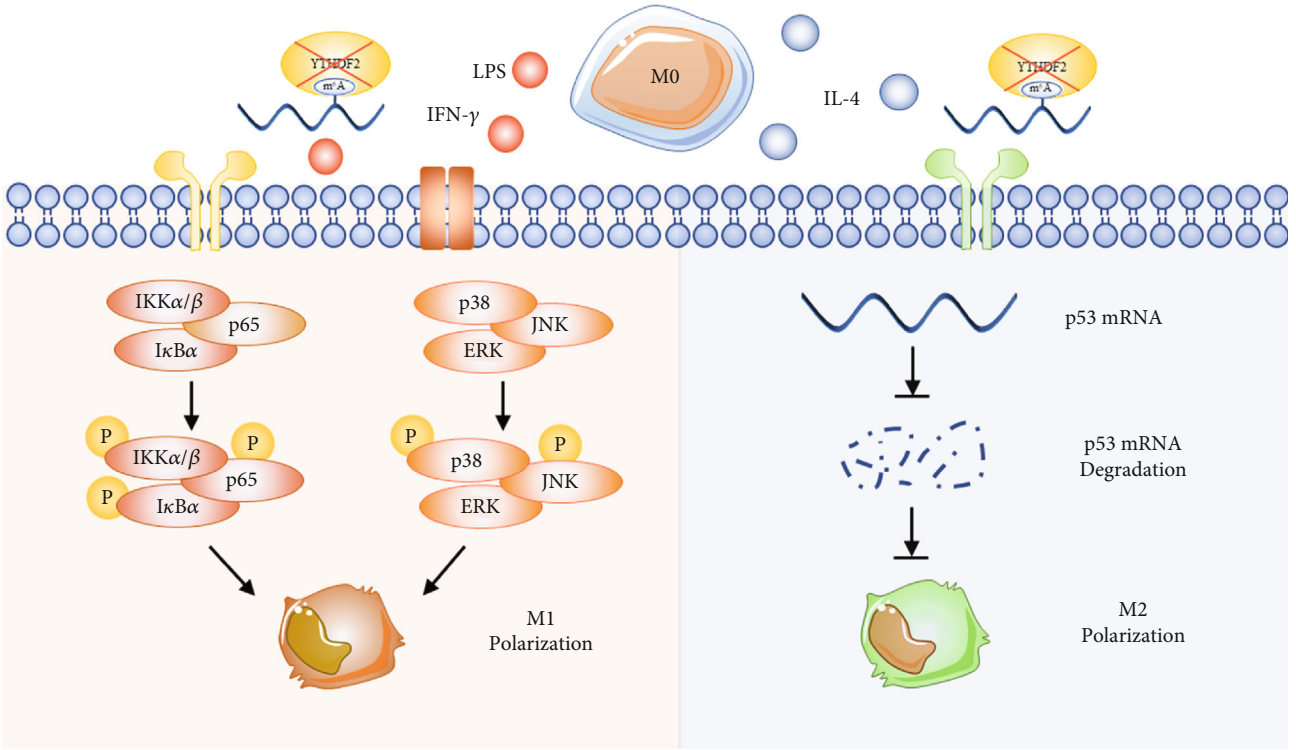

Figure 6: Role of m6A "reader" YTHDF2 in polarization of M1/M2 macrophages. YTHDF2 suppression promotes polarization of M1 cells via MAPK and NF-κB pathway activation. Moreover, depleting YTHDF2 stabilizes p53 mRNA and upregulates its expression, thereby inhibiting the polarization of M2 macrophages.

cascade of signal transduction, which leads to various cellular responses. However, not all cells within an organism are identical. They differ in the amount of proteins involved in signal transduction. These differences shape cellular communication and responses to intracellular signaling. So, there might be a negative regulation responsible for the expression level of TGF-β to begin to reduce after a sharp increase [38]. After confirming the activation of M1/M2 phenotypes, YTHDF2 mRNA and protein expression were determined. As presented in our result, YTHDF2 expression increased significantly within M1 and M2 polarized cells, indicating that YTHDF2 might be involved in regulating macrophage polarization.

YTHDF2 can selectively recognize m^6A to regulate mRNA degradation [15, 19]. Studies have shown that YTHDF2 enhances the capacity of self-renewal of the leukemia stem cells and neural stem/progenitor cells by suppressing the stability of multiple mRNAs critical for cell expansion [39]. YTHDF2 depletion in zebrafish embryos slows down the decline of maternal mRNAs that been m^6A-modified and impedes the cell cycle, thereby restraining the growth development during vertebrate embryogenesis [29]. In the study of infectious diseases, YTHDF2 upregulation promotes HIV-1 and HBV levels as well as viral replication ability [40, 41]. Most recently, a study by our team found that YTHDF2 negatively regulates the mRNA expression levels of MAP2K4 and MAP4K4 via destabilizing their mRNA transcripts, which inhibits the inflammatory response in LPS-stimulated inflammatory reactions [24]. For exploring YTHDF2's effect on macrophage polarization, YTHDF2 expression was silenced in BMDMs, and M1 and M2 markers levels were examined. IL-1β, IL-6, iNOS, TNF-α, CD86, as well as CD16/32 levels were upregulated within YTHDF2-silenced M1 cells. Meanwhile, in YTHDF2-silenced M2 cells, the secretion of M2 markers IL-10, TNF-α, ARG-1, FIZZ, CD206, and DECTIN-1 experienced a significant reduction. Therefore, these findings demonstrated that the expression of YTHDF2 is increased in both M1/M2 cells and that YTHDF2 might have different roles during the orientation of macrophages, with YTHDF2 inhibiting M1 but promoting the M2 phenotype.

Our preliminary RNA sequence results found that genes differentially expressed in YTHDF2-silenced macrophages were mainly enriched in the p53 signaling pathway. The gene p53 is the most common tumor suppressor gene in human cancer [42, 43]. It functions as a crucial regulatory node through monitoring the expression of genes associated with metabolism, cell cycle arrest, and apoptosis [44–46]. Studies in cancer have found that inflammation is a vital aspect when it comes to determining its predisposition [47, 48] and p53 has recently been discovered working as a regulator in various inflammatory diseases [25, 26, 27, 49]. As a guardian of homeostasis, p53 plays a protective role by inhibiting the local inflammation of rheumatoid arthritis patients and collagen-induced osteoarthritis in mice [49].

p53 also controls immunity by directly impeding the activation of p65 promoter in the NF-κB signaling and negatively regulating its transcriptional expression of its downstream genes IL-6, Cox-2, and Nos2 [25]. Recent studies found that p53 can regulate macrophage polarization [26, 27, 50–52]. Macrophages lacking p53 promoted the responses to LPS stimulation, producing more pro-inflammatory M1 marker genes, like IL-6, TNF-α, and MIP-2 [26]. When marrow-derived macrophages activated towards to M2 phonotype, cells display endogenous p53 activity and the p53 activation can in turn inhibit expression of M2 genes [27]. The p53 activator Nutlin-3a in bone marrow-derived macrophages can reduce the expression of M2 subtype [51]. To investigate whether p53 involved in the activation of YTHDF2-deficent macrophages, we examined the expression of p53 in macrophages after YTHDF2 knockdown. As shown in the result, YTHDF2 silencing did not significantly affect p53 level within M1 cells; however, p53 increased within YTHDF2-silenced M2 cells. To further determine the role of p53, the p53 inhibitor Pifithrin-α (PFT-α) was used to suppress the p53 expression in YTHDF2-knockdown cells. According to the above findings, PFT-α pretreatment further increased TNF-α and IL-6 levels within YTHDF2-knockdown M1 cells, but the reduction of TGF-β and IL-10 within YTHDF2-knockdown M2 subtype was reversed. Collectively, YTHDF2 promoted M2 polarization by regulating p53, but did not repress the M1 polarization directly through p53.

Accumulating evidences suggest that m^{6}A may regulate the stability of the RNA through the effects of YTHDF2 [29]. The C-terminal YTH domain (YTHDF2-C) of YTHDF2 can selectively bind m^{6}A, whereas P/Q/N enriched N-terminal region promote target mRNA migration into cytoplasmic foci (P bodies) while recruiting RNA import of CCR4-NOT deadenylase complex [53]. To investigate the role of YTHDF2 in destabilizing the gene transcripts of related cytokines in macrophage polarization, we measured the stability of *IL-6*, *IL-10*, *TNF-α*, *p53*, and *TGF-β* mRNAs in YTHDF2-depletion cells. According to our results, YTHDF2 silencing promoted p53 mRNA stability in M2 macrophages but had little effect on p53 stability in M1 macrophages. We further analyzed and predicted p53 mRNA on the m^{6}A database SRAMP and found that p53 mRNA may have 11 m^{6}A modification sites, while among other polarization-related factors, only IL-6 and ARG1 have a few m^{6}A modification sites, which contains 3 and 1, respectively. This might explain why loss of YTHDF2 exhibited no detectable effect on the mRNA stability of TNF-α and IL-6 in M1 cells or TGF-β and IL-10 in M2 cells. Therefore, we concluded that YTHDF2 may encourage M2 polarization by promoting the degradation of p53 mRNA, but inhibit M1 polarization leaving the mRNA stability of inflammatory factors unaffected.

MAPK and NF-κB pathways have been identified as key pathways for inflammation and M1 macrophage polarization [54–56]. Recent studies discovered that YTHDF2 upregulation can inhibit ERK and MEK activation within liver cancer cells [23]. For verifying whether YTHDF2 regulates M1 polarization by deactivating MAPK and NF-κB pathways, we detected some critical molecules related to the above pathways for their phosphorylation levels after silencing YTHDF2. In our results, IKKα/β, p65, IκBα, p38, and JNK phosphorylation levels significantly elevated after YTHDF2 silencing, but ERK phosphorylation level was suppressed. Studies have found that ERK1/2 mainly function during cell growth, proliferation, and differentiation, while p38 and JNK play essential roles in inflammation, cytokine production, and apoptosis. Besides, the activation of ERK can be suppressed by JNK and p38 kinase. These might explain the inactivation of ERK in YTHDF2-knockdown M1 macrophages. Furthermore, we inhibited the above pathways to validate their effects on regulating M1 markers' expression. Our results stated that inhibitors of NF-κB, p38, and JNK pathways downregulated IL-6 and TNF-α levels in YTHDF2-depleted M1 cells, confirming that YTHDF2 impeded macrophage M1 polarization by inhibiting NF-κB, p38, and JNK signaling pathways.

To sum up, the m^{6}A reader YTHDF2 increased its expression within M1 and M2 polarized cells. YTHDF2 silencing encouraged M1 but diminished M2 macrophage polarization. Mechanistically, silencing YTHDF2 promoted the stability of *p53* mRNA and its expression level, thereby impeding M2 macrophage polarization; YTHDF2 depletion facilitated M1 polarization by triggering both MAPK and NF-κB pathways (Figure 6). In this study, YTHDF2 was identified with its regulatory role during M1/M2 polarization. Our present research on m^{6}A reader YTHDF2 may offer an alternative approach for the understanding of macrophage plasticity and probably a newfound target for treating inflammatory diseases.

Data Availability

All data utilized in the present work can be obtained from corresponding author upon reasonable request.

Conflicts of Interest

All authors declared no competing interest.

Authors' Contributions

Luhui Cai and Di Li contributed equally to this work. All authors have contributed significantly and agree with the version for submission.

Acknowledgments

The present work was funded by the National Natural Science Foundation of China (82100994) and Guangdong Basic and Applied Basic Research Foundation (2019A1515110141).

References

[1] T. Lawrence and G. Natoli, "Transcriptional regulation of macrophage polarization: enabling diversity with identity," *Nature Reviews. Immunology*, vol. 11, no. 11, pp. 750–761, 2011.

[2] S. Gordon and F. O. Martinez, "Alternative activation of macrophages: mechanism and functions," *Immunity*, vol. 32, no. 5, pp. 593–604, 2010.

[3] O. Takeuchi and S. Akira, "Pattern recognition receptors and inflammation," *Cell*, vol. 140, no. 6, pp. 805–820, 2010.

[4] F. O. Martinez and S. Gordon, "The M1 and M2 paradigm of macrophage activation: time for reassessment," *F1000Prime Reports*, vol. 6, 2014.

[5] K. A. Jablonski, S. A. Amici, L. M. Webb et al., "Novel markers to delineate murine M1 and M2 macrophages," *PLoS One*, vol. 10, no. 12, article e0145342, 2015.

[6] A. C. Trombetta, S. Soldano, P. Contini et al., "A circulating cell population showing both M1 and M2 monocyte/macrophage surface markers characterizes systemic sclerosis patients with lung involvement," *Respiratory Research*, vol. 19, no. 1, p. 186, 2018.

[7] R. Deshpande, H. Khalili, R. G. Pergolizzi, S. D. Michael, and M. D. Y. Chang, "Estradiol down-regulates LPS-induced cytokine production and NF-κB activation in murine macrophages," *American Journal of Reproductive Immunology*, vol. 38, no. 1, pp. 46–54, 1997.

[8] S. U. Islam, J. H. Lee, A. Shehzad, E. M. Ahn, Y. Lee, and Y. Lee, "Decursinol angelate inhibits LPS-induced macrophage polarization through modulation of the NFκB and MAPK signaling pathways," *Molecules*, vol. 23, no. 8, p. 1880, 2018.

[9] X. Huang, Y. Li, M. Fu, and H. B. Xin, "Polarizing macrophages in vitro," *Methods in Molecular Biology*, vol. 1784, pp. 119–126, 2018.

[10] A. Shapouri-Moghaddam, S. Mohammadian, H. Vazini et al., "Macrophage plasticity, polarization, and function in health and disease," *Journal of Cellular Physiology*, vol. 233, no. 9, pp. 6425–6440, 2018.

[11] P. Italiani and D. Boraschi, "From monocytes to M1/M2 macrophages: phenotypical vs. Functional Differentiation," *Frontiers in Immunology*, vol. 5, 2014.

[12] S. Geula, S. Moshitch-Moshkovitz, D. Dominissini et al., "Stem cells. m6A mRNA methylation facilitates resolution of naïve pluripotency toward differentiation," *Science*, vol. 347, no. 6225, pp. 1002–1006, 2015.

[13] Y. Yue, J. Liu, and C. He, "RNA N6-methyladenosine methylation in post-transcriptional gene expression regulation," *Genes & Development*, vol. 29, no. 13, pp. 1343–1355, 2015.

[14] Q. Cui, H. Shi, P. Ye et al., "mA RNA methylation regulates the self-renewal and tumorigenesis of glioblastoma stem cells," *Cell Reports*, vol. 18, no. 11, pp. 2622–2634, 2017.

[15] X. Wang, Z. Lu, A. Gomez et al., "N6-methyladenosine-dependent regulation of messenger RNA stability," *Nature*, vol. 505, no. 7481, pp. 117–120, 2014.

[16] L. Wen, W. Sun, D. Xia, Y. Wang, J. Li, and S. Yang, "The m6A methyltransferase METTL3 promotes LPS-induced microglia inflammation through TRAF6/NF-κB pathway," *NeuroReport*, vol. 33, no. 6, pp. 243–251, 2022.

[17] J. T. Yu, X. W. Hu, H. Y. Chen et al., "DNA methylation of FTO promotes renal inflammation by enhancing m(6)A of PPAR-alpha in alcohol-induced kidney injury," *Pharmacological Research*, vol. 163, article 105286, 2021.

[18] D. Jian, Y. Wang, L. Jian et al., "METTL14 aggravates endothelial inflammation and atherosclerosis by increasing FOXO1 N6-methyladeosine modifications," *Theranostics*, vol. 10, no. 20, pp. 8939–8956, 2020.

[19] X. Wang, B. S. Zhao, I. A. Roundtree et al., "N(6)-methyladenosine modulates messenger RNA translation efficiency," *Cell*, vol. 161, no. 6, pp. 1388–1399, 2015.

[20] M. Li, X. Zhao, W. Wang et al., "Ythdf2-mediated m6A mRNA clearance modulates neural development in mice," *Genome Biology*, vol. 19, no. 1, p. 69, 2018.

[21] C. Zhang, Y. Chen, B. Sun et al., "mA modulates haematopoietic stem and progenitor cell specification," *Nature*, vol. 549, no. 7671, pp. 273–276, 2017.

[22] M. Chen, L. Wei, C. T. Law et al., "RNA N6-methyladenosine methyltransferase-like 3 promotes liver cancer progression through YTHDF2-dependent posttranscriptional silencing of SOCS2," *Hepatology*, vol. 67, no. 6, pp. 2254–2270, 2018.

[23] L. Zhong, D. Liao, M. Zhang et al., "YTHDF2 suppresses cell proliferation and growth via destabilizing the EGFR mRNA in hepatocellular carcinoma," *Cancer Letters*, vol. 442, pp. 252–261, 2019.

[24] R. Yu, Q. Li, Z. Feng, L. Cai, and Q. Xu, "m6A reader YTHDF2 regulates LPS-induced inflammatory response," *International Journal of Molecular Sciences*, vol. 20, no. 6, p. 1323, 2019.

[25] T. Cooks, C. C. Harris, and M. Oren, "Caught in the cross fire: p53 in inflammation," *Carcinogenesis*, vol. 35, no. 8, pp. 1680–1690, 2014.

[26] G. Liu, Y. J. Park, Y. Tsuruta, E. Lorne, and E. Abraham, "p53 attenuates lipopolysaccharide-induced NF-kappaB activation and acute lung injury," *Journal of Immunology*, vol. 182, no. 8, pp. 5063–5071, 2009.

[27] L. Li, D. S. Ng, W. C. Mah et al., "A unique role for p53 in the regulation of M2 macrophage polarization," *Cell Death and Differentiation*, vol. 22, no. 7, pp. 1081–1093, 2015.

[28] D. Dominissini, S. Moshitch-Moshkovitz, S. Schwartz et al., "Topology of the human and mouse m^6A RNA methylomes revealed by m^6A-seq," *Nature*, vol. 485, no. 7397, pp. 201–206, 2012.

[29] B. S. Zhao, X. Wang, A. V. Beadell et al., "m^6A-dependent maternal mRNA clearance facilitates zebrafish maternal-to-zygotic transition," *Nature*, vol. 542, no. 7642, pp. 475–478, 2017.

[30] Z. Li, P. Qian, W. Shao et al., "Suppression of mA reader Ythdf2 promotes hematopoietic stem cell expansion," *Cell Research*, vol. 28, no. 9, pp. 904–917, 2018.

[31] K. Tsai, D. G. Courtney, and B. R. Cullen, "Addition of m6A to SV40 late mRNAs enhances viral structural gene expression and replication," *PLoS Pathogens*, vol. 14, no. 2, article e1006919, 2018.

[32] S. K. Biswas and A. Mantovani, "Macrophage plasticity and interaction with lymphocyte subsets: cancer as a paradigm," *Nature Immunology*, vol. 11, no. 10, pp. 889–896, 2010.

[33] M. Stein, S. Keshav, N. Harris, and S. Gordon, "Interleukin 4 potently enhances murine macrophage mannose receptor activity: a marker of alternative immunologic macrophage activation," *American Journal of Reproductive Immunology*, vol. 176, pp. 287–292, 1997.

[34] L. Zhu, Q. Zhao, T. Yang, W. Ding, and Y. Zhao, "Cellular metabolism and macrophage functional polarization," *International Reviews of Immunology*, vol. 34, no. 1, pp. 82–100, 2015.

[35] L. Bosurgi, Y. G. Cao, M. Cabeza-Cabrerizo et al., "Macrophage function in tissue repair and remodeling requires IL-4 or IL-13 with apoptotic cells," *Science*, vol. 356, no. 6342, pp. 1072–1076, 2017.

[36] Y. Liu, Z. Liu, H. Tang et al., "The N(6)-methyladenosine m6A-forming enzyme METTL3 facilitates M1 macrophage polarization through the methylation ofSTAT1mRNA," *American Journal of Physiology. Cell Physiology*, vol. 317, no. 4, pp. C762–C775, 2019.

[37] X. Gu, Y. Zhang, D. Li, H. Cai, L. Cai, and Q. Xu, "N6-methyladenosine demethylase FTO promotes M1 and M2 macrophage activation," *Cellular Signalling*, vol. 69, article 109553, 2020.

[38] J. Fiebelkow, A. Guendel, B. Guendel et al., "The tyrosine phosphatase SHP2 increases robustness and information transfer within IL-6-induced JAK/STAT signalling," *Cell Communication and Signaling: CCS*, vol. 19, no. 1, p. 94, 2021.

[39] J. Paris, M. Morgan, J. Campos et al., "Targeting the RNA m(6)A reader YTHDF2 selectively compromises cancer stem cells in acute myeloid leukemia," *Cell Stem Cell*, vol. 25, no. 1, pp. 137–148.e6, 2019.

[40] W. Lu, N. Tirumuru, C. St Gelais et al., "N6-Methyladenosine-binding proteins suppress HIV-1 infectivity and viral production," *The Journal of Biological Chemistry*, vol. 293, no. 34, pp. 12992–13005, 2018.

[41] H. Imam, G. W. Kim, S. A. Mir, M. Khan, and A. Siddiqui, "Interferon-stimulated gene 20 (ISG20) selectively degrades N6-methyladenosine modified hepatitis B virus transcripts," *PLoS Pathogens*, vol. 16, no. 2, article e1008338, 2020.

[42] L. Bouaoun, D. Sonkin, M. Ardin et al., "TP53 variations in human cancers: new lessons from the IARC TP53 database and genomics data," *Human Mutation*, vol. 37, no. 9, pp. 865–876, 2016.

[43] K. T. Bieging, S. S. Mello, and L. D. Attardi, "Unravelling mechanisms of p53-mediated tumour suppression," *Nature Reviews. Cancer*, vol. 14, no. 5, pp. 359–370, 2014.

[44] F. Kruiswijk, C. F. Labuschagne, and K. H. Vousden, "p53 in survival, death and metabolic health: a lifeguard with a licence to kill," *Nature Reviews. Molecular Cell Biology*, vol. 16, no. 7, pp. 393–405, 2015.

[45] L. Jiang, N. Kon, T. Li et al., "Ferroptosis as a p53-mediated activity during tumour suppression," *Nature*, vol. 520, no. 7545, pp. 57–62, 2015.

[46] M. P. Baar, R. M. C. Brandt, D. A. Putavet et al., "Targeted apoptosis of senescent cells restores tissue homeostasis in response to chemotoxicity and aging," *Cell*, vol. 169, no. 1, pp. 132–147.e16, 2017.

[47] C. Guerra, M. Collado, C. Navas et al., "Pancreatitis-induced inflammation contributes to pancreatic cancer by inhibiting oncogene-induced senescence," *Cancer Cell*, vol. 19, no. 6, pp. 728–739, 2011.

[48] T. Cooks, I. S. Pateras, O. Tarcic et al., "Mutant p53 prolongs NF-κB activation and promotes chronic inflammation and inflammation-associated colorectal cancer," *Cancer Cell*, vol. 23, no. 5, pp. 634–646, 2013.

[49] Y. Yamanishi, D. L. Boyle, M. J. Pinkoski et al., "Regulation of joint destruction and inflammation by p53 in collagen-induced arthritis," *The American Journal of Pathology*, vol. 160, no. 1, pp. 123–130, 2002.

[50] S. Mukhopadhyay, T. M. Antalis, K. P. Nguyen, M. H. Hoofnagle, and R. Sarkar, "Myeloid p53 regulates macrophage polarization and venous thrombus resolution by inflammatory vascular remodeling in mice," *Blood*, vol. 129, no. 24, pp. 3245–3255, 2017.

[51] X. Y. He, C. Xiang, C. X. Zhang et al., "p53 in the myeloid lineage modulates an inflammatory microenvironment limiting initiation and invasion of intestinal tumors," *Cell Reports*, vol. 13, no. 5, pp. 888–897, 2015.

[52] A. Lujambio, L. Akkari, J. Simon et al., "Non-cell-autonomous tumor suppression by p53," *Cell*, vol. 153, no. 2, pp. 449–460, 2013.

[53] H. Du, Y. Zhao, J. He et al., "YTHDF2 destabilizes m(6)A-containing RNA through direct recruitment of the CCR4-NOT deadenylase complex," *Nature Communications*, vol. 7, no. 1, 2016.

[54] M. R. Gwinn and V. Vallyathan, "Respiratory burst: role in signal transduction in alveolar macrophages," *Journal of Toxicology and Environmental Health. Part B, Critical Reviews*, vol. 9, no. 1, pp. 27–39, 2006.

[55] C. P. Chang, Y. C. Su, P. H. Lee, and H. Y. Lei, "Targeting NFKB by autophagy to polarize hepatoma-associated macrophage differentiation," *Autophagy*, vol. 9, no. 4, pp. 619–621, 2013.

[56] J. G. Bode, C. Ehlting, and D. Häussinger, "The macrophage response towards LPS and its control through the p38(MAPK)-STAT3 axis," *Cellular Signalling*, vol. 24, no. 6, pp. 1185–1194, 2012.

Hindawi
Disease Markers
Volume 2022, Article ID 7243146, 11 pages
https://doi.org/10.1155/2022/7243146

Research Article

SN-38 Sensitizes BRCA-Proficient Ovarian Cancers to PARP Inhibitors through Inhibiting Homologous Recombination Repair

Shengbin Lin,[1] **Jiaxin Tian**,[1] **Qiang He**,[1] **Minyi Yang**,[1] **Zuyang Chen**,[1,2] **Alexey A. Belogurov Jr.**,[3] **Xiao Li**,[4] **Fan Zhang**,[5] **Yongzhu Liu**,[2] **and Guo Chen**[1,6]

[1]*Department of Medical Biochemistry and Molecular Biology, School of Medicine, Jinan University, Guangzhou 510632, China*
[2]*Department of Gynecology, The Sixth Affiliated Hospital of Guangzhou Medical University, Qingyuan People's Hospital, Guangdong 511500, China*
[3]*Shemyakin-Ovchinnikov Institute of Bioorganic Chemistry of the Russian Academy of Sciences, Miklukho-Maklaya 16/10, 117997 Moscow, Russia*
[4]*Tianjin Key Laboratory of Human Development and Reproductive Regulation, Tianjin Central Hospital of Gynecology Obstetrics, Tianjin 300100, China*
[5]*The 5th Affiliated Hospital, Guangzhou Medical University, Guangzhou 510700, China*
[6]*School of Biopharmacy, China Pharmaceutical University, Nanjing 211198, China*

Correspondence should be addressed to Xiao Li; apple_lixiao@sina.com, Fan Zhang; 2014687007@gzhmu.edu.cn, Yongzhu Liu; lyz_1995@yeah.net, and Guo Chen; gchen84@jnu.edu.cn

Received 10 August 2022; Accepted 16 September 2022; Published 11 October 2022

Academic Editor: Jingang Huang

As a multifunctional protein posttranslational modification enzyme in eukaryotic cells, Poly-ADP-ribose polymerase (PARP) acts as a DNA damage sensor, which helps to repair DNA damage through recruiting repair proteins to the DNA break sites. PARP inhibitors offer a significant clinical benefit for ovarian cancer with *BRCA1/2* mutations. However, the majority of ovarian cancer patients harbor wild-type (WT) *BRCA1/2* status, which narrows its clinical application. Here, we identified a small compound, SN-38, a CPT analog, which sensitizes *BRCA*-proficient ovarian cancer cells to PARP inhibitor treatment by inhibiting homologous recombination (HR) repair. SN-38 treatment greatly enhanced PARP inhibitor olaparib induced DNA double-strand breaks (DSBs) and DNA replication stress. Meanwhile, the combination of SN-38 and olaparib synergistically induced apoptosis in ovarian cancer. Furthermore, combination administration of SN-38 and olaparib induced synergistic antitumor efficacy in an ovarian cancer xenograft model *in vivo*. Therefore, our study provides a novel therapeutic strategy to optimize PARP inhibitor therapy for patients with *BRCA*-proficient ovarian cancer.

1. Introduction

As the genetic material for all the living cells, DNA is fragile and easily damaged by endogenous and exogenous sources including reactive oxygen species (ROS), environmental and dietary carcinogens, and radiation [1]. In response to various types of damage, cells activate complicated signal cascades, which help the cell to repair the damaged DNA before dividing [2]. Cell fate after DNA damage was determined by factors involved in DNA damage recognition, repair, and injury tolerance, as well as activation of apoptosis, necrosis, autophagy, and senescence [3]. And these pathways that determine cell fate are not independent of each other [4]. The signaling pathways that are associated with DNA damage and repair play key roles in the initiation and progression of cancer [5]. They are also important in determining the outcome of cancer treatment with genotoxic drugs. Developing drugs or therapies based on the molecular basis of these pathways is important to optimize cancer treatment [6]. Currently, a number of cancer therapeutics

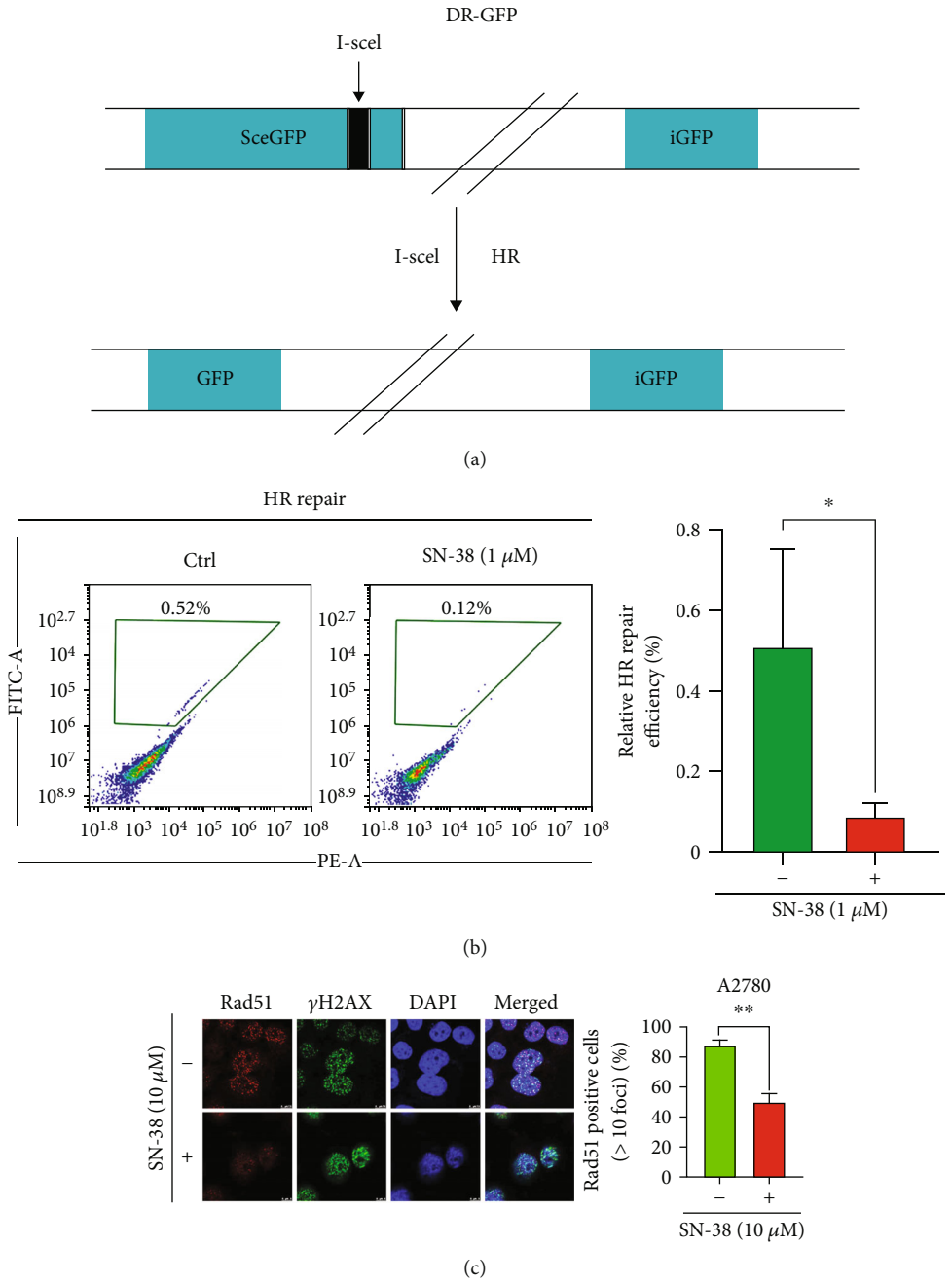

Figure 1: SN-38 inhibits homologous recombination repair in BRCA-proficient ovarian cancer cells. (a) Schematic diagram of HR reporter system. The expression of wild-type GFP can be rescued only by HR repair, resulting in GFP fluorescence. (b) HR repair activities were measured in cells treated with SN-38 (1 μM) or control (Ctrl). Data represent the mean ± SD, $n = 3$ per group. $^{*}P < 0.05$, by 2-tailed t -test. (c) Immunostaining analysis of IR-induced Rad51 in SN-38 (10 μM) treated or untreated A2780 cells. $^{**}P < 0.01$, by 2-tailed t-test.

are designed to induce unrepairable DNA damage in cancer cells, such as tumor radiotherapy and chemotherapy [7].

As a multifunctional protein posttranslational modifying enzyme, PARP catalyzes poly-ADP-ribosylation on various substrate proteins, and it is a key protein in base excision repair (BER) [8]. When DNA damage occurs, PARP1 and its homolog PARP2, which are the first responders of DNA damage, recognize the damage site firstly, and then, they recruit other repair proteins to complete the damage repair process [9]. PARP inhibitor binds to PARP1/2 and inhibits their enzymatic activity, resulting in the accumulation of unrepairable single-strand breaks (SSB) and finally transformed into the double-strand breaks (DSBs), which highly reply on homologous recombination- (HR-) mediated pathway to repair. Thus, cells with HR repair deficiency are particularly susceptible to PARP inhibition. Taking advantage of this principle, PARP inhibitor is developed, and it is the first anticancer drug successfully approved for clinical use by using the concept of synthetic lethality [10, 11]. Therefore, HR repair capacity is the primary factor that

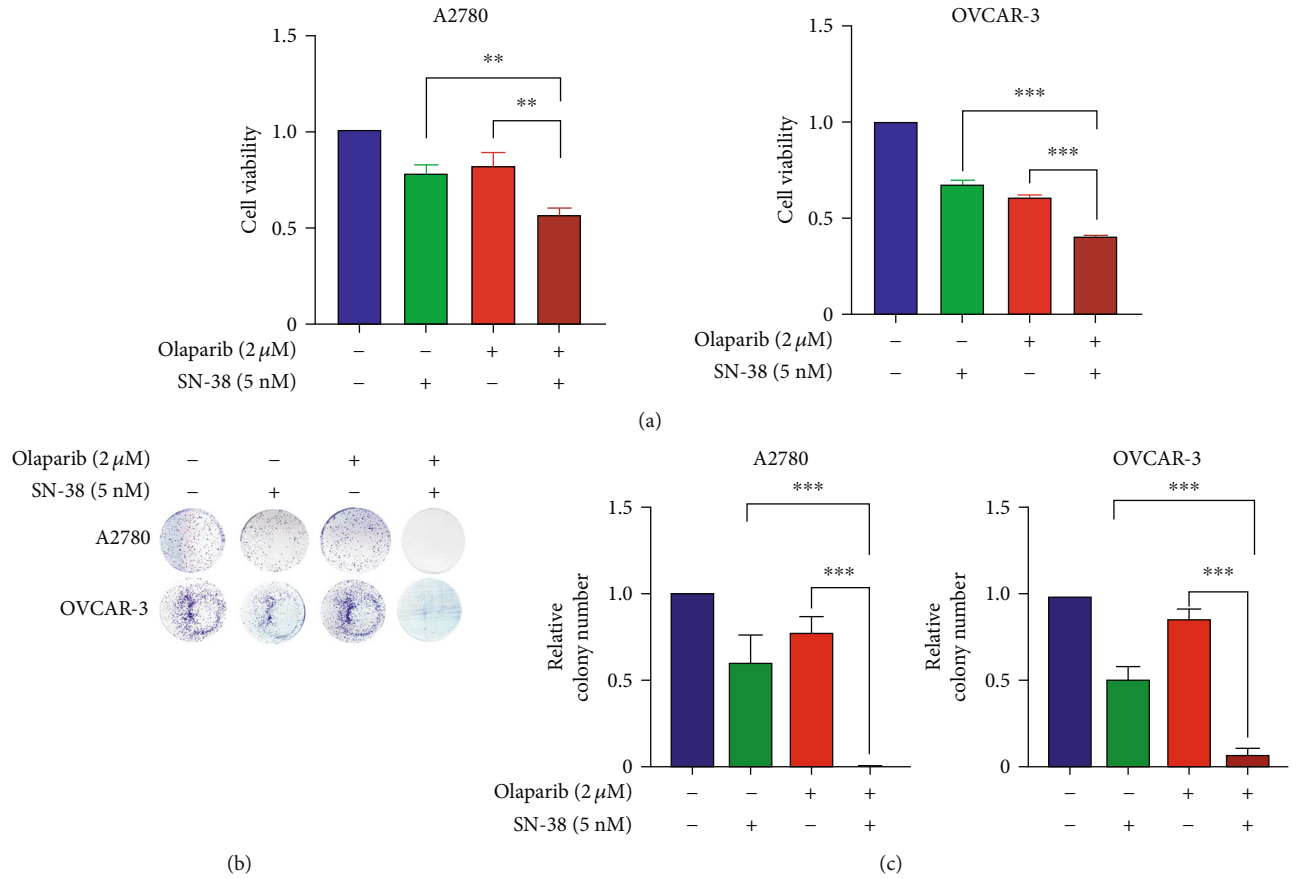

FIGURE 2: SN-38 sensitizes BRCA-proficient ovarian cancers to PARP inhibitors. (a) A2780 and OVCAR-3 cells were treated with 2 μM olaparib, 5 nM SN-38, or their combination for 72 hrs, and the cell viability was measured by CCK8. (b, c) Colony formation survival analysis of A2780 and OVCAR-3 cells were treated with the indicated concentration of olaparib and SN-38. Representative colony formations were shown (b) and the relative number of colonies was quantified and normalized to untreated parental cells (c). $^{**}P < 0.01$ and $^{***}P < 0.001$, by two-tailed t-test.

determines the PARP inhibitor efficacy; if the HR pathway is also dysfunctional at this time, it will produce a synthetic lethal effect, to have a stronger killing effect on tumor cells [12].

Synthetic lethality is a process in which defects in two different genes or pathways jointly lead to cell death. PARP inhibitor is the first FDA-approved anticancer drug, which utilizes this concept and specifically kills cancer cells with impaired HR repair capacity [13]. However, in *BRCA1/2*-proficient ovarian cancers, PARP inhibitors' therapeutic effects are relatively low [14]. How to improve the therapeutic effects of PARP inhibitor in *BRCA1/2*-proficient ovarian cancers is still an urgent problem needed to be solved at this stage [15]. In this study, we identified a compound SN-38, an analog of the natural compound camptothecin (CPT), potently inhibited HR repair activity and sensitize ovarian cancer cells to PARP inhibitor treatment *in vitro* and *in vivo*. SN-38 (7-ethyl-10-hydroxycamptothecin), a TOP1 inhibitor, is an active metabolite of irinotecan, which is widely used in ovarian cancer treatment [16–18]. Therefore, our study provided a novel strategy and potential drug candidate to optimize future PARP inhibitor therapy in ovarian cancer patients.

2. Materials and Methods

2.1. Cell Culture. Tow *BRCA1/2*-proficient ovarian cancer cell lines including A2780 and OVCAR3 were purchased from American Type Culture Collection (ATCC). Cells were grown in RPMI 1640 medium (ATCC modification) (Gibco, Thermo Fisher, USA) supplemented with 10% fetal bovine serum (FBS) (Hyclone, Thermo Fisher, USA) and 1% penicillin/streptomycin (Corning, USA). Each cell line was passage every 3 6 days. All cells were maintained at 37°C in a 5% CO_2 and 95% air atmosphere incubator.

2.2. Reagents. Anti-β-actin (sc-47778) antibody was purchased from Santa Cruz Biotechnology (Santa Cruz, CA). Anti-Ki67 (#9027) and anti-cleaved caspase 3 (#9579) antibodies were purchased from Cell Signaling Technology (Danvers, MA). Anti-γH2AX (05-636) antibody was purchased from Millipore (Billerica, MA). Anti-pRPA2 S33 (A300-246A) and anti-RPA2 (A300-244A) antibodies were purchased from Bethyl Laboratories (Montgomery, TX). Olaparib and SN-38 were obtained from Selleckchem (Houston, TX). Cells were transfected with indicated plasmids using Lipofectamine™ 3000 transfection reagent

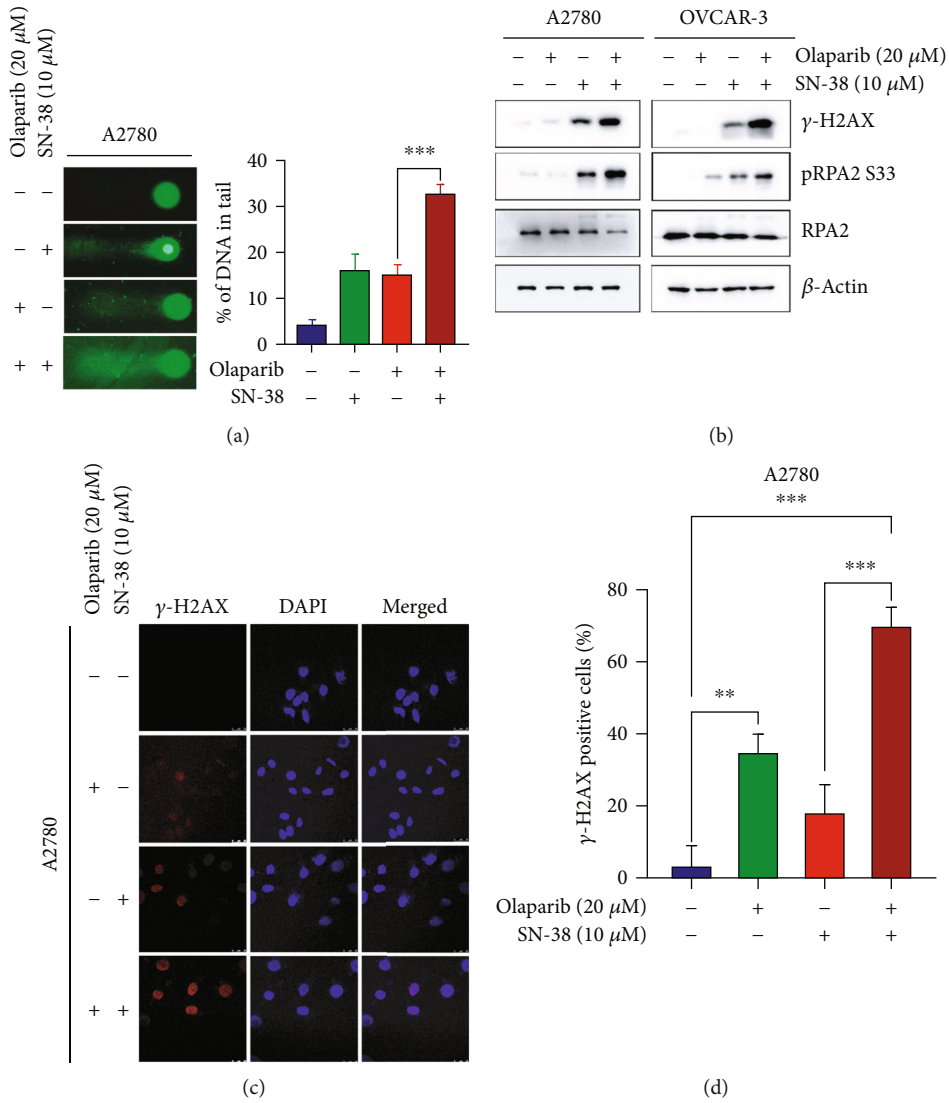

Figure 3: SN-38 and PARP inhibitor olaparib synergistically induces DNA damage and DNA replication stress. (a) A2780 cells were treated with the indicated concentration of olaparib and SN-38 for 24 hrs, followed by a comet assay of DNA damage. Representative image (left) and quantification of tail moments (right) were represented. (b) OVCAR-3 cells and A2780 cells were treated with indicated compounds, followed by western blot (b) and immunostaining (c, d) analysis of γH2AX. Scale bar is 25 μM. The percentage of γ-H2AX-positive cells (≥5 foci) and the number of γ-H2AX foci per cell was determined by counting at least 100 cells from each sample. Data were represented as the mean ± SD, $n = 3$ per group. $^{**}P < 0.01$ and $^{***}P < 0.001$, by 2-tailed t-test.

(Thermo Fisher Scientific, USA) according to the manufacturer's instructions.

2.3. HR Repair Reporter Assays. We used U2OS-DRGFP cells that harbor a chromosome-integrated DR-GFP reporter to measure HR efficiency. U2OS-DR-GFP cells were equally planted into two 60 mm cell culture dishes as the control group and the experimental group. Cells were transfected with 3 μg of I-SceI expression plasmid pCBA-Sce-I using Lipofectamine™ 3000 (Thermo Fisher Scientific). 24 hours after the transfection, cells were treated with 1 μM of SN-38 or DMSO, and 24 hours after treatment, cells were collected and subjected to flow cytometry analysis to determine percentages of GFP-positive cells.

2.4. Immunofluorescence Analysis. A2780 cells grown in the chamber slider were firstly irradiated with 10 Gy of radiation and then treated with or without SN-38 (10 μM) for 2 hours. After treatment, cells were washed with PBS and fixed with 4% paraformaldehyde for 10 min at room temperature. Cells were then permeabilized with 0.3% Triton-100 for 10 min on ice. After extensively washing with PBS, cells were incubated with primary antibodies including Rad51 (1: 200) and γH2AX (1 : 500) overnight at 4°C. After washing, cells were incubated with Alexa Fluor secondary antibodies (1 : 1000) at room temperature for 1 hr. Then, image acquisition was performed after washing with PBS and mounting with DAPI.

2.5. Colony Formation. Equal numbers of cells were seeded onto six-well plates in triplicate, treated with different

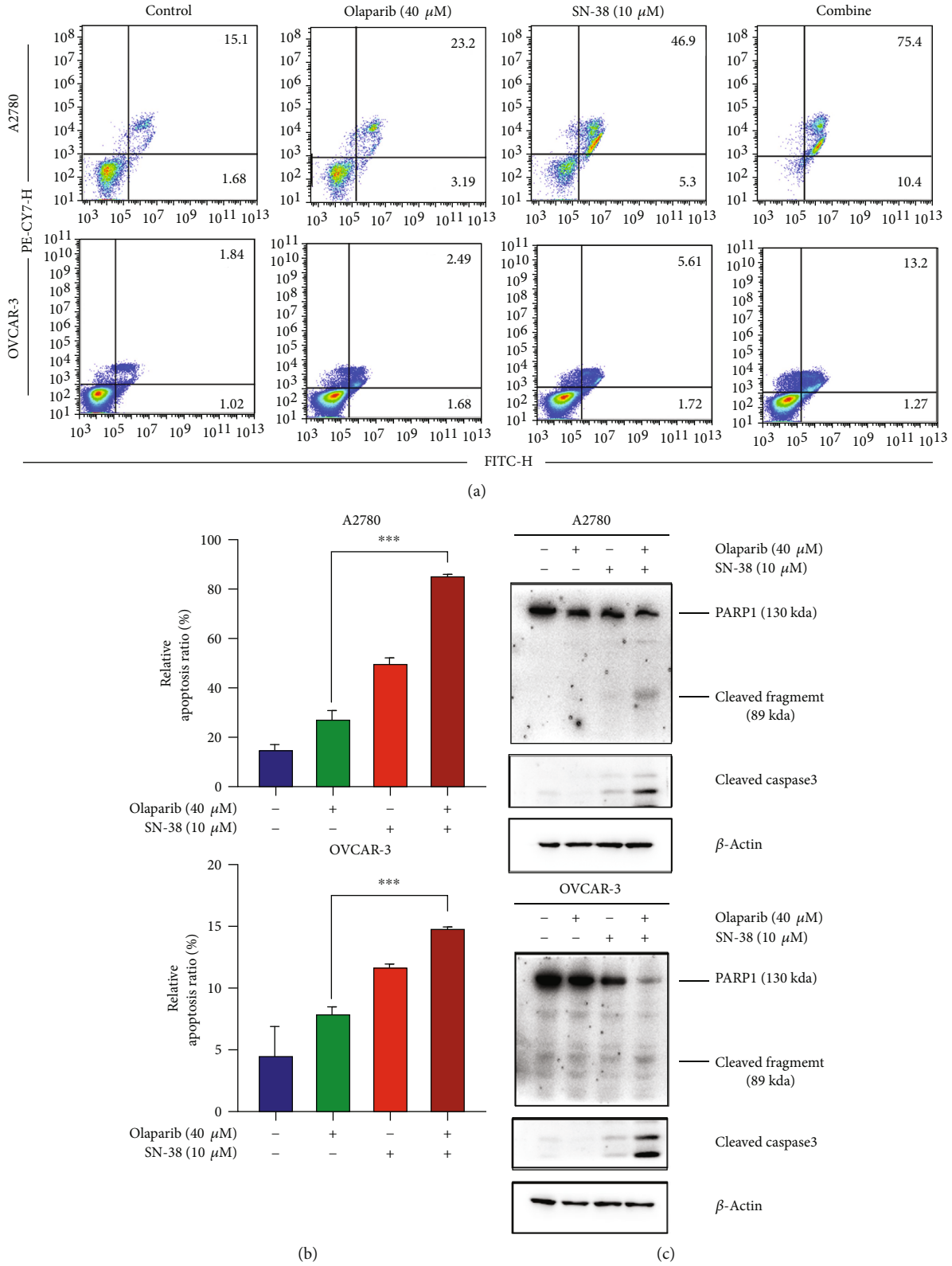

FIGURE 4: SN-38 and olaparib combination cause BRCA-proficient ovarian cancer cells apoptosis. A2780 cells were treated with 40 μM olaparib, 10 μM SN-38, or their combination as indicated, and cell apoptosis was analyzed at 48 hrs after treatment by annexin V staining (a, b) and western blot (c) analysis of cleaved caspase 3. Data were represented as the mean ± SD, $n = 3$ per group. $^{***}P < 0.001$, by 2-tailed t-test.

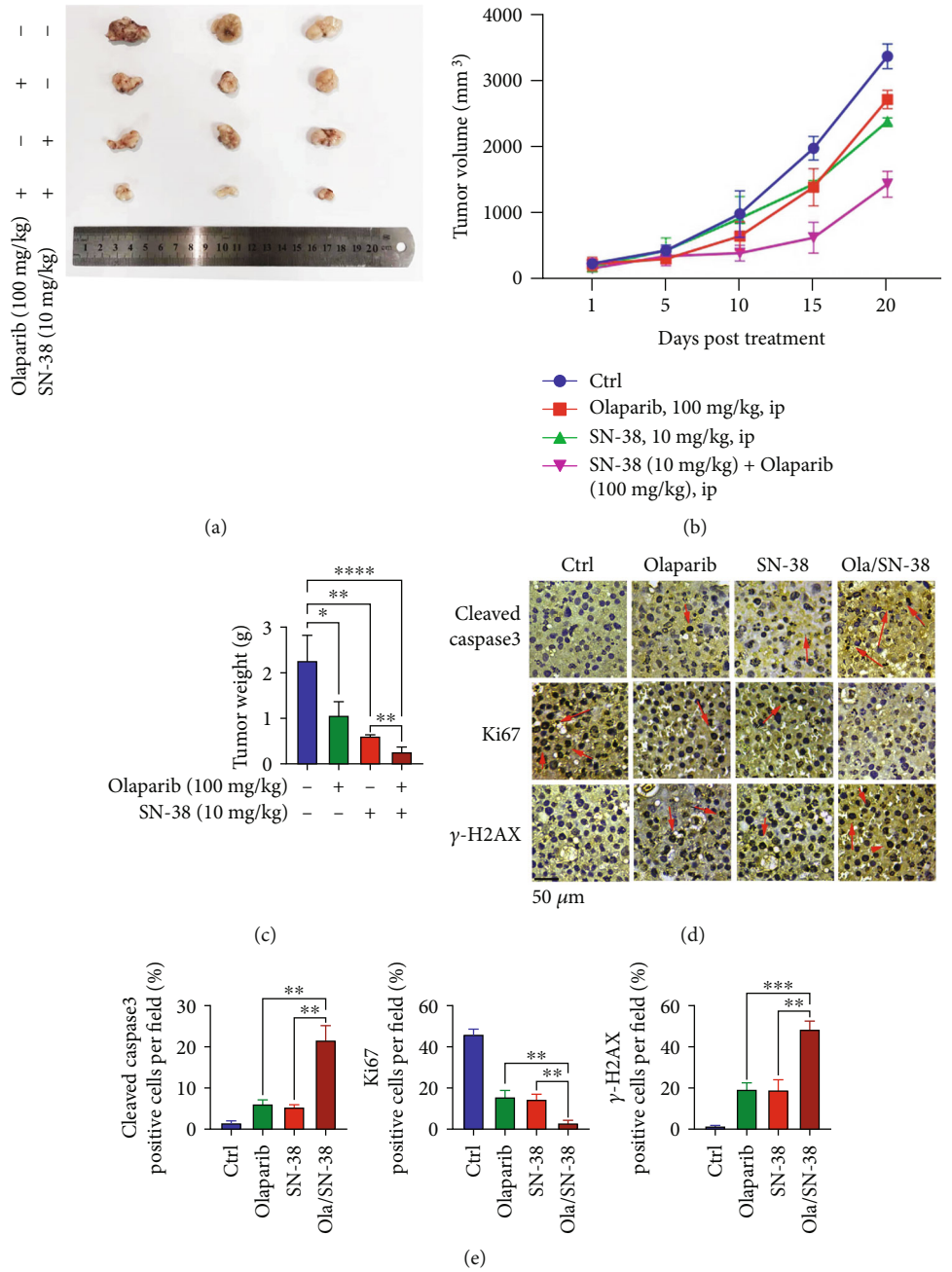

Figure 5: SN-38 enhances the antitumor efficacy of olaparib in an A2780 subcutaneous xenograft model. Mice bearing A2780 xenograft were divided into 4 groups, and each group received 100 mg/kg olaparib, 10 mg/kg SN-38 alone, or their combination; tumor volumes were measured every 5 days. Tumor volumes were measured (a) and tumor growth curve (b) was shown. Tumors were weighed and shown in (c). (d, e) Immunohistochemistry (IHC) analysis of Ki67 in the tumors derived from the 4 groups of mice mentioned above. $^{*}P < 0.05$, $^{**}P < 0.01$, and $^{***}P < 0.001$ by 2-tailed t-test.

concentrations of various compounds, and incubated for 14–20 days. Then, colonies were fixed and stained with 0.5% crystal violet. The colonies were counted using ImageJ software (NIH) or manually. All cell survival assays were performed at least in triplicate.

2.6. CCK8 Assay. Cell viability assay was performed using A CCK8 Kit (Beyotime, China). 5×10^3 of cells were suspended with fresh solution and then seeded into 96-well plates. 24 hrs later, olaparib and SN-38 were added into each well. 48 hrs later, a 10 μL of CCK8 agent was added into each well. The plates were incubated at 37°C for 1.5 hours, and then, the absorbance values at OD 450 nm were measured using an ELISA plate reader (BioTek, Winooski, VT, USA).

2.7. Comet Assay. The comet assay was performed using an OxiSelect™ Comet Assay Kit (#ADI-900-166, ENZO Life Science) according to manufacturer's instructions. Briefly,

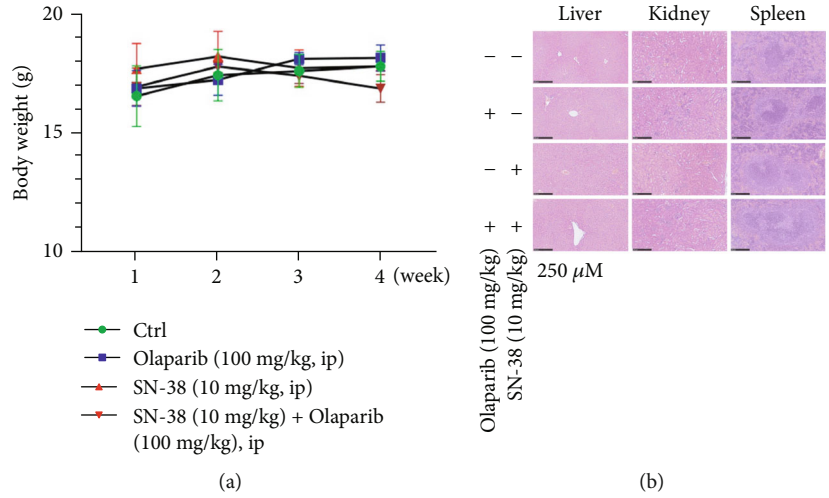

FIGURE 6: SN-38 and olaparib combination exhibits no obvious toxicity in mice. (a) The body weights of mice in each group were weighed every week, and the weight change curve was made. (b) HE staining histological analysis of paraffin-embedded sections of the liver, spleen, and kidney in each group.

cells were plated into a 6-well plate and treated with olaparib, SN-38, or their combination. 24 hrs after treatment, cells were collected, washed, and resuspended in ice-cold PBS (without Mg^{2+} and Ca^{2+}) at a final concentration of 1×10^5 cells/mL. Then, we mixed 10 μL of cell sample with 100 μL of OxiSelect™ comet agarose and immediately transferred 75 μL onto OxiSelect™ comet slides. The sliders were then placed at 4°C for 30 minutes and immersed in prechilled lysis solution for 30 to 60 minutes. After tapping off the excess buffer, the sliders were immersed in freshly prepared alkaline solution (pH > 13) for 60 minutes at room temperature, in the dark. Then, the sliders were electrophoresed in TBE buffer for 30 minutes at room temperature at 15 V (1 V/cm) and 300 mA. After electrophoresis, we dipped slide in 70% ethanol for 5 minutes and air dry samples and stained with 100 μL/well of 1× Vista Green DNA dye in the dark for 30 min at room temperature. Slides were viewed with a fluorescence microscope (Olympus).

2.8. Annexin V/Propidium Iodide Staining. Apoptosis was measured using annexin V/PI costaining as previously described [19]. Briefly, A2780 or OVCAR-3 cells were treated with olaparib, SN-38, or their combination for 48 hrs. After treatment, cells were collected by centrifuge at 1000 rpm for 5 min and washed with PBS. The pellet was then resuspended in a 100 μL binding buffer. Then, annexin V-FITC reagent and PI solution were incubated with each sample for 15 min in the dark at room temperature. Cell samples were then analyzed by flow cytometry (FACScan, BD Biosciences). Each sample was collected as 30,000 events and analyzed by FlowJo software (FlowJov10).

2.9. Cancer Xenograft Study. Six-week-old female nude mice were purchased from GemPharmatech Co., Ltd. (Nanjing, China) and housed under pathogen-free conditions. All the animal experiments were approved by the Institutional Animal Care and Use Committee of Jinan University. 1×10^7 of A2780 cells was subcutaneously implanted into mouse flanks. When tumor volume reached around 100 mm^3, tumor-bearing mice were randomly divided into 4 groups and orally administrated with olaparib (100 mg/kg), SN-38 (10 mg/kg), or their combination according to previous studies [20, 21]. We monitored tumor growth and measured tumor volume with a caliper every 5 days, and tumor volumes were calculated as $V = (L \times W^2)/2$ (L, length; W, width).

2.10. Immunohistochemistry (IHC). Tumor sections were first deparaffinized with 100% xylene, followed by rehydration using gradient ethanol (100%, 90%, 70%, 30%, and 0%). After inactivation of endogenous peroxidase by 3% hydrogen peroxide and heat-based retrieval antigen in citrate buffer, IHC staining was then performed using R.T.U. Vectastain Kit (Vector Laboratories) according to the manufacturer's instructions. Primary antibody dilutions were anti-Ki67 (1 : 500), anti-γH2AX (1 : 200), and anti-cleaved caspase 3 (1 : 200). All positive cells in tumor tissues were scored at 400x magnification. Percentage of positive cells was determined from three separate fields in each of three independent tumor samples.

2.11. Hematoxylin-Eosin (HE) Staining. Tissue damages including necrosis, congestion, and vacuolar degeneration were evaluated by hematoxylin-eosin (HE) staining as previously described [22]. Briefly, sliders were immersed in Harris hematoxylin solution for 10 seconds and then immersed in the eosin staining solution for 10-30 seconds after three times washing with water. After thoroughly washing with water, sliders were dehydrated by ascending alcohol solutions (50%, 70%, 80%, 95%, and 100%) and mounted.

2.12. Statistics. Data shown were from one representative experiment of at least three independent experiments and are expressed as mean ± SD. The statistical significance of the difference between groups was analyzed with a two-sided Student's *t*-test.

3. Results

3.1. SN-38 Inhibits Homologous Recombination (HR) in Ovarian Cancer Cells. The base excision repair (BER) is the primary pathway responsible for repairing single-strand breaks [23]. PARP1 is an important BER protein, and PARP inhibitor could disrupt BER by binding to the NAD^+ catalytic site of PARP1 and subsequently caused DNA DSBs, which highly depend on HR pathway to repair [24]. If HR is inhibited at the same time, synthetic lethal effects could be produced [25]. Thus, HR activity could determine the PARP inhibitor sensitivity in cancer cells. We utilized the HR repair reporter system, which harbors an engineered GFP gene inactivated by insertion of the I-SceI endonuclease recognition site [26]. Only after the I-SceI-induced DSB is repaired by HR repair pathway, active GFP can be restored (Figure 1(a)). Thus, we can measure the HR repair activity by measuring the GFP expression. By using this system, we found that small molecule SN-38 significantly decreased levels of HR activity (Figure 1(b)). Rad51 recombinase catalyzes homologous pairing and strand exchange during HR and Rad51 foci are considered as the marker for HR repair [27]. To confirm that SN-38 could inhibit HR, we next evaluated the percentage of Rad51 foci-positive cells after SN-38 treatment by immunofluorescence assay. Our results showed that the percentage of Rad51 foci positive cells was significantly reduced in A2780 cells after SN-38 treatment (Figure 1(c)), which further validated that SN-38 inhibits HR.

3.2. Combination of SN-38 and Olaparib Synergistically Inhibits Ovarian Cancer Growth. Given that HR repair activity dictates olaparib sensitivity, we next evaluated ovarian cancer cell growth in presence of olaparib, SN-38 alone, or their combination. As shown in Figure 2(a), combination treatment of SN-38 and olaparib inhibited cancer cell growth greater than SN-38 or olaparib treatment alone. Meanwhile, the number of colonies formed by the combined treatment was also significantly reduced compared with that of the single treatment (Figures 2(b) and 2(c)). Thus, these results demonstrated that the antiproliferative effect of SN-38 and olaparib combination is a general phenomenon in *BRAC*-proficient ovarian cancer cells.

3.3. Combination of Olaparib and SN-38 Induced Greater DNA Damage. DNA damage plays an important role in cancer radio-chemotherapy efficacy, especially in PARP inhibitor efficacy. Excessive damages that exceed the DNA repair capacity of cells can lead to cell death [28]. Here, we determined whether the compound combination enhanced DNA damage using an alkaline comet assay for detection of both SSBs (single-strand breaks) and DSBs. As shown in Figure 3(a), compared to each single drug treatment, the combination of the SN-38 and olaparib generated markedly increased tail intensity in A2780 cells, suggesting that more severe DNA damage was induced in combination treatment.

γH2AX is the phosphorylation of H2AX at its S139 site, which is considered as a sensitive molecular marker for DNA double-strand breaks (DSBs) [29]. We then measured γH2AX levels after compound treatments by western blot and immunofluorescence assay. As shown in Figures 3(b)–3(d), we detected a greater level of γH2AX in cells treated with two-drug combinations compared with SN-38 or olaparib alone. PARP inhibitor induced DNA DSBs primarily resulted from unrepaired single-strand breaks (SSBs), which are generated from accumulated DNA replication stress. Consistently, we also detected a significant increase in RPA2 S33 phosphorylation, which is phosphorylated by ATR when exposure of single-stand DNA and is extensively used as a surrogate marker for DNA replication stress [30, 31].

3.4. Combination of Olaparib and SN-38 Synergistically Induced Apoptosis. DNA damage can lead to cell apoptosis whose activation is a key mechanism by which cytotoxic drugs kill tumor cells [32]. We conducted annexin V-PI staining and performed flow cytometry analysis to measure the cell apoptosis induced by drug treatments. As shown in Figures 4(a) and 4(b), the combined treatment led to a significant increase of the apoptotic population in A2780 and OVCAR3 cells compared to each compound treatment alone. Caspase 3 is a critical executioner of apoptosis, and it is cleaved into an active form during cell apoptosis [33]. As is shown in Figure 4(c), the combined treatment showed greater cleavage of caspase 3 and PARP1 than either SN-38 or olaparib treatment alone. These results demonstrated that the combination of SN-38 and olaparib induced extensive apoptosis in ovarian cancer cells.

3.5. SN-38 Enhances the Antitumor Efficacy of Olaparib in A2780 Xenografts. We then used A2780 ovarian cancer xenograft model to subsequently investigate the antitumor efficacy of the compound combination. SN-38 (10 mg/kg), olaparib (100 mg/kg), and their combination were administered to mice bearing tumors as described in Materials and Methods. Tumor volumes and body weights were measured every 5 days. As shown in Figures 5(a)–5(c), the use of SN-38 or olaparib alone resulted in a certain inhibition of tumor growth, while stronger antitumor efficacy was observed in the combination treatment. In addition, immunohistochemistry (IHC) analysis of the cell proliferation marker Ki67, apoptosis marker cleaved caspase 3, and DNA damage marker γH2AX was performed to further evaluate the therapeutic efficacy of treatments. Inconsistent with tumor growth, Ki67 positive cells were dramatically reduced, while cleaved caspase 3 and γH2AX-positive cells were increased, in tumor tissues from mice receiving combination treatment (Figures 5(d) and 5(e)).

3.6. Combination of SN-38 and Olaparib Exhibited No Obvious Toxicity. We next evaluated the toxicity of treatments. Both SN-38 and the combination treatment did not cause a significant reduction in body weights (Figure 6(a)). Meanwhile, we also did not detect significant tissue toxicity on the liver, kidney, and spleen from mice treated with SN-38 alone or in combination with olaparib (Figure 6(b)). These results indicate that combination with SN-38 is a safe therapeutic strategy for PARP inhibitor therapy.

4. Discussion

PARP inhibitor is the first FDA-approved anticancer agent which utilizes synthetic lethality concept, and homologous recombination (HR) repair capacity is considered as the primary factor determining PARP inhibitor sensitivity. Developing agents inhibit HR repair which could render drug susceptible to PARP inhibitor insensitive cancer. Based on this premise, our studies demonstrated the first evidence that a combination of the PARP inhibitors and a small compound named SN-38, which individually have poor therapeutic effects, exhibited a greatly synergistic impact on *BRCA1/2*-proficient ovarian cancer. Since *BRAC1/2* genes play important roles in homologous recombination- (HR-) mediated DNA repair, thus, *BRAC1/2* mutant cancers are hypersensitive to PARP inhibitors. Mutations of *BRAC1/2* lead to the inhibition of cancer cell's HR repair capacity and the formation of synthetic lethal effects with PARP inhibitors. However, a significant number of cancers have normal *BRAC1/2* gene status, resulting in limited therapeutic efficacy for PARP inhibitors. Therefore, it is urgent to seek novel strategies to optimize PARP inhibitor therapy, such as in combination with other agents for *BRCA1/2*-proficient ovarian cancer. Here, we identified a small molecule SN-38, which could inhibit HR repair activity in ovarian cancer cells and verified the synergistic antitumor effects of SN-38 and olaparib combination in *BRCA1/2*-proficient ovarian cancer cells. Our data also showed that SN-38 combination with PARP inhibitors leads to significant accumulation of DNA damage as well as cell apoptosis, promoting cancer cell death. SN-38 exerts high potency against a variety of human cancers including ovarian cancer; however, its side effects and narrow therapeutic window hindered its monotherapy application in clinical therapy [34]. To exploit the therapeutic potential of SN-38, a number of antibody drug conjugate (ADC) preparations have been developed to ameliorate its adverse effects [35–37]. There are also some reviews of bioanalytical methods for SN-38 and some analyses from a clinical pharmacology perspective [38]. And the antibody-SN-38 conjugates are currently evaluated in phase II clinical trial on ovarian cancer patients [39]. Here, we show that SN-38 could be used as PARP inhibitor sensitizer and provide a novel strategy to apply SN-38 in future ovarian cancer treatment.

As a critical component of HR repair machinery, RAD51 facilitates DNA strand exchange and recombination. Our study suggests that the HR inhibiting activity of SN-38 was resulted or partially resulted from Rad51 recruitment. In addition, our results also showed that the combination of SN-38 and PARP inhibitor olaparib significantly caused replication stress, as well as apoptosis, in ovarian cancer cells. Thus, our findings suggest that a combination of PARP inhibitor with SN-38 could cause extensive DNA damage and DNA replication stress, subsequently leading to cancer cell apoptosis, therefore sensitizing *BRCA1/2*-proficient ovarian cancer cells to PARP inhibitors.

Taking together, our results herein demonstrated the synergistic effects of the PARP inhibitors and the SN-38 compound in HR-proficient ovarian cancer cells *in vitro* and xenograft tumors derived from *BRCA1/2*-proficient ovarian cancer cells in vivo, which do not respond well to the PARP inhibitors alone. Further, our findings provide evidence for the clinical development of PARP inhibitors in BRAC-proficient ovarian cancer patients.

5. Conclusions

Here, we identified a small compound SN-38, a CPT analog, which sensitizes BRCA-proficient ovarian cancer cells to PARP inhibitor treatment by inhibiting homologous recombination (HR) repair. In other words, our study provides a novel therapeutic strategy to optimize PARP inhibitor therapy for patients with BRCA-proficient ovarian cancers.

Data Availability

The datasets used and/or analyzed during the current study are available from the corresponding author on reasonable request.

Ethical Approval

The authors are accountable for all aspects of the work in ensuring that questions related to the accuracy or integrity of any part of the work are appropriately investigated and resolved. The study was conducted in accordance with the Declaration of Helsinki (as revised in 2013). This study was approved by the institutional review board of Jinan University (No. 2021531-02).

Consent

Written informed consent was given by all participants.

Conflicts of Interest

The authors declare no competing financial interests.

Authors' Contributions

S Lin and G Chen conceived and designed the study. G Chen and J Tian provided administrative support. Z Chen and Q He made great contribution to the provision of study materials or patients. M Yang and J Tian contributed to the collection and assembly of data. Q He and Y Liu assisted in data analysis and interpreted the data. All authors contributed to manuscript writing and provided final approval of manuscript. Shengbin Lin and Jiaxin Tian contributed equally to this work.

Acknowledgments

This work was supported by the National Natural Science Foundation of China (82073042 to Guo Chen), Guangdong Basic and Applied Basic Research Foundation (2022B1515020105 to Guo Chen), and open research funds from the Sixth Affiliated Hospital of Guangzhou Medical University, Qingyuan People's Hospital (202011-205 to Guo Chen).

References

[1] T. Lindahl and D. Barnes, "Repair of endogenous DNA damage," in *Cold Spring Harbor Symposia on Quantitative Biology*, Cold Spring Harbor Laboratory Press, 2000.

[2] C. J. Lord and A. Ashworth, "The DNA damage response and cancer therapy," *Nature*, vol. 481, no. 7381, pp. 287–294, 2012.

[3] D. Zhang, B. Tang, X. Xie, Y. F. Xiao, S. M. Yang, and J. W. Zhang, "The interplay between DNA repair and autophagy in cancer therapy," *Cancer Biology & Therapy*, vol. 16, no. 7, pp. 1005–1013, 2015.

[4] W.-T. Chen, N. D. Ebelt, T. H. Stracker, B. Xhemalce, C. L. van den Berg, and K. M. Miller, "ATM regulation of IL-8 links oxidative stress to cancer cell migration and invasion," *eLife*, vol. 4, article e07270, 2015.

[5] K. Bahmed, C. R. Lin, H. Simborio et al., "The role of DJ-1 in human primary alveolar type II cell injury induced by e-cigarette aerosol," *American Journal of Physiology-Lung Cellular and Molecular Physiology*, vol. 317, no. 4, pp. L475–L485, 2019.

[6] S. Moufarrij, M. Dandapani, E. Arthofer et al., "Epigenetic therapy for ovarian cancer: promise and progress," *Clinical Epigenetics*, vol. 11, no. 1, pp. 1–11, 2019.

[7] G. Wang, H. Zhou, L. Tian et al., "A prognostic DNA damage repair genes signature and its impact on immune cell infiltration in glioma," *Frontiers in Oncology*, vol. 11, 2021.

[8] C. Wang, W. Xu, J. An et al., "Poly(ADP-ribose) polymerase 1 accelerates vascular calcification by upregulating Runx2," *Nature Communications*, vol. 10, no. 1, pp. 1–12, 2019.

[9] P. Wyrsch, C. Blenn, J. Bader, and F. R. Althaus, "Cell death and autophagy under oxidative stress: roles of poly (ADP-ribose) polymerases and Ca2+," *Molecular and Cellular Biology*, vol. 32, no. 17, pp. 3541–3553, 2012.

[10] A. Poveda, A. Oaknin, I. Romero et al., "A phase I dose-finding, pharmacokinetics and genotyping study of olaparib and lurbinectedin in patients with advanced solid tumors," *Scientific Reports*, vol. 11, no. 1, p. 4433, 2021.

[11] V. Weigert, T. Jost, M. Hecht et al., "PARP inhibitors combined with ionizing radiation induce different effects in melanoma cells and healthy fibroblasts," *BMC Cancer*, vol. 20, no. 1, p. 775, 2020.

[12] V. Kruse, S. Rottey, O. de Backer, S. van Belle, V. Cocquyt, and H. Denys, "PARP inhibitors in oncology: a new synthetic lethal approach to cancer therapy," *Acta Clinica Belgica*, vol. 66, no. 1, pp. 2–9, 2011.

[13] C. J. Lord and A. Ashworth, "PARP inhibitors: Synthetic lethality in the clinic," *Science*, vol. 355, no. 6330, pp. 1152–1158, 2017.

[14] A. Ashworth and C. J. Lord, "Synthetic lethal therapies for cancer: what's next after PARP inhibitors?," *Nature Reviews Clinical oncology*, vol. 15, no. 9, pp. 564–576, 2018.

[15] M. S. Wicha, "Development of synthetic lethal'strategies to target BRCA1-deficient breast cancer," *Breast Cancer Research*, vol. 11, no. 5, pp. 1-2, 2009.

[16] F. Musa, B. Pothuri, S. V. Blank et al., "Phase II study of irinotecan in combination with bevacizumab in recurrent ovarian cancer," *Gynecologic Oncology*, vol. 144, no. 2, pp. 279–284, 2017.

[17] D. M. Gershenson, "Irinotecan in epithelial ovarian cancer," *Oncology*, vol. 16, 5 Supplement 5, pp. 29–31, 2002.

[18] D. V. T. Wong, H. V. Ribeiro-Filho, C. W. S. Wanderley et al., "SN-38, the active metabolite of irinotecan, inhibits the acute inflammatory response by targeting toll-like receptor 4," *Cancer Chemotherapy and Pharmacology*, vol. 84, no. 2, pp. 287–298, 2019.

[19] L. C. Crowley, B. J. Marfell, A. P. Scott, and N. J. Waterhouse, "Quantitation of apoptosis and necrosis by annexin V binding, propidium iodide uptake, and flow cytometry," *Cold Spring Harbor Protocols*, vol. 2016, no. 11, 2016.

[20] T. Nanbu, N. Umemura, E. Ohkoshi, K. Nanbu, H. Sakagami, and J. Shimada, "Combined SN-38 and gefitinib treatment promotes CD44 degradation in head and neck squamous cell carcinoma cells," *Oncology Reports*, vol. 39, no. 1, pp. 367–375, 2018.

[21] K. Sun, K. Mikule, Z. Wang et al., "A comparative pharmacokinetic study of PARP inhibitors demonstrates favorable properties for niraparib efficacy in preclinical tumor models," *Oncotarget*, vol. 9, no. 98, pp. 37080–37096, 2018.

[22] Z. Zou, X. Hu, T. Luo et al., "Naturally-occurring spinosyn A and its derivatives function as argininosuccinate synthase activator and tumor inhibitor," *Nature Communications*, vol. 12, no. 1, pp. 1–15, 2021.

[23] K. Ha, W. Fiskus, D. S. Choi et al., "Histone deacetylase inhibitor treatment induces 'BRCAness' and synergistic lethality with PARP inhibitor and cisplatin against human triple negative breast cancer cells," *Oncotarget*, vol. 5, no. 14, pp. 5637–5650, 2014.

[24] M.-F. Langelier, L. Zandarashvili, P. M. Aguiar, B. E. Black, and J. M. Pascal, "NAD^+ analog reveals PARP-1 substrate-blocking mechanism and allosteric communication from catalytic center to DNA-binding domains," *Nature Communications*, vol. 9, no. 1, pp. 1–13, 2018.

[25] J. M. Cleary, A. J. Aguirre, G. I. Shapiro, and A. D. D'Andrea, "Biomarker-guided development of DNA repair inhibitors," *Molecular Cell*, vol. 78, no. 6, pp. 1070–1085, 2020.

[26] L. Tian, C. Chen, Y. Guo et al., "mTORC2 regulates ribonucleotide reductase to promote DNA replication and gemcitabine resistance in non-small cell lung cancer," *Neoplasia*, vol. 23, no. 7, pp. 643–652, 2021.

[27] A. Demeyer, H. Benhelli-Mokrani, B. Chénais, P. Weigel, and F. Fleury, "Inhibiting homologous recombination by targeting RAD51 protein," *Biochimica et Biophysica Acta (BBA)-Reviews on Cancer*, vol. 1876, no. 2, article 188597, 2021.

[28] W. P. Roos and B. Kaina, "DNA damage-induced cell death by apoptosis," *Trends in Molecular Medicine*, vol. 12, no. 9, pp. 440–450, 2006.

[29] A. Ivashkevich, C. E. Redon, A. J. Nakamura, R. F. Martin, and O. A. Martin, "Use of the γ-H2AX assay to monitor DNA damage and repair in translational cancer research," *Cancer Letters*, vol. 327, no. 1-2, pp. 123–133, 2012.

[30] J. G. Glanzer, S. Liu, L. Wang, A. Mosel, A. Peng, and G. G. Oakley, "RPA inhibition increases replication stress and suppresses tumor growth," *Cancer Research*, vol. 74, no. 18, pp. 5165–5172, 2014.

[31] V. M. Vassin, R. W. Anantha, E. Sokolova, S. Kanner, and J. A. Borowiec, "Human RPA phosphorylation by ATR stimulates DNA synthesis and prevents ssDNA accumulation during DNA-replication stress," *Journal of Cell Science*, vol. 122, no. 22, pp. 4070–4080, 2009.

[32] K.-M. Debatin, "Apoptosis pathways in cancer and cancer therapy," *Cancer Immunology, Immunotherapy*, vol. 53, no. 3, pp. 153–159, 2004.

[33] S. Kumar, "Caspase function in programmed cell death," *Cell Death & Differentiation*, vol. 14, no. 1, pp. 32–43, 2007.

[34] S. Palakurthi, "Challenges in SN38 drug delivery: current success and future directions," *Expert Opinion on Drug Delivery*, vol. 12, no. 12, pp. 1911–1921, 2015.

[35] T. M. Cardillo, S. V. Govindan, R. M. Sharkey, P. Trisal, and D. M. Goldenberg, "Humanized anti-Trop-2 IgG-SN-38 conjugate for effective treatment of diverse epithelial cancers: preclinical studies in human cancer xenograft models and monkeys," *Clinical Cancer Research*, vol. 17, no. 10, pp. 3157–3169, 2011.

[36] S. V. Govindan, T. M. Cardillo, S. J. Moon, H. J. Hansen, and D. M. Goldenberg, "CEACAM5-targeted therapy of human colonic and pancreatic cancer xenografts with potent labetuzumab-SN-38 immunoconjugates," *Clinical Cancer Research*, vol. 15, no. 19, pp. 6052–6061, 2009.

[37] S. V. Govindan, T. M. Cardillo, R. M. Sharkey, F. Tat, D. V. Gold, and D. M. Goldenberg, "Milatuzumab–SN-38 conjugates for the treatment of CD74+ cancers," *Molecular Cancer Therapeutics*, vol. 12, no. 6, pp. 968–978, 2013.

[38] M. Ramesh, P. Ahlawat, and N. R. Srinivas, "Irinotecan and its active metabolite, SN-38: review of bioanalytical methods and recent update from clinical pharmacology perspectives," *Biomedical Chromatography*, vol. 24, no. 1, pp. 104–123, 2010.

[39] D. Stewart and M. Cristea, "Antibody–drug conjugates for ovarian cancer: current clinical development," *Current Opinion in Obstetrics and Gynecology*, vol. 31, no. 1, pp. 18–23, 2019.

Hindawi
Disease Markers
Volume 2022, Article ID 4607966, 19 pages
https://doi.org/10.1155/2022/4607966

Research Article

Ferulic Acid Mitigates Growth and Invasion of Esophageal Squamous Cell Carcinoma through Inducing Ferroptotic Cell Death

Yu Cao, Hong Zhang, Jianming Tang, and Rui Wang

Department of Thoracic Surgery, The Third Affiliated Hospital of Chongqing Medical University, Chongqing 401120, China

Correspondence should be addressed to Rui Wang; 650614@hospital.cqmu.edu.cn

Received 14 July 2022; Revised 2 September 2022; Accepted 6 September 2022; Published 11 October 2022

Academic Editor: Fu Wang

Objective. Ferroptosis is an iron- and ROS-dependent form of cell death initiated by lipid peroxidation. The rapidly developing study of ferroptosis has facilitated its application in cancer therapeutics. The current study is aimed at investigating the functional property of ferulic acid (FA, a phenolic acid substance) on inducing ferroptosis in antiesophageal squamous cell carcinoma (ESCC). *Methods.* ESCC cells were administrated with gradient doses of FA or with ferroptosis inhibitor deferoxamine. Cellular growth was measured with CCK-8 and colony formation experiments. LDH, caspase-3, MDA, SOD, GSH, and iron were assayed with corresponding kits. Apoptotic level was evaluated through Annexin V-FITC apoptosis staining, with migration and invasion utilizing Transwell assays. Through quantitative RT-PCR, angiogenesis-relevant genes VEGFA and PDGFB were detected. ROS generation was measured via DCFH-DA probe. Immunoblotting was conducted for monitoring ACSL4, SLC7A11, HO-1, and GPX4. *Results.* FA administration observably mitigated cellular viability and colony formation capacity and motivated LDH release, caspase-3 activity, and apoptosis in EC-1 and TE-4 cells. In addition, migration and invasion together with angiogenesis of ESCC cells were restraint by FA. FA exposure led to the increase of MDA content, ROS production, and iron load as well as the reduction of SOD activity and GSH content. Also, FA augmented the activities of ACSL4 and HO-1, with lessening SLC7A11 and GPX4. Nonetheless, deferoxamine restrained the effect of FA on ESCC ferroptosis. *Conclusion.* Altogether, FA may act as a ferroptosis inducer and thus attenuates cell growth and invasion of ESCC, which boosts the clinical application of FA in ESCC therapeutics.

1. Introduction

Esophageal cancer remains one of the most lethal cancers worldwide [1]. There were an estimated 604,100 newly diagnosed cases and 544,100 death cases globally in 2020 [2]. 957,000 new cases and 880,000 deaths are expected by 2040. Males are predominant in esophageal cancer, with male-to-female incidence and mortality ratios of 2 : 1 and 3 : 1 [3]. Esophageal squamous cell carcinoma (ESCC) is the dominating histological form, occupying 85% of all esophageal cancer cases, especially African and Asian populations [4]. Risk factors for ESCC mainly cover genetics, diet and nutrition, gastric atrophy, infection and microbiology, metabolism, epidemiology, and environment, etc. [5]. The progression of ESCC primarily contains pure epithelial hyperplasia, dysplasia, preinvasive carcinoma, invasive carcinoma, and metastasis stages [6]. Surgical resection and chemoradiotherapy remain the prime therapeutic options for combating this deadly malignancy [7]. Nonetheless, clinical outcomes are still unfavorable as a result of the limited efficacy together with serious adverse reactions. Despite the development of large-scale next-generation sequencing, the development of molecularly targeted agents (cetuximab, bevacizumab, agents targeting surface antigens and immune checkpoints, etc.) is still in its early stages. The new agents may be applied alone or combined with other therapeutic options, thus improving the therapeutic efficacy together with outcomes [8–10]. Nonetheless, adverse events, first-rank doses, and available combination regimens still require in-depth exploration.

Ferroptosis is a reactive oxygen species- (ROS-) dependent form of cell death with two major biochemical traits, iron accumulation and lipid peroxidation [11]. Ferroptotic cells often exhibit necrotic-like morphological alterations such as disruption of plasma membrane integrity, swelling of cytoplasm and cytoplasmic organelles, and moderate condensation of chromatins [12]. At the ultrastructural levels, cells that experience ferroptosis often display mitochondrial abnormalities. Ferroptotic cell death occurs primarily by extrinsic or transporter-dependent signaling (reduced cysteine or glutamine uptake, enhanced iron uptake, etc.) as well as intrinsic or enzyme-mediated signaling (GPX4 suppression, etc.) [13]. Excessive or defective ferroptotic cell death may result in pathological cell damage and malignant processes. Accumulated evidence demonstrates the potential of inducing ferroptosis for ESCC treatment. For instance, SLC7A11-mediated suppression of ferroptotic cell death induces NRF2-associated the resistance of ESCC radiotherapy [14]. ESCC stem-like cells hit back ferroptosis through activating Hsp27-GPX4 signaling [15]. 5-Aminolevulinic acid exerts an anti-ESCC property through inducing ferroptosis [16]. Oridonin enhances ferroptosis of ESCC cells via attenuating gamma-glutamyl cycle [17]. circPVT1 mitigates 5-fluorouracil chemosensitivity via resisting ferroptosis in ESCC cells [18]. Hence, more efforts are required for the design and development of anti-ESCC agents on the basis of ferroptosis induction.

Ferulic acid (4-hydroxy-3-methoxycinnamic acid, FA), a phenolic acid substance, is broadly distributed in the plant kingdom, which is usually covalently conjugated with lignin, polysaccharide, etc. of plant cell walls [19]. As a bioactive substance with multiple functions, FA is capable of removing redundant ROS and free radicals, thus resisting oxidative injury as well as lowering inflammatory response [20]. In addition, it exerts a potent anti-cancer property through modulating multiple pathways [21]. Limited evidence proposes the relationships of FA with ferroptosis in pathological state [22]. Nonetheless, the anti-ESCC property and mechanisms of FA are still unexplored. The current study put forward the hypothesis that FA mitigated growth of ESCC via inducing ferroptotic cell death.

2. Materials and Methods

2.1. Cell Culture. ESCC cells TE-4 and EC-1 (Cell Bank of Shanghai Institute of Cell Biology, China) were cultivated in Roswell Park Memorial Institute (RPMI) 1640 medium (Corning, USA) plus 10% fetal bovine serum (FBS; Invitrogen, USA) together with 1% penicillin/streptomycin (HyClone, USA) at 37°C in 5% CO_2. FA (purity ≥ 95%) was acquired from Aladdin (China). ESCC cells were administrated with a gradient of FA dissolved by dimethyl sulfoxide (DMSO) for distinct time points. Additionally, ESCC cells were exposed to 50 μM deferoxamine (DFO; Aladdin, China) to mitigate ferroptosis.

2.2. Cell Viability Assay. ESCC cells were seeded onto 96-well plates (5×10^3 cells/well), and cell viability was assayed with Cell Counting Kit-8 (CCK-8; Abcam, USA) in line with the manufacturer's protocol. Viable cells were quantified through detecting the absorbance value at 450 nm utilizing a microplate reader.

2.3. Lactate Dehydrogenase (LDH) Release and Caspase-3 Activity Assay. LDH release level was monitored with LDH cytotoxicity assay kit (Abcam, USA) in line with the manufacturer's instruction. In brief, ESCC cells were lysed and exposed to pyruvate and nicotinamide adenine dinucleotide (NADH) for 15 min at 37°C. Absorbance value at 530 nm was quantified with a microplate reader. Caspase-3 activity was measured utilizing its assay kit (Abcam, USA) in accordance with the manufacturer's protocols. Absorbance value at 405 nm was quantified with a microplate reader.

2.4. Colony Formation Assay. ESCC cells were seeded onto a 6-well plate (1×10^3 cells/well) and inculcated for 2 weeks. The colonies were fixed with 4% paraformaldehyde for 15 min and dyed with 0.5% crystal violet for 5 min. Afterwards, the colonies were counted under a light microscope.

2.5. Annexin V-FITC Apoptosis Staining. Apoptotic level was assayed with Annexin V-FITC/propidium iodide (PI) apoptosis detection kit (Beyotime, China). ESCC cells were collected via trypsinization without EDTA. After washing twice with ice-cold phosphate buffer saline (PBS), they were prepared as a single-cell suspension and dual-dyed utilizing 5 μL Annexin V-FITC together with 10 μL propidium iodide away from light for 5 min at room temperature (RT). The proportion of apoptotic cells was quantified with FACSCalibur flow cytometer (BD Biosciences, USA).

2.6. Transwell Assays. Transwell assays were adopted for detecting cellular migration and invasion. ESCC cells were cultivated in serum-free medium (SFM) for 24 h, which were inoculated into the upper chamber coated with Matrigel (for invasion assay) or uncoated (for migration assay). 200 μL SFM with 1×10^5 ESCC cells was added to the upper chamber, with the same medium plus 10% FBS adding to the lower chamber. Afterwards, the cells were grown at 37°C for 24 h. The migrated or invaded cells attached to the lower surface of the upper chamber were fixed with 4% paraformaldehyde, and dyed with 0.1% crystal violet. Images were photographed and counted.

2.7. RNA Extraction and Quantitative RT-PCR Analysis. Total RNA of ESCC cells was extracted with TRIzol reagent. RNA concentration and purity were assessed utilizing spectrophotometry. Complementary DNA was synthesized with PrimeScript RT Reagent kit (Takara, Japan). RT-PCR was conducted on CFX96 PCR system (Bio-Rad, USA) together with SYBR Green Supermix (Bio-Rad). Primer sequences included: VEGFA, 5′-AGGGCAGAATCATCACGAAGT-3′ (forward), 5′-AGGGTCTCGATTGGATGGCA-3′ (reverse); PDGFB, 5′-CTCGATCCGCTCCTTTGATGA-3′ (forward), 5′-CGTTGGTGCGGTCTATGAG-3′ (reverse); and GAPDH, 5′-CGAGATCCCTCCAAAATCAA-3′ (forward), 5′-TGTGGTCATGAGTCCTTCCA-3′ (reverse). Gene expression was computed with $2^{-\Delta\Delta Ct}$ approach.

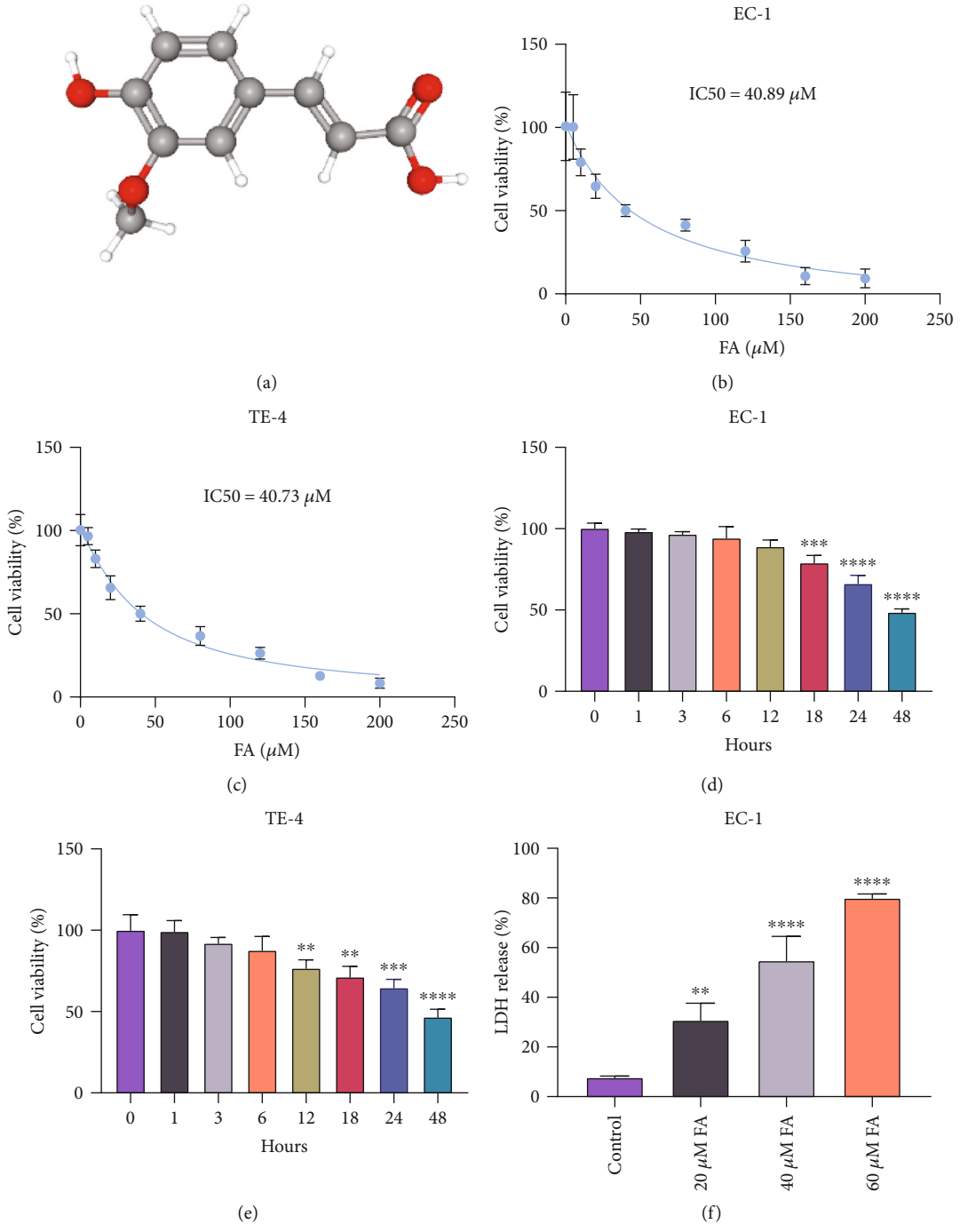

Figure 1: Continued.

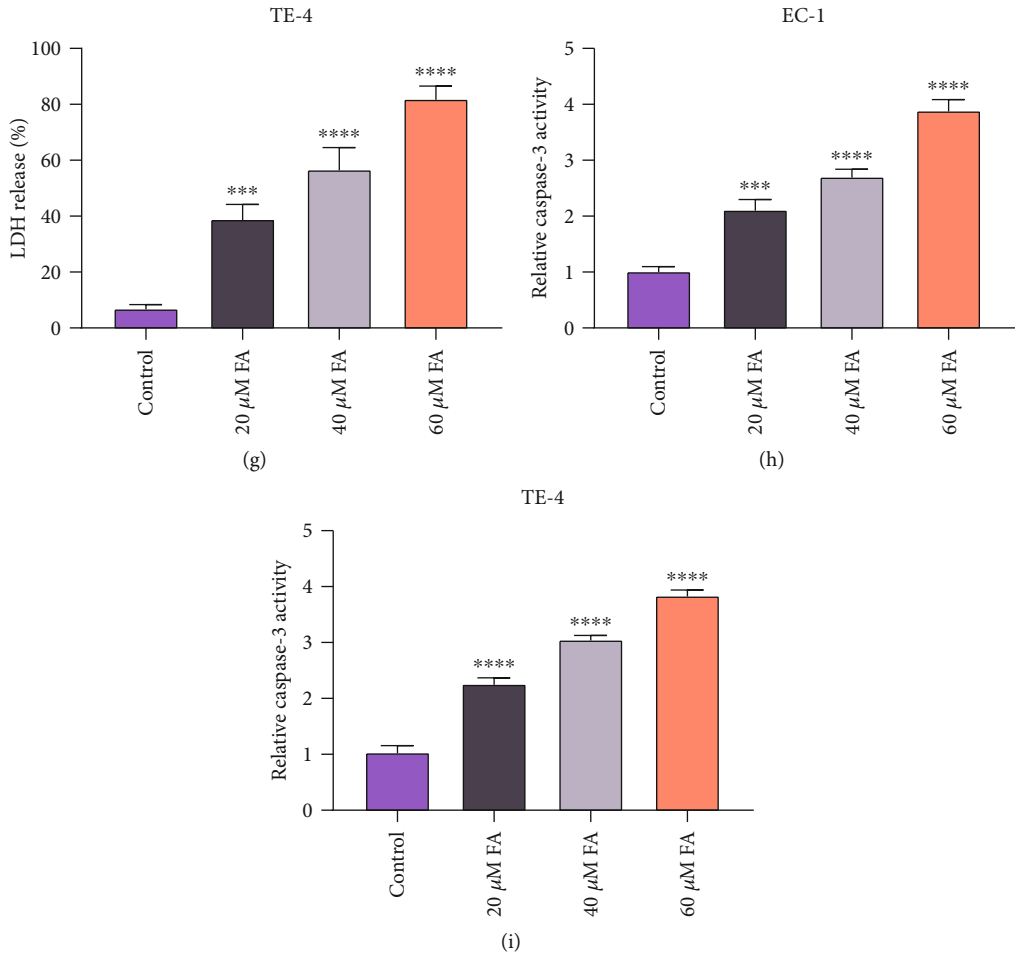

Figure 1: FA exposure mitigates cellular viability and induces LDH release and caspase-3 activity of ESCC cells. (a) Chemical structure of FA from the PubChem database. (b, c) Viable EC-1 and TE-4 cells that were exposed to gradient doses of FA for 48 h were quantified through CCK-8, and IC50 values of FA were computed. (d, e) 40 μM FA was administrated to EC-1 and TE-4 cells for a series of time points, and cellular viability was monitored via CCK-8. (f, g) LDH release level was monitored in EC-1 and TE-4 cells with 48 h administration of 20 μM, 40 μM, and 60 μM FA through LDH cytotoxicity assay kit. (h, i) Caspase-3 activity was quantified in EC-1 and TE-4 cells with 48 h exposure of 20 μM, 40 μM, and 60 μM FA utilizing caspase-3 activity assay kit. p was computed through one- or two-way ANOVA test. Significance level was denoted as $^{**}p < 0.01$, $^{***}p < 0.001$, and $^{****}p < 0.0001$.

2.8. Measurement of Malondialdehyde (MDA), Superoxide Dismutase (SOD), and Glutathione (GSH). In line with the manufacturer's instruction, MDA content and SOD activity were monitored and normalized in ESCC cells that were collected and ultrasonicated through corresponding kits (Abcam, USA). Total quantity of glutathione was tested by GSH and GSSG assay kit following the manufacturer's instruction (Abcam, USA). GSH content was assessed in contrast to the standard curves of GSH.

2.9. ROS Generation Assay. ESCC cells were seeded onto 96-well plates and exposed to 10 μM dichlorodihydrofluorescein diacetate (DCFH-DA; Sigma-Aldrich, USA) probe for 20 min at 37°C. Thereafter, they were instantly submitted to a fluorescence microscope (Olympus, Tokyo, Japan).

2.10. Iron Detection. Iron content in ESCC cells was monitored with iron assay kit in line with the manufacturer's instruction (Beyotime, China). Cells were homogenized via five volumes of iron assay buffer and centrifugated at 13,000 g lasting 10 min at 4°C. Thereafter, iron reducer was added to supernatant mixture and treated for 30 min at room temperature, followed by iron probe protecting against light for 1 h. The absorbance value was monitored at 593 nm.

2.11. Immunoblotting. Protein extraction was conducted through homogenizing ESCC cells in radioimmunoprecipitation assay (RIPA) reagent (Sigma-Aldrich, USA) supplemented with protease inhibitors. The homogenate was centrifugated at 12,000 rpm at 4°C for 20 min, and the supernatant was harvested. The concentration of proteins was assessed with bicinchoninic acid (BCA) protein assay kit (Pierce, USA). Afterwards, the proteins were loaded onto SDS polyacrylamide gel, separated through electrophoresis, and transferred onto nitrocellulose membranes via electroblotting. The membranes were blocked by 5% skim milk for 1 h at RT, followed by incubation with primary antibody of ACSL4 (1/10000; ab155282; Abcam), SLC7A11 (1/1000; ab175186), HO-1 (1/2000;

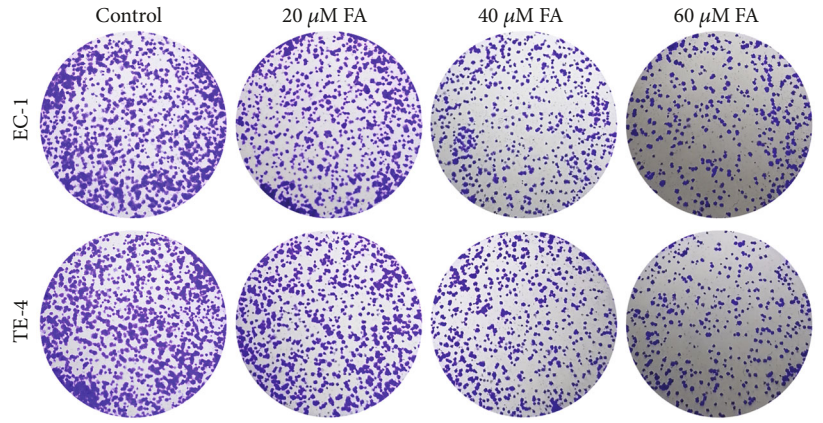

(a)

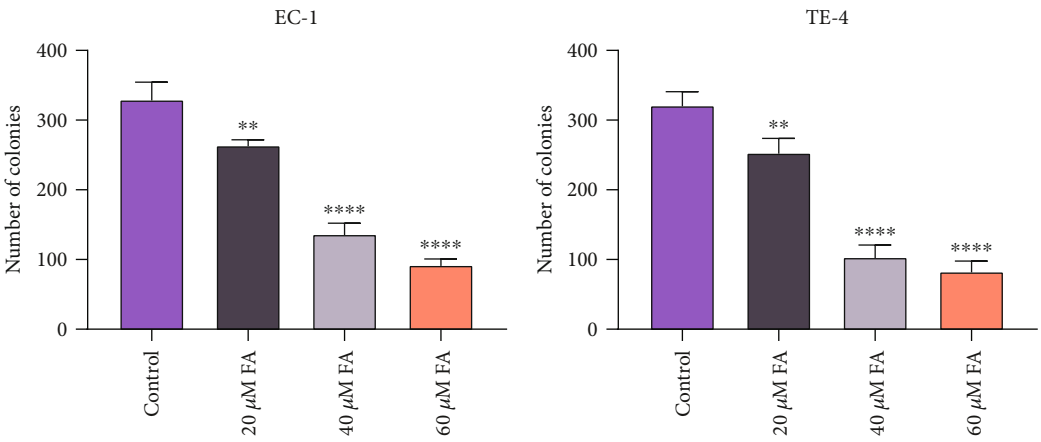

(b) (c)

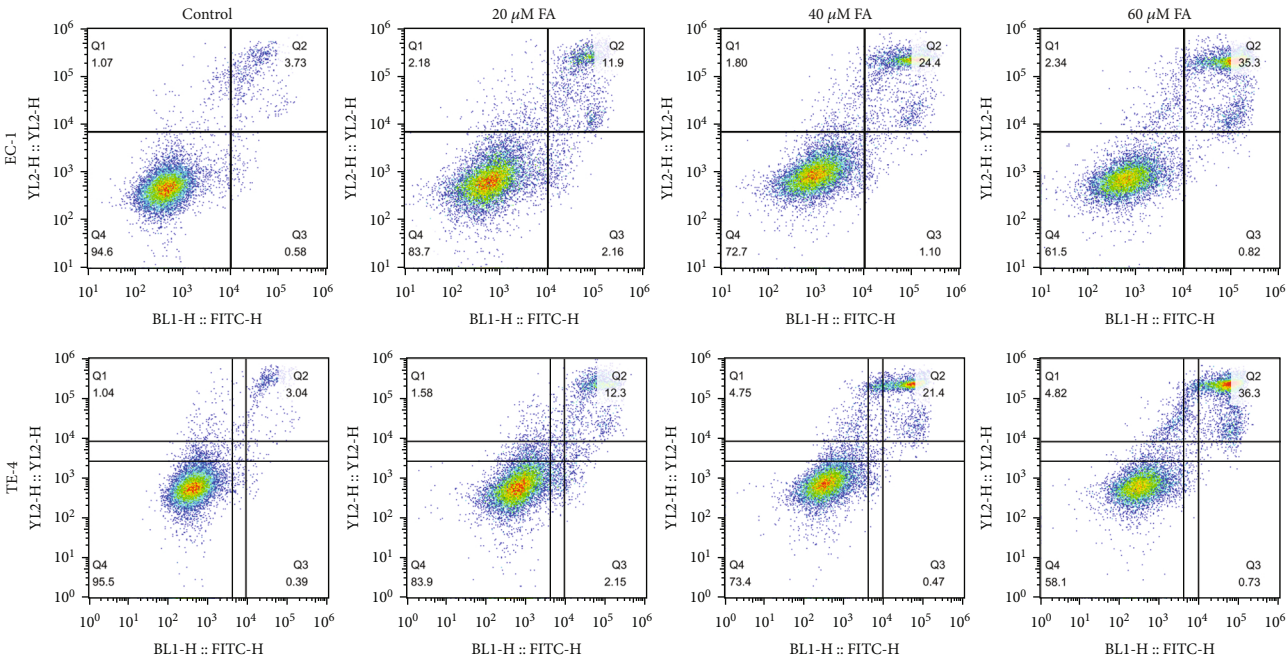

(d)

Figure 2: Continued.

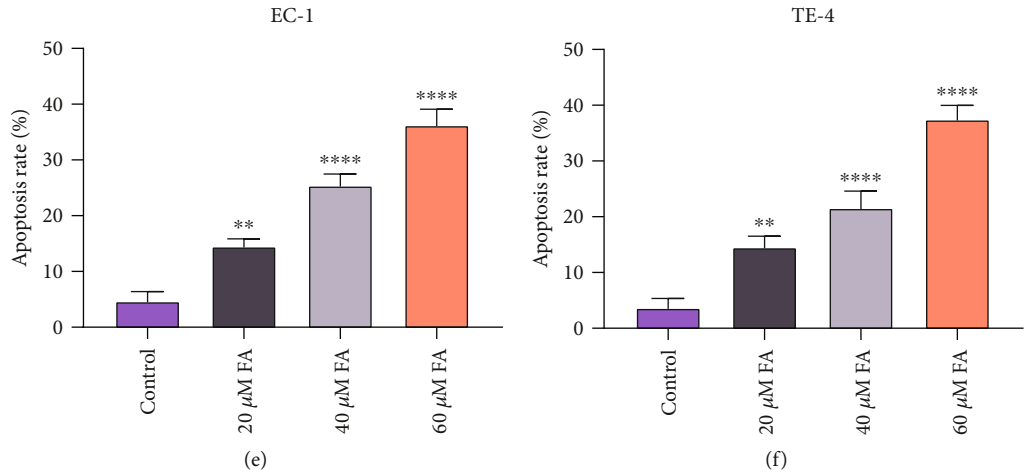

Figure 2: FA administration impairs colony formation capacity and motivates apoptosis in ESCC cells. (a–c) The colonies were counted when EC-1 and TE-4 cells were administrated with 20 μM, 40 μM, and 60 μM FA for 48 h. (d–f) Apoptotic level of EC-1 and TE-4 cells with 48 h administration of 20 μM, 40 μM, and 60 μM FA was tested via Annexin V-FITC apoptosis staining. p was computed through one-way ANOVA test. Significance level was denoted as $^{**}p < 0.01$ and $^{****}p < 0.0001$.

ab52947), GPX4 (1/2000; ab41787), or GAPDH (1/10000; ab128915) diluted in 5% skim milk overnight at 4°C. After washing with PBS, the membranes were incubated with horseradish peroxidase- (HRP-) conjugated anti-IgG antibody (1/500; ab7085) for 1 h at RT. Signal was visualized with enhanced chemiluminescence (ECL) and viewed utilizing FluorChem® M MultiFluor system (Cell Biosciences, USA).

2.12. Statistics and Analysis. All data are expressed as the standard error of mean. One- or two-way analysis of variance (ANOVA) test was conducted with GraphPad Prism 8.0.1 software (GraphPad, USA) for comparing differences between groups. $p < 0.05$ denotes statistical significance.

3. Results

3.1. FA Exposure Mitigates Cellular Viability and Induces LDH Release and Caspase-3 Activity of ESCC Cells. Figure 1(a) illustrates the chemical structure of FA that was acquired from the PubChem database. For investigating the property of FA on ESCC cellular viability, gradient doses of FA were administrated to ESCC cells for 48 h. Following 48 h exposure, IC50 values of EC-1 and TE-4 were separately 40.98 μM and 40.73 μM (Figures 1(b) and 1(c)). In addition, the optimal time point was determined when ESCC cells were exposed to 40 μM FA. As illustrated in Figures 1(d) and 1(e), the cellular viability was notably attenuated under 48 h exposure. We also investigated the influence of FA on cytotoxicity of ESCC cells through monitoring LDH release. As a result, 20 μM, 40 μM, and 60 μM FA exposure observably motivated LDH release in EC-1 and TE-4 cells in a dose-dependent manner (Figures 1(f) and 1(g)). In addition, caspase-3 activity was tested in ESCC cells administrated with 20 μM, 40 μM, and 60 μM FA for 48 h. The data showed the notable stimulative function of FA on caspase-3 activity of ESCC cells (Figures 1(h) and 1(i)). Altogether, FA administration led to the reduction of cellular viability as well as the increase of LDH release and caspase-3 activity in ESCC cells.

3.2. FA Administration Impairs Colony Formation Capacity and Motivates Apoptosis in ESCC Cells. For assessing whether FA exposure resulted in the growth suppression of FA on ESCC cells, the colonies were counted when EC-1 and TE-4 cells were administrated with 20 μM, 40 μM, and 60 μM FA for 48 h. As a result, the data demonstrated that colony formation capacity of ESCC cells was dramatically impaired by gradient doses of FA (Figures 2(a)–2(c)). In addition, apoptotic level was tested through Annexin V-FITC apoptosis staining. As illustrated in Figures 2(d)–2(f), 48 h administration of 20 μM, 40 μM, and 60 μM FA memorably motivated apoptosis of EC-1 and TE-4 cells. Hence, above findings suggested that FA led to growth suppression of ESCC cells.

3.3. FA Exerts a Suppressive Effect on Migration, Invasion, and Angiogenesis in ESCC Cells. Through adopting Transwell experiments, the current study investigated the influence of FA on migratory and invasive capacities of ESCC cells. As illustrated in Figures 3(a)–3(c), the number of migratory EC-1 and TE-4 cells was observably diminished under 48 h exposure of 20 μM, 40 μM, and 60 μM FA. In addition, FA administration contributed to the reduction of invasive EC-1 and TE-4 cells (Figures 3(d)–3(f)). Hence, FA exerted a suppressive property on migration together with invasion in ESCC cells. Afterwards, the impact of FA on ESCC angiogenesis was assessed through measuring angiogenesis-relevant genes. Consequently, 48 h administration of 20 μM, 40 μM, and 60 μM FA memorably lessened the levels of VEGFA and PDGFB mRNAs in C-1 and TE-4 cells (Figures 3(g)–3(j)), indicating that FA led to the angiogenesis suppression of ESCC cells.

3.4. FA Administration Leads to Oxidative Stress Damage of ESCC Cells through Lipid Peroxidation and ROS Generation. The loss of redox homeostasis results in the pathogenesis of ESCC [23]. One of the consequences of oxidative stress is lipid peroxidation, which is reflected by MDA at the cellular level. Under administrated with 20 μM, 40 μM, and 60 μM FA for

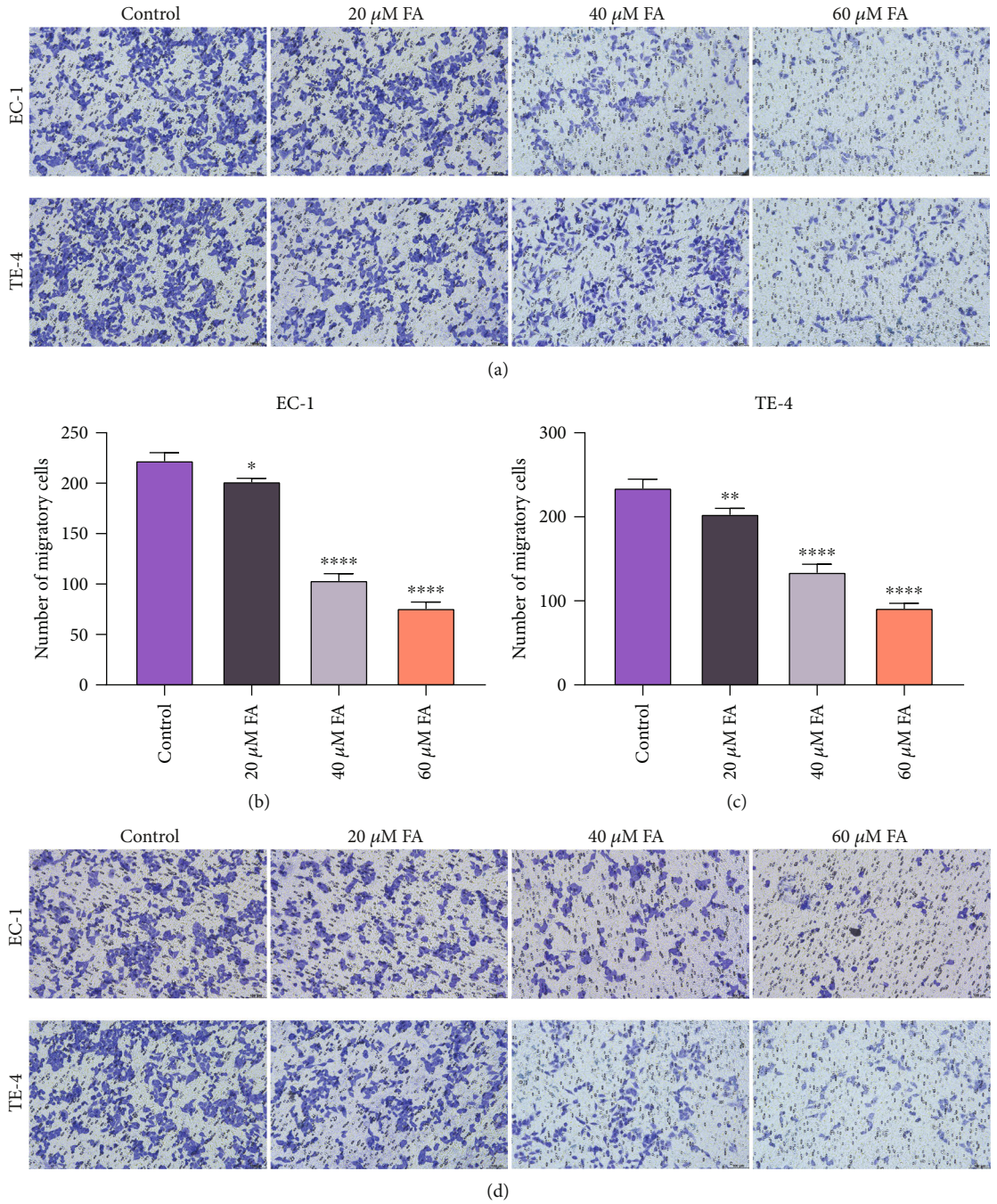

Figure 3: Continued.

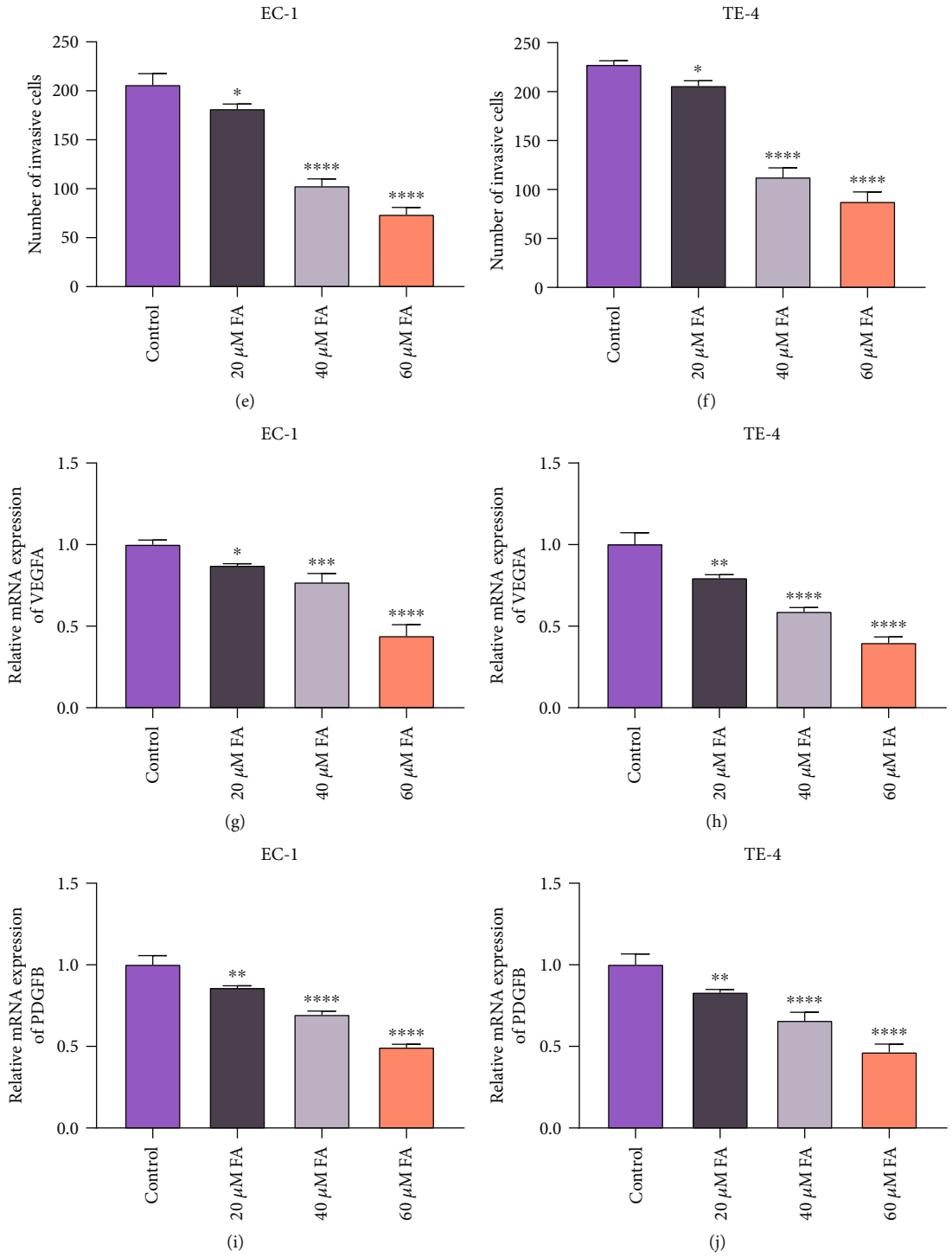

Figure 3: FA exerts a suppressive effect on migration, invasion, and angiogenesis in ESCC cells. (a–c) The migratory cells were counted when EC-1 and TE-4 cells were administrated with 20 μM, 40 μM, and 60 μM FA for 48 h via Transwell experiment. Scale bar, 100 μm. (d–f) The invasive EC-1 and TE-4 cells with 48 h administration of 20 μM, 40 μM, and 60 μM FA were counted through Transwell experiment. Scale bar, 100 μm. (g, h) VEGFA mRNA level was measured in EC-1 and TE-4 cells that were administrated with 20 μM, 40 μM, and 60 μM FA for 48 h utilizing quantitative RT-PCR analysis. (i, j) PDGFB mRNA level was tested in EC-1 and TE-4 cells with 48 h administration of 20 μM, 40 μM, and 60 μM FA through adopting quantitative RT-PCR analysis. p was computed through one-way ANOVA test. Significance level was denoted as $^{*}p < 0.05$, $^{**}p < 0.01$, $^{***}p < 0.001$, and $^{****}p < 0.0001$.

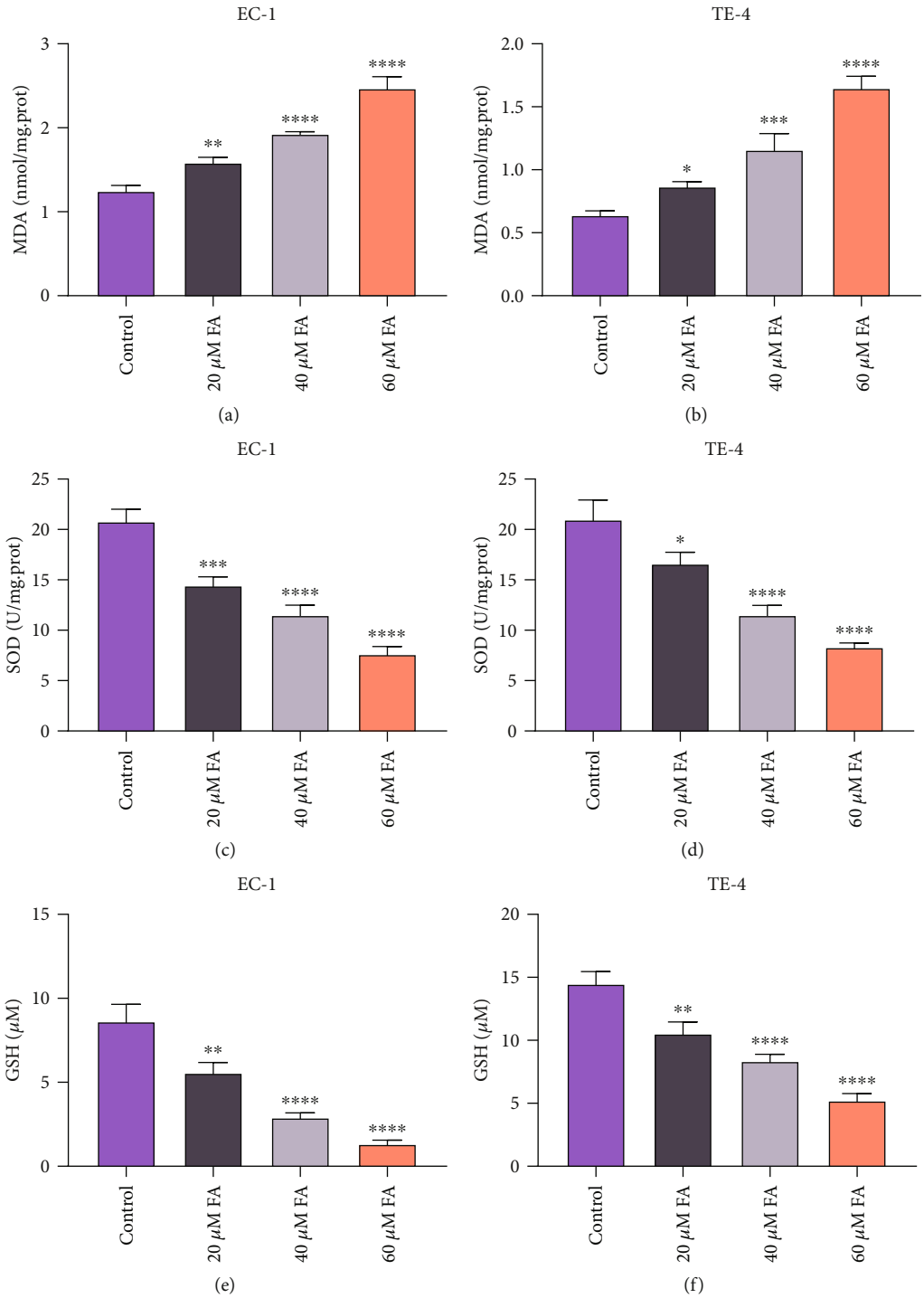

Figure 4: Continued.

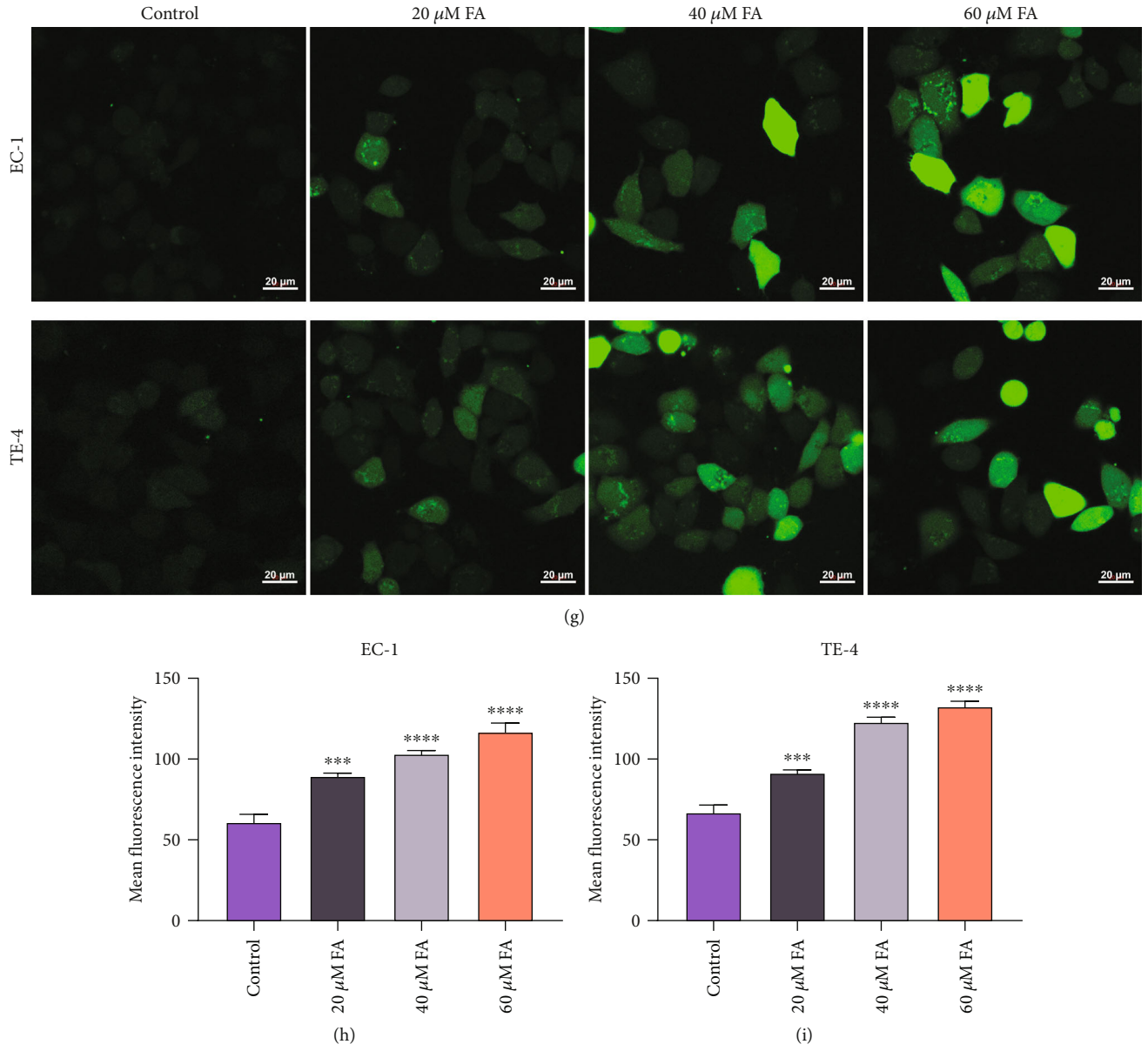

Figure 4: FA administration leads to oxidative stress damage of ESCC cells through lipid peroxidation and ROS generation. (a, b) MDA content was detected in EC-1 and TE-4 cells with 48 h administration of 20 μM, 40 μM, and 60 μM FA through MDA content kit. (c, d) SOD activity was monitored and normalized in ESCC cells that were administrated with 20 μM, 40 μM, and 60 μM FA for 48 h utilizing SOD activity kit. (e, f) GSH content was quantified in EC-1 and TE-4 cells following exposure to 20 μM, 40 μM, and 60 μM FA for 48 h. (g–i) Intracellular ROS accumulation was tested in EC-1 and TE-4 cells with 48 h administration of 20 μM, 40 μM, and 60 μM FA utilizing DCFH-DA probe. Scale bar, 20 μm. p was computed through one-way ANOVA test. Significance level was denoted as $^{*}p < 0.05$, $^{**}p < 0.01$, $^{***}p < 0.001$, and $^{****}p < 0.0001$.

48 h, MDA content was notably elevated in EC-1 and TE-4 cells (Figures 4(a) and 4(b)). SOD and GSH are important members of the antioxidant enzyme system. SOD activity together with GSH content in EC-1 and TE-4 cells were observably lessened by FA treatment (Figures 4(c)–4(f)). Afterwards, intracellular ROS generation was monitored in EC-1 and TE-4 cells utilizing DCFH-DA probe. Consequently, 48 h administration of 20 μM, 40 μM, and 60 μM FA dramatically motivated ROS generation in ESCC cells (Figures 4(g)–4(i)). Hence, FA enabled to result in oxidative stress damage of ESCC cells via lipid peroxidation and ROS production.

3.5. FA Exposure Contributes to Ferroptotic Cell Death of ESCC Cells. Further analysis was conducted for assessing whether FA impacted ferroptosis of ESCC cells. We measured iron content in ESCC cells with 48 h administration of 20 μM, 40 μM, and 60 μM FA. The data showed that FA notably increased iron content in EC-1 and TE-4 cells in a dose-dependent manner (Figures 5(a) and 5(b)). In addition, ferroptosis-relevant markers (ACSL4, SLC7A11, HO-1, and GPX4) were determined via immunoblotting. Both in EC-1 and TE-4 cells, FA exposure dramatically augmented the activities of ACSL4 and HO-1 as well as lessened the

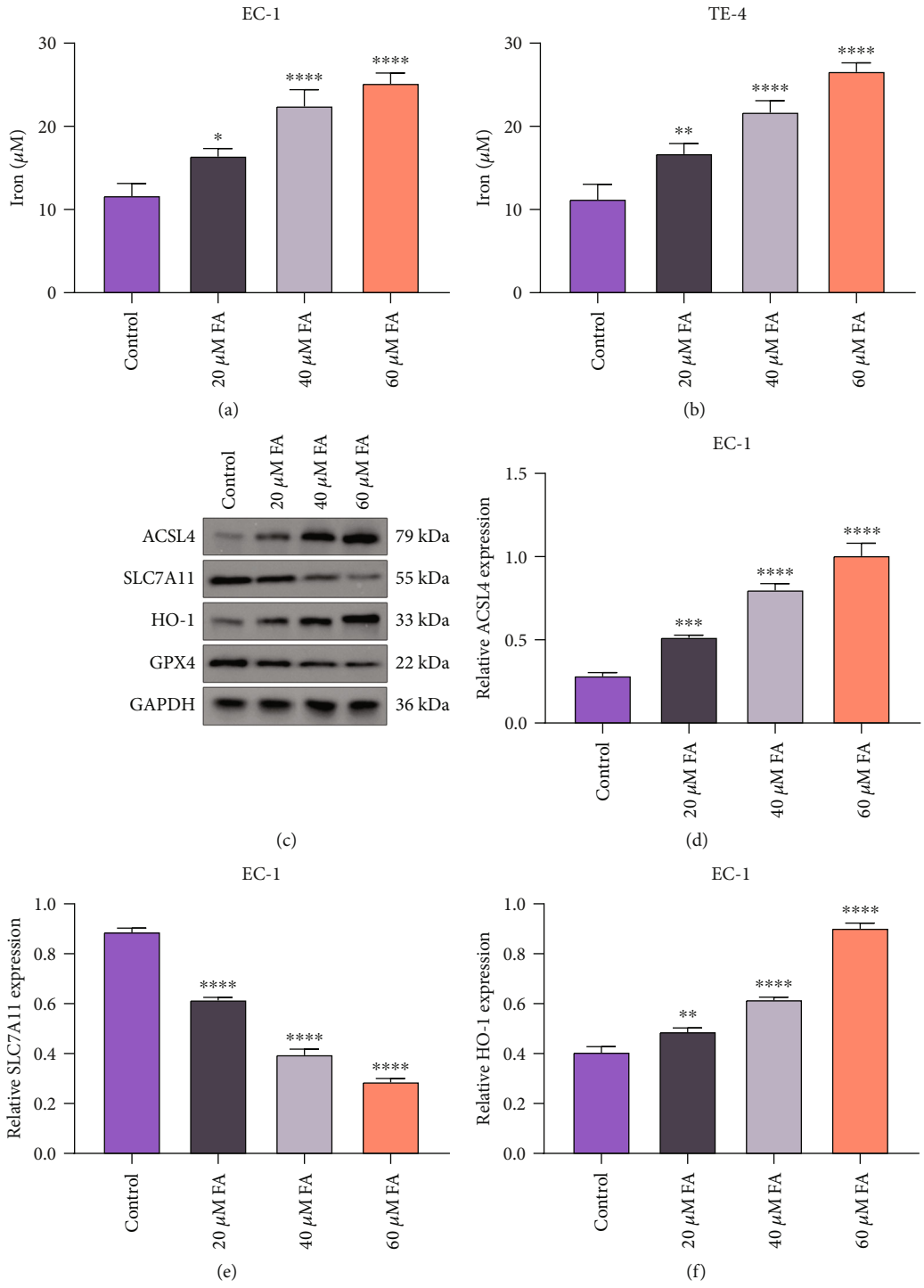

Figure 5: Continued.

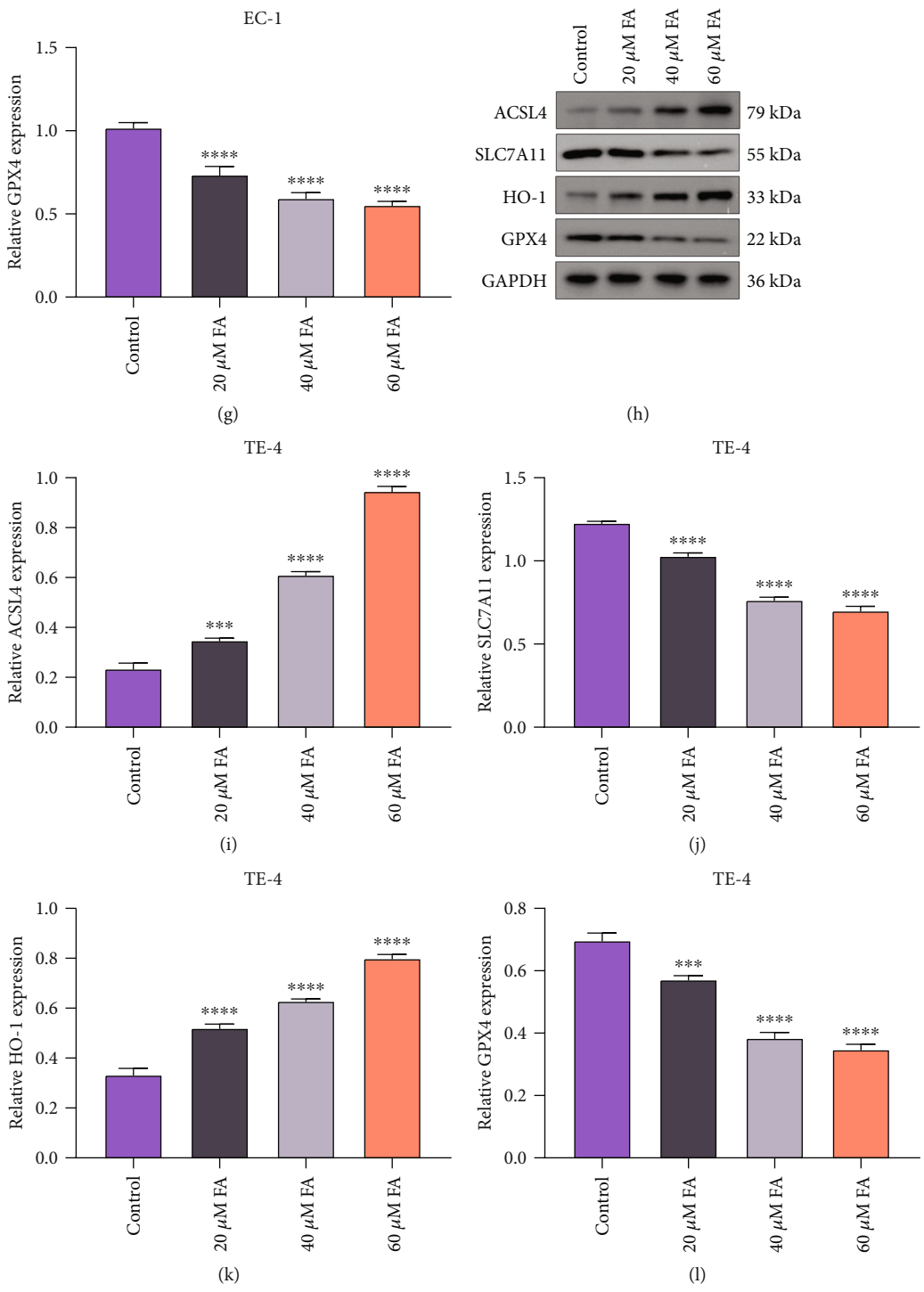

Figure 5: FA exposure contributes to ferroptotic cell death of ESCC cells. (a, b) Iron content was detected in EC-1 and TE-4 cells with 48 h administration of 20 μM, 40 μM, and 60 μM FA through iron content kit. (c–g) Activities of ACSL4, SLC7A11, HO-1, and GPX4 were measured in EC-1 cells following exposure to 20 μM, 40 μM, and 60 μM FA for 48 h through immunoblotting. (h–l) Activities of ACSL4, SLC7A11, HO-1, and GPX4 were tested in TE-4 cells that were administrated with 20 μM, 40 μM, and 60 μM FA for 48 h via adopting immunoblotting. p was computed through one-way ANOVA test. Significance level was denoted as $^{*}p < 0.05$, $^{**}p < 0.01$, $^{***}p < 0.001$, and $^{****}p < 0.0001$.

activities of SLC7A11 and GPX4 (Figures 5(c)–5(l)). These data demonstrated that FA exposure resulted in ferroptotic cell death of ESCC cells.

3.6. DFO Impairs the Stimulative Effect of FA on Lipid Peroxidation and ROS Generation in ESCC Cells. Ferroptosis is an iron-dependent cell death correlated to peroxidation of

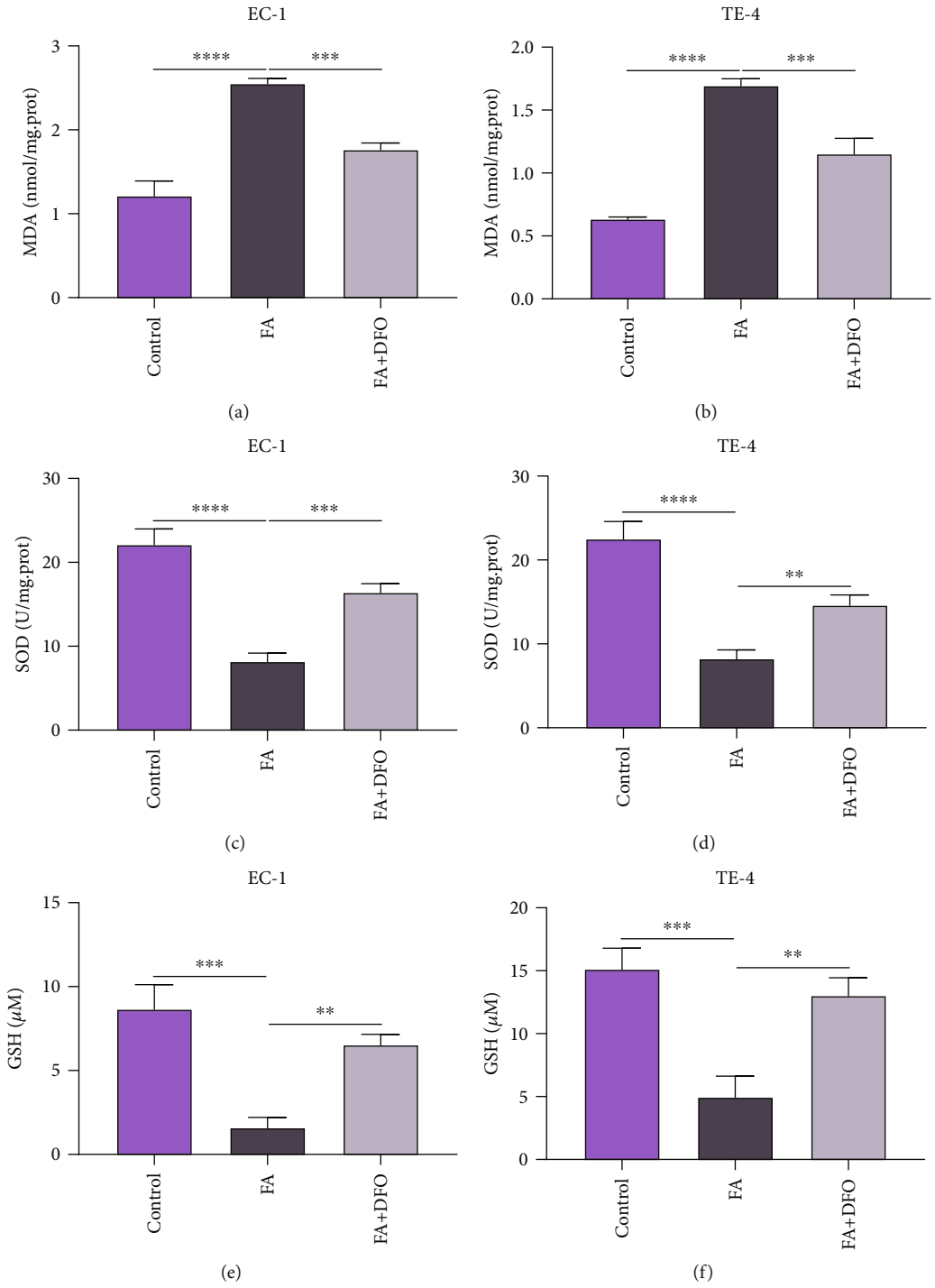

Figure 6: Continued.

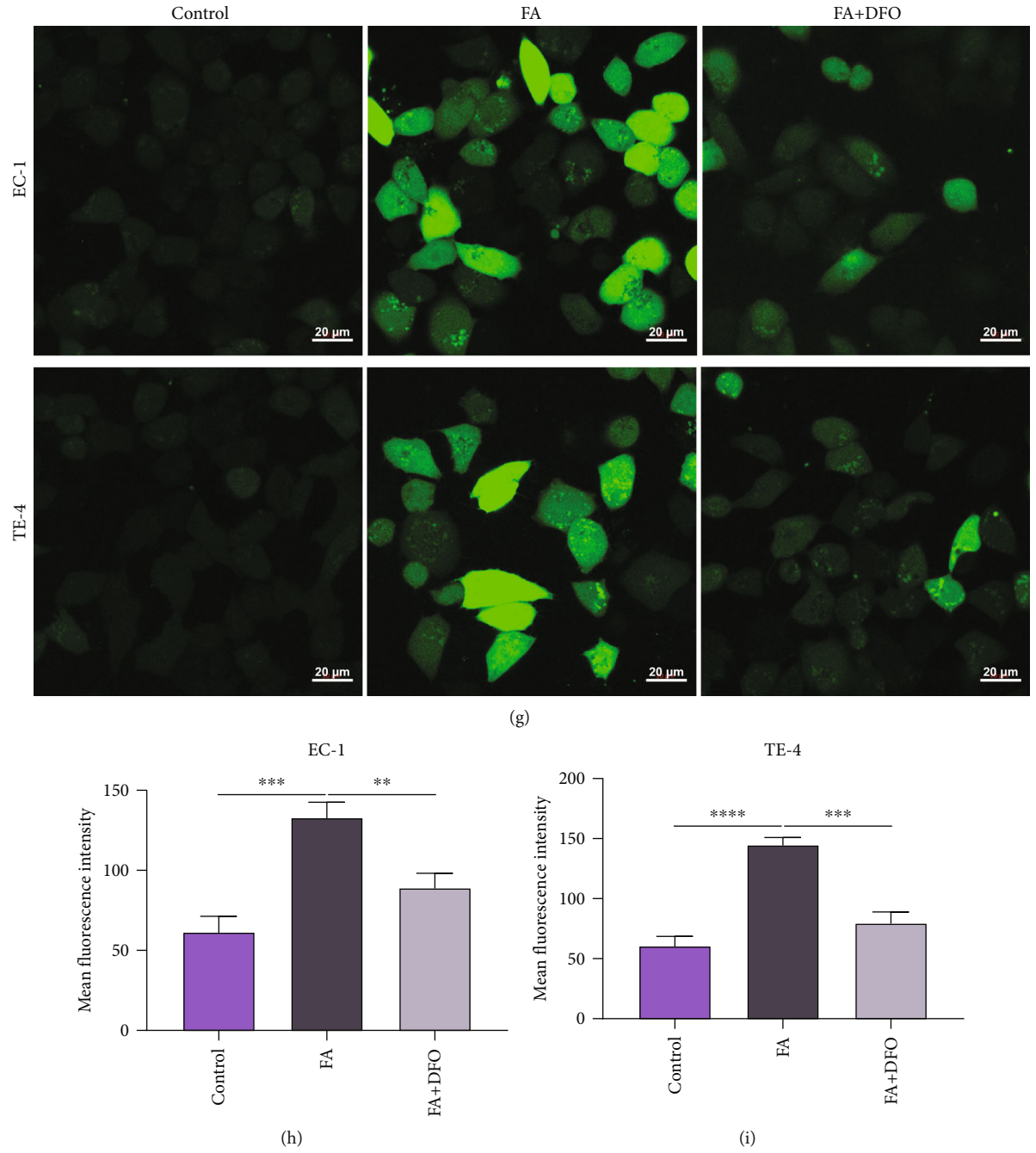

Figure 6: DFO impairs the stimulative effect of FA on lipid peroxidation and ROS generation in ESCC cells. (a, b) MDA content was measured in EC-1 and TE-4 cells with 48 h administration of 40 μM FA and 50 μM DFO by MDA content kit. (c, d) SOD activity was tested in EC-1 and TE-4 cells that were administrated with 40 μM FA and 50 μM DFO for 48 h through adopting SOD activity kit. (e, f) GSH content was assayed in EC-1 and TE-4 cells under exposure to 40 μM FA and 50 μM DFO for 48 h. (g–i) Intracellular ROS accumulation was assessed in EC-1 and TE-4 cells with 48 h administration of 40 μM FA and 50 μM DFO via DCFH-DA probe. Scale bar, 20 μm. p was computed through one-way ANOVA test. Significance level was denoted as $^{**}p < 0.01$, $^{***}p < 0.001$, and $^{****}p < 0.0001$.

lipids. EC-1 and TE-4 cells were coadministrated with 40 μM FA and 50 μM ferroptosis inhibitor DFO for 48 h to observe whether DFO hindered the stimulative effect of FA on lipid peroxidation and ROS production. The data showed that DFO notably whittled the stimulative effect of FA on MDA content together with the suppressive effect on SOD activity and GSH content in EC-1 and TE-4 cells (Figures 6(a)–6(f)). In addition, FA-induced ROS generation was observably weakened by DFO in ESCC cells (Figures 6(g)–6(i)). Hence, DFO enabled to impair the stimulative effect of FA on lipid peroxidation together with intracellular ROS accumulation in ESCC cells.

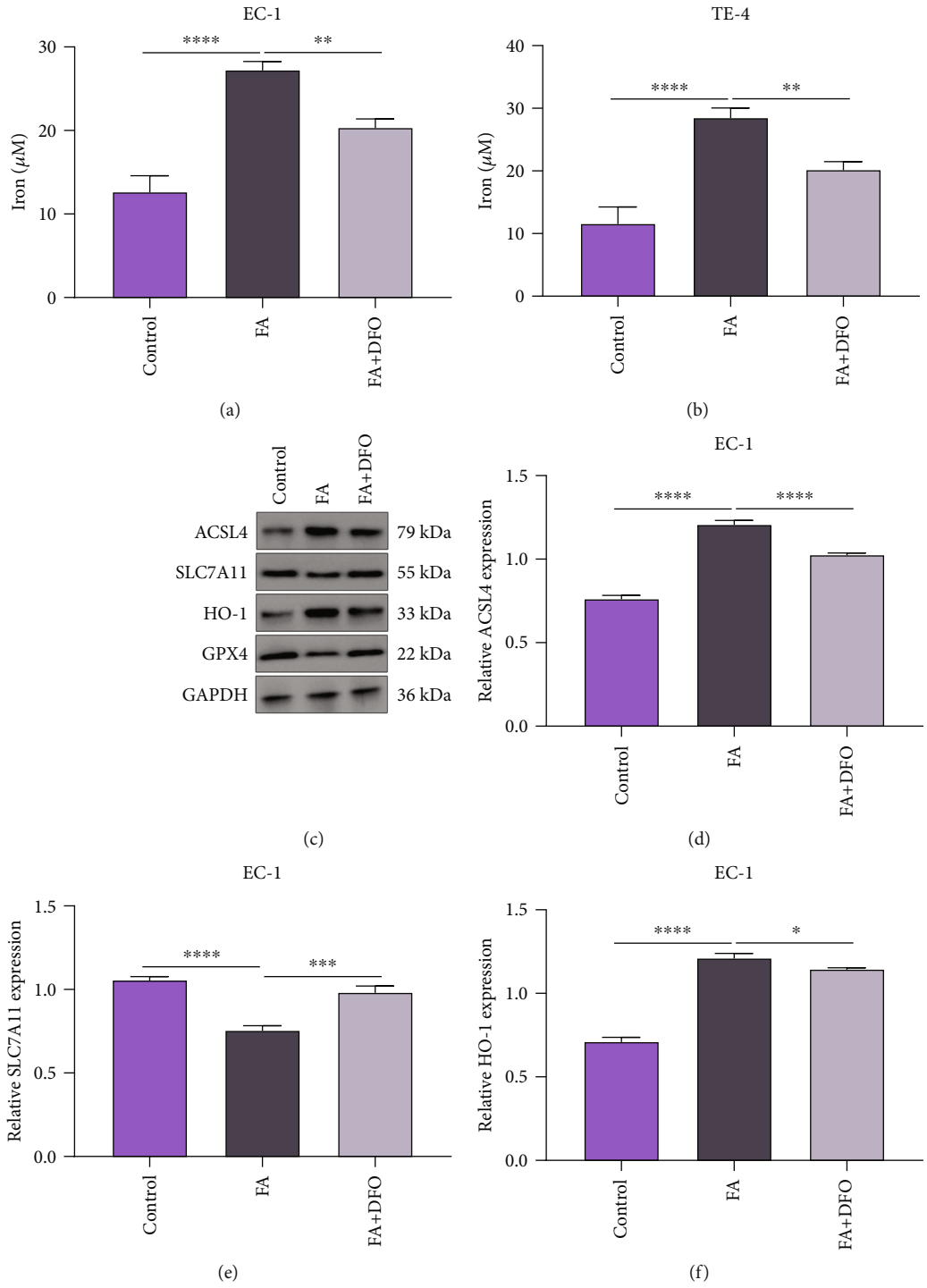

Figure 7: Continued.

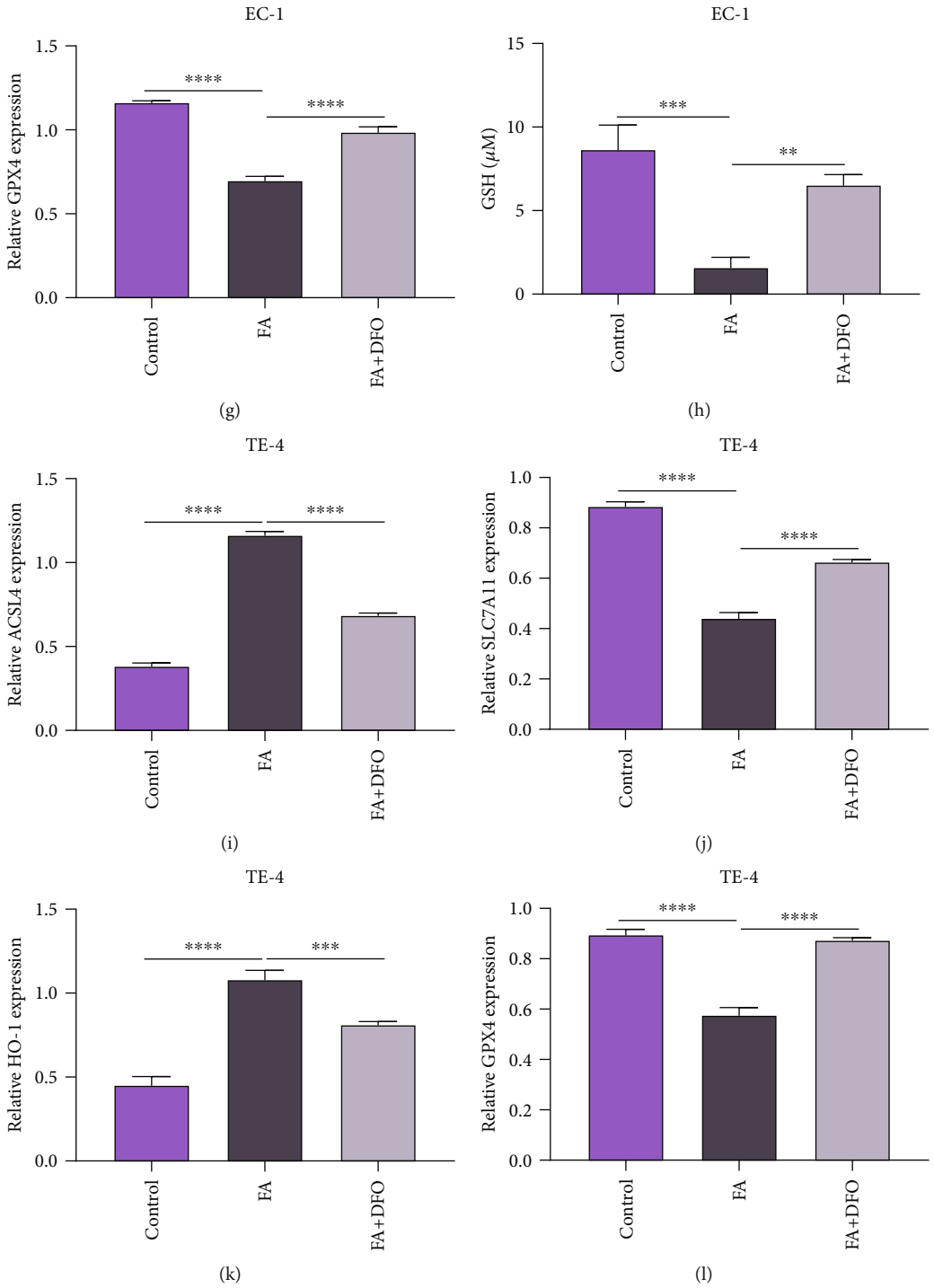

Figure 7: DFO restrains the stimulative effect of FA on ferroptotic cell death of ESCC cells. (a, b) Iron content was measured in EC-1 and TE-4 cells with 48 h administration of 40 μM FA and 50 μM DFO. (c–g) Activities of ACSL4, SLC7A11, HO-1, and GPX4 were tested in EC-1 cells with administration of 40 μM FA and 50 μM DFO for 48 h via immunoblotting. (h–l) Activities of ACSL4, SLC7A11, HO-1, and GPX4 were monitored in TE-4 cells that were exposed to 40 μM FA and 50 μM DFO for 48 h via immunoblotting. p was computed through one-way ANOVA test. Significance level was denoted as $^{*}p < 0.05$, $^{**}p < 0.01$, $^{***}p < 0.001$, and $^{****}p < 0.0001$.

3.7. DFO Restrains the Stimulative Effect of FA on Ferroptotic Cell Death of ESCC Cells. The current study conducted in-depth analysis to assess the property of FA on inducing ESCC ferroptosis. The data showed that DFO markedly lessened the iron content of FA-administrated EC-1 and TE-4 cells (Figures 7(a) and 7(b)). Administration with FA observably heightened the activities of ACSL4 and HO-1 and lessened the activities of SLC7A11 and GPX4 in EC-1 and TE-4 cells, which was reversed by DFO co-administration (Figures 7(c)–7(l)). Hence, DFO restrained

the stimulative effect of FA on ferroptotic cell death of ESCC cells.

4. Discussion

Ferroptosis is an iron- and lipid ROS-dependent cell death type, which morphologically, biologically, and genetically differentiates from other cell death types [24]. Evidence demonstrates the crucial functions of ferroptotic cell death against ESCC [25]. Ferroptosis is mitigated in ESCC and acts as a dynamic tumor suppressor in ESCC progression, suggesting that inducing ferroptosis may be applied as a potential interventional target for ESCC therapy [16]. Hence, small molecules reprogramming ESCC cells to experience ferroptotic cell death are regarded as potent agents for treating ESCC.

The potency of FA in cancer therapeutics has been proposed in other cancer types. For instance, FA attenuates proliferation and induces apoptosis through blocking PI3K/Akt signaling in osteosarcoma [26]. In addition, it mitigates cellular viability together with colony formation in pancreatic cancer [27]. Nonetheless, whether FA mitigated ESCC progression has not been reported. The current experiments demonstrated that FA attenuated cellular viability and colony formation capacity and motivated LDH release, caspase-3 activity, and apoptosis in EC-1 and TE-4 cells. Thus, ESCC cells might be vulnerable to FA. In addition, we observed the suppressive effect of FA on migration and invasion together with angiogenesis through VEGFA and PDGFB in ESCC cells, consistent with previously published literature [28, 29].

Ferroptosis is initiated by redox imbalance between the generation of oxidants and antioxidants, triggered by the aberrant expression and activities of various redox-active enzymes generating free radicals together with lipid oxidant products [30]. This cell death form has the features of elevated levels of lipid hydroperoxides and iron overload, resulting in caspase- and necrosome-independent cell death [31]. FA administration resulted in the increase of MDA content, ROS production, and iron load as well as the reduction of SOD activity and GSH content. ACSL4 may dictate the sensitivity ferroptotic cell death through shaping cellular lipid compositions [32]. Also, phosphorylation of ACSL4 by PKCβII amplifies lipid peroxidation to trigger ferroptosis [33]. Inducing ferroptosis enables to attenuate lung cancer cell growth together with migration [34]. HO-1 is recognized as a survival indicator of cancer cells as well as a ferroptosis inducing molecule [35]. The cystine/glutamate antiporter SLC7A11 is utilized for importing cystine for glutathione biosynthesis as well as antioxidant defense [36]. Recently, SLC7A11 mediated by NRF2 enhances ESCC radiosensitivity via attenuating ferroptotic cell death [14]. In addition, SLC7A11 functions as an independent prognostic indicator in human ESCC [37]. Selenium-containing enzyme GPX4 is regarded as a central inhibitor of ferroptotic cell death, and its activity depends upon glutathione generated from SLC7A11 activation [38]. In ESCC cells, FA augmented the activities of ACSL4 and HO-1, with cutting down SLC7A11 and GPX4. In addition, DFO restrained the effect of FA on ESCC ferroptosis. Altogether, FA mitigated growth together with invasion of ESCC through inducing ferroptotic cell death.

5. Conclusion

Thus, the current study is aimed at investigating the functional property of FA on inducing ferroptotic cell death in anti-ESCC. Our findings unveiled FA as a novel ferroptosis inducer, thus attenuating cell growth and invasion of ESCC, which might boost the clinical application of FA in ESCC therapeutics.

Abbreviations

ESCC: Esophageal squamous cell carcinoma
ROS: Reactive oxygen species
FA: Ferulic acid
DMSO: Dimethyl sulfoxide
DFO: Deferoxamine
CCK-8: Cell Counting Kit-8
LDH: Lactate dehydrogenase
RT: Room temperature
SFM: Serum-free medium
MDA: Malondialdehyde
SOD: Superoxide dismutase
GSH: Glutathione
DCFH-DA: Dichlorodihydrofluorescein diacetate.

Data Availability

The datasets analyzed during the current study are available from the corresponding author on reasonable request.

Conflicts of Interest

The authors declare no conflicts of interest.

References

[1] Y. M. Yang, P. Hong, W. W. Xu, Q. Y. He, and B. Li, "Advances in targeted therapy for esophageal cancer," *Signal Transduction and Targeted Therapy*, vol. 5, no. 1, p. 229, 2020.

[2] E. Morgan, I. Soerjomataram, H. Rumgay et al., "The global landscape of esophageal squamous cell carcinoma and esophageal adenocarcinoma incidence and mortality in 2020 and projections to 2040: new estimates from GLOBOCAN 2020," *Gastroenterology*, vol. 163, no. 3, pp. 649–658.e2, 2022.

[3] H. Sung, J. Ferlay, R. L. Siegel et al., "Global cancer statistics 2020: GLOBOCAN estimates of incidence and mortality worldwide for 36 cancers in 185 countries," *CA: a Cancer Journal for Clinicians*, vol. 71, no. 3, pp. 209–249, 2021.

[4] X. Zhang, Y. Wang, and L. Meng, "Comparative genomic analysis of esophageal squamous cell carcinoma and adenocarcinoma: new opportunities towards molecularly targeted therapy," *Acta Pharmaceutica Sinica B*, vol. 12, no. 3, pp. 1054–1067, 2022.

[5] M. Tarazi, S. Chidambaram, and S. R. Markar, "Risk factors of esophageal squamous cell carcinoma beyond alcohol and smoking," *Cancers*, vol. 13, no. 5, p. 1009, 2021.

[6] S. He, J. Xu, X. Liu, and Y. Zhen, "Advances and challenges in the treatment of esophageal cancer," *Acta Pharmaceutica Sinica B*, vol. 11, no. 11, pp. 3379–3392, 2021.

[7] A. P. Thrift, "Global burden and epidemiology of Barrett oesophagus and oesophageal cancer," *Nature Reviews Gastroenterology & Hepatology*, vol. 18, no. 6, pp. 432–443, 2021.

[8] H. Wang, H. Tang, Y. Fang et al., "Morbidity and mortality of patients who underwent minimally invasive esophagectomy after neoadjuvant chemoradiotherapy vs neoadjuvant chemotherapy for locally advanced esophageal squamous cell carcinoma: a randomized clinical trial," *JAMA Surgery*, vol. 156, no. 5, pp. 444–451, 2021.

[9] K. Kato, B. C. Cho, M. Takahashi et al., "Nivolumab versus chemotherapy in patients with advanced oesophageal squamous cell carcinoma refractory or intolerant to previous chemotherapy (ATTRACTION-3): a multicentre, randomised, open-label, phase 3 trial," *The Lancet Oncology*, vol. 20, no. 11, pp. 1506–1517, 2019.

[10] H. Luo, J. Lu, Y. Bai et al., "Effect of camrelizumab vs placebo added to chemotherapy on survival and progression-free survival in patients with advanced or metastatic esophageal squamous cell carcinoma: the ESCORT-1st randomized clinical trial," *JAMA*, vol. 326, no. 10, pp. 916–925, 2021.

[11] X. Niu, L. Chen, Y. Li, Z. Hu, and F. He, "Ferroptosis, necroptosis, and pyroptosis in the tumor microenvironment: perspectives for immunotherapy of SCLC," *Seminars in Cancer Biology*, 2022.

[12] W. Liu, B. Chakraborty, R. Safi, D. Kazmin, C. Y. Chang, and D. P. McDonnell, "Dysregulated cholesterol homeostasis results in resistance to ferroptosis increasing tumorigenicity and metastasis in cancer," *Nature Communications*, vol. 12, no. 1, p. 5103, 2021.

[13] L. Chen, X. Niu, X. Qiao et al., "Characterization of interplay between autophagy and ferroptosis and their synergistical roles on manipulating immunological tumor microenvironment in squamous cell carcinomas," *Frontiers in Immunology*, vol. 12, article 739039, 2022.

[14] L. Feng, K. Zhao, L. Sun et al., "SLC7A11 regulated by NRF2 modulates esophageal squamous cell carcinoma radiosensitivity by inhibiting ferroptosis," *Journal of Translational Medicine*, vol. 19, no. 1, p. 367, 2021.

[15] C. C. Liu, H. H. Li, J. H. Lin et al., "Esophageal cancer stem-like cells resist ferroptosis-induced cell death by active Hsp27-GPX4 pathway," *Biomolecules*, vol. 12, 2022.

[16] Y. Shishido, M. Amisaki, Y. Matsumi et al., "Antitumor effect of 5-aminolevulinic acid through ferroptosis in esophageal squamous cell carcinoma," *Annals of Surgical Oncology*, vol. 28, no. 7, pp. 3996–4006, 2021.

[17] J. Zhang, N. Wang, Y. Zhou et al., "Oridonin induces ferroptosis by inhibiting gamma-glutamyl cycle in TE1 cells," *Phytotherapy Research*, vol. 35, no. 1, pp. 494–503, 2021.

[18] W. Yao, J. Wang, F. Meng et al., "Circular RNA CircPVT1 inhibits 5-fluorouracil chemosensitivity by regulating ferroptosis through miR-30a-5p/FZD3 axis in esophageal cancer cells," *Frontiers in Oncology*, vol. 11, article 780938, 2021.

[19] A. Gupta, A. K. Singh, M. Loka, A. K. Pandey, and A. Bishayee, "Ferulic acid-mediated modulation of apoptotic signaling pathways in cancer," *Advances in Protein Chemistry and Structural Biology*, vol. 125, pp. 215–257, 2021.

[20] D. Li, Y. X. Rui, S. D. Guo, F. Luan, R. Liu, and N. Zeng, "Ferulic acid: a review of its pharmacology, pharmacokinetics and derivatives," *Life Sciences*, vol. 284, article 119921, 2021.

[21] C. Senthil Kumar, R. Thangam, S. A. Mary, P. R. Kannan, G. Arun, and B. Madhan, "Targeted delivery and apoptosis induction of trans-resveratrol-ferulic acid loaded chitosan coated folic acid conjugate solid lipid nanoparticles in colon cancer cells," *Carbohydrate Polymers*, vol. 231, article 115682, 2020.

[22] X. Liu, K. Qi, Y. Gong et al., "Ferulic acid alleviates myocardial ischemia reperfusion injury via upregulating AMPKα2 expression-mediated ferroptosis depression," *Journal of Cardiovascular Pharmacology*, vol. 79, no. 4, pp. 489–500, 2021.

[23] Z. Liu, S. Gu, T. Lu et al., "IFI6 depletion inhibits esophageal squamous cell carcinoma progression through reactive oxygen species accumulation via mitochondrial dysfunction and endoplasmic reticulum stress," *Journal of Experimental & Clinical Cancer Research*, vol. 39, no. 1, p. 144, 2020.

[24] H. Wang, Y. Cheng, C. Mao et al., "Emerging mechanisms and targeted therapy of ferroptosis in cancer," *Molecular Therapy*, vol. 29, no. 7, pp. 2185–2208, 2021.

[25] C. Liang, X. Zhang, M. Yang, and X. Dong, "Recent progress in ferroptosis inducers for cancer therapy," *Advanced Materials*, vol. 31, article e1904197, 2019.

[26] T. Wang, X. Gong, R. Jiang, H. Li, W. Du, and G. Kuang, "Ferulic acid inhibits proliferation and promotes apoptosis via blockage of PI3K/Akt pathway in osteosarcoma cell," *American Journal of Translational Research*, vol. 8, no. 2, pp. 968–980, 2016.

[27] U. Fahrioğlu, Y. Dodurga, L. Elmas, and M. Seçme, "Ferulic acid decreases cell viability and colony formation while inhibiting migration of MIA PaCa-2 human pancreatic cancer cells in vitro," *Gene*, vol. 576, no. 1, pp. 476–482, 2016.

[28] S. J. Yue, P. X. Zhang, Y. Zhu et al., "A ferulic acid derivative FXS-3 inhibits proliferation and metastasis of human lung cancer A549 cells via positive JNK signaling pathway and negative ERK/p38, AKT/mTOR and MEK/ERK signaling pathways," *Molecules*, vol. 24, no. 11, article 2165, 2019.

[29] G. W. Yang, J. S. Jiang, and W. Q. Lu, "Ferulic acid exerts antiangiogenic and anti-tumor activity by targeting fibroblast growth factor receptor 1-mediated angiogenesis," *International Journal of Molecular Sciences*, vol. 16, no. 10, pp. 24011–24031, 2015.

[30] S. Yuan, C. Wei, G. Liu et al., "Sorafenib attenuates liver fibrosis by triggering hepatic stellate cell ferroptosis via HIF-1α/SLC7A11 pathway," *Cell Proliferation*, vol. 55, article e13158, 2022.

[31] H. Ma, X. Wang, W. Zhang et al., "Melatonin suppresses ferroptosis induced by high glucose via activation of the Nrf2/HO-1 signaling pathway in type 2 diabetic osteoporosis," *Oxidative Medicine and Cellular Longevity*, vol. 2020, Article ID 9067610, 18 pages, 2020.

[32] S. Doll, B. Proneth, Y. Y. Tyurina et al., "ACSL4 dictates ferroptosis sensitivity by shaping cellular lipid composition," *Nature Chemical Biology*, vol. 13, no. 1, pp. 91–98, 2017.

[33] H. L. Zhang, B. X. Hu, Z. L. Li et al., "PKCβII phosphorylates ACSL4 to amplify lipid peroxidation to induce ferroptosis," *Nature Cell Biology*, vol. 24, no. 1, pp. 88–98, 2022.

[34] P. Chen, Q. Wu, J. Feng et al., "Erianin, a novel dibenzyl compound in Dendrobium extract, inhibits lung cancer cell growth and migration via calcium/calmodulin-dependent ferroptosis," *Signal Transduction and Targeted Therapy*, vol. 5, no. 1, p. 51, 2020.

[35] P. Chen, X. Li, R. Zhang et al., "Combinative treatment of β-elemene and cetuximab is sensitive to KRAS mutant colorectal cancer cells by inducing ferroptosis and inhibiting epithelial-

mesenchymal transformation," *Theranostics*, vol. 10, no. 11, pp. 5107–5119, 2020.

[36] P. Yadav, P. Sharma, S. Sundaram, G. Venkatraman, A. K. Bera, and D. Karunagaran, "SLC7A11/ xCT is a target of miR-5096 and its restoration partially rescues miR-5096-mediated ferroptosis and anti-tumor effects in human breast cancer cells," *Cancer Letters*, vol. 522, pp. 211–224, 2021.

[37] A. Shiozaki, D. Iitaka, D. Ichikawa et al., "xCT, component of cysteine/glutamate transporter, as an independent prognostic factor in human esophageal squamous cell carcinoma," *Journal of Gastroenterology*, vol. 49, no. 5, pp. 853–863, 2014.

[38] Y. Sun, N. Berleth, W. Wu et al., "Fin56-induced ferroptosis is supported by autophagy-mediated GPX4 degradation and functions synergistically with mTOR inhibition to kill bladder cancer cells," *Cell Death & Disease*, vol. 12, no. 11, p. 1028, 2021.

Hindawi
Disease Markers
Volume 2022, Article ID 8809956, 19 pages
https://doi.org/10.1155/2022/8809956

Research Article

Application of Cytochrome C-Related Genes in Prognosis and Treatment Prediction of Lung Adenocarcinoma

Min Tang,[1] **Guoqing Li**,[2] **Liang Chen**,[3] **and Jing Tu**[2]

[1]*Department of Oncology, Chongqing General Hospital, Chongqing 401147, China*
[2]*Department of Pulmonary and Critical Care Medicine, Chongqing General Hospital, Chongqing 401147, China*
[3]*Intensive Care Unit, Chongqing General Hospital, Chongqing 401147, China*

Correspondence should be addressed to Jing Tu; tujing2019@ucas.edu.cn

Received 22 August 2022; Revised 11 September 2022; Accepted 14 September 2022; Published 3 October 2022

Academic Editor: Fu Wang

Lung adenocarcinoma (LUAD) is the most common subtype of nonsmall cell lung cancer. Cytochrome c (Cyt c), which is produced from mitochondria, interacts with a protein called Apaf-1 to form the heptameric apoptosome. This heptameric apoptosome then activates the caspase cascade, which ultimately results in the execution of apoptosis. The purpose of our research was to discover a new prognostic model that is based on cytochrome c-related genes (CCRGs) for LUAD patients. Through LASSO regression analysis conducted on the LUAD datasets included in the TCGA datasets, a CCRGs signature was created. The diagnostic accuracy of the multigene signature was verified by an independent source using the GSE31210 and GSE72094 datasets. The GO and KEGG enrichment analysis were performed. In this study, there were 159 differentially expressed CCRGs in the TCGA dataset, while there were 68 differentially expressed CCRGs in the GSE31210 dataset. Additionally, there were 57 genes that overlapped across the two datasets. Using LASSO and Cox regression analysis, a signature consisting of 12 differentially expressed CCRGs was developed from the total of 57 such genes. On the basis of their risk ratings, patients were categorized into high-risk and low-risk categories, with low-risk patients having lower risk scores and a greater likelihood of surviving the disease. Univariate and multivariate analyses both concluded that this signature is an independent risk factor for LUAD. ROC curves demonstrated that this risk signature is capable of accurately predicting the 1-year, 2-year, 3-year, and 5-year survival rates of patients who have LUAD. The infiltration of antigen-presenting cells was higher in the low-risk group, such as aDCs, DCs, pDCs, and iDCs. The expression of multiple immune checkpoints was significantly higher in the low-risk group, such as BTLA, CD28, and CD86. Finally, we showed that the signature can be used to predict the drug sensitivity of already available or under investigational drugs. Overall, patient classification and individualized therapy options may benefit from this study's development of a powerful gene signature with high value for prognostic prediction in LUAD.

1. Introduction

One of the most frequent forms of cancer is the lung cancer which has reached epidemic proportions in recent years [1]. It poses a significant threat to human health and quality of life, ranking third most frequent behind breast and prostate cancers [2, 3]. Researchers studying cancer all over the world have been concentrating their efforts on the lung cancer. Nonsmall cell lung cancer (NSCLC) is the most common histological subtype of lung cancer and accounts for roughly 85 percent of newly diagnosed cases [4, 5]. Lung adenocarcinoma, also known as LUAD, is a subtype of NSCLC that has a high morbidity and mortality rate. In recent years, there have been considerable advancements in the treatment choices for persons who have been diagnosed with LUAD [6, 7]. These options include chemotherapy, radiation, and immunotherapy. Despite this, there is still a percentage of patients who have distant metastases and are unable to be treated effectively at an early stage due to a lack of sensitive biomarkers, resulting in poor 5-year survival rates [8, 9]. Hence, it is of the utmost need to find more efficient biomarkers for early diagnosis, therapy, and evaluation of prognosis.

A large protein complex known as the "apoptosome" is formed when cytochrome c (Cyt c) is released from mitochondria and interacts with an adaptor protein called apoptotic protease activating factor-1 (Apaf-1) [10, 11]. This complex then recruits and activates caspase-9, which begins the caspase cascade and the process of apoptosis. Thus, in the process of apoptosome-mediated caspase activation, the interaction between Cyt c and Apaf-1 is a crucial upstream event [12]. The "Warburg effect" describes the tendency of most cancer cells to rely more heavily on aerobic glycolysis rather than OxPhos as their primary source of energy [13, 14]. Cancer cells must go through the process of metabolic reprogramming in order to boost anabolic biomass production, which is necessary for cell growth. Cancer is characterized by a number of key features, including dysregulation of cellular energetics and resistance to cell death. Cyt c is a protein that sits at the crossroads of several different pathways that can lead to both of these different carcinogenesis mechanisms [15, 16]. The significance of Cyt c in tumor angiogenesis, cell proliferation, as well as cellular differentiation and apoptosis has been shown by previous research. Nevertheless, the possible regulatory mechanism it possesses is not completely understood. In the past 20 years, there has been a recent uptick in research on the microenvironment of cancers, namely how immune cells play a pivotal part in the development of cancer. Cyt c has been shown in previous research to be able to influence the status of a tumor's immune microenvironment in a number of distinct ways, including encouraging the recruitment of innate immune cells and inhibiting the differentiation and functions of adaptive immune cells [17, 18]. Thus, it is necessary to conduct additional research on the link between Cyt c and immunity in LUAD in order to come up with innovative approaches to the treatment.

In our work, our group is aimed at thoroughly examining the roles of cytochrome c-related genes in LUAD and at developing a novel model based on cytochrome c-related gene signature. We anticipate that the findings of our research will provide a more in-depth understanding of the role that cytochrome c-related genes play in LUAD.

2. Methods and Materials

2.1. Data Acquisition. The transcriptome data of 535 LUAD and 59 para-tumor samples were retrieved from TCGA datasets. The clinical data and mutation data were also downloaded for survival analysis and tumor mutation burden (TMB) analysis, respectively. The GSE31210 dataset consisted of 226 tumor samples and 20 nontumor samples was obtained from GEO datasets. The GSE72094 dataset was downloaded as validation dataset, including 442 LUAD patients. The cytochrome c-related genes (CCRGs) were downloaded from GeneCards database (https://www.genecards.org), and 781 genes were screened for subsequent analysis according to the relevance score greater than 10 (Table S1).

2.2. Functional Enrichment Analysis of Differentially Expressed CCRGs. The differentially expressed CCRGs of TCGA dataset and GSE31210 were examined by the use of FDR < 0.05 and |logFC| > 1 using 'limma' package [19]. Subsequently, the 'Venn' package used to find out their intersection genes. The GO analysis was conducted in Metascape (https://metascape.org). The KEGG analysis was conducted using 'clusterProfiler' package [20].

3. Construction of a CCRGs Signature

A univariate Cox regression analysis was used to identify prognosis-related CCRGs utilizing the TCGA dataset as a training cohort. To create the prognostic CCRGs signature, we used LASSO Cox regression analysis, an approach that can prevent over fitting. The signature was as risk score = $e^{\mathrm{sum}(\mathrm{eachgene's normalizedexpression} \times \mathrm{eachgene's correspondingcoefficient})}$. Patients were sorted into high-risk group and low-risk group as the median score of CRGs signature was the threshold.

3.1. Verification of CCRGs Signature Performance. Using the GSE31210 and GSE72094 as testing cohorts, the contents of verifying the performance including survival analysis, ROC curve, PCA, and t-SNE analysis were performed. Univariate and multivariate assays were carried out to explore the independent performance.

3.2. Immune Microenvironment and the CCRGs Signature. By the use of the ESTIMATE algorithm, the enrichment degree of immune cells and stromal cells in each sample was calculated [21]. The single sample gene set enrichment analysis (ssGSEA) was conducted to estimate the enrichment scores of sixteen immune cells to explore the relationship between the signature and immune cells using 'GSEABase' package [22].

3.3. Immunotherapy and the CCRGs Signature. The relationship between the signature and immune checkpoints was also explored to explore whether immune checkpoint blockade (ICB) was different in different groups of patients. Tumor Immune Dysfunction and Exclusion (TIDE) algorithm could predict the effect of different groups of patients on anti-PD-1 and anti-CTLA-4 immunotherapy. The TIDE score was negatively correlated with the response effect of ICB treatment.

3.4. Tumor Mutation Burden and the CCRGs Signature. Higher TMB was associated with better ICB outcomes. We compared the difference in TMB between the two risk groups to predict the effect of ICB therapy. The mutation of CCRGs was explored on the cBioPortal database (http://www.cbioportal.org).

3.5. Chemotherapy and the CCRGs Signature. The CellMiner (https://discover.nci.nih.gov/cellminer) is a public database resource that provides drug sensitivity information files. We downloaded drug sensitivity information files from it and selected gene targeting drugs, which were approved by the Food and Drug Administration (FDA). The *P* value was shorted from small to large, and the first 16 analysis results were visualized.

3.6. Statistical Analysis. All statistical analyses were performed by R software (Version 4.2.1). A *P* value less than

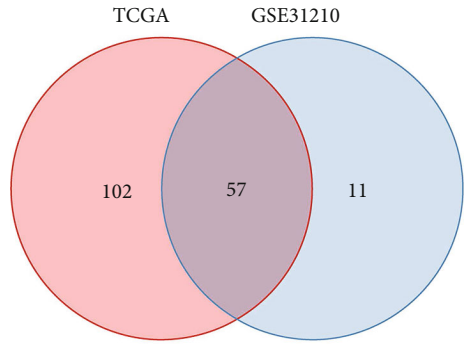

(a)

(b)

Figure 1: Continued.

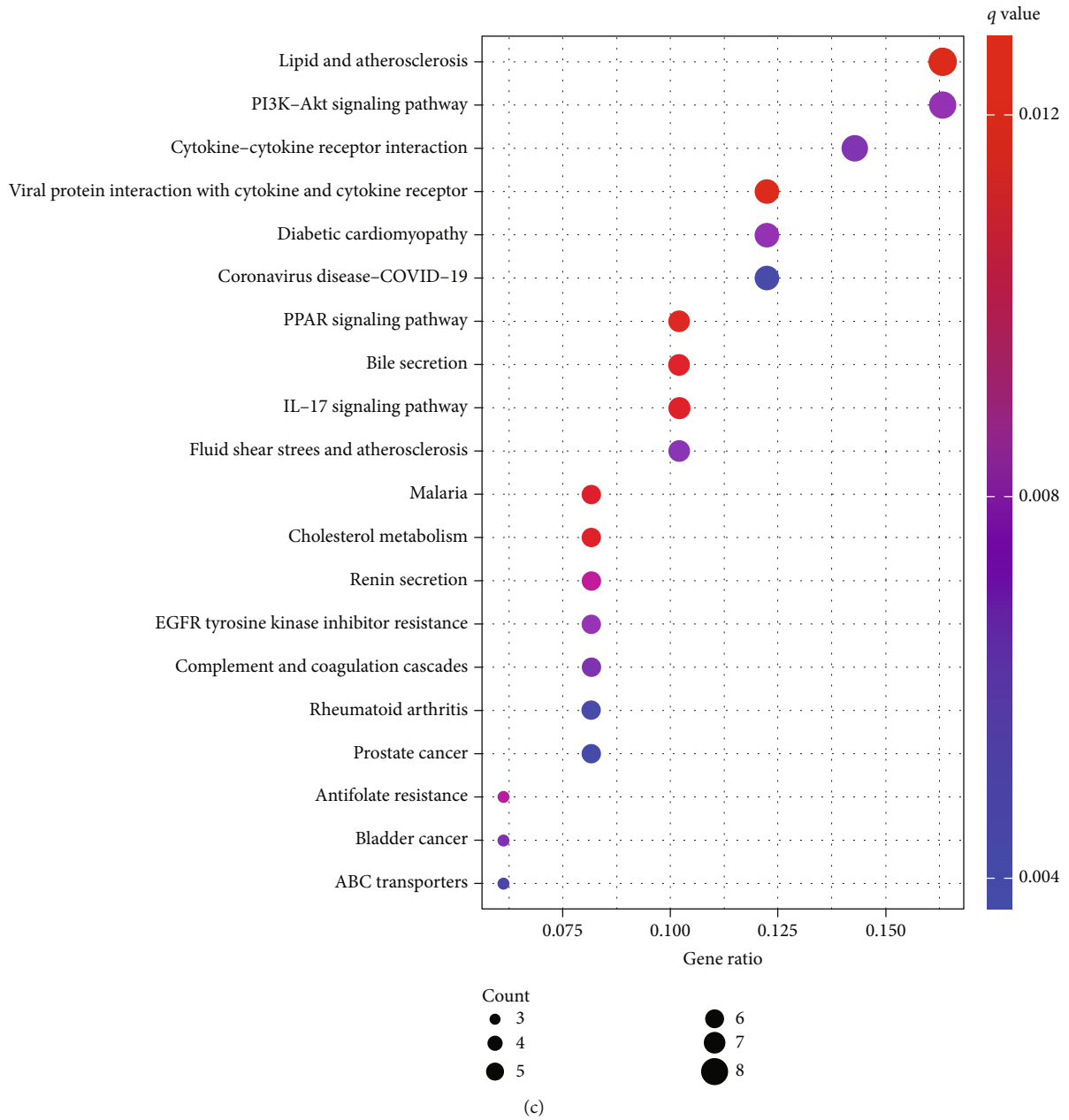

(c)

Figure 1: Continued.

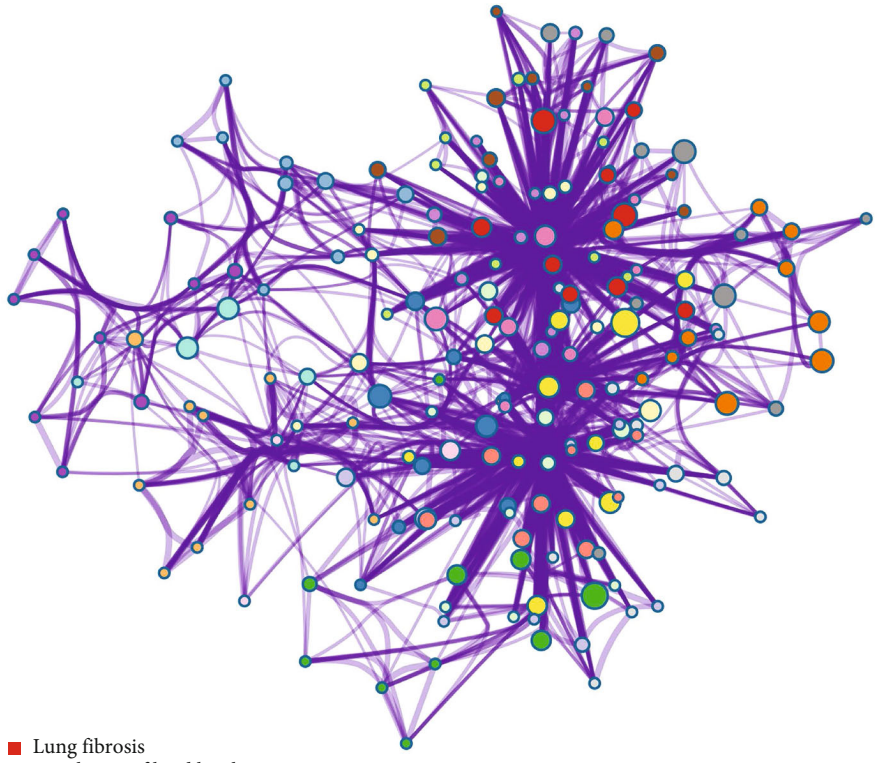

(d)

Figure 1: The expression and function enrichment of differentially expressed 57 CCRGs. (a) Venn Diagram. (b) Heatmap. (c) KEGG analysis. (d) GO analysis.

0.05 was considered statistically different. Student's t-test and one-way ANOVA were, respectively, employed to evaluate two or multiple groups, for statistical significance. Differences in LUAD patient survival were assessed using the Kaplan-Meier method. A Cox regression analysis was adopted to assess the prognostic factors. Differences were considered statistically significant when $P < 0.05$.

4. Result

4.1. Differentially Expressed CCRGs and Functional Enrichment. There were 159 differentially expressed CCRGs in TCGA dataset and 68 differentially expressed CCRGs in GSE31210, and there were 57 intersect genes (Figure 1(a)). The heatmap was used to show the differential expression of these 57 genes (Figure 1(b)). The KEGG analysis showed that 57 genes were enriched in PI3K-Akt signaling pathway, PPAR signaling pathway, EGFR tyrosine kinase inhibitor resistance, and so on (Figure 1(c)). GO assays revealed that 57 genes were participated in lung fibrosis, regulation of lipid localization, cellular response to lipid, and so on (Figure 1(d)). Our data may indicate that 57 genes were involved in the development of lung diseases and were related to EGFR-TKI treatment of lung cancer.

4.2. Construction of the CCRGs Signature. Of the 57 differentially expressed CCRGs, 20 genes were associated with prognosis (Figure 2(a)). Finally, a 12-CCRGs signature was

	p value	Hazard ratio
SFTPC	0.001	0.931 (0.891–0.973)
CYP27C1	0.043	1.229 (1.007–1.502)
CYP24A1	0.009	1.105 (1.025–1.190)
CYP4B1	<0.001	0.856 (0.794–0.924)
LPL	0.022	0.885 (0.797–0.982)
UBE2C	0.008	1.148 (1.036–1.272)
FGF2	0.015	1.482 (1.079–2.035)
SLC2A1	<0.001	1.293 (1.150–1.454)
MIF	0.022	1.230 (1.030–1.469)
BIRC5	0.001	1.238 (1.088–1.408)
CDKN3	<0.001	1.327 (1.147–1.535)
KRT8	<0.001	1.445 (1.205–1.734)
MMP1	0.047	1.078 (1.001–1.161)
CDK1	<0.001	1.286 (1.116–1.481)
CCNB1	<0.001	1.343 (1.158–1.557)
CDC20	0.003	1.200 (1.064–1.353)
OLR1	0.033	0.880 (0.782–0.990)
MKI67	<0.001	1.321 (1.139–1.532)
FA2H	0.041	1.132 (1.005–1.274)
ADRB2	0.001	0.673 (0.530–0.856)

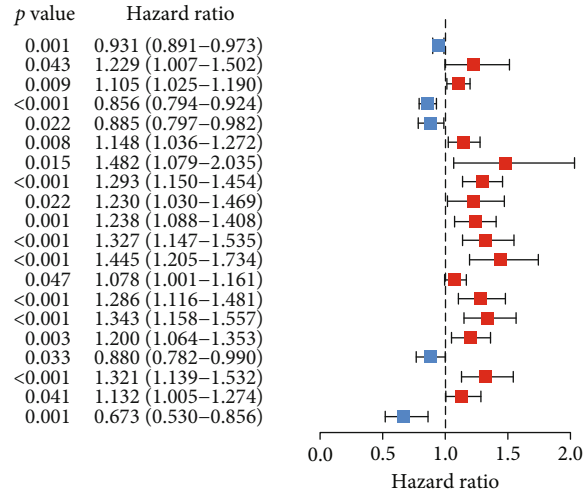

(a)

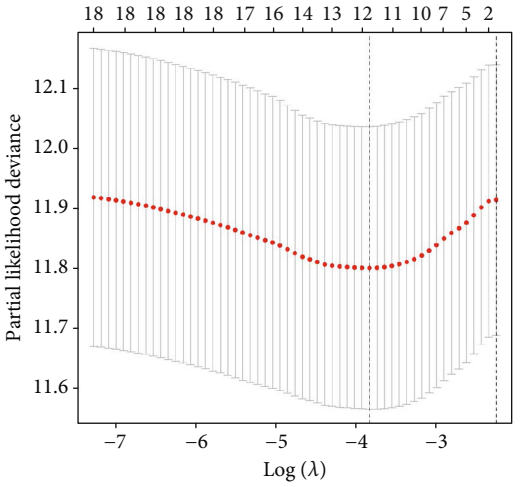

(b)

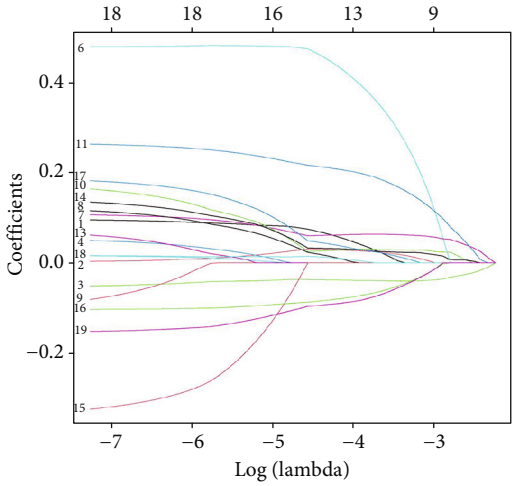

(c)

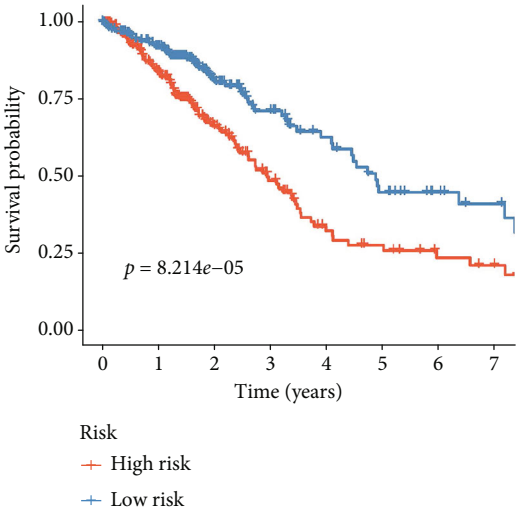

(d)

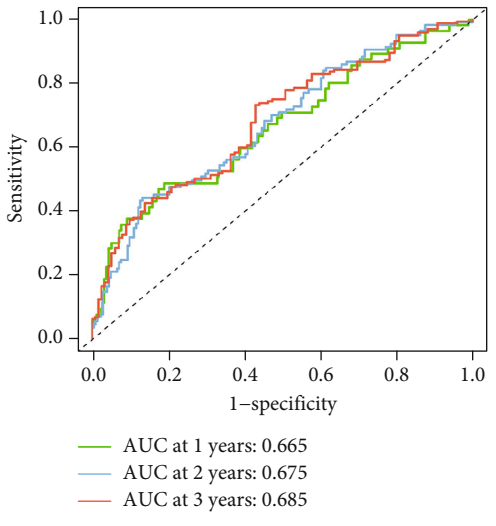

(e)

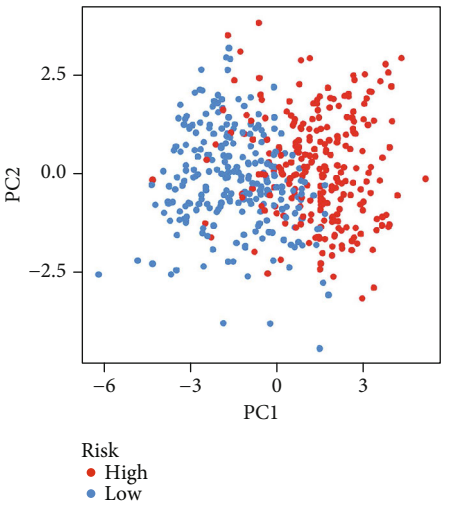

(f)

Figure 2: Continued.

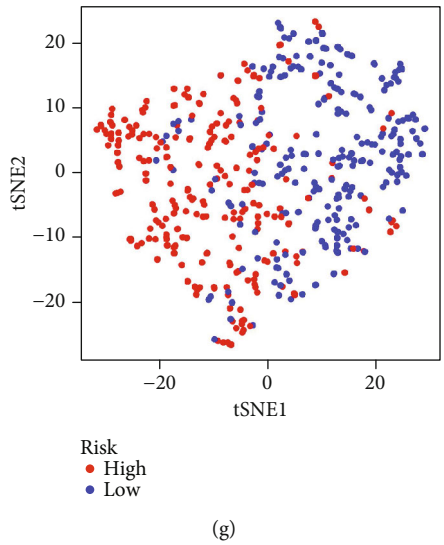

(g)

Figure 2: The construction of the CCRGs signature using TCGA training cohort. (a) Screening prognosis-related genes. (b) The process of selecting the appropriate penalty parameters. (c) The process of selecting 12-CCRGs to construct the signature. (d) The survival analysis. (e) The ROC curve. (f) PCA. (g) The t-SNE analysis.

constructed using LASSO Cox regression analysis (Figures 2(b) and 2(c)). The risk score = (0.034772098 ∗ CYP27C1) + (0.025435421 ∗ CYP24A1) + (−0.038721339 ∗ CYP4B1) + (0.378091608 ∗ FGF2) + (0.063388606 ∗ SLC 2A1) + (0.030467492) ∗ CDKN3 + (0.193865279) ∗ KRT8 + (0.027231488 ∗ CCNB1) + (−0.069261881 ∗ OLR1) + (0.026932373 ∗ MKI67) + (0.002432304) ∗ FA2H + (−0.07 8693326 ∗ ADRB2). The survival analysis of TCGA dataset showed that the survival probability of high-risk group was distinctly lower than the low-risk group (Figure 2(d)). The AUC at 1, 2, and 3 years were 0.665, 0.675, and 0.685 (Figure 2(e)). PCA and t-SNE analyses demonstrated that high-risk group patients were clearly distinguished from low-risk group (Figures 2(f) and 2(g)).

4.3. Validation of the CCRGs Signature. The GSE31210 and GSE72094 were used to validate the performance of CCRGs signature. The survival probability of high-risk groups in two testing datasets was lower than the low-risk groups (Figures 3(a) and 3(b)). The AUC of GSE31210 at 1, 2, and 3 years were 0.664, 0.668, and 0.611 (Figure 3(c)). The AUC of GSE72094 at 1, 2, and 3 years were 0.689, 0.669, and 0.671 (Figure 3(d)). The result of PCA and t-SNE analyses also showed that patients in two groups were clearly distinguished (Figures 3(e)–3(h)). What is more, the Cox assays were both showed that the CCRGs signature was an independent predictor (Figures 3(i) and 3(j)). The result all demonstrated that the 12-CCRGs signature had stable performance.

4.4. Immune Microenvironment and the CCRGs Signature. The infiltration degree of immune cells and stromal cells were negatively related to risk-score (Figures 4(a) and 4(b)), suggesting a distinct association between risk-score and immune microenvironment. The infiltration of antigen-presenting cells was higher in the low-risk group, such as aDCs, DCs, pDCs, and iDCs (Figure 4(c)). The infiltration of T helper cells and TIL was also higher in the low-risk group. Correspondingly, the antigen presentation process and HLA expression in the low-risk group were more active (Figure 4(d)).

4.5. Immunotherapy and the CCRGs Signature. The expression of multiple immune checkpoints was significantly higher in the low-risk group, such as BTLA, CD28, and CD86. While the expression of PDCD1 (also known as PD-1) was higher in the high-risk group, it may indicate that the high-risk group had a better response to anti-PD-1 immunotherapy (Figure 5(a)). Further, the TIDE score of high-risk group was lower than the low-risk group, also indicating the high-risk group had a better response to anti-PD-1 or anti-CTLA4 immunotherapy (Figure 5(b)).

4.6. Tumor Mutation Burden and the CCRGs Signature. The TMB of high-risk group was 94.63% and significantly higher than the low-risk group, indicating that the high-risk group may have better ICB outcomes than the low-risk group (Figures 6(a)–6(c)). There were mutations in all 12 CCRGs (Figures 7(a)–7(m)) except FGF2, the common mutation type was amplification. The mutation rate of MKI67 was 6%, ranking the first at all 12 CCRGs, and the mutation rate of FGF2 was only 0.5%. Mutations in these genes may affect the effect of treatment.

4.7. Chemotherapy and the CCRGs Signature. Many of 12 signature CCRGs were sensitive to EGFR-TKI, such as CYP24A1, FA2H, FGF2, KRT8, and MKI67 were sensitive to Afatinib, ADRB2, CYP24A1, FA2H, FGF2, and MKI67 were sensitive to Dacomitinib, and SLC2A1, ADRB2, FGF2, and KRT8 were sensitive to Dasatinib. However, CYP27C1, CYP4B1, CDKN3, CCNB1, and OLR1 were

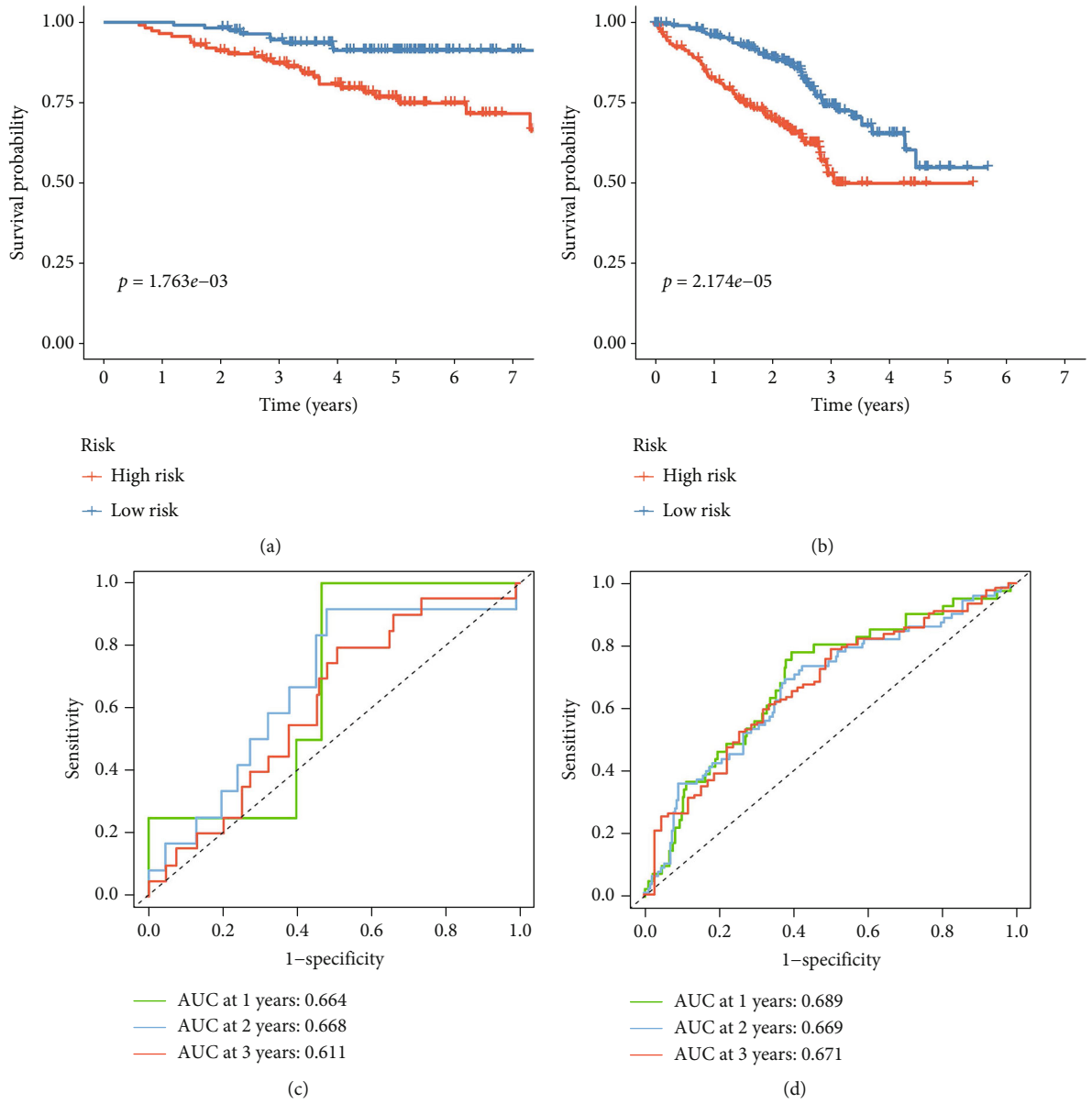

Figure 3: Continued.

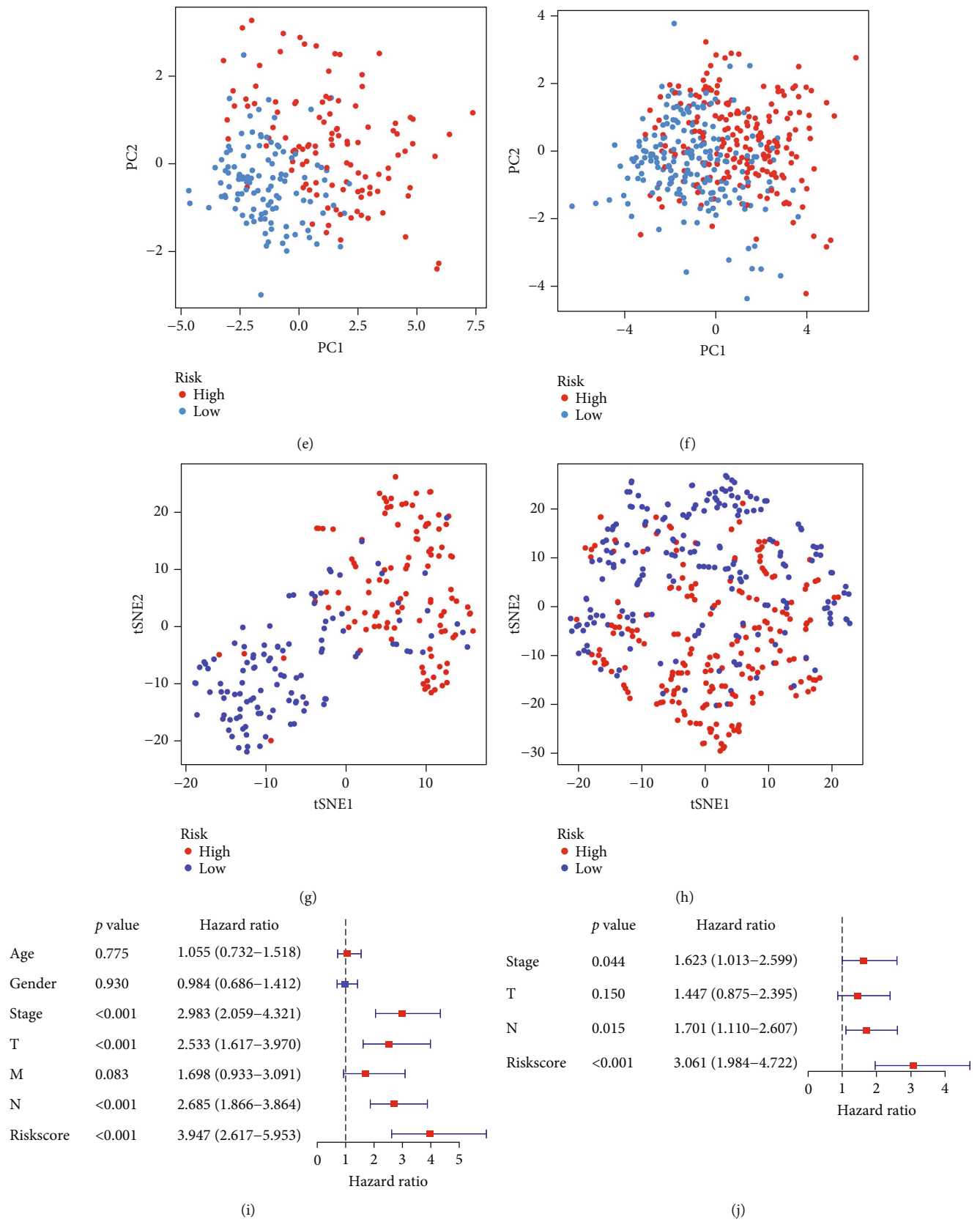

Figure 3: Validation of the CCRGs signature using two GEO datasets. (a) The survival analysis of GSE31210. (b) The survival analysis GSE72094. (c) The ROC curve of GSE31210. (d) The ROC curve of GSE72094. (e) PCA of GSE31210. (f) PCA of GSE72094. (g) The t-SNE analysis of GSE31210. (h) The t-SNE analysis of GSE72094. (i) Independence analysis using univariate Cox regression analysis. (j) Independence analysis using multivariate Cox regression analysis.

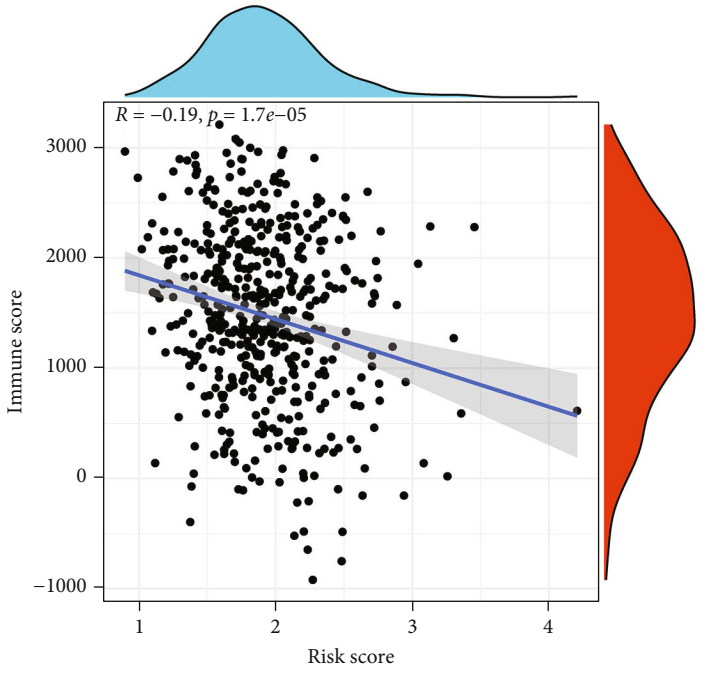

(a)

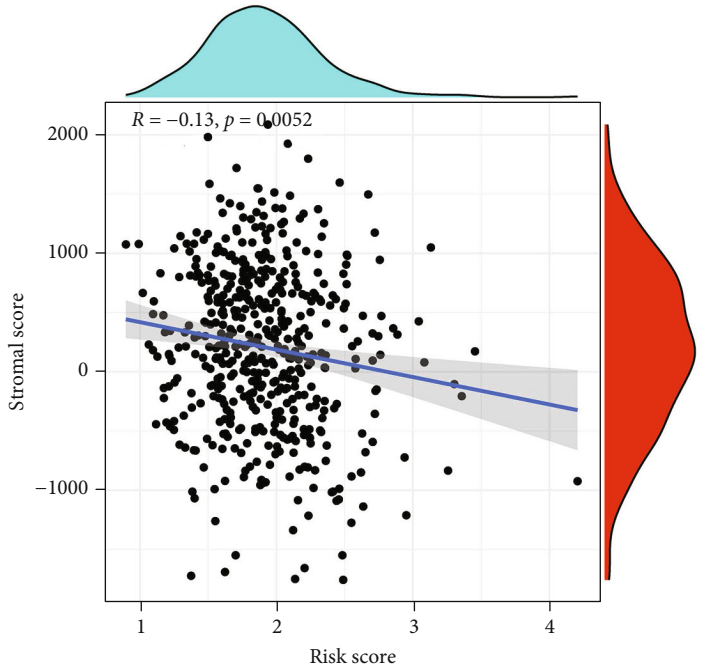

(b)

Figure 4: Continued.

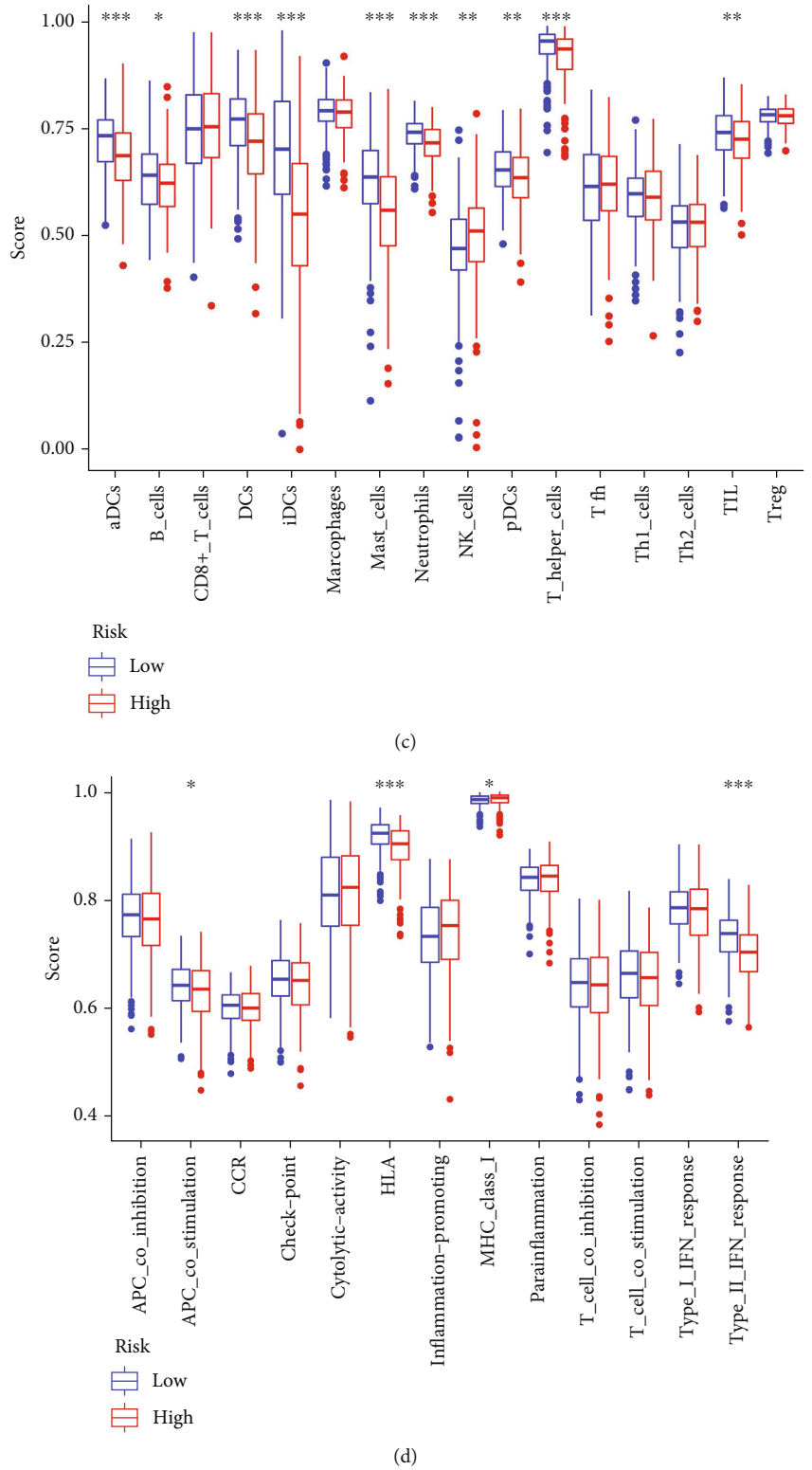

Figure 4: Immune related analysis of the CCRGs signature. (a) The infiltration of immune cells using ESTIMATE algorithm. (b) The infiltration of stromal cells using ESTIMATE algorithm. (c) The infiltration of immune cells using ssGSEA. (d) The analysis of immune related functions.

resistant to many drugs. CDKN3 and CCNB1 were both resistant to Denileukin Diftitox (Ontak). CYP4B1 was resistant to Encorafenib, Pazopanib, Carmustine, and so on. CYP27C1 was sensitive to Ibrutinib, while it was resistant to Cobimetinib, Trametinib, Oxaliplatin, and so on. It was shown that there were no OLR1 sensitive drugs, but many resistant drugs, such as Sulfatinib, Paclitaxel, Vinblastine, and Vincristine (Figure 8).

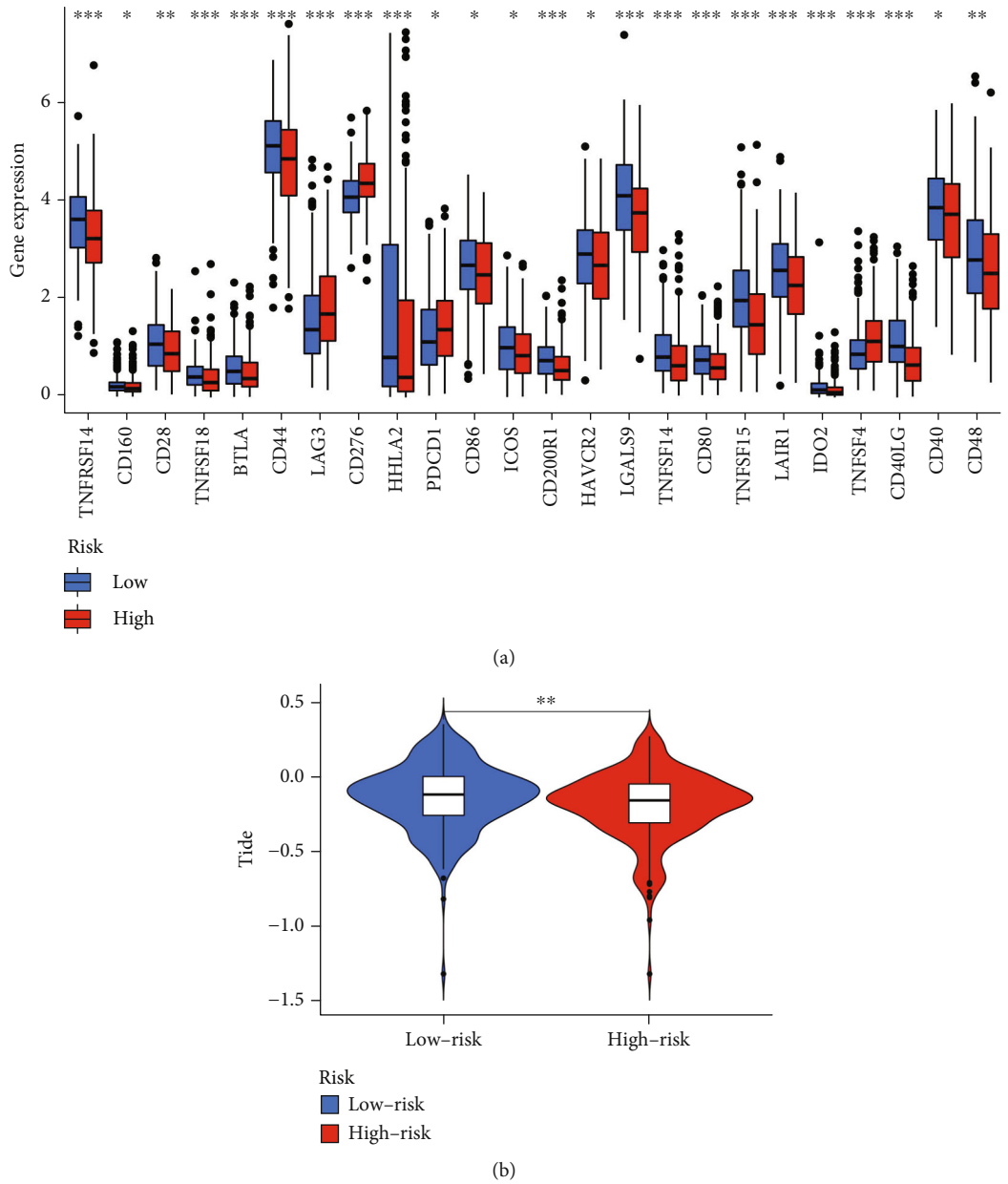

Figure 5: The application of the CCRGs signature in predicting the effect of immunotherapy. (a) The expression of immune checkpoint in predicting the effect of immunotherapy. (b) TIDE algorithm in predicting the effect of immunotherapy.

5. Discussion

When it comes to health issues, lung cancer is ranked in second place, and it is the leading cause of death due to cancer in the entire world [23]. Nonsmokers are thought to have the highest prevalence of LUAD than smokers. Because of the proliferation of antismoking campaigns, the incidence of LUAD is quickly climbing to alarming levels [24, 25]. Even though there has been significant progress made in the treatment of cancer, the overall survival rate of LUAD patients continues to be unsatisfactory because there are no good early prognostic indications [26, 27]. More and more pieces of evidence have emerged in recent years linking CCRGs to the initiation and progression of various cancers. The results suggest a role for CCRGs in tumor development and progression. Therefore, to improve the outcomes of LUAD patients, it is absolutely necessary to locate reliable CCRGs markers. Because of this work, a predictive risk signature that is based on CCRGs has been successfully established for predicting the overall survival of patients with LUAD.

We firstly analyzed TCGA and GSE31210 to screen the differentially expressed CCRGs and identified 57 intersect genes. The KEGG analysis showed that 57 genes were enriched in PI3K-Akt signaling pathway, PPAR signaling pathway, EGFR tyrosine kinase inhibitor resistance, and so on, suggesting that the 57 differentially expressed CCRGs play an important role in tumor progression. After doing a

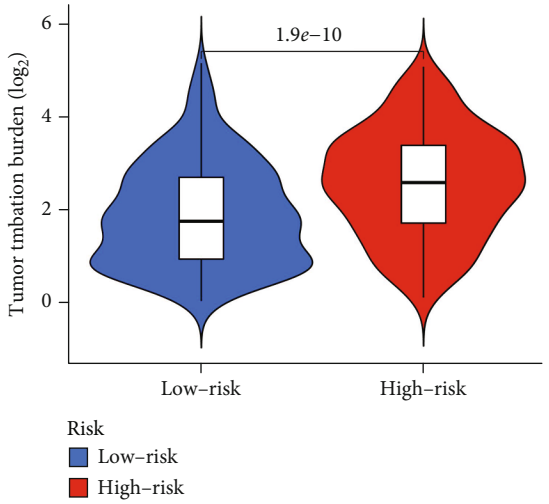

(a)

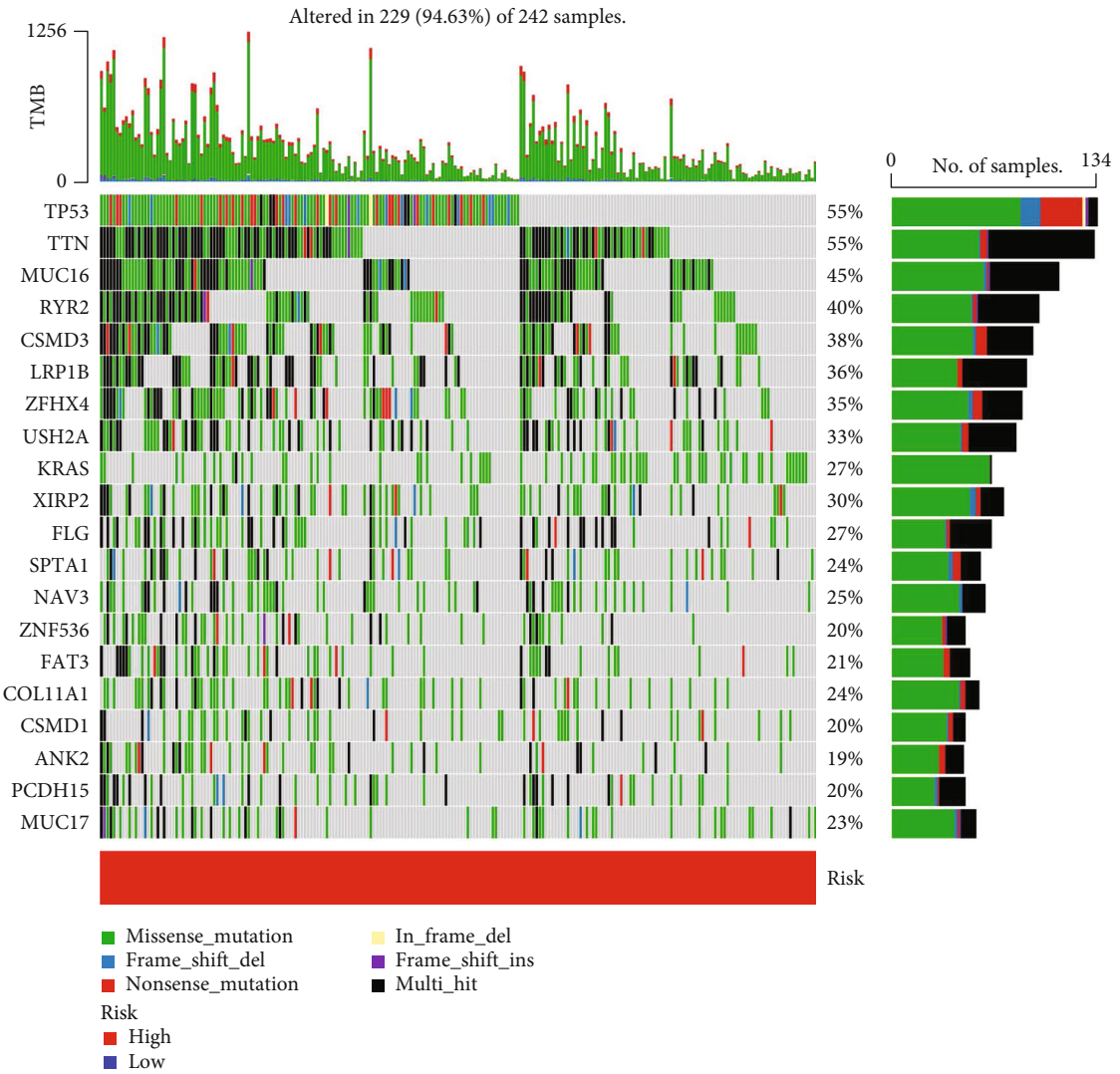

(b)

Figure 6: Continued.

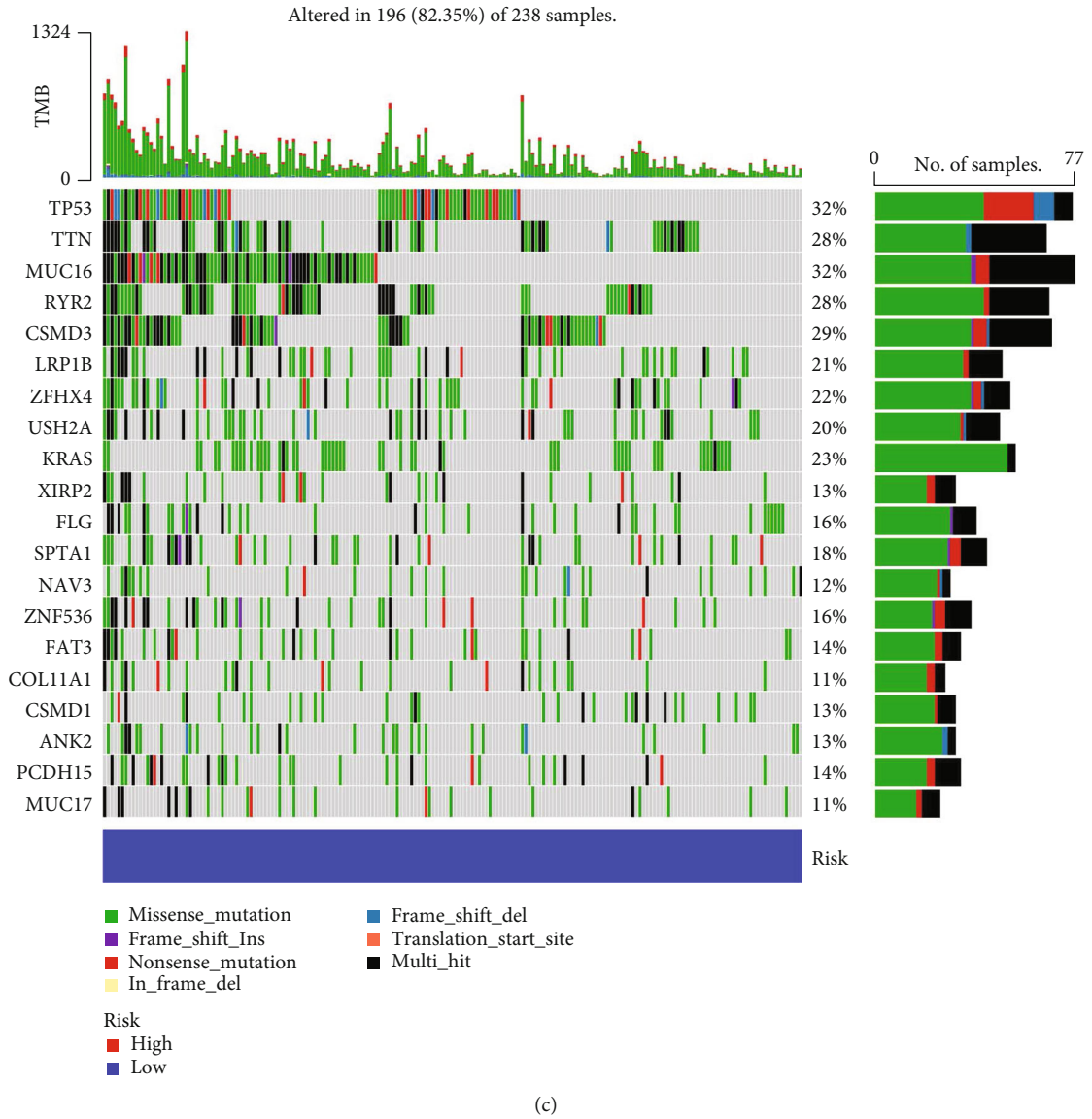

(c)

Figure 6: TMB and the CCRGs signature. (a) Comparison of TMB in two risk groups. (b) TMB of high-risk group. (c) TMB of low-risk group.

LASSO Cox analysis, we isolated 16 CCRGs from these DEGs in order to construct a predictive signature consisting of 12 CCRGs. These genes had a role in the development of malignancies and had an impact on the prognosis of patients by recognizing and presenting antigens in the immune system. The function of the 12 CCRGs has been reported in several tumors, including LUAD. For instance, it was found that the degree of CCNB1 expression was clinically linked with a number of clinicopathological characteristics, such as gender, smoking status, tumor stage, and tumor stage. According to the findings of a survival analysis, a greater level of CCNB1 was associated with a more dismal outcome in terms of both overall survival and disease-free survival. In terms of its functionality, the degradation of CCNB1 by APC11 via UBA52 ubiquitylation was essential for the development of the cell cycle and the proliferation of NSCLC cell lines [28]. Mo et al. reported that the inhibition of CYP27C1 led to an increase in cell proliferation, migration, and invasion through the control of the signaling cascade involving IGF-1R, Akt, and p53 [29]. Xie et al. found that KRT8 is overexpressed in LUAD tissues, and its expression may be able to independently predict poor OS and RFS for LUAD patients, but not for LUSC patients. However, KRT8 is not overexpressed in LUSC tissues [30]. Xu et al. reported that in NSCLC cells, treatment with VEGFR2-TKIs led to an increase in the expression of ADRB2. By blocking the ADRB2 signaling pathway in NSCLC cells in vitro and in vivo, propranolol, a common ADRB2 antagonist, dramatically increased the therapeutic efficacy of VEGFR2-TKIs. This was demonstrated both in vitro and in vivo. Mechanically, NSCLC patients developed resistance to VEGFR2-TKIs as a result of the treatment-induced overexpression of ADRB2 and the strengthening of the interaction between ADRB2 and VEGFR2. Additionally, cells became more sensitive to VEGFR2-TKIs after the suppression of the ADRB2, CREB, and PSAT1 signaling pathway [31]. Overall, our

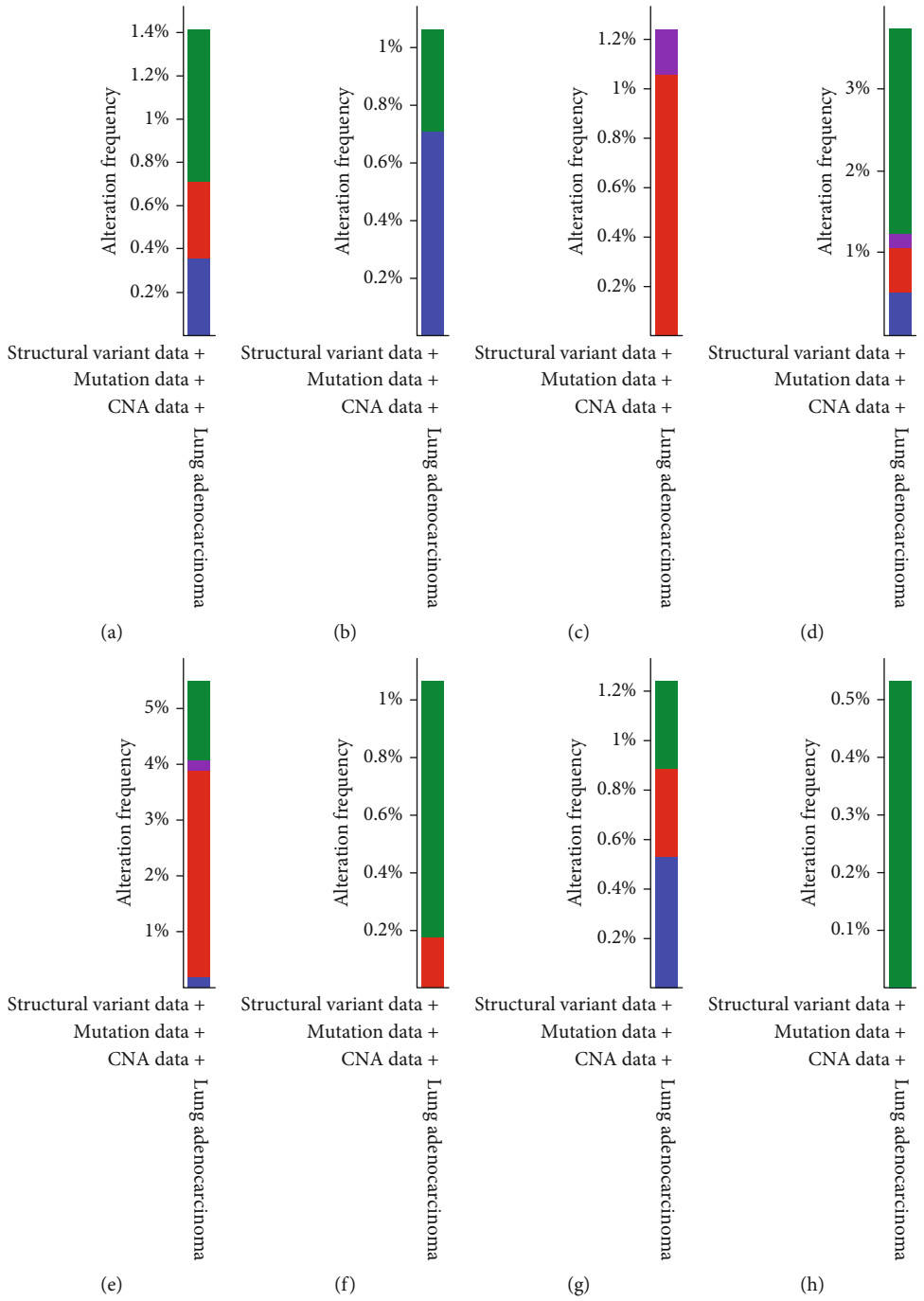

Figure 7: Continued.

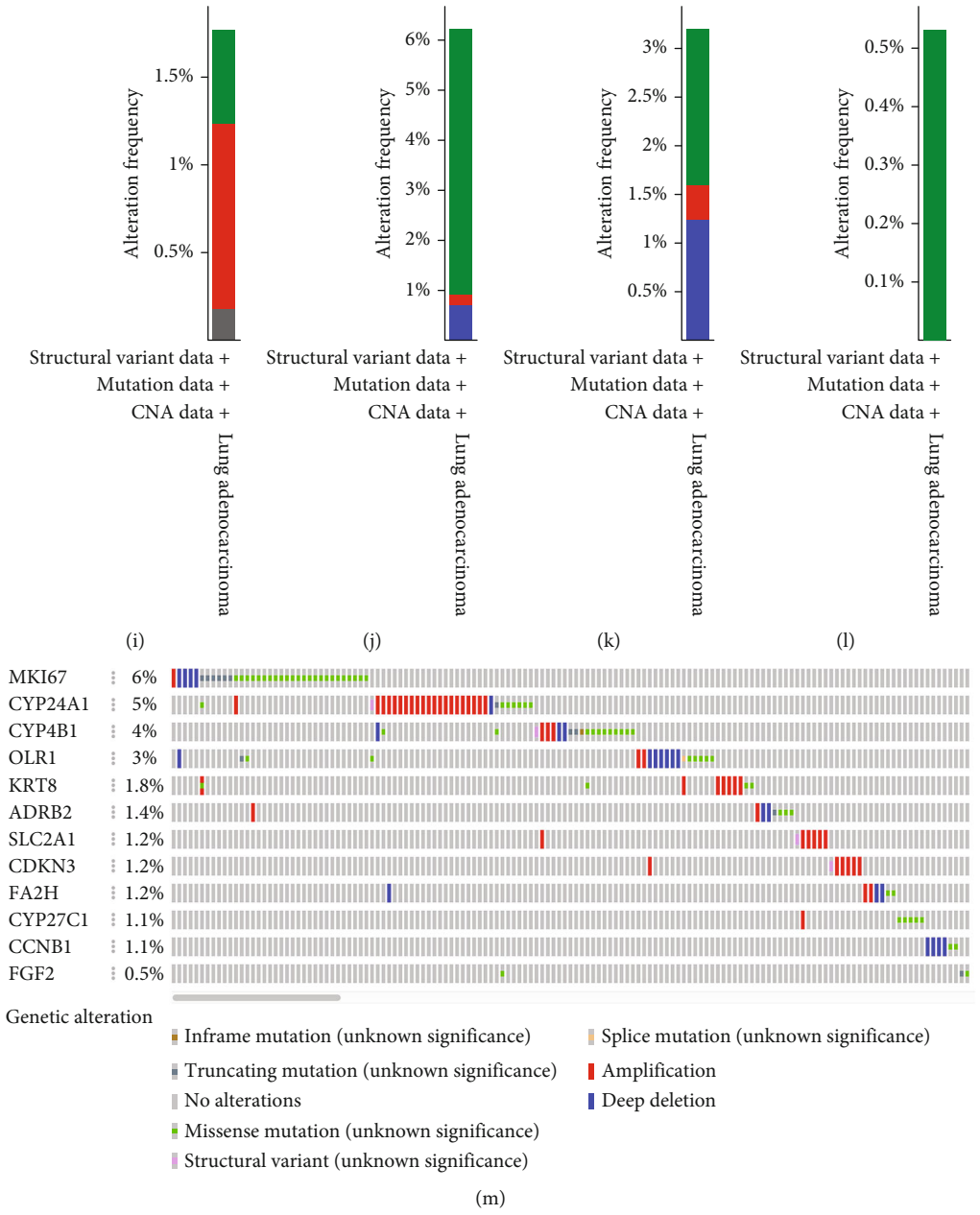

Figure 7: The mutation of 12 CCRGs. (a) ADRB2. (b) CCNB1. (c) CDKN3. (d) CYP4B1. (e) CYP24A1. (f) CYP27C1. (g) FA2H. (h) FGF2. (i) KRT8. (j) MKI67. (k) OLR1. (l) SLC2A1. (m) Summary of mutations in 12 CCRGs.

findings suggested the 12 CCRGs served as tumor promotor or tumor suppressors.

All patients diagnosed with LUAD were split into two groups according to our model (high group and low group). According to the results of the survival tests, the new prognostic signature was able to assist medical professionals in classifying patients diagnosed with LUAD into two categories that have considerably different OS. The prognostic signature's ROC showed reasonable predictive accuracy in OS prediction for patients with LUAD, and it displayed good discrimination capacity of OS in subgroup analysis. The risk score of the prognostic signature was found to be capable of functioning as an independent prognostic factor after being subjected to multivariate Cox regression analysis. In addition, our findings were supported by further evidence found in the datasets GSE31210 and GSE72094.

Immunotherapy is a relatively new approach to cancer treatment that is receiving a growing amount of attention across a variety of cancer types, including LUAD [32]. However, the identification of patients who are most likely to benefit from immunotherapy is still something that has to be watched. For the treatment of patients who have cancer, immunotherapy checkpoint inhibitors are now being used and evaluated in either preclinical or clinical trials [33, 34]. This is because immunotherapy checkpoint inhibitors are an essential part of the immunotherapy strategy. The immunological milieu of the tumors is highly infiltrated with immune cells and contains a wide variety of

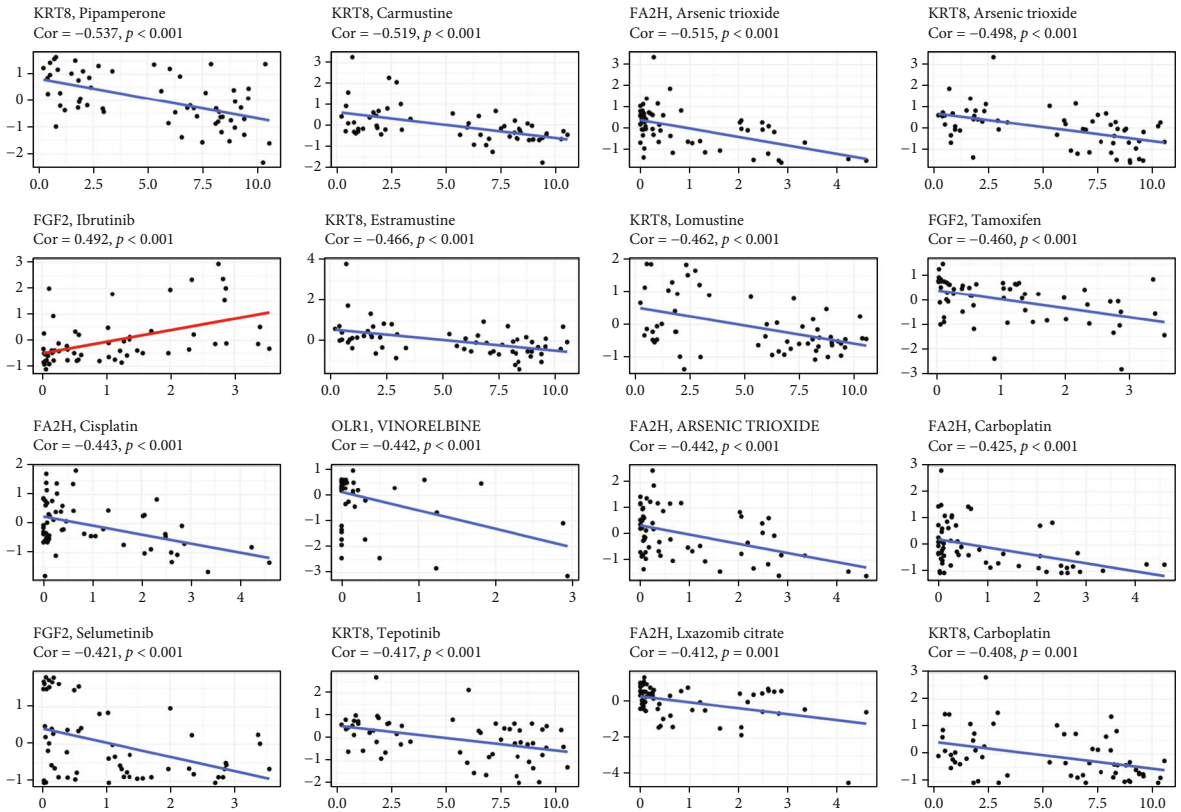

Figure 8: The application of the CCRGs signature in predicting the effect of chemotherapy.

immunomodulatory chemicals. This may have a significant bearing on the immunotherapeutic resistance and efficacy of the disease. We discovered that high-risk groups with shorter OS exhibited lower scores in aDCs, DCs, pDCs, and iDCs. These findings implied that an imbalanced and dynamic immune modulation was involved in the progression of LUAD. In addition, the elevated levels of T cell exhaustion markers that are brought about by continuous antigenic stimulation can result in the functional loss of CD8+ T cells [35, 36]. The expression of multiple immune checkpoints was significantly higher in the low-risk group, such as BTLA, CD28, and CD86. While the expression of PD-1 was higher in the high-risk group, it may indicate that the high-risk group had a better response to anti-PD-1 immunotherapy. Further, the TIDE score of high-risk group was lower than the low-risk group, also indicating the high-risk group had a better response to anti-PD-1 or anti-CTLA4 immunotherapy. Thus, a potential therapeutic approach for LUAD may consist of combining immunotherapy with the targeting of Cytochrome c-related ICD.

A key contributor to unfavorable clinical outcomes in cancer patients undergoing chemotherapy is the development of acquired resistance. If genes of sensitivity to anticancer treatments could be identified, it would be possible to improve the antitumor efficacy of chemotherapeutic drugs while simultaneously reducing their hazardous side effects. Then, we inquired as to whether particular regulators have the ability to forecast how a drug will react in a patient and the possible treatments that are available for LUAD. We found that many of 12 signature CCRGs were sensitive to EGFR-TKI, such as CYP24A1, FA2H, FGF2, KRT8, and MKI67 were sensitive to Afatinib, ADRB2, CYP24A1, FA2H, FGF2, and MKI67 were sensitive to Dacomitinib, and SLC2A1, ADRB2, FGF2, and KRT8 were sensitive to Dasatinib. Our findings suggested the genes in our prognostic model can be used as targets to predict drug sensitivity.

However, our study has several limitations. Firstly, the data originated from two different datasets, each of which had a small sample size. Moving forward, more thorough analyses will need to be conducted using large-scale and independent cohorts. Secondly, it should be noted that the clinical information that is offered by the TCGA data set is insufficient. There is a lack of knowledge regarding stages and grades for some individuals, in addition to a lack of data regarding treatments such as surgery, radiation, or chemotherapy. Thirdly, on the basis of investigations conducted in vitro and in vivo, the underlying molecular processes of LUAD that were investigated in this work have not been determined. Additional studies are necessary to broaden our understanding of cytochrome c and to foster the developments of novel therapeutic methods for LUAD patients.

6. Conclusion

In summary, we developed a reliable CCRGs genes signature that is capable of accurately assessing the clinical outcome of LUAD patients. Besides, we identified the immune microenvironments and immune targets were different between risk

groups, which may be an explanation for unfavorable outcome in the high-risk group. In the meanwhile, our research might identify potentially useful targets that can boost the efficiency of cancer immunotherapy.

Data Availability

The data are available from the corresponding author upon request.

Conflicts of Interest

All authors declare no competing interests.

Acknowledgments

The study was supported by the High-level Medical Research Personnel Training Project of Chongqing, China, Beijing Health Alliance Charitable Foundation of China (WS817D).

Supplementary Materials

Table S1 781 cytochrome c-related genes. *(Supplementary Materials)*

References

[1] R. L. Siegel, K. D. Miller, and A. Jemal, "Cancer statistics, 2019," *CA: A Cancer Journal for Clinicians*, vol. 69, no. 1, pp. 7–34, 2019.

[2] C. Xia, X. Dong, H. Li et al., "Cancer statistics in China and United States, 2022: profiles, trends, and determinants," *Chinese Medical Journal*, vol. 135, no. 5, pp. 584–590, 2022.

[3] C. de Martel, D. Georges, F. Bray, J. Ferlay, and G. M. Clifford, "Global burden of cancer attributable to infections in 2018: a worldwide incidence analysis," *The Lancet Global Health*, vol. 8, no. 2, pp. e180–e190, 2020.

[4] R. S. Herbst, D. Morgensztern, and C. Boshoff, "The biology and management of non-small cell lung cancer," *Nature*, vol. 553, no. 7689, pp. 446–454, 2018.

[5] N. Duma, R. Santana-Davila, and J. R. Molina, "Non-small cell lung cancer: epidemiology, screening, diagnosis, and treatment," *Mayo Clinic Proceedings*, vol. 94, no. 8, pp. 1623–1640, 2019.

[6] E. N. Imyanitov, A. G. Iyevleva, and E. V. Levchenko, "Molecular testing and targeted therapy for non-small cell lung cancer: current status and perspectives," *Critical Reviews in Oncology/Hematology*, vol. 157, article 103194, 2021.

[7] E. D. Deeks, "Ceritinib: a review in ALK-positive advanced NSCLC," *Targeted Oncology*, vol. 11, no. 5, pp. 693–700, 2016.

[8] S. P. L. Saw, B. H. Ong, K. L. M. Chua, A. Takano, and D. S. W. Tan, "Revisiting neoadjuvant therapy in non-small-cell lung cancer," *The Lancet Oncology*, vol. 22, no. 11, pp. e501–e516, 2021.

[9] D. R. Camidge, R. C. Doebele, and K. M. Kerr, "Comparing and contrasting predictive biomarkers for immunotherapy and targeted therapy of NSCLC," *Nature Reviews Clinical Oncology*, vol. 16, no. 6, pp. 341–355, 2019.

[10] Y. P. Ow, D. R. Green, Z. Hao, and T. W. Mak, "Cytochrome *c* : functions beyond respiration," *Nature Reviews Molecular Cell Biology*, vol. 9, no. 7, pp. 532–542, 2008.

[11] F. J. Bock and S. W. G. Tait, "Mitochondria as multifaceted regulators of cell death," *Nature Reviews Molecular Cell Biology*, vol. 21, no. 2, pp. 85–100, 2020.

[12] H. A. Kalpage, V. Bazylianska, M. A. Recanati et al., "Tissue-specific regulation of cytochrome c by post-translational modifications: respiration, the mitochondrial membrane potential, ROS, and apoptosis," *FASEB Journal*, vol. 33, no. 2, pp. 1540–1553, 2019.

[13] D. A. Mavridou, S. J. Ferguson, and J. M. Stevens, "Cytochrome c assembly," *IUBMB Life*, vol. 65, no. 3, pp. 209–216, 2013.

[14] Z. S. Aghamiri, M. Mohsennia, and H. A. Rafiee-Pour, "Immobilization of cytochrome c and its application as electrochemical biosensors," *Talanta*, vol. 176, pp. 195–207, 2018.

[15] P. Manickam, A. Kaushik, C. Karunakaran, and S. Bhansali, "Recent advances in cytochrome c biosensing technologies," *Biosensors & Bioelectronics*, vol. 87, pp. 654–668, 2017.

[16] X. Jiang and X. Wang, "Cytochrome *C*-mediated apoptosis," *Annual Review of Biochemistry*, vol. 73, no. 1, pp. 87–106, 2004.

[17] R. Kumar, T. A. Bhat, E. M. Walsh et al., "Cytochromec deficiency confers apoptosome and mitochondrial dysfunction in African-American men with prostate cancer," *Cancer Research*, vol. 79, no. 7, pp. 1353–1368, 2019.

[18] N. Yadav, R. Gogada, J. O'Malley et al., "Molecular insights on cytochrome *c*and nucleotide regulation of apoptosome function and its implication in cancer," *Biochimica et Biophysica Acta (BBA) - Molecular Cell Research*, vol. 1867, no. 1, article 118573, 2020.

[19] M. E. Ritchie, B. Phipson, D. Wu et al., "Limma powers differential expression analyses for RNA-sequencing and microarray studies," *Nucleic Acids Research*, vol. 43, no. 7, article e47, 2015.

[20] G. Yu, L. G. Wang, Y. Han, and Q. Y. He, "clusterProfiler: an R package for comparing biological themes among gene clusters," *Omics: A Journal of Integrative Biology*, vol. 16, no. 5, pp. 284–287, 2012.

[21] H. Chakraborty and A. Hossain, "R package to estimate intracluster correlation coefficient with confidence interval for binary data," *Computer Methods and Programs in Biomedicine*, vol. 155, pp. 85–92, 2018.

[22] A. Subramanian, P. Tamayo, V. K. Mootha et al., "Gene set enrichment analysis: a knowledge-based approach for interpreting genome-wide expression profiles," *Proceedings of the National Academy of Sciences of the United States of America*, vol. 102, no. 43, pp. 15545–15550, 2005.

[23] A. G. Pallis and K. N. Syrigos, "Lung cancer in never smokers: disease characteristics and risk factors," *Critical Reviews in Oncology/Hematology*, vol. 88, no. 3, pp. 494–503, 2013.

[24] H. A. Hamann, E. S. Ver Hoeve, L. Carter-Harris, J. L. Studts, and J. S. Ostroff, "Multilevel opportunities to address lung cancer stigma across the cancer control continuum," *Journal of Thoracic Oncology: Official Publication of the International Association for the Study of Lung Cancer*, vol. 13, no. 8, pp. 1062–1075, 2018.

[25] L. Succony, D. M. Rassl, A. P. Barker, F. M. McCaughan, and R. C. Rintoul, "Adenocarcinoma spectrum lesions of the lung: detection, pathology and treatment strategies," *Cancer Treatment Reviews*, vol. 99, article 102237, 2021.

[26] F. Nasim, B. F. Sabath, and G. A. Eapen, "Lung cancer," *The Medical Clinics of North America*, vol. 103, no. 3, pp. 463–473, 2019.

[27] B. C. Bade and C. S. Dela Cruz, "Lung cancer 2020," *Clinics in Chest Medicine*, vol. 41, no. 1, pp. 1–24, 2020.

[28] F. Wang, X. Chen, X. Yu, and Q. Lin, "Degradation of CCNB1 mediated by APC11 through UBA52 ubiquitination promotes cell cycle progression and proliferation of non-small cell lung cancer cells," *American Journal of Translational Research*, vol. 11, no. 11, pp. 7166–7185, 2019.

[29] H. Y. Mo, Q. Y. Wei, Q. H. Zhong et al., "Cytochrome P450 27C1 level dictates lung cancer tumorigenicity and sensitivity towards multiple anticancer agents and its potential interplay with the IGF-1R/Akt/p53 signaling pathway," *International Journal of Molecular Sciences*, vol. 23, no. 14, p. 7853, 2022.

[30] L. Xie, Y. Dang, J. Guo et al., "High KRT8 expression independently predicts poor prognosis for lung adenocarcinoma patients," *Genes*, vol. 10, no. 1, p. 36, 2019.

[31] Y. Xu, J. Wang, X. Wang et al., "Targeting ADRB2 enhances sensitivity of non-small cell lung cancer to VEGFR2 tyrosine kinase inhibitors," *Cell Death Discovery*, vol. 8, no. 1, p. 36, 2022.

[32] L. B. Kennedy and A. K. S. Salama, "A review of cancer immunotherapy toxicity," *CA: A Cancer Journal for Clinicians*, vol. 70, no. 2, pp. 86–104, 2020.

[33] A. Steven, S. A. Fisher, and B. W. Robinson, "Immunotherapy for lung cancer," *Respirology*, vol. 21, no. 5, pp. 821–833, 2016.

[34] M. Abbott and Y. Ustoyev, "Cancer and the immune system: the history and background of immunotherapy," *Seminars in Oncology Nursing*, vol. 35, no. 5, article 150923, 2019.

[35] C. U. Blank, W. N. Haining, W. Held et al., "Defining 'T cell exhaustion'," *Nature Reviews Immunology*, vol. 19, no. 11, pp. 665–674, 2019.

[36] E. J. Wherry and M. Kurachi, "Molecular and cellular insights into T cell exhaustion," *Nature Reviews Immunology*, vol. 15, no. 8, pp. 486–499, 2015.

Hindawi
Disease Markers
Volume 2022, Article ID 7356297, 15 pages
https://doi.org/10.1155/2022/7356297

Research Article

Prognostic Value of an Integrin-Based Signature in Hepatocellular Carcinoma and the Identification of Immunological Role of LIMS2

Fengning Ye,[1] Hao Le,[2] Fan He,[1] Hao Tu,[1] Dengfa Peng,[2] and Sini Ruan[3]

[1]*Ultrasound Imaging Department, The National Hospital of Enshi Autonomous Prefecture, Enshi, China*
[2]*First Surgical Department, The National Hospital of Enshi Autonomous Prefecture, Enshi, China*
[3]*Ultrasound Imaging Department I, The Central Hospital of Enshi Tujia and Miao Autonomous Prefecture, Enshi, China*

Correspondence should be addressed to Dengfa Peng; pengdf666@stu.cpu.edu.cn and Sini Ruan; rsl1980526@163.com

Received 14 August 2022; Revised 6 September 2022; Accepted 7 September 2022; Published 29 September 2022

Academic Editor: Fu Wang

Objective. Evidence proves that integrins affect almost every step of hepatocellular carcinoma (HCC) progression. The current study aimed at constructing an integrin-based signature for prognostic prediction of HCC. *Methods*. TCGA-LIHC and ICGC-LIRI-JP cohorts were retrospectively analyzed. Integrin genes were analyzed via univariate Cox regression, followed by generation of a prognostic signature with LASSO approach. Independent factors were input into the nomogram. WGCNA was adopted to select this signature-specific genes. Gene Ontology (GO) enrichment together with Kyoto Encyclopedia of Genes and Genomes (KEGG) pathway analysis were conducted to explore the function of the dysregulated genes. The abundance of tumor microenvironment components was estimated with diverse popular computational methods. The relative importance of genes from this signature was estimated through random-forest method. *Results*. Eight integrin genes (ADAM15, CDC42, DAB2, ITGB1BP1, ITGB5, KIF14, LIMS2, and SELP) were adopted to define an integrin-based signature. Each patient was assigned the riskScore. High-riskScore subpopulation exhibited worse overall survival, with satisfying prediction efficacy. Also, the integrin-based signature was independent of routine clinicopathological parameters. The nomogram (comprising integrin-based signature, and stage) accurately inferred prognostic outcome, with the excellent net benefit. Genes with the strongest positive interaction to low-riskScore were primarily linked to biosynthetic, metabolic, and catabolic processes and immune pathways; those with the strongest association with high-riskScore were principally associated with diverse tumorigenic signaling. The integrin-based signature was strongly linked with tumor microenvironment components. Among the genes from this signature, LIMS2 possessed the highest importance, and its expression was proven through immunohistochemical staining. *Conclusion*. Altogether, our study defined a quantitative integrin-based signature that reliably assessed HCC prognosis and tumor microenvironment features, which possessed the potential as a tool for prognostic prediction.

1. Introduction

Liver cancer remains the sixth most commonly diagnosed cancer together with the third most deadly cancer, with an estimated 906,000 new cases as well as 830,000 deaths globally [1]. Asian countries have the highest incidence of primary liver cancer cases, reporting approximately 72.5% of the world's cases [2]. Hepatocellular carcinoma (HCC) contributes 80% of all cases worldwide [3]. Elderly male together with Asian populations are still the highest risk groups for HCC. The preferred therapy of HCC remains surgery, which is the only method to achieve long-term survival and even a cure [4]. Radiofrequency ablation is the treatment of choice for malignancies that are extremely early in their stages as well as tumors that are early in their stages but cannot be removed surgically [5]. Ultrasound is well poised to address this need due to its low cost, portability, safety, and excellent temporal resolution. The role of ultrasound for HCC screening has been well established and supported by multiple international guidelines. Nonetheless, HCC patients are

generally in intermediate or advanced stages. Transcatheter arterial chemoembolization is the standard of care for patients with intermediate HCC, resulting to the median survival of 25–30 months [6]. Molecular-targeted agents, sorafenib, etc. have been developed against advanced HCC [7]. Regrettably, liver toxicity and weak anti-tumor effect contribute to treatment failure and low survival benefit. Recently, immune-based therapies have generated notable improvement in clinical outcome of HCC [8]. Despite this, current immunotherapies only induce durable response for minority of HCC patients. Altogether, it is of significance to select potent therapeutic targets, and determine more reliable tools for stratifying HCC patients together with prognostic prediction.

Integrins cross the plasma membrane as well as connect the extracellular matrix (ECM) to the cytoskeleton, as elementary cell adhesion receptors mediating cellular and tissue functions [9]. Altered expression of integrins is commonly detected in HCC [10]. They profoundly affect almost every step of HCC progression from primary tumor development to metastases [10, 11]. Additionally, integrins correlate to the acquisition of drug resistance and immune escape [12, 13]. In addition to tumor cells, integrins are present in components within tumor microenvironment, which critically regulate their contributions to tumor progression [14]. For instance, SPON2 facilitated the recruitment of M1-like macrophages as well as mitigates HCC metastases through integrin signaling [10]. Cancer-associated fibroblasts facilitate vascular invasion of HCC through lowering integrin β1 [15]. Blockade of integrin signaling can attenuate HCC progression through hindering key signaling events in tumor microenvironment and tumor cells. Hence, integrins together with integrin-dependent functions have been regarded as attractive therapeutic targets against HCC [16]. In addition to this, integrins may become imaging biomarkers for evaluating the efficacy of anti-angiogenic or antitumor agents [17]. Moreover, integrin-targeted nanoparticles with varying anti-tumoral payloads are a definitely promising research field to lower toxicity linked to systemic radio- or chemotherapy [18]. To date, the now prognostic model based on integrin-related genes were rarely reported. Based on accumulated evidence, the current study conducted a comprehensive analysis of multidimensional integrin-relevant genomic data across HCC, and defined a quantitative integrin-based signature that may evaluate HCC prognostic outcome together with tumor microenvironment traits, which might open up a novel insight into improving HCC outcomes together with determining patients' therapeutic regimens.

2. Materials and Methods

2.1. Data Acquisition. Transcriptome data and clinical information of HCC patients were acquired from TCGA-LIHC as the training cohort. Under removal of patients with incomplete survival data, 343 HCC patients were included. Another RNA-seq dataset ICGC-LIRI-JP with 229 HCC samples obtained from the ICGC database were adopted for verification.

2.2. Collection of Integrin Gene Set. The Molecular Signatures Database offers the annotated gene sets that involve biochemical pathways, signaling cascades, and expression profiling from published research together with other biological concepts [19]. We collected 128 integrin genes from this popular database, involving four biological process terms (integrin activation, integrin-mediated signaling pathway, positive regulation of integrin activation, and regulation of integrin activation) together with one cellular component terms (integrin complex).

2.3. Definition of an Integrin-Based Signature. Prognostic significance of integrin genes was firstly evaluated. Through adopting univariate-cox regression approach, integrin genes with $p < 0.05$ were selected, and input into least absolute shrinkage and selection operator (LASSO) [20]. This analysis was conducted utilizing glmnet package [21]. The regression coefficient was computed utilizing multivariate-cox regression. The integrin-based signature-derived riskScore was generated through combination of regression coefficient together with transcript level of each integrin gene in this signature. With the median riskScore, patients were classified as low- and high-riskScore subpopulations. This classification was verified through PCA and tSNE approaches. Overall survival (OS) analysis was implemented with Kaplan–Meier (K-M) method together with log-rank test. Area under the receiver operating characteristic curve (AUC) was computed with "timeROC" package. Uni- together with multivariate-cox regression methods were adopted for inferring the independency of the integrin-based signature as a prognostic parameter. Through the use of subgroup analysis, we were able to deduce the sensitivity of this signature in prognostic prediction.

2.4. Nomogram Construction. Nomogram was generated through incorporating independent risky factors (riskScore and stage) via adopting rms package. ROC curves were utilized for reflecting the predictive capability of the nomogram. Concordance index (C-index) was employed to estimate the nomogram discrimination through bootstrap approach with 1000 resamples. Calibration curve was graphically assessed through drawing the actual OS rate against the probability predicted by this nomogram, with the 45° line for the ideal prediction. Decision curve analysis was employed to evaluate the net benefit of the nomogram, routine clinicopathological parameters, and riskScore.

2.5. Weighted Gene Coexpression Network Analysis (WGCNA). WGCNA package [22] was adopted to select the riskScore-specific modules. The transcriptome profiling was utilized as input for WGCNA, and riskScore was computed as well as defined as the clinical traits. A signed scale-free coexpression gene network was guaranteed via setting an appropriate power β value and scale-free R^2 value as the soft threshold parameters. Afterwards, we constructed a coexpression matrix in accordance with β value, and the input gene expression matrix for classifying genes with similar expression pattern into the same gene module, thus producing a coexpression module. Association of module

Eigengenes with riskScore were estimated with Eigengenes function. Heatmap was generated for visualizing the association of each coexpression module with riskScore. Modules with the strongest association with riskScore were selected as the riskScore-specific modules.

2.6. Functional Enrichment Analysis. Gene Ontology (GO) enrichment together with Kyoto Encyclopedia of Genes and Genomes (KEGG) pathway analysis were conducted through adopting clusterProfiler package [23]. For preventing high false discovery rate (FDR) in multiple tests, q -value was inferred for FDR control. A gene set was regarded as significantly enriched if a $p < 0.05$ and false discovery rate <0.025.

2.7. Estimation of Tumor Microenvironment Components. Seven computational approaches were employed to infer components within tumor microenvironment. Tumor Immune Estimation Resource (TIMER) adopts deconvolution approach to estimate the level of six tumor-infiltrating immune subsets from gene expression profiling [24]. CIBERSORT applies transcriptome profiles with a predefined immune signature matrix to calculate the deconvolution of 22 tumor-infiltrating immune cells in a given sample on the basis of support-vector regression [25]. quanTIseq quantifies the fraction of 10 immune cell types utilizing bulk RNA-sequencing data [26]. MCPcounter quantifies the absolute abundance of 8 immune together with 2 stromal cell subsets within heterogeneous tissues through transcriptomic profiles [27]. XCELL infers 64 immune, and stromal cell types via adopting gene signature-based approach [28]. EPIC estimates the proportion of immune and cancer cells utilizing bulk gene expression profiling [29]. Associations of riskScore and genes in the integrin-based signature with the abundance of tumor microenvironment components were estimated with Spearman's correlation test.

2.8. Random-Forest Analysis. The relative importance of genes in the integrin-based signature was ranked via implementing random-forest analysis, and the gene with the highest importance was determined. LIMS2 transcript level was compared between low- and high-riskScore subpopulations. Association of LIMS2 transcript level with riskScore was inferred with Spearman's correlation test. Immunohistochemical staining of LIMS2 in HCC and normal tissue was acquired from the Human Protein Atlas.

2.8.1. Patients and Tissue Samples. The study was approved by the Ethic Committee of The National Hospital of Enshi Autonomous Prefecture. Written informed consent on the use of clinical specimens from each patient was achieved. Eight pairs of HCC tissues and matched nontumor tissues were acquired from HCC patients with written informed consents who received surgical resection at The National Hospital of Enshi Autonomous Prefecture. These tissue samples were confirmed by pathological diagnoses and stored at -80°C until use.

2.8.2. RT-qPCR. Total RNA from HCC specimens and nontumor specimens was extracted by the use of the TRIzol kit (Invitrogen, China). A reverse transcription kit was applied to synthesize the cDNA. Based on the instructions of the SYBR Premix Ex Taq kit (Takara, Dalian, China), Real-time PCR experiments were carried out. The relative quantification of genes was assessed using the $2^{-\Delta\Delta Ct}$ method. The primer sequences were presented as follows: LIMS2 5′-GCACCGGCACTATGAGAAGAA-3′ (forward) and 5′-ACGGGCTTCATGTCGAACTC-3′ (reverse), GAPDH 5′-GCCACATCGCTCAGACACCAT-3′, and 5′-CCCATA CGACTGCAAAGACCC-3′.

2.9. Statistical Analysis. All statistical tests were conducted with R software (R Statistical Software, R Foundation for Statistical Computing, Vienna, Austria). $p < 0.05$ indicated statistical significance.

3. Results

3.1. Definition of an Integrin-Based Signature for HCC Prognostic Outcome. To observe the prognostic signature of integrin genes, the current study carried out univariate-cox regression analysis in TCGA-LIHC cohort. Among 128 integrin genes, 35 exhibited significant correlations to OS (Figure 1(a)). Among them, FBLN1, FLNA, ITGB1, ITGA3, LAMA5, CDH17, SRC, COL16A1, ITGA2, ZYX, ITGAM, ITGAV, NME2, ABL1, CD63, ILK, PTGER4, PRKD1, ADAM9, PTK2, ITGA5, DAB2, ADAM15, BCAR1, ITGB5, LIMS1, RCC2, CTNNA1, ITGB1BP1, KIF14, RAP1B, and CDC42 act as risky factors, with LIMS2, SELP, and APOA1 as protective factors. These prognostic integrin genes were adopted for defining an integrin-based signature with LASSO approach (Figures 1(b) and 1(c)). The formula of the integrin-based signature was as follows: riskScore = 0.0827089185245466, *ADAM15 transcript level + 0.0709032023435198, *CDC42 transcript level + 0.128150636135253, *DAB2 transcript level + 0.196471754226477, *ITGB1BP1 transcript level + 0.121662581037157, *ITGB5 transcript level + 0.207623740869238, *KIF14 transcript level + (−0.31147424622991), *LIMS2 transcript level + (−0.0983574871616035), and *SELP transcript level (Figure 1(d)). With K-M curve together with log-rank test, the prognostic implication of each gene in integrin-based signature was further verified across TCGA-LIHC. Consequently, highly expressed SELP and LIMS2 correlated to more favorable OS, with highly expressed KIF14, ITGB5, DAB2, CDC42, ADAM15, and ITGB1BP1 linked to poorer OS (Figures 1(e)–1(l)).

3.2. The Integrin-Based Signature Excellently Predicts HCC's OS Outcome. We stratified TCGA-LIHC together with ICGC-LIRI-JP cases into low- and high-riskScore subpopulations following the median riskScore (Figures 2(a) and 2(b)). Both in two cohorts, more dead cases were observed in high-riskScore subpopulation (Figures 2(c) and 2(d)). ADAM15, CDC42, DAB2, ITGB1BP1, ITGB5, and KIF14 displayed higher transcript level in high- than low-

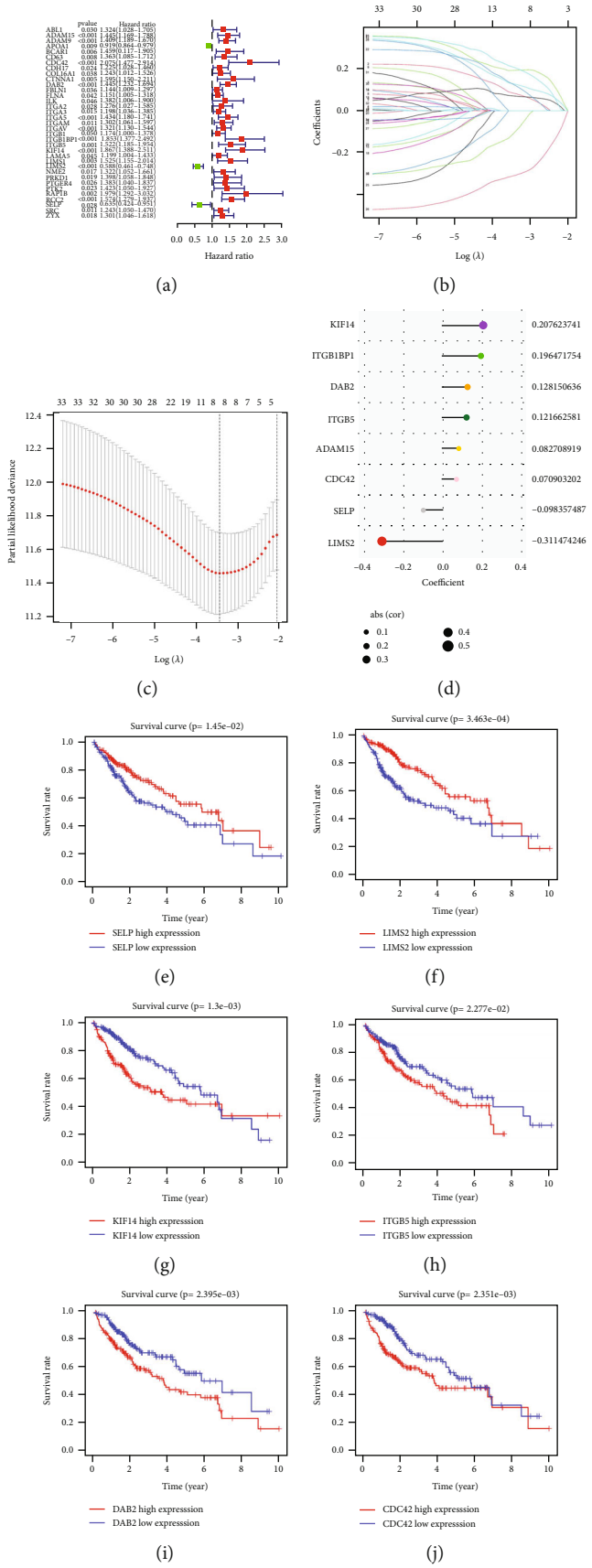

Figure 1: Continued.

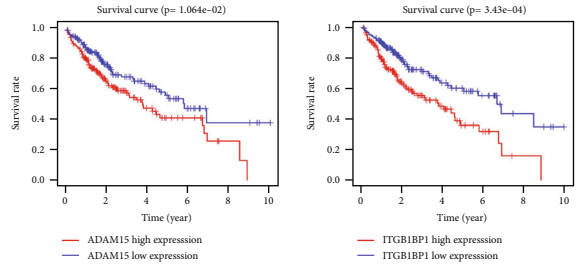

Figure 1: Definition of an integrin-based signature for HCC prognostic outcome in TCGA-LIHC cohort. (a) Forest diagram illustrates the significant correlations of 35 integrin genes with HCC OS. Red, risky factor; and green, protective factor. (b) LASSO coefficient profiling of 35 prognostic integrin genes describes that the alterations in the magnitude of the variable coefficients shrinks as the penalty value increases. (c) Penalty diagram shows the partial likelihood deviance under diverse penalty values. (d) The coefficient of each gene in the integrin-based signature. (e–l) K-M curves of OS outcomes between highly and lowly expressed SELP, LIMS2, KIF14, ITGB5, DAB2, CDC42, ADAM15, or ITGB1BP1 groups. OS difference was estimated with log-rank test.

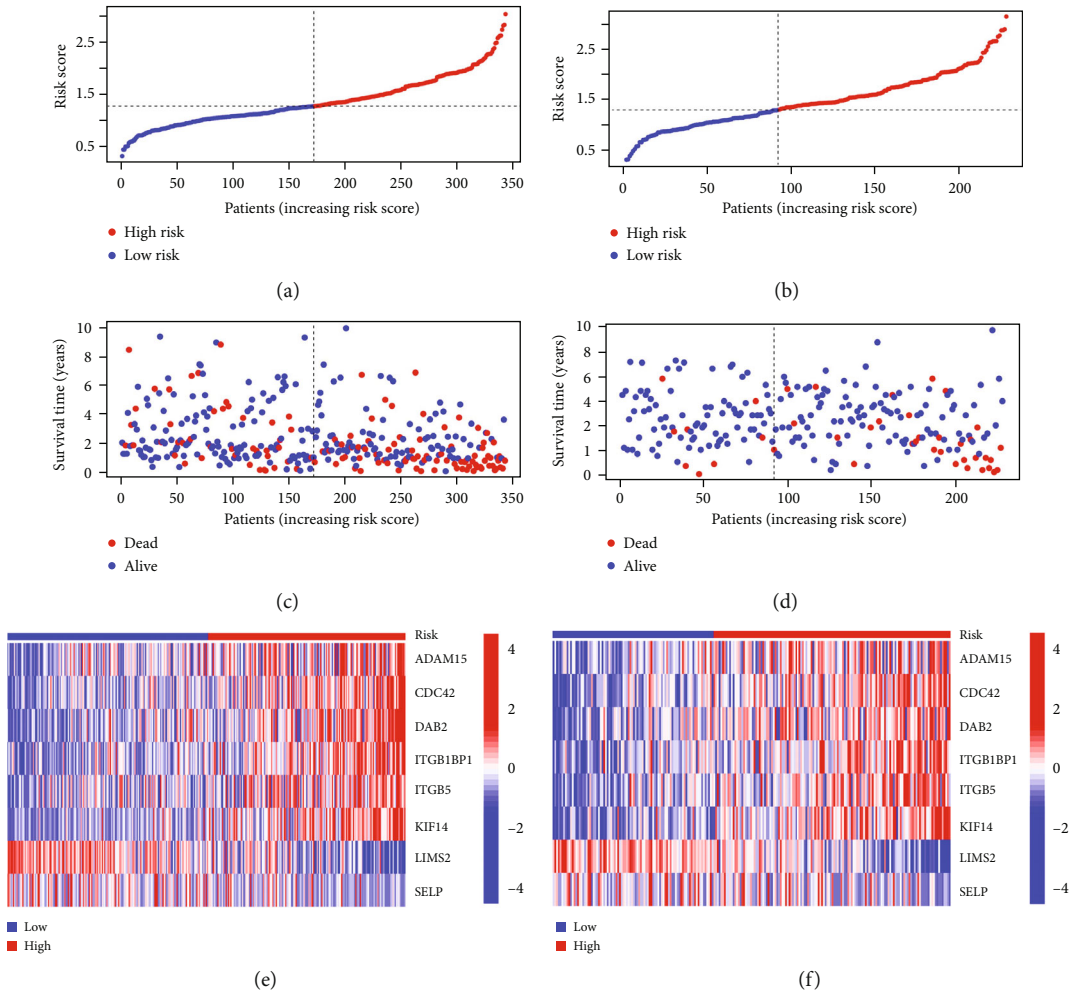

Figure 2: Calculation of the integrin-based signature-derived riskScore in TCGA-LIHC together with ICGC-LIRI-JP cohorts. (a) Distribution of riskScore across TCGA-LIHC cases. Vertical dashed line denotes the median riskScore. TCGA-LIHC cases are classified as low- and high-riskScore subpopulations. (b) Distribution of riskScore across ICGC-LIRI-JP cases. (c) Survival time and status across TCGA-LIHC cases with increasing riskScore. Blue, alive; red, dead. (d) Survival time and status across ICGC-LIRI-JP cases with increasing riskScore. (e) Heatmap visualizes transcript level of genes in the integrin-based signature across low- and high-riskScore subpopulations from TCGA-LIHC cohort. Blue, low transcript level; red, high transcript level. (f) Heatmap exhibits transcript level of genes in the integrin-based signature across low- and high-riskScore subpopulations from ICGC-LIRI-JP cohort.

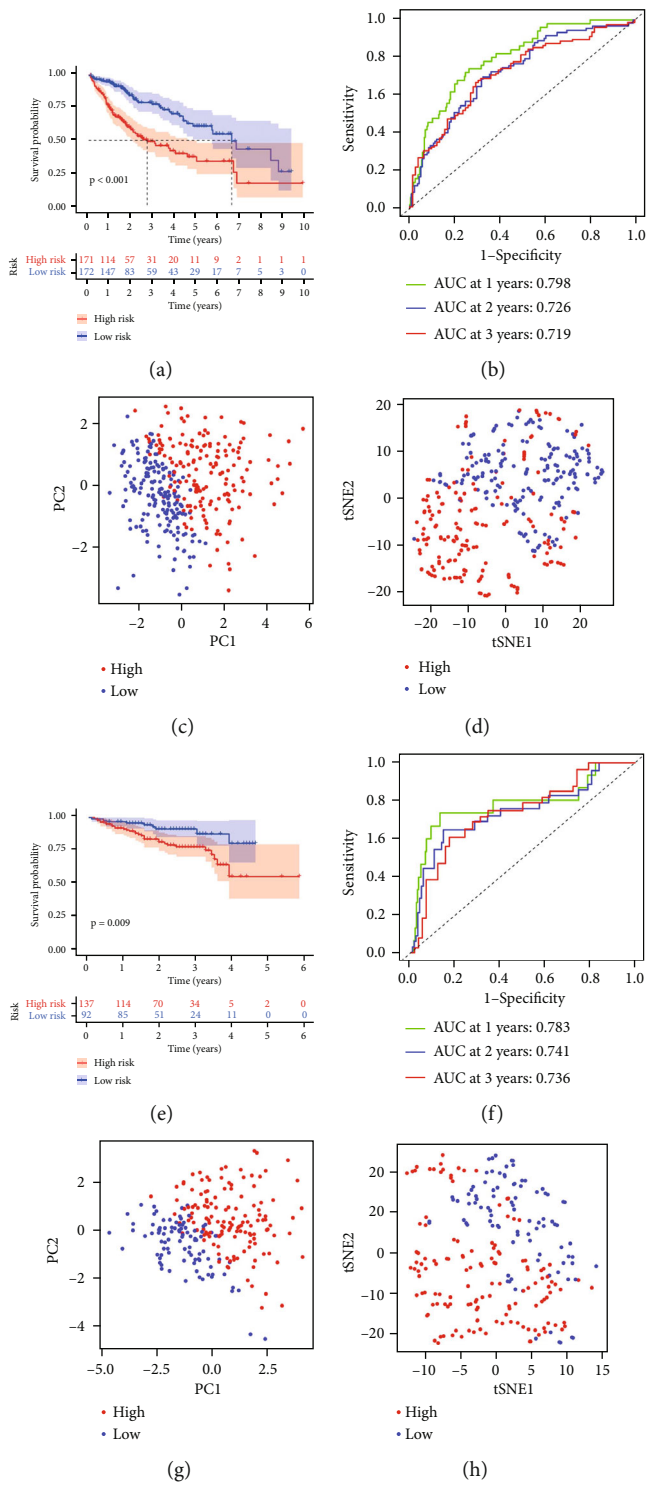

Figure 3: The integrin-based signature excellently predicts HCC's OS outcome. (a) K-M curves depict the OS outcome of two subpopulations stratified by the median riskScore in TCGA-LIHC cohort. OS difference was inferred with log-rank test. (b) ROC curves validate the prediction efficacy of riskScore for OS at one, two together with three years in TCGA-LIHC cohort. (c) PCA plots demonstrate the discrepancy between low- and high-riskScore subpopulations from TCGA-LIHC cohort at the transcriptome level. (d) tSNE plots prove the discrepancy between low- and high-riskScore subpopulations from TCGA-LIHC cohort at the transcriptome level. (e) K-M curves show the OS outcome of two subpopulations stratified by the median riskScore in ICGC-LIRI-JP cohort. OS difference was computed utilizing log-rank test. (f) ROC curves validate the prediction efficacy of riskScore for OS at one, two together with three years in ICGC-LIRI-JP cohort. (g) PCA plots demonstrate the discrepancy between low- and high-riskScore subpopulations from ICGC-LIRI-JP cohort at the transcriptome level. (h) tSNE plots prove the discrepancy between low- and high-riskScore subpopulations from ICGC-LIRI-JP cohort at the transcriptome level.

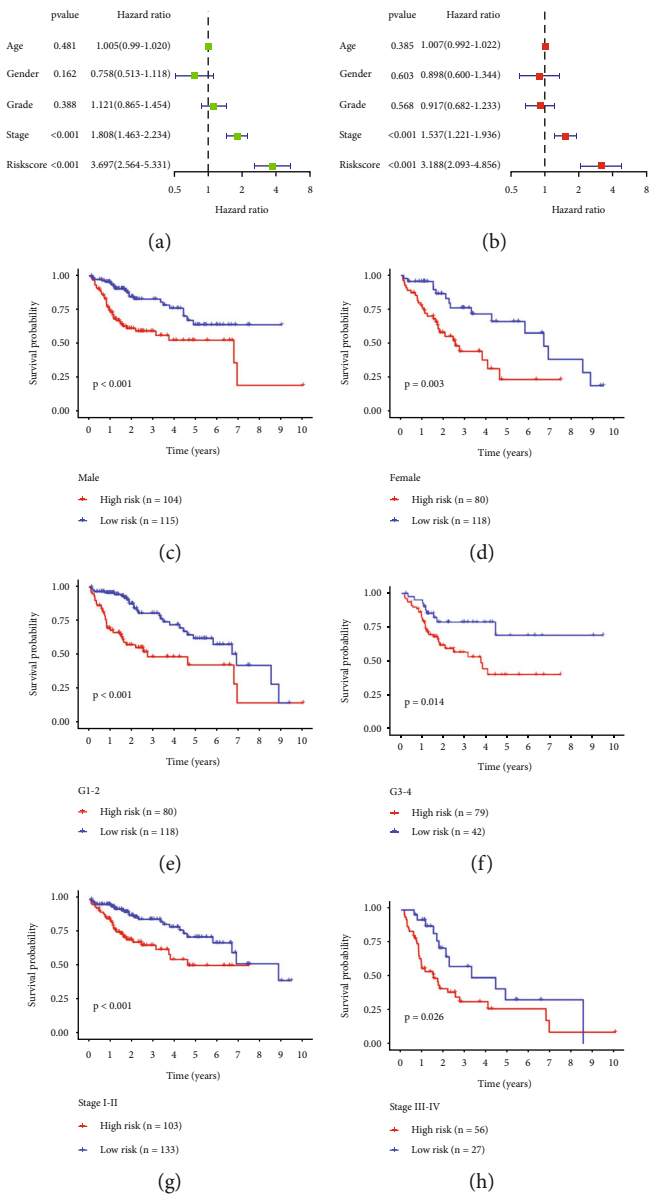

Figure 4: The integrin-based signature is independent of routine clinicopathological parameters across TCGA-LIHC. (a, b) Forest diagram shows the associations of riskScore and routine clinicopathological parameters with OS outcome utilizing uni- and multivariate-cox regression approaches. (c–h) K-M curves of low- and high-riskScore subpopulations in diverse subgroups stratified by routine clinicopathological parameters.

riskScore subpopulation, with lower transcript level of SELP, and LIMS2 in high-riskScore subpopulation across TCGA-LIHC as well as ICGC-LIRI-JP cases (Figures 2(e) and 2(f)).

Afterwards, OS outcome was compared between subpopulations across TCGA-LIHC. In contrast to high-riskScore patients, those with low-riskScore possessed the notable advantage in OS outcome (Figure 3(a)). ROC curves were plotted to investigate the prediction efficacy of the integrin-based signature. Consequently, AUC values of OS at one, two together with three years were all exceeding 0.7 (Figure 3(b)), proving that this signature excellently predicted HCC's OS outcome. To verify the discrepancy between low- and high-riskScore subpopulations, we adopted PCA and tSNE approaches across TCGA-LIHC. As a result, low-riskScore patients signally distinguished from those with high-riskScore at the transcriptome level (Figures 3(c) and 3(d)).

Next, the current study observed whether the integrin-based signature generalized to other cohorts. Similarly, we computed riskScore of patients from ICGC-LIRI-JP cohort, which were then classified as low- and high-riskScore subpopulations. As expected, poorer OS outcome was proven in high-riskScore subpopulation (Figure 3(e)). In addition, AUC values of OS at one, two together with three years were all over 0.7 (Figure 3(f)). PCA and tSNE demonstrated the arresting discrepancy between subpopulations (Figures 3(g) and 3(h)).

The integrin-based signature is independent of routine clinicopathological parameters.

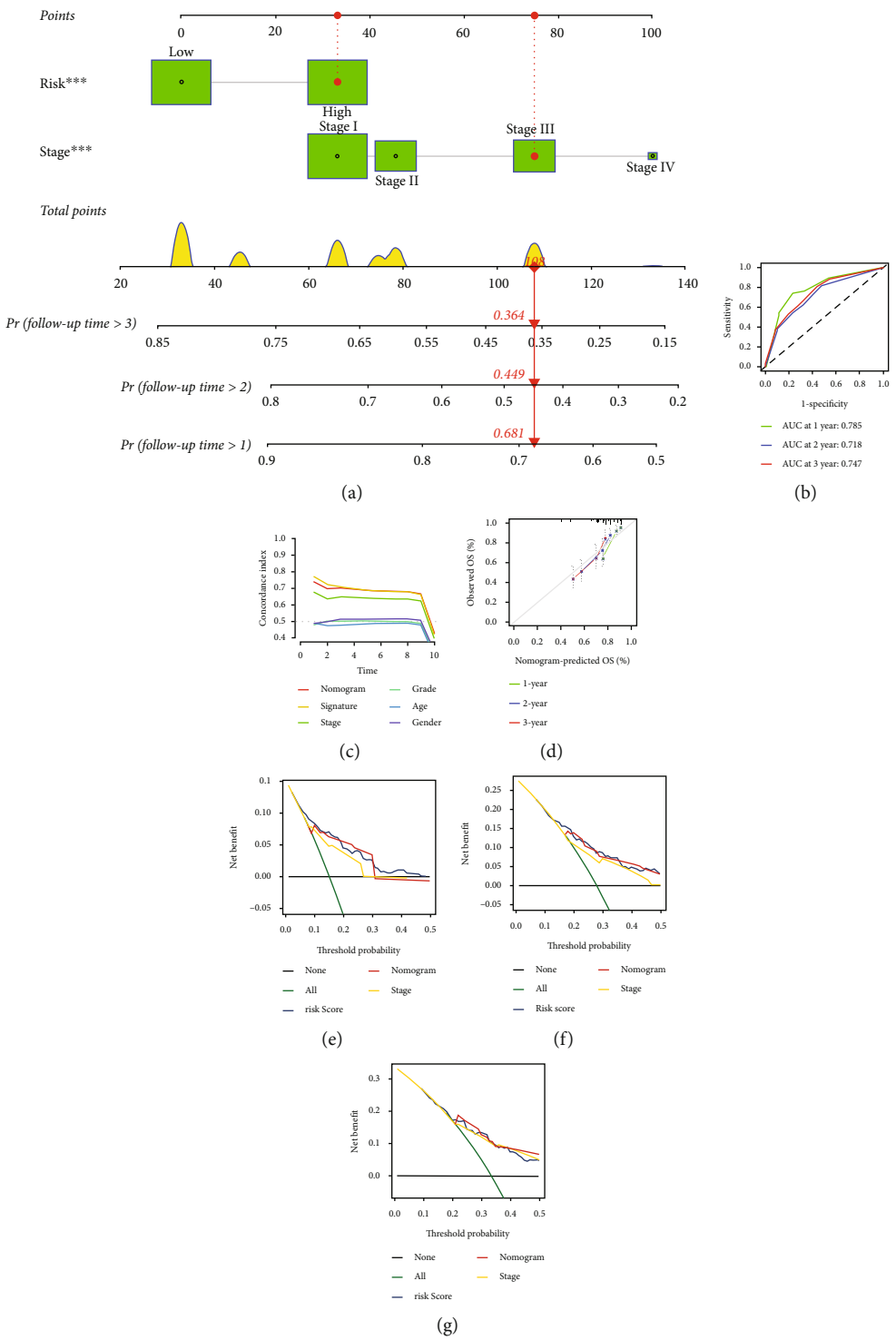

Figure 5: Generation of an integrin-based signature- and stage-based nomogram into HCC clinical practice in TCGA-LIHC cohort. (a) The nomogram incorporating two independent risky factors (riskScore together with stage) for HCC. (b) ROC curves of OS at one, two together with three years. (c) The C-indices of various variables in short- and long-term OS outcomes. (d) Calibration plots of the nomogram for predicting the probability of OS at one, three, together with five years. (e–g) Decision curve analysis curves for inferring the bet benefits.

Next, the present study estimated the associations of riskScore and routine clinicopathological parameters with OS outcome across TCGA-LIHC utilizing univariate-cox regression approach. Consequently, riskScore together with stage were linked with poor OS outcome (Figure 4(a)). Multivariate-cox regression approach was adopted to infer whether riskScore was independent of routine clinicopathological parameters. As illustrated in Figure 4(b), riskScore together with stage acted as independent risky factors of TCGA-LIHC. The sensitivity of riskScore in prognosis

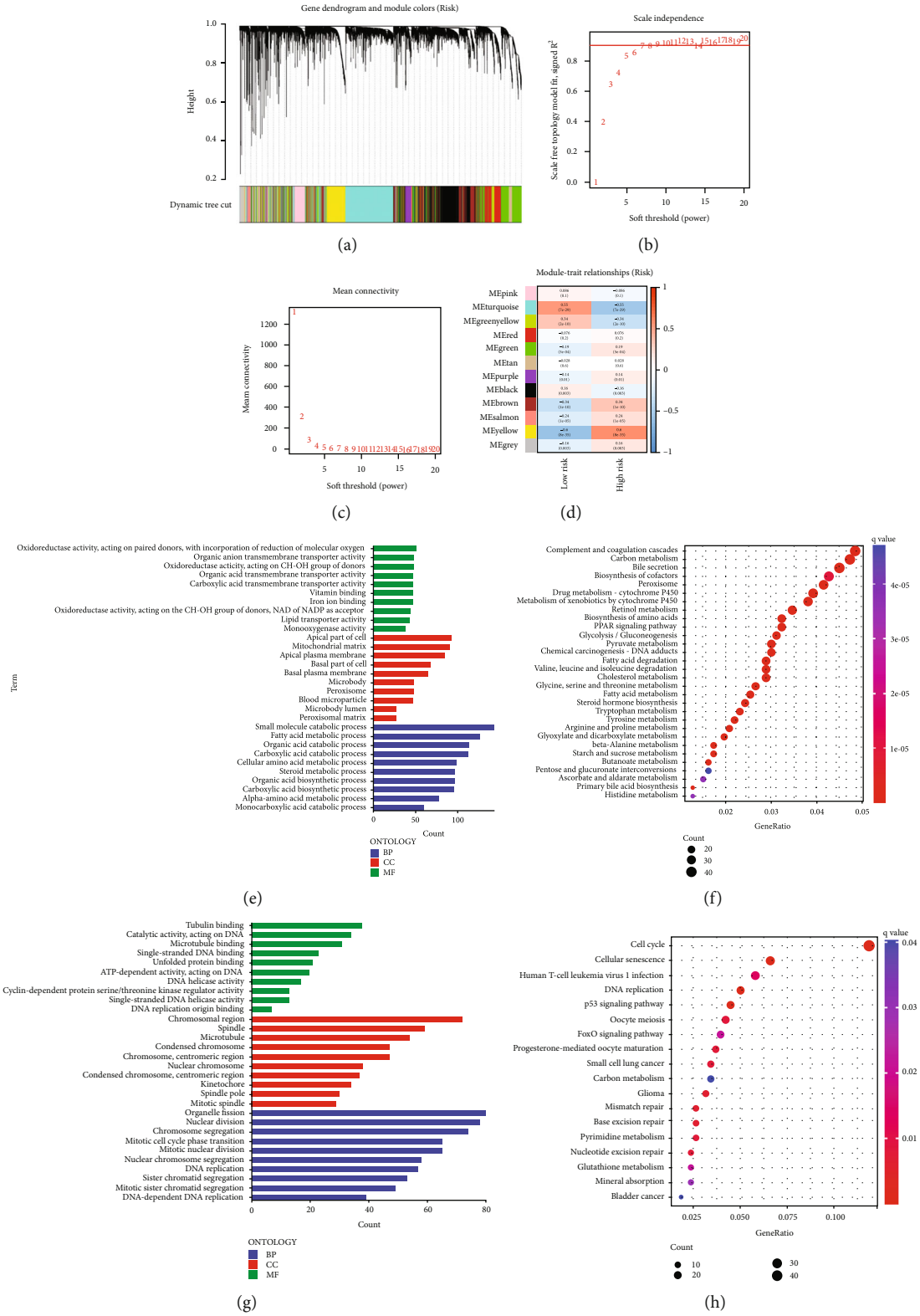

Figure 6: Selection of integrin-based signature-specific genes across TCGA-LIHC. (a) Gene dendrogram acquired through average linkage hierarchical clustering. The colored row below the dendrogram depicts the module assignment determined with dynamic tree cut approach. (b, c) Selection of the optimal soft threshold in accordance with scale independence together with mean connectivity. (d) Associations of coexpression modules with low- and high-riskScore specimens. Each module comprises correlation coefficient together with p value. (e) GO enrichment terms of genes in turquoise module. The length of the columns indicates the count of enriched genes. (f) KEGG pathways of genes in turquoise module. Red denotes high enrichment, and blue denotes low enrichment. The size of the dots represents the count of enriched genes. (g, h) GO enrichment terms together with KEGG pathways of genes in yellow module.

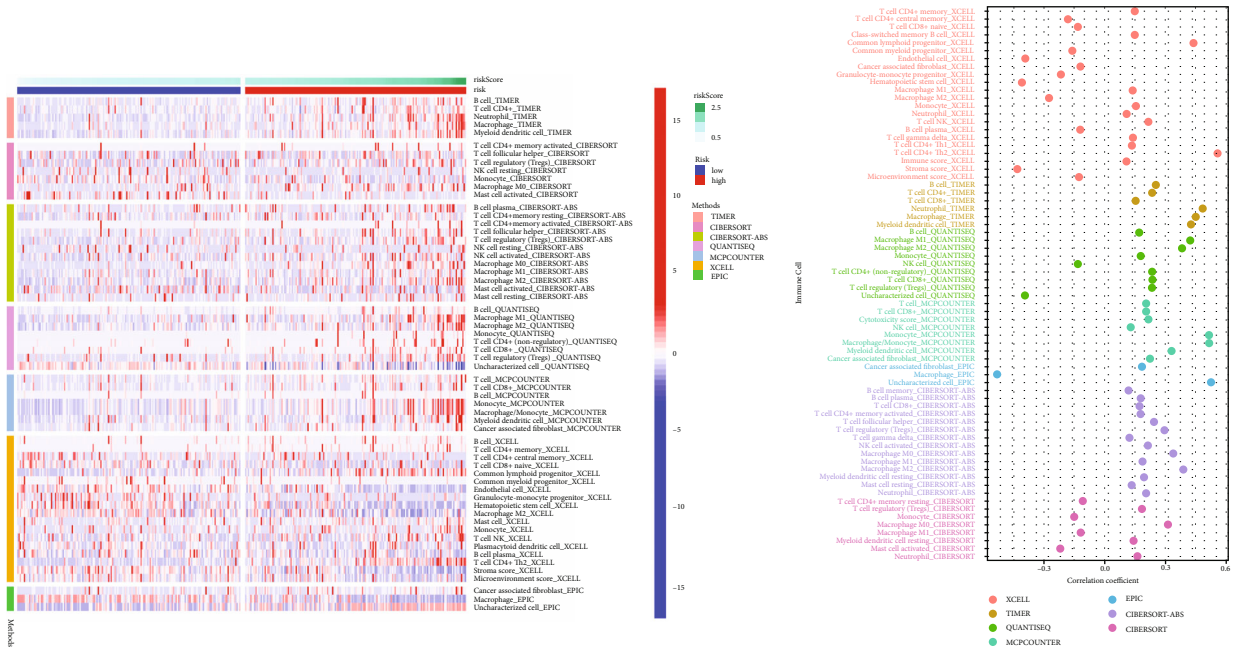

(a) (b)

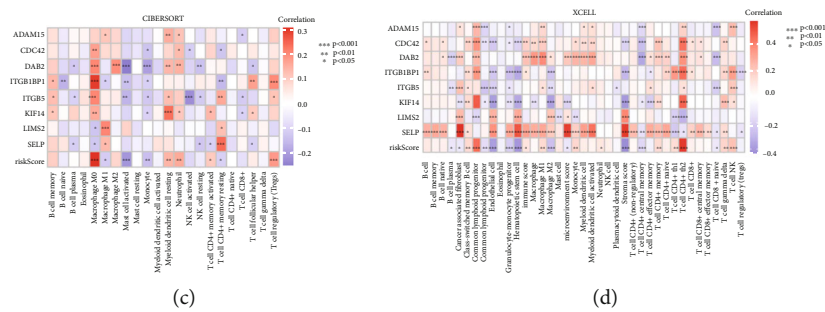

(c) (d)

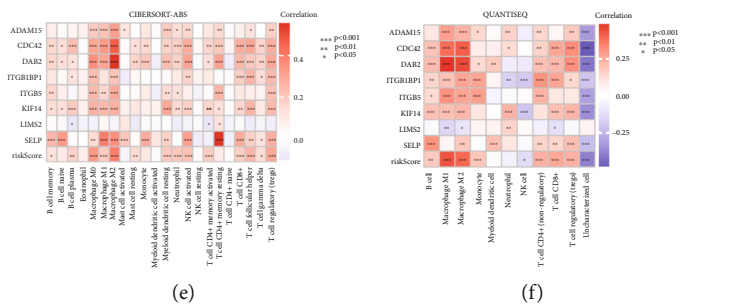

(e) (f)

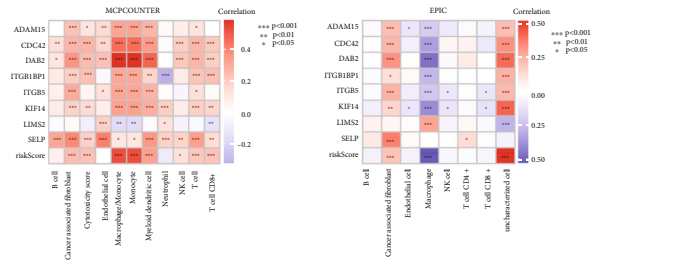

(g) (h)

FIGURE 7: Continued.

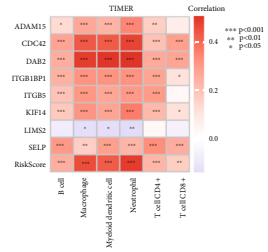

(i)

Figure 7: Interactions of the integrin-based signature with components within tumor microenvironment across TCGA-LIHC. (a) Heatmap illustrates the abundance of tumor microenvironment components in low- and high-riskScore subpopulations utilizing diverse computational approaches. (b) Associations of riskScore with the abundance of tumor microenvironment components. (c–i) Interactions of genes from the integrin-based signature and riskScore with the abundance of tumor microenvironment components computed through CIBERSORT, XCELL, CIBERSORT-ABS, QuantTIseq, MCPcounter, EPIC together with TIMER approaches. $^{*}p < 0.05$; $^{**}p < 0.01$; $^{***}p < 0.001$.

prediction was measured in diverse subgroups stratified by routine clinicopathological parameters (sex, grade, or stage). In each subgroup, high-riskScore subpopulation possessed worse OS outcome in contrast to low-riskScore subpopulation (Figures 4(c)–4(h)).

3.3. Generation of an Integrin-Based Signature- and Stage-Based Nomogram into HCC Clinical Practice. Two independent risky factors (riskScore together with stage) were selected for generating a nomogram for HCC prognostic prediction (Figure 5(a)). Firstly, points for riskScore and stage were derived in TCGA-LIHC cases. Total points were acquired through adding the points of two risky factors, and the corresponding location of the point of each patient was observed in the line of total points. At last, the probability of one-, three- together with five-year OS for HCC was referred through plotting a straight line on the bottom three rows. ROC curves and C-indices were adopted for evaluating the prediction accuracy of the nomogram. AUC values of OS at one, two together with three years were all over 0.7 (Figure 5(b)), and the C-indices were over 0.7 for short- and long-term OS outcomes (Figure 5(c)). In addition, calibration curve illustrated that the one-, three- together with five-year OS probability predicted by this nomogram was consistent with the actual OS rate (Figure 5(d)). Above evidence proved the excellent prediction efficacy of this nomogram. Decision curve analysis curves at one-, three- together with five-year OS displayed the potential for clinical application as well as better net benefits (Figures 5(e)–5(g)).

3.4. Selection of Integrin-Based Signature-Specific Genes. WGCNA was employed for identifying integrin-based signature-specific genes across TCGA-LIHC. Transcriptome data and clinical trait (low- and high-riskScore) were input into WGNCA. The first power value when the index of scale-free topologies was up to 0.90 was set as the optimal soft threshold power (β) for establishing a scale-free network, and genes with similar expression patterns were assigned to the same coexpression module utilizing dynamic tree cut approach, thus generating 12 coexpression modules (Figures 6(a)–6(c)). Afterwards, associations of coexpression modules with low- and high-riskScore were evaluated. Turquoise module exhibited the strongest positive interaction to low-riskScore (Figure 6(d)). In addition, yellow module displayed the strongest positive association with high-riskScore. Thus, genes in turquoise and yellow modules were regarded as integrin-based signature-specific genes.

Next, biological implication of integrin-based signature-specific genes was assessed. Genes in turquoise module were primarily linked to biosynthetic, metabolic, and catabolic processes together with immune pathways (Figures 6(e) and 6(f)). Genes in yellow module primarily correlated to diverse tumorigenic signaling (Figures 6(g) and 6(h)).

3.5. Interactions of the Integrin-Based Signature with Components within Tumor Microenvironment. Diverse computational approaches were adopted for inferring the interactions of the integrin-based signature with components within tumor microenvironment across TCGA-LIHC. Overall, high-riskScore exhibited higher abundance of immunosuppressive cells, and the riskScore was positively correlated to immunosuppressive cells (Figures 7(a) and 7(b)). In addition, genes from the integrin-based signature (ADAM15, CDC42, DAB2, ITGB1BP1, ITGB5, KIF14, SELP, and LIMS2) were strongly linked with the abundance of components within tumor microenvironment (Figures 7(c)–7(i)).

3.6. The Importance of LIMS2 from the Integrin-Based Signature in HCC. Random-forest approach was adopting for assessing the relative importance of genes in the integrin-based signature. Consequently, LIMS2 possessed the highest importance (Figure 8(a)). In contrast to low-riskScore subpopulation, lower transcript level of LIMS2 was observed in high-riskScore subpopulation (Figure 8(b)). In addition, LIMS2 transcript level was negatively linked to riskScore (Figure 8(c)). Immunohistochemical staining demonstrated that LIMS2 protein displayed low expression level in normal tissue, without detection in HCC tissue (Figures 8(d) and 8(e)). Finally, we performed RT-PCR and found that LIMS2 expression was distinctly decreased in HCC specimens compared with nontumor specimens (Figure 8(f)).

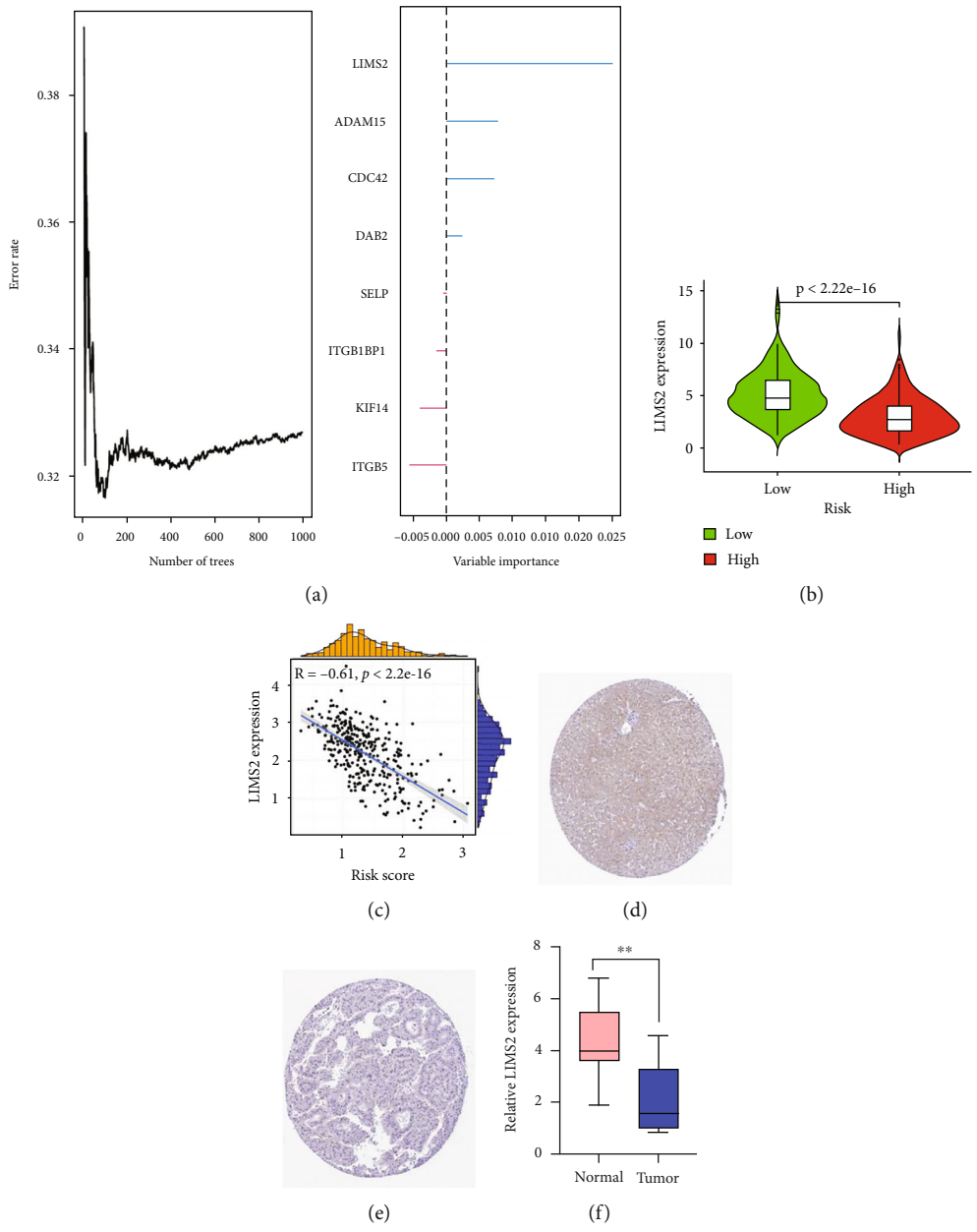

Figure 8: The importance of LIMS2 from the integrin-based signature in HCC. (a) Assessment of the relative importance of genes in the integrin-based signature through adopting random-forest approach across TCGA-LIHC. (b) Transcript level of LIMS2 in low- and high-riskScore subpopulations across TCGA-LIHC. (c) Association of transcript level of LIMS2 with integrin-based signature-derived riskScore across TCGA-LIHC. (d, e) Immunohistochemical images of LIMS2 in normal and HCC tissues from the Human Protein Atlas. Bar, 200 μm. (f) RT-PCR was applied to examine the expression of LIMS2 in HCC specimens and nontumor specimens. $^{**}p < 0.01$.

4. Discussion

Despite the notable improvement in HCC research, patients' outcome remains depressing [30]. Hence, it is imperative to search for novel tools for HCC prognostic prediction. Evidence demonstrates that integrins affect almost every step of HCC progression [10]. Herein, eight integrin genes (ADAM15, CDC42, DAB2, ITGB1BP1, ITGB5, KIF14, LIMS2, and SELP) were selected and adopted to define an integrin-based signature. High-riskScore subpopulation displayed worse OS, with satisfying prediction efficacy. In addition, the integrin-based signature was independent of routine clinicopathological parameters. To facilitate clinical practice, we produced the integrin-based signature- and stage-based nomogram that accurately inferred prognostic outcome, with the excellent net benefit.

Accumulated evidence proves the significance of genes from the integrin-based signature in HCC. For instance, ADAM15 metalloproteinase, a multidomain disintegrin protease, is linked to prognostic outcome, infiltration of immune cells together with apoptosis in HCC [31]. CDC42 stimulates tumor growth, angiogenesis together with metastatic potential of HCC [32]. DAB2 mitigates tumor growth and metastasis of HCC [33]. ITGB1BP1 induces HCC

metastasis through epithelial-mesenchymal transition [34]. ITGB5 motivates HCC tumorigenesis via elevating β-catenin stability [35]. KIF14 suppression may interfere with cell cycle progression together with cytokinesis through hindering p27 ubiquitination signaling in HCC [36]. In addition, KIF14 expedites growth and sorafenib resistance in HCC [37]. Microwave responsive nanoplatform through SELP-mediated drug delivery exhibits the excellent efficacy in treating HCC with distant metastasis [38].

To unveil the mechanisms underlying the integrin-based signature-derived riskScore, specific genes were selected, respectively. Genes with the strongest positive interaction to low-riskScore were primarily correlated to biosynthetic, metabolic, and catabolic processes and immune pathways. In addition, genes with the strongest association with high-riskScore were principally linked with diverse tumorigenic signaling. Above data reflected the prognostic difference between low- and high-riskScore subpopulations. Tumorigenesis-related inflammation results in the accumulation of immune cells within tumors together with the surrounding environment, which contributed to tissue remodeling as well as damage in their functions [39]. Immune cells and nonimmune components comprise the immediate surrounding of tumor cells, named tumor microenvironment [40]. Components within tumor microenvironment exert dual roles in HCC. Tumor microenvironment was in charge of immune surveillance together with immunoediting [41]. In addition, it facilitates invasive tumor growth, metastatic potential as well as evasion from immune surveillance [42]. The current evidence proved the interactions of the integrin-based signature and their genes with tumor microenvironment components across HCC.

Among genes from the integrin-based signature, LIMS2 possessed the highest importance. LIMS2 was negatively linked with riskScore and exhibited low expression in HCC. Additionally, its expression in HCC was proven via immunohistochemical staining. Previously, LIMS2 inhibition contributed to enlargement of liver and tumorigenesis [43]. Epigenetic silencing of LIMS2 has been found in gastric cancer [44]. Extracellular vesicles secreted by mesenchymal stem cells inhibit the progression of cervical cancer by transferring the microRNA miR-331-3p, which reduces the level of methylation of LIMS2 in cancer cells [45]. Our study presented for the first time the importance of LIMS2 in HCC. LIMS2 might become a potent therapeutic target of HCC.

Nonetheless, this study has a few disadvantages. Firstly, we utilized the LASSO approach to filter prognostic integrin genes. Regrettably, the disadvantages of this approach itself possibly resulted in missing some integrin genes with equally important contributions when adjusting the regression coefficients. In addition, clinical features incorporated in the independent analysis of the prognostic signature together with the establishment of the nomogram were traditionally considered crucial factors influencing HCC tumorigenesis. Nonetheless, a few clinical elements with similar contributions, dietary habits, etc., were not incorporated in our study as a result of insufficient patients' information, which might impact our conclusions. In addition, the efficacy of the prognostic signature used to assess immunotherapeutic response will be further proven in large clinical trials.

5. Conclusion

In summary, the integrin-based signature was generated and verified, which possessed predictive significance of HCC prognostic outcome. Our findings supported the notions that integrin genes notably correlated to patients' outcome. In clinical practice, to measure the transcript level of only ADAM15, CDC42, DAB2, ITGB1BP1, ITGB5, KIF14, LIMS2, and SELP might be a cost-effective application and enabled to offer accurate prognostic prediction of HCC.

Abbreviations

HCC: Hepatocellular carcinoma
ECM: Extracellular matrix
LASSO: Least absolute shrinkage and selection operator
OS: Overall survival
K-M: Kaplan–Meier
AUC: Area under the receiver operating characteristic curve
C-index: Concordance index
WGCNA: Weighted gene coexpression network analysis
GO: Gene ontology
KEGG: Kyoto Encyclopedia of Genes and Genomes
FDR: False discovery rate.

Data Availability

The data presented in this study are available from the corresponding authors on reasonable request.

Conflicts of Interest

The authors declared no conflicts of interest.

Authors' Contributions

Fengning Ye and Hao Le contributed equally to this work.

References

[1] H. Sung, J. Ferlay, R. L. Siegel et al., "Global cancer statistics 2020: GLOBOCAN estimates of incidence and mortality worldwide for 36 cancers in 185 countries," *CA: a Cancer Journal for Clinicians*, vol. 71, no. 3, pp. 209–249, 2021.

[2] C. H. Zhang, Y. Cheng, S. Zhang, J. Fan, and Q. Gao, "Changing epidemiology of hepatocellular carcinoma in Asia," *Liver International*, vol. 42, no. 9, pp. 2029–2041, 2022.

[3] H. Rumgay, J. Ferlay, C. de Martel et al., "Global, regional and national burden of primary liver cancer by subtype," *European Journal of Cancer*, vol. 161, pp. 108–118, 2022.

[4] J. M. Llovet, R. Pinyol, R. K. Kelley et al., "Molecular pathogenesis and systemic therapies for hepatocellular carcinoma," *Nature Cancer*, vol. 3, no. 4, pp. 386–401, 2022.

[5] T. Su, M. Huang, J. Liao et al., "Insufficient radiofrequency ablation promotes hepatocellular carcinoma metastasis through N6-methyladenosine mRNA methylation-dependent mechanism," *Hepatology*, vol. 74, no. 3, pp. 1339–1356, 2021.

[6] L. Liu, J. Zhuang, J. Tan et al., "Doxorubicin-loaded UiO-66/Bi2S3nanocomposite-enhanced synergistic Transarterial chemoembolization and photothermal therapy against hepatocellular carcinoma," *ACS Applied Materials & Interfaces*, vol. 14, no. 6, pp. 7579–7591, 2022.

[7] M. Kudo, K. Ueshima, O. Yokosuka et al., "Sorafenib plus low-dose cisplatin and fluorouracil hepatic arterial infusion chemotherapy versus sorafenib alone in patients with advanced hepatocellular carcinoma (SILIUS): a randomised, open label, phase 3 trial," *The Lancet Gastroenterology & Hepatology*, vol. 3, no. 6, pp. 424–432, 2018.

[8] T. Yau, Y. K. Kang, T. Y. Kim et al., "Efficacy and safety of nivolumab plus ipilimumab in patients with advanced hepatocellular carcinoma previously treated with sorafenib: the CheckMate 040 randomized clinical trial," *JAMA Oncology*, vol. 6, no. 11, p. e204564, 2020.

[9] J. Z. Kechagia, J. Ivaska, and P. Roca-Cusachs, "Integrins as biomechanical sensors of the microenvironment," *Nature Reviews. Molecular Cell Biology*, vol. 20, no. 8, pp. 457–473, 2019.

[10] Y. L. Zhang, Q. Li, X. M. Yang et al., "SPON2 promotes M1-like macrophage recruitment and inhibits hepatocellular carcinoma metastasis by distinct integrin-rho GTPase-Hippo pathways," *Cancer Research*, vol. 78, no. 9, pp. 2305–2317, 2018.

[11] F. Sun, J. Wang, Q. Sun et al., "Interleukin-8 promotes integrin β3 upregulation and cell invasion through PI3K/Akt pathway in hepatocellular carcinoma," *Journal of Experimental & Clinical Cancer Research*, vol. 38, no. 1, p. 449, 2019.

[12] P. Busenhart, A. Montalban-Arques, E. Katkeviciute et al., "Inhibition of integrin $\alpha v\beta 6$ sparks T-cell antitumor response and enhances immune checkpoint blockade therapy in colorectal cancer," *Journal for Immunotherapy of Cancer*, vol. 10, no. 2, p. e003465, 2022.

[13] T. H. Jang, W. C. Huang, S. L. Tung et al., "MicroRNA-485-5p targets keratin 17 to regulate oral cancer stemness and chemoresistance via the integrin/FAK/Src/ERK/β-catenin pathway," *Journal of Biomedical Science*, vol. 29, no. 1, p. 42, 2022.

[14] E. Duong, T. B. Fessenden, E. Lutz et al., "Type I interferon activates MHC class I-dressed CD11b(+) conventional dendritic cells to promote protective anti-tumor CD8(+) T cell immunity," *Immunity*, vol. 55, pp. 308–323, 2022.

[15] X. Zheng, P. Wang, L. Li et al., "Cancer-associated fibroblasts promote vascular invasion of hepatocellular carcinoma via downregulating Decorin-integrin β1 signaling," *Frontiers in Cell and Development Biology*, vol. 9, p. 678670, 2021.

[16] J. S. Desgrosellier and D. A. Cheresh, "Integrins in cancer: biological implications and therapeutic opportunities," *Nature Reviews. Cancer*, vol. 10, no. 1, pp. 9–22, 2010.

[17] R. Sharma, P. O. Valls, M. Inglese et al., "Fluciclatide PET as a biomarker of response to combination therapy of pazopanib and paclitaxel in platinum-resistant/refractory ovarian cancer," *European Journal of Nuclear Medicine and Molecular Imaging*, vol. 47, no. 5, pp. 1239–1251, 2020.

[18] A. D. Tagalakis, V. Jayarajan, R. Maeshima et al., "Integrin-targeted, short interfering RNA nanocomplexes for neuroblastoma tumor-specific delivery achieveMYCNsilencing with improved survival," *Advanced Functional Materials*, vol. 31, no. 37, p. 2104843, 2021.

[19] A. Liberzon, C. Birger, H. Thorvaldsdóttir, M. Ghandi, J. P. Mesirov, and P. Tamayo, "The molecular signatures database (MSigDB) hallmark gene set collection," *Cell Systems*, vol. 1, no. 6, pp. 417–425, 2015.

[20] L. Chen, X. Niu, X. Qiao et al., "Characterization of interplay between autophagy and ferroptosis and their synergistical roles on manipulating immunological tumor microenvironment in squamous cell carcinomas," *Frontiers in Immunology*, vol. 12, p. 739039, 2022.

[21] S. Engebretsen and J. Bohlin, "Statistical predictions with glmnet," *Clinical Epigenetics*, vol. 11, no. 1, p. 123, 2019.

[22] P. Langfelder and S. Horvath, "WGCNA: an R package for weighted correlation network analysis," *BMC Bioinformatics*, vol. 9, no. 1, p. 559, 2008.

[23] G. Yu, L. G. Wang, Y. Han, and Q. Y. He, "clusterProfiler: an R package for comparing biological themes among gene clusters," *Omics*, vol. 16, no. 5, pp. 284–287, 2012.

[24] T. Li, J. Fu, Z. Zeng et al., "TIMER2.0 for analysis of tumor-infiltrating immune cells," *Nucleic Acids Research*, vol. 48, no. W1, pp. W509–w514, 2020.

[25] A. M. Newman, C. L. Liu, M. R. Green et al., "Robust enumeration of cell subsets from tissue expression profiles," *Nature Methods*, vol. 12, no. 5, pp. 453–457, 2015.

[26] F. Finotello, C. Mayer, C. Plattner et al., "Molecular and pharmacological modulators of the tumor immune contexture revealed by deconvolution of RNA-seq data," *Genome Medicine*, vol. 11, no. 1, p. 34, 2019.

[27] E. Becht, N. A. Giraldo, L. Lacroix et al., "Estimating the population abundance of tissue-infiltrating immune and stromal cell populations using gene expression," *Genome Biology*, vol. 17, no. 1, p. 218, 2016.

[28] D. Aran, Z. Hu, and A. J. Butte, "xCell: digitally portraying the tissue cellular heterogeneity landscape," *Genome Biology*, vol. 18, no. 1, p. 220, 2017.

[29] J. Racle and D. Gfeller, "EPIC: a tool to estimate the proportions of different cell types from bulk gene expression data," *Methods in Molecular Biology*, vol. 2120, pp. 233–248, 2020.

[30] X. Liu, X. Niu, and Z. Qiu, "A five-gene signature based on stromal/immune scores in the tumor microenvironment and its clinical implications for liver cancer," *DNA and Cell Biology*, vol. 39, no. 9, pp. 1621–1638, 2020.

[31] J. H. Xu, Y. J. Guan, Y. C. Zhang et al., "ADAM15 correlates with prognosis, immune infiltration and apoptosis in hepatocellular carcinoma," *Aging (Albany NY)*, vol. 13, no. 16, pp. 20395–20417, 2021.

[32] R. Wang, N. Zhao, S. Li et al., "MicroRNA-195 suppresses angiogenesis and metastasis of hepatocellular carcinoma by inhibiting the expression of VEGF, VAV2, and CDC42," *Hepatology*, vol. 58, no. 2, pp. 642–653, 2013.

[33] C. Sun, X. Yao, Q. Jiang, and X. Sun, "miR-106b targets DAB2 to promote hepatocellular carcinoma cell proliferation and metastasis," *Oncology Letters*, vol. 16, no. 3, pp. 3063–3069, 2018.

[34] Y. Y. Zhang, L. Q. Kong, X. D. Zhu et al., "CD31 regulates metastasis by inducing epithelial-mesenchymal transition in hepatocellular carcinoma via the ITGB1-FAK-Akt signaling pathway," *Cancer Letters*, vol. 429, pp. 29–40, 2018.

[35] Z. Lin, R. He, H. Luo et al., "Integrin-β5, a miR-185-targeted gene, promotes hepatocellular carcinoma tumorigenesis by regulating β-catenin stability," *Journal of Experimental & Clinical Cancer Research*, vol. 37, no. 1, p. 17, 2018.

[36] H. Xu, C. Choe, S. H. Shin et al., "Silencing of KIF14 interferes with cell cycle progression and cytokinesis by blocking the p27(Kip1) ubiquitination pathway in hepatocellular carcinoma," *Experimental & Molecular Medicine*, vol. 46, no. 5, p. e97, 2014.

[37] C. Cheng, X. Wu, Y. Shen, and Q. Li, "KIF14 and KIF23 promote cell proliferation and chemoresistance in HCC cells, and predict worse prognosis of patients with HCC," *Cancer Management and Research*, vol. Volume 12, pp. 13241–13257, 2020.

[38] J. Xu, X. Cheng, L. Tan et al., "Microwave responsive nanoplatform via P-selectin mediated drug delivery for treatment of hepatocellular carcinoma with distant metastasis," *Nano Letters*, vol. 19, no. 5, pp. 2914–2927, 2019.

[39] X. Niu, L. Chen, Y. Li, Z. Hu, and F. He, "Ferroptosis, necroptosis, and pyroptosis in the tumor microenvironment: perspectives for immunotherapy of SCLC," in *Seminars in Cancer Biology*, Academic Press, 2022.

[40] Y. Xu, W. Liao, Q. Luo, D. Yang, and M. Pan, "Histone acetylation regulator-mediated acetylation patterns define tumor malignant pathways and tumor microenvironment in hepatocellular carcinoma," *Frontiers in Immunology*, vol. 13, p. 761046, 2022.

[41] J. Sheng, J. Zhang, L. Wang et al., "Topological analysis of hepatocellular carcinoma tumour microenvironment based on imaging mass cytometry reveals cellular neighbourhood regulated reversely by macrophages with different ontogeny," *Gut*, vol. 71, no. 6, pp. 1176–1191, 2022.

[42] H. Ma, Z. Kang, T. K. Foo, Z. Shen, and B. Xia, "Disrupted BRCA1-PALB2 interaction induces tumor immunosuppression and T-lymphocyte infiltration in HCC through cGAS-STING pathway," *Hepatology*, 2022.

[43] S. Donthamsetty, V. S. Bhave, W. M. Mars et al., "Role of PINCH and its partner tumor suppressor Rsu-1 in regulating liver size and tumorigenesis," *PLoS One*, vol. 8, no. 9, p. e74625, 2013.

[44] S. K. Kim, H. R. Jang, J. H. Kim et al., "The epigenetic silencing of LIMS2 in gastric cancer and its inhibitory effect on cell migration," *Biochemical and Biophysical Research Communications*, vol. 349, no. 3, pp. 1032–1040, 2006.

[45] S. Yang, L. Wang, L. Gu et al., "Mesenchymal stem cell-derived extracellular vesicles alleviate cervical cancer by delivering miR-331-3p to reduce LIMS2 methylation in tumor cells," *Human Molecular Genetics*, 2022.

Hindawi
Disease Markers
Volume 2022, Article ID 4764609, 12 pages
https://doi.org/10.1155/2022/4764609

Research Article

Prognostic Value of Combination of Controlling Nutritional Status and Tumor Marker in Patients with Radical Non-Small-Cell Lung Cancer

Keru Ma,[1] **Hao Wang**,[2] **Xiangyu Jiang**,[1] **Chengyuan Fang**,[1] **and Jianqun Ma**[1]

[1]*Department of Thoracic Surgery, Harbin Medical University Cancer Hospital, Harbin, China*
[2]*Department of Gastrointestinal Surgery, Harbin Medical University Cancer Hospital, Harbin, China*

Correspondence should be addressed to Jianqun Ma; jianqunma@aliyun.com

Received 9 August 2022; Revised 5 September 2022; Accepted 7 September 2022; Published 23 September 2022

Academic Editor: Fu Wang

Background. Controlling nutritional status (CONUT) and tumor markers are associated with prognosis in patients with non-small-cell lung cancer (NSCLC). This study is aimed at exploring the potential usefulness of T-CONUT, constructed by combining CONUT and tumor markers, for NSCLC patients undergoing radical surgery. *Methods*. A total of 483 patients with NSCLC underwent radical surgical resection. The receiver characteristic operating curve (ROC) was used to select the tumor marker with the highest predictive performance, and CONUT was combined with this marker to construct the T-CONUT. The Kaplan–Meier method and log-rank test were used to analyze the overall survival (OS), and chi-square analysis was used to analyze the association between T-CONUT and clinicopathological characteristics. The independent risk factors were analyzed by Cox regression. A nomogram was constructed by R studio. Calibration plots, the *c*-index, and decision curves were evaluated for the performance of the nomogram. *Results*. ROC analysis showed that the predictive performance of CYFRA21–1 was better than that of CEA, NSE, and SCC. CYFRA21–1 was selected for combining with CONUT to construct T-CONUT. Elevated T-CONUT indicates poor prognosis of patients. Histological type, pTNM, and T-CONUT are independent risk factors associated with patient prognosis. The areas under the curve of the nomogram for predicting 3- and 5-year OS were 0.760 and 0.761, respectively. *Conclusion*. T-CONUT comprising CYFRA21–1 and CONUT can effectively predict the prognosis of NSCLC patients.

1. Introduction

Lung cancer (LC) has the second highest incidence of all cancers and is the leading cause of cancer death [1]. The pathological subtypes of LC are classified into non-small-cell lung cancer (NSCLC) and small-cell lung cancer (SCLC), of which NSCLC is the most common pathological type, accounting for 85% of LCs [2]. Despite significant improvements in treatment in recent years, the prognosis for NSCLC remains poor, with a median survival time of only 30.5 months [3]. Accurately predicting the prognosis of NSCLC patients still faces great challenges, and there are even some differences in the prognosis of patients at the same stage [4].

LC is a malignant tumor with a high incidence of malnutrition and cachexia. Malnutrition has been reported in 26% of NSCLC patients, while 46% of patients are at risk [5]. Malnutrition is not only a common problem faced by NSCLC patients at diagnosis but also a frequent sign during chemotherapy and adjuvant therapy. Esophagitis or anorexia caused by chemoradiotherapy may affect the treatment plan and increase the nutritional burden [6, 7]. Malnutrition can adversely affect the prognosis of patients with NSCLC, such as affected quality of life, treatment-resistant, and increased mortality [8, 9]. Therefore, it is necessary to develop fast, simple, and accurate markers to accurately identify the nutritional status of NSCLC patients before surgery, which is of great value for guiding clinical treatment and predicting prognosis.

Controlling nutritional status (CONUT) is calculated from serum albumin (Alb), total cholesterol (TC), and

peripheral lymphocyte count (TLC) [10], which relate to a variety of nutritional indicators that can enable quick assessment of nutritional status and allow the prognosis of NSCLC patients to be accurately predicted [11–13]. In addition to directly reflecting nutritional status, CONUT indirectly reflects the activity of tumor lesions. Elevated CONUT is often accompanied by higher levels of tumor markers [14] that help monitor tumor recurrence and metastasis [15, 16]. Increasing evidence confirms that the T-CONUT score, as jointly constructed from CONUT and tumor marker values, can not only provide a comprehensive preoperative nutritional assessment but also be a natural monitor of tumor activity. Researchers have shown its predictive value in colorectal cancer [17]. In addition, the nomogram constructed by tumor markers can effectively predict the prognosis of NSCLC patients [18]. However, there are few studies on T-CONUT in NSCLC, and the decision of whether to construct a nomogram with T-CONUT for better evaluation of the prognosis of NSCLC still needs to be further explored.

As a result, this study compared the predictive value of different tumor markers for the prognosis of NSCLC patients and selected the tumor marker with the highest predictive performance when combined with CONUT to construct T-CONUT. A nomogram was constructed based on the clinicopathological features of the patients.

2. Materials and Methods

2.1. Patients. This study retrospectively analyzed NSCLC patients who underwent radical surgical resection at the Department of Thoracic Surgery, Cancer Hospital Affiliated to Harbin Medical University, from December 2011 to May 2016. The diagnosis of NSCLC was based on the intraoperative pathological tissue obtained and confirmed by two pathologists. The patients received routine preoperative examinations during hospitalization, including CT, bone scan, electrocardiogram, routine hematology, and tumor markers. The clinicopathological information of patients was stored in the case system of the Cancer Hospital Affiliated to Harbin Medical University, including gender, age, tumor size, tumor location, and pTNM staging. The above content is in line with the eighth edition of the AJCC Staging Manual [19].

The inclusion criteria were as follows: (1) pathologically diagnosed patients with NSCLC; (2) undergo radical surgery; (3) patients without other malignancies.

The exclusion criteria were as follows: (1) preoperative radiotherapy or chemotherapy; (2) treatment with steroids; (3) autoimmune diseases; (4) serious infection; (5) hematological malignancies.

All patients underwent routine review after surgery, including chest CT, abdominal ultrasound, blood tumor markers, superficial lymph node ultrasound, and head MRI.

2.2. Hematology Parameters. Patients underwent routine hematology tests one week before surgery. Prognostic nutritional index (PNI) is calculated as peripheral blood lymphocyte count ($\times 10^9$/ml) $\times$ 5 + serum albumin value (g/l) [20]. Systemic inflammation score (SIS) was calculated as follows: Alb < 40 g/l and LMR < 4.44 scored 2; Alb ≥ 40 g/l or LMR ≥ 4.44 scored 1; Alb ≥ 40 g/l and LMR ≥ 4.44 scored 0 [21]. CONUT was calculated by Alb and TLC, which was divided into normal (0-1), mild (2-4), moderate (5-8), and severe (9-12, 14).

Table 1: Patient characteristics.

Clinicopathological features	Patients 483(%)
Sex	
Male	281 (58.2)
Female	202 (41.8)
Age (years)	
≤60	284 (58.8)
>60	199 (41.2)
BMI (kg/m^2), median, range	23.39 (14.69-32.1)
SCC (ng/ml)	
≤1.5	409 (84.7)
>1.5	74 (15.3)
CEA (ng/ml)	
≤5	327 (67.7)
>5	156 (32.3)
NSE (ng/ml)	
≤15.2	369 (76.4)
>15.2	114 (23.6)
CYFRA21-1 (ng/ml)	
≤3.3	259 (53.6)
>3.3	224 (46.4)
Smoking history	
No	227 (47.0)
Yes	256 (53.0)
Tumor location	
Left lung	192 (39.8)
Right lung	291 (60.2)
Histological type	
Squamous cell carcinoma	157 (32.5)
Adenocarcinoma	301 (62.3)
Others	25 (5.2)
pTNM	
I	269 (55.7)
II	81 (16.8)
III	133 (27.5)
CONUT	
<2	330 (68.3)
≥2	153 (31.7)
PNI	
≥52.48	203 (42.0)
<52.48	280 (58.0)
SIS	
0	175 (36.2)
1	215 (44.5)
2	93 (19.3)

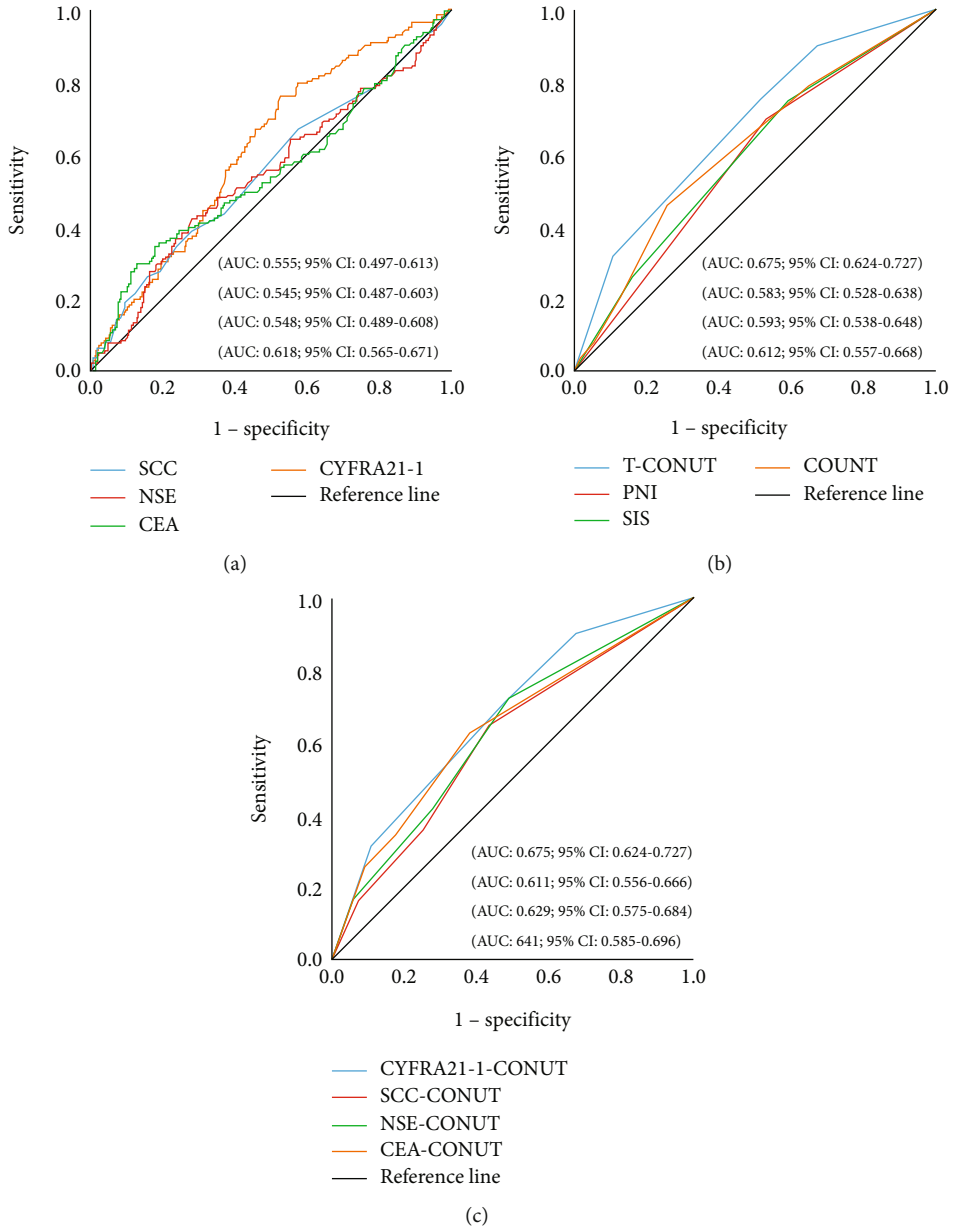

Figure 1: ROC of tumor markers and nutritional markers among total patients. (a) Comparison of predictive performance of different tumor markers. (b) Comparison of predictive performance of T-CONUT with nutritional markers. (c) Comparison of predictive performance of different tumor markers combined with CONUT.

2.3. Construction of T-CONUT. At first, a receiver characteristic operating curve (ROC) of carcinoembryonic antigen (CEA), cytokeratin 19 fragment (CYFRA21–1), neuron specific enolase (NSE), and squamous cell associated antigen (SCC) was established individually for the NSCLC patients. Then, the area under the curve (AUC) was calculated to determine the optimal cutoff values. The values above the cutoff were considered high, otherwise were considered to be low. Based on the tumor markers and the CONUT values, the patients were divided into four groups: group 1—tumor markers and CONUT both below the cutoff point; group 2—tumor markers below but CONUT above the cutoff point; group 3—tumor markers above while CONUT below the cutoff point; and group 4—tumor markers and CONUT both above the cutoff point.

2.4. Statistical Analysis. Overall survival (OS) was defined as the follow-up time from the time of operation to the time of death or the last survival. If the patients were alive at the last follow-up, they were included in this study. ROC was used to calculate the AUC. The optimal cut-off value was calculated using the "Youden index." Kaplan-Meier method with Long-rank was used to analyze survival curves. Cox regression models were used to analyze the calculation of hazard ratios (HRs) and 95% confidence intervals (CIs) and to identify independent risk factors. T-ROC and nomogram

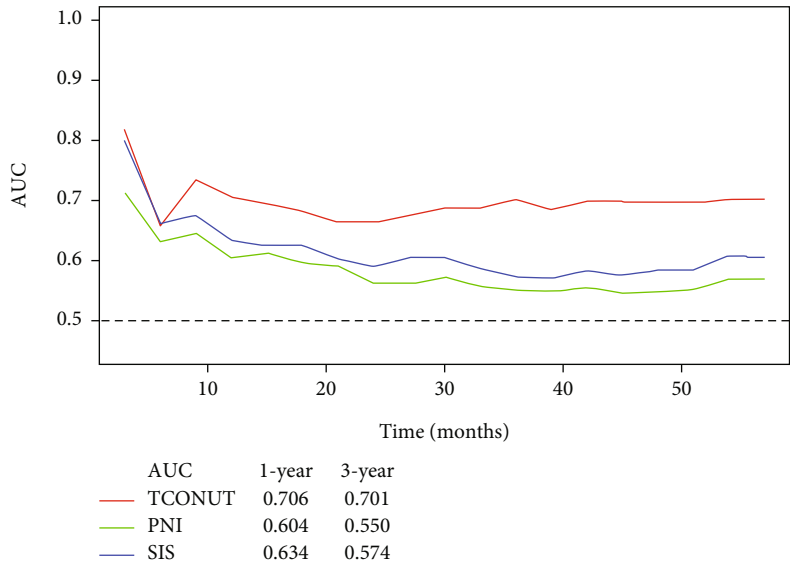

Figure 2: Time-dependent ROC curves for the T-CONUT, PNI, and SIS. The horizontal axis represents month after surgery, and the vertical axis represents the estimated AUC for survival at the time of interest. Red, green, and blue solid lines represent the estimated AUCs for the T-CONUT, PNI, and SIS, respectively.

were performed by R studio. Calibration plots, decision curve, and *c*-index were used to validate the performance of nomogram. All analyses were performed using SPSS for Windows version 25.0 and R software version 4.1.2 for statistical analysis, $P < 0.05$ was considered statistically significant.

3. Results

3.1. Patient Characteristics. The study included 483 patients, 281 males and 202 females, with a median age of 58 (range 25-78) and BMI at 23.39 (range 14.69-32.1). Among them, there were 269 at stage I, 81 at stage II, and 133 at stage III, according to the pTNM definition (Table 1).

3.2. Accuracy Comparison of Different Prognostic Markers. To select tumor markers suitable for evaluating NSCLC according to ROC, CYFRA21-1 and CONUT had the highest AUC (Figures 1(a) and 1(b)), and the cutoff values of CYFRA21-1, CONUT, and PNI are 2.75, 2, and 52.48.

After finding that CYFRA21-1 and CONUT have the highest AUC, we construct T-CONUT according to the cutoff values of CYFRA21-1 and CONUT. The patients in group 1-group 4 were 125 (25.9%), 71 (14.7%), 205 (42.4%), and 82 (17%), respectively. The prognostic accuracy of T-CONUT, PNI, and SIS was compared by ROC and T-ROC. The results showed that T-CONUT had the highest AUC, which indicated that T-CONUT had high accuracy in predicting OS (Figures 1(b) and 2).

Furthermore, we combine different tumor markers with CONUT and ROC showed that the cutoff values of SCC, NSE, and CEA are 1.15, 14.18, and 6.63. Then, we combine different tumor markers with CONUT, respectively. The AUC of CYFRA21-1-CONUT was higher than that of SCC-CONUT, NSE-CONUT, and CEA-CONUT (Figure 1(c)).

3.3. T-CONUT and Patient Survival. Chi-square analysis showed that T-CONUT was associated with sex, SCC, NSE ($P < 0.001$), smoking history, histological type, and pTNM stage and was significantly correlated (Table 2).

The survival curve showed that the 5-year OS rate of CONUT ≥ 2 was significantly lower than that of CONUT < 2 (54.5% vs. 74.8%) (Figure 3(a)); the 5-year OS rate of CYFRA21-1 > 2.75 was significantly lower than that of CYFRA21-1 ≤ 2.75 (59.0% vs. 81.4%) (Figure 3(b)); for T-CONUT, the 5-year OS rates of group 1-group 4 were 87.6%, 70.7%, 66.8%, and 38.6% (Figure 3(c)). Obviously, elevated T-CONUT indicates poor prognosis of patients.

According to pTNM, for stage I, the 5-year OS rates of T-CONUT group 1-4 were 97.4%, 82.7%, 74.3%, and 60.1%. For stage II, the 5-year OS rates of T-CONUT groups 1-4 were 72.4%, 66.7%, 60.8%, and 42.0%. For stage III, the 5-year survival rates of T-CONUT groups 1-4 were 63.8%, 27.3%, 57.2%, and 23.3% (Figures 4(a)–4(c)).

The Cox found that histological type, pTNM, and T-CONUT were independent risk factors (Table 3).

3.4. Construction of a Nomogram. Histological type, pTNM, and T-CONUT were independent risk factors; we combined these factors to construct a nomogram (Figure 5(a)). ROC showed that nomogram had the highest AUC in 3-year and 5-year OS, the sensitivity were 75.5% and 64.6%, and the specificity were 85.2% and 52.5% (Figures 5(b) and 5(d)). The *c*-index was 0.725. Calibration plots and decision curve showed good predictive performance of nomogram (Figures 5(c), 5(f), and 6).

4. Discussion

Preoperative nutritional status is crucial for lung cancer patients, and malnutrition adversely affects lung cancer patients, whether for treatment, quality of life, or predicting

Table 2: Chi-square analysis of T-CONUT and patient characteristics.

Clinicopathological features	Group 1 (125)	Group 2 (71)	Group 3 (205)	Group 4 (82)	*P*
Sex					**0.001**
Male	56 (44.8)	41 (57.7)	126 (61.5)	58 (70.7)	
Female	69 (55.2)	30 (42.3)	79 (38.5)	24 (29.3)	
Age (years)					0.209
≤60	78 (62.4)	47 (66.2)	110 (53.7)	49 (59.8)	
>60	47 (37.6)	24 (33.8)	95 (46.3)	33 (40.2)	
BMI (kg/m^2)					0.093
≤23.39	58 (46.4)	34 (47.9)	96 (46.8)	51 (62.2)	
>23.39	67 (53.6)	37 (52.1)	109 (53.2)	31 (37.8)	
SCC (ng/ml)					**<0.001**
≤1.5	120 (96.0)	65 (91.5)	166 (81.0)	58 (70.7)	
>1.5	5 (4.0)	6 (8.5)	39 (19.0)	24 (29.3)	
CEA (ng/ml)					0.275
≤5	86 (68.8)	49 (69.0)	144 (70.2)	48 (58.5)	
>5	39 (31.2)	22 (31.0)	61 (29.8)	34 (41.5)	
NSE (ng/ml)					**<0.001**
≤15.2	111 (88.8)	67 (94.4)	137 (66.8)	54 (65.9)	
>15.2	14 (11.2)	4 (5.6)	68 (33.2)	28 (34.1)	
Smoking history					**0.003**
No	73 (58.4)	39 (54.9)	80 (39.0)	35 (42.7)	
Yes	52 (41.6)	32 (45.1)	125 (61.0)	47 (57.3)	
Tumor location					0.302
Left lung	51 (40.8)	29 (40.8)	73 (35.6)	39 (47.6)	
Right lung	74 (59.2)	42 (59.2)	132 (64.4)	43 (52.4)	
Histological type					**<0.001**
Squamous cell carcinoma	17 (13.6)	21 (29.6)	88 (42.9)	31 (37.8)	
Adenocarcinoma	105 (84.0)	46 (64.8)	108 (52.7)	42 (51.2)	
Others	3 (2.4)	4 (5.6)	9 (4.4)	9 (11.0)	
pTNM					**<0.001**
I	84 (67.2)	48 (67.6)	110 (53.7)	27 (32.9)	
II	17 (13.6)	12 (16.9)	32 (15.6)	20 (24.4)	
III	24 (19.2)	11 (15.5)	63 (30.7)	35 (42.7)	

prognosis. Malnutrition in lung cancer patients may be caused by insufficient intake, impaired function, and complications of adjuvant therapy [22, 23]. A previous study reported that 42.8% of lung cancer patients had malnutrition, a proportion which is significantly higher than for some digestive system tumors such as gastric cancer and colorectal cancer [23]. Therefore, accurately assessing the nutritional status of LC patients is of great significance for better tolerance of adjuvant therapy, nutritional intervention guidance, and prognosis.

In this study, we found that the CONUT score could effectively predict the prognosis of NSCLC patients undergoing radical surgery. CONUT had the highest AUC, which was consistent with previous studies [24]. Part of the reason is that CONUT contains total cholesterol levels, which can reflect inflammation in the body, liver function, changes in body fluids and energy reserves. However, the calculation methods of PNI and SIS do not include total cholesterol. Hikage et al. showed that CONUT has high sensitivity in patients with hypocholesterolemia [25], and changes in total cholesterol levels can effectively judge postoperative recovery and tumor aggressiveness. Total cholesterol levels tend to decrease when tumors recur, suggesting that CONUT can more comprehensively and accurately reflect the nutritional status of NSCLC [26]. In addition, there are certain differences in the nutritional status of ethnic groups in different regions. For example, the obesity rate in Western countries is higher than in Eastern countries, and the obesity rate in economically developed regions is higher than in low-income regions [27–29]. Therefore, some specific nutritional scores help better predict prognosis [30, 31]. Our institution is a high-capacity center in Northeast China, and the results also have certain applicable value. Although our results may have limited clinical applicability, this does not prevent us from making recommendations for LC experts: for LC patients with a high incidence of malnutrition, variations

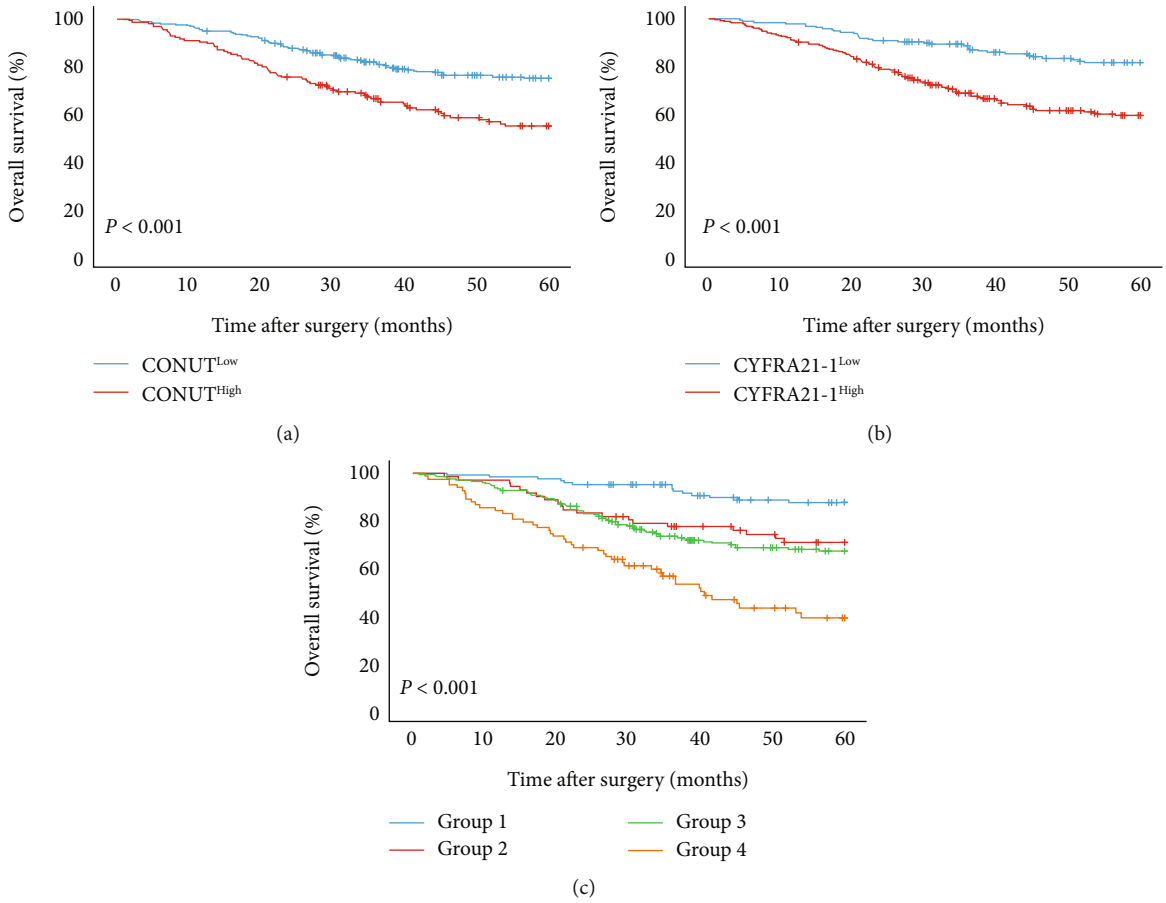

Figure 3: Kaplan–Meier analysis of OS of overall NSCLC patients. (a) Association of the CONUT with the OS of overall patients. (b) Association of the CYFRA21-1 with the OS of overall patients. (c) Association of the T-CONUT with the OS of overall patients.

in the nutritional status of lung cancer patients with different physiques in different regions needs to be recognized. At the same time, we also call for multicenter and large-sample studies to use region and ethnicity as independent evaluation factors for nutritional indicators, which will help to more accurately assess the nutritional status of patients before surgery.

We found that elevated CONUT was associated with poor prognosis, suggesting that poor nutritional status will lead to poor prognosis. This finding indicates that different nutritional indicators play different roles in NSCLC patients. Albumin is synthesized by the liver and has antitumor oxidative properties [32]. Decreased albumin reflects a loss of body defenses and reduced responsiveness to antitumor therapy [33]. Guner et al. showed that albumin was more prognostic than NLR and PLR [34], and the score weight of albumin in the CONUT score was twice that of other indicators, which also shows that albumin has importance for the prognosis of patients. Cholesterol participates in the basic structure of cell membranes and maintains cell physiological functions through intracellular signal transduction. Decreased cholesterol levels suggest both a lack of energy storage and metabolic imbalances that contribute to the development and progression of cancer [35]. As an important part of the immune system, lymphocytes inhibit tumor cell growth, invasion, and migration by exerting cytotoxic functions, and their decreased levels suggest a poor prognosis for patients [36]. These mechanisms explain why elevated CONUT is associated with poor patient outcomes.

Notably, some studies have found that CONUT is significantly associated with tumor marker levels, and when CONUT is elevated, it is often accompanied by higher tumor marker levels [14, 37]. Selecting specific tumor markers according to different tumor tissues helps to accurately determine the biological behavior of tumors. The T-CONUT constructed by Yamamoto et al. combines CEA and CONUT and can effectively predict the prognosis of colorectal cancer patients [17]. T-CONUT constructed by Wang et al. as a combination of CA19-9 and CONUT can well predict the prognosis of patients with pancreatic ductal adenocarcinoma [38]. These studies suggest that the combined score can provide more comprehensive prognostic information and better serve patients. They also provide a good theoretical basis for us to combine tumor markers with CONUT as T-CONUT may have better predictive performance for NSCLC.

ROC showed that CYFRA21-1 was more accurate in predicting prognosis than CEA, SCC, and NSE, which was consistent with previous studies [39]. Although the sensitivity of tumor markers depends on tumor tissue classification,

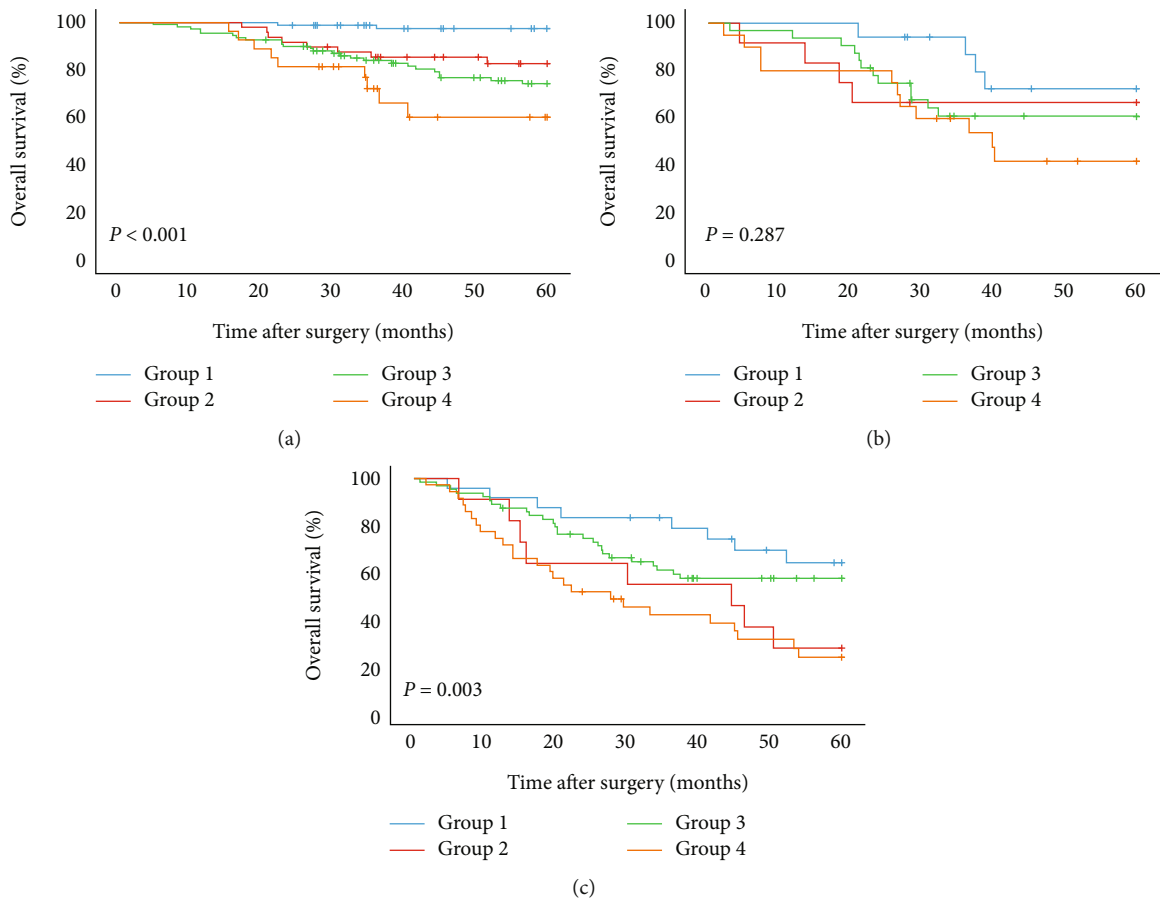

Figure 4: Kaplan–Meier analysis of OS of NSCLC patients at each pTNM stage according to the T-CONUT. (a) Association of the T-CONUT with the OS of patients with stage I NSCLC. (b) Association of the T-CONUT with the OS of patients with stage II NSCLC. (c) Association of the T-CONUT with the OS of patients with stage III NSCLC.

different studies have shown that CYFRA21-1 can effectively assess the prognosis of NSCLC patients. Zhang et al. found that CYFRA21-1 was an independent risk factor associated with the prognosis of lung adenocarcinoma whose predictive power was better than that of CEA and CSE [16]. Reinmuth et al. showed that CYFRA21-1 was more sensitive to lung squamous cell carcinoma than CEA, NSE, and SCC [40]. These results suggest that CYFRA21-1 still has good applicability, even for different histological types. In addition, we combined different tumor markers with CONUT and still found that T-CONUT, constructed with CYFRA21-1 and CONUT, had the highest AUC. This indicates that CYFRA21-1-CONUT is more suitable for predicting the prognosis of NSCLC patients; it can provide simple, accurate, and rapid preoperative evaluation and has definite applicable value.

After constructing T-CONUT from CYFRA21-1 and CONUT, we found that strong tumor aggression was associated with increased T-CONUT, suggesting that greater aggression would lead to lower nutritional status. In addition, we also found that when T-CONUT scores were higher, there was a significantly increased proportion of patients who smoked. Smoking is one of the causes of LC. Smoking may suppress appetite and affect eating [41] while anorexia can lead to insufficient nutritional intake and weight loss. As anorexia progresses, lung cancer patients may eventually develop refractory cachexia [42]. Smoking can also lead to more aggressive lung cancer, acquisition of drug resistance, and ultimately, poor prognosis [43, 44]. Therefore, smoking cessation will not only reduce the incidence of LC but also help improve nutritional status.

Clinically, pTNM staging can accurately assess the biological behavior of NSCLC and predict prognosis. However, nutritional status gradually decreases with increasing pTNM staging, and pTNM staging based on macroscopic anatomy cannot provide microscopic blood prognostic information. Some blood nutritional markers, such as albumin serum and total cholesterol, have the advantages of being cheap and easy to apply and can allow rapid preoperative assessment. More importantly, these blood nutritional markers can accurately predict the prognosis of patients with NSCLC. Li et al. constructed a nomogram based on pTNM staging and the albumin-fibrin ratio to accurately predict the prognosis of NSCLC [45]. Guo et al. constructed a combination of N stage and serum albumin to globulin ratio as a nomogram to accurately predict long-term survival in NSCLC [46]. Zeng et al. constructed C-reactive protein and TNM staging as a nomogram which can accurately predict the prognosis of NSCLC patients undergoing radical surgery [47]. These studies demonstrate that predictive

Table 3: The Cox regression of overall patients.

Clinicopathological features	Univariate analysis		Multivariate analysis	
	HR (95% CI)	*P*	HR (95% CI)	*P*
Sex		0.111		
Male	1			
Female	0.757 (0.537-1.066)			
Age	0.994 (0.976-1.014)	0.566		
BMI	0.954 (0.907-1.002)	0.061		
SCC	1.059 (1.004-1.117)	**0.034**	1.015 (0.952-1.081)	0.655
CEA	1.000 (0.997-1.004)	0.811		
NSE	0.999 (0.995-1.004)	0.786		
Smoking history		0.513		
No	1			
Yes	1.117 (0.802-1.555)			
Tumor location		0.484		
Left lung	1			
Right lung	1.130 (0.803-1.589)			
Histological type		**0.014**		**0.004**
Squamous cell carcinoma	1		1	
Adenocarcinoma	1.230 (0.845-1.791)	0.280	1.856 (1.211-2.843)	**0.005**
Others	2.558 (1.364-4.797)	**0.003**	2.513 (1.316-4.801)	**0.005**
pTNM		**<0.001**		**<0.001**
I	1		1	
II	2.806 (1.771-4.445)	**<0.001**	2.614 (1.619-4.222)	**<0.001**
III	4.036 (2.757-5.907)	**<0.001**	3.248 (2.183-4.834)	**<0.001**
T-CONUT		**<0.001**		**<0.001**
0	1		1	
1	2.749 (1.389-5.443)	**0.004**	2.720 (1.352-5.471)	**0.005**
2	3.254 (1.823-5.808)	**<0.001**	3.252 (1.800-5.874)	**<0.001**
3	7.204 (3.948-13.145)	**<0.001**	4.716 (2.470-9.003)	**<0.001**
PNI		**0.002**		0.336
≥52.48	1		1	
<52.48	1.744 (1.219-2.495)		1.243 (0.798-1.938)	
SIS		**0.003**		0.466
0	1		1	
1	1.746 (1.167-2.612)	**0.007**	1.315 (0.840-2.057)	0.231
2	2.175 (1.374-3.442)	**0.001**	1.338 (0.761-2.353)	0.311

models constructed from anatomical staging and nutritional markers can personalize patient risk stratification, reduce prognostic bias, and serve patients better. Notably, we combined different tumor markers with CONUT and ROC and showed that CYFRA21-1-CONUT had the highest AUC. Moreover, Cox analysis showed that T-CONUT constructed from CYFRA21-1 and CONUT, histological type, and pTNM stage were independent risk factors associated with patient prognosis. Afterward, we integrated the above parameters to construct a nomogram model. However, although a nomogram built with CYFRA21-1-CONUT had the highest AUC, the AUC values for ROCs in this study were not as high as expected. We think this may be due to the small sample size, also recognizing that a larger sample will be required for validation. Nevertheless, the AUC of the nomogram in predicting the patient's OS at both 3 and 5 years was higher than that of pTNM staging. This indicates that T-CONUT can supplement pTNM staging with more comprehensive prognostic information. This study suggests that the nomogram constructed with T-CONUT can provide clinicians with more comprehensive tumor prognostic information, which is helpful for comprehensively grasping the biological behavior of the tumor, and its prognostic performance is higher than that of traditional pTNM staging. The calibration plot showed that the nomogram performed well in predicting the status of patients at 3 and 5 years. The advantages of the nomogram also show that both nutritional status and pTNM staging play an important role in

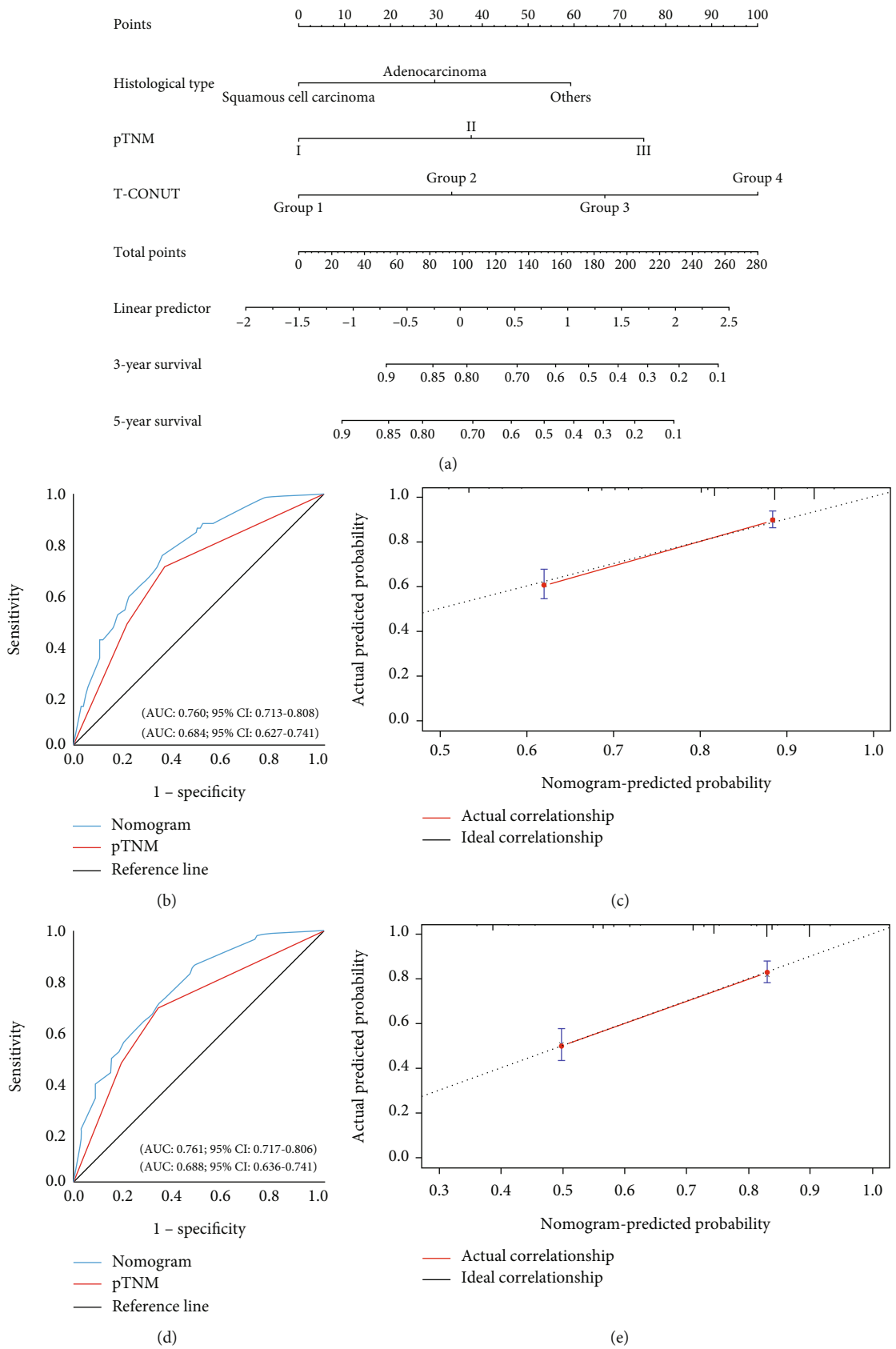

Figure 5: (a) Nomogram model predicting the 3- and 5-year OS of all patients. (b) ROC curve of the nomogram model predicting the 3-year OS of all patients. (c) Calibration curve for 3-year nomogram predictions. (d) ROC curve of the nomogram model predicting the 5-year OS of all patients. (e) Calibration curve for 3-year nomogram predictions.

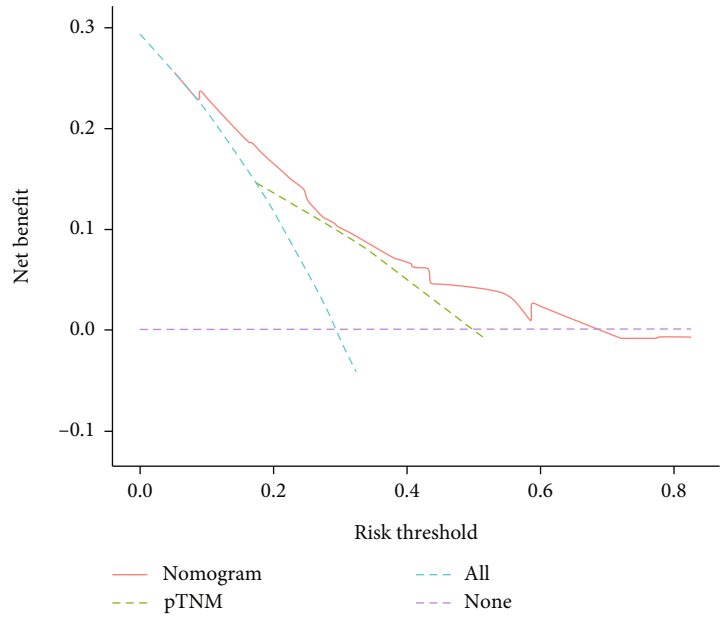

Figure 6: Decision curve analysis for the 5-year survival predictions. In the decision curve analysis, the *y*-axis indicates net benefit, calculated by summing the benefits (true positives) and subtracting the harms (false positives). The nomogram model (red dotted line) had the highest net benefit compared with the pTNM staging system (green dotted line). The straight line represents the assumption that all the patients will die, and the horizontal line represents the assumption that none of the patients will die.

predicting the prognosis of NSCLC. Some nutritional markers supplement pTNM staging with more comprehensive prognostic information. The nomogram combined with staging can better serve NSCLC patients and is worthy of clinical application.

4.1. Research Limitations. There are some limitations to this retrospective study. First, the results of this study require multicenter validation. Second, we only collected the information of tumor markers and nutritional markers of patients before surgery, and dynamic monitoring of these indicators can help predict prognosis more accurately.

5. Conclusion

The T-CONUT constructed by the combination of CYFRA21-1 and CONUT can effectively predict the prognosis of NSCLC patients. An elevated T-CONUT group suggested a poor prognosis. Furthermore, the nomogram constructed by T-CONUT combined with the clinicopathological features of the patients helps to better serve NSCLC patients.

Data Availability

The data used to support the findings of the manuscript are available by contacting the corresponding author upon reasonable request.

Ethical Approval

All procedures followed were in accordance with the ethical standards of the Human Subjects Responsibility Committee (institutional and national) and the 1964 Declaration of Helsinki and subsequent editions. This study was approved by the Ethics Committee of the Cancer Hospital Affiliated to Harbin Medical University (ChiECRCT20210277).

Conflicts of Interest

The authors declare that they have no conflict of interest.

Authors' Contributions

Keru Ma and Hao Wang designed and conceived this project, and they contributed equally to this work. Keru Ma, Hao Wang, and Xiangyu Jiang interpreted and analyzed the data. Jianqun Ma revised the manuscript for important intellectual content, and Keru Ma, Hao Wang, Xiangyu Jiang, and Chengyuan Fang participated in the patient information collection. Keru Ma and Hao Wang contributed equally to the work as first authors.

Acknowledgments

This work was supported by the Haiyan Foundation of the Harbin Medical University Cancer Hospital (under grants JJZD2018-01 and JJZD2020-01).

References

[1] H. Sung, J. Ferlay, R. L. Siegel et al., "Global cancer statistics 2020: GLOBOCAN estimates of incidence and mortality worldwide for 36 cancers in 185 countries," *CA: a Cancer Journal for Clinicians*, vol. 71, no. 3, pp. 209–249, 2021.

[2] D. Planchard, S. Popat, K. Kerr et al., "Metastatic non-small cell lung cancer: ESMO Clinical Practice Guidelines for

diagnosis, treatment and follow-up†," *Annals of Oncology*, vol. 29, p. iv192, 2018.

[3] M. Maemondo, A. Inoue, K. Kobayashi et al., "Gefitinib or chemotherapy for non-small-cell lung cancer with mutated EGFR," *The New England Journal of Medicine*, vol. 362, no. 25, pp. 2380–2388, 2010.

[4] R. Govindan, J. Bogart, and E. E. Vokes, "Locally advanced non-small cell lung cancer: the past, present, and future," *Journal of Thoracic Oncology*, vol. 3, no. 8, pp. 917–928, 2008.

[5] M. Kovarik, M. Hronek, and Z. Zadak, "Clinically relevant determinants of body composition, function and nutritional status as mortality predictors in lung cancer patients," *Lung Cancer*, vol. 84, no. 1, pp. 1–6, 2014.

[6] N. Kiss and A. Curtis, "Current insights in nutrition assessment and intervention for malnutrition or muscle loss in people with lung cancer: a narrative review," *Advances in Nutrition*, vol. 13, 2022.

[7] M. E. Cooley, "Symptoms in adults with lung cancer: a systematic research review," *Journal of Pain and Symptom Management*, vol. 19, no. 2, pp. 137–153, 2000.

[8] J. Polański, B. Jankowska-Polańska, and G. Mazur, "Relationship between nutritional status and quality of life in patients with lung cancer," *Cancer Management and Research*, vol. 13, pp. 1407–1416, 2021.

[9] J. Polański, B. Jankowska-Polańska, I. Uchmanowicz et al., "Malnutrition and quality of life in patients with non-small-cell lung cancer," *Advances in Experimental Medicine and Biology*, vol. 1021, pp. 15–26, 2017.

[10] J. Ignacio de Ulíbarri, A. González-Madroño, N. G. de Villar et al., "CONUT: a tool for controlling nutritional status. First validation in a hospital population," *Nutrición Hospitalaria*, vol. 20, no. 1, pp. 38–45, 2005.

[11] S. Takamori, G. Toyokawa, M. Shimokawa et al., "A novel prognostic marker in patients with non-small cell lung cancer: musculo-immuno-nutritional score calculated by controlling nutritional status and creatine kinase," *Journal of Thoracic Disease*, vol. 11, no. 3, pp. 927–935, 2019.

[12] T. Ohba, S. Takamori, R. Toyozawa et al., "Prognostic impact of the controlling nutritional status score in patients with non-small cell lung cancer treated with pembrolizumab," *Journal of Thoracic Disease*, vol. 11, no. 9, pp. 3757–3768, 2019.

[13] G. Toyokawa, Y. Kozuma, T. Matsubara et al., "Prognostic impact of controlling nutritional status score in resected lung squamous cell carcinoma," *Journal of Thoracic Disease*, vol. 9, no. 9, pp. 2942–2951, 2017.

[14] D. Kuroda, H. Sawayama, J. Kurashige et al., "Controlling nutritional status (CONUT) score is a prognostic marker for gastric cancer patients after curative resection," *Gastric Cancer*, vol. 21, no. 2, pp. 204–212, 2018.

[15] H. Chen, F. Fu, Y. Zhao et al., "The prognostic value of preoperative serum tumor markers in non-small cell lung cancer varies with radiological features and histological types," *Frontiers in Oncology*, vol. 11, article 645159, 2021.

[16] L. Zhang, D. Liu, L. Li et al., "The important role of circulating CYFRA21-1 in metastasis diagnosis and prognostic value compared with carcinoembryonic antigen and neuron-specific enolase in lung cancer patients," *BMC Cancer*, vol. 17, no. 1, p. 96, 2017.

[17] M. Yamamoto, H. Saito, C. Uejima et al., "Prognostic value of combined tumor marker and controlling nutritional status (CONUT) score in colorectal cancer patients," *Yonago Acta Medica*, vol. 62, no. 1, pp. 124–130, 2019.

[18] X. Lv, Z. Wu, J. Cao et al., "A nomogram for predicting the risk of lymph node metastasis in T1-2 non-small-cell lung cancer based on PET/CT and clinical characteristics," *Translational Lung Cancer Research*, vol. 10, no. 1, pp. 430–438, 2021.

[19] A. G. Nicholson, K. Chansky, J. Crowley et al., "The International Association for the Study of Lung Cancer lung cancer staging project: proposals for the revision of the clinical and pathologic staging of small cell lung cancer in the forthcoming eighth edition of the TNM classification for lung cancer," *Journal of Thoracic Oncology*, vol. 11, no. 3, pp. 300–311, 2016.

[20] J. Y. Liu, H. M. Dong, W. L. Wang et al., "The effect of the prognostic nutritional index on the toxic side effects of radiochemotherapy and prognosis after radical surgery for gastric cancer," *Cancer Management and Research*, vol. 13, pp. 3385–3392, 2021.

[21] S. Li, Z. Wang, W. Zhang, J. Li, K. Zhou, and G. Che, "Systemic inflammation score: a novel risk stratification tool for postoperative outcomes after video-assisted thoracoscopic surgery lobectomy for early-stage non-small-cell lung cancer," *Cancer Management and Research*, vol. 11, pp. 5613–5628, 2019.

[22] D. De Ruysscher, C. Faivre-Finn, K. Nackaerts et al., "Recommendation for supportive care in patients receiving concurrent chemotherapy and radiotherapy for lung cancer☆," *Annals of Oncology*, vol. 31, no. 1, pp. 41–49, 2020.

[23] B. G. Na, S. S. Han, Y. A. Cho et al., "Nutritional status of patients with cancer: a prospective cohort study of 1, 588 hospitalized patients," *Nutrition and Cancer*, vol. 70, no. 8, pp. 1228–1236, 2018.

[24] S. C. Lee, J. G. Lee, S. H. Lee et al., "Prediction of postoperative pulmonary complications using preoperative controlling nutritional status (CONUT) score in patients with resectable non-small cell lung cancer," *Scientific Reports*, vol. 10, no. 1, p. 12385, 2020.

[25] M. Hikage, Y. Taniyama, T. Sakurai et al., "The influence of the perioperative nutritional status on the survival outcomes for esophageal cancer patients with neoadjuvant chemotherapy," *Annals of Surgical Oncology*, vol. 26, no. 13, pp. 4744–4753, 2019.

[26] A. Niendorf, H. Nägele, D. Gerding, U. Meyer-Pannwitt, and A. Gebhardt, "Increased LDL receptor mRNA expression in colon cancer is correlated with a rise in plasma cholesterol levels after curative surgery," *International Journal of Cancer*, vol. 61, no. 4, pp. 461–464, 1995.

[27] X. Li, C. Wu, J. Lu et al., "Cardiovascular risk factors in China: a nationwide population-based cohort study," *The Lancet Public Health*, vol. 5, no. 12, pp. e672–e681, 2020.

[28] B. A. Swinburn, G. Sacks, K. D. Hall et al., "The global obesity pandemic: shaped by global drivers and local environments," *Lancet*, vol. 378, no. 9793, pp. 804–814, 2011.

[29] J. C. Brown, S. Yang, E. F. Mire et al., "Obesity and cancer risk in white and black adults: a prospective cohort study," *Obesity (Silver Spring)*, vol. 29, no. 6, pp. 960–965, 2021.

[30] O. Bouillanne, G. Morineau, C. Dupont et al., "Geriatric nutritional risk index: a new index for evaluating at-risk elderly medical patients," *The American Journal of Clinical Nutrition*, vol. 82, no. 4, pp. 777–783, 2005.

[31] R. C. Thirlby and J. Randall, "A genetic "obesity risk index" for patients with morbid obesity," *Obesity Surgery*, vol. 12, no. 1, pp. 25–29, 2002.

[32] V. Arroyo, R. García-Martinez, and X. Salvatella, "Human serum albumin, systemic inflammation, and cirrhosis," *Journal of Hepatology*, vol. 61, no. 2, pp. 396–407, 2014.

[33] J. P. Xiong, J. Y. Long, W. Y. Xu et al., "Albumin-to-alkaline phosphatase ratio: a novel prognostic index of overall survival in cholangiocarcinoma patients after surgery," *World journal of gastrointestinal oncology*, vol. 11, no. 1, pp. 39–47, 2019.

[34] A. Guner, S. Y. Kim, J. E. Yu et al., "Parameters for predicting surgical outcomes for gastric cancer patients: simple is better than complex," *Annals of Surgical Oncology*, vol. 25, no. 11, pp. 3239–3247, 2018.

[35] S. A. Törnberg, L. E. Holm, J. M. Carstensen, and G. A. Eklund, "Cancer incidence and cancer mortality in relation to serum cholesterol," *Journal of the National Cancer Institute*, vol. 81, no. 24, pp. 1917–1921, 1989.

[36] B. Z. Qian, "Inflammation fires up cancer metastasis," *Seminars in Cancer Biology*, vol. 47, pp. 170–176, 2017.

[37] M. Shiihara, R. Higuchi, W. Izumo et al., "Impact of the controlling nutritional status score on severe postoperative complications of pancreaticoduodenectomy for pancreatic cancer," *Langenbeck's Archives of Surgery*, vol. 406, no. 5, pp. 1491–1498, 2021.

[38] A. Wang, B. Sun, M. Wang et al., "Predictive value of CONUT score combined with serum CA199 levels in postoperative survival of patients with pancreatic ductal adenocarcinoma: a retrospective study," *Peer J*, vol. 8, p. e8811, 2020.

[39] M. J. Edelman, L. Hodgson, P. Y. Rosenblatt et al., "CYFRA 21-1 as a prognostic and predictive marker in advanced non-small-cell lung cancer in a prospective trial: CALGB 150304," *Journal of Thoracic Oncology*, vol. 7, no. 4, pp. 649–654, 2012.

[40] N. Reinmuth, B. Brandt, M. Semik et al., "Prognostic impact of Cyfra21-1 and other serum markers in completely resected non-small cell lung cancer," *Lung Cancer*, vol. 36, no. 3, pp. 265–270, 2002.

[41] Y. H. Jo, D. A. Talmage, and L. W. Role, "Nicotinic receptor-mediated effects on appetite and food intake," *Journal of Neurobiology*, vol. 53, no. 4, pp. 618–632, 2002.

[42] K. Fearon, F. Strasser, S. D. Anker et al., "Definition and classification of cancer cachexia: an international consensus," *The Lancet Oncology*, vol. 12, no. 5, pp. 489–495, 2011.

[43] L. Zhang, J. Li, J. Hu et al., "Cigarette smoke extract induces EGFR-TKI resistance via promoting EGFR signaling pathway and ROS generation in NSCLC cell lines," *Lung Cancer*, vol. 109, pp. 109–116, 2017.

[44] O. Arrieta, A. D. Campos-Parra, C. Zuloaga et al., "Clinical and pathological characteristics, outcome and mutational profiles regarding non-small-cell lung cancer related to wood-smoke exposure," *Journal of Thoracic Oncology*, vol. 7, no. 8, pp. 1228–1234, 2012.

[45] S. Q. Li, Y. H. Jiang, J. Lin et al., "Albumin-to-fibrinogen ratio as a promising biomarker to predict clinical outcome of non-small cell lung cancer individuals," *Cancer Medicine*, vol. 7, no. 4, pp. 1221–1231, 2018.

[46] X. Guo, J. Shao, B. Zhai et al., "Relationship and prognostic significance between preoperative serum albumin to globulin ratio and CT features of non-small cell lung cancer," *European Journal of Radiology*, vol. 128, article 109039, 2020.

[47] Q. Zeng, N. Xue, D. Dai et al., "A nomogram based on inflammatory factors C-reactive protein and fibrinogen to predict the prognostic value in patients with resected non-small cell lung cancer," *Journal of Cancer*, vol. 8, no. 5, pp. 744–753, 2017.

Hindawi
Disease Markers
Volume 2022, Article ID 2876170, 12 pages
https://doi.org/10.1155/2022/2876170

Research Article

lncRNA PCGEM1 Regulates the Progress of Colorectal Cancer through Targeting miR-129-5p/SOX4

Bingsheng Guan, Fazhi Chen, Zhenpeng Wu, Cunchuan Wang, and Jingge Yang

Department of Gastrointestinal Surgery, First Affiliated Hospital of Jinan University, Guangzhou, China

Correspondence should be addressed to Jingge Yang; dryangjg@126.com

Received 1 July 2022; Revised 17 August 2022; Accepted 9 September 2022; Published 20 September 2022

Academic Editor: Fu Wang

Prostate cancer gene expression marker 1 (PCGEM1) has abnormal expression level in a variety of malignant tumor. However, the relationship between PCGEM1 and colorectal cancer is still unclear yet. This study is aimed at identifying the role of PCGEM1 in colorectal cancer. qRT-PCR was used to examine the expressions of the expression of lncRNA PCGEM1 and SOX4 in CRC tissues and cell lines. The biological functions of lncRNA PCGEM1 and SOX4 were examined by CCK-8 assay, Transwell assay, immunohistochemistry, western blotting, RNA interference, and gene overexpression techniques. Bioinformatics analysis was used to find the potential downstream molecule of PCGEM1 and miR-129-5p. The relationship between PCGEM1, miR-129-5p, and SOX4 was assessed by dual luciferase activity assay. We found that PCGEM1 is overexpressed in colorectal cancer cells and tissues, while miR-129-5p is underexpressed. SOX4 is overexpressed in colorectal cancer cells and tissues. Functionally, PCGEM1 silencing can significantly inhibit the proliferation, invasion, and migration of colorectal cancer cells. Mechanically, PCGEM1 acted as a sponge for miR-129-5p and absorbed its expression, and miR-129-5p was found to target SOX4, constructing the axis of PCGEM1/miR-129-5p/SOX4 in colorectal cancer. In conclusion, PCGEM1 mediates the proliferation, invasion, and migration of colorectal cancer cells by targeting miR-129-5p/SOX4 axis.

1. Background

Colorectal cancer (CRC) is a common digestive system tumor nowadays. According to the global cancer statistics, CRC is the third most common cause of cancer occurrence and the second most common cause of cancer-related death in the world [1–3]. Therefore, CRC has made a great negative impact on people's life and property security. Despite many forms of treatment, some patients have a poor prognosis. Understanding the molecular mechanisms of CRC is conducive to better treatment of CRC.

According to the human transcriptome analysis with the Human Genome Project (HGP), only about 2% of human base sequence has the ability to code protein. The remaining 98% of human base sequence can only be transcribed into noncoding RNAs (ncRNAs). A majority of ncRNAs are long noncoding RNA (lncRNA), which has at least 200 base pairs in lengths [4]. Previous research indicated that LncRNAs has a significant relationship with different cancers [5, 6], some work as cancer-promoting lncRNA and some as cancer-suppressing lncRNA [7].

Prostate cancer gene expression marker 1 (lncRNA PCGEM1) was first reported in prostate cancer. However, some researches showed that PCGEM1 has abnormal expression level in a variety of malignant tumors, which can affect the progress of cancer cells, including cervical carcinoma, renal carcinoma, gastric cancer, and endometrial carcinoma [8–11]. The effect of PCGEM1 in CRC has not been well studied yet; we hypothesize that PCGEM1 could participate in regulating the development of colorectal cancer. Therefore, this study is aimed at analyzing the expression of PCGEM1 in colorectal cells and tissues; at analyzing the effect of PCGEM1 on the proliferation, invasion, and migration of colorectal cancer; and at uncovering the mechanisms involved, so as to clarify the role of PCGEM1/miR-129-5p/SOX4 axis in colorectal cancer.

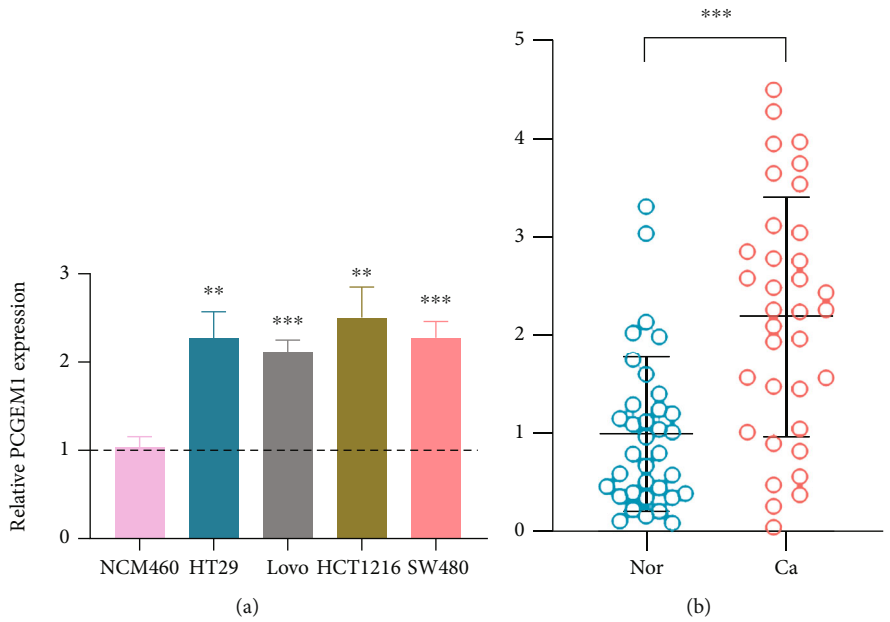

Figure 1: (a) Expression level of PCGEM1 in colorectal cancer cells. (b) Expression level of PCGEM1 in colorectal cancer tissues.

2. Methods

2.1. Clinical Cases and Tissue Samples. From June 2019 to January 2020, we performed surgical resection for 35 patients diagnosed with CRC in our hospital; these patients did not receive any chemoradiotherapy before surgery. Paired colorectal cancer tissue and adjacent normal tissue were collected from all patients. During surgery, resected tissue samples were immediately frozen in liquid nitrogen and stored at -80°C for further RNA isolation.

2.2. Cell Culture. Colorectal cancer cells (HT29, LoVo, SW480) and normal colonic epithelial cell (NCM460) were provided by the Shanghai Institute of Biochemistry and Cell Biology at the Chinese Academy of Sciences. Colorectal cancer cell (HCT116) was provided by the Guangzhou LaiSe Biological Technology Company. Cells were cultured in an incubator (culture conditions include constant temperature of 37°C and 5% CO_2).

2.3. RNA Extraction and qRT-PCR. TRIzol reagent was used to extract the total RNA of colorectal cancer cells and normal cells. The isolated RNA was reverse-transcribed into cDNA and then performed qRT-PCR using the Fluorescence Quantitative Reverse Transcription Kit (Solarbio, Beijing, China). Relative data were normalized to GAPDH. The gene primer sequences were as follows: lncRNA PCGEM1 forward primer, 5′-ACAGCTCCTGGAAGAG GACT-3′, reverse primer, 5′-TTTTCCAAAGGGTCCG CTGT-3′.

2.4. CCK-8 Experiment. A Cell Counting Kit-8 was used to examine the proliferation ability of colorectal cancer cells (HCT116, SW480). In each well of the 96-well plate, 100 μl of cell fluid with the logarithmic phase growing cells was added. After culturing in an incubator for 24 h, their absorbance at 450 nm was measured with a microplate analyzer.

2.5. Transwell Experiment. Transwell experiment was conducted to examine the invasion and migration ability of colorectal cancer cells (HCT116, SW480). After the fusion of colorectal cancer cells reached 70-90%, the cells were digested and counted by trypsin, and the concentration of the cell suspension was adjusted to 1×10^5/mL in serum-free medium. These cells were transferred to an incubator and cultured for 16-30 hours and then fixed with 4% paraformaldehyde for 15-30 min. The staining solution was gently cleaned with PBS, and the number of cells in different fields was counted under the visual field of the inverted microscope.

2.6. Immunohistochemistry. Paired colorectal cancer tissue and adjacent normal tissue were collected. 4% PFA was used for tissue fixation and paraffin-embedded tissue sections. After paraffin removal and flush with PBS fluid, each slice was added the first antibody and the second antibody. And then, ultrapure water was used to rinse the slices, and the color rendering was observed under a color microscope by using DAB color rendering reagent box.

2.7. Western Blotting (WB). After lysed in lysis buffer, cells were transferred to Eppendorf tubes. Bovine serum albumin (BSA) standard dilution buffer was diluted to 500 μg/mL and used to determine the standard curve of protein concentration. The tested sample was added to the 96-well plate and used for colorimetric reaction. Bio-Rad vertical electrophoresis system was used for cataphoresis. After adding the first antibody and the second antibody, chemiluminescence detection kit was used for chemiluminescence protein detection.

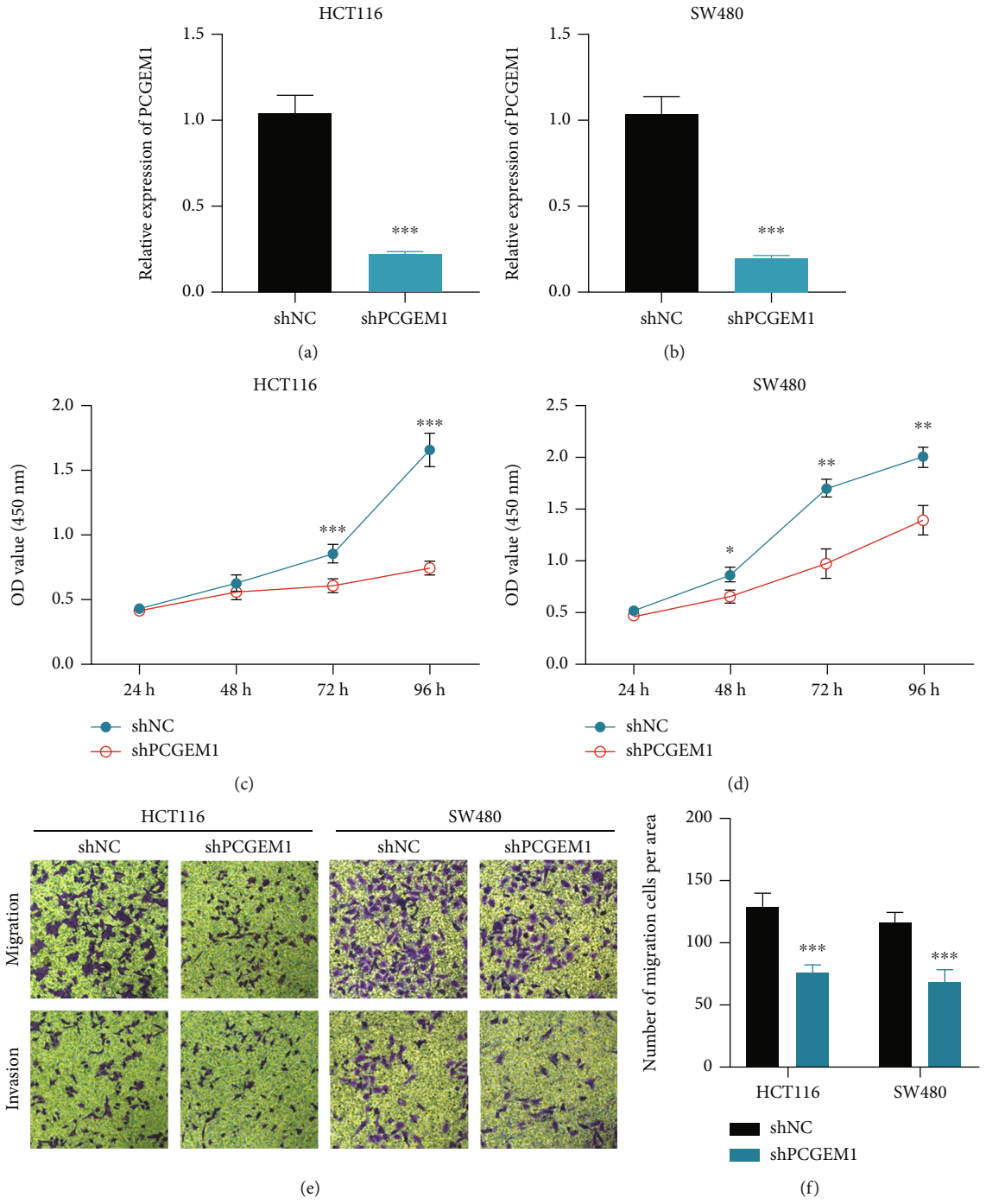

Figure 2: Continued.

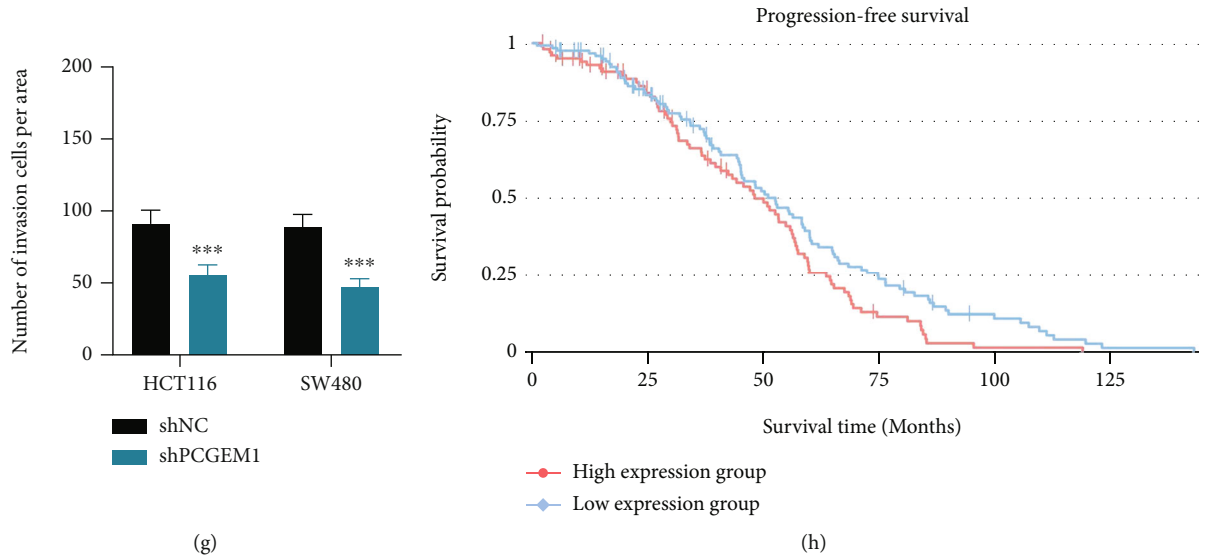

Figure 2: (a–d) Effect of PCGEM1 knockdown on the proliferation of HCT116 and SW480 cells. (e–g) Effect of PCGEM1 knockdown on the invasion and migration of HCT116 and SW480 cells. (h) Survival analysis curve of PCGEM1 and progression-free survival.

2.8. Dual Luciferase Activity Assay. LINC00071 (PCGEM1) 3′UTR gene fragment was generated, and then, wild-type PCGEM1 (PCGEM1 WT) and mutant PCGEM1 (PCGEM1 Mut) were cloned into PsichecKTM-2 vector by homologous recombination method. Then, colony PCR and gene sequencing were performed to verify the success of the vector construction. Then, Lipofectamine 2000 was used to introduce the above plasmids together with miR-129-5p inhibitor and its mimics into HCT116 and SW480 cells. After 48 hours, the cells were collected and lysed. The luciferase activity of each group was detected by Promega double luciferase detection kit.

2.9. Statistical Analysis. All statistical analyses were performed using the SPSS software 20.0 and graphed using the GraphPad Prism software. Student's *t*-test or one-way ANOVA was used to determine differences between groups. $P < 0.05$ was considered statistically significant.

3. Results

3.1. Expression of lncRNA PCGEM1 in Colorectal Cancer. In experiments of cell level, we found that when compared with NCM60, the four colorectal cancer cell lines (HT29, LoVo, HCT116, and SW480) had significant increased expression level of PCGEM1, with the multiples of 2.28, 2.20, 2.51, and 2.28 (Figure 1(a)). Similar results were also found in experiments of tissue level, which indicated that the PCGEM1 expression in colorectal cancer tissues was 2.35 times higher than that in adjacent normal tissue (Figure 1(b)).

3.2. Biological Behavior of lncRNA PCGEM1 in Colorectal Cancer. In cellular function experiments, cell proliferation curve showed that PCGEM1 knockdown could significantly inhibit the proliferation of HCT116 and SW480 cells (Figures 2(a)–2(d)), which means that PCGEM1 can promote the proliferation of colorectal cancer cells. In addition, the results of Transwell analysis revealed that the invasion and migration ability of colorectal cancer cells were significantly reduced after PCGEM1 knockdown (Figures 2(e)–2(g)).

When considering the relationship between PCGEM1 and patients' survival outcomes, the results from online database lnCAR showed that patients with low PCGEM1 expression had significantly higher progression-free survival than those with high PCGEM1 expression (Figure 2(h)). These results indicate that PCGEM1 serves as an oncogene in colorectal cancer.

3.3. lncRNA PCGEM1 Downregulates the Expression of miR-129-5p. Through miRcode software, we found that there were binding sites between PCGEM1 3′UTR and miR-129-5p, which means that miR-129-5p may be the downstream target gene of lncRNA PCGEM1.

In experiments of cell and tissue levels, it was proved that miR-129-5p is downregulated in colorectal cancer (Figures 3(a) and 3(b)). In addition, the Pearson correlation analysis found a significant correlation between PCGEM1 and miR-129-5p expression levels in colorectal cancer tissue (Pearson $r = -0.3788$, $P = 0.0248$) (Figure 3(c)).

In order to explore whether PCGEM1 can target the expression level of miR-129-5p, RNA interference and gene overexpression techniques were used to detect the effects of PCGEM1 overexpression and knockdown on miR-129-5p (Figures 3(d) and 3(e)); the results indicated that lncRNA PCGEM1 can regulate the expression level of miR-129-5p as a miRNA sponge. Moreover, dual luciferase activity assay was used to verify that miR-129-5p can target binding to PCGEMA.

3.4. miR-129-5p Mediates Colorectal Cancer Tumorigenesis by Targeting SOX4. The results above showed that PCGEM1 can act as an oncogene in colorectal cancer and targets the expression of miR-129-5p. In order to explore the

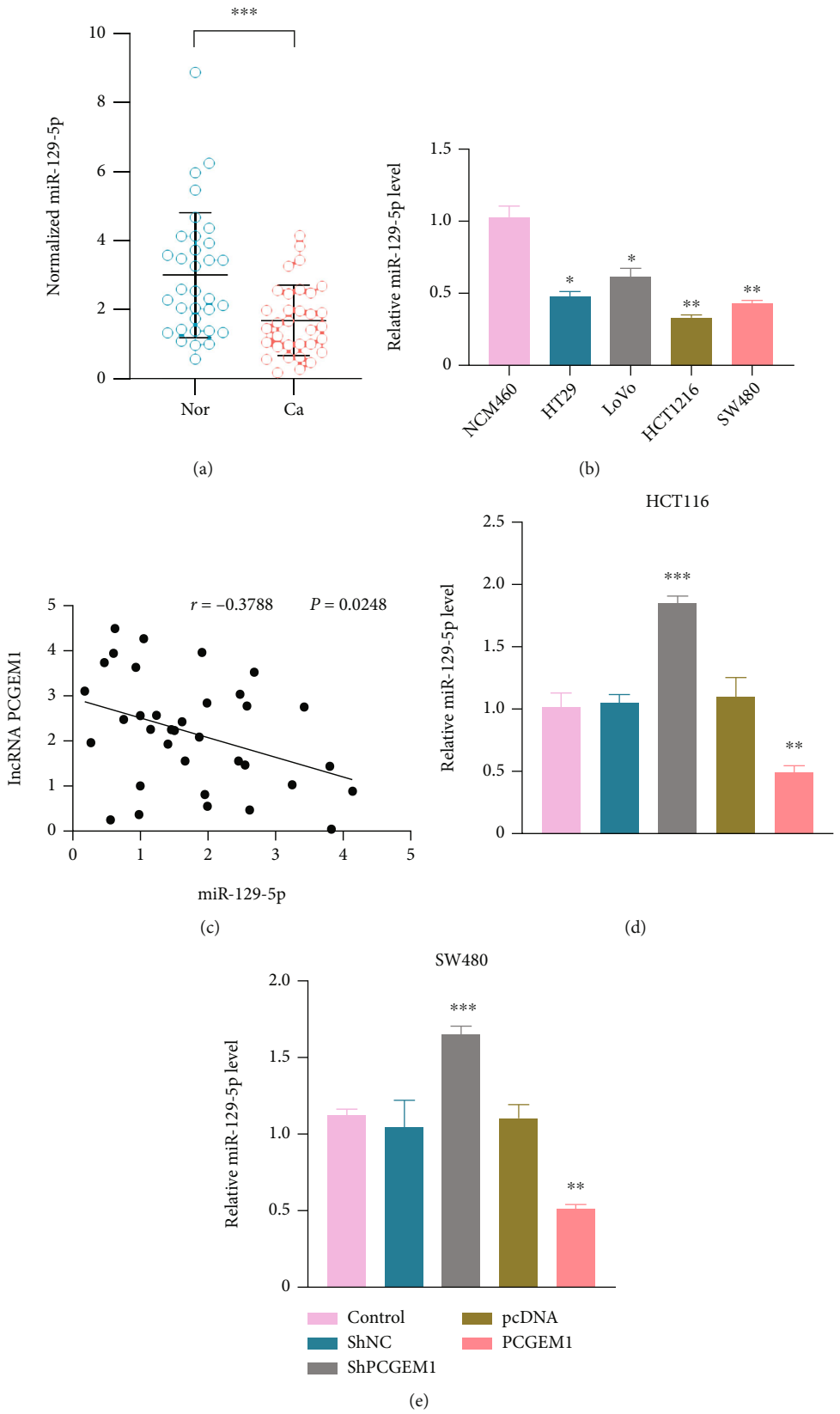

Figure 3: (a, b) Expression level of PCGEM1 in colorectal cancer cells and tissues. (c) Correlation analysis between PCGEM1 and miR-129-5p expression levels. (d, e) Effect of PCGEM1 overexpression and knockdown on miR-129-5p level.

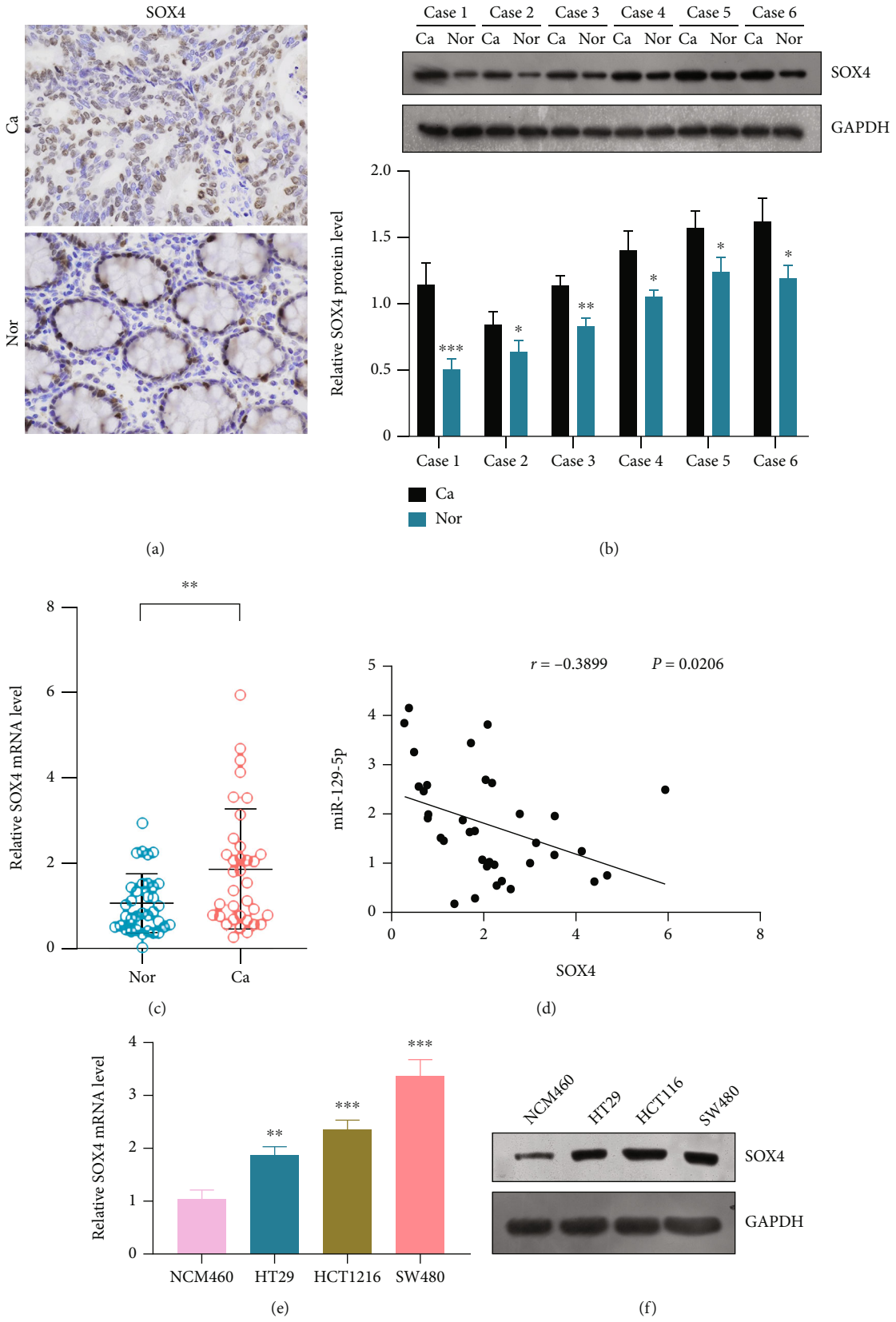

Figure 4: (a–c) SOX4 expression in colorectal cancer tissue detected by immunohistochemistry, western blotting, and RT-qPCR. (e, f) SOX4 expression in colorectal cancer tissue detected by RT-qPCR and western blotting.

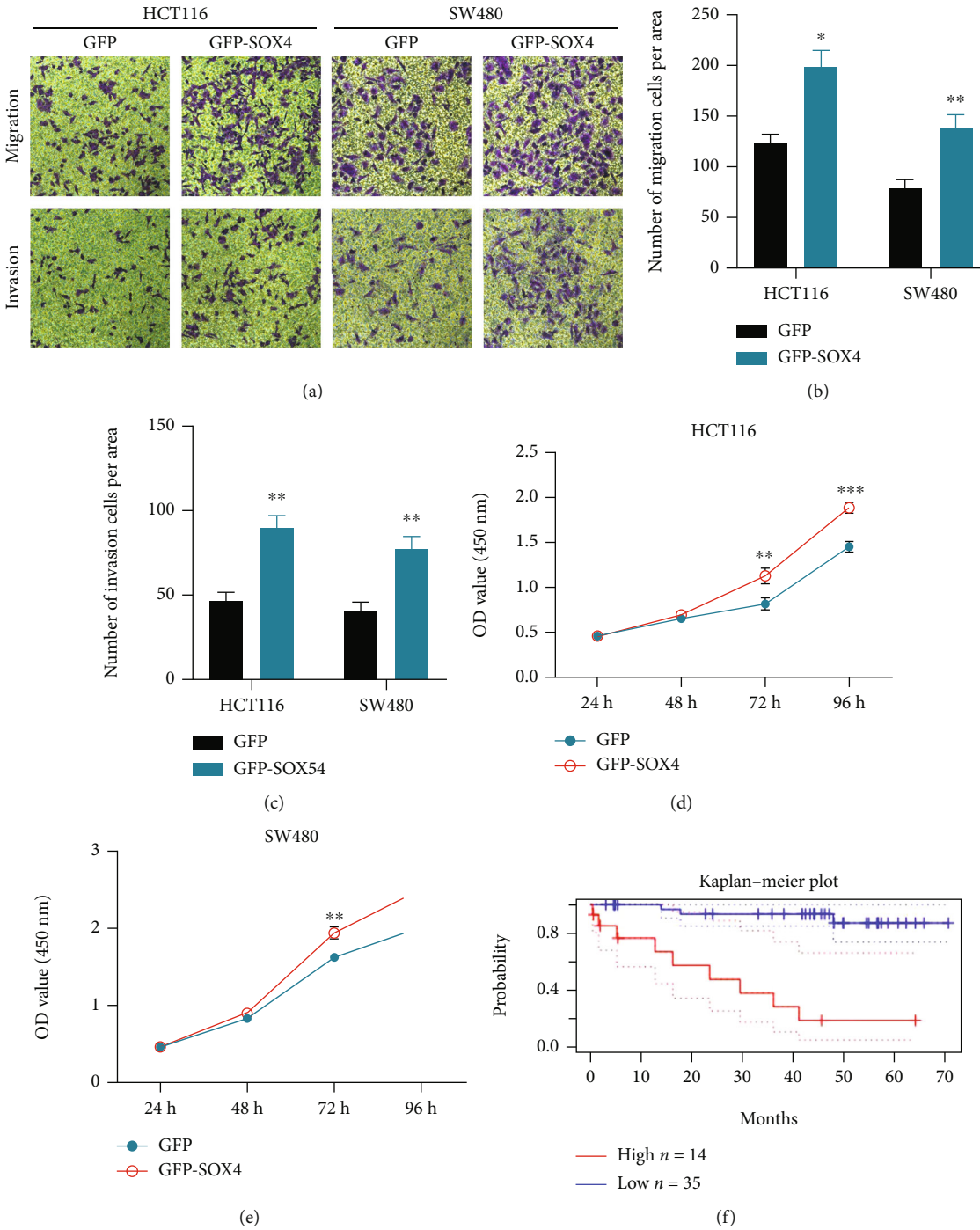

Figure 5: Continued.

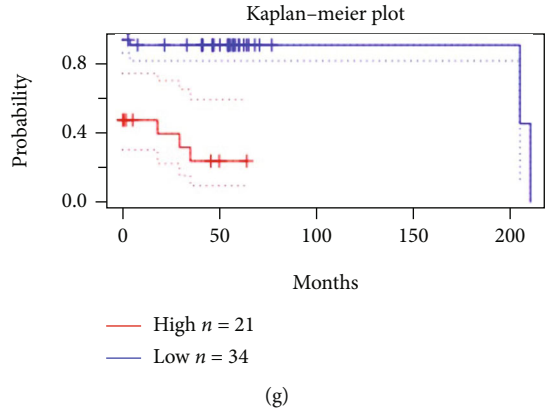

(g)

Figure 5: (a–c) Effect of SOX4 overexpression on the invasion and migration of HCT116 and SW480 cells. (d, e) Effect of SOX4 overexpression on the proliferation of HCT116 and SW480 cells. (f, g) Survival analysis curve of SOX4 expression and tumor-free survival and disease-specific survival.

downstream molecular mechanisms, the TargetScan software was used to find the potential downstream gene, which revealed that SOX4 had some potential binding sites with miR-129-5p. Immunohistochemistry, western blotting, and RT-qPCR found that SOX4 expression was upregulated in clinical colorectal cancer tissue (Figures 4(a)–4(c)). Similar results were also found in colorectal cancer cells (Figures 4(e) and 4(f)).

In the study of cellular function, overexpression of SOX4 can significantly promote the proliferation, invasion, and migration of colorectal cell (Figures 5(a)–5(e)). Survival analyses revealed that patients with low SOX4 expression had significantly higher tumor-free survival and disease-specific survival than those with high SOX4 expression (Figures 5(f) and 5(g)).

Regarding the relationship between miR-129-5p and SOX4, correlation analysis revealed that miR-129-5p expression was negatively related with SOX4 (Pearson $r = -0.3899$, $P = 0.0206$) (Figure 4(d)). The results of RT-qPCR and western blotting displayed that overexpression of miR-129-5p can significantly inhibit the expression of SOX4 mRNA (Figures 6(a) and 6(b)). Furthermore, dual luciferase activity assay confirmed that SOX4 is a target gene of miR-129-5p (Figure 6(c)).

3.5. lncRNA PCGEM1 Upregulates the Expression of SOX4 by Targeting miR-129-5p. In order to explore whether the molecular pathway of PCGEM1/miR-129-5p/SOX4 exists in colorectal cancer or not, we subsequently analyze the effect of PCGEM1 on SOX4, which found that PCGEM1 silencing can significantly reduce endogenous SOX4 mRNA and protein expression in colorectal cancer cells (Figures 6(d) and 6(e)), which would be recovered by miR-129-5p silencing (Figure 6(f)). The results of rescue experiments confirmed that SOX4 served as the functional protein of PCGEM1/miR-129-5p in colorectal cancer.

4. Discussion

lncRNA is a hotspot in the study of mechanism of malignant tumor in these years. lncRNA PCGEM1 has been proved to participate in the progress of several cancers. However, the effect and mechanism of PCGEM1 in colorectal cancer is still unknown. A better understanding of the specific therapeutic targets for CRC is essential to advance and improve effective treatment methods.

In this study, dysregulated lncRNA PCGEM1 was found in colorectal cancer tissues/cells and identified to be significantly upregulated. Cellular functional studies showed that lncRNA PCGEM1 silencing inhibited the proliferation, invasion, and migration of colorectal cancer. These results revealed that PCGEM1 can act as a cancer-promoting gene for the progress of PCGEM1. lncRNA and miRNA are both noncoding genes, and lncRNA can act as a miRNA sponge so as to regulate the function of miRNA. For example, previous research results indicated that lncRNA PCGEM1 can regulate the expression of miR-642a-5p in cervical carcinoma [8], the expression of miR-433-3p in renal carcinoma [9], the expression of miR-590-3p in non-small-cell lung cancer [12], and so on.

Bioinformatics analysis is helpful for us to find the potential downstream molecule during the study of mechanism. Using this method, it was found that miR-129-5p is a potential downstream target of lncRNA PCGEM1, which means that lncRNA PCGEM1 can target miR-129-5p as a miRNA sponge. The regulation axis of PCGEM1/miR-129-5p has been reported in gastric cancer and cervical cancer in previous studies [13, 14]. However, our study represents the first publication to confirm this axis in colorectal cancer, with the evidences from correlation analysis and dual luciferase activity assay. In addition, overexpressing and silencing PCGEM1 in colorectal cancer cells could make the expression level of miR-129-5p downregulated and upregulated, respectively, suggesting that PCGEM1 can negatively target miR-129-5p. Regarding the expression level of miR-129 in cancer, the results in literature are inconsistent, with elevated level in oral carcinoma and reduced level in gastric cancer, lung cancer, and breast cancer [15–17]. These differences may be attributed to the fact that different tumors have different internal microenvironments. In our study, decreased miR-129-5p level was found in cellular level and tissue level.

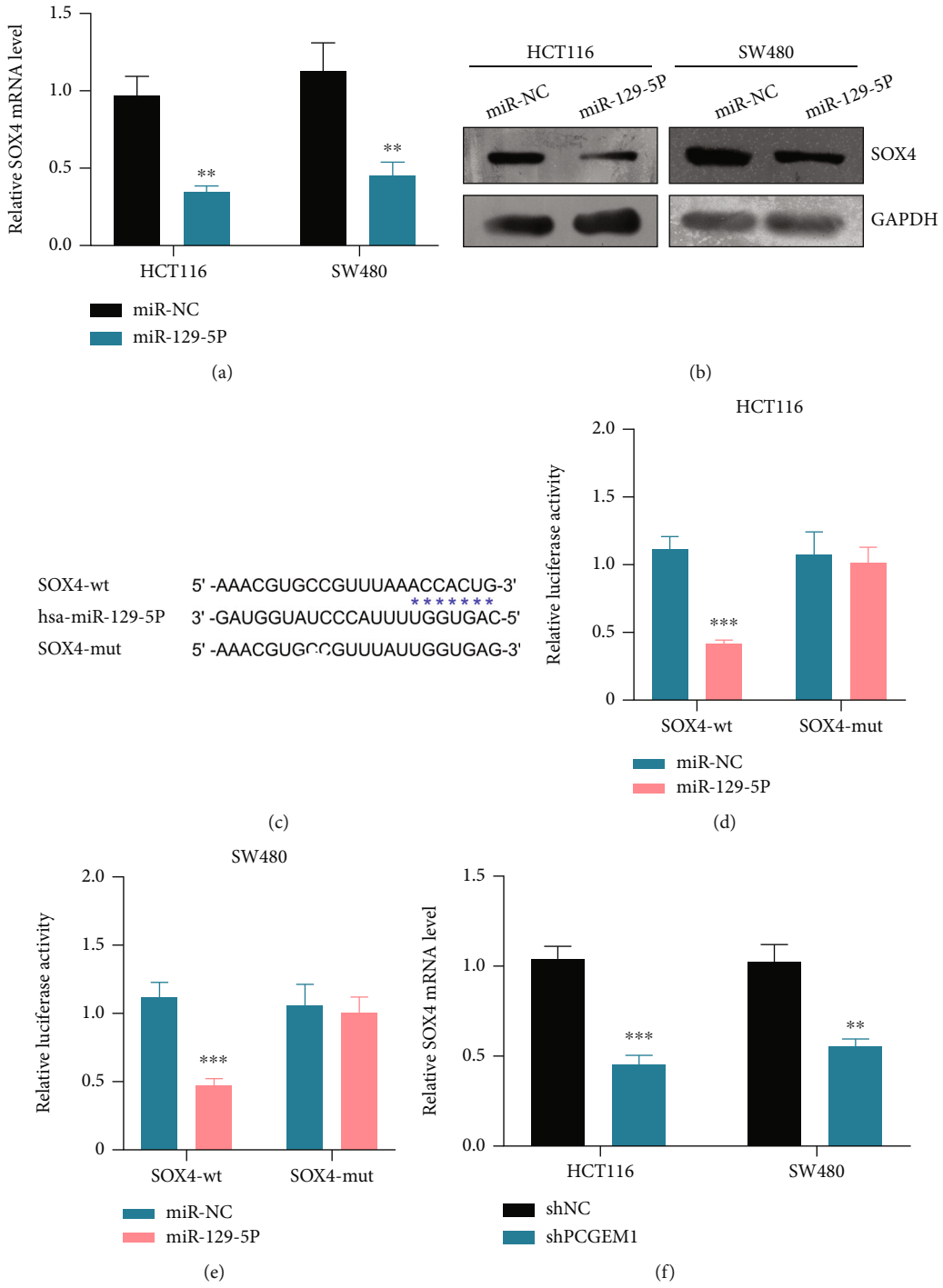

Figure 6: Continued.

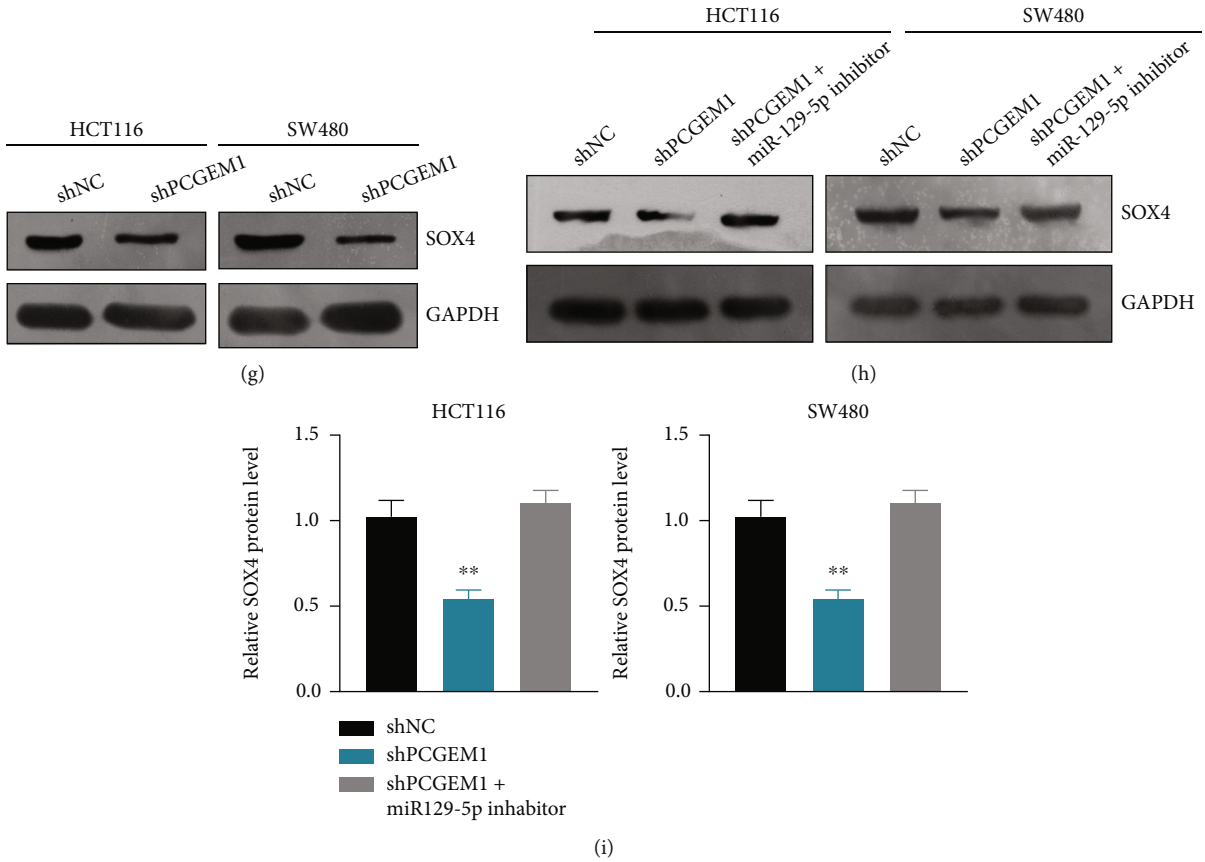

Figure 6: (a, b) Effect of miR-129-5p on SOX4 expression detected by RT-qPCR and western blotting. (c) Dual luciferase activity assay for confirming the relation between SOX4 and miR-129-5p. (d, e) Effect of PCGEM1 knockdown on SOX4 expression detected by RT-qPCR and western blotting. (f) Rescue experiments for confirming the axis of PCGEM1/miR-129-5p/SOX4.

According to the role of miRNA in tumor development, miRNA can be divided into cancer-promoting miRNA and cancer-suppressing miRNA. From the above results, we found that miR-129-5p can act as a cancer-suppressing miRNA in colorectal cancer. Previous research results showed that miR-129-5p has multiple target genes. For example, miR-129-5p can regulate the expression of COL1A1 so as to promote the progression of gastric cancer [17], regulate YWHAB to affect the progression of lung cancer [16], and target ETV1 to inhibit prostate cancer proliferation [18]. But for colorectal cancer, what is the potential target gene for miR-129-5p, bioinformatics analysis was used again in our study, and SOX4 was found.

Upregulated expression of SOX4 in colorectal cancer was identified in our study, which was consistent with previous researches [19]. In addition, overexpressing SOX4 can increase the invasion and migration ability of colorectal cancer cell, which means that SOX4 can act as a cancer-promoting gene for colorectal cancer. In colorectal cancer, SOX4 has been reported as a target gene of some miRNAs, including miRNA-212, miRNA-130a, miRNA-133a, and miRNA-539 [20–23]. However, the axis of miR-129-5p/SOX4 in colorectal cancer has not been reported yet. In our study, cell functional studies and dual luciferase activity assay confirmed the existence of miR-129-5p/SOX4 axis in colorectal cancer. Furthermore, rescue experiments indicated that lncRNA PCGEM1 can regulate colorectal cancer proliferation, invasion, and migration through targeting miR-129-5p/SOX4.

To the best of our knowledge, this study represents the first report to confirm the axis of lncRNA PCGEM1/miR-129-5p/SOX4 in colorectal cancer. However, some limitation should be pointed out. At first, the sample size of clinical patients is not large enough, and more follow-up data need to be collected to further evaluate the relationship between the expression levels of lncRNA PCGEM1, miR-129-5p, and SOX4 in colorectal cancer tissues and patient prognosis. In addition, this study only conducted in vitro cell experiments and clinical tissue detection; in vivo experiments in animal models are needed to further clarify the role of lncRNA PCGEM1/miR-129-5p/SOX4 regulatory axis in colorectal cancer.

5. Conclusion

This study finds that lncRNA PCGEM1 and SOX4 are overexpressed in colorectal cancer, while miR-129-5p is underexpressed. PCGEM1 mediates the proliferation, invasion, and migration of colorectal cancer cells by targeting miR-129-5p and regulates the expression of SOX4.

Abbreviations

PCGEM1: Prostate cancer gene expression marker 1
CRC: Colorectal cancer
HGP: Human Genome Project
ncRNAs: Noncoding RNAs
lncRNA: Long noncoding RNA
qRT-PCR: Quantitative real-time PCR
CCK-8: Cell Counting Kit-8
WB: Western blotting
BSA: Bovine serum albumin.

Data Availability

The analyzed datasets generated during the study are available from the corresponding author on reasonable request.

Ethical Approval

Ethical consent was approved by the Ethics Committee of First Affiliated Hospital of Jinan University, Guangzhou, China.

Consent

Informed consent was obtained from all patients.

Conflicts of Interest

The authors declare that they have no competing interests.

Authors' Contributions

Bingsheng Guan was responsible for the conceptualization, methodology, investigation, writing of the original draft, and funding acquisition. Fazhi Chen was responsible for the validation and resources. Zhenpeng Wu was responsible for the investigation and visualization. Cunchuan Wang was responsible for the validation, resources, and supervision. Jingge Yang was responsible for the conceptualization, validation, resources, and writing—review and editing. All authors reviewed the manuscript.

Acknowledgments

The work was supported by the Fundamental Research Funds for the Central Universities (21622304) and the Basic and Applied Basic Research Project of Guangzhou Basic Research Program (SL2023A04J01245).

References

[1] F. Bray, J. Ferlay, I. Soerjomataram, R. L. Siegel, L. A. Torre, and A. Jemal, "Global Cancer Statistics 2018: GLOBOCAN estimates of incidence and mortality worldwide for 36 cancers in 185 countries," *CA: a Cancer Journal for Clinicians*, vol. 68, no. 6, pp. 394–424, 2018.

[2] R. L. Siegel, K. D. Miller, A. Goding Sauer et al., "Colorectal cancer statistics, 2020," *CA: a Cancer Journal for Clinicians*, vol. 70, no. 3, pp. 145–164, 2020.

[3] H. Sung, J. Ferlay, R. L. Siegel et al., "Global Cancer Statistics 2020: GLOBOCAN estimates of incidence and mortality worldwide for 36 cancers in 185 countries," *CA: a Cancer Journal for Clinicians*, vol. 71, no. 3, pp. 209–249, 2021.

[4] J. E. Wilusz, H. Sunwoo, and D. L. Spector, "Long noncoding RNAs: functional surprises from the RNA world," *Genes & Development*, vol. 23, no. 13, pp. 1494–1504, 2009.

[5] A. Bhan, M. Soleimani, and S. S. Mandal, "Long noncoding RNA and cancer: a new paradigm," *Cancer Research*, vol. 77, no. 15, pp. 3965–3981, 2017.

[6] Y. Zhang and L. Tang, "The application of lncRNAs in cancer treatment and diagnosis," *Recent Patents on Anti-Cancer Drug Discovery*, vol. 13, no. 3, pp. 292–301, 2018.

[7] K. C. Wang and H. Y. Chang, "Molecular mechanisms of long noncoding RNAs," *Molecular Cell*, vol. 43, no. 6, pp. 904–914, 2011.

[8] Y. Liu, Y. Wang, X. Shen et al., "Down-regulation of lncRNA PCGEM1 inhibits cervical carcinoma by modulating the miR-642a-5p/LGMN axis," *Experimental and Molecular Pathology*, vol. 117, article 104561, 2020.

[9] X. Cai, X. Zhang, L. Mo, J. Zhu, and H. Yu, "LncRNA PCGEM1 promotes renal carcinoma progression by targeting miR-433-3p to regulate FGF2 expression," *Cancer Biomarkers*, vol. 27, no. 4, pp. 493–504, 2020.

[10] H. Jiang, S. Guo, Y. Zhao et al., "Circulating long non-coding RNA PCGEM1 as a novel biomarker for gastric cancer diagnosis," *Pathology, Research and Practice*, vol. 215, no. 10, article 152569, 2019.

[11] Q. Li, F. Shen, and L. Zhao, "The relationship between lncRNA PCGEM1 and STAT3 during the occurrence and development of endometrial carcinoma," *Biomedicine & Pharmacotherapy*, vol. 107, pp. 918–928, 2018.

[12] H. Wen, H. Feng, Q. Ma, and C. Liang, "LncRNA PCGEM1 induces proliferation and migration in non-small cell lung cancer cells through modulating the miR-590-3p/SOX11 axis," *BMC Pulmonary Medicine*, vol. 21, no. 1, p. 234, 2021.

[13] T. Zhang, H. Piao, S. Guo et al., "LncRNA PCGEM1 enhances metastasis and gastric cancer invasion through targeting of miR-129-5p to regulate P4HA2 expression," *Experimental and Molecular Pathology*, vol. 116, article 104487, 2020.

[14] Y. Xu, H. Zhu, H. Ma, L. Yuan, Q. Hu, and L. Yang, "LINC01305 inhibits malignant progression of cervical cancer via miR-129-5p/Sox4 axis," *American Journal of Translational Research*, vol. 12, no. 11, pp. 7581–7592, 2020.

[15] L. Scapoli, A. Palmieri, L. L. Muzio et al., "MicroRNA expression profiling of oral carcinoma identifies new markers of tumor progression," *International Journal of Immunopathology and Pharmacology*, vol. 23, no. 4, pp. 1229–1234, 2010.

[16] C. Xu, Z. Du, S. Ren, X. Liang, and H. Li, "MiR-129-5p sensitization of lung cancer cells to etoposide-induced apoptosis by reducing YWHAB," *Journal of Cancer*, vol. 11, no. 4, pp. 858–866, 2020.

[17] Q. Wang and J. Yu, "MiR-129-5p suppresses gastric cancer cell invasion and proliferation by inhibiting COL1A1," *Biochemistry and Cell Biology*, vol. 96, no. 1, pp. 19–25, 2018.

[18] G. Gao, D. Xiu, B. Yang et al., "miR-129-5p inhibits prostate cancer proliferation via targeting ETV1," *Oncotargets and Therapy*, vol. Volume 12, pp. 3531–3544, 2019.

[19] B. Wang, Y. Li, F. Tan, and Z. Xiao, "Increased expression of SOX4 is associated with colorectal cancer progression," *Tumor Biology*, vol. 37, no. 7, pp. 9131–9137, 2016.

[20] T. Y. Mou, R. R. Zhang, and Y. N. Wang, "MiRNA-212 acts as a tumor-suppressor in colorectal carcinoma through targeting

SOX4," *European Review for Medical and Pharmacological Sciences*, vol. 23, no. 24, pp. 10751–10760, 2019.

[21] T. H. Ha, H. Y. Kim, Y. M. Kim, and S. Hong, "MicroRNA-130a modulates a radiosensitivity of rectal cancer by targeting SOX4," *Neoplasia*, vol. 21, no. 9, pp. 882–892, 2019.

[22] X. Lei, L. Li, and X. Duan, "Long non-coding RNA ABHD11-AS1 promotes colorectal cancer development through regulation of miR-133a/SOX4 axis," *Bioscience Reports*, vol. 38, no. 6, 2018.

[23] J. Zhao, J. Xu, and R. Zhang, "MicroRNA-539 inhibits colorectal cancer progression by directly targeting SOX4," *Oncology Letters*, vol. 16, no. 2, pp. 2693–2700, 2018.

Hindawi
Disease Markers
Volume 2022, Article ID 6545266, 9 pages
https://doi.org/10.1155/2022/6545266

Research Article

KIAA0101 and IL2RA Were Identified as Core Genes in Hormone-Resistant Nephropathy

Ying Chen, Shuyi Qian, Yinyin Chen, Kanghan Liu, Wei Yin, and Xun Luo

Department of Nephrology, Hunan Provincial People's Hospital, The First Affiliated Hospital of Hunan Normal University, Changsha Clinical Research Center for Kidney Disease, Hunan Clinical Research Center for Chronic Kidney Disease, Changsha 410005, China

Correspondence should be addressed to Xun Luo; luox@hunnu.edu.cn

Received 30 June 2022; Accepted 26 August 2022; Published 17 September 2022

Academic Editor: Fu Wang

Objectives. To analyze the tissue heterogeneity of hormone-sensitive and drug-resistant nephrotic syndrome genes using a bioinformatics approach and to analyze gene-related functional pathways. *Methods*. The limma package of R software was used to screen differential genes from the nephropathy datasets GSE145969 and GSE189734. The differential genes were analyzed for functional and pathway enrichment in terms of biological processes, cellular components, and molecular functions. The Metascape tool was used to construct protein networks for the differential genes, and the results were imported into Cytoscape software for visualization. The genes were identified as key modules and genes using the MCODE plug-in. Gene set enrichment analysis was performed for the HALLMARK analysis of the two microarray key genes to obtain the relevant pathways. *Results*. GSE145969 screened 351 differential genes, 168 upregulated genes, and 183 downregulated genes. The differential genes were enriched in biological processes, cellular components, and molecular functions, such as myocardial contraction, intracellular nonmembrane organelles, and structural molecular activities. The protein-protein interaction (PPI) network contained 140 nodes, with the highest-scoring module containing seven genes, and the MCODE plug-in calculated the downseed. The key gene was KIAA0101, whose HALLMARK pathway was significantly enriched in the mTORC1 signaling pathway. A total of 263 differential genes were screened by GSE189734, and they were enriched in biological processes, molecular functions, and cellular components, such as immune system processes, signaling receptor binding, and the cytoplasmic matrix. The PPI network contained 253 nodes, with the highest-scoring module containing 37 genes. The seed gene obtained through the MCODE plug-in calculation was IL2RA, whose HALLMARK pathway was significantly enriched in the KRAS signaling pathway. *Conclusion*. By analyzing the gene sets of different tissues in nephropathy, two key genes, namely KIAA0101 and IL2RA, were obtained. Their gene function enrichment is related to cell growth, development, and reproduction. Therefore, IL2RA and KIAA0101 can be used as diagnostic markers for hormone-resistant nephropathy.

1. Introduction

Chronic kidney disease (CKD) is a global public health problem that will eventually evolve into renal failure and cardiovascular disease [1]. Steroid-sensitive nephrotic syndrome (SSNS) is one of the most common chronic diseases in children [2], but half of the children with SSNS will have at least four relapses per year or at least two relapses within six months after the initial visit, a condition known as frequently recurrent nephrotic syndrome (FRNS) [3]. In some of these children with FRNS, two consecutive relapses occur after a period of reduction or discontinuation of steroid therapy, a condition defined as steroid-dependent nephrotic syndrome [4]. Steroid-resistant nephrotic syndrome (SRNS) is a heterogeneous disease that includes both immune-based genes and a monogenic etiology [5]. The incidence of nephrotic syndrome is regionally dependent, with rates of 1.2–1.8 cases per 100,000 children per year in Germany [6], 3–3.5 cases per 100,000 children per year in Paris and surrounding areas [7], and 6.49 cases per 100,000 children per year in Japan [8]. Among the affected young children, males predominate, with a male-to-female ratio of 2 : 1 [9].

More than 85% of patients with nephrotic syndrome respond to corticosteroids, but about 10%–15% still do not respond to steroids or develop steroid resistance [5]. The median age of onset of SRNS is 4.4 years [10], with an early age of onset concentrated in early childhood.

With the development of bioinformatics technology, it has become an important way to obtain disease-related information for further analysis using techniques such as microarrays or multiple sequencing methods. Moreover, by grouping disease gene expression profiles for study, the causative genes can eventually be screened. The study of SSNS can be facilitated by analyzing hormone-sensitive and drug-resistant nephrotic syndrome gene-related pathways. In this study, we plan to determine the key genes of hormone-resistant nephropathy by analyzing different tissue microarrays for differential expression and gene function enrichment.

2. Methods and Materials

2.1. Sample Source. This study found two datasets related to hormone-resistant nephrotic syndrome based on the Gene Expression Omnibus (GEO, https://www.ncbi.nlm.nih.gov/geo/) gene expression databases: GSE145969 and GSE189734. The GSE145969 dataset collected data from 16 SSNS and 12 SRNS patients. The clinical information was divided into two groups: hormone sensitivity (steroid-sensitive) and hormone resistance (steroid-resistant). The GSE189734 dataset collected data on three SSNS and three SRNS patients.

2.2. Differential Expression Analysis to Screen for Differential Genes. The limma package of R software was used to analyze the differential expression of mRNA in the two microarrays. The results of the differential expression analysis for each microarray are shown in a volcano plot with a screening threshold of $p < 0.05$, $|\mathrm{FC}| \geq 1.5$ for differentially expressed genes (DEGs).

2.3. Differential Gene Function and Pathway Enrichment Analysis. In order to further study the functions of the above genes, the ClusterProfiler program package in R software was used to perform gene function enrichment analysis on DEGs to obtain gene ontological- (GO-) related pathways. GO includes Molecular Function (MF), Biological Process (BP) and Cellular Component (CC). $p < 0.01$ is statistically significant, and the results are presented as bubble plots.

2.4. Protein-Protein Interaction (PPI) Network Analysis. To further investigate the interaction relationship between differentially expressed genes, we performed PPI analysis on the DEGs. The DEGs were analyzed using Metascape (https://metascape.org/) to obtain the PPI relationship network. The MCODE plug-in in Cytoscape software was used to screen the important functional modules in the PPI network, select the highest-scoring cluster and seed genes in that cluster for subsequent analysis, and position the seed genes as key genes.

2.5. Single Gene Set Enrichment Analysis (GSEA). Based on the median expression value of key genes, the samples were divided into two groups: high and low expressions. The HALLMARK pathway was observed using a single GSEA. The screening threshold was $|NES| > 1$, and the p value was set to <0.05.

3. Results

3.1. Screening of Differential Genes Using Differential Expression Analysis. The differential analysis of GSE145969 yielded 351 differential genes (Figure 1(a)), including 168 upregulated genes and 183 downregulated genes. The differential analysis of GSE189734 produced 263 differential genes (Figure 1(b)), which were all upregulated genes.

3.2. Functional Enrichment Analysis of Differential Genes. GO functional enrichment analysis was performed on the differential genes of the two microarrays. The significantly enriched biological process terms for the genes of the GSE189734 microarray included immune system processes, cellular responses to chemical stimuli, and cellular responses to organic substances (Figure 2(a)). The significantly enriched molecular function terms included signaling receptor binding and enzyme site binding (Figure 2(b)). The significantly enriched cellular component terms included cytoplasmic matrix, cytoplasmic vesicles, intracellular vesicles, and cell membranes (Figure 2(c)). The significantly enriched biological process terms included cardiac contraction and hair cycle regulation (Figure 2(d)). The significantly enriched cellular component terms included intracellular nonmembrane organelles and nucleoli (Figure 2(e)). The significantly enriched molecular function terms included structural molecular activity, ion-gated channel activity, and gated channel activity (Figure 2(f)).

3.3. PPI Network Analysis. The two-dataset DEGs were analyzed using Metascape, and the PPI network constituted by the DEGs contained 140 nodes and 253 node action relationships (Figures 3(a) and 3(b)). The two datasets were analyzed for GO functional enrichment, and the results showed that the GSE145969 chip gene was significantly enriched in the positive regulation of neuron projection development and gene silencing by RNA (Figure 3(c)). The GSE189734 dataset gene was significantly enriched in cytokine signaling in the immune system and in cell activation (Figure 3(d)). The highest-scoring clusters were obtained using the MCODE plug-in in Cytoscape. The modules contained seven nodes with 18 edges and 37 nodes with 368 edges (Figures 3(e) and 3(f)).

3.4. GSEA of Key Genes. The key genes from the MCODE plug-in analysis were used as the key genes: KIAA0101 for the GSE145969 dataset and IL2RA for the GSE189734 chip. The GSEA of the HALLMARK pathway was performed separately. IL2RA was significantly enriched in the KRAS signaling pathway (Figure 4(b)).

4. Discussion

With the rapid development of biological sciences and genetics, we have gained a deeper understanding of

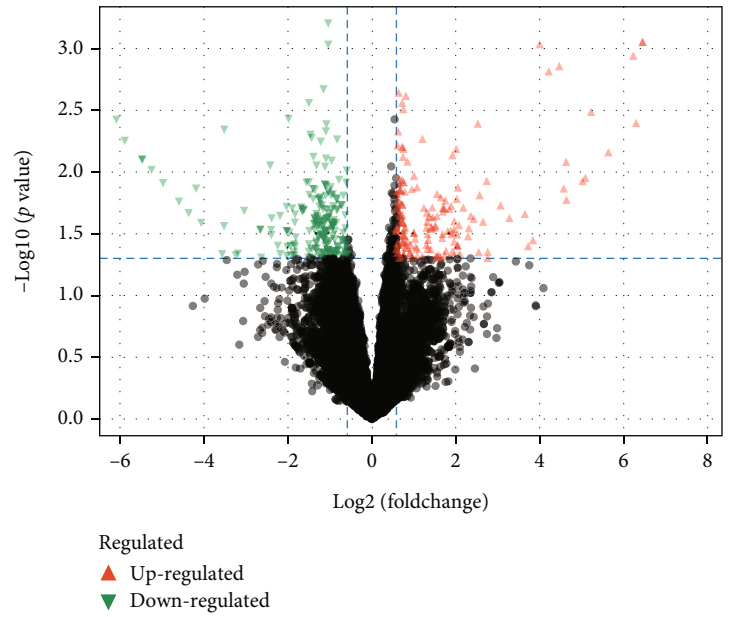

(a) GSE145969 differential gene volcano map

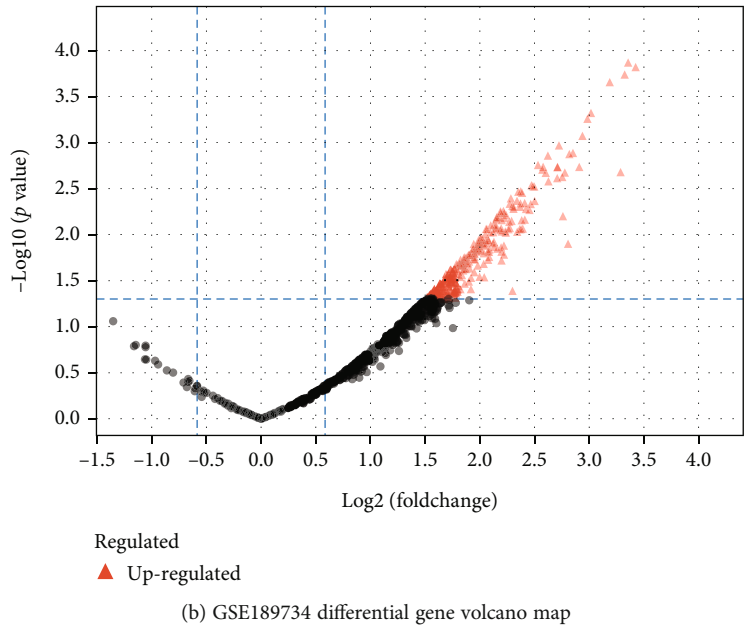

(b) GSE189734 differential gene volcano map

FIGURE 1: Results of the differential expression analysis. Note: The figure shows a volcano plot. The screening criteria are $p < 0.05$ and $|FC| \geq 1.5$. The green portion of the figure denotes the downregulated genes, and the red portion denotes the upregulated genes.

nephrotic syndrome. In recent years, the epidemiology of nephrotic syndrome has been in a stable state and largely unchanged, but the pathology associated with it is constantly evolving. The nephrotic syndrome is reflected by urinary polyprotein, hypoproteinemia, edema, and other available clinical features, such as hyperlipidemia [11]. The pathogenesis of nephropathy is related to several factors; the most common of which is diabetic nephropathy, one of the most common microvascular complications among diabetic patients [12].

In this study, we selected different tissue samples from nephropathy for analysis, with GSE189734 containing six samples and GSE145969 containing 28 samples. Differential expression analysis was performed on the two microarrays. A total of 263 DEGs were obtained for GSE189734, and 351 genes were obtained for GSE145969, including 168 upregulated genes and 183 downregulated genes. Their functional enrichment analyses and pathways were analyzed separately. The GSE145969 dataset was functionally enriched in the positive regulation of neuron projection development. Neuron projection is established through an extremely complex transcriptional crossover, and genes operate by regulating the developmental drivers of the projection neuron subtype and another subtype [13]. Satb2 and Ctip2 are the

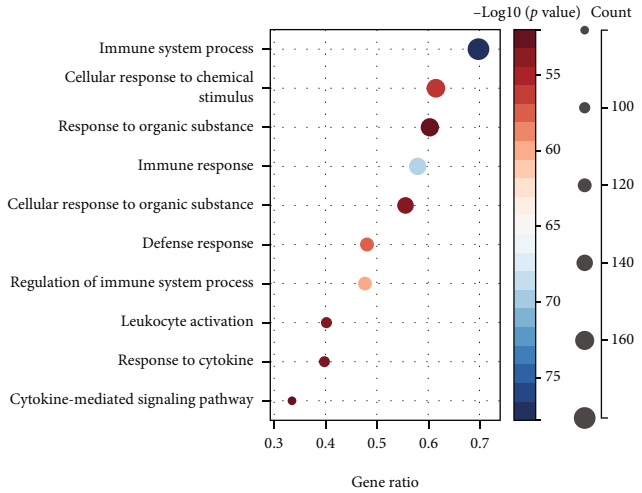

(a) Bioprocess terminology for DEG in GSE189734

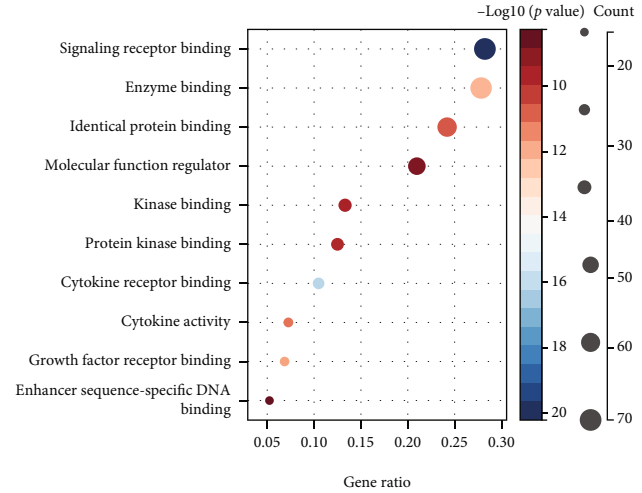

(b) Molecular functional terminology of DEG in GSE189734

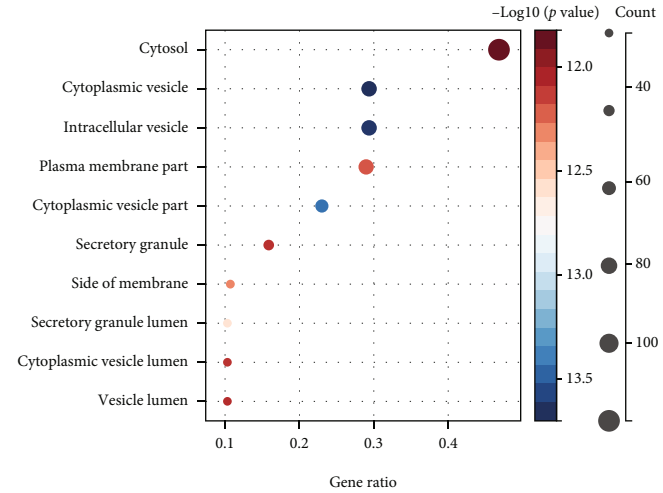

(c) Cellular component terminology for DEG in GSE189734

Figure 2: Continued.

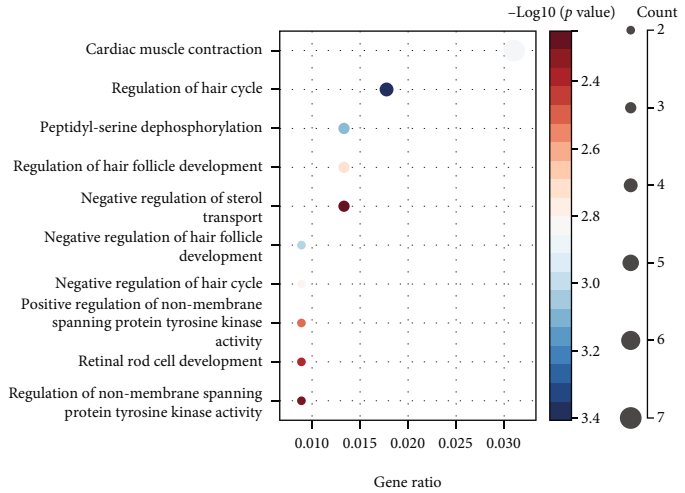

(d) Bioprocess terminology for DEG in GSE145969

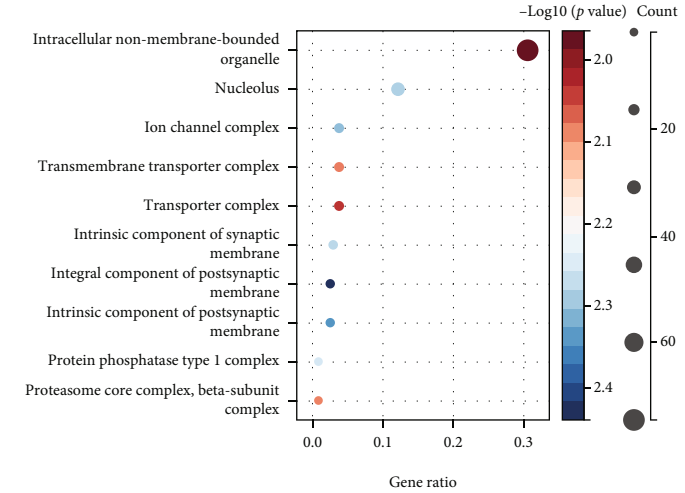

(e) Cellular component terminology for DEG in GSE145969

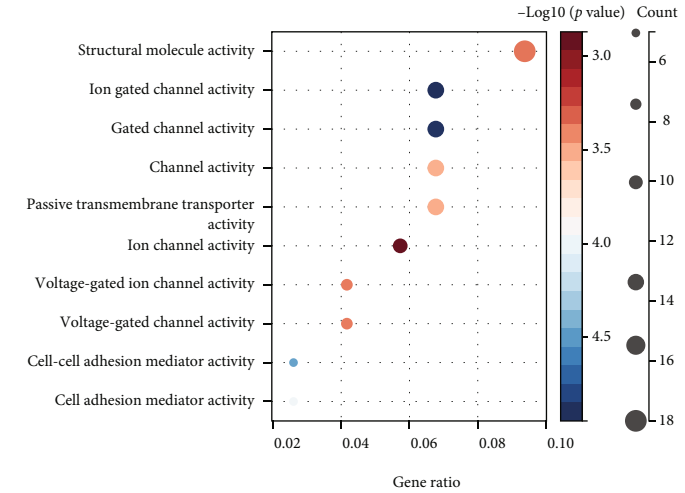

(f) Molecular functional terminology of DEG in GSE145969

Figure 2: Results of the GSE189734 and GSE145969 gene functional enrichment analysis. Note: The results are shown by bubble plots for the first 10 functional pathways of genes, with a screening threshold of $p < 0.01$.

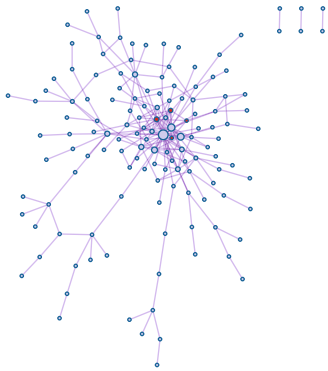

(a) Interaction relationship network of DEGs in GSE145969

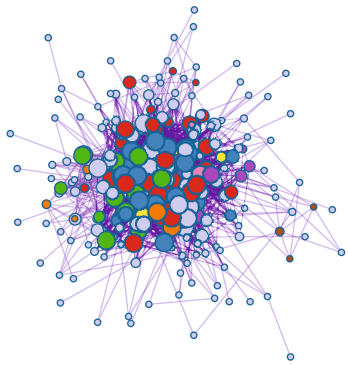

(b) Interaction relationship network of DEGs in GSE189734

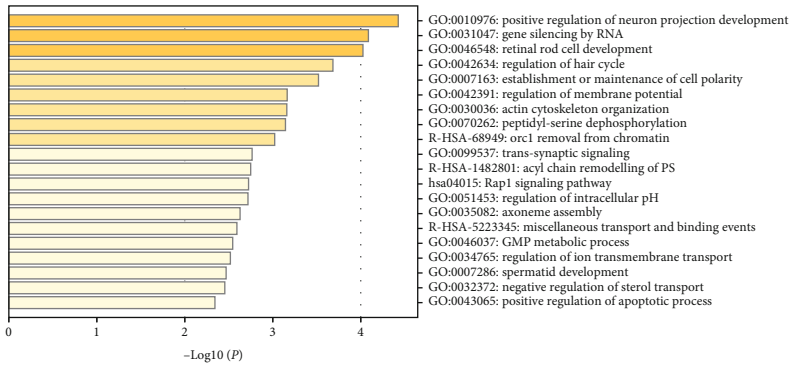

(c) Functional and pathway enrichment analysis of DEGs in GSE145969

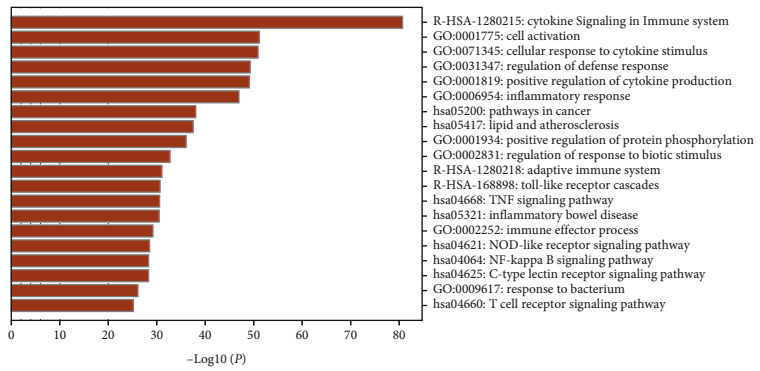

(d) Functional and pathway enrichment analysis of DEGs in GSE189734

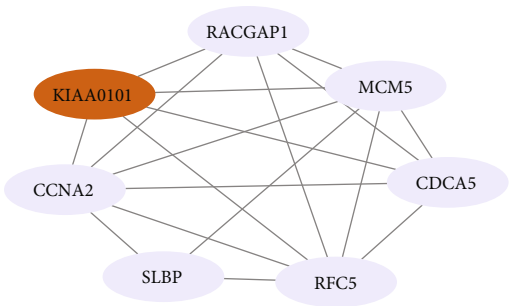

(e) Top scoring gene modules in GSE145969 based on MCODE algorithm analysis in Cytoscape

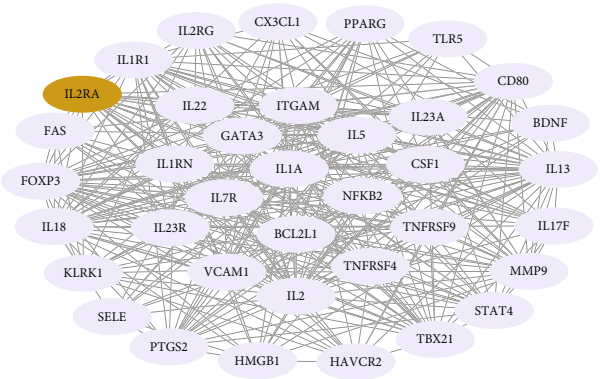

(f) Top scoring gene modules in GSE189734 based on MCODE algorithm analysis in Cytoscape

Figure 3: Results of the PPI analysis of GSE145969 and GSE189734. Note: As the result of the MCODE plug-in in Metascape had only one cluster and contained fewer genes, Cytoscape was used to recreate the map.

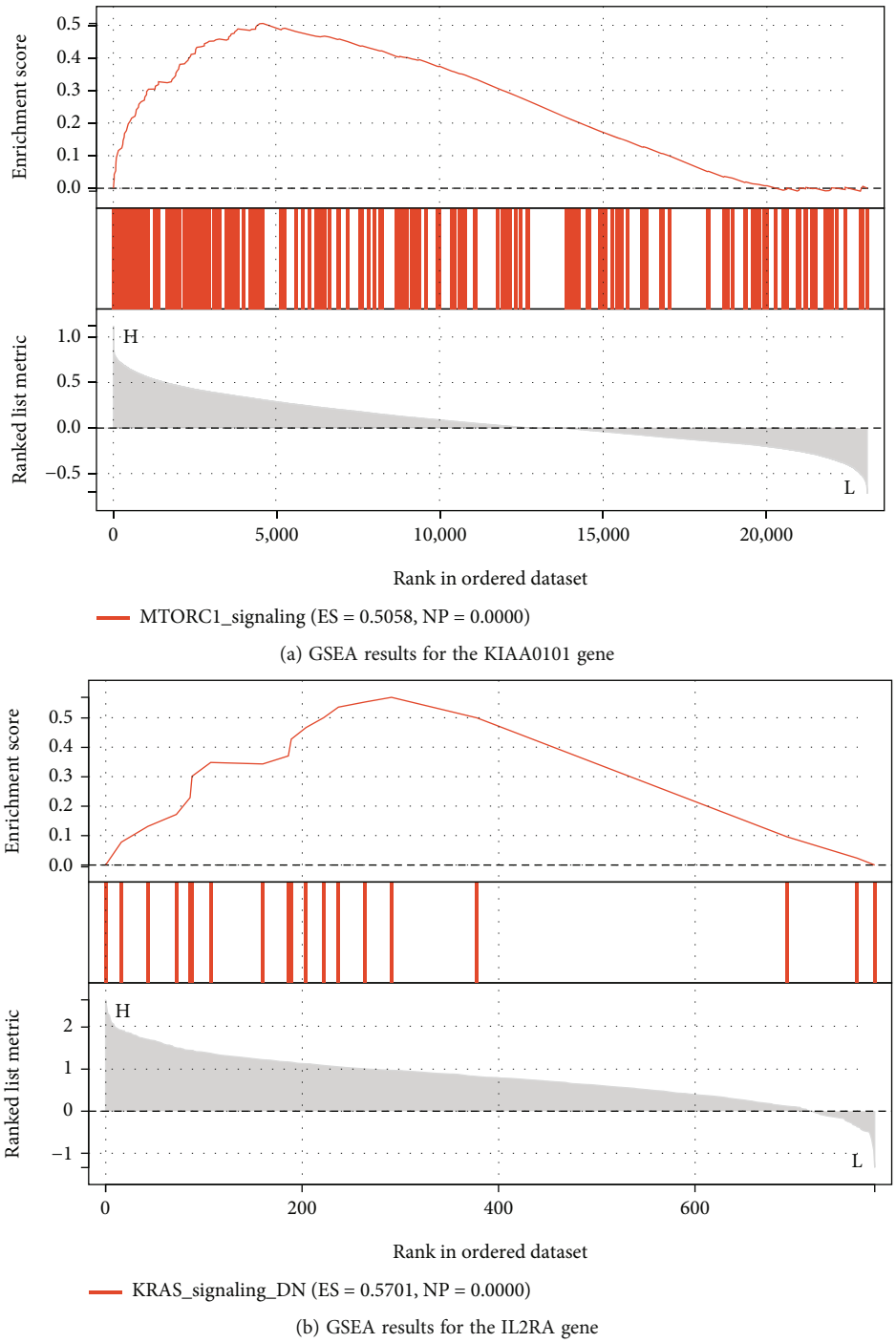

(a) GSEA results for the KIAA0101 gene

(b) GSEA results for the IL2RA gene

Figure 4: Results of the GSEA of the key genes. Note: The threshold value is $|NES| > 1$, and the p value is <0.05.

two transcription factors that generally play a role in projection neuron development, with Satb2 acting as a repressor of Ctip2 [14]. The functions of the GSE189734 dataset are enriched in cytokine signaling in the immune system. The immune system is controlled by a variety of cytokines, which act through the Janus tyrosine kinases and the signal transduction and activators of transcription to achieve their functions [15]. In addition, the protein network models were constructed separately for the DEGs, and the genes were scored using the MCODE plug-in, resulting in the highest-scoring gene modules. The results showed that GSE189734 had 253 nodes and that the highest-scoring module contained 37 genes and 368 edges. GSE145969 had 140 nodes, and the highest-scoring module contained 7 genes and 18 edges. Clearly, the GSE189734 dataset genes were more closely related. The seed genes IL2RA and KIAA0101 were selected as the key genes for the GSEA of the HALLMARK pathway. The results showed that KIAA0101 was significantly enriched in the mTORC1 signaling pathway, while IL2RA was significantly enriched in the KRAS signaling pathway.

The KIAA0101 gene was found to be associated with the prognosis of several tumors, and its bioinformatics analysis revealed that it is an independent prognostic factor for malignant pleural mesothelioma [16]. It was also found to be a diagnostic biomarker of breast cancer prognosis in a study on breast cancer [17]. In addition, KIAA0101 is a diagnostic and prognostic marker for lung adenocarcinoma and is even associated with the gene regulatory network and immune infiltration of lung adenocarcinoma [18]. The IL2RA gene regulates proliferation, differentiation, apoptosis, and leukemogenesis and is associated with a variety of diseases, such as acute myeloid leukemia prognosis [19]. Single nucleotide polymorphisms in the IL2RA gene affect the pathogenesis of multiple sclerosis by encoding IL-2Rα [20]. An mTOR signaling pathway is closely related to the MAPK pathway and controls cell growth by interacting to determine anabolism and catabolism. The mTORC1 signaling pathway transduces functions that regulate metabolism, translation, and autophagy [21] [22]. The overexpression of mTORC1 causes disease; therefore, mTORC1 inhibitors are used to treat various diseases [23]. KRAS is a member of the Ras family, which is a common protooncogene with a mutation rate of up to 30% [24], and is associated with a variety of cancers with poor prognoses. There are several KRAS markers in mutated cancers, such as pancreatic, colorectal, lung, and genitourinary cancers [25]. Ras proteins regulate multiple programs of cell growth, reproduction, and metabolism by signaling to pathways, such as the MAPK pathway and P13K, thus facilitating oncogenic transformation [26]. The results of the study showed that similar gene function pathways were obtained by analyzing different tissue samples from nephropathy and that all were related to cell growth, development, and reproduction.

In conclusion, hormone-resistant nephropathy was identified by two key genes, IL2RA and KIAA0101, and the signaling pathways involved were the KRAS signaling pathway and the mTORC1 signaling pathway. We hypothesize that the two genes exert their effects by influencing two signaling pathways to regulate cell growth, development, and reproduction, and that IL2RA and KIAA0101 could be used as hormone-resistant nephropathy diagnostic markers.

Data Availability

This study found two datasets related to hormone-resistant nephrotic syndrome based on the Gene Expression Omnibus (GEO, https://www.ncbi.nlm.nih.gov/geo/)

Conflicts of Interest

The authors declare that they have no conflicts of interest.

Acknowledgments

The research was supported by Natural Science Foundation of Hunan Province under the grant number 2019JJ80004.

References

[1] A. S. Levey, K. U. Eckardt, Y. Tsukamoto et al., "Definition and classification of chronic kidney disease: a position statement from kidney disease: improving global outcomes (KDIGO)," *Kidney International*, vol. 67, no. 6, pp. 2089–2100, 2005.

[2] A. Sinha, A. Bagga, S. Banerjee et al., "Steroid sensitive nephrotic syndrome: revised guidelines," *Indian Pediatrics*, vol. 58, no. 5, pp. 461–481, 2021.

[3] K. Iijima, M. Sako, K. Kamei, and K. Nozu, "Rituximab in steroid-sensitive nephrotic syndrome: lessons from clinical trials," *Pediatric Nephrology*, vol. 33, no. 9, pp. 1449–1455, 2018.

[4] S. L. Schulman, B. A. Kaiser, M. S. Polinsky, R. Srinivasan, and H. J. Baluarte, "Predicting the response to cytotoxic therapy for childhood nephrotic syndrome: superiority of response to corticosteroid therapy over histopathologic patterns," *The Journal of Pediatrics*, vol. 113, no. 6, pp. 996–1001, 1988.

[5] J. M. Lee, A. Kronbichler, J. I. Shin, and J. Oh, "Current understandings in treating children with steroid-resistant nephrotic syndrome," *Pediatric Nephrology*, vol. 36, no. 4, pp. 747–761, 2021.

[6] I. Franke, M. Aydin, C. E. Llamas Lopez et al., "The incidence of the nephrotic syndrome in childhood in Germany," *Clinical and Experimental Nephrology*, vol. 22, no. 1, pp. 126–132, 2018.

[7] C. Dossier, N. Lapidus, F. Bayer et al., "Epidemiology of idiopathic nephrotic syndrome in children: endemic or epidemic," *Pediatric Nephrology*, vol. 31, no. 12, pp. 2299–2308, 2016.

[8] K. Kikunaga, K. Ishikura, C. Terano et al., "High incidence of idiopathic nephrotic syndrome in east Asian children: a nationwide survey in Japan (JP-SHINE study)," *Clinical and Experimental Nephrology*, vol. 21, no. 4, pp. 651–657, 2017.

[9] J. A. Kari, "Changing trends of histopathology in childhood nephrotic syndrome in western Saudi Arabia," *Saudi Medical Journal*, vol. 23, no. 3, pp. 317–321, 2002.

[10] D. Mekahli, A. Liutkus, B. Ranchin et al., "Long-term outcome of idiopathic steroid-resistant nephrotic syndrome: a multicenter study," *Pediatric Nephrology*, vol. 24, no. 8, pp. 1525–1532, 2009.

[11] S. Banerjee, "Steroid resistant nephrotic syndrome," *Indian Journal of Pediatrics*, vol. 69, no. 12, pp. 1065–1069, 2002.

[12] Q. Han, H. Zhu, X. Chen, and Z. Liu, "Non-genetic mechanisms of diabetic nephropathy," *Frontiers in Medicine*, vol. 11, no. 3, pp. 319–332, 2017.

[13] L. C. Greig, M. B. Woodworth, M. J. Galazo, H. Padmanabhan, and J. D. Macklis, "Molecular logic of neocortical projection neuron specification, development and diversity," *Nature Reviews Neuroscience*, vol. 14, no. 11, pp. 755–769, 2013.

[14] K. Harb, E. Magrinelli, C. S. Nicolas et al., "Area-specific development of distinct projection neuron subclasses is regulated by postnatal epigenetic modifications," *eLife*, vol. 5, article e09531, 2016.

[15] A. Yoshimura, H. Nishinakamura, Y. Matsumura, and T. Hanada, "Negative regulation of cytokine signaling and immune responses by SOCS proteins[J]," *Arthritis Research & Therapy*, vol. 7, no. 3, pp. 100–111, 2005.

[16] P. Lin, Y. Zhao, X. Li, and Z. Liang, "KIAA0101 in malignant pleural mesothelioma: a potential diagnostic and prognostic marker," *Combinatorial Chemistry & High Throughput Screening*, vol. 25, no. 9, pp. 1498–1506, 2022.

[17] J. Liu, Y. He, C. Li et al., "Increased KIAA0101 gene expression associated with poor prognosis in breast cancer," *Translational Cancer Research*, vol. 10, no. 9, pp. 4009–4019, 2021.

[18] S. Hu, W. Zeng, W. Zhang et al., "KIAA0101 as a new diagnostic and prognostic marker, and its correlation with gene regulatory networks and immune infiltrates in lung adenocarcinoma," *Aging (Albany NY)*, vol. 13, no. 1, pp. 301–339, 2020.

[19] C. H. Nguyen, A. Schlerka, A. M. Grandits et al., "IL2RAPromotes aggressiveness and stem cell-related properties of acute myeloid leukemia," *Cancer Research*, vol. 80, no. 20, pp. 4527–4539, 2020.

[20] S. Buhelt, H. M. Laigaard, M. R. von Essen et al., "IL2RA methylation and gene expression in relation to the multiple sclerosis-associated gene variant rs2104286 and soluble IL-2Rα in CD8+ T cells," *Frontiers in Immunology*, vol. 12, no. 12, article 676141, 2021.

[21] Y. Rabanal-Ruiz, E. G. Otten, and V. I. Korolchuk, "mTORC1 as the main gateway to autophagy," *Essays in Biochemistry*, vol. 61, no. 6, pp. 565–584, 2017.

[22] K. J. Condon and D. M. Sabatini, "Nutrient regulation of mTORC1 at a glance," *Journal of Cell Science*, vol. 132, no. 21, article jcs222570, 2019.

[23] G. Lei, L. Zhuang, and B. Gan, "mTORC1 and ferroptosis: regulatory mechanisms and therapeutic potential," *BioEssays*, vol. 43, no. 8, article e2100093, 2021.

[24] D. Uprety and A. A. Adjei, "KRAS: from undruggable to a druggable cancer target," *Cancer Treatment Reviews*, vol. 89, article 102070, 2020.

[25] J. Timar and K. Kashofer, "Molecular epidemiology and diagnostics of KRAS mutations in human cancer," *Cancer Metastasis Reviews*, vol. 39, no. 4, pp. 1029–1038, 2020.

[26] J. Luo, "KRAS mutation in pancreatic cancer," *Seminars in Oncology*, vol. 48, no. 1, pp. 10–18, 2021.

Hindawi
Disease Markers
Volume 2022, Article ID 1226697, 15 pages
https://doi.org/10.1155/2022/1226697

Research Article

ANTXR1 Regulates Erythroid Cell Proliferation and Differentiation through wnt/β-Catenin Signaling Pathway *In Vitro* and in Hematopoietic Stem Cell

Tingting Jin,[1,2] **Zhaojun Zhang**,[3] **Yuanyuan Han**,[1,2] **Di Li**,[2] **Juan Liu**,[1] **Minmin Jiang**,[2] **Ryo Kurita**,[4] **Yukio Nakamura**,[4] **Fangfang Hu**,[5] **Xiangdong Fang**,[3] **Shengwen Huang**,[1,2,6] **and Zhaolin Sun**[1,7]

[1]*School of Medicine, Guizhou University, Guiyang, Guizhou 550025, China*
[2]*Prenatal Diagnosis Center, Guizhou Provincial People's Hospital, Guiyang, Guizhou 550002, China*
[3]*CAS Key Laboratory of Genome Sciences and Information, Beijing Institute of Genomics, Chinese Academy of Sciences, Beijing 100101, China*
[4]*Cell Engineering Division, RIKEN Bio Resource Center, Tsukuba, Ibaraki 305-0074, Japan*
[5]*Department of Laboratory, Guizhou Provincial People's Hospital, Guiyang, Guizhou 550002, China*
[6]*NHC Key Laboratory of Pulmonary Immunological Diseases, Guizhou Provincial People's Hospital, Guiyang, Guizhou 550002, China*
[7]*Department of Urology, Guizhou Provincial People's Hospital, Guiyang, Guizhou 550002, China*

Correspondence should be addressed to Xiangdong Fang; fangxd@big.ac.cn, Shengwen Huang; hsw713@sina.com, and Zhaolin Sun; szl5926186@163.com

Received 29 June 2022; Revised 21 July 2022; Accepted 29 July 2022; Published 27 August 2022

Academic Editor: Fu Wang

Erythropoiesis is a highly complex and sophisticated multistage process regulated by many transcription factors, as well as noncoding RNAs. Anthrax toxin receptor 1 (ANTXR1) is a type I transmembrane protein that binds the anthrax toxin ligands and mediates the entry of its toxic part into cells. It also functions as a receptor for the Protective antigen (PA) of anthrax toxin, and mediates the entry of Edema factor (EF) and Lethal factor (LF) into the cytoplasm of target cells and exerts their toxicity. Previous research has shown that ANTXR1 inhibits the expression of γ-globin during the differentiation of erythroid cells. However, the effect on erythropoiesis from a cellular perspective has not been fully determined. This study examined the role of ANTXR1 on erythropoiesis using K562 and HUDEP-2 cell lines as well as cord blood $CD34^+$ cells. Our study has shown that overexpression of ANTXR1 can positively regulate erythrocyte proliferation, as well as inhibit GATA1 and ALAS2 expression, differentiation, and apoptosis in K562 cells and hematopoietic stem cells. ANTXR1 knockdown inhibited proliferation, promoted GATA1 and ALAS2 expression, accelerated erythrocyte differentiation and apoptosis, and promoted erythrocyte maturation. Our study also showed that ANTXR1 may regulate the proliferation and differentiation of hematopoietic cells, though the Wnt/β-catenin pathway, which may help to establish a possible therapeutic target for the treatment of blood disorders.

1. Introduction

Hematopoietic stem cells (HSCs) can self-renew and differentiate into erythroid lines [1]. By dividing into megakaryocytic erythroid progenitors (MEPs) through common myeloid progenitor cells (CMPs) and erythroblasts through erythroid blast-forming units (BFU-E) and erythroid colony-forming units (CFU-E), HSCs form reticulocytes through the terminal differentiation stage, and then enter the bloodstream and become mature red blood cells, highly specialized functional cells. In this process, new erythrocytes are continuously generated, and the spontaneous elimination of senescent

erythrocytes maintains a dynamic balance. Blood disorders such as sickle cell anemia, β-thalassemia, and sideroblastic anemia are often caused by red blood cells with abnormal morphology and function [2–4]. Life-long blood transfusions or bone marrow transplantation may be required in severe cases of blood diseases with complications. Therefore, promoting the production of effective red blood cells is an effective treatment for hemolytic anemia. Previous studies have shown that erythropoiesis is regulated by many microenvironmental factors, such as miRNAs and transcription factors, particularly the crucial GATA1.

Initially, Krüppel-like factor 1 (KLF1 or EKLF, erythroid Krüppel-like factor) and GATA1 primitively and definitively regulate erythropoiesis under physiological and pathological conditions by targeting different erythroid-specific genes [5], but their regulatory networks remain unclear. Anthrax toxin receptor 1 (ANTXR1) is a membrane protein discovered 20 years ago, and it plays an important role in extracellular matrix homeostasis, angiogenesis, and cell proliferation [6, 7]. A recent study has found that ANTXR1 is a target of Runx2 and regulates the proliferation and apoptosis of chondrocytes [8]. The role of ANTXR1 in tumor development has been demonstrated in previous studies, but no studies have examined its effects on hematopoiesis and erythrocyte differentiation. Until now, two single-nucleotide polymorphisms (SNPs), known as rs4527238 and rs35685045, have been associated with the expression of fetal hemoglobin (HbF) in patients with sickle cell anemia [9–11]. We overexpressed and interfered with ANTXR1 in K562 cells, cord blood $CD34^+$ cells, and HUDEP-2 cells in the early stage and found that the expression of the γ-globin gene was inversely proportional to the expression of the ANTXR1 gene, and interfering with the gene inhibited cell proliferation.

Canonical Wnt signaling has been implicated in the regulation of hematopoiesis. Wnt signaling pathways play important roles in self-renewal of hematopoietic stem cells [12]. The knockout of β-catenin in the mouse hematopoietic system results in impaired HSCs self-renewal [13]. HSCs self-renewal is impaired, and hematopoietic reconstitution capacity is reduced when Wnt inhibitors, such as Axin1, DKK1, and Wif1, are overexpressed in bone marrow stromal cells and osteoblasts [14–16]. There is evidence that hematopoietic stem cells and their hematopoietic microenvironment can receive and respond to Wnt signaling. However, the role of ANTXR1 in regulating erythroid cell proliferation and differentiation through the Wnt/β-catenin signaling pathway has not been proven. In this study, differentiated erythroid cell models were used to investigate the role of ANTXR1 in the proliferation and differentiation of erythroid cells and its possible mechanisms. Based on the findings of this study, we might be able to promote the production of red blood cells that are more effective in the treatment of blood disorders.

2. Materials and Methods

2.1. Cell culture. K562 cell line was purchased from Shanghai Institute of Biological Sciences, China. Cord blood (CB) samples were obtained from the Obstetrics Department of Beijing Maternity Hospital. The institutional ethical committee of Guizhou Provincial People's Hospital approved the study. All methods were conducted following Declaration of Helsinki guidelines and regulations. HUDEP-2 cells were donated by RIKEN Tsukuba Branch, Ibaraki, Japan.

K562 cells were cultured in RPMI-1640 medium containing 10% fetal bovine serum (FBS) and 1% streptomycin/penicillin. The culture media was changed once daily and passaged once every two days. The erythroid differentiation of K562 was induced for three days with 50 μmol/L hemin and cultured in a 37°C, 5% CO2 incubator.

Isolated $CD34^+$ cells (STEMCELL,#17896) were first plated in StemSpan SFEM II (STEMCELL Technologies) supplemented with 50 ng/mL SCF, 50 ng/mL, Flt3 ligand, 50 ng/mL TPO, and 2% penicillin-streptomycin for 7 days according to the manufacturer's instructions. On day 7, the cells were cultured to promote erythroid differentiation using conditions modified from those reported previously [10]. The cells were inoculated for 7 days at a density of 5×10^5/mL in StemSpan SFEM II medium containing 10 ng/mL SCF, 10 ng/mL IL-3, 3 IU/mL EPO, and 2% penicillin-streptomycin, followed by the addition of 10 ng/mL SCF, 3 IU/mL EPO, and 2% penicillin-streptomycin and culture for a further 3 days. 1 IU/mL EPO and 2% penicillin-streptomycin were then added continually to the SFEM II medium for a further 6 days, resulting in a total incubation time of 16 days.

Culture of the HUDEP-2 cells for erythroid differentiation involved: (1) transfer of the cells to the erythroid differentiation medium (EDM) containing Iscove's modified Dulbecco's medium (IMDM), 2% penicillin-streptomycin solution (10,000 U/mL stock concentration), 500 μg/mL human holo-transferrin, 10 μg/mL recombinant human insulin solution, 3 IU/mL heparin, 3% inactivated human plasma, and 3 IU/mL Epoetin alfa (Epogen, Amgen); (2) culture for 4 days in EDM containing 100 ng/mL SCF and 1 μg/mL doxycycline; and (3) culture for 3 days in EDM containing 1 μg/mL doxycycline.

2.2. Overexpression and Knockdown of ANTXR1-Transfected K562 Cells, Cord Blood $CD34^+$, and HUDEP-2 Cells. Semiattached K562 cells were cultured in RPMI 1640 (Gibco) supplemented with 10% FBS (Gibco), penicillin 100 units/mL, and streptomycin 100 μg/mL at 37°C in a humidified 5% CO_2 incubator overnight. K562 cells were seeded at a density of 5×10^5 cells per well, then transfected with the overexpression (OE) plasmids (titer 1×10^8 transduction unit (TU)/mL, multiplicity of infection MOI = 30) and control plasmids (titer 1×10^7 TU/mL, MOI = 30) transfected into K562 cells, and were cultured with fresh RPMI-1640 medium containing 10% fetal bovine serum for 48 h. The NC-shRNA and ANTXR1-sh5 sequences were designed by online software (https://www.sigmaaldrich.cn/CN/zh/semi-configurators/shrna?activeLink=productSearch). The K562 cells were infected with the shNC (titer 1×10^8 TU/mL, MOI = 20) virus or ANTXR1-sh5 (titer 4×10^8 TU/mL, MOI = 20) virus with Invitrogen Lipofectamine™ 3000 Transfection Reagent following the commercial protocol. On the second day of erythroid differentiation, $CD34^+$ cells

were infected with the virus, and the culture medium was changed after 8 hours of infection. HUDEP-2 lentivirus infection was the same as K562 cells infection, and GFP-positive cells were screened by flow cytometry.

2.3. qRT-PCR. For the detection of mRNA expression, total RNA was reversed and transcribed into cDNA using the $2^{-\Delta\Delta Ct}$ method. The PCR was carried out at 95°C for 10 min; 95°C for 10s, and 60°C for 30s for 40 cycles. Each sample was repeated 3 times. The gene expression of the *ANTXR1*, *GATA1*, and *ALAS2* was detected by RT-PCR. The primers of the target genes are shown in Table 1.

2.4. Flow Cytometry. Approximately 1×10^6 of K562 and $CD34^+$ cells were collected and washed twice with $1 \times$ PBS. The cells were then permeabilized using TritonX-100 (Beyotime, #P0096) for 20 minutes. Following immunostaining, antibodies to CD235a-APC (#REA175) and CD71-PE (Miltenyi Company, Germany, #AC102) were added. The cells were incubated for 30 minutes at room temperature in the dark, and fluorescence-activated cell sorting (FACS) machine was then used to analyze CD71 and CD235a expression.

2.5. Benzidine Staining. Benzidine hydrochloride powder (10 mg) was dissolved in 1 mL of 0.5 M glacial acetic acid solution. 50 μL of the above solution was added to 1 μL of 30% hydrogen peroxide to prepare a benzidine work solution. About 0.5 million cells were spread on the slide after two washes with 100 μL $1 \times$ PBS and incubated at room temperature for 5 min following addition of 1 μl benzidine solution to the cell suspension. The staining results were observed, and about 200 cells in a field were counted under a microscope. The positive rates of blue-stained cells in 3 different fields were calculated. Benzidine staining was used to determine K562 cell differentiation by synthesizing hemoglobin.

2.6. Wright-Giemsa Staining. The entire glass slide area smeared with cells was covered with drip dye solution A (0.8-1.0 mL) and then evenly stained for 1 min. Later, solution B (which has a volume twice that of solution A) was added, washed, and stained for approximately 8 minutes each. The slide was then gently rinsed to remove the residual dye solution, air-dried, and observed under the microscope for the effect of ANTXR1 on K562 cells during erythroid differentiation.

2.7. Western Blot. Using a collection of 1×10^6 cells from the overexpression, knockdown, and control groups, western blotting was used to determine protein expression in transfected cells. In brief, the cells were washed three times with PBS, and 200 μL of protein lysis buffer was added to extract the total protein. The protein concentration was determined with the BCA protein assay. After loading 20 μg total protein in the SDS-PAGE, it was run for 5 min at 95°C using protein sample buffer. The protein was transferred into a PVDF membrane through electrophoresis at 120 V for 2 h. The membrane was then blocked with 5% bovine serum albumin for 1 h at room temperature. The primary ANTXR1 antibody of the target gene 1 : 1000 (ab21270, Abcam), anti-phospho-β-catenin (Ser33/37/Thr41) 1 : 1000 (ab246504, Abcam), anti-β-catenin 1 : 2000 (#8480, CST), anti-GATA1 1 : 1000 (ab133274, Abcam), anti-ALAS2 1 : 1000 (ab184964, Abcam), anti-GAPDH 1 : 3000 (ab181602, Abcam), and anti-GSK3β1:3000 (ab32391, Abcam) was added, respectively, for each detection and incubated overnight at 4°C. The membrane was washed thrice with TBST, 5 min each time, and incubated with a secondary antibody for 1 h at room temperature. The membrane was then re-washed thrice with TBST, and the band was developed with ECL Iuminescence solution. Finally, immunoreactive protein bands were visualized using the ECL system, and the protein bands were analyzed using Image J software (http://imagej.nih.gov/ij).

Table 1: List of primers used for RT-qPCR assays.

Gene	Primer sequence (5′-3′)
GAPDH	F: GCACCGTCAAGGCTGAGAAC
	R: TGGTGAAGACGCCAGTGGA
ANTXR1	F: CGGATTGCGGACAGTAAGGAT
	R:TCCTCTCACGACAACTTGAAATG
GATA1	F: CTGTCCCCAATAGTGCTTATGG
	R:GAATAGGCTGCTGAATTGAGGG
ALAS2	F: CCAAACAGGAACTGGTGAGTC
	R:TCATTCGTTCGTCCTCAGTG

2.8. Cell Proliferation Assay. We aimed to detect the effect of ANTXR1 on the proliferation of K562 cells and $CD34^+$ cells. Cell proliferation assay was done using Biyuntian Cell Counting Kit-8 (#C0038, Biyuntian Biotech, Jiangsu, China). The experimental and the control cells were plated into a 96-well plate at a density of 1×10^4 cells/well, and the K562 cell line were divided into groups at 12, 24, 48, and 72 hours according to protocol; 10 μL of CCK-8 solution was added to the well plates at various times, and the OD absorbance value of each well at 450 nm was detected by a microplate reader at 12, 24, 48 and 72 hours. Cord blood $CD34^+$ cells were evaluated for cell proliferation on D6, D7, D8, and D9.

2.9. Apoptosis Assay. The apoptosis experiment was performed with an Annexin V-PE apoptosis detection kit (#C1065S, Biyuntian, Jiangsu, China.). The cord blood $CD34^+$ cells of the experimental and the control group were centrifuged at 300*g* to remove the supernatant. The cells were then washed with $1 \times$ PBS, and the supernatant was discarded. Later, 195 μL Annexin V-PE binding solution was added, and the cells were gently resuspended before adding 5 μL Annexin V-PE with gentle mixing. The mixture was incubated in the dark at room temperature for 15 minutes, washed with $1 \times$ PBS, resuspended in 500 μL of $1 \times$ PBS, and placed on ice for flow cytometry detection.

2.10. Immunofluorescence Staining. To detect the localization of ANTXR1 and LRP6 in K562 cell line, we collected 1×10^6 cells from the experimental and the control group. The cells were then centrifuged, washed twice with $1 \times$ PBS,

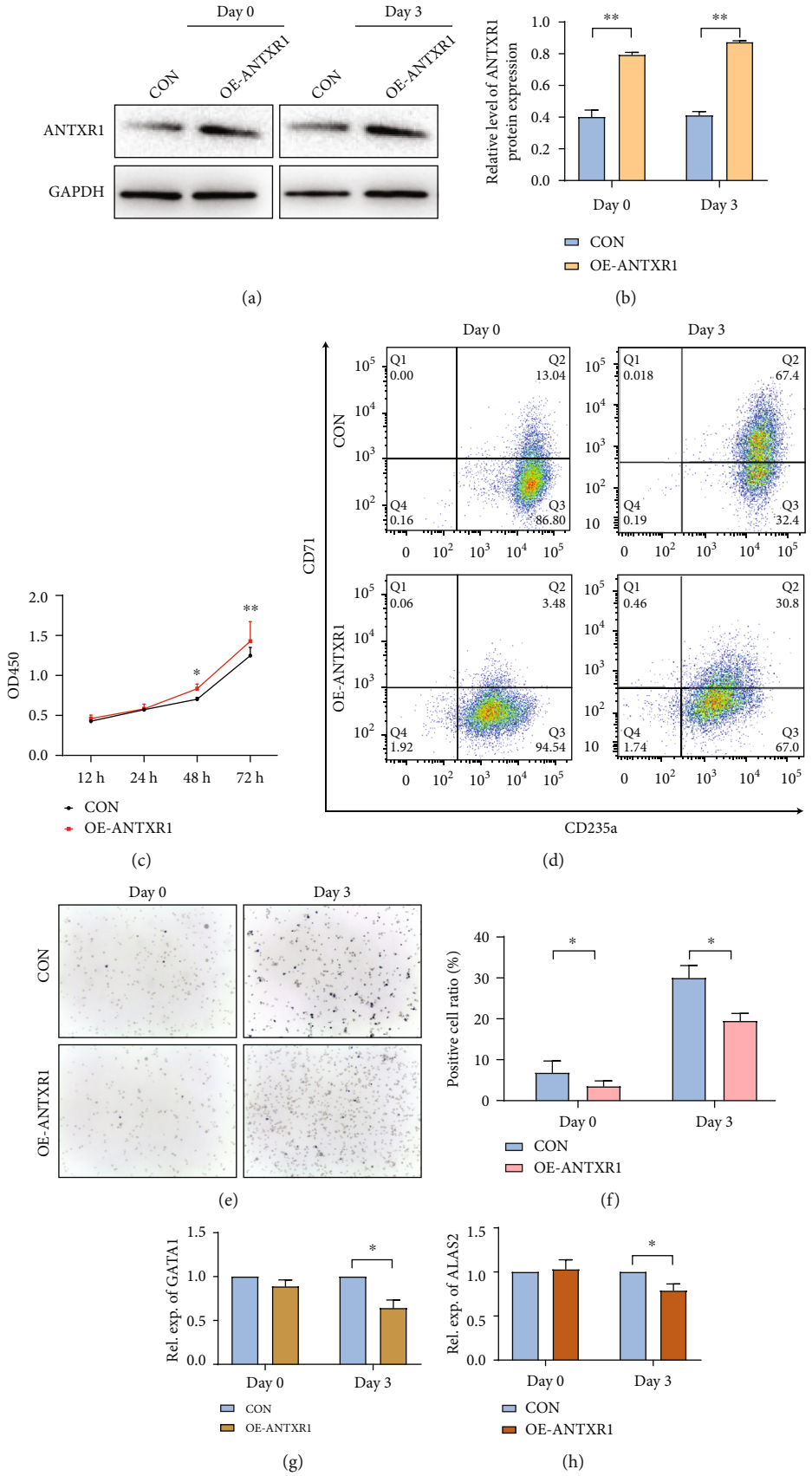

Figure 1: Continued.

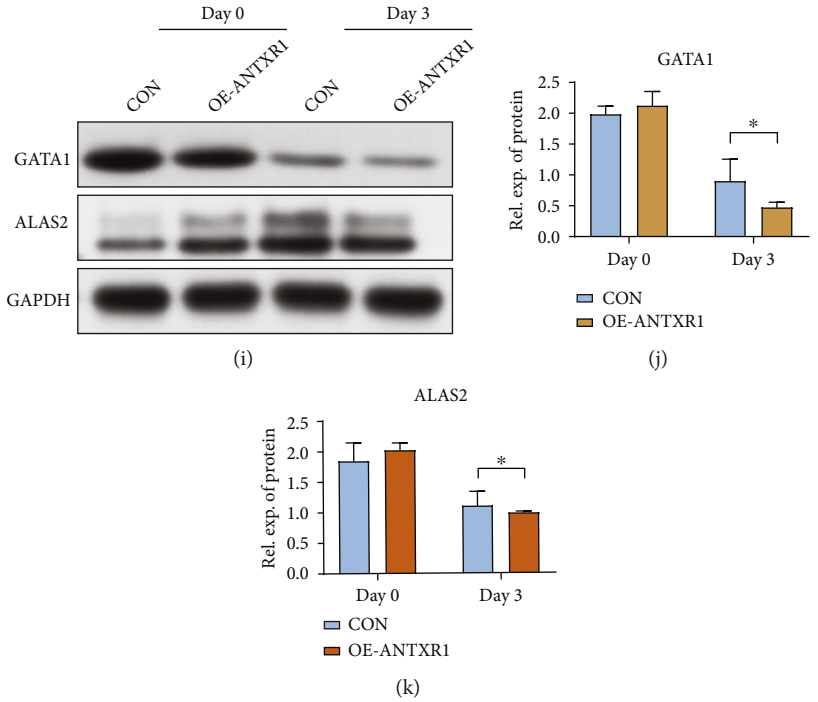

Figure 1: ANTXR1 promotes erythroid cell proliferation and inhibits erythroid cell differentiation and apoptosis in K562 cells. (a) Western blot analysis was used to detect ANTXR1 (45 kDa) expression after transfection of K562 cells with *ANTXR1* overexpression vectors. (b) Quantification of western blots. (c) CCK8 proliferation assay of K562 cells at 12 h, 24 h, 48 h, and 72 h. (d) Flow cytometry detection of CD71 and CD235a expression in K562 erythroid differentiation. (e) Benzidine staining-positive cells. (f) Changes in the proportion of benzidine-positive cells. (g, h) Quantitative reverse transcription polymerase chain reaction (qRT-PCR) was used to determine the mRNA expression levels of GATA1 and ALAS2 in K562 erythrocytes induced by overexpression of ANTXR1. (i) Western blot analysis was used to detect GATA1 (45 kDa) and ALAS2 (65 kDa) protein expression in K562 erythrocytes induced by overexpression of ANTXR1. (j, k) Quantification of western blots. Error bars represent standard deviation of three independent experiments. $^{*}P < 0.05$, $^{**}P < 0.01$.

and resuspended in 20 μL of 1 × PBS. Cells were later introduced onto glass slides to air dry naturally. The cells were fixed for 30 min using 4% paraformaldehyde. Later, rinsing was done three times with 1 × PBS for 5 min each time before air-drying the cells naturally. Cells were permeabilized with TritonX-100 at room temperature for 15 min and then rinsed thrice with 1 × PBS for 5 min. The samples were then blocked with 5% BSA/PBS solution for 30 min at room temperature before blocking with 50 μL of primary antibodies ANTXR1 1 : 100 (ab21270, Abcam) and LRP6 1 : 100 (ab75358, Abcam). Cells were incubated overnight at 4°C and rinsed thrice with 1 × PBS. Later, 50 μL of fluorescein-labeled secondary antibody (#A-11037, Thermo Fisher Scientific) was added and incubated in the dark for 1 h at room temperature. The samples were then rinsed thrice with 1 × PBS, stained with DAPI, and observed in a laser confocal microscope.

2.11. Statistical Analysis. Data were analyzed using SPSS17.0 software and presented as mean ± standard deviation. The experiments were independently repeated three times, and the statistical significance between groups was determined by an independent *t*-test, and $^{*}P < 0.05$ or $^{**}P < 0.01$ was considered a significant difference.

3. Results

3.1. ANTXR1 Effects on Erythrocyte Differentiation during Erythroid Differentiation. To determine the effect of ANTXR1 overexpressing on erythroid differentiation, ANTXR1 was cloned into the pHAGE-fEF-1a-IRES-ZsGreen-2 vector. In the following experiments, the vector was transfected into K562 and cord blood $CD34^{+}$ cells, while cells transfected with an empty vector were used as controls. Western blot was performed to confirm transfection efficiency 48-72 hours after transfection. According to the results, ANTXR1 expression was significantly increased during the induction of erythroid in K562 cells compared with the control group (Figures 1(a) and 1(b)). There was no statistical difference in cell proliferation compared with the control group before 48 hours. Cell proliferation was significantly increased in the OE-ANTXR1 group compared to the control at 48-72 h (Figure 1(c)). ANTXR1 was found to promote proliferation in the study. Flow cytometry analysis showed that the double-positive ratio of overexpression ANTXR1, CD71, and CD235a was significantly reduced compared with the control group, indicating that ANTXR1 inhibited the erythroid differentiation of K562 cells (Figure 1(d)). In comparison to the control group, the proportion of positive

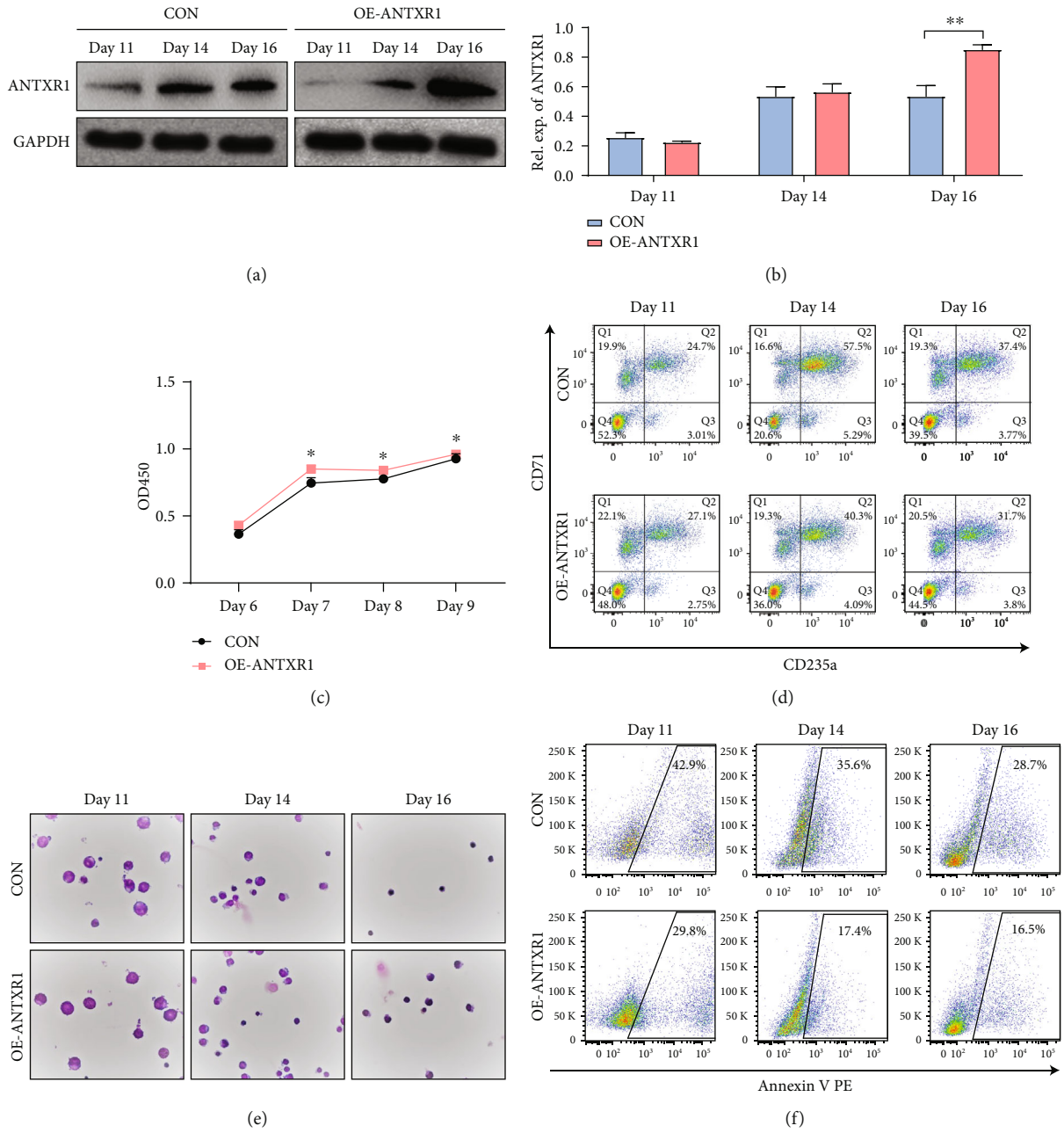

Figure 2: ANTXR1 promotes erythroid cell proliferation and inhibits erythroid cell differentiation and apoptosis in cord blood CD34$^+$ cells. (a) Western blot analysis was used to detect ANTXR1 levels after transfection of cord blood CD34$^+$ cells with *ANTXR1* overexpression vectors. (b) Quantification of western blots. (c) CCK8 assay of cord blood CD34$^+$ cells proliferation at D6, D7, D8, and D9. (d) Flow cytometry detection of CD71 and CD235a expression in cord blood CD34$^+$ cells during erythroid differentiation. (e) Wright-Giemsa staining results of cord blood CD34$^+$ cells. (f) Flow cytometry to detect the expression of apoptotic cells in the differentiation of cord blood CD34$^+$ cells. Error bars represent standard deviation of three independent experiments. $^*P < 0.05$, $^{**}P < 0.01$.

cells detected by benzidine staining decreased (Figures 1(e) and 1(f)). In addition, ANTXR1 overexpression inhibited the GATA1 and ALAS2 expression at mRNA and protein levels among the days of D0 to D3 with erythroid differentiation (Figures 1(g)–1(k)).

3.2. ANTXR1 Promotes Erythroid Cell Proliferation and Inhibits Erythroid Cell Differentiation and Apoptosis in Cord Blood CD34$^+$ Cells. An increase in ANTXR1 expression was observed in cord blood CD34$^+$ cells on days 14 and 16 during erythroid induction (Figures 2(a) and 2(b)). CD34$^+$ cells proliferated from day 7 after ANTXR1 overexpression (Figure 2(c)). According to flow cytometry results, the OE-ANTXR1 showed reduced CD71 and CD235a expression compared with the control group, which indicated that ANTXR1 inhibited the differentiation of cord blood CD34$^+$ cells into erythroid (Figure 2(d)). Wright-Giemsa results also showed that ANTXR1 overexpression increased CD34$^+$

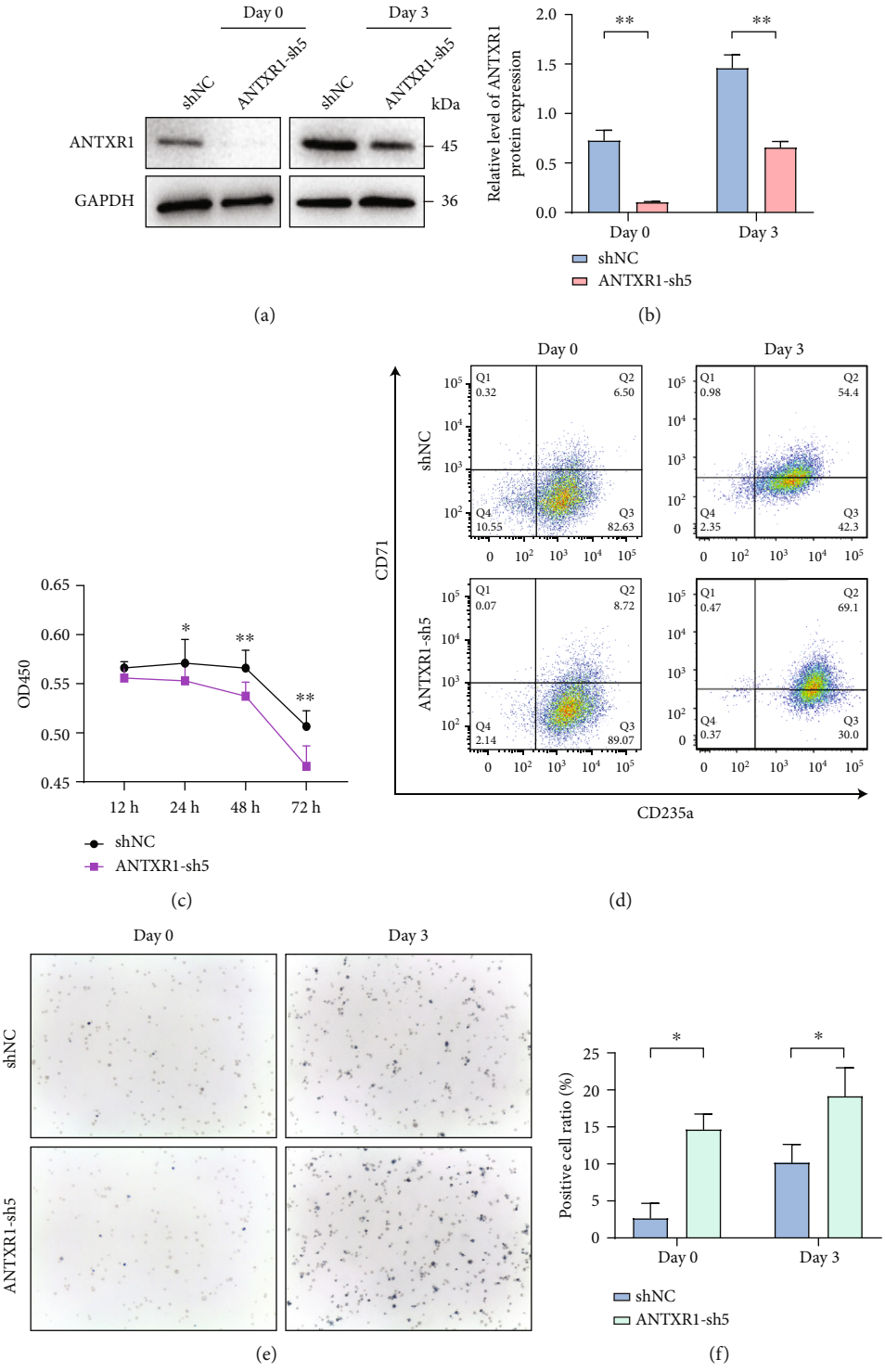

Figure 3: Continued.

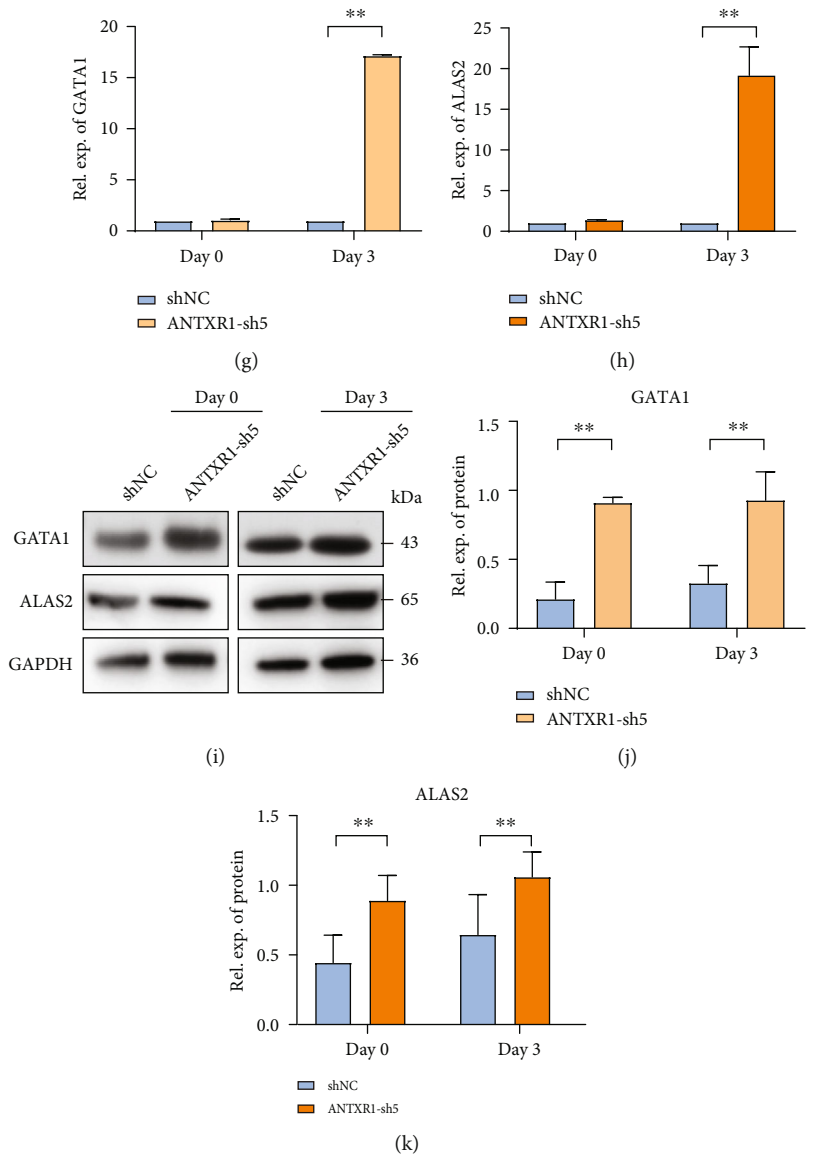

Figure 3: Interfering with ANTXR1 inhibits erythroid cell proliferation and promotes erythroid cell differentiation and apoptosis in K562 cells. (a) Western blot analysis was used to detect ANTXR1 levels after transfection of K562 cells with *ANTXR1* interfering vectors. (b) Quantification of western blots. (c) CCK8 assay of K562 cells proliferation at 12 h, 24 h, 48 h, and 72 h. (d) Flow cytometry detection of CD71 and CD235a expression in K562 cells erythroid differentiation. (e) Benzidine staining-positive cells. (f) Changes in the proportion of benzidine-positive cells. (g, h) Quantitative reverse transcription polymerase chain reaction (qRT-PCR) was used to determine the mRNA expression levels of GATA1 and ALAS2 in K562 erythrocytes induced by interfering with ANTXR1. (i) GATA1 and ALAS2 protein expression in K562 erythrocytes induced by interfering with ANTXR1. (j, k) Quantification of western blots. Error bars represent standard deviation of three independent experiments. $^{*}P < 0.05$, $^{**}P < 0.01$.

erythroid cell volume, whereas the cells with nuclear shift and nuclear shrinkage was significantly reduced compared to those in the control group (Figure 2(e)).

Apoptosis experiment results showed a significantly higher apoptosis rate in the CON group (42.9%, 35.6%, and 28.7%) on days 11, 14, and 16 of cord blood $CD34^{+}$ cell differentiation than that in the OE-ANTXR1 group (29.8%, 17.4%, and 16.5%) (Figure 2(f)). The results of these studies confirm that ANTXR1 regulates erythroid proliferation and differentiation in K562 cells and cord blood $CD34^{+}$ cells during erythroid induction.

3.3. ANTXR1 Silencing Inhibits Cell Proliferation and Promotes Erythroid Differentiation. To further confirm the role of ANTXR1 in erythroid differentiation, we silenced the ANTXR1 expression in K562, cord blood $CD34^{+}$ cells, and HUDEP-2 cells with short hair RNA (shRNA). After transfection with shRNA, ANTXR1 expression in these three cell lines was significantly reduced compared to the control group cells transfected with shNC (Figures 3(a) and 3(b), 4(a), and 5(a)). ANTXR1 silencing significantly reduced the proliferative capacity of K562 cells after 24 h (Figure 3(c)). The flow cytometry results showed that during erythroid

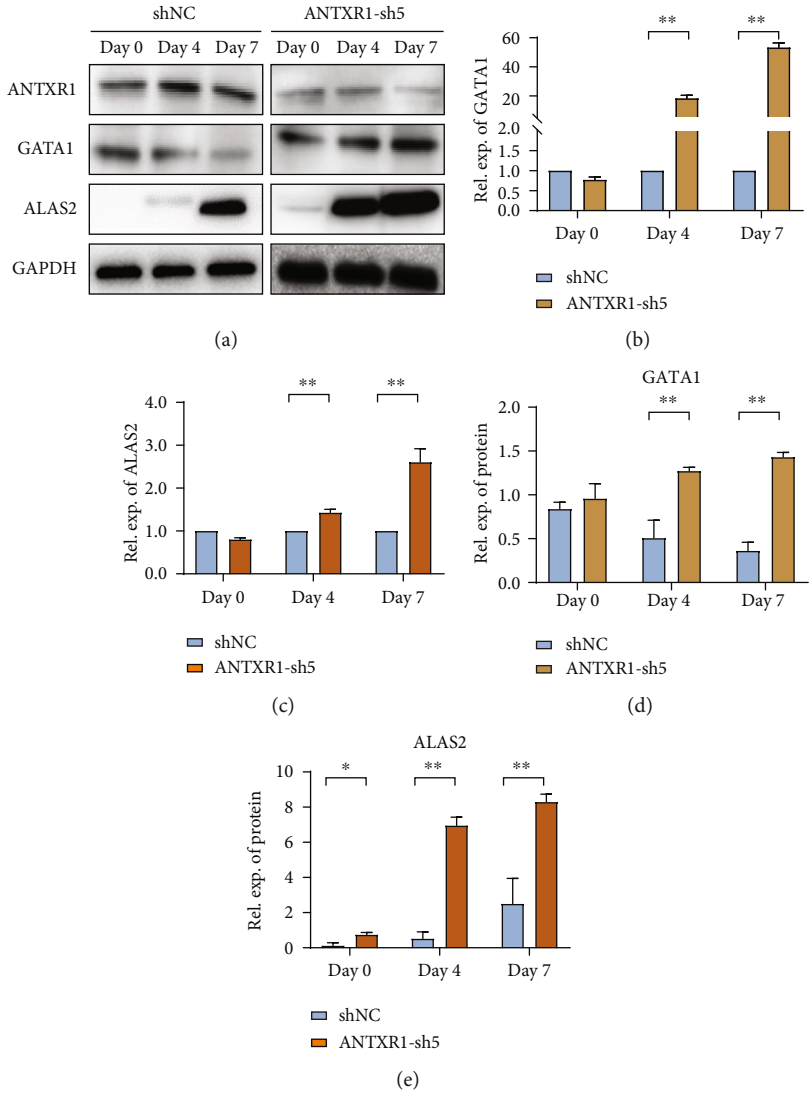

Figure 4: ANTXR1 silencing promotes erythroid cell differentiation in HUDEP-2 cells by interval consecutive analysis. (a) Analysis of GATA1 and ALAS2 protein expressions in HUDEP-2 cells following the knockdown of ANTXR1 the gene expression levels by western blotting and qRT-PCR. (b, c) The relative protein expression levels of GATA1 and ALAS2 were detected after HUDEP-2 cells were transfected with ANTXR1-sh5. (d, e) Quantification of western blots. Error bars represent standard deviation of three independent experiments. $^{*}P < 0.05$, $^{**}P < 0.01$.

differentiation of K562, the proportion of CD71 and CD235a double-positive cells was significantly increased by interfering with ANTXR1 (Figure 3(d)). The benzidine staining showed that ANTXR1 silencing increased the proportion of the positive cells (Figures 3(e) and 3(f)). In addition, ANTXR1 silencing increased the GATA1 and ALAS2 expressions at mRNA and protein levels from days D0 to D3 throughout the erythroid differentiation (Figures 3(g)–3(k)).

We also found the same GATA1 and ALAS2 expressions trend in HUDEP-2 (Figures 4(a)–4(e)). Similar cell proliferation, differentiation, and apoptosis results were observed in cord blood $CD34^{+}$ cells after ANTXR1 silencing, and $CD34^{+}$ cell proliferation decreased from day 7 (Figure 5(b)). There was a significant increase in CD71 and CD235a expression compared to the shNC group, suggesting that ANTXR1 induced erythroid differentiation in cord blood $CD34^{+}$ cells (Figure 5(c)). The Wright-Giemsa results also showed that during $CD34^{+}$ cells erythroid differentiation, ANTXR1 silencing could induce a smaller volume of cord blood $CD34^{+}$ cells, and the cells with nuclear shift and shrinkage were significantly higher after Day 14 (Figure 5(d)). In addition, the apoptosis rate of shNC group (10.7%, 19.5%, and 36.3%) at days 11, 14, and 16 in cord blood $CD34^{+}$ cells was significantly lower than ANTXR1-sh5 group (23.8%, 40.8%, and 42.2%, respectively (Figure 5(e)). Thus, we speculate that ANTXR1 regulated the proliferation and differentiation of erythroid cells during erythroid induction.

3.4. ANTXR1 Regulates Erythroid Cell Differentiation through the Wnt/β-Catenin Pathway. Recent studies have shown that the Wnt signaling pathway induces blood cell maturation by regulating the hematopoietic microenvironment

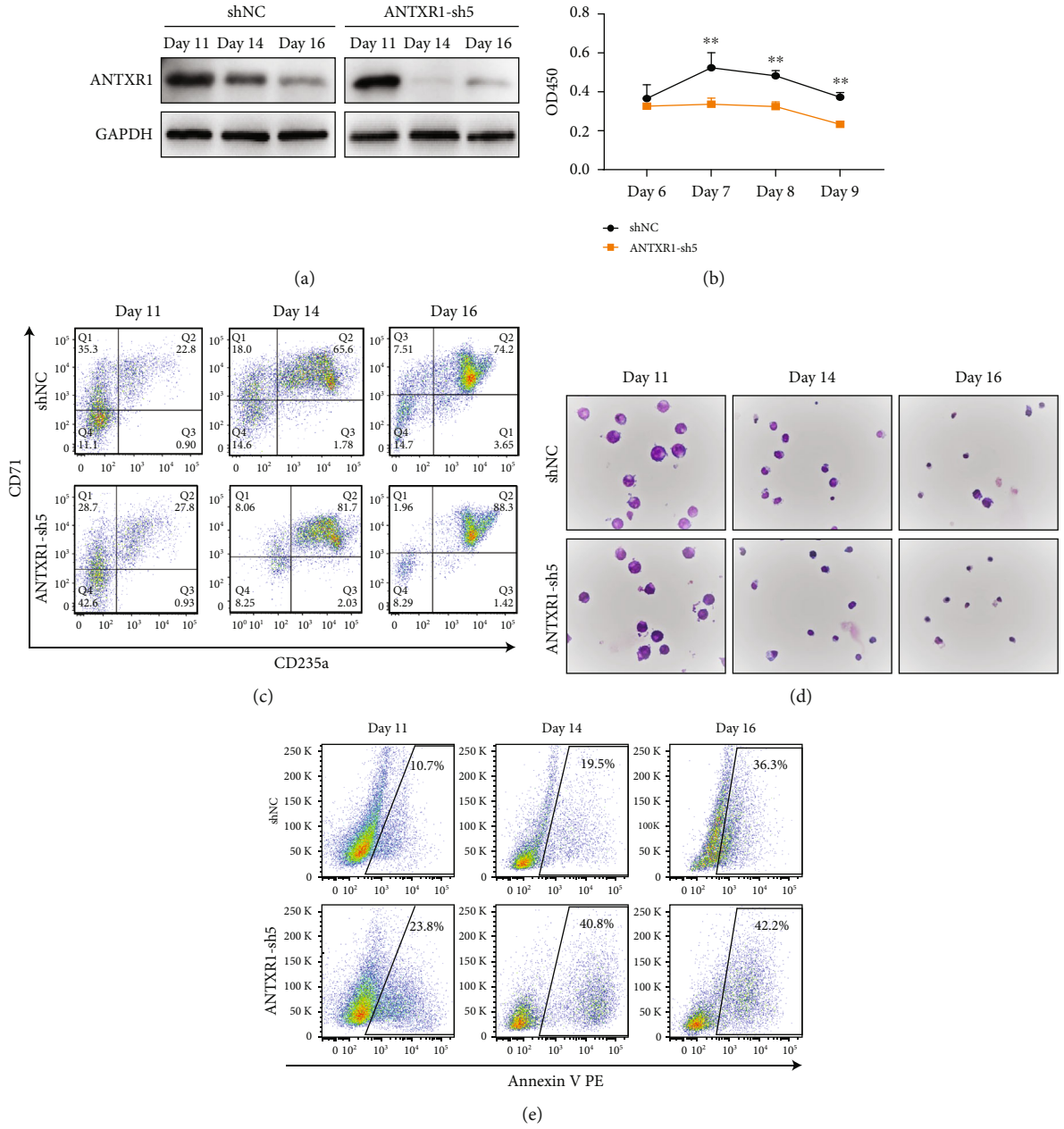

Figure 5: knockdown of ANTXR1 decreased erythroid cell proliferation and promoted erythroid cell differentiation and apoptosis in cord blood CD34$^+$ cells. (a) Western blot analysis was used to detect ANTXR1 levels after transfection of cord blood CD34$^+$ cells with *ANTXR1* interference vectors. (b) CCK8 assay of cord blood CD34$^+$ cells proliferation at D6, D7, D8, and D9. (c) Flow cytometry detection of CD71 and CD235a expression in cord blood CD34$^+$ cells during erythroid differentiation. (d) Wright-Giemsa staining results of cord blood CD34$^+$ cells. (e) Flow cytometry to detect the expression of apoptotic cells in the differentiation of cord blood CD34$^+$ cells. Error bars represent standard deviation of three independent experiments. $^*P < 0.05$, $^{**}P < 0.01$.

[17]. For instance, overexpression of Axin can block Wnt signaling and further inhibit HSCs proliferation in vitro [15]. Immunofluorescence results showed that ANTXR1 and Wnt upstream protein LRP6 were colocalized on the cell membrane of K562 cells in order to determine whether the Wnt signaling pathway is also involved in the regulation of erythroid differentiation by ANTXR1 (Figure 6(a)). Our previous research shows that ANTXR1 interacted with LRP6 to activate Wnt/β-catenin signaling pathway in K562 cell line, but whether this interaction is direct or indirect is still unclear. In this experiment, overexpression of *ANTXR1* upregulated the β-catenin expression but down-regulated the P-β-catenin and GS3β expressions. ANTXR1 knockdown reduced β-catenin expression but increased P-β-catenin and GS3β expressions as demonstrated by western blotting analysis (Figure 6(b)). The Wnt/β-catenin pathway may be involved in the ANTXR1 regulation of erythroid differentiation.

To further test and verify the mechanisms of ANTXR1 and Wnt/β-catenin in the regulation of erythroid differentiation, different concentrations of XAV939 (a chemical that

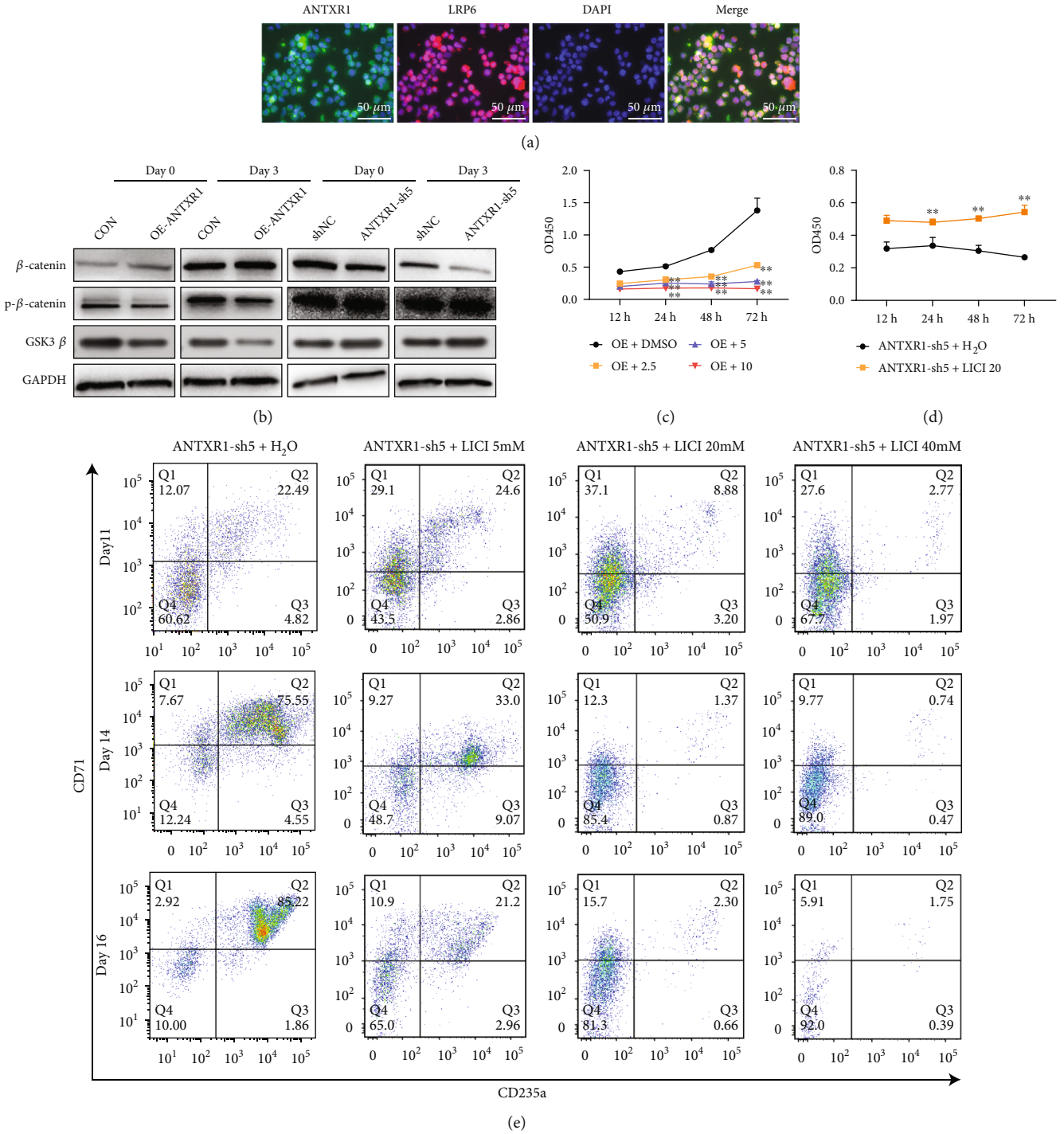

Figure 6: The Wnt/β-catenin signaling pathway cooperates with ANTXR1 in regulating erythroid cell differentiation. (a) The expression of ANTXR1 and LRP6 in K562 cells was detected by immunofluorescence with a confocal laser scanning microscope. ANTXR1 was labeled with 428 nm FITC, which represents green; LRP6 was labeled with Texas red; and nuclei were stained by DAPI to compare to the cell membrane. The merged images indicate the localization of ANTXR1 and LRP6 in the cell membrane, which the overlay of green and red give yellow. (b) The protein levels of β-catenin (92 kDa), P-β-catenin (85 kDa), and GS3β (46 kDa) were measured by western blotting after K562 cells were overexpressed or knocked down by ANTXR1. (c) Respectively, with K562 cells overexpressing ANTXR1 treated with 2.5, 5, and 10 μmol/L of XAV939 for 24 h. Cell proliferation was determined by CCK-8. (d) K562 cells knockdown ANTXR1 treated with 20 mM LiCl for 24 h, and cell proliferation was determined by CCK-8. (e) Cord blood $CD34^+$ cells knockdown ANTXR1 treated with 5, 20, and 40 mM LiCl for 24 h, respectively. Flow cytometry detection of CD71 and CD235a expression. Error bars represent standard deviation of three independent experiments. $^*P < 0.05$, $^{**}P < 0.01$.

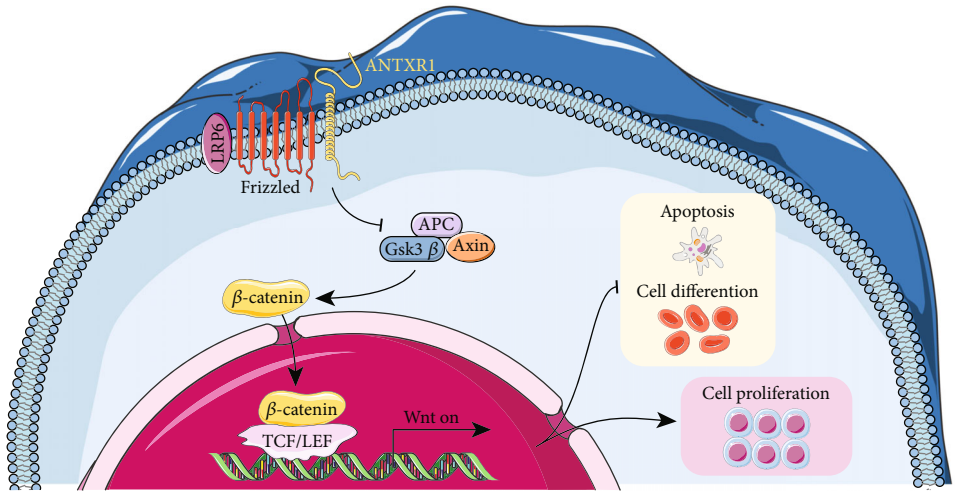

Figure 7: The hypothetical molecular mechanism of ANTXR1 affecting erythroid cell proliferation and differentiation through wnt/β-catenin signaling pathway.

inhibits the regulation of Wnt pathway transcription factor β-catenin) were firstly added to K562 cell line that stably overexpress ANTXR1. Different concentrations of LiCl (a special Wnt activator that functions by inhibiting the activity of GSK3β) were also analyzed. Compared to the DMSO control group, cell proliferation significantly decreased with increasing XAV939 concentration in K562 cells (Figure 6(c)). In contrast, the proliferation of cells in the ANTXR1-sh5 + LiCl20 group was significantly increased compared with the control group (Figure 6(d)). We used flow cytometry to investigate further the Wnt/β-catenin pathway in the erythroid differentiation of hematopoietic stem cells. After interfering with ANTXR1 in cord blood $CD34^+$ cells and adding various LiCl concentrations, the double positivity of CD71 and CD235a decreased with the increasing LiCl dose, showing a dose-effect relationship (Figure 6(e)). Taken together, these observations confirmed that Wnt/β-catenin has a role in the regulation of ANTXR1 on erythroid differentiation, proliferation, and differentiation. The specific regulation mechanism needs to be further studied.

4. Discussion

The hematopoietic microenvironment is mainly regulated by various cytokines. Hematopoietic cells with disrupted gene expression exhibit a state known as "stressed hematopoiesis," which causes abnormal hematopoietic cell proliferation due to the increased cellular oxidative stress level and early erythrocyte apoptosis [18–20]. Transplantation of hematopoietic stem cells is the primary treatment for many blood diseases, but it is frequently difficult to obtain sufficient HSCs and transplantable donors for this procedure. In addition, an inefficient hematopoietic reconstruction system is still a fundamental cause of hematopoietic engraftment failure [21, 22]. Our study provides theoretical bases for improving effective erythroid expansion by exploring mechanism that membrane protein ANTXR1 regulates the proliferation and differentiation of erythroid cells through wnt/β-catenin signaling pathway for the first time.

ANTXR1 was initially found in tumor vascular endothelial cells and promote tumor vascular endothelial formation [23]. ANTXR1 gene mutation can also cause growth retardation, alopecia, pseudo-anodontia, and GAPO syndrome (GAPOS) [24, 25]. ANTXR1 plays an important role in chondrocyte proliferation, and its overexpression causes chondrocyte apoptosis and matrix mineralization [8]. In addition, ANTXR1 inhibition has been reported to reduce esophageal tumor cell proliferation, block the G0/G1 phase, and promote cell apoptosis [26].

Our findings showed that ANTXR1 overexpression promoted K562 cell proliferation, decreased the erythrocyte transcription factors GATA1 and ALAS2 expressions, and delayed the differentiation and apoptosis of the erythroid cell. On the other hand, ANTXR1 knockdown inhibited the erythroid cells proliferation, promoted the GATA1 and ALAS2 expressions, and inhibited the erythroid cell apoptosis. GATA1 is expressed in the erythroid, and its DNA binding region can recognize the specific gene regulatory region of erythrocytes, which is an essential regulatory factor for erythroid development [27, 28]. ALAS2 is the key enzyme for heme synthesis, which can promote hematopoietic cell differentiation by increasing hemoglobin synthesis [29]. Therefore, we speculated that ANTXR1 was involved in regulating erythroid differentiation. This indicates that ANTXR1 may be a new factor that affects the proliferation and differentiation of erythroid cells.

The Wnt/β-catenin pathway plays a role in cell proliferation and cycle changes and the maintenance and differentiation of stem cell self-renewal [30]. A large amount of unphosphorylated catenin will be present in the cytoplasm when the Wnt pathway is activated. Upon entering the nucleus, β-catenin binds to transcription factor (TCF) protein and acts as a co-activator of TCF to stimulate transcription of Wnt target genes. Our previous research

found that there was an interaction between ANTXR1 and LRP6, the colocalization of ANTXR1 and LRP6 in cell membrane indicated that ANTXR1 regulates erythroid proliferation and differentiation is probably through interacting with the membrane protein LRP6 and activating the Wnt/β-catenin signaling pathway [31]. However, it is not clear whether ANTXR1 involved in regulating erythroid proliferation and differentiation by interacting with LRP6. It has been shown that overexpression of Axin to block Wnt signaling can inhibit HSCs proliferation in vitro [16]. The transduction of β-catenin into HSCs of transgenic Bcl-2 mice resulted in increased HSCs phenotype during in vitro culture [32]. Overexpression of Wnt inhibitory factors in bone marrow stromal cells or/and osteoblasts can break the quiescent state of HSCs, resulting in impaired HSCs self-renewal and reduced hematopoietic reconstitution in vivo [15, 33, 34]. Activating β-catenin signaling with GSK3β inhibitors can improve the HSCs expansion in vitro and promote the hematopoietic reconstitution ability of HSCs in vivo [35–37].

Our study shows that ANTXR1 activates the Wnt/β-catenin signaling pathway and promotes the proliferation of erythroid cells through inhibit GATA1 and ALAS2 transcription. In contrast, ANTXR1 knockdown reduced the β-catenin expression, and Wnt/β-catenin signaling was also inhibited, GATA1 and ALAS2 expressions were increased and promote erythroid differentiation. It has therefore been proposed that ANTXR1 may affect the proliferation and differentiation of erythroid cells through the Wnt/β-catenin signaling pathway.

Recent studies have found that the Wnt signaling pathway strengthens the differential effect on HSCs self-renewal [38]. The Wnt/β-catenin signaling pathway may affect the proliferation and differentiation of hematopoietic stem cells in a dose-response-dependent manner at different levels. Two times the normal level of Wnt pathway activity promotes HSCs proliferation, and more than four times the Wnt pathway activity impairs HSCs self-renewal and proliferation. In this study, overexpression of ANTXR1 increased the activity of Wnt pathway and increased the proliferation of HSCs cells. We speculate that the activity of Wnt pathway may be at a normal low level. Further studies are needed to determine the effect of Wnt pathway activation induced by different expression levels of ANTXR1 on erythrocyte proliferation and differentiation. In addition, STRING database shows that the downstream transcription factor JUN of the Wnt/β-catenin pathway interacts with GATA1. As an important protein of the Wnt pathway, Wnt1 and JUN may also interact (https://cn.string-db.org/cgi/network?taskId=bjU1mtYXnzEc&sessionId=bw0iWzp61fNp). Our previous research showed that ANTXR1 regulates γ-globin expression is mainly activating the Wnt/β-catenin signaling pathway, which initiates the expression of the downstream transcription factor c-Jun. Erythrocyte differentiation and development are accompanied by globin production. Therefore, this study suggests that GATA1/ALAS2, an important transcription factor for hematopoiesis and erythrocyte differentiation, may also interact with the c-Jun gene in Wnt/β-catenin to regulate erythrocyte proliferation and differentiation [39, 40]. However, further investigation is needed to determine whether ANTXR1 interacts with Wnt1. The use of gene expression profiles in peripheral blood for the diagnosis of autoimmune diseases, leukemia, and other genetic disorders is becoming increasingly common in clinical settings. The participation of all hematopoietic cells in the hematopoietic system, whether directly or indirectly, is highly dependent on the stage of hematopoietic development.

In summary, ANTXR1 may play essential roles in regulating the HSCs microenvironment through Wnt signaling pathway (Figure 7) that may indirectly trigger Axin1, DKK1, and Wif1 [41–43]. It requires further understanding of ANTXR1 in regulating hematopoiesis in a gene network. In conclusion, due to the complex mechanism of Wnt pathway regulation of HSCs self-renewal and maintenance, ANTXR1 modulates erythroid cell proliferation and differentiation, but many unknowns are still to be revealed. The findings of this research might provide a novel approach for treating blood disorders and improve the proliferation of hematopoietic stem cells.

Abbreviations

EF: Edema factor
LF: Lethal factor
ANTXR1: Anthrax toxin receptor 1
HSCs: Hematopoietic stem cells
MEPs: Megakaryocytic erythroid progenitors
CMPs: Common myeloid progenitor cells
BFU-E: Erythroid blast-forming units
CFU-E: Erythroid colony-forming units
KLF1: Krüppel-like factor 1
SNP: Single-nucleotide polymorphism
CB: Cord blood
HbF: Fetal hemoglobin
FBS: Fetal bovine serum
HUDEP-2: Human umbilical cord blood-derived erythroid progenitor-2
GATA1: GATA-binding factor 1 or GATA-1 (also termed erythroid transcription factor)
ALAS2: 5'-Aminolevulinate synthase 2
GAPOS: GAPO syndrome
TCF: Transcription factor
shRNA: Short hair RNA.

Data Availability

The data used to support the findings of this study are included within the article.

Ethical Approval

The study was approved by the Institutional Review Board of the Ethics Committee of Guizhou Provincial People's Hospital. All methods were carried out in accordance with Declaration of Helsinki guidelines and regulations.

Consent

Written informed consent was obtained from the patients for publication of this study. Documentation of the written consent will be provided to the journal upon request.

Conflicts of Interest

The authors declare no competing financial interests.

Authors' Contributions

T.T.J. performed experiments, analyzed data, and wrote the manuscript; Z.J.Z. designed researched, collected, and analyzed the data; Y.Y.H., J.L., and D.L. performed partial experiments; R.K. and Y.N. provided HUDEP-2 cell line; M.M.J and F.F.H. partially analyzed data and constructed figures and tables; Z.L.S. and X.D.F. coordinated the study and revised manuscript drafts; S.W.H. paned and conceived the project.

Acknowledgments

We thank all laboratory staff of the Genomics Science and Information Laboratory, the Chinese Academy of Sciences, and the Central Laboratory of Guizhou Provincial People's Hospital for their assistance in this study. This work was supported by the National Natural Science Foundation of China [grant number 81960040] and the Guizhou Provincial Science and Technology Projects [grant numbers 20165670, 20205011, Gzwjkj2020-1-171, and ZK2021493].

References

[1] R. G. Hawley, A. Ramezani, and T. S. Hawley, "Hematopoietic stem cells," *Methods Enzymol*, vol. 419, pp. 149–179, 2006.

[2] E. O. Wakefield, A. Pantaleao, J. M. Popp et al., "Describing perceived racial bias among youth with sickle cell disease," *Journal of Pediatric Psychology*, vol. 43, no. 7, pp. 779–788, 2018.

[3] N. Hussein, S. Weng, J. Kai, and N. Qureshi, "Preconception risk assessment for thalassaemia, sickle cell disease, cystic fibrosis and Tay-Sachs disease," *Cochrane Database Systematic Reveviews*, vol. 2021, no. 10, article CD010849, 2015.

[4] J. J. Fernández, D. R. C. García, I. Fernández-Urién et al., "Mediterranean lymphoma, an uncommon case of iron-deficiency anemia," *Acta gastro-enterologica Belgica*, vol. 80, no. 2, pp. 337–339, 2017.

[5] M. Y. Gao and Y. Z. Zheng, "Research progress on transcriptional regulation mechanism of erythropoiesis," *International Journal of blood transfusion and hematology*, vol. 43, no. 5, pp. 457–460, 2020.

[6] A. Nanda, E. B. Carsonwalter, and S. Seaman, "TEM8 interacts with the cleaved C5 domain of collagen alpha 3(VI)," *Cancer Research*, vol. 64, no. 3, p. 817, 2004.

[7] E. A. Werner, P. Kowalczyk, and V. Faundez, "Anthrax toxin receptor 1/tumor endothelium marker 8 mediates cell spreading by coupling extracellular ligands to the actin cytoskeleton," *Journal of Biological Chemistry*, vol. 281, no. 32, pp. 23227–23236, 2006.

[8] Q. Jiang, X. Qin, C. A. Yoshida et al., "Antxr1, which is a target of Runx2, regulates chondrocyte proliferation and apoptosis," *International Journal of Molecular Sciences*, vol. 21, no. 7, p. 2425, 2020.

[9] A. Chaudhary, M. B. Hilton, S. Seaman et al., "TEM8/ANTXR1 blockade inhibits pathological angiogenesis and potentiates tumoricidal responses against multiple cancer types," *Cancer Cell*, vol. 21, no. 2, pp. 212–226, 2012.

[10] V. Vathipadiekal, J. J. Farrell, S. Wang et al., "A candidate transacting modulator of fetal hemoglobin gene expression in the Arab-Indian haplotype of sickle cell anemia," *American Journal of Hematology*, vol. 91, no. 11, pp. 1118–1122, 2016.

[11] Z. A. Al-Ali, R. K. Fallatah, E. A. Aljaffer et al., "ANTXR1 intronic variants are associated with fetal hemoglobin in the Arab Indian haplotype of sickle cell disease," *Acta Haematol*, vol. 140, no. 1, pp. 55–59, 2018.

[12] Z. Xu, A. M. Robitaille, and J. D. Berndt, "Wnt/β-catenin signaling promotes self-renewal and inhibits the primed state transition in naïve human embryonic stem cells," *Proceedings of the National Academy of Sciences*, vol. 113, no. 42, pp. E6382–E6390, 2016.

[13] C. Zhao, J. Blum, A. Chen et al., "Loss of beta-catenin impairs the renewal of normal and CML stem cells in vivo," *Cancer Cell*, vol. 12, no. 6, pp. 528–541, 2007.

[14] H. E. Fleming, V. Janzen, C. L. Celso et al., "Wnt signaling in the niche enforces hematopoietic stem cell quiescence and is necessary to preserve self-renewal in vivo," *Cell Stem Cell*, vol. 2, no. 3, pp. 274–283, 2008.

[15] C. Schaniel, D. Sirabella, J. Qiu, X. Niu, I. R. Lemischka, and K. A. Moore, "Wnt-inhibitory factor 1 dysregulation of the bone marrow niche exhausts hematopoietic stem cells," *Blood*, vol. 118, no. 9, p. 2420, 2011.

[16] T. Reya, A. W. Duncan, L. Ailles et al., "A role for Wnt signalling in self-renewal of haematopoietic stem cells," *Nature*, vol. 423, no. 6938, pp. 409–414, 2003.

[17] S. Hotra and P. W. Kincade, "Wnt-related molecules and signal pathway equilibrium in hematopoiesis," *Cell Stem Cell*, vol. 4, no. 1, pp. 27–36, 2009.

[18] X. Tian, F. Cong, H. Guo, J. Fan, G. Chao, and T. Song, "Downregulation of Bach1 protects osteoblasts against hydrogen peroxide-induced oxidative damage in vitro by enhancing the activation of Nrf2/ARE signaling," *Chemico-Biological Interactions*, vol. 309, article 108706, 2019.

[19] Y. Cao, Y. Fang, J. Cai et al., "ROS functions as an upstream trigger for autophagy to drive hematopoietic stem cell differentiation," *Hematology*, vol. 21, no. 10, pp. 613–618, 2016.

[20] A. T. Taher, D. J. Weatherall, and M. D. Cappellini, "Thalassaemia," *Lancet*, vol. 391, no. 10116, pp. 155–167, 2018.

[21] R. Seggewiss and H. Einsele, "Immune reconstitution after allogeneic transplantation and expanding options for immunomodulation: an update," *Blood*, vol. 115, no. 19, pp. 3861–3868, 2010.

[22] N. Pineault and L. Boyer, "Cellular-based therapies to prevent or reduce thrombocytopenia," *Transfusion*, vol. 51, no. 4, article 72s81s, 2011.

[23] T. Y. Besschetnova, T. Ichimura, N. Katebi, B. S. Croix, J. V. Bonventre, and B. R. Olsen, "Regulatory mechanisms of anthrax toxin receptor 1-dependent vascular and connective tissue homeostasis," *Matrix Biology*, vol. 42, pp. 56–73, 2015.

[24] Y. Bayram, D. Pehlivan, E. Karaca et al., "Whole exome sequencing identifies three novel mutations in ANTXR1 in

families with GAPO syndromeAmerican journal of medical genetics Part A," vol. 164A, no. 9, pp. 2328–2334, 2014.

[25] D. Chen, P. Bhat-Nakshatri, C. Goswami, S. Badve, and H. Nakshatri, "ANTXR1, a stem cell-enriched functional biomarker, connects collagen signaling to cancer stem-like cells and metastasis in breast cancer," *Cancer Research*, vol. 73, no. 18, pp. 5821–5833, 2013.

[26] Y. Ren, W. He, M. L. Qi, X. W. Chen, L. W. Liang, and J. M. Feng, "Effect of silencing antxr1 gene by RNA interference on proliferation and apoptosis of esophageal cancer Eca109 cells," *South China Journal of National Defense Medicine*, vol. 30, no. 12, pp. 761–765, 2016.

[27] C. Y. Luo and J. W. Wang, "GATA-1 and erythropoiesis," *International Journal of Internal Medicine*, vol. 35, no. 6, pp. 360–363, 2008.

[28] L. Gutiérrez, T. Nikolic, T. B. van Dijk et al., "Gata l regulates dendritic-cell development and survival," *Blood*, vol. 110, no. 6, pp. 1933–1941, 2007.

[29] S. Rio, M. Gastou, N. Karboul et al., "Regulation of globin-heme balance in diamond-Blackfan anemia by HSP70/GATA1," *Blood*, vol. 133, no. 12, pp. 1358–1370, 2019.

[30] J. R. Miller, "The Wnts," *Genome Biology*, vol. 3, 2002.

[31] F. Haack, T. Köster, and A. M. Uhrmacher, "Receptor/raft ratio is a determinant for LRP6 phosphorylation and WNT/β-catenin signaling," *Frontiers in Cell and Developmental Biology*, vol. 9, article 706731, 2021.

[32] M. Ming, S. Wang, W. Wu et al., "Activation of Wnt/β-catenin protein signaling induces mitochondria-mediated apoptosis in hematopoietic progenitor cells," *Journal of biological chemistry*, vol. 287, no. 27, pp. 22683–22690, 2012.

[33] M. J. Nemeth and D. M. Bodine, "Regulation of hematopoiesis and the hematopoietic stem cell niche by Wnt signaling pathways," *Cell Research*, vol. 17, no. 9, pp. 746–758, 2007.

[34] L. Gattinoni, X. S. Zhong, D. C. Palmer et al., "Wnt signaling arrests effector T cell differentiation and generates $CD8^+$ memory stem cells," *Nature Medicine*, vol. 15, no. 7, pp. 808–813, 2009.

[35] J. J. Trowbridge, A. Xenocostas, R. T. Moon, and M. Bhatia, "Glycogen synthase kinase-3 is an in vivo regulator of hematopoietic stem cell repopulation," *Nature Medcine*, vol. 12, no. 1, pp. 89–98, 2006.

[36] K. H. Ko, T. Holmes, P. Palladinetti et al., "GSK-3beta inhibition promotes engraftment of ex vivo-expanded hematopoietic stem cells and modulates gene expression," *Stem Cells*, vol. 29, no. 1, pp. 108–118, 2011.

[37] J. Huang, M. Nguyen-McCarty, E. O. Hexner, G. Danet-Desnoyers, and P. S. Klein, "Maintenance of hematopoietic stem cells through regulation of Wnt and mTOR pathways," *Nature Medicine*, vol. 18, no. 12, pp. 1778–1785, 2012.

[38] T. C. Luis, B. A. Naber, P. P. Roozen et al., "Canonical wnt signaling regulates hematopoiesis in a dosage-dependent fashion," *Cell Stem Cell*, vol. 9, no. 4, pp. 345–356, 2011.

[39] R. Dan and T. G. O'Brien, "AP-1 activity affects the levels of induced erythroid and megakaryocytic differentiation of K562 cells. Archives of Biochemistry & Biophysics," *Archives of Biochemistry & Biophysics*, vol. 352, no. 2, pp. 298–305, 1998.

[40] K. E. Elagib, M. Xiao, I. M. Hussaini et al., "Jun blockade of erythropoiesis: role for repression of GATA-1 by HERP2," *Molecular & Cellular Biology*, vol. 24, no. 17, pp. 7779–7794, 2004.

[41] W. Goessling, T. E. North, S. Loewer et al., "Genetic interaction of PGE2 and Wnt signaling regulates developmental specification of stem cells and regeneration," *Cell*, vol. 136, no. 6, pp. 1136–1147, 2009.

[42] M. C. Nostro, X. Cheng, G. M. Keller, and P. Gadue, "Wnt, activin, and BMP signaling regulate distinct stages in the developmental pathway from embryonic stem cells to Blood," *Cell Stem Cell*, vol. 2, no. 1, pp. 60–71, 2008.

[43] S. Singbrant, G. Karlsson, M. Ehinger et al., "Canonical BMP signaling is dispensable for hematopoietic stem cell function in both adult and fetal liver hematopoiesis, but essential to preserve colon architecture," *Blood, The Journal of the American Society of Hematology*, vol. 115, no. 23, pp. 4689–4698, 2010.

Hindawi
Disease Markers
Volume 2022, Article ID 5638675, 13 pages
https://doi.org/10.1155/2022/5638675

Research Article

Prognostic Significance of CCDC137 Expression and Its Association with Immune Infiltration in Hepatocellular Carcinoma

Lu Bai,[1] Zhao-Xu Yang,[2] Jian-Shan Liu,[2] De-Sheng Wang ,[2] and Heng-Chao Yu [2]

[1]*Department of Clinical Laboratory, Xijing Hospital, Air Force Military Medical University, Xian, China*
[2]*Department of Hepatobiliary Surgery, Xijing Hospital, Air Force Military Medical University, Xian, China*

Correspondence should be addressed to De-Sheng Wang; wangdesh@163.com and Heng-Chao Yu; yuhech1982@163.com

Received 1 July 2022; Revised 8 August 2022; Accepted 11 August 2022; Published 24 August 2022

Academic Editor: Fu Wang

Globally, hepatocellular carcinoma (HCC) is one of the most common causes of cancer-associated mortalities. The clinical outcome of HCC patients remains poor due to distant metastasis and recurrence. In recent years, growing evidences have confirmed that the coiled-coil domain-containing (CCDC) family proteins are involved in the progression of several diseases. However, the expression and clinical significance of the coiled-coil domain-containing 137 (CCDC137) in hepatocellular carcinoma (HCC) have not been investigated. Level 3 mRNA expression profiles and clinicopathological data were obtained in TCGA-LIHC. Differentially expressed genes (DEGs) were screened between 371 HCC and 50 nontumor specimens. The prognostic value of CCDC137 was analyzed in HCC patients. The correlations between CCDC137 and cancer immune infiltrates were investigated. In this study, a total of 2897 DEGs were obtained: 2451 genes were significantly upregulated and 446 genes were significantly downregulated. KEGG assays revealed that these DEGs were involved in tumor progression. Among 2897 DEGs, we found that CCDC137 expression was distinctly increased in HCC specimens compared with nontumor specimens. A high level of CCDC137 expression was related to an advanced tumor stage and grade. Moreover, patients with higher levels of CCDC137 expression had a shorter overall survival and disease-free survival than patients with lower CCDC137 levels. CCDC137 expression was positively correlated with infiltrating levels of several immune cells, such as CD8 T cells and Th2 cells. Finally, in vitro experiments confirmed that CCDC137 expression was highly expressed in HCC cells, and its knockdown suppressed the proliferation of HCC cells. Taken together, our findings revealed that CCDC137 might be used as a biomarker for immune infiltration and poor prognosis in HCC, which offered fresh insight on potential therapies for HCC.

1. Introduction

Hepatocellular carcinoma (HCC) is one of the leading causes of cancer-related death worldwide [1]. According to the Global Cancer Statistics, for the year 2020, there were around 906,000 newly diagnosed instances of liver cancer and approximately 830,000 deaths caused by liver cancer worldwide that year [2]. Although the majority of HCC develop in individuals who have a history of established hepatic conditions, there are a number of risk factors that are known to promote the development and progression of HCC [3, 4]. Some of these risk factors include aflatoxin B, excessive use of tobacco and alcohol, prolonged infection with hepatitis B or C virus (HBV or HCV), and exposure to iron overload [5, 6]. At the moment, surgical removal of the tumor is the recommended course of treatment for head and neck cancer caused by HCC. Despite this, the recurrence rate of HCC is still quite high, and the survival rate at five years is often less than fifty percent [7]. Therefore, it is of the utmost importance that the pathogenesis of HCC should be investigated in order to search for useful diagnostic markers and treatment targets in HCC patients.

Characterizing prognostic factors in patients with HCC has benefited greatly from the use of transcriptome profiling, which has resulted in the generation of a number of prospective biomarkers with the potential to have clinical use [8].

However, there is a lack of consistency among different studies and the indicated signatures only provide limited predictive information. This is partially due to the small sample size and the technical variables that were used [9, 10]. An increasing number of studies, made possible by developments in gene chips and high-throughput sequencing, have demonstrated that the dysregulated mRNAs have a significant amount of potential to predict HCC prognosis [11, 12]. In addition, even though the genetic and epigenetic alterations that occur in tumor cells are essential to the progression of tumors, there is an increasing body of evidence indicating that the interaction between tumor cells and the normal cells that surround them also plays an important role in both of these processes. A complex network made up of extracellular matrix, inflammatory cells, endothelial cells, fibroblast cells, mesenchymal stem cells, and tumor cells is referred to as the tumor microenvironment (TME) [13, 14]. Over the course of the past several years, an increasing number of researches have concentrated on locating novel prognostic biomarkers implicated in the microenvironment of HCC [15]. For instance, it has been reported that CD96 showed varied levels of expression in the majority of cancerous and neighboring normal tissues. CD96 had a major impact on the prognosis of several different malignancies. Because CD96 is involved in a wide variety of immune responses, is responsible for immune cell infiltration, and influences the malignant properties of different cancers, it is a candidate for use as a biomarker in determining patient prognosis and immune infiltration in a number of different cancers [16, 17].

In this study, we screened a novel HCC-associated gene CCDC137 which was rarely reported in previous studies. First, we presented data that CCDC137 was substantially expressed in HCC and that its upregulation was predictive of a poor prognosis for individuals with HCC. Moreover, we analyzed its association with immune Infiltration. For the purposes of this investigation, all of the data came from publicly available sources, and the analyses were carried out using Webtools and the R programming language. Our findings suggested CCDC137 as a novel biomarker for HCC patients.

2. Materials and Methods

2.1. Cell Lines and Cell Transfection. iCell (Xuhui, Shanghai, China) was the supplier of both the HCC Cells (MHCC97H, HepG2, HCCLM3, Hep3B, and SMMC-7721) and the LO2 cells which served as the control cells. RPMI-1640 served as the medium for their cultivation (with 10 percent fetal bovine serum). The cell culture condition was 37°C and 5% CO_2. The small interfering RNAs (siRNAs) (siRNA-control and siRNA-CCDC137) were obtained from JiMa Biological Corporation (Shanghai, Pudong, China). Lipofectamine 2000 reagent kits, manufactured by Guanghua Biotech in Changsha, Hunan Province, China, were utilized in the cell transfection process. The procedure followed the guidelines included with the reagent kits.

2.2. Quantitative Real-Time PCR. The TRIzol reagents (Invitrogen, Carlsbad, CA, USA) were utilized in order to get the total RNA. cDNA was produced from the isolated RNA by employing the PrimeScript RT Reagent Kit (Takara, Japan) in the process of reverse transcription. Next, synthesized cDNA was subjected to RT-qPCR using the Fast SYBR Green PCR Kit (Applied Biosystems, Foster City, CA, USA) on an ABI PRISM 7300 instrument (Applied Biosystems). $2^{-\Delta\Delta Ct}$ method was utilized in order to calculate the fold changes in target genes. The primer sequences were presented as follows: CCDC137 5′-ACGGGGCCTATATCCA CCG-3′ (forward) and 5′-CGTCGGACTTTATCTAGTC GCC-3′ (reverse); GAPDH 5′-GGAGCGAGATCCCTCC AAAAT-3′ and 5′-GGCTGTTGTCATACTTCTCATGG-3′.

2.3. CCK-8 Assay. Transfected HCCLM3 and MHCC97H cells were seeded at a density of 2×10^3 cells per well in 96-well plates, and the plates were then incubated with RPMI-1640 media for 24, 48, 72, or 96 hours, depending on the experiment. After that, all of the cells were allowed to remain in an environment containing 10 μL of CCK-8 reagents for a period of four hours. After discarding the medium, dimethyl sulfoxide was included in the experiment. After 10 minutes of shaking, a Microplate Absorbance Reader was used to measure the color reaction at 450 nm.

3. Data Source

The mRNA expression patterns and the related clinical information from the patients with HCC were gathered from TCGA. This was calculated on an Illumina HiSeq RNA-seq platform, and as of March 5, 2022, the platform had 371 HCC tissues and 50 nontumorous liver tissues. Because the data from TCGA are openly and freely accessible to the public, the local ethics committees were not required to give their approval for the study.

3.1. Identification of DEGs between HCC and Noncancerous Tissues. The limma R package was utilized in the determination of the DEG. DEGs that had an absolute log2 fold change (FC) of more than two and an adjusted p value of less than 0.05 were determined to be eligible for further investigation.

3.2. Gene Ontology (GO) and Kyoto Encyclopedia of Genes and Genomes (KEGG) Pathway Enrichment Analysis of DEGs. The software package "clusterProfiler" of R was used to execute GO and KEGG results for visualization of the diverse genes shared by the two distinct groups of high-risk patients, and the appropriate graphs were generated afterward.

4. Gene Expression Profiling Interactive Analysis (GEPIA)

Further confirmation of the strongly linked genes was accomplished through the use of the internet database GEPIA (http://gepia.cancer-pku.cn/index.html). GEPIA is an interactive online database that consists of 9,736 tumor samples and 8,587 normal samples from TCGA and the GTEx projects. These projects analyze the RNA sequencing expression of the samples. In 33 distinct forms of cancer,

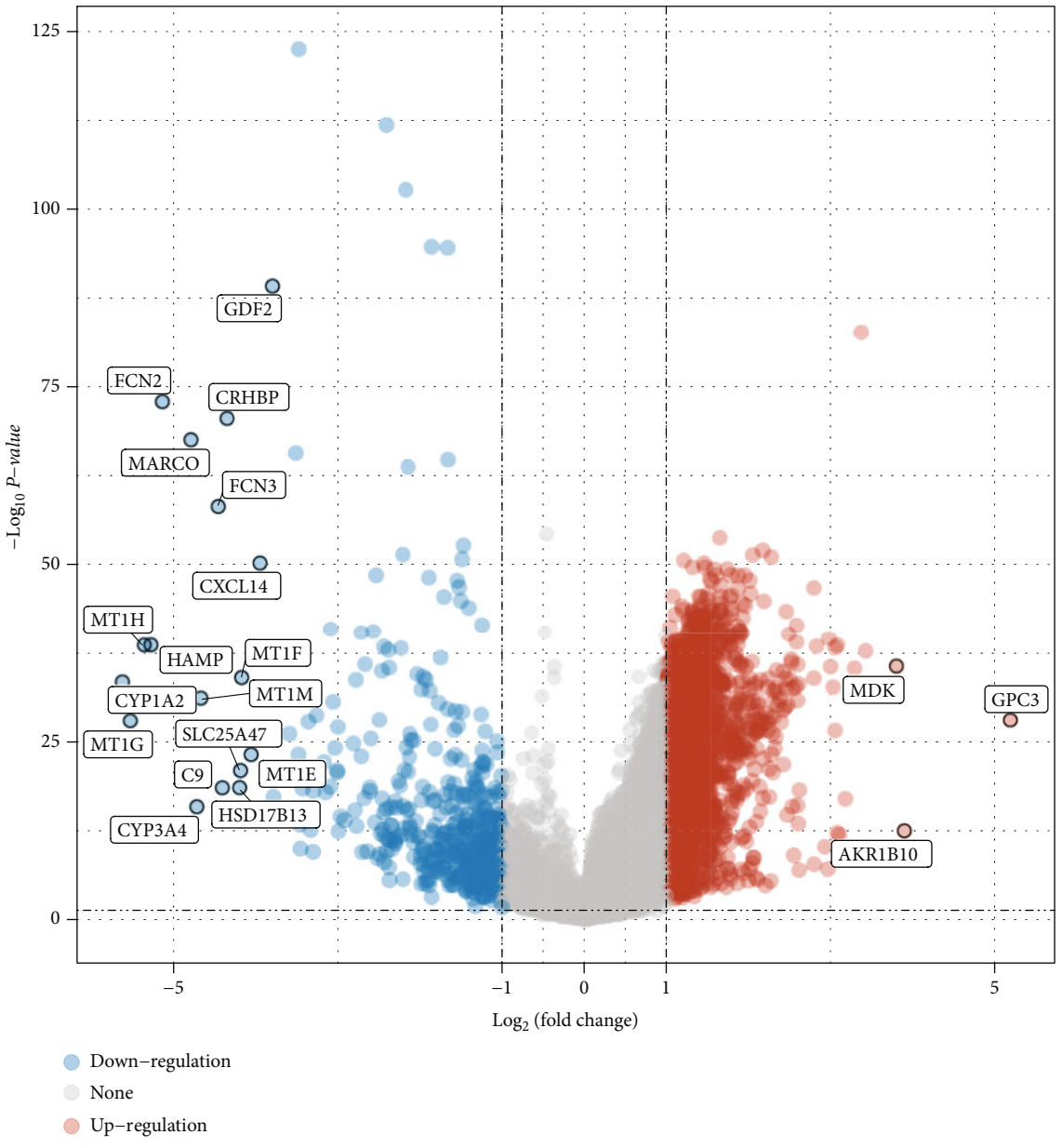

(a)

Figure 1: Continued.

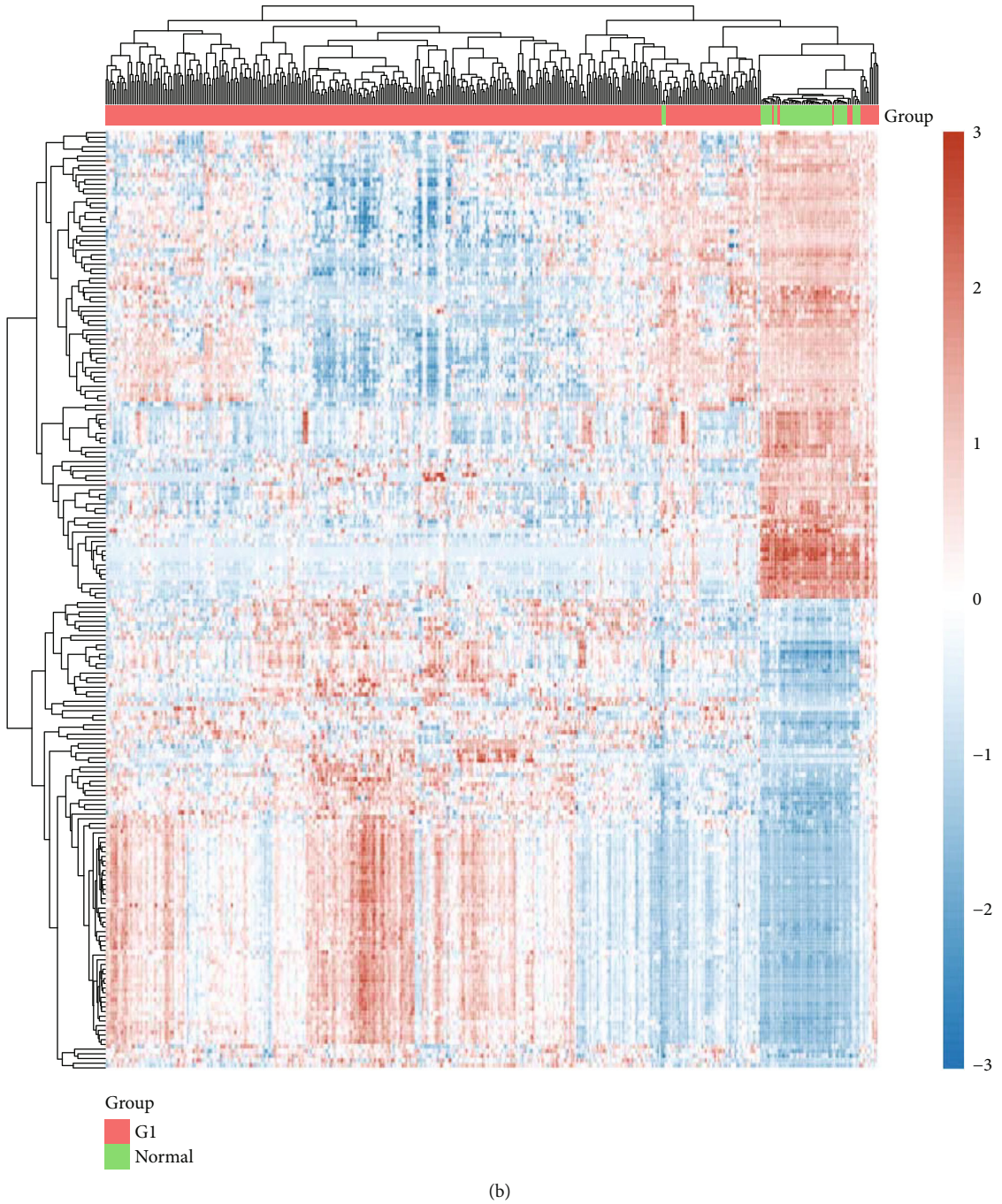

(b)

Figure 1: Differentially expressed genes between HCC specimens and nontumor specimens using (a) volcano map and (b) heat map based on TCGA datasets.

the log-rank test and the Mantel-Cox test were used in conjunction with GEPIA to develop survival curves. These survival curves were based on gene expression and included overall survival and disease-free survival.

4.1. Immune Infiltration Analysis. We determined the degree of infiltration of 28 different immune cell types by using the single-sample gene set enrichment analysis (ssGSEA) method from the GSVA R package. Our calculations were based on the expression levels of genes found in 28 different published gene sets that are associated with immune cells.

4.2. Statistical Analysis. All statistical analyses were conducted by R (4.0.2). The significance of CCDC137 in HCC specimens and nontumor tissues was assessed by the paired Wilcoxon test. Survival curves were plotted by the Kaplan-Meier method, and the log-rank test evaluated the significance. All hypothetical tests were two-sided, and a p value < 0.05 was considered significant.

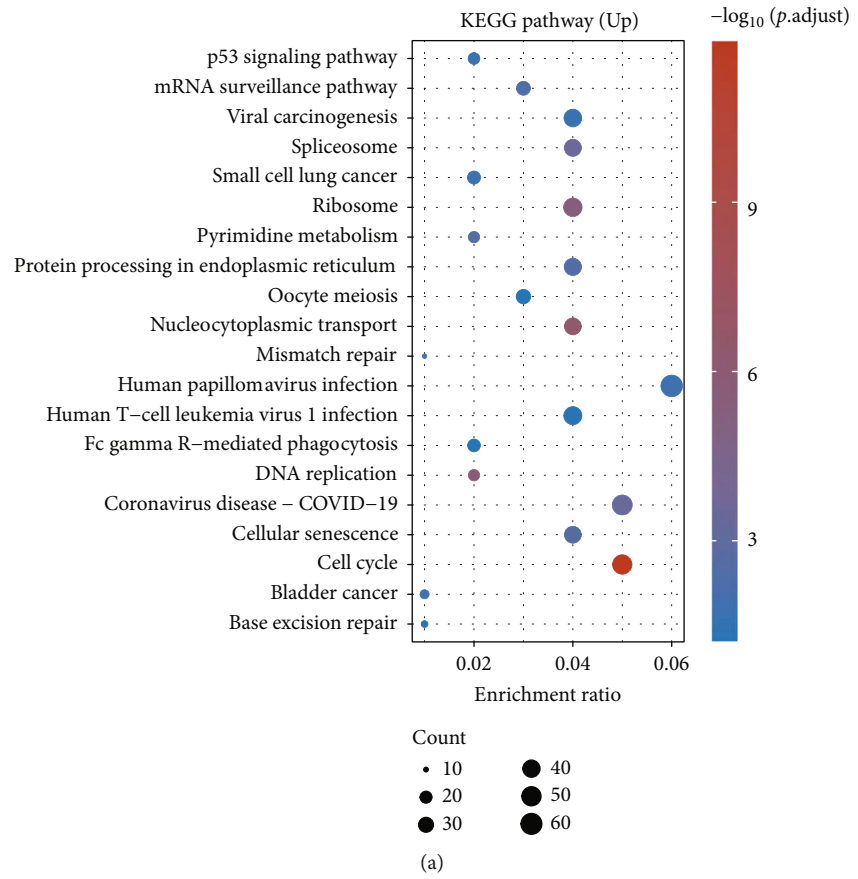

(a)

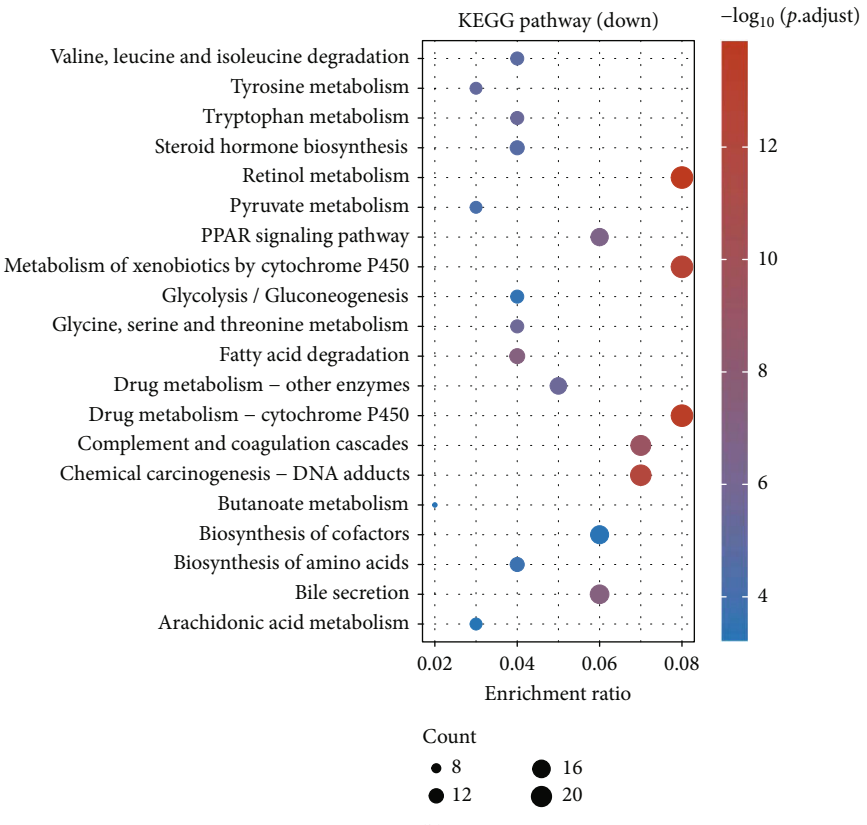

(b)

Figure 2: Continued.

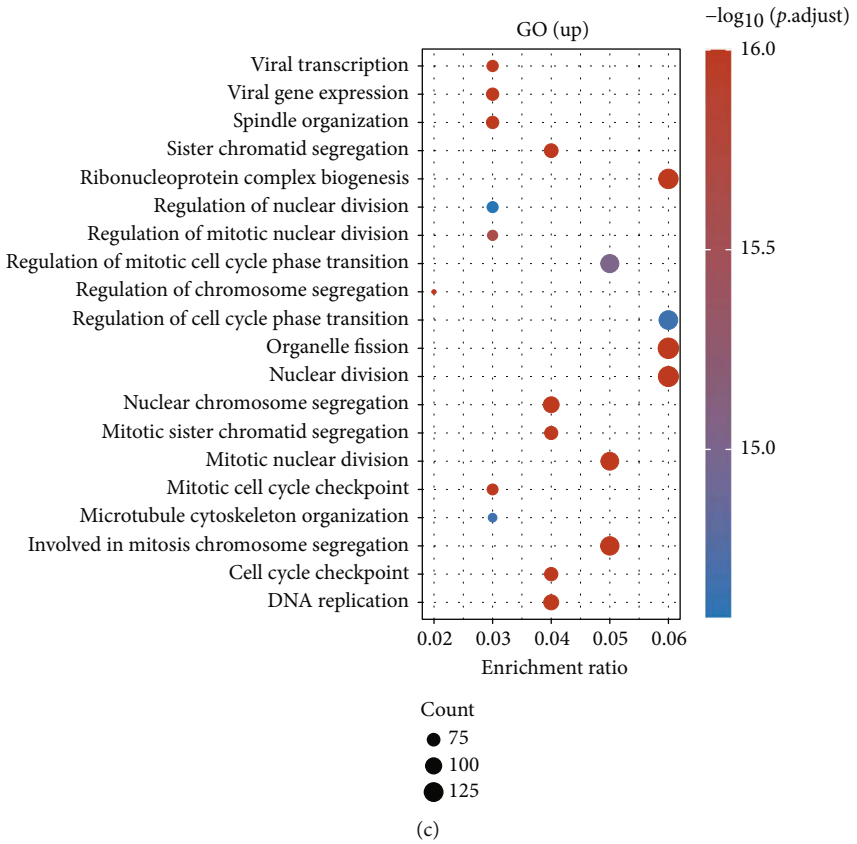

(c)

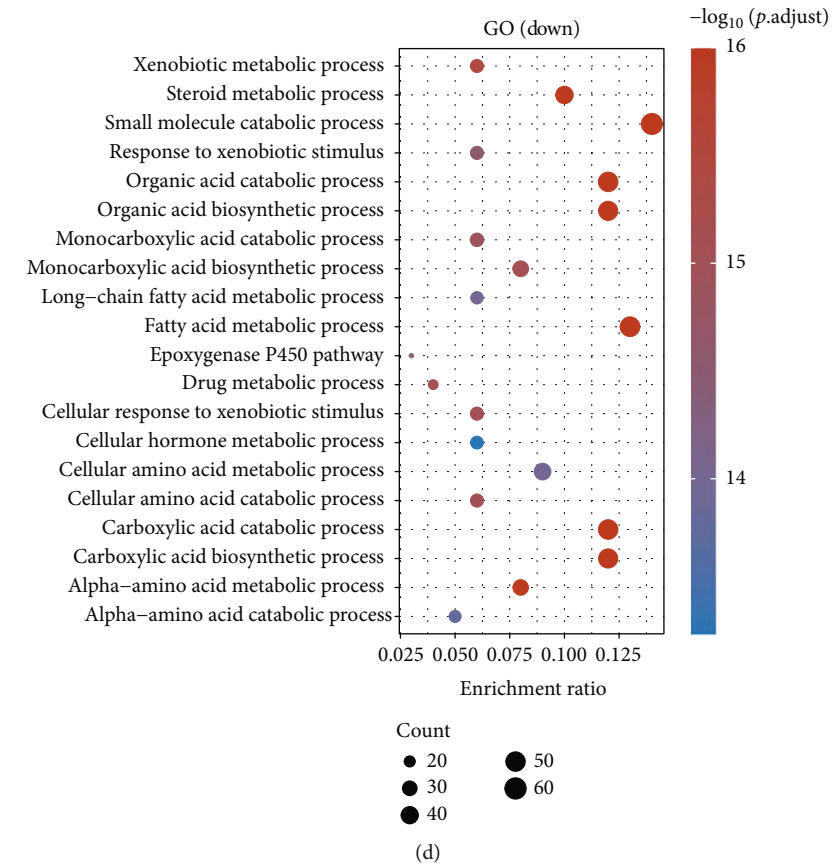

(d)

Figure 2: Results of GO and KEGG analyses. (a, b) KEGG pathway analysis in TCGA dataset. (c, d) GO analysis in TCGA dataset.

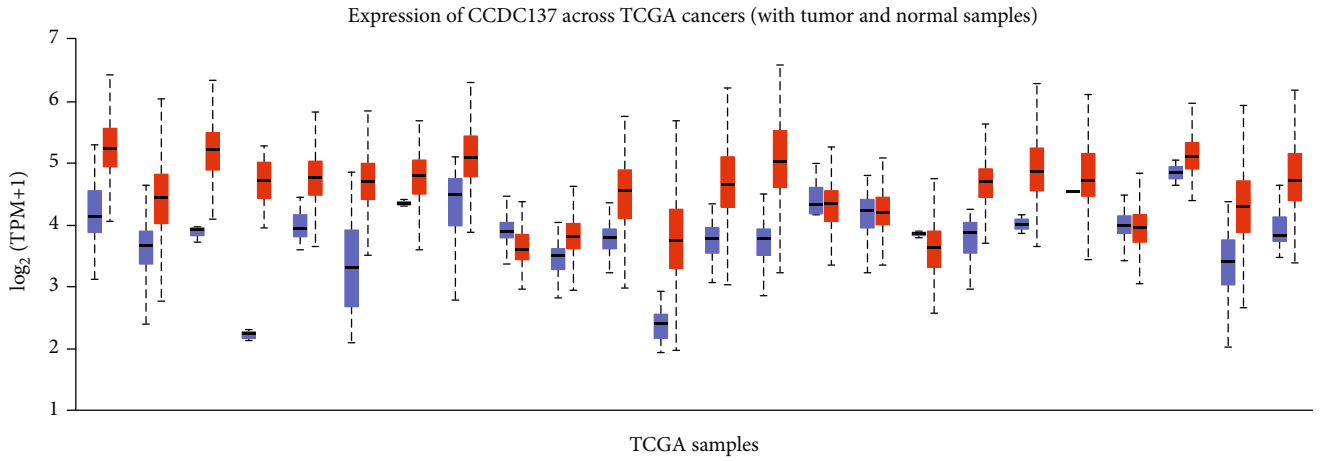

(a)

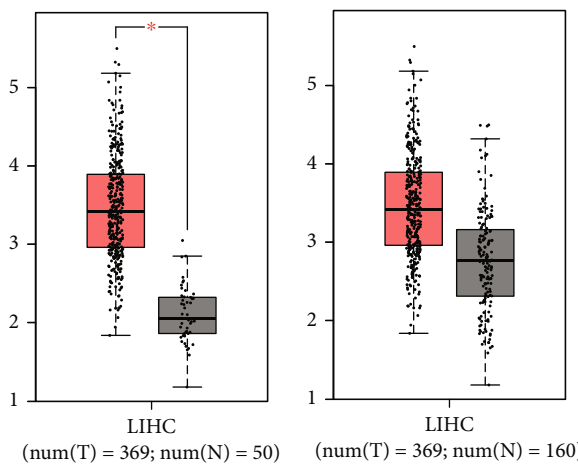

(b) (c)

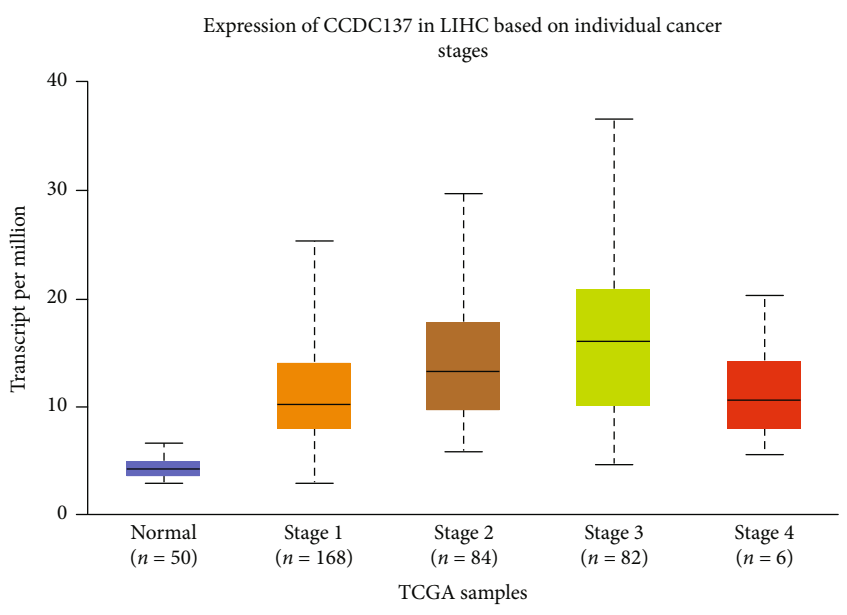

(d)

Figure 3: Continued.

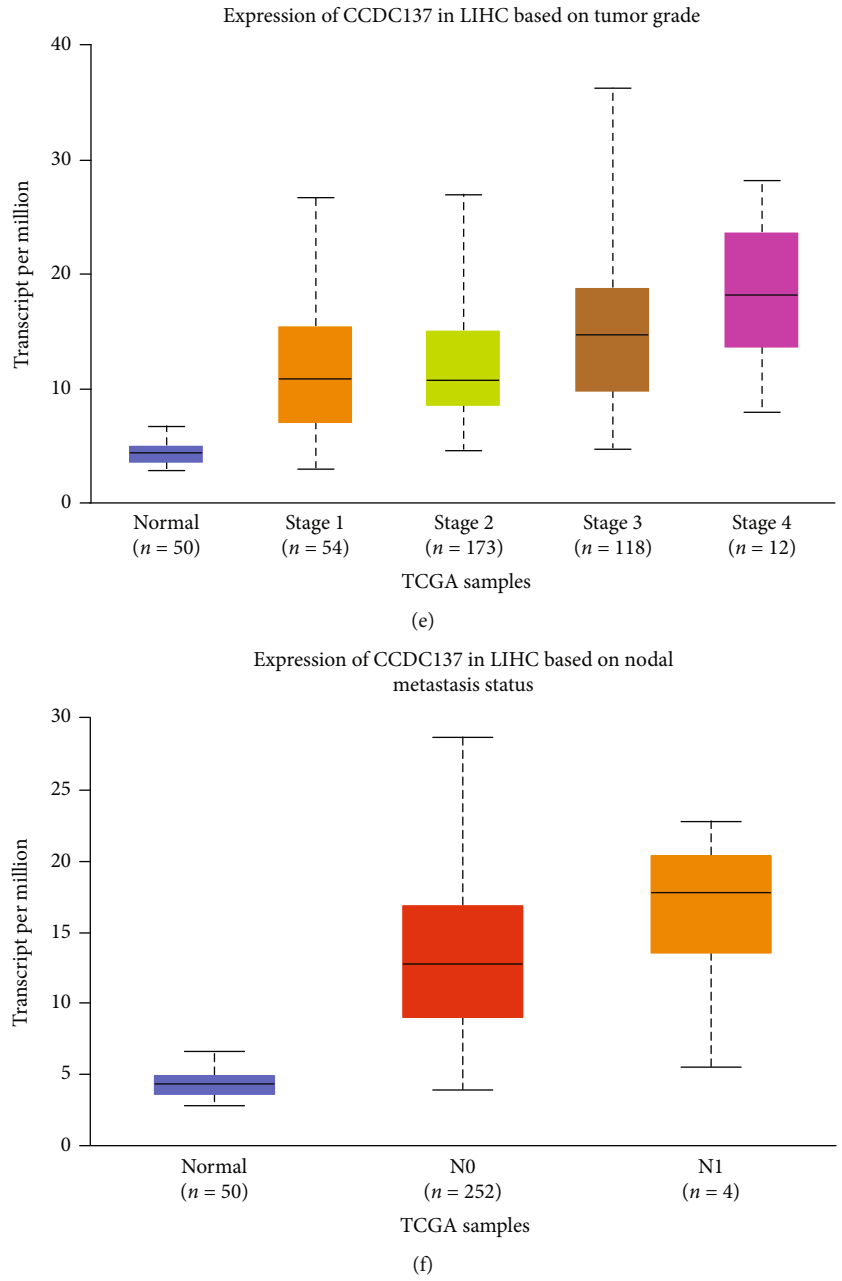

Figure 3: CCDC137 expression in HCC and its association with clinical progress. (a) CCDC137 expression levels in different cancer types from TCGA database analyzed. (b, c) Upregulation of CCDC137 expression in HCC samples compared with nontumor samples based on TCGA datasets and GTEx data. (d–f) CCDC137 expression was associated with clinicopathological characteristics in HCC patients, including (d) clinical stage, (e) tumor grade, and (f) nodal metastasis status.

5. Results

5.1. Identification of DEGs in HCC. In this work, a retrospective analysis of the data was performed on a total of 371 cases with HCC and 50 specimens without tumors taken from TCGA datasets. The limma software was utilized in the analysis of the DEGs. A total of 2897 DEGs were obtained: 2,451 genes were significantly upregulated, and 446 genes were significantly downregulated (Figures 1(a) and 1(b)).

5.2. Functional Correlation Analysis. Enrichment analysis using the KEGG database was carried out in order to investigate the function of DEGs. The results indicated that the 2451 upregulated genes were mainly associated with p53 signaling pathway, mRNA surveillance pathway, viral carcinogenesis, spliceosome, small cell lung cancer, and ribosome (Figure 2(a)). 446 downregulated genes were mainly associated with valine, leucine, and isoleucine degradation, tyrosine metabolism, tryptophan metabolism, steroid hormone biosynthesis, retinol metabolism, pyruvate metabolism, and

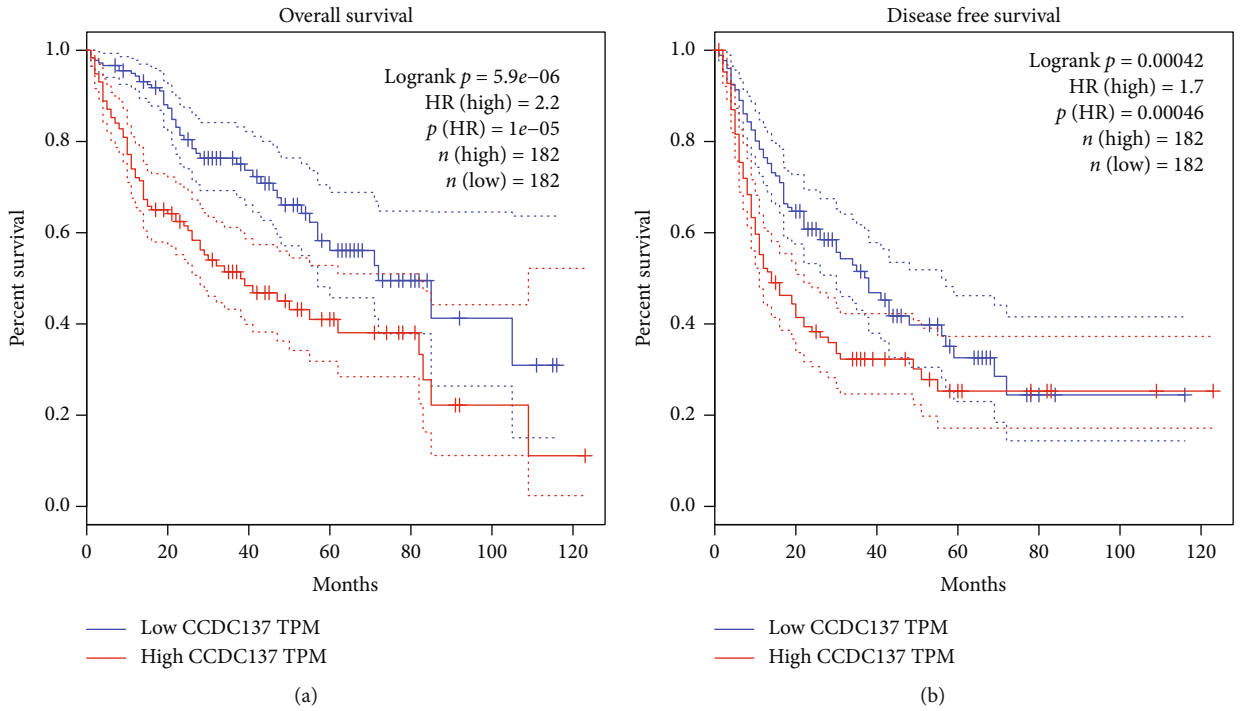

Figure 4: Predictive value of CCDC137 expression for clinical outcomes in HCC patients. Survival analysis for (a) overall survival and (b) disease-free survival of HCC patients with low and high CCDC137 expressions (based on median expression) in TCGA database.

PPAR signaling pathway (Figure 2(b)). Then, we performed GO assays and found that 2451 upregulated genes were mainly enriched in viral transcription, viral gene expression, spindle organization, sister chromatid segregation, ribonucleoprotein complex biogenesis, and regulation of nuclear division (Figure 2(c)). Moreover, 446 downregulated genes were enriched in xenobiotic metabolic process, steroid metabolic process, small molecule catabolic process, response to xenobiotic stimulus, organic acid catabolic process, and organic acid biosynthetic process (Figure 2(d)).

5.3. CCDC137 Expression Was Distinctly Increased in HCC. CCDC137 was the gene that caught our attention out of the 2,451 that were elevated. In order to determine whether or not CCDC137 expression was correlated with cancer, we analyzed its levels in a variety of tumors as well as the normal tissues. According to information obtained from TCGA database, the expression of CCDC137 was significantly increased in the majority of kinds of cancers (Figure 3(a)). In addition, CCDC137 expression was distinctly increased in HCC specimens compared with nontumor specimens (Figure 3(b)). Although data from TCGA and GTEx database did not show a distinct change of CCDC137 expression between HCC specimens and nontumor specimens, an overall trend can be observed (Figure 3(c)). After that, we investigated the relationship between the expression of CCDC137 and the clinical stages, and we discovered that a high level of CCDC137 expression was related with an advanced tumor stage and grade (Figure 3(d) and Figure 3(e)). More importantly, we found that metastasis HCC specimens showed an increased expression of CCDC137 compared with nonmetastasis HCC specimens (Figure 3(f)).

5.4. Correlations between CCDC137 and Prognosis. In order to investigate the possible connection between CCDC137 expression and the prognosis of HCC patients, we computed Kaplan-Meier curves for overall survival and made a comparison between those patients whose CCDC137 expression was high and those whose expression was low. The results showed that patients with higher levels of CCDC137 expression had a shorter overall survival ($p = 5.9e - 06$, Figure 4(a)) and disease-free survival ($p = 0.00042$, Figure 4(b)) than patients with lower CCDC137 expression levels. Based on our findings, CCDC137 might be a useful prognostic biomarker for patients with HCC.

5.5. The Correlation between CCDC137 Expression and Immune Infiltration. The Spearman correlation test was used to investigate the relationship between the amount of CCDC137 expression and the amount of immune cell infiltration that was measured using single-sample sequence set enrichment analysis (ssGSEA). The expression of HTRA3 was negatively correlated with the abundance of acquired immunocytes (NK cells, cytotoxic cells, mast cells, neutrophils, DC, CD8 T cells, Th17 cells, and TReg) and positively correlated with the abundance of innate immunocytes (NK CD56bright cells, Th2 cells, and TFH) (Figure 5).

5.6. The Potential Roles of CCDC137 in HCC Progression. In order to verify the aforementioned findings, an aberrant expression of CCDC137 was analyzed in HCC cells using real-time quantitative PCR. As shown in Figure 6(a), we found that the level of expression of CCDC137 in five HCC cells was much higher than that that in LO2 cells. In order to investigate the role that CCDC137 plays in HCC,

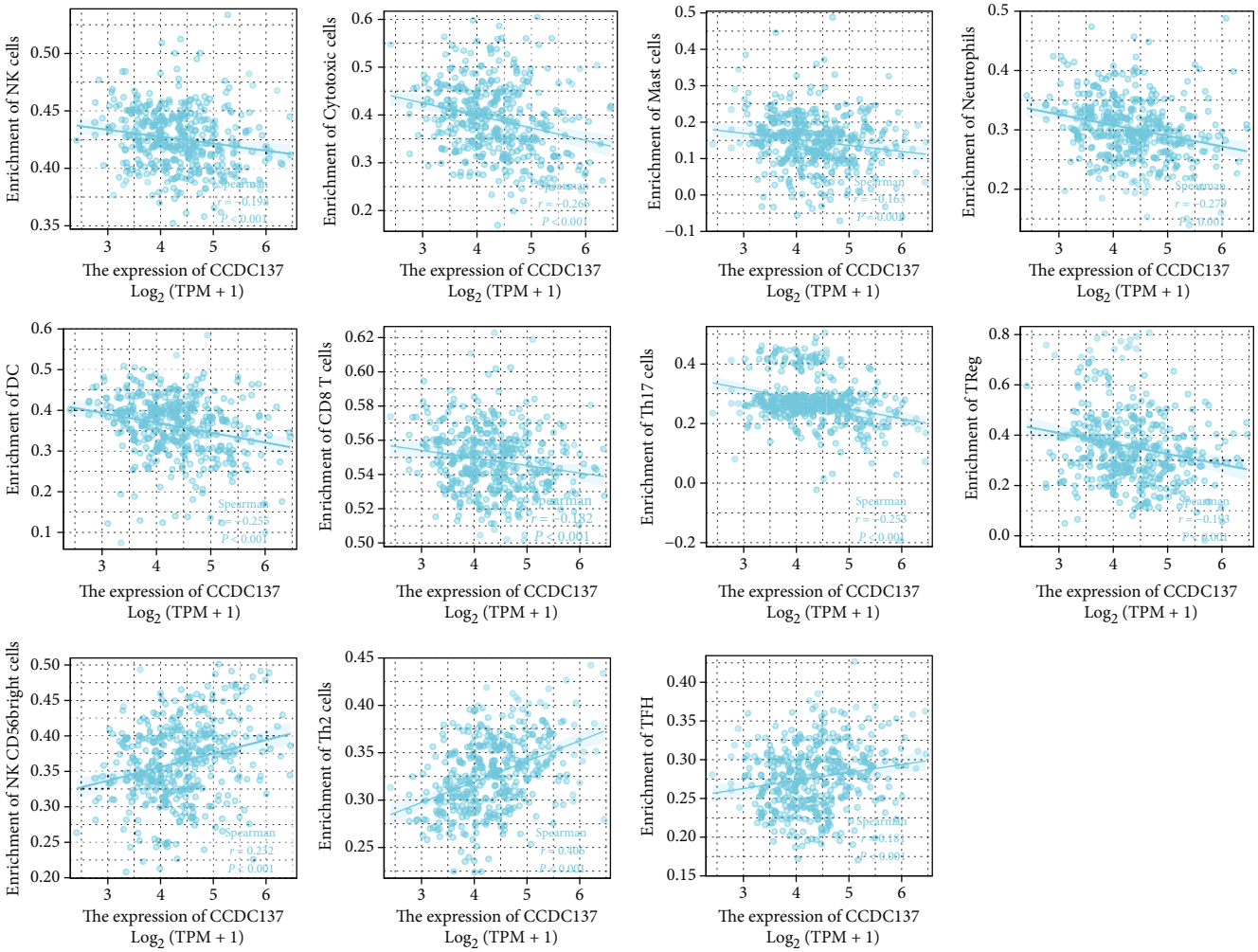

Figure 5: Correlation of immune cell infiltration and CCDC137 expression in HCC patients.

siRNA targeting CCDC137 was transfected into MHCC97H and HCCLM3 cells due to their relatively higher level compared with other HCC cells. CCDC137 expression in HCCLM3 and MHCC97H cells was found to be drastically reduced thanks to CCDC137 siRNA, as demonstrated by RT-qPCR (Figure 6(b)). CCK-8 data showed that the inhibition of CCDC137 expression led to a reduction in the rate of cell proliferation in HCCLM3 and MHCC97H cells (Figures 6(c) and 6(d)). These results indicate that upregulation of CCDC137 aggravated the malignancy of HCC cells.

6. Discussion

HCC continues to be a significant threat to public health all over the world, primarily because there are no enough reliable diagnostic tools and curative options [18]. The majority of patients identified with HCC are already in advanced stages, at which point the tumors are no longer resectable [19]. Discoveries of new biomarkers and molecular pathways have a significant clinical impact on the treatment of HCC.

Coiled-coil domain-containing (CCDC) is a structural motif that had been identified in proteins, and it exhibited an important role in a number of biological progresses, including membrane fusion, drug transport, control of gene expression, drug extrusion, and cell division [20, 21]. In addition, research has shown that the structure of the CCDC gene or the epigenetic alterations associated with it are linked to a wide variety of cancerous tumors [22]. It is believed that CCDC is involved in tumor growth and invasion of malignant tumor cells, in addition to other biological characteristics. CCDC performs a wide variety of vitally important biological functions. For instance, gastric tissues have an abundance of CCDC43 expression. Expression of CCDC43 has been linked to a number of aspects of gastric cancer, including tumor differentiation, distant metastasis, and clinical outcome of patients. The overexpression of CCDC43 in GC cells is correlated with increased rates of cell proliferation, invasion, and metastasis. It is possible for CCDC43 to upregulate and stabilize ADRM1, which would then lead to the formation of the ubiquitin-mediated proteasome [23]. In addition, Guo et al. performed pancancer analysis and identified CCDC137 as a tumor promoter and predictor of poor survivals for many tumor patients. A high level of CCDC137 has been linked to a tumor's immunosuppressive condition and has the potential to contribute to an increased infiltration of TAMs and CAFs [24]. However,

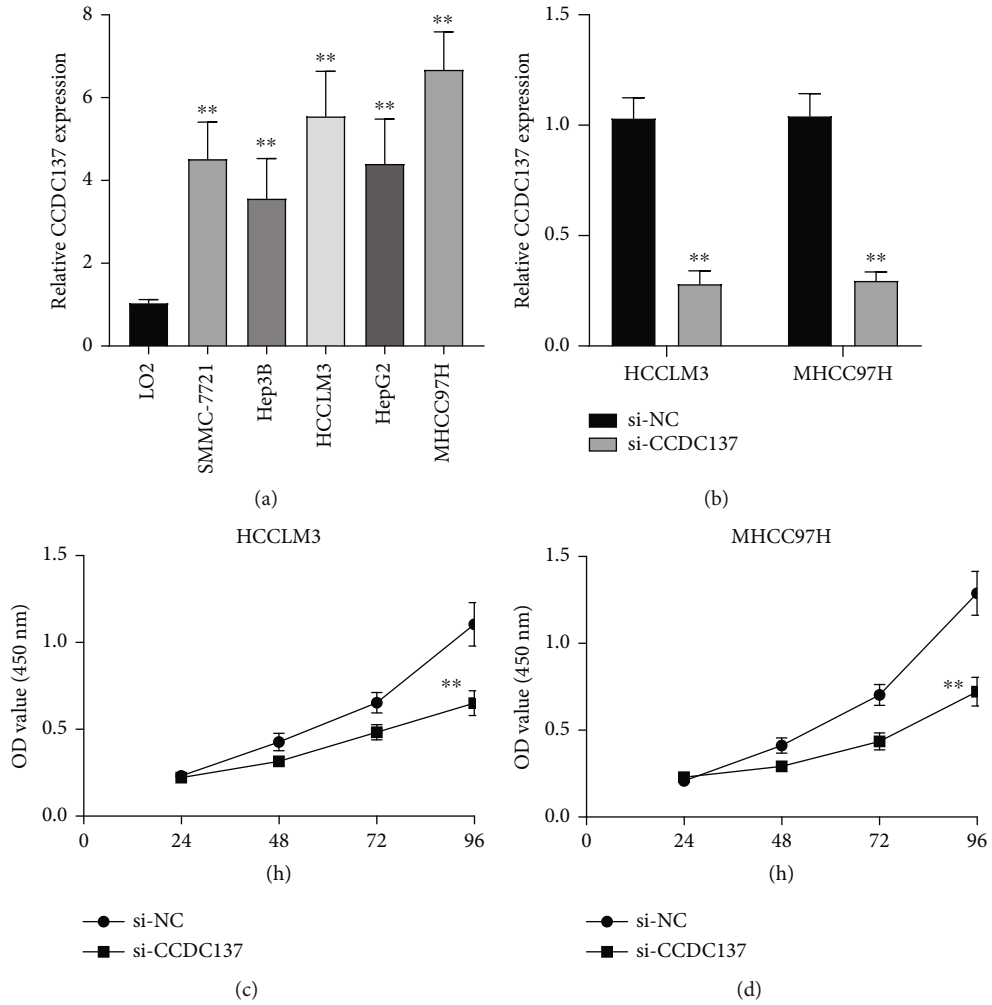

Figure 6: Knockdown of CCDC137 suppressed the proliferation of HCC cells. (a) RT-PCR for CCDC137 expression in five HCC cells and LO2 cells. (b) The expressions of CCDC137 in HCCLM3 and MHCC97H cells with its siRNA. (c, d) The proliferation of HCC cells after CCDC137 knockdown was examined by the use of CCK-8 assays. $^{**}p < 0.01$.

the expression and function of CCDC137 in HCC have not been investigated. In this study, we discovered that the expression of CCDC137 was significantly elevated in HCC patients, and its high levels were linked to an advanced clinical stage and grade. Survival assays revealed that high CCDC137 expression was associated with shorter overall survival and disease-free survival in HCC patients. On the other hand, we also performed in vitro assays and confirmed that CCDC137 expression was distinctly increased in HCC cells. Further CCK-8 assays confirmed that CCDC137 knockdown suppressed the proliferation of HCC cells. In general, our research indicated that CCDC137 may have a role in the progression of HCC, suggesting that it may be an oncogene and underlining the fact that it may be employed as a potential biomarker and therapeutic target.

The immunological milieu of the liver is extremely complicated because it contains a high number of innate immune cells and immune cells that behave similarly to innate immune cells [25]. It is widely held that a persistent inflammatory response is one of the primary factors that leads to the development of HCC [26, 27]. Chen et al. revealed that a favorable prognosis can be predicted by the presence of CD8+ T lymphocytes, B cells, and dendritic cells in the tumor, but a poor prognosis can be predicted by the presence of cancer-associated fibroblasts [28]. By upregulating immunological checkpoints and proinflammatory cytokines, immune cells promote the growth of tumors by allowing them to escape the body's immune system. When the immunological checkpoint is bypassed, it has been demonstrated that the host immune system is capable of producing effective antitumor immunity against tumor antigens. As a result, immunotherapy has arisen as a treatment option that can be considered for patients who have advanced HCC [29, 30]. It was indicated by our work that CCDC137 has a considerable relationship with the immune cells, particularly in NK cells, cytotoxic cells, mast cells, neutrophils, DC, CD8 T cells, Th17 cells, Treg and NK CD56bright cells, Th2 cells, and TFH. Based on our findings, CCDC137 may play a significant role in the regulation and recruitment of immune cells that infiltrate HCC.

7. Conclusion

Our findings suggested CCDC137 as a novel HCC-associated gene which was highly expressed in HCC. In addition, CCDC137 was found to be a useful biomarker for determining the prognosis of patients with HCC, and it was found that the expression of this biomarker has a substantial association with immune infiltrations.

Data Availability

The data used in this research are available from the corresponding authors upon reasonable request.

Conflicts of Interest

The authors declare that they have no conflicts of interest.

Authors' Contributions

Lu Bai, Zhao-Xu Yang, and Jian-Shan Liu contributed equally to this work.

Acknowledgments

This work was supported by the National Natural Science Foundation of China (81672341) and Shaanxi Provincial Fund (2019JM-170).

References

[1] S. Caruso, D. R. O'Brien, S. P. Cleary, L. R. Roberts, and J. Zucman-Rossi, "Genetics of hepatocellular carcinoma: approaches to explore molecular diversity," *Hepatology*, vol. 73, Supplement 1, pp. 14–26, 2021.

[2] A. Cucchetti, J. Zhong, S. Berhane et al., "The chances of hepatic resection curing hepatocellular carcinoma," *Journal of Hepatology*, vol. 72, no. 4, pp. 711–717, 2020.

[3] S.-Y. Fan, C. Eiser, and M.-C. Ho, "Health-related quality of life in patients with hepatocellular carcinoma: a systematic review," *Clinical Gastroenterology and Hepatology*, vol. 8, no. 7, pp. 559–564.e10, 2010.

[4] D. Miki, H. Ochi, C. N. Hayes, H. Aikata, and K. Chayama, "Hepatocellular carcinoma: towards personalized medicine," *Cancer Science*, vol. 103, no. 5, pp. 846–850, 2012.

[5] J. M. Llovet, F. Castet, M. Heikenwalder et al., "Immunotherapies for hepatocellular carcinoma," *Nature Reviews Clinical Oncology*, vol. 19, no. 3, pp. 151–172, 2022.

[6] T. K.-W. Lee, X.-Y. Guan, and S. Ma, "Cancer stem cells in hepatocellular carcinoma — from origin to clinical implications," *Nature Reviews Gastroenterology & Hepatology*, vol. 19, no. 1, pp. 26–44, 2022.

[7] P. A. Shah, R. Patil, and S. A. Harrison, "NAFLD-related hepatocellular carcinoma: the growing challenge," *Hepatology*, 2022.

[8] E. Juárez-Hernández, D. Motola-Kuba, N. C. Chávez-Tapia, M. Uribe, and V. Barbero Becerra, "Biomarkers in hepatocellular carcinoma: an overview," *Gastroenterología y Hepatología*, vol. 11, no. 6, pp. 549–558, 2017.

[9] S. Gill, "The evolving treatment landscape of hepatocellular carcinoma: more choices, more responsibility," *Current Oncology*, vol. 27, Suppl 3, pp. S136–s137, 2020.

[10] V. Klungboonkrong, D. Das, and G. McLennan, "Molecular mechanisms and targets of therapy for hepatocellular carcinoma," *Journal of Vascular and Interventional Radiology*, vol. 28, no. 7, pp. 949–955, 2017.

[11] A. Mazzola, A. Costantino, S. Petta et al., "Recurrence of hepatocellular carcinoma after liver transplantation: an update," *Future Oncology*, vol. 11, no. 21, pp. 2923–2936, 2015.

[12] B. M. Hussen, K. H. Tamizkar, H. J. Hidayat, M. Taheri, and S. Ghafouri-Fard, "The role of circular RNAs in the development of hepatocellular carcinoma," *Pathology - Research and Practice*, vol. 223, article 153495, 2021.

[13] I. Vitale, E. Shema, S. Loi, and L. Galluzzi, "Intratumoral heterogeneity in cancer progression and response to immunotherapy," *Nature Medicine*, vol. 27, no. 2, pp. 212–224, 2021.

[14] O. Meurette and P. Mehlen, "Notch signaling in the tumor microenvironment," *Cancer Cell*, vol. 34, no. 4, pp. 536–548, 2018.

[15] C. Lu, D. Rong, B. Zhang et al., "Current perspectives on the immunosuppressive tumor microenvironment in hepatocellular carcinoma: challenges and opportunities," *Molecular Cancer*, vol. 18, no. 1, p. 130, 2019.

[16] W. C. Dougall, S. Kurtulus, M. J. Smyth, and A. C. Anderson, "TIGIT and CD96: new checkpoint receptor targets for cancer immunotherapy," *Immunological Reviews*, vol. 276, no. 1, pp. 112–120, 2017.

[17] L. Martinet and M. J. Smyth, "Balancing natural killer cell activation through paired receptors," *Nature Reviews. Immunology*, vol. 15, no. 4, pp. 243–254, 2015.

[18] S. Lin, K. Hoffmann, and P. Schemmer, "Treatment of hepatocellular carcinoma: a systematic review," *Cancer*, vol. 1, no. 3-4, pp. 144–158, 2012.

[19] J. S. Lee and S. S. Thorgeirsson, "Comparative and integrative functional genomics of HCC," *Oncogene*, vol. 25, no. 27, pp. 3801–3809, 2006.

[20] P. P. Priyanka and S. Yenugu, "Coiled-coil domain-containing (CCDC) proteins: functional roles in general and male reproductive physiology," *Reproductive Sciences*, vol. 28, no. 10, pp. 2725–2734, 2021.

[21] C. Wang, H. Li, L. Wu et al., "Coiled-coil domain-containing 68 downregulation promotes colorectal cancer cell growth by inhibiting ITCH-mediated CDK4 degradation," *Frontiers in Oncology*, vol. 11, article 668743, 2021.

[22] T. Hua, J. Ding, J. Xu, Y. Fan, Z. Liu, and J. Lian, "Coiled-coil domain-containing 68 promotes non-small cell lung cancer cell proliferation *in vitro*," *Oncology Letters*, vol. 20, no. 6, p. 1, 2020.

[23] J. Wang, X. Wu, W. Dai et al., "The CCDC43-ADRM1 axis regulated by YY1, promotes proliferation and metastasis of gastric cancer," *Cancer Letters*, vol. 482, pp. 90–101, 2020.

[24] L. Guo, B. Li, Z. Lu et al., "CCDC137 is a prognostic biomarker and correlates with immunosuppressive tumor microenvironment based on pan-cancer analysis," *Frontiers in Molecular Biosciences*, vol. 8, article 674863, 2021.

[25] P. Zimmermann and N. Curtis, "Factors that influence the immune response to vaccination," *Clinical Microbiology Reviews*, vol. 32, no. 2, 2019.

[26] Y. Chen and Z. Tian, "HBV-induced immune imbalance in the development of HCC," *Frontiers in Immunology*, vol. 10, p. 2048, 2019.

[27] C. Donisi, M. Puzzoni, P. Ziranu et al., "Immune checkpoint inhibitors in the treatment of HCC," *Frontiers in Oncology*, vol. 10, article 601240, 2021.

[28] J. Chen, A. Schmitt, B. Chen et al., "Nilotinib hampers the proliferation and function of $CD8^+$ T lymphocytes through inhibition of T cell receptor signalling," *Journal of Cellular and Molecular Medicine*, vol. 12, no. 5b, pp. 2107–2118, 2008.

[29] M. De Ridder, H. Jiang, G. Van Esch et al., "IFN-γ^+ $CD8^+$ T lymphocytes: possible link between immune and radiation responses in tumor-relevant hypoxia," *International Journal of Radiation Oncology • Biology • Physics*, vol. 71, no. 3, pp. 647–651, 2008.

[30] A. Obata-Onai, S. Hashimoto, N. Onai et al., "Comprehensive gene expression analysis of human NK cells and $CD8^+$ T lymphocytes," *International Immunology*, vol. 14, no. 10, pp. 1085–1098, 2002.

Hindawi
Disease Markers
Volume 2022, Article ID 6734105, 9 pages
https://doi.org/10.1155/2022/6734105

Research Article

Bioinformatics Analysis Based on TCGA: MUC16 Mutation Correlates with Clinical Outcome in Gastric Cancer

Liang Huang, Shuang Zheng, Junhui Fu, Meng Zhang, Xiaogang Ge, and Ning Mu

Department of General Surgery, Taizhou First People's Hospital, Taizhou, China

Correspondence should be addressed to Ning Mu; mnwsq@163.com

Received 26 June 2022; Revised 25 July 2022; Accepted 27 July 2022; Published 23 August 2022

Academic Editor: Fu Wang

The prognosis of gastric cancer (GC) is difficult to predict due to the disease's complex genetic and phenotypic characteristics. MUC16 has been reported to be involved in the progression of several tumors. In this study, we aimed to explore whether MUC16 mutation had any impact on the prognosis or treatments of GC patients. Additionally, this analysis uncovered possible critical pathways related with these systems. On the cBioPortal, we were able to locate the pertinent data of patients with MUC16 mutations. And then, GSEA analysis identified differences in mRNA levels between mutant and wild-type MUC16 patients in terms of biological function annotation and pathways. The KEGG and GO analyses were also performed using the differentially expressed genes (DEGs). There were 139 individuals with GC who had the MUC16 mutation, which accounts for 32 percent, and the remaining patients had the MUC16 wild type. Survival assays revealed that patients with the MUC16 mutation had longer overall survival and disease-free survival. GSEA analysis revealed that cell cycle, cysteine and methionine metabolism, Huntington's disease, one carbon pool by folate, pyrimidine metabolism, pyruvate metabolism, RNA degradation, spliceosome, and valine leucine and isoleucine degradation were distinctly enriched in patients with MUC16 mutation type. Moreover, we identified 323 DEGs. Among them, 162 genes were upregulated, and 161 genes were downregulated. GO and KEGG assays indicated DEGs as enriched in pancreatic secretion, neuroactive ligand-receptor interaction, protein digestion and absorption, fat digestion and absorption, and glycerolipid metabolism. Overall, our data revealed that the MUC16 mutation in GC may affect the development of patients by altering several genes and pathways, indicating the importance of MUC16 mutation in the treatments of GC on an individual basis.

1. Introduction

Gastric cancer (GC) is the most common malignant tumor of the digestive system [1]. Despite the fact that there has been considerable advancement in terms of treatments, it remains the second leading cause of mortality due to cancer [2, 3]. In China, both the incidence and mortality rates of GC have been on the rise [4]. After surgery, patients typically undergo a variety of treatments, such as chemoradiation and chemotherapy, in an effort to delay or eliminate the likelihood of a cancer returning [5, 6]. Despite the fact that these treatments have led to an increase in patient survival rates, the overall survival rate for patients diagnosed with GC remains at roughly 30 percent worldwide [7, 8]. Therefore, the purpose of our research was to investigate potential biomarkers for the prognostic evaluation of GC patients.

Growing studies have confirmed that gene mutations are very important in disease program [9]. Chromosomal abnormalities, such as recurrent somatic mutations, copy number alterations, and oncogenic structural DNA rearrangements, have been uncovered in cases of primary germ cell cancer [10, 11]. In the field of ovarian cancer research, the biomarker MUC16 (which was formerly known as CA125) has been employed extensively, and its expression has been found to be related with the course of the disease [12]. Significant progress has been made in understanding the structure and activities of this protein, as well as the part it plays in essential processes, such as the prevention of epithelial damage and the development of human cancer [13, 14]. Ovarian, pancreatic, breast, and lung cancers have been found to exhibit aberrantly high levels of MUC16 [15–18]. MUC16 and its ligands have emerged as prospective

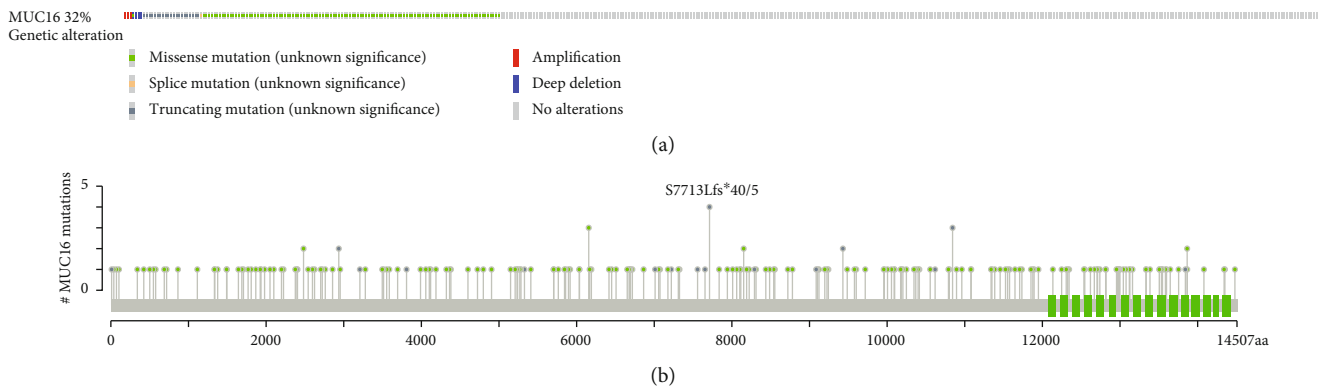

Figure 1: Mutation frequency (a) and types (b) of MUC16 in GC reproduced from the Cancer Genome Atlas (TCGA) datasets.

therapeutic intervention targets thanks to their dysregulation and functional involvements. This has allowed monoclonal antibodies and immunotherapy to be utilized in their investigation. MUC16 is one of the genes in GC that is most susceptible to mutations. A variable MUC16 status may have an impact on the progression of cancer, the prognosis of the disease, and treatment options, and it may also cause certain patients to have a natural resistance or sensitivities to treatment tests [19, 20]. Thus, investigating the changes that take place in the important signaling pathways in patients who have the MUC16 mutation and determining the significance of these changes in tumor developments could assist us in gaining a deeper understanding of the pathogenesis of the disease, which will provide additional evidence for the individualized treatment of GC. In this research, we aimed to determine whether or not MUC16 mutations are linked to the clinical prognosis of GC patients.

2. Materials and Methods

2.1. RNA-Seq Data. From the database of the Cancer Genome Atlas (TCGA) (https://portal.gdc.cancer.gov/), an RNA-Seq dataset of GC was obtained, together with the clinical characteristics that corresponded to it. The website of the cBioPortal for Cancer Genomics was searched in order to collect the corresponding information associated to patients who had the MUC16 mutation (http://www.cbioportal.org/index.do).

2.2. Gene Set Enrichment Analysis (GSEA). MUC16 mutation and wild-type patients were compared using GSEA v3.0 to find differences in gene mRNA expressions of biological functions, which allowed us to better comprehend the effects of the MUC16 mutation on various biological function gene sets in the GC patient population [21]. It was decided that there would be 5 different permutations. It was determined that the enrichment results were statistically significant if they met the criteria of a nominal P value threshold of 0.05 and a false discovery rate (FDR q-val) of less than 0.25.

2.3. Identification of Differentially Expressed Genes (DEGs). An R package called EdgeR, which is used for analyzing abnormal expressions of RNA-Seq count data, was applied in accordance with the user's guide in order to screen DEG between patients with the MUC16 mutation and those with the wild-type form of GC. The following criteria were used to identify DEGs: |fold change (FC)| greater than 2; both the P value and the FDR were less than 0.05. The DEGs were applied for subsequent bioinformatics research.

2.4. Functional Enrichment Analysis. We used the "http://org.Hs.eg.db" package to convert gene symbols into Entrez IDs, and then, we used the "cluster Profiler," "ggplot2," and "enrich plot" packages to do pathway enrichment analysis on the DEGs based on the GO database and KEGG. The assays were performed on the DEGs. After applying the FDR approach, the P values were recalculated, and significantly enriched pathways were determined to have an FDR of 0.25 or lower.

2.5. Statistical Analysis. The Student's t-test was applied to compare the MUC16 expressions between the MUC16 mutation and wild-type GC tissues. Kaplan-Meier plots and log rank tests were used for survival analysis. Controlling the FDR in edgeR and GSEA required an adjustment for multiple testing using the Benjamini-Hochberg method, respectively. All statistical analyses were performed in RStudio (version 3.6.8), and we considered a P value <0.05 to be statistically significant.

3. Results

3.1. Data Information. We collected the information for 441 GC specimens and nontumor specimens RNA-Seq datasets from the TCGA database. These datasets included complete follow-up data. There were 139 individuals with GC who had the MUC16 mutation, which accounts for 32 percent, and the remaining patients had the MUC16 wild type (Figure 1(a)). Amplification, truncating, and deep deletion mutations as well as inframe and missense variants spanned the entire gene. Other mutation categories included missense mutations (Figure 1(b)). The website known as cBioPortal for Cancer Genomics was applied in order to acquire these data.

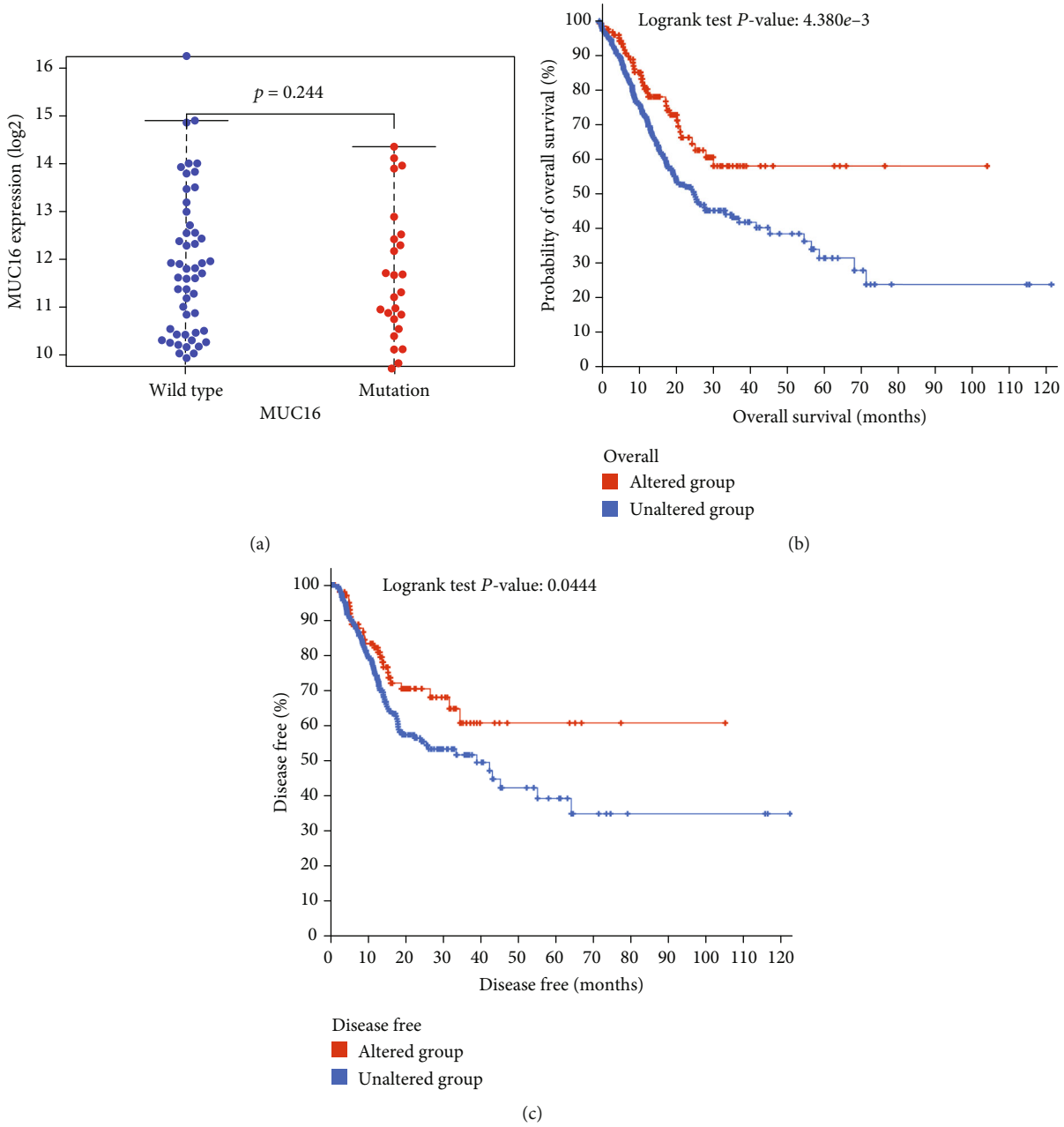

Figure 2: Mutations of MUC16 were related to the clinical outcome of GC patients. (a) The MUC16 mutation has been shown to correlate with the expression of mRNA. (b and c) The Kaplan-Meier survival curves, stratified by the MUC16 mutation, for patients with GC.

3.2. Clinical Impact of MUC16 Mutation in GC Progress and Prognosis. The second thing that we did was look into how the MUC16 mutation affected the progression of GC and the prognosis. We began by determining the levels of MUC16 in both the wild-type and mutant groups. According to the findings, MUC16 did not differ between GC specimens that had the wild-type and GC specimens that contained mutations ($P > 0.244$, Figure 2(a)). Survival assays revealed that patients with the MUC16 mutation had longer overall survival (Figure 2(b), $P = 4.380e-3$) and disease-free survival ($P = 0.0444$, Figure 2(c)), suggesting that the MUC16 mutation suppressed the developments of GC. Patients who carried the MUC16 mutation can benefit from receiving intervention at an earlier stage.

3.3. GSEA. All of these studies point to the fact that the MUC16 mutation played an important part in the progression of GC, the prognosis, and the choice of drugs. In order to study the mechanism and to collect more evidence, we began by analyzing the effects that the MUC16 mutation had on the processes that occur within cells. At initially, we used the GSEA method to conduct research on a number of different biological functional gene sets. As exhibited in Figure 3, we observe that cell cycle, cysteine and methionine

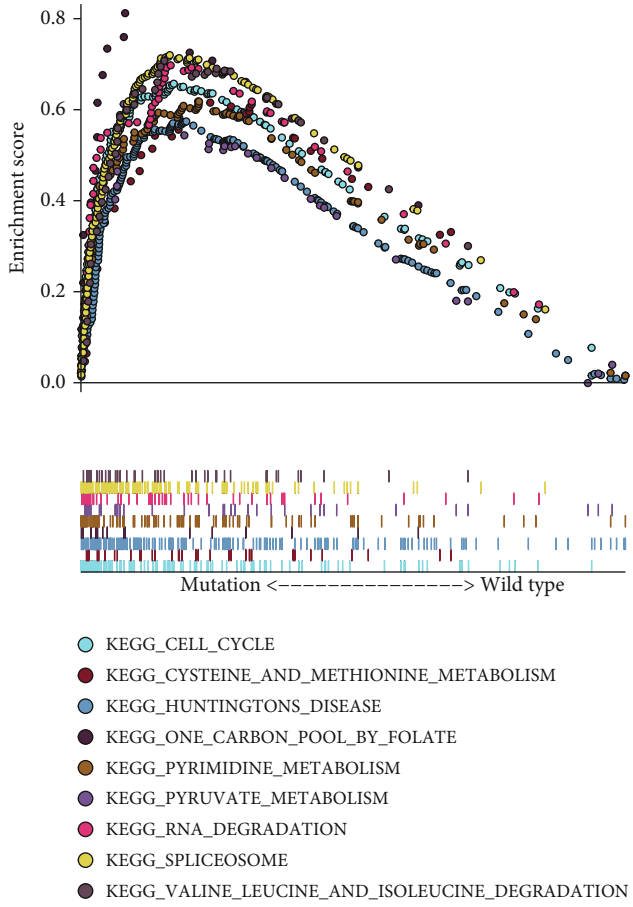

Figure 3: The gene set enrichment analysis (GSEA) was used to investigate the variations in gene enrichment observed in patients with the MUC16 wild-type and MUC16 mutant alleles.

metabolism, Huntington's disease, one carbon pool by folate, pyrimidine metabolism, pyruvate metabolism, RNA degradation, spliceosome and valine leucine, and isoleucine degradation were significantly enriched. Our findings revealed that the MUC16 mutation could suppress GC progression via regulating several tumor-related pathways in cell cycle, RNA degradation, and metabolism.

3.4. Identification of DEGs. We identified the DEGs in order to conduct further research into the pathways and genes that were involved in the MUC16 mutation. For the purpose of DEG screen, RNA-Seq datasets from 113 GC patients carrying the MUC16 mutation and additional MUC16 wild-type patients were employed. As a result of the in-silico study, a total of 323 genes were determined to be DEGs by using the criterion of having a |fold change (FC)| more than 2.0 and $P < 0.05$. We found that 162 genes were upregulated, and 161 genes were downregulated throughout the entire set of genes mentioned above (Figure 4(a)). The heatmap of the DEGs is shown in Figure 4(b).

3.5. Functional and Pathway Enrichment Analyses of DEGs. Enrichment studies for the GO and KEGG pathways were carried out in order to investigate the functional properties of the DEGs. In BP, the terms were mainly associated with epidermis development, keratinocyte differentiation, epidermal cell differentiation, skin development, and keratinization (Figure 5(a)). In CC, they were related to secretory granule lumen, cytoplasmic vesicle lumen, vesicle lumen, blood microparticle, and primary lysosome (Figure 5(b)). In MF, term enrichment mainly involved endopeptidase activity, serine-type peptidase activity, serine hydrolase activity, serine-type endopeptidase activity, and receptor ligand activity (Figure 5(c)). The results of KEGG assays revealed that the most distinctly enriched biological processes included pancreatic secretion, neuroactive ligand-receptor interaction, protein digestion and absorption, fat digestion and absorption, and glycerolipid metabolism (Figure 5(d)).

4. Discussion

The general outcome of advanced GC is quite poor, and only a few number of molecular targets have been demonstrated to be useful for GC [22, 23]. In order to successfully apply cancer precision medicine, the identification of biomarkers or signatures that can predict prognosis and therapeutic outcomes is an essential component. There have been reports of improvements in prognostic and therapeutic benefits brought about by the utilization of biomarkers in the treatment of colorectal cancer, breast cancer, lung cancer, and other types of cancer [24–26]. Nevertheless, the current initiatives consistently prioritize predictive accuracy over explanatory capacity. In recent years, an increasing number of studies have indicated that tumor mutation burden (TMB) is often referred to as a biomarker correlated with clinical responses to immune checkpoint blockade (ICB) in the treatment of nonsmall-cell lung cancer, cervical cancer, and GC [27–29]. Extensive sequencing of the genome using either next-generation sequencing (NGS) or whole-exome sequencing is used for TMB identification. Recently, the clinical prognosis of cancer patients can be predicted with the help of relatively straightforward procedures, such as the identification of single gene mutations, as has been demonstrated in a number of studies. Numerous studies have demonstrated that mutations in genes related to genomic integrity, such as TP53 and ATR, can lead to genomic instability and thus contribute to a high genomic mutation rate [30–32]. This is the case because these mutations can cause genomic instability. Therefore, investigating the association between the mutations of important genes and the clinical outcomes of GC patients is helpful for guiding immunotherapy on GC sufferers.

MUC16 is a unique glycoprotein, and its expression can be found in the cell membrane and a soluble form [13]. As a biomarker for ovarian cancer, MUC16 has been extensively used, and its expression has been shown to be related with the course of the disease [12]. Additionally, MUC16 has been shown to be useful in both the diagnosis and monitoring of the disease. In addition to this, it has been reported that increased quantities of soluble MUC16 were found in a variety of cancers, including breast cancer, mesothelioma, gastric cancer, colorectal adenocarcinoma,

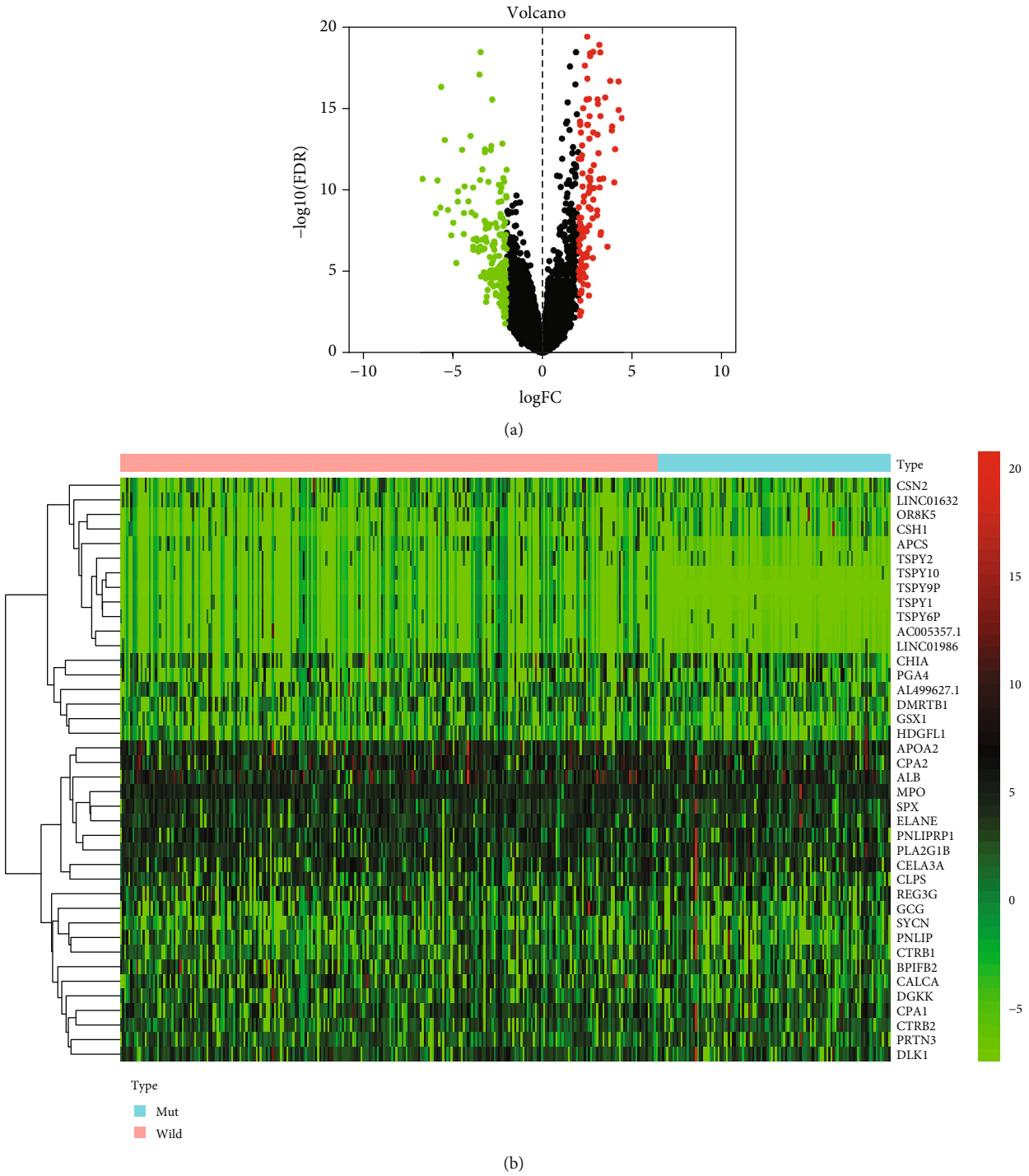

Figure 4: RNA-Seq datasets from 113 MUC16 mutation-bearing and other MUC16 wild-type GC patients were used for DEG screening. (a) Volcano plot of DEGs. (b) Heatmap of DEGs.

and some others [19, 33–35]. Comparative studies using MUC16 and other tumor markers, such as carcinoembryonic antigen, have been conducted on colorectal adenocarcinomas [36]. MUC16 has been found to have potential relevance as a future serological marker (CEA) [37]. A correlation has been shown between the upregulation of MUC16 and the progression of pancreatic ductal adenocarcinoma. According to the findings of a number of research, MUC16 may play a role in the evolution of GC. However, its association with clinical outcome was rarely reported. In order to encourage customized treatment, our goal was to determine the clinical importance of the MUC16 mutation in terms of the course and prognosis of GC. Our group further observed that about 32% of patients carried the MUC16 mutation among 441 cases, including missense mutation, splice mutation, truncating mutation, amplification, and deep deletion. According to the findings

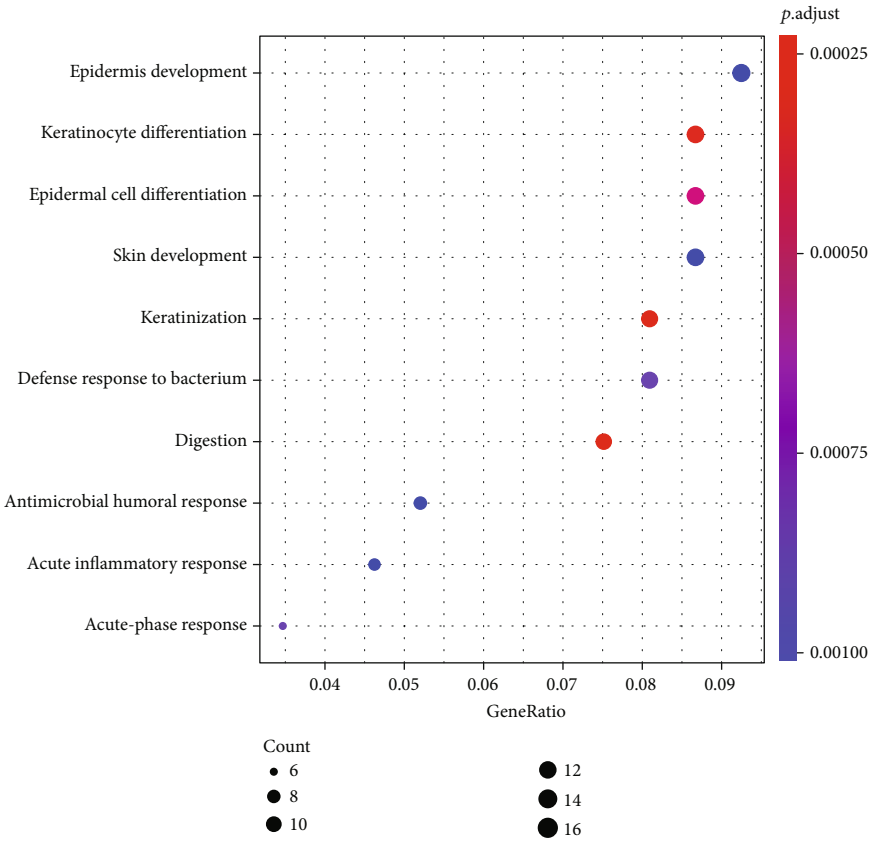

(a)

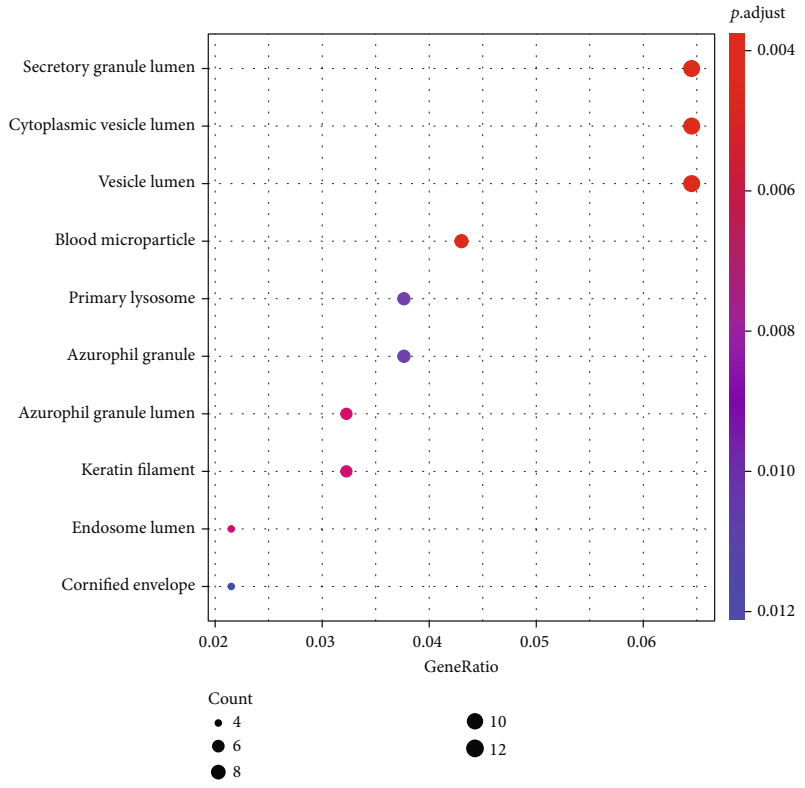

(b)

Figure 5: Continued.

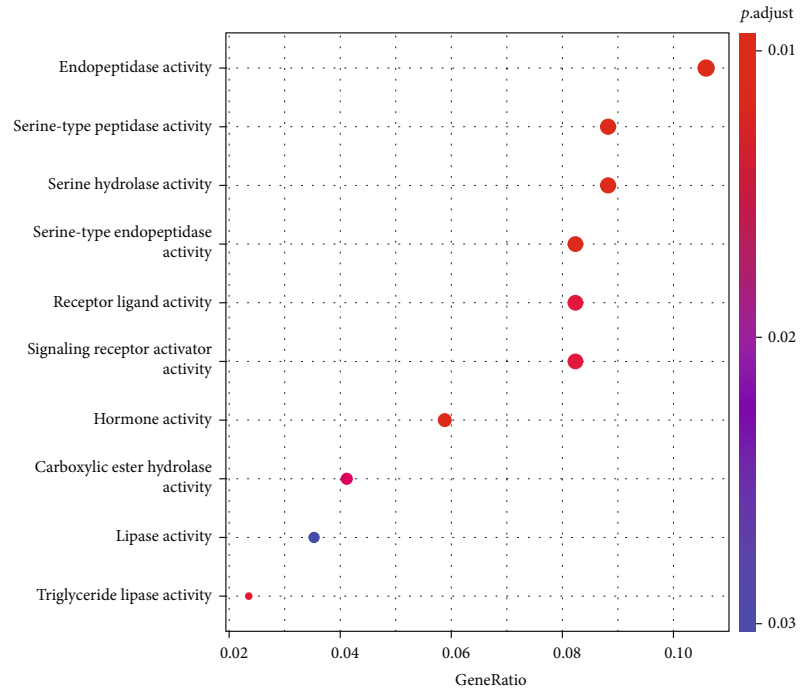

(c)

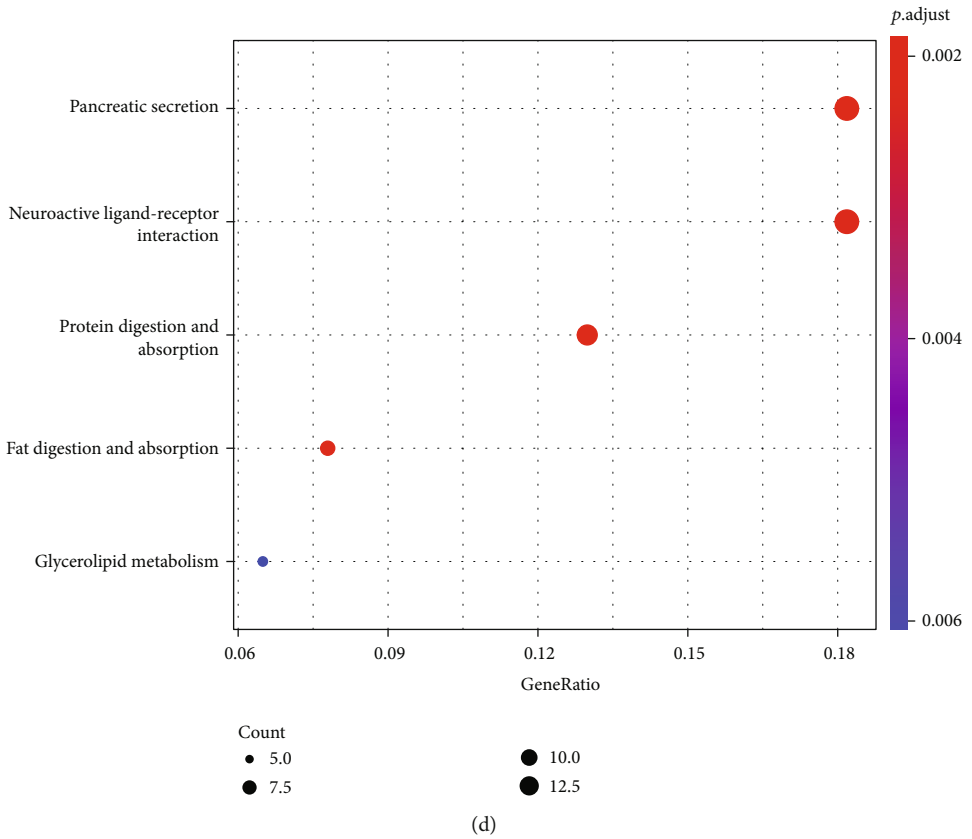

(d)

Figure 5: GO and KEGG assays were applied to explore the possible function of DEGs. (a–c) The GO enrichment terms of DEGs. (d) The KEGG assays of DEGs.

of a clinical study, GC patients with the MUC16 mutation have a significantly poorer prognosis in survival and disease-free survival. All of these findings suggest that the MUC16 mutation in GC patients should be given more attention in clinical practice, which is in line with the findings of some recent studies. The detection of mutations in tumor genes has been brought into clinical practice, which enables physicians to accurately determine the prognosis of patients and choose more effective and tailored treatment regimens. Our findings give evidence that individuals with gastric cancer who have the MUC16 wild type were more likely to develop distant metastases and that the clinical outcome of the disease is worse, suggesting that active treatments were essential for these patients in order to achieve a favorable prognosis. Patients with GC who have the MUC16 wild type may need more complete examinations to discover early metastatic tumor specimens. Alternatively, they may require earlier use of targeted therapies in order to cope with a poor illness prognosis.

Regarding the mechanisms, we performed an analysis on the RNA-Seq dataset of GC that was retrieved from TCGA in order to determine the important pathways and genes that are linked with the MUC16 mutation. These analyses were involved in the application of bioinformatics. GSEA analysis in the present study suggested that cell cycle, cysteine and methionine metabolism, Huntington's disease, one carbon pool by folate, pyrimidine metabolism, pyruvate metabolism, RNA degradation, spliceosome and valine leucine, and isoleucine degradation were significantly enriched. Our findings revealed that the MUC16 mutation may suppress GC progression via regulating several pathways in cell cycle, RNA degradation, and metabolism.

We identified the DEGs in order to conduct further research into the pathways and genes that were involved in the MUC16 mutation. There were a total of 323 genes that were found to be DEGs. GO assays revealed that 323 genes were involved in epidermis development, keratinocyte differentiation, epidermal cell differentiation, secretory granule lumen, cytoplasmic vesicle lumen, vesicle lumen, endopeptidase activity, and serine hydrolase activity. The results of KEGG assays revealed that the most distinctly enriched biological processes included pancreatic secretion, neuroactive ligand-receptor interaction, protein digestion and absorption, fat digestion and absorption, and glycerolipid metabolism. Our findings provided evidence that the MUC16 mutation plays a role in the progression of cells and sheds light on a potentially effective therapeutic target in patients who carry the MUC16 mutation, which can be used to form tailored treatment recommendations.

5. Conclusion

In conclusion, we demonstrated that the MUC16 mutation was related with the clinical outcomes of GC patients. Our research identified the probable pathways and key genes that were related to the MUC16 mutation in GC, which could potentially contribute to the development of therapeutic methods and predictive and prognostic tools for this particular subgroup of patients suffering from GC.

Data Availability

The datasets used and/or analyzed during the current study are available from the corresponding author upon reasonable request.

Conflicts of Interest

The authors declare that they have no competing interests.

Acknowledgments

This word was supported by Scientific Research Project of Taizhou Science and Technology Bureau in Zhejiang Province (NO. 20ywa47).

References

[1] A. P. Thrift and H. B. El-Serag, "Burden of gastric cancer," *Clinical Gastroenterology and Hepatology*, vol. 18, no. 3, pp. 534–542, 2020.

[2] D. E. Guggenheim and M. A. Shah, "Gastric cancer epidemiology and risk factors," *Journal of Surgical Oncology*, vol. 107, no. 3, pp. 230–236, 2013.

[3] S. Li, H. Zhang, K. Chen et al., "Application of chitosan/alginate nanoparticle in oral drug delivery systems: prospects and challenges," *Drug Delivery*, vol. 29, no. 1, pp. 1142–1149, 2022.

[4] S. Xiao and L. Zhou, "Gastric cancer: metabolic and metabolomics perspectives (review)," *International Journal of Oncology*, vol. 51, no. 1, pp. 5–17, 2017.

[5] T. Tsukamoto, M. Nakagawa, Y. Kiriyama, T. Toyoda, and X. Cao, "Prevention of gastric cancer: eradication of helicobacter pylori and beyond," *International Journal of Molecular Sciences*, vol. 18, no. 8, p. 1699, 2017.

[6] J. Dong and A. P. Thrift, "Alcohol, smoking and risk of oesophago-gastric cancer," *Best Practice & Research. Clinical Gastroenterology*, vol. 31, no. 5, pp. 509–517, 2017.

[7] Q. Guo, Y. Yuan, Z. Jin et al., "Association between tumor vasculogenic mimicry and the poor prognosis of gastric cancer in China: an updated systematic review and meta-analysis," *BioMed Research International*, vol. 2016, 2408648 pages, 2016.

[8] S. K. McKinley, P. Singh, K. Yin et al., "Disease spectrum of gastric cancer susceptibility genes," *Medical Oncology*, vol. 38, no. 5, p. 46, 2021.

[9] A. Gutiérrez-Martínez, W. Q. G. Sew, M. Molano-Fernández, M. Carretero-Junquera, and H. Herranz, "Mechanisms of oncogenic cell competition-paths of victory," *Seminars in Cancer Biology*, vol. 63, pp. 27–35, 2020.

[10] R. Asselta, L. Di Tommaso, M. Perrino et al., "Mutation profile and immunoscore signature in thymic carcinomas: an exploratory study and review of the literature," *Thorac Cancer*, vol. 12, no. 9, pp. 1271–1278, 2021.

[11] H. Nakagawa and M. Fujita, "Whole genome sequencing analysis for cancer genomics and precision medicine," *Cancer Science*, vol. 109, no. 3, pp. 513–522, 2018.

[12] M. Felder, A. Kapur, J. Gonzalez-Bosquet et al., "MUC16 (CA125): tumor biomarker to cancer therapy, a work in progress," *Molecular Cancer*, vol. 13, no. 1, p. 129, 2014.

[13] A. Aithal, S. Rauth, P. Kshirsagar et al., "MUC16 as a novel target for cancer therapy," *Expert Opinion on Therapeutic Targets*, vol. 22, no. 8, pp. 675–686, 2018.

[14] J. Núñez, R. de la Espriella, G. Miñana et al., "Antigen carbohydrate 125 as a biomarker in heart failure: a narrative review," *European Journal of Heart Failure*, vol. 23, no. 9, pp. 1445–1457, 2021.

[15] S. Lheureux, C. Gourley, I. Vergote, and A. M. Oza, "Epithelial ovarian cancer," *Lancet*, vol. 393, no. 10177, pp. 1240–1253, 2019.

[16] R. Bhatia, S. K. Gautam, A. Cannon et al., "Cancer-associated mucins: role in immune modulation and metastasis," *Cancer Metastasis Reviews*, vol. 38, no. 1-2, pp. 223–236, 2019.

[17] M. Zhang, S. Cheng, Y. Jin, Y. Zhao, and Y. Wang, "Roles of CA125 in diagnosis, prediction, and oncogenesis of ovarian cancer," *Biochimica Et Biophysica Acta. Reviews on Cancer*, vol. 1875, no. 2, article 188503, 2021.

[18] I. Lakshmanan, S. Salfity, P. Seshacharyulu et al., "MUC16 regulates TSPYL5 for lung cancer cell growth and chemoresistance by suppressing p53," *Clinical Cancer Research*, vol. 23, no. 14, pp. 3906–3917, 2017.

[19] H. Shen, M. Guo, L. Wang, and X. Cui, "MUC16 facilitates cervical cancer progression via JAK2/STAT3 phosphorylation-mediated cyclooxygenase-2 expression," *Genomics*, vol. 42, no. 2, pp. 127–133, 2020.

[20] P. Giamougiannis, P. L. Martin-Hirsch, and F. L. Martin, "The evolving role of MUC16 (CA125) in the transformation of ovarian cells and the progression of neoplasia," *Carcinogenesis*, vol. 42, no. 3, pp. 327–343, 2021.

[21] A. Subramanian, P. Tamayo, V. K. Mootha et al., "Gene set enrichment analysis: a knowledge-based approach for interpreting genome-wide expression profiles," *Proceedings of the National Academy of Sciences of the United States of America*, vol. 102, no. 43, pp. 15545–15550, 2005.

[22] P. Hohenberger and S. Gretschel, "Gastic cancer," *Lancet*, vol. 362, no. 9380, pp. 305–315, 2003.

[23] T. Aoyama and T. Yoshikawa, "Adjuvant therapy for locally advanced gastric cancer," *Surgery Today*, vol. 47, no. 11, pp. 1295–1302, 2017.

[24] L. Wu and X. Qu, "Cancer biomarker detection: recent achievements and challenges," *Chemical Society Reviews*, vol. 44, no. 10, pp. 2963–2997, 2015.

[25] C. L. Sawyers, "The cancer biomarker problem," *Nature*, vol. 452, no. 7187, pp. 548–552, 2008.

[26] W. Li, C. Li, T. Zhou et al., "Role of exosomal proteins in cancer diagnosis," *Molecular Cancer*, vol. 16, no. 1, p. 145, 2017.

[27] S. S. Joshi and B. D. Badgwell, "Current treatment and recent progress in gastric cancer," *CA: a Cancer Journal for Clinicians*, vol. 71, no. 3, pp. 264–279, 2021.

[28] T. A. Chan, M. Yarchoan, E. Jaffee et al., "Development of tumor mutation burden as an immunotherapy biomarker: utility for the oncology clinic," *Annals of Oncology*, vol. 30, no. 1, pp. 44–56, 2019.

[29] D. L. Jardim, A. Goodman, D. de Melo Gagliato, and R. Kurzrock, "The challenges of tumor mutational burden as an immunotherapy biomarker," *Cancer Cell*, vol. 39, no. 2, pp. 154–173, 2021.

[30] M. Hallek, "Chronic lymphocytic leukemia: 2020 update on diagnosis, risk stratification and treatment," *American Journal of Hematology*, vol. 94, no. 11, pp. 1266–1287, 2019.

[31] M. Olivier, M. Hollstein, and P. Hainaut, "TP53 mutations in human cancers: origins, consequences, and clinical use," *Cold Spring Harbor Perspectives in Biology*, vol. 2, no. 1, article a001008, 2010.

[32] Z. Qiu, N. L. Oleinick, and J. Zhang, "ATR/CHK1 inhibitors and cancer therapy," *Radiotherapy and Oncology*, vol. 126, no. 3, pp. 450–464, 2018.

[33] D. Thomas, S. Sagar, X. Liu et al., "Isoforms of MUC16 activate oncogenic signaling through EGF receptors to enhance the progression of pancreatic cancer," *Molecular Therapy*, vol. 29, no. 4, pp. 1557–1571, 2021.

[34] T. Einama, Y. Yamagishi, Y. Takihata et al., "Co-expression of mesothelin and CA125/MUC16 is a prognostic factor for breast cancer, especially in luminal-type breast cancer patients," *Biomarker Research*, vol. 9, no. 1, p. 78, 2021.

[35] X. Xiang, M. Feng, M. Felder et al., "HN125: a novel immunoadhesin targeting MUC16 with potential for cancer therapy," *Journal of Cancer*, vol. 2, pp. 280–291, 2011.

[36] R. Pandey, M. Zhou, Y. Chen et al., "Molecular pathways associated with Kallikrein 6 overexpression in colorectal cancer," *Genes (Basel)*, vol. 12, no. 5, p. 749, 2021.

[37] K. Björkman, H. Mustonen, T. Kaprio et al., "CA125: a superior prognostic biomarker for colorectal cancer compared to CEA, CA19-9 or CA242," *Tumour Biology*, vol. 43, no. 1, pp. 57–70, 2021.

Hindawi
Disease Markers
Volume 2022, Article ID 3144742, 8 pages
https://doi.org/10.1155/2022/3144742

Research Article

The Landscape of Early Growth Response Family Members 1-4 in Hepatocellular Carcinoma: Their Biological Roles and Diagnostic Utility

Jinlong Liang,[1] **Jingyi Wang**,[2] **Jinshui Zeng**,[1] **Zhibo Bai**,[1] **Zhiyuan Zheng**,[1] **Yue Zheng**,[1] **Fengqi Jiang**,[3] **and Di Wu**[3]

[1]*Department of General Surgery, Xiamen Fifth Hospital, Xiamen, China*
[2]*Medical Department, Xiamen Fifth Hospital, Xiamen, China*
[3]*Department of General Surgery, Heilongjiang Provincial Hospital, Harbin, China*

Correspondence should be addressed to Jinlong Liang; liang111@163.com, Fengqi Jiang; 15945684810@163.com, and Di Wu; wudi0629@126.com

Received 18 June 2022; Revised 27 July 2022; Accepted 29 July 2022; Published 22 August 2022

Academic Editor: Fu Wang

The incidence of hepatocellular carcinoma (HCC), which is one of the most frequent types of cancer seen all over the world, is steadily growing from year to year. EGR genes are members of the early growth response (EGR) gene family. It has been shown that EGR genes play an increasingly essential role in the development of tumors and the progression of numerous malignancies. However, the possible diagnostic and prognostic roles of EGR genes in HCC have only been examined in a limited number of studies. Expression and methylation data on EGR family members were obtained from TCGA datasets. The prognostic values of EGR members were studied. Additionally, the correlations of EGR members with immune cells were assessed through the single-sample gene set enrichment analysis (ssGSEA). In this study, we found that the expression of EGR1, EGR2, EGR3, and EGR4 was distinctly decreased in HCC specimens compared with nontumor specimens. ROC assays confirmed that they have a strong ability in screening HCC specimens from nontumor specimens. According to the findings of Pearson's correlation, EGR1, EGR2, EGR3, and EGR4 were found to have a negative association with the methylation level. Survival study revealed that EGR1, EGR2, and EGR3 were associated with the clinical outcome of HCC patients. Immune cell enrichment analysis demonstrated that the expressions of all EGR members were positively related to the levels of most types of immune cells, such as macrophages, NK cells, B cells, T cells, eosinophils, and CD8 T cells. Overall, the current work demonstrated the expression mode and prognostic value of EGR members in HCC in a comprehensive manner, offering insights for further research of the EGR family as possible clinical biomarkers in HCC.

1. Introduction

Hepatocellular carcinoma (HCC) is a highly predominant malignancy with high mortality, and its incidence has continued to increase worldwide [1]. HCC falls within the category of heterogeneous diseases, and its development is frequently brought on by a number of different etiologies, such as the hepatitis B virus, metabolic syndrome, and long-term usage of alcohol [2, 3]. Despite the fact that many different therapeutic treatments have been applied over the past few years, HCC is still responsible for over 60,000 fatalities and nearly 750,000 diagnoses annually [4, 5]. The poor prognosis of HCC is mostly attributable to the cancer's tendency to spread rapidly inside the liver and to spread to other organs [6, 7]. Few particular biomarkers have been developed and made available for clinical application in diagnosis and prognosis up until this point. Thus, the development of novel biomarkers that have the capability of predicting the outcome of HCC patients is an absolute necessity.

A family of zinc-finger transcription factors called immediate-early gene (IEG) zinc-finger transcription factors is made up of the early growth response (EGR) genes: EGR1,

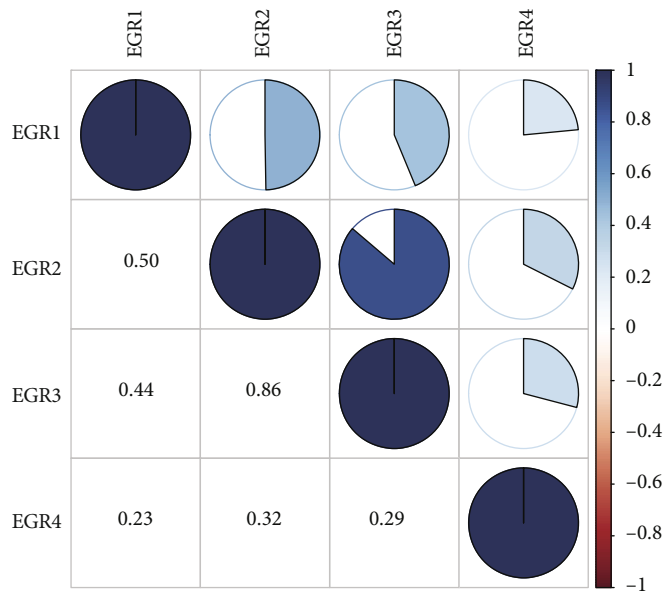

Figure 1: Associations between EGR family members.

EGR2, EGR3, and EGR4 [8]. IEGs exhibit high amounts of messenger ribonucleic acid (mRNA) transcription within thirty to forty-five minutes of being stimulated, which satisfies the criteria of the term "rapidly activated in response to a stimulus." [9, 10]. The EGR proteins operate as transcription factors, binding to DNA to control the expression of a large number of genes that are downstream. It is likely that the potential targeting genes play an important role played by EGRs in a variety of biological processes, including memory formation and reconsolidation, synaptic plasticity, inflammation, vascularization, myelination, and growth factor regulation [11, 12]. As a tumor-inhibitor factor, EGR1 exhibited a dysregulated level in several types of tumors [13, 14]. The regulation of the transcription of the heparin enzyme is one of the biological roles that EGR1 performs in tumor cells. Depending on the type of tumor, EGR1 can either play an inhibitory role or an activating role [15]. Lei et al. reported that through the epigenetically mediated silence of DKK1 and the modulation of the Wnt/-catenin pathway, the EGR1-induced overexpression of the lncRNA FOXD2-AS1 contributed to the advancement of hepatocellular carcinoma [16]. In addition to this, researchers have found that EGR2 is only weakly expressed in HCC, and that it can prevent HCC cells from growing, migrating, and invading other cells. This suggests that EGR2 may have an anticancer effect [17]. It was found that the expressions of EGR3 were typically suppressed in HCC specimens and cells. Through the overexpression of Fas ligand, the ectopic expression of EGR3 was able to contribute to the suppression of cell growth and the induction of apoptosis in HCC cells [18]. Similarly, it was also widely reported that EGR4 was implicated in the advancement of a number of different cancers [19, 20]. Based on these findings, EGR members are likely to be crucial regulators in the growth of tumors.

The genetic map of HCC has continued to advance thanks to the discovery of genomics, which has enabled these advancements. Nevertheless, there is a pressing need to find effective gene therapy targets for HCC. Based on recently updated public resources and bioinformatics assays, the expressing profiles and diagnostic values of the EGR family members were exhaustively evaluated in this study.

2. Materials and Methods

2.1. Data Collection. Both the clinical messages and the gene expression data from the TCGA website (https://portal.gdc.cancer.gov/) were retrieved. The gene expression data were of the form of level 3 RNA-seq FPKM dataset. There were a total of 374 cases of HCC and 50 cases of normal tissue that were downloaded and evaluated.

2.2. Comparison of Expressions of the EGR Family in HCC and Nontumor Tissues. The expressions of the EGR family were determined using the HTSeq level 3 data on the genome mRNA expression by the use of the software Perl 5.26. The limma package found in *R* 3.6.0 software was used for the analysis of the differential expressions of members of the EGR family in HCC samples in comparison to nontumor samples. The pheatmap program was applied in order to create a visual representation of the results.

2.3. Correlations between mRNA Expressions and Methylation of the EGR Members in HCC. We downloaded data from Illumina Human Methylation 450 K using the GDC Data Transfer Tool, which was approved by TCGA. The data concerned the methylation levels of cg sites in the gene promoter regions of differentially expressed EGR members in HCC tissues. Following that, we made use of the corrplot software to conduct additional research into the relationship between methylation and EGR expressions in HCC. An annotation was performed on the data obtained from

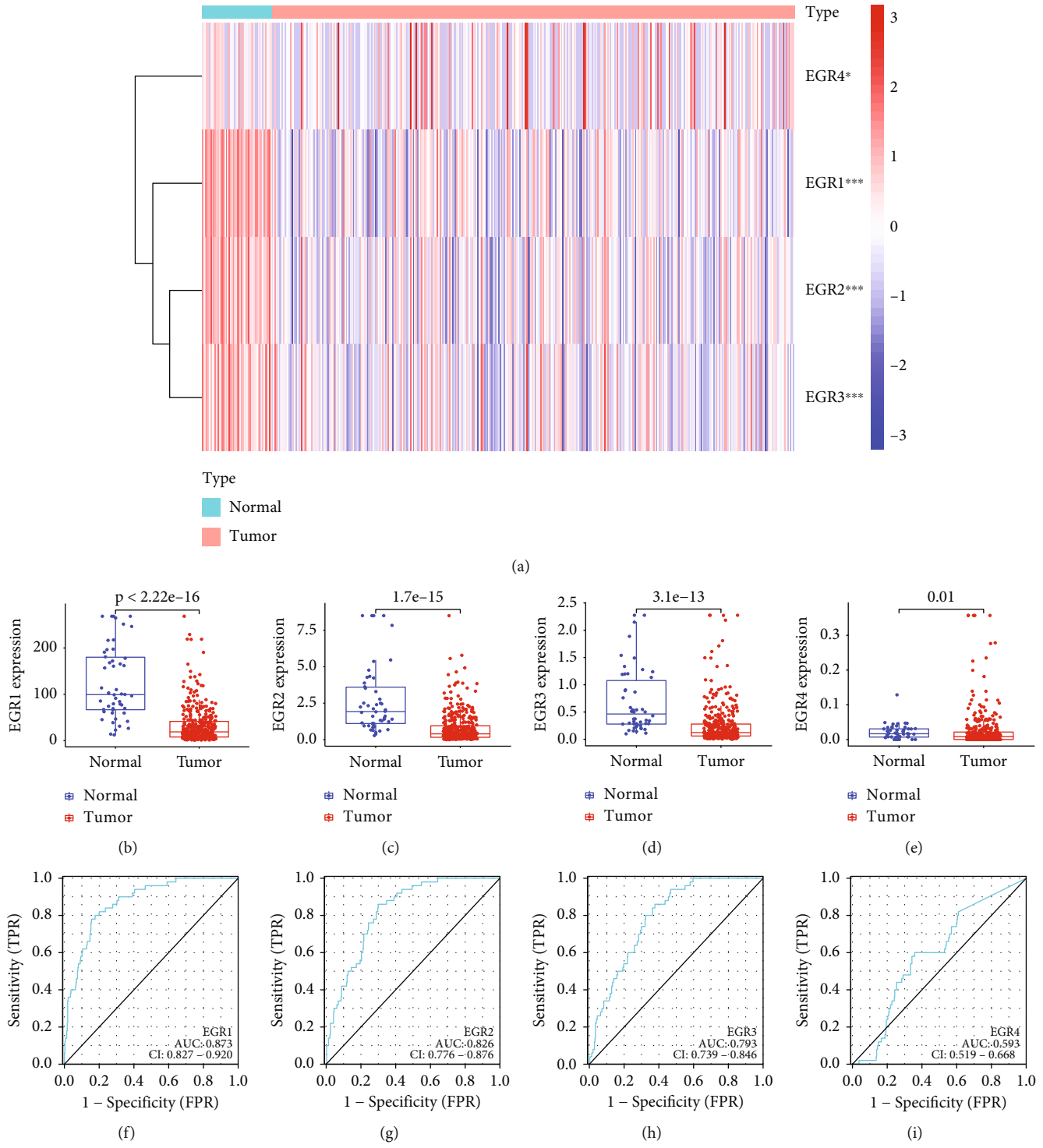

Figure 2: Identification of the dysregulated EGR family members in HCC and their diagnostic value. (a) Heat map showing the expressing pattern of EGR family members between HCC specimens and nontumor specimens. (b)–(e) The expression of EGR1, EGR2, EGR3, and EGR4 was distinctly decreased in HCC specimens compared with nontumor specimens. (f)–(i) The diagnostic value of EGR1, EGR2, EGR3, and EGR4 in screening HCC specimens from normal specimens using ROC analysis.

Illumina Human Methylation 450 K using the annotation file that can be found on the official Illumina website.

2.4. Receiver Operating Characteristic (ROC) Curve Analysis. We determined the diagnostic value of the expressions of EGR members in distinguishing HCC patients by performing a receiver operating curve (ROC) analysis. This allowed us to examine the area under the curve (AUC) value as well as a cutoff value according to the maximum of the Youden index. Finally, we determined the diagnostic value of the

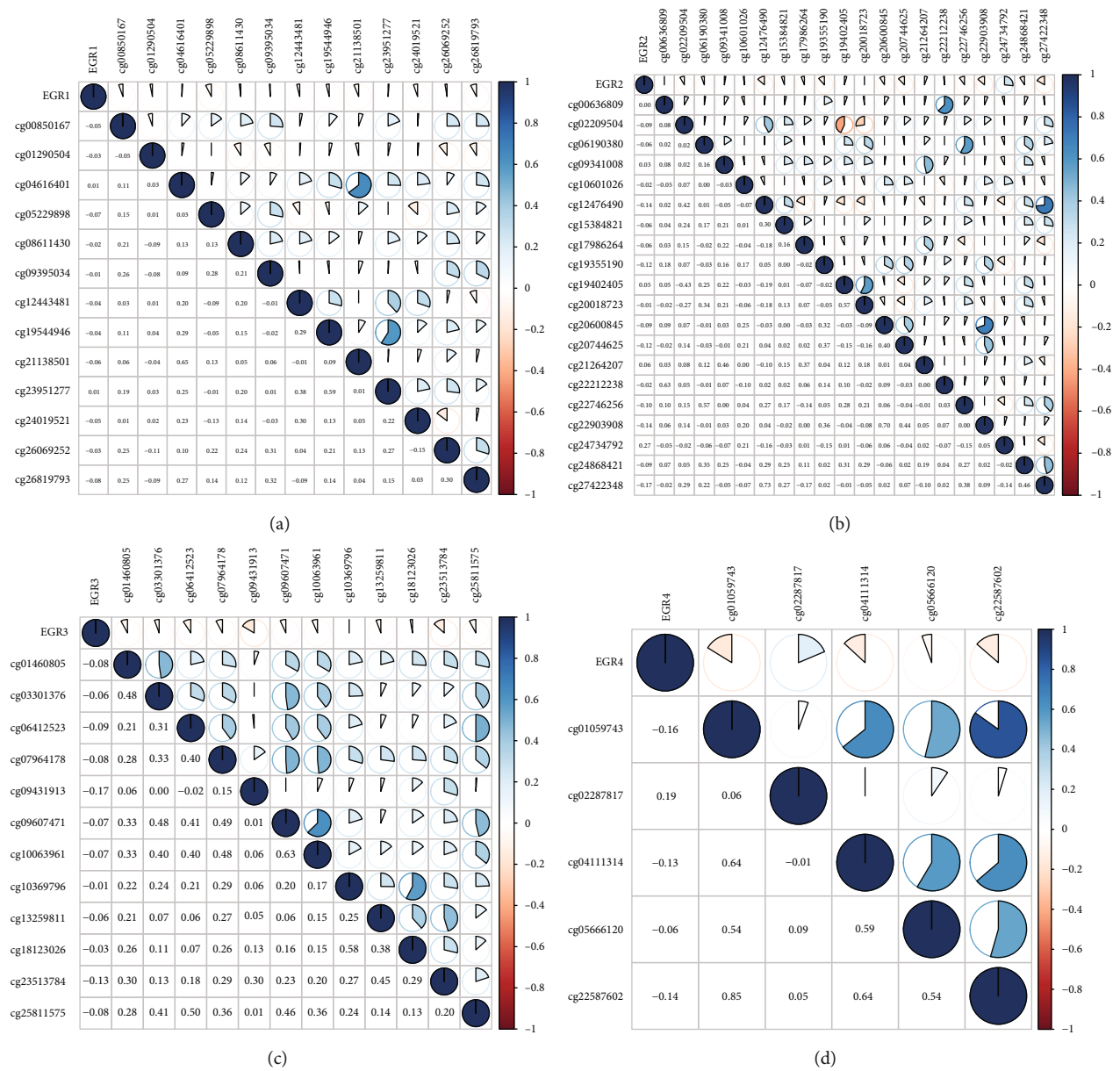

Figure 3: Pearson's correlation between methylation levels and expressions of (a) EGR1, (b) EGR2, (c) EGR3, and (d) EGR4. There was a negative association between the expression level of EGR members and their methylation status in HCC.

expressions of EGR members. The definition of the Youden index is sensitivity plus specificity minus one.

2.5. Computational Deconvolution of Infiltrating Immune Cells. We performed the deconvolution analysis using single sample gene set enrichment analysis (ssGSEA) to infer the presence in TCGA-LIHC in order to examine the correlations of the infiltrating immune cell subsets in HCC samples with the expressions of the EGR family. Our goal was to determine whether or not there was a relationship between the two. Spearman's correlation coefficient was used to analyze the associations between the expressions of EGR family members and the abundance scores of immune cells.

2.6. Statistical Analysis. All statistical analyses were carried out using *R* 3.6.1 software. $p < 0.05$ was regarded as statistically significant.

3. Results

3.1. Expression Status of EGR Members and Their Diagnostic Value in HCC Tissues. Firstly, the mRNA expression data on EGR members (EGR 1-4) from 374 HCC and 50 normal control samples that were received from TCGA were analyzed with Perl software. These samples came from individuals who had been diagnosed with cancer. Pearson's correlation of EGR family genes was determined, and the corrplot software was used to determine whether or not

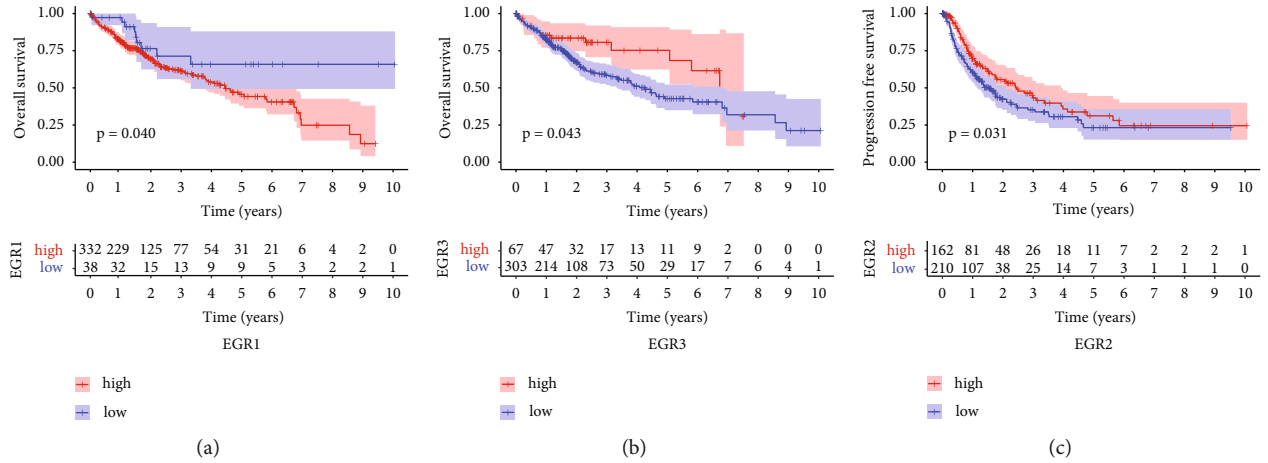

Figure 4: Kaplan-Meier curves estimating the prognostic value of (a) EGR1, (b) EGR3, and (c) EGR2 in patients with HCC.

these genes were connected with each other. Figure 1 demonstrates that there was a meaningful degree of correlation between the genes in the EGR family.

As exhibited in Figure 2(a), the limma program was applied to evaluate the differentially expressed EGR members, and the pheatmap tool was applied to illustrate the results. We found that the expression of EGR1, EGR2, EGR3, and EGR4 was distinctly decreased in HCC specimens compared with nontumor specimens (Figures 2(b)–2(e)). Then, we explored whether the levels of EGR members had a diagnostic potential. The results of the ROC tests indicated that the low EGR1 expression had an AUC value of 0.873 (95 percent confidence interval: 0.827 to 0.920) for HCC (Figure 2(f)). The low EGR2 expression resulted in an AUC value of 0.826 for HCC, with a 95% confidence interval ranging from 0.776 to 0.876 (Figure 2(g)). The low EGR3 expression resulted in an AUC value of 0.793 for HCC, with a 95% confidence interval ranging from 0.739 to 0.846 (Figure 2(h)). The low EGR4 expression resulted in an AUC value of 0.593 for HCC, with a 95% confidence interval ranging from 0.519 to 0.668 (Figure 2(i)). According to our findings, EGR1, EGR2, and EGR3 could be potential diagnostic criteria for HCC.

3.2. Correlation of EGR Expression and Methylation in HCC. One of the most prevalent ways that genes are controlled is through a process known as methylation of their promoter regions. We identified four differentially expressed EGR members in HCC, and they are distinct lowly expressed in HCC specimens. According to the findings of Pearson's correlation, EGR1, EGR2, EGR3, and EGR4 were found to have a negative association with the methylation level (Figures 3(a)–3(d)). According to these findings, there was a negative association between the expression level of EGR members and their methylation status in HCC.

3.3. The Prognostic Value of EGR Members in HCC Patients. Kaplan-Meier methods were utilized so that we could investigate the clinical importance of EGR members in HCC patients. As can be seen in Figure 4(a), we found that patients with high EGR1 expression levels displayed lower overall survival rates than patients with low EGR1 expression levels ($p = 0.040$). On the other hand, a high expressions of EGR3 were related to a prolonged overall survival in HCC patients (Figure 4(b)). In addition, our research revealed that individuals with HCC who had low EGR2 expression had a progression-free survival rate that was much lower ($p = 0.0031$, Figure 4(c)). According to the results of our research, EGR1, EGR2, and EGR3 have the potential to serve as a prognostic biomarker for patients with HCC.

3.4. Correlation between EGR Members and Tumor Immune Infiltrating Cells. We used ssGSEA to investigate the potential immunomodulatory mechanism of EGR members in the regulation of tumor-infiltrating immune cells. Specifically, we were interested in determining whether or not there was a relationship between the expressions of EGR members in TCGA HCC samples and immune infiltrating cells. The data revealed that the expressions of EGR were positively related to the levels of Idc, Tem, macrophages, Th1 cells, NK cells, B cells, T cells, eosinophils, CD8 T cells, T helper cells, neutrophils, TFH, mast cells, DC, NK CD56bright cells, Tcm, cytotoxic cells, aDC, and NK CD56dim cells (Figure 5(a)). The expression of EGR2 was positively correlated with the expression levels of macrophages, Th1 cells, iDC, Tem, TFH, NK cells, B cells, T cells, T helper cells, mast cells, neutrophils, aDC, eosinophils, CD8 T cells, Th2 cells, NK CD56dim cells, NK CD56bright cells, DC, cytotoxic cells, Tgd, Tcm, and pDC (Figure 5(b)). In a manner parallel to this, we discovered that the expression of EGR3 and EGR was favorably related with the majority of different types of immune cells (Figures 5(c) and 5(d)).

4. Discussion

Immunotherapy, gene therapy, and molecular targeted therapy are just some of the cutting-edge therapeutic options that are now being researched and developed for HCC [21, 22]. Despite this, the outcomes for patients with HCC remain dismal because there are currently no effective therapeutic approaches [23]. A comprehensive understanding of

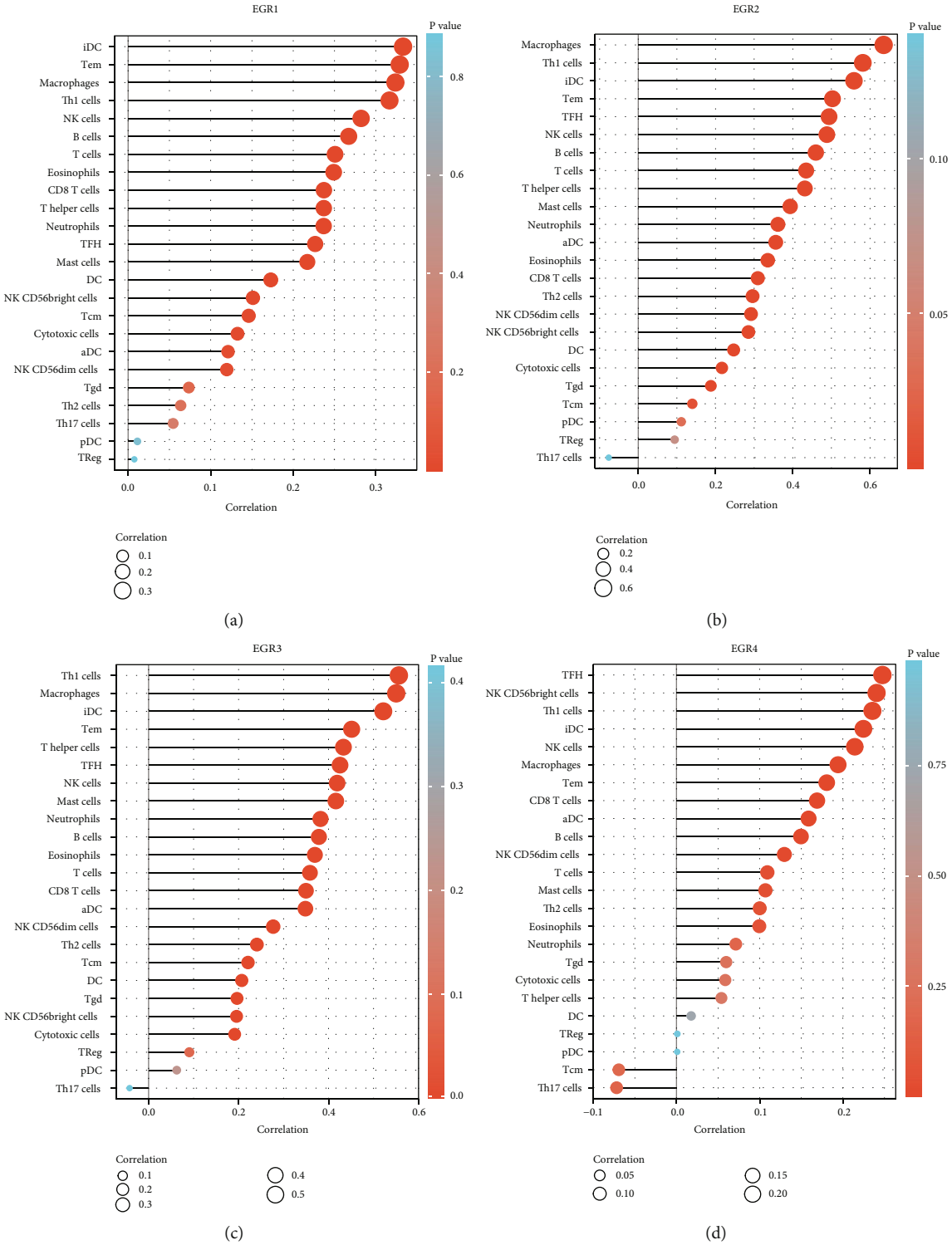

Figure 5: Correlation between EGR family members, including (a) EGR1, (b) EGR2, (c) EGR3, and (d) EGR4, and expression of immune cells (ssGSEA).

the molecular processes underlying tumor genesis and progression is necessary for the development of novel prognostic and therapeutic strategies with the goal of improving the prognosis of patients diagnosed with HCC.

Members of the EGR family are garnering an increasing amount of interest as a result of the significant roles they play in cancer [24]. According to accumulating evidence, the EGR family proteins act as tumor suppressor or oncoprotein regulators to control the growth and migration of cells as well as the metabolic process [25, 26]. This and other biological processes like autophagy and their abnormal expression have been confirmed in a variety of cancers. Even

though a number of studies have found that members of the EGR family demonstrate dysregulation in HCC, the diagnostic and prognostic relevance of these genes has only rarely been investigated. In this study, to our knowledge, this is the first time that a complete examination of EGR family members based on TCGA datasets has been carried out. We showed that the expression of EGR1, EGR2, EGR3, and EGR4 was significantly lowered in HCC specimens in comparison to nontumor specimens, which suggested that members of the EGR family may serve as a tumor suppressor in the progression of HCC. In addition, ROC assays validated their diagnostic utility by demonstrating that they can distinguish HCC specimens from nontumor tissues. In addition, the EGR1 and EGR3 expression was related with overall survival in HCC patients, whereas the EGR2 expression was connected with progression-free survival in patients with HCC. Our findings were consistent with previous studies.

DNA methylation (DNAm) is one of the epigenetic processes that occurs most frequently [27]. It entails the reversible addition of a methyl group, most frequently to cytosines in the context of CpG dinucleotides, but it does not alter the DNA sequences of the genome [28, 29]. When it comes to cancer diagnosis, the methylation status of DNA is, in general, more trustworthy than the gene expression. In addition, DNA methylation, which serves as the fundamental component of epigenetic changes, plays an important part in the control of cellular processes as well as the development of cancer [30, 31]. Epigenetic modifications in DNA methylation were shown to be relevant to the progression and metastasis of HCC in an increasing number of studies. According to Pearson's correlation, among the four differentially expressed EGR members (EGR1, EGR2, EGR3, and EGR4), the methylation level influences the majority of expression levels, particularly with regard to EGR1 and EGR3. These findings were consistent with earlier researches that demonstrated an inverse relationship between the methylation of EGR and its expression in patients diagnosed with HCC.

Within the immune microenvironment, stromal cells have the ability to alter the carcinogenic properties of tumor cells [32, 33]. Tumor-infiltrating lymphocytes (TILs) are one type of immune cell that plays a significant part in the genesis and progression of cancerous growths [34, 35]. TILs help develop and sustain an immunosuppressive milieu, facilitate immune escape, and ultimately contribute to the progression of tumors by establishing a complex intercellular interaction network [36, 37]. In this study, we discovered that the expression of EGR4, EGR3, EGR2, and EGR1 was positively associated with the expression of a large number of immune cells, which suggested that the enhancement of innate immunity was accompanied by a reduction in adaptive immunity. Additionally, in the tumor microenvironment, invading NK cells and TAMs have high immunosuppressive activities, which decreased the release of IFN- and promotes malfunction in T cells [38]. More and more evidences have confirmed that the existence of gene indicators for CD8 T cells and T helper 1 cells contributes to favorable long-term survivals [39, 40]. Taken together, according to the results of our research, EGR4, EGR3, EGR2, and EGR1 may play an important part in the TME and TICs, and they were strongly associated with immune regulation and the change of the TME.

There are several drawbacks to our study. This study is limited since it is retrospective; hence, there are no data from prospective real-world studies included in it. Second, basic experimental researches were not performed to expand on the results.

5. Conclusion

This was the first and most extensive examination of the expressing profiles and clinical importance of EGR members in HCC cases. Our findings could offer a clinically valuable tool for early detection and better prognostic care as well as optimizing the immunotherapy that is related with HCC patients.

Data Availability

The data used to support the findings of this study are available from the corresponding authors upon request.

Conflicts of Interest

The authors have no conflicts of interest to declare.

Authors' Contributions

Jinlong Liang and Jingyi Wang contributed equally to this work as co-first authors.

Acknowledgments

This work was supported by the Fujian Provincial Department of Science and Technology Guidance Program (No. 2021D011, No. 2022D033), Xiamen Health Care Guidance Program (No. 3502Z20214ZD1255), and Scientific Research Project of Heilongjiang Provincial Health Commission (No. 20210404080106).

References

[1] R. L. Siegel, K. D. Miller, and A. Jemal, "Cancer statistics, 2020," *CA: a Cancer Journal for Clinicians*, vol. 70, no. 1, pp. 7–30, 2020.

[2] F. Piñero, M. Dirchwolf, and M. G. Pessôa, "Biomarkers in hepatocellular carcinoma: diagnosis, prognosis and treatment response assessment," *Cell*, vol. 9, no. 6, article 1370, 2020.

[3] A. Villanueva, "Hepatocellular Carcinoma," *The New England Journal of Medicine*, vol. 380, no. 15, pp. 1450–1462, 2019.

[4] S. Yang, J. Wang, S. Wang, A. Zhou, G. Zhao, and P. Li, "Roles of small extracellular vesicles in the development, diagnosis and possible treatment strategies for hepatocellular carcinoma (review)," *International Journal of Oncology*, vol. 61, no. 2, 2022.

[5] G. Testino, S. Leone, V. Patussi, E. Scafato, and P. Borro, "Hepatocellular carcinoma: diagnosis and proposal of treatment," *Minerva Medica*, vol. 107, no. 6, pp. 413–426, 2016.

[6] D. Arif, T. Mettler, and O. A. Adeyi, "Mimics of hepatocellular carcinoma: a review and an approach to avoiding histopathological diagnostic missteps," *Human Pathology*, vol. 112, pp. 116–127, 2021.

[7] T. Flecken, H. C. Spangenberg, and R. Thimme, "Immunobiology of hepatocellular carcinoma," *Langenbeck's Archives of Surgery*, vol. 397, no. 5, pp. 673–680, 2012.

[8] C. K. Go, S. Gross, R. Hooper, and J. Soboloff, "EGR-mediated control of STIM expression and function," *Cell Calcium*, vol. 77, pp. 58–67, 2019.

[9] B. Wang, H. Guo, H. Yu, Y. Chen, H. Xu, and G. Zhao, "The role of the transcription factor EGR1 in cancer," *Frontiers in Oncology*, vol. 11, article 642547, 2021.

[10] A. M. Beckmann and P. A. Wilce, "Egr transcription factors in the nervous system," *Neurochemistry International*, vol. 31, no. 4, pp. 477–510, 1997, discussion 517-6.

[11] Y. Ying, X. Ma, J. Fang et al., "EGR2-mediated regulation of m^6A reader IGF2BP proteins drive RCC tumorigenesis and metastasis via enhancing S1PR3 mRNA stabilization," *Cell Death & Disease*, vol. 12, no. 8, p. 750, 2021.

[12] Y. Kwon, M. Kim, Y. Kim, M. S. Jeong, H. S. Jung, and D. Jeoung, "EGR3-HDAC6-IL-27 Axis mediates allergic inflammation and is necessary for tumorigenic potential of cancer cells enhanced by allergic inflammation-promoted cellular interactions," *Frontiers in Immunology*, vol. 12, article 680441, 2021.

[13] L. Li, A. H. Ameri, S. Wang et al., "EGR1 regulates angiogenic and osteoclastogenic factors in prostate cancer and promotes metastasis," *Oncogene*, vol. 38, no. 35, pp. 6241–6255, 2019.

[14] S. K. Saha, S. M. R. Islam, T. Saha et al., "Prognostic role of EGR1 in breast cancer: a systematic review," *BMB Reports*, vol. 54, no. 10, pp. 497–504, 2021.

[15] H. Guo and L. Zhang, "EGR1/2 inhibits papillary thyroid carcinoma cell growth by suppressing the expression of PTEN and BAX," *Biochemical Genetics*, vol. 59, no. 6, pp. 1544–1557, 2021.

[16] T. Lei, X. Zhu, K. Zhu, F. Jia, and S. Li, "EGR1-induced upregulation of lncRNA FOXD2-AS1 promotes the progression of hepatocellular carcinoma via epigenetically silencing DKK1 and activating Wnt/β-catenin signaling pathway," *Cancer Biology & Therapy*, vol. 20, no. 7, pp. 1007–1016, 2019.

[17] T. Zeng, D. Wang, J. Chen et al., "LncRNA-AF113014 promotes the expression of Egr2 by interaction with miR-20a to inhibit proliferation of hepatocellular carcinoma cells," *PLoS One*, vol. 12, no. 5, article e0177843, 2017.

[18] S. Zhang, C. Xia, C. Xu et al., "Early growth response 3 inhibits growth of hepatocellular carcinoma cells via upregulation of Fas ligand," *International Journal of Oncology*, vol. 50, no. 3, pp. 805–814, 2017.

[19] X. Gong, L. Zou, M. Wang et al., "Gramicidin inhibits cholangiocarcinoma cell growth by suppressing *EGR4*," *Artificial Cells, Nanomedicine, and Biotechnology*, vol. 48, no. 1, pp. 53–59, 2020.

[20] J. Mookerjee-Basu, R. Hooper, S. Gross et al., "Suppression of Ca2+signals byEGR4 controls Th1 differentiation and anticancer immunityin vivo," *EMBO Reports*, vol. 21, no. 5, article e48904, 2020.

[21] B. Ruf, B. Heinrich, and T. F. Greten, "Immunobiology and immunotherapy of HCC: spotlight on innate and innate-like immune cells," *Cellular & Molecular Immunology*, vol. 18, no. 1, pp. 112–127, 2021.

[22] Y. Zongyi and L. Xiaowu, "Immunotherapy for hepatocellular carcinoma," *Cancer Letters*, vol. 470, pp. 8–17, 2020.

[23] Y. Jiang, Q. J. Han, and J. Zhang, "Hepatocellular carcinoma: mechanisms of progression and immunotherapy," *World Journal of Gastroenterology*, vol. 25, no. 25, pp. 3151–3167, 2019.

[24] M. H. Chien, W. J. Lee, Y. C. Yang et al., "KSRP suppresses cell invasion and metastasis through miR-23a-mediated EGR3 mRNA degradation in non-small cell lung cancer," *Biochimica et Biophysica Acta (BBA) - Gene Regulatory Mechanisms*, vol. 2017, pp. 1013–1024, 2017.

[25] K. Morita, T. Okamura, S. Sumitomo, Y. Iwasaki, K. Fujio, and K. Yamamoto, "Emerging roles of Egr2 and Egr3 in the control of systemic autoimmunity," *Rheumatology*, vol. 55, Supplement 2, pp. ii76–ii81, 2016.

[26] S. H. Shin, I. Kim, J. E. Lee, M. Lee, and J. W. Park, "Loss of _EGR3_ is an independent risk factor for metastatic progression in prostate cancer," *Oncogene*, vol. 39, no. 36, pp. 5839–5854, 2020.

[27] L. D. Moore, T. Le, and G. Fan, "DNA methylation and its basic function," *Neuropsychopharmacology*, vol. 38, no. 1, pp. 23–38, 2013.

[28] S. Horvath and K. Raj, "DNA methylation-based biomarkers and the epigenetic clock theory of ageing," *Nature Reviews. Genetics*, vol. 19, no. 6, pp. 371–384, 2018.

[29] H. Hashimoto, P. M. Vertino, and X. Cheng, "Molecular coupling of DNA methylation and histone methylation," *Epigenomics*, vol. 2, no. 5, pp. 657–669, 2010.

[30] M. Kulis and M. Esteller, "DNA methylation and cancer," *Advances in Genetics*, vol. 70, pp. 27–56, 2010.

[31] A. Koch, S. C. Joosten, Z. Feng et al., "Analysis of DNA methylation in cancer: location revisited," *Nature Reviews. Clinical Oncology*, vol. 15, no. 7, pp. 459–466, 2018.

[32] T. F. Gajewski, H. Schreiber, and Y. X. Fu, "Innate and adaptive immune cells in the tumor microenvironment," *Nature Immunology*, vol. 14, no. 10, pp. 1014–1022, 2013.

[33] Z. E. Stine, Z. T. Schug, J. M. Salvino, and C. V. Dang, "Targeting cancer metabolism in the era of precision oncology," *Nature Reviews Drug Discovery*, vol. 21, no. 2, pp. 141–162, 2022.

[34] D. C. Hinshaw and L. A. Shevde, "The tumor microenvironment innately modulates cancer progression," *Cancer Research*, vol. 79, no. 18, pp. 4557–4566, 2019.

[35] C. M. Laumont, A. C. Banville, M. Gilardi, D. P. Hollern, and B. H. Nelson, "Tumour-infiltrating B cells: immunological mechanisms, clinical impact and therapeutic opportunities," *Nature Reviews Cancer*, vol. 22, no. 7, pp. 414–430, 2022.

[36] P. Darvin, S. M. Toor, V. Sasidharan Nair, and E. Elkord, "Immune checkpoint inhibitors: recent progress and potential biomarkers," *Experimental & Molecular Medicine*, vol. 50, no. 12, pp. 1–11, 2018.

[37] D. S. Chen and I. Mellman, "Oncology meets immunology: the cancer-immunity cycle," *Immunity*, vol. 39, no. 1, pp. 1–10, 2013.

[38] S. Gomez, T. Tabernacki, J. Kobyra, P. Roberts, and K. B. Chiappinelli, "Combining epigenetic and immune therapy to overcome cancer resistance," *Seminars in Cancer Biology*, vol. 65, pp. 99–113, 2020.

[39] M. Hofmann, C. Tauber, N. Hensel, and R. Thimme, "$CD8^+$ T cell responses during HCV infection and HCC," *Journal of Clinical Medicine*, vol. 10, no. 5, p. 991, 2021.

[40] B. Tang, J. Zhu, Z. Zhao et al., "Diagnosis and prognosis models for hepatocellular carcinoma patient's management based on tumor mutation burden," *Journal of Advanced Research*, vol. 33, pp. 153–165, 2021.

Hindawi
Disease Markers
Volume 2022, Article ID 1930185, 11 pages
https://doi.org/10.1155/2022/1930185

Research Article

KDELR3 Is a Prognostic Biomarker Related to the Immune Infiltration and Chemoresistance of Anticancer Drugs in Uveal Melanoma

Jingnan Zhang,[1] Juan Zhang,[2] Jing Guan,[2] Lisha Yu,[2] and Shilong Yan[3]

[1]*Department of Pharmacy, Linyi Central Hospital, Linyi, Shandong, China*
[2]*Department of Traditional Chinese Medicine, Qingdao Eighth People's Hospital, Qingdao, Shandong, China*
[3]*Department of Cataract, Jinan Aier Eye Hospital, Jinan, Shandong, China*

Correspondence should be addressed to Shilong Yan; shilongy828@163.com

Received 27 June 2022; Revised 31 July 2022; Accepted 1 August 2022; Published 21 August 2022

Academic Editor: Fu Wang

Uveal melanoma (UM) is an intraocular malignancy in adults in which approximately 50% of patients develop metastatic diseases and have a poor clinical outcome. Immunotherapies are quickly becoming a need, and recent research has produced some amazing achievements in this area. In the current investigation, an attempt was made to evaluate the prognostic usefulness of KDELR3 in UM, particularly its connection with tumor-infiltrating lymphocytes (TILs). The expression patterns of mRNAs and related clinical data of 80 UM patients were obtained from The Cancer Genome Atlas (TCGA). By using RT-PCR, we were able to investigate whether or not UM cells and D78 cells expressed KDELR3. The Kaplan-Meier approach, as well as univariate and multivariate tests, was utilized in order to investigate the potential predictive significance of KDELR3 expression. The associations between KDELR3 and TILs and immunological checkpoints were analyzed in order to evaluate the effect that KDELR3 may have on UM immunotherapy. On the basis of the differential expression of KDELR3, a distribution of the half-maximal inhibitory concentration (IC50) of various targeted medicines was observed. In this study, we found that the expression of KDELR3 was distinctly increased in most types of tumors. In addition, KDELR3 was highly expressed in UM cells. Moreover, patients with high KDELR3 expression exhibited a shorter overall survival and disease-free survival than those with low KDELR3 expression. Multivariate analyses confirmed that KDELR3 expression was an independent prognostic factor for overall survival and disease-free survival in patients with UM. Furthermore, KDELR3 expression was demonstrated to be positively correlated with macrophage M1, T cell CD8, T cell follicular helper, dendritic cell resting, and T cell CD4 memory activated. Meanwhile, the expression of KDELR3 was related to several immune checkpoints. The IC50 of AP-24534, BHG712, bleomycin, camptothecin, cisplatin, cytarabine, GSK1070916, and tipifarnib was higher in the KDELR3 high-expression group. In conclusion, KDELR3 may be applied as a potential diagnostic and prognostic biomarker for UM patients.

1. Introduction

Uveal melanoma (UM) is the most prevalent form of intraocular cancer found in adults around the world [1]. It is a malignant tumor that begins in the melanocytes of the eye's choroid plexus, iris, and ciliary body [2]. The development of early metastases is the primary contributor to the disease' alarmingly high mortality rate [3, 4]. Because the biology behind the beginnings and spread of UM is unknown, there is currently no effective treatment available for patients who have already developed metastatic illness [5, 6]. It is estimated that almost half of UM patients will have further deterioration, and the clinical outcome for the patients remains poor [7]. The use of chemotherapy and targeted therapies typically does not result in the maintenance of long-term tumor control. Thus, immunotherapy is increasingly

emerging as a potentially useful treatment option [8, 9]. Meanwhile, it is essential to investigate potential new prognostic biomarkers or therapeutic targets that are effective.

The KDEL (Lys-Asp-Glu-Leu) receptor family, also known as the KDELR family, is an important protein family that plays a role in recycling the chaperones and maintaining the dynamic balance of trafficking between the Golgi and the endoplasmic reticulum (ER) [10, 11]. Recent researches have shown evidence to imply that KDELRs are essential components of the Golgi transport control mechanism. KDELR is responsible for initiating transport via the Golgi complex after it binds to the heterotrimeric signaling G protein G (q/11), where it then activates the proteins [12, 13]. The third confirmed member of the KDEL family is referred to as KDELR3. KDELR3 expression in arteriosclerosis macrophages might be noticeably different from that in nonarteriosclerosis tissues, and the higher expression level in nonarteriosclerosis tissues, which can be used as a potential predictive factor [14]. In addition, a number of investigations have found that the expression of KDELR3 was markedly aberrant in a variety of malignancies, including hepatocellular carcinoma and prostate adenocarcinoma [15, 16]. However, its expression and clinical significance in UM have not been investigated.

The vast majority of immune system components have been linked to both the beginning and the development of UM [17]. In the context of tumor immunity, tumor cells serve the function of antigens, and immune cells and leukocytes penetrate the tumor tissue via chemotaxis in order to mount an immunological defense [18, 19]. In addition, immune evasion is a significant contributor to the development of tumors. At the moment, a wide variety of novel immunotherapies are being utilized in UM, some of which are PD-1, PD-L1, and CTLA-4 inhibitors [20–22]. However, these methods are only useful for a small number of individuals, and the vast majority of patients have either a limited or nonexistent response to the treatment, particularly when the UM is in a more advanced stage. Therefore, in order to investigate the potential diagnostic application of new biomarkers, it is necessary to perform exhaustive studies on the association that exists between key genes and overall survival in UM.

In the present investigation, we began by conducting pan-cancer assays, and we discovered that the level of KDELR3 was noticeably elevated in the majority of different kinds of cancers. After that, we discovered that the level of KDELR3 expression was considerably elevated in UM cells. In addition, we investigated the expression of KDELR3 in UM and investigated the connection between the level of KDELR3 expression and the prognosis of patients with UM. Finally, exhaustive bioinformatics studies were carried out in order to investigate the underlying mechanisms of KDELR3. This study contributes to the following individualized diagnosis and treatment of UM by providing relevant information.

2. Materials and Methods

2.1. Cell Lines and Culture. The uveal melanoma cell lines (MUM-2C, OCM-1A, MUM-2B, and C918) and one melanocyte cell line (D78) were purchased from purchase Chinese Academy of Sciences (Beijing, China). DMEM was used as the medium for the cultivation of D78, OCM-1A, and MUM-2C, while RPMI 1640 was utilized for the upkeep of C918 and MUM-2B.

2.2. RNA Isolation and RT-PCR. Extraction of total RNAs from grown cells was carried out using TRIzol (Life Technologies) in accordance with the procedure provided by the manufacturer. cDNAs were reverse transcribed using HiScript III Reverse Transcriptase (Vazyme) using oligo (dT) and random hexamers, then qRT-PCR analysis was performed on them, and then they were put through PCR and qPCR analysis. Real-time quantitative PCR was carried out using ChamQ SYBR qPCR Master Mix (Vazyme) and either a 7900HT Fast Real-Time PCR System or an ABI Prism 7900HT Real-Time PCR System (Applied Biosystems). The relative expression of genes was quantified to GAPDH. The primer sequences were presented as follows: KDELR3 5′-TCCCAGTCATTGGCCTTTCC-3′ (forward) and 5′-CCAGTTAGCCAGGTAGAGTGC-3′ (reverse) and GAPDH 5′-GGAGCGAGATCCCTCCAAAAT-3′ and 5′-GGCTGTTGTCATACTTCTCATGG-3′.

2.3. Data Resource and Preprocessing. The GDC Data Transfer Tool was used to retrieve the RNA expression profiles of 80 UM patients from TCGA database in FPKM format. In addition, mRNA and lncRNA expression data were also retrieved. On the UCSC Xena website, the pertinent clinicopathological characteristics, such as sex, age, and cancer stage, were retrieved. Table 1 contains an in-depth presentation of the clinical features.

2.4. Functional Enrichment Analysis. We separated the samples from TCGA datasets into two groups based on the median expression level of KDELR3 and screened the dysregulated genes between the two groups using the "limma" program [23]. This was done so that we could gain a deeper understanding of the underlying mechanism of KDELR3. Then, we examined the genes in the two groups using the Gene Ontology (GO) and the Kyoto Encyclopedia of Genes and Genomes (KEGG) assays to see if they were abundant in significant biological processes. Then, we used the "http://org.Hs.eg.db" package to convert the gene symbols into Entrez IDs, and we used the "cluster Profiler," "ggplot2," and "enrich plot" packages to conduct a pathway enrichment analysis for the DEGs based on the GO database and KEGG. This was done by combining the results of the pathway enrichment analysis with the DEGs. After applying the false discovery rate (FDR) approach, the P values were recalculated, and significantly enriched pathways were determined to have an FDR of 0.25 or lower.

2.5. Tumor-Infiltrating Immune Cells (TICs) Profile. Using the LM22 signature, the CIBERSORT algorithm was utilized to conduct an analysis of the percentage of immune cells that had penetrated the tumor microenvironment (TME) [24]. The LM22 signature, which consists of 547 genes, was utilized to detect 22 different types of immune cells that had

Table 1: Correlation between tissue KDELR3 expression level and clinicopathological characteristics.

Characteristic	Low expression of KDELR3	High expression of KDELR3	p
n	40	40	
Pathologic T stage, n (%)			0.644
T2	8 (10%)	6 (7.5%)	
T3	17 (21.2%)	15 (18.8%)	
T4	15 (18.8%)	19 (23.8%)	
Pathologic N stage, n (%)			0.579
N0	28 (35.4%)	24 (30.4%)	
NX	12 (15.2%)	15 (19%)	
Pathologic M stage, n (%)			0.128
M0	28 (35.9%)	23 (29.5%)	
M1	0 (0%)	4 (5.1%)	
MX	12 (15.4%)	11 (14.1%)	
Pathologic stage, n (%)			0.113
Stage II	22 (27.8%)	17 (21.5%)	
Stage III	18 (22.8%)	18 (22.8%)	
Stage IV	0 (0%)	4 (5.1%)	
Gender, n (%)			1.000
Female	17 (21.2%)	18 (22.5%)	
Male	23 (28.7%)	22 (27.5%)	
Age, n (%)			0.502
≤60	22 (27.5%)	18 (22.5%)	
>60	18 (22.5%)	22 (27.5%)	
Age, mean ± SD	57.95 ± 14.03	65.35 ± 13	0.017

infiltrated the tissue. In addition, we investigated the difference between KDELR3 expression and the immune cells that had penetrated the TME by performing difference and correlation analysis.

2.6. Correlation Analysis. The Cancer Regulome Explorer (http://explorer.cancerregulome.org/) enables users to search, filter, and visualize analytical results generated from TCGA data and explore associations among heterogeneous features. On the chromosomal level, we utilized it to display the expression of KDELR3 as well as its association with other variables that are associated with malignancies. In order to investigate the degree of association that exists between KDELR3 and immunological checkpoints, a Pearson's analysis was carried out. The "pheatmap" tool in R was used to present the results of the analysis.

2.7. IC50 Score. When determining the efficacy of a medicine or the response of a sample to treatment, one of the most essential indicators to look at is the half-maximal inhibitory concentration, also known as the IC50. The sample-based transcriptome, which makes use of the Genomics of Drug Sensitivity in Cancer (GDSC) database, which is the biggest publicly available pharmacogenomics resource, can predict the response of each sample to the targeting and/or immunotherapy of UM.

2.8. Statistical Analysis. Statistical analysis was performed in R v. 4.0.2 (R Core Team, Massachusetts, USA) and GraphPad Prism v. 8.01 (GraphPad Software, La Jolla, CA, USA). The Wilcoxon rank-sum test was utilized in order to carry out analyses on box plots. Spearman's coefficient was utilized in order to carry out the correlation study. In order to investigate the nature of the connection that exists between KDELR3 expression levels and clinicopathological characteristics, both the chi-square and t-tests were carried out. The Kaplan-Meier method was utilized in the construction of the survival curves (log-rank test). Survival data were evaluated through the univariate and multivariate Cox regression analysis. A $p < 0.05$ was deemed to be statistically significant.

3. Results

3.1. The mRNA Expression of KDELR3 in Cancers. In order to determine whether or not KDELR3 expression was correlated with cancer, we analyzed its levels in a variety of tumors as well as the normal tissues. Data from TCGA datasets showed that KDELR3 mRNA expression was distinctly higher in ACC, BLCA, BRCA, CESC, CHOL, COAD, DLBC, ESCA, GBM, HNSC, KIRP, LIHC, LUAD, LUSC, OV, PAAD, PRAD, PEAD, SARC, SKCM, STAD, THCA, THYM, UCEC, and UCS tumor specimens compared to that in normal specimens, suggesting that it could serve as a tumor promoter in the progression of diverse tumors (Figure 1(a)). Nevertheless, TCGA datasets did not contain any normal uveal specimens. Therefore, it is unknown whether KDELR3 demonstrated a dysregulated behavior in UM. Therefore, we utilized RT-PCR to investigate the level of KDELR3 in D78 cells and four different UM cell lines. We discovered that the level of KDELR3 expression was noticeably elevated in UM cells in comparison to D78 cells (Figure 1(b)).

3.2. Correlation of KDELR3 Expression with Clinicopathological Features. Further investigation into the relationship between KDELR3 and the clinicopathological features of UM was carried out so that we could determine the clinical significance of KDELR3 in UM. The patients diagnosed with UM were separated into two groups based on the mean expression of KDELR3 (high KDELR3 expression group and low KDELR3 expression group). As exhibited in Table 1, our investigation revealed that the level of KDELR3 was not connected to any clinical parameters, including age, gender, or stage ($p > 0.05$).

3.3. The Prognostic Value of KDELR3 Expression in UM. After that, we used the Kaplan-Meier method to determine whether or not the levels of KDELR3 expression can accurately predict the prognosis of patients with UM. Patients who had high levels of KDELR3 expression had a shorter overall survival (Figure 2(a), $p < 0.001$) and disease-free

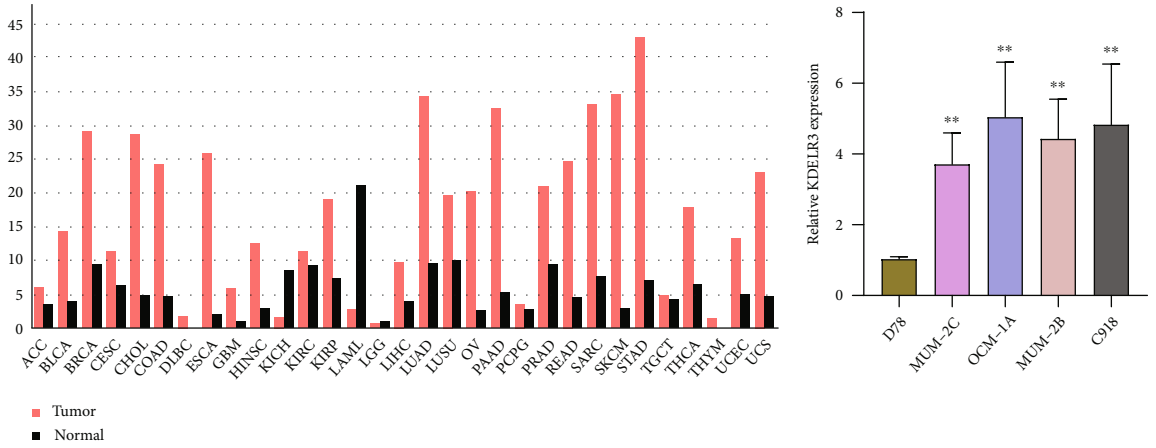

Figure 1: KDELR3 expression levels in human cancers. (a) Using data from TCGA database, GEPIA was able to assess the levels of KDELR3 expression in a variety of tumor types. (b) RT-PCR was utilized in order to investigate whether KDELR3 was expressed in MUM-2C, OCM-1A, MUM-2B, C918, and D78.

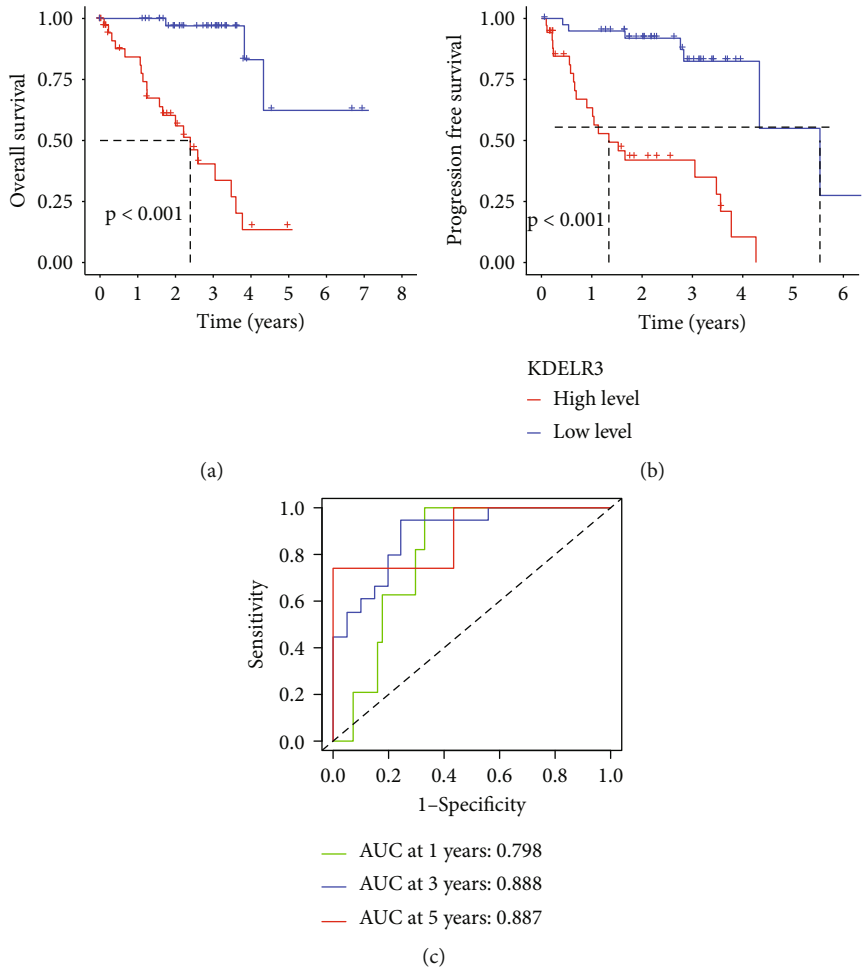

Figure 2: Prognostic value of KDELR3 expression in UM patients. (a, b) In TCGA datasets, Kaplan-Meier survival curves and log-rank tests were performed on high-risk and low-risk score groups. (c) The AUC for 1-, 2-, and 3-year overall survival in TCGA datasets.

Table 2: Univariate and multivariate analysis of the associations of overall survival with various clinicopathologic parameters and KDELR3 expression in uveal melanoma patients.

Characteristics	Total (*N*)	Univariate analysis Hazard ratio (95% CI)	*p* value	Multivariate analysis Hazard ratio (95% CI)	*p* value
Pathologic T stage	80				
T2	14	Reference			
T3	32	3.138 (0.401-24.558)	0.276		
T4	34	4.572 (0.590-35.428)	0.146		
Pathologic N stage	79				
N0	52	Reference			
NX	27	0.890 (0.360-2.198)	0.800		
Pathologic M stage	78				
M0	51	Reference			
M1 and MX	27	0.924 (0.373-2.287)	0.865		
Pathologic stage	79				
Stage II	39	Reference			
Stage III and stage IV	40	1.502 (0.629-3.585)	0.360		
Age	80				
≤60	40	Reference			
>60	40	2.123 (0.914-4.933)	0.080	2.528 (1.055-6.061)	**0.038**
Gender	80				
Female	35	Reference			
Male	45	1.542 (0.651-3.652)	0.325		
KDELR3	80				
Low	40	Reference			
High	40	12.517 (3.685-42.512)	**<0.001**	13.397 (3.931-45.657)	**<0.001**

survival (Figure 2(b), $p < 0.001$) than those who had low levels of KDELR3 expression. These findings were demonstrated by statistical analysis. Time-dependent ROC analysis indicated the prognostic accuracies were 0.798 at 1 year, 0.888 at 3 years, and 0.887 at 5 years, respectively (Figure 2(c)). In order to assess whether the KDELR3 expression level was an independent factor for prognostic prediction in UM patients, both univariate and multivariate analyses were carried out. We observed that KDELR3 expression was an independent prognostic factor for overall survival (HR = 13.397; 95% CI: 3.931-45.657; $p < 0.001$, Table 2) and disease-free survival (HR = 17.116; 95% CI: 3.961-73.971; $p < 0.001$, Table 3) in patients with UM.

3.4. Function Enrichment Analysis of DEGs. Our group evaluated dysregulated genes in UM specimens that were in the high KDELR3 expression group in order to gain a better understanding of the role that KDELR3 plays in UM. Then, we utilized these genes in GO and KEGG analyses that we carried out. Figure 3(a) contains a list of the top 30 most enriching GO terms. In BP, the DEGs were mainly associated with RNA catabolic process, mRNA catabolic process, establishment of protein localization to membrane, translational initiation, and viral gene expression. In CC, they were related to mitochondrial inner membrane, cell-substrate junction, focal adhesion, ribosome, and ribosomal subunit. In MF, the DEGs mainly involved in cadherin binding, ubiquitin-like protein ligase binding, ubiquitin protein ligase binding, structural constituent of ribosome, and ribonucleoprotein complex binding. The results of KEGG assays revealed that the most distinctly enriched biological processes included pathways of neurodegeneration-multiple diseases, amyotrophic lateral sclerosis, Alzheimer's disease, Parkinson's disease, Huntington's disease, prion disease, and thermogenesis (Figure 3(b)).

3.5. Correlation Analysis between KDELR3 Expression and Infiltrating Immune Cells. TIICs are a crucial component of the intricate microenvironment that plays a role in regulating the development and progression of numerous malignancies [25, 26]. Survival rates from cancer can be accurately predicted based on factors such as the number of lymphocytes that infiltrate the tumor and their activity level. As a result, we investigated whether or not there was a connection between immune cell infiltration and KDELR3 expression. We explored the relationship of KDELR3 expression and immune infiltration level based on CIBERSORT in order to identify whether KDELR3 expression was connected with the immune infiltration level in a variety of malignancies. The results indicated that KDELR3 expression was positively associated with macrophage M1, T cell CD8, T cell follicular helper, dendritic cell resting, and T cell CD4 memory activated, while negatively associated with NK cell resting, B cell naïve, eosinophils, neutrophils,

Table 3: Univariate and multivariate analyses of the associations of progression-free survival with various clinicopathologic parameters and KDELR3 expression in uveal melanoma patients.

Characteristics	Total (*N*)	Univariate analysis Hazard ratio (95% CI)	*p* value	Multivariate analysis Hazard ratio (95% CI)	*p* value
Pathologic T stage	80				
T2	14	Reference			
T3	32	2.512 (0.314-20.124)	0.386		
T4	34	4.433 (0.572-34.338)	0.154		
Pathologic N stage	79				
N0	52	Reference			
NX	27	0.985 (0.391-2.483)	0.974		
Pathologic M stage	78				
M0	51	Reference			
M1 and MX	27	1.024 (0.405-2.585)	0.961		
Pathologic stage	79				
Stage II	39	Reference			
Stage III and stage IV	40	1.607 (0.640-4.033)	0.312		
Age	80				
≤60	40	Reference			
>60	40	1.872 (0.785-4.461)	0.157		
Gender	80				
Female	35	Reference			
Male	45	1.351 (0.558-3.275)	0.505		
KDELR3	80				
Low	40	Reference			
High	40	17.116 (3.961-73.971)	**<0.001**	17.116 (3.961-73.971)	**<0.001**

monocytes, mast cell resting, and T cell CD4 memory resting (Figure 4). According to the results of our research, the level of immune infiltration in UM was directly proportional to the amount of KDELR3 expression.

3.6. Correlation Analysis between KDELR3 Expression and Immune Checkpoint Molecules in UM. Subsequently, we determined the linear correlation between the expression of immune checkpoint related genes (CD86, PDCD1, CD48, CD80, CD276, TNFSF18, TNFRSF8, and TNFRSF18) and risk scores using Spearman's rank correlation coefficient. These genes include CD86, PDCD1, CD48, CD80, CD276, TNFSF18, TNFRSF8, and TNFRSF18. The results indicated that the expression of immunosuppression-related genes had positive correlation with KDELR3 expression in TCGA datasets (Figure 5).

3.7. IC50 Score. When determining how well patients may respond to targeted medication therapy, IC50 is an essential metric to use [27, 28]. We were able to predict changes in the IC50 scores of chemotherapeutic drugs between different KDELR3 expression groups by using data from GDSC. The IC50 of AP-24534, BHG712, bleomycin, camptothecin, cisplatin, cytarabine, GSK1070916, and tipifarnib was higher in the KDELR3 high-expression group (Figure 6). Therefore, these data demonstrate that there was a statistically significant difference in the distribution of IC50 values for targeted drugs among the different KDELR3 expression groups.

4. Discussion

UM is a malignant primary intraocular tumor that affects adults at a higher rate than any other type of malignant primary intraocular tumor [29]. The majority of UM are often treated with surgery or radiotherapy, which typically results in survival rates that are comparable over the short term [30, 31]. Because of its unique biology and clinical behavior, around fifty percent of patients will be given a bad prognosis, which may include disease recurrence and dissemination. To date, conventional methods have not been able to provide a survival benefit or exact prognostic prediction for these patients. On the other hand, more recent systemic treatments, in particular immunotherapies and targeted therapy, have dramatically improved patient survival. Nevertheless, the discovery of novel prognostic indicators was of utmost significance for patients diagnosed with UM. In this work, we conducted a retrospective analysis to choose biomarkers that linked with the immunological milieu of the tumor in order to predict prognosis and identify the segment of the population that would benefit the most from immune checkpoints.

The role of KDELR3, which was only recently shown to be associated with tumors, was seldom ever mentioned. The

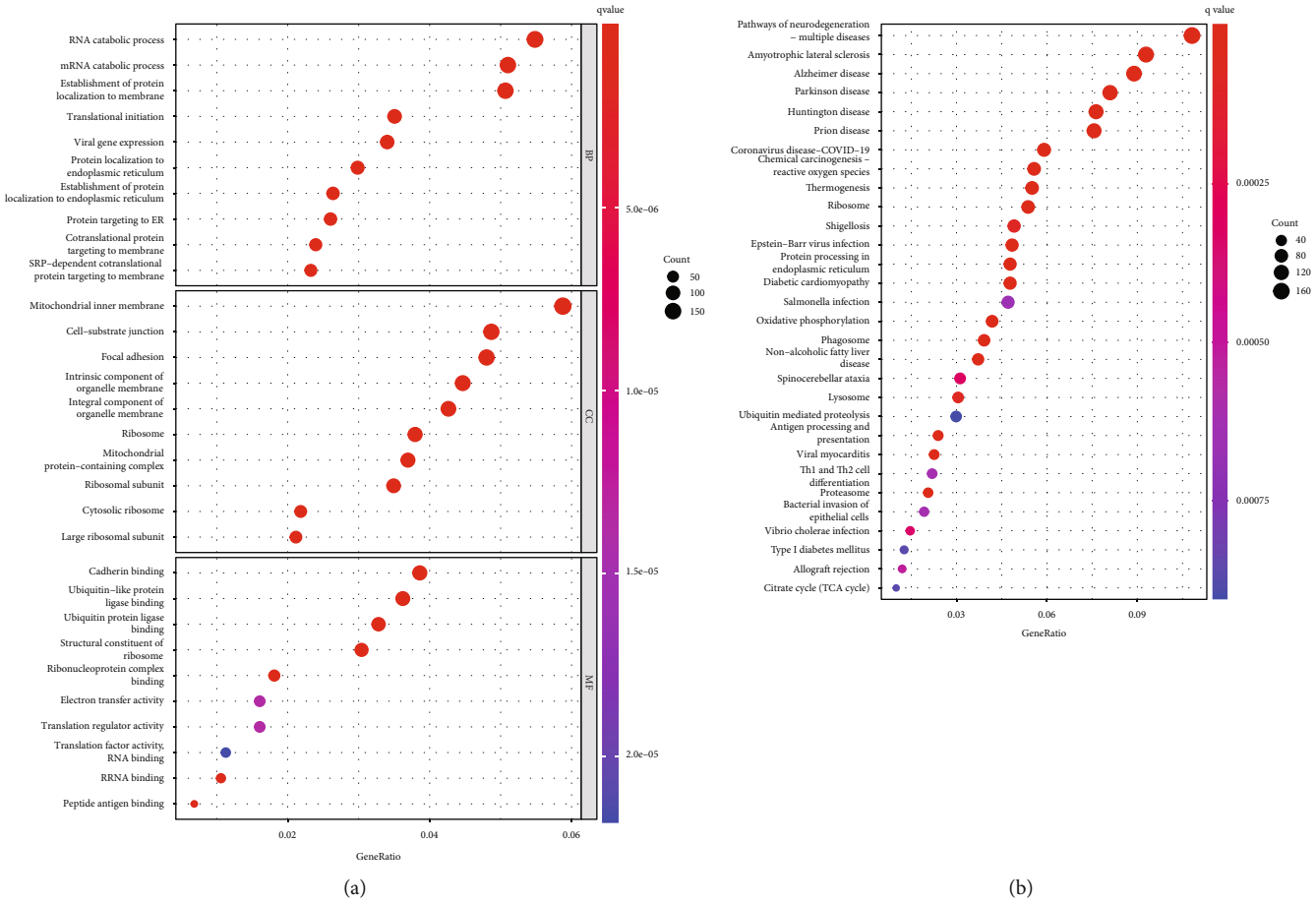

Figure 3: Enrichment analysis in TCGA UM cohort. (a) Gene ontology enrichment. (b) Kyoto Encyclopedia of Genes and Genomes pathway analyses.

KDELR3 gene is a member of the KDEL endoplasmic reticulum protein retention receptor family. Its product, KDELR3, is translated into proteins. According to the findings of the study carried out by Marie and colleagues, the inhibition of KDELR3 led to a reduction in the amount of melanoma cells that colonized the lungs during experimental metastasis assays. This was accomplished by modulating the activity of the metastasis suppressor KAI1 [32]. However, the expression and clinical significance of KDELR3 in UM have not been investigated. In this study, the mRNA expression of KDELR3 was shown to be significantly greater in the majority of different tumors, which suggested that it may play a role as an oncogenic molecule in the development of a variety of different malignancies. When compared with D78 cells, the level of KDELR3 in UM cells was found to be noticeably higher thanks to the findings of RT-PCR. In patients diagnosed with UM, we found that the level of KDELR3 expression acted as an independent predictive factor for both overall survival and survival free of illness. In general, the results of our study revealed that KDELR3 could be a predictive biomarker for UM patients.

We carried out a GO and KEGG function enrichment analysis using the genes that were dysregulated between the high KDELR3 expression group and the low KDELR3 expression group in order to gain a deeper understanding of the possible role that KDELR3 played in the progression of tumors. Our findings suggested that KDELR3 may play an important role in the progression of neurodegeneration-multiple diseases, amyotrophic lateral sclerosis, Alzheimer's disease, Parkinson's disease, Huntington's disease, prion disease, and thermogenesis.

Cancer tissues consist of not only malignant neoplastic cells but also immune cells, fibroblasts, endothelial cells, and an abundant collection of cytokines, chemokines, and growth factors [33]. The TME is formed by these components and their complex interaction with one another. The various cellular compartments that make up the TME are able to critically regulate tumorigenesis, which is essential not only to tumor initiation, malignant progression, and metastasis but also to response to therapy [34, 35]. In the TME, the majority of host cells that are drawn to and activated are immune cells. Determining appropriate immunotherapy treatment plans for cancer patients now relies significantly on the detection of immune cells that can serve as biomarkers in the cancer immunological microenvironment. The quantity of immune cells and how they are distributed is the single most critical element in determining the eventual course of a tumor, including whether or not it will inhibit or promote carcinogenesis, cell metastasis, cell migration, and tumor angiogenesis [36, 37]. Nevertheless,

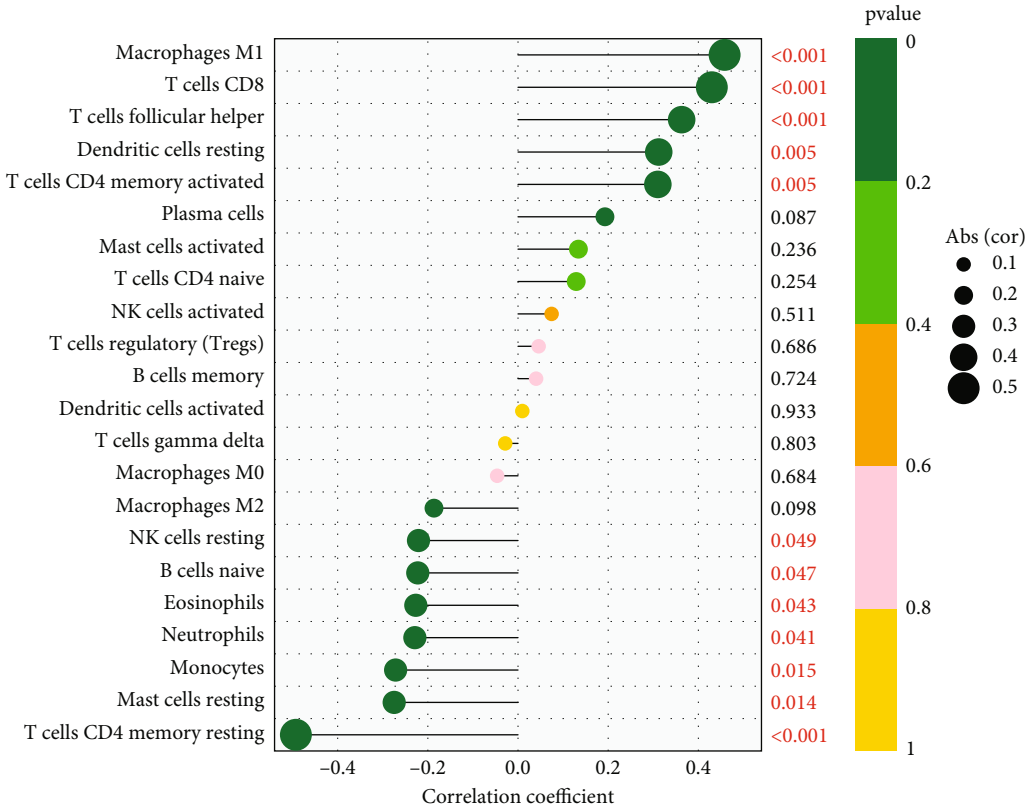

Figure 4: Analysis of the correlation between the amount of KDELR3 expression and the amount of immune infiltration.

the immunological microenvironment in the many forms of cancer is intricate and heterogeneous. In this study, we found that KDELR3 expression was positively associated with macrophage M1, T cell CD8, T cell follicular helper, dendritic cell resting, and T cell CD4 memory activated, while negatively associated with NK cell resting, B cell naïve, eosinophils, neutrophils, monocytes, mast cell resting, and T cell CD4 memory resting. According to the findings that we obtained, the level of immune infiltration in UM was directly proportional to the amount of KDELR3 expression. In recent years, immune checkpoint blockade therapy has emerged as one of the most important immunotherapies for the treatment of cancers. This therapy is credited for fundamentally altering the landscape of cancer treatment. Inducing a long-lasting anticancer response and removing a block in the immune system are the goal of immunotherapy that blocks immunological checkpoints [38, 39]. In addition, we discovered that the expression of genes linked to immunosuppression had a positive connection with the expression of KDELR3 in TCGA datasets. When determining how well patients may respond to targeted medication therapy, IC50 is an essential metric to use. We were able to predict changes in the IC50 scores of chemotherapeutic drugs between different KDELR3 expression groups by using data from GDSC. The IC50 of AP-24534, BHG712, bleomycin, camptothecin, cisplatin, cytarabine, GSK1070916, and tipifarnib was higher in the KDELR3 high-expression group. Consequently, these findings showed that the IC50 distributions of targeted drugs in distinct KDELR3 expression groups were statistically significant.

However, despite the fact that we conducted an exhaustive and methodical study on KDELR3, we found nothing. This study has certain caveats and restrictions to it. First, the findings were based on data that was collected in the past, and more data collected in the present was required to prove the clinical relevance of it. Second, experiments in vivo and in vitro are required to validate our findings about the possible functions of KDELR3. If these experiments are successful, the credibility of our findings will be significantly increased. Third, despite the fact that KDELR3 expression was highly connected to immune cell infiltration and the prognosis of human malignancies, we do not have any direct proof that KDELR3 played a role in immune infiltration and hence influenced the prognosis. Therefore, the methods via which KDELR3 participated in immune modulation are still a mystery, and the precise pathway needed additional research.

5. Conclusions

Our research contributed to a better understanding of the potential function of KDELR3 mRNA in tumor immunology as well as its relevance as a prognostic indicator. It was found that the levels of KDELR3 mRNA connected with both the prognosis and the immune infiltration levels in UM, indicating that it can be employed as a biomarker for

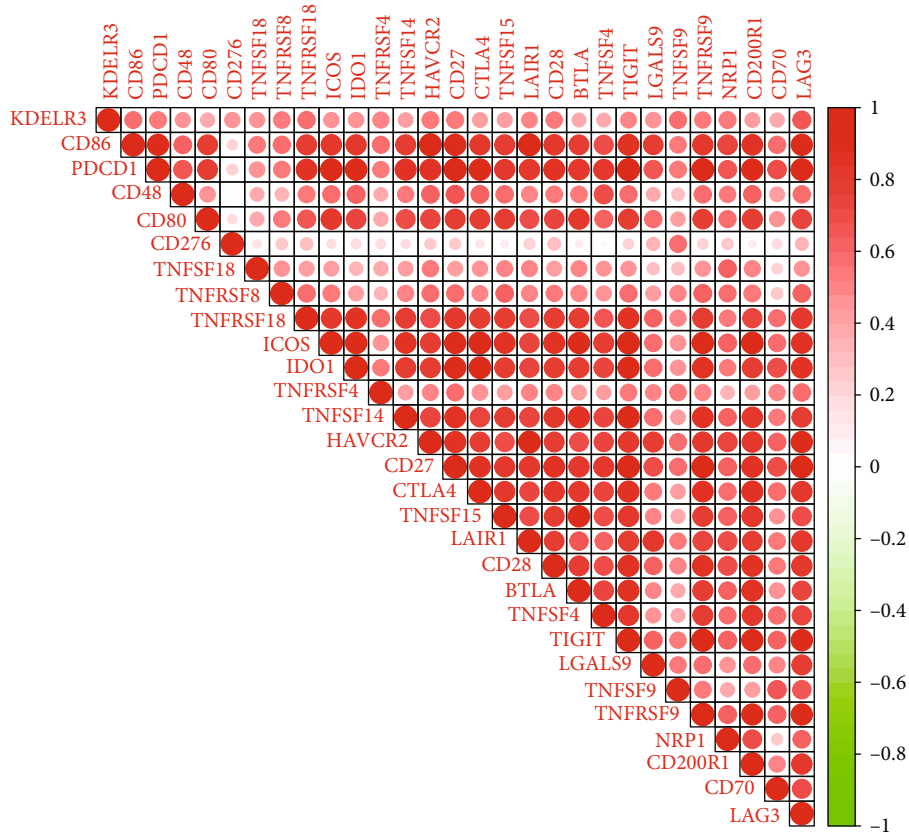

Figure 5: The differential expression of immune checkpoint molecules in TCGA cohorts between the high-risk group and the low-risk group.

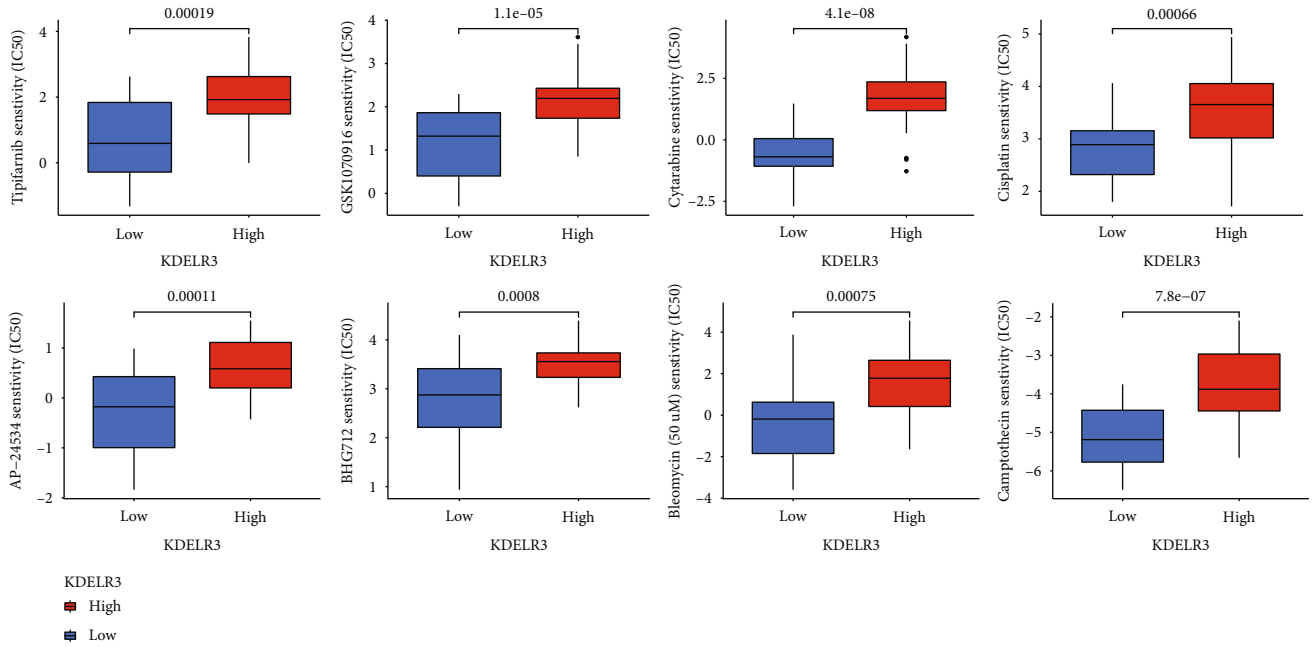

Figure 6: Distribution of IC50 scores of targeted drugs in different KDELR3 expression groups via ACLBI website.

predicting the outcome of the disease. It is necessary to investigate the possibility that KDELR3 inhibitors would cause interference with immune cells.

Data Availability

The data used to support the findings of this study are included within the article. Further inquiries can be directed to the corresponding author.

Conflicts of Interest

The authors declare that they have no competing interests.

References

[1] M. J. Jager, C. L. Shields, C. M. Cebulla et al., "Uveal melanoma," *Nature Reviews. Disease Primers*, vol. 6, no. 1, p. 24, 2020.

[2] K. N. Smit, M. J. Jager, A. de Klein, and E. Kiliç, "Uveal melanoma: towards a molecular understanding," *Progress in Retinal and Eye Research*, vol. 75, article 100800, 2020.

[3] A. Amaro, R. Gangemi, F. Piaggio et al., "The biology of uveal melanoma," *Cancer Metastasis Reviews*, vol. 36, no. 1, pp. 109–140, 2017.

[4] I. H. Bronkhorst and M. J. Jager, "Uveal melanoma: the inflammatory microenvironment," *Journal of Innate Immunity*, vol. 4, no. 5-6, pp. 454–462, 2012.

[5] C. Rodriguez-Vidal, D. Fernandez-Diaz, B. Fernandez-Marta et al., "Treatment of metastatic uveal melanoma: systematic review," *Cancers (Basel)*, vol. 12, no. 9, p. 2557, 2020.

[6] R. S. Seedor, M. Orloff, and T. Sato, "Genetic landscape and emerging therapies in uveal melanoma," *Cancers (Basel)*, vol. 13, no. 21, p. 5503, 2021.

[7] D. Martinez-Perez, D. Viñal, I. Solares, E. Espinosa, and J. Feliu, "Gp-100 as a novel therapeutic target in uveal melanoma," *Cancers (Basel)*, vol. 13, no. 23, p. 5968, 2021.

[8] J. Y. Niederkorn, "Immune escape mechanisms of intraocular tumors," *Progress in Retinal and Eye Research*, vol. 28, no. 5, pp. 329–347, 2009.

[9] M. Z. Afzal, R. Mabaera, and K. Shirai, "Metastatic uveal melanoma showing durable response to anti-CTLA-4 and anti-PD-1 combination therapy after experiencing progression on anti-PD-1 therapy alone," *Journal for Immunotherapy of Cancer*, vol. 6, no. 1, p. 13, 2018.

[10] G. P. Solis, O. Bilousov, A. Koval, A. M. Lüchtenborg, C. Lin, and V. L. Katanaev, "Golgi-resident Gαo promotes protrusive membrane dynamics," *Cell*, vol. 170, no. 5, pp. 939–955.e24, 2017.

[11] R. Yan, K. Chen, B. Wang, and K. Xu, "SURF4-induced tubular ERGIC selectively expedites ER-to-Golgi transport," *Developmental Cell*, vol. 57, no. 4, pp. 512–525.e8, 2022.

[12] T. Stauber, J. C. Simpson, R. Pepperkok, and I. Vernos, "A role for kinesin-2 in COPI-dependent recycling between the ER and the Golgi complex," *Current Biology*, vol. 16, no. 22, pp. 2245–2251, 2006.

[13] M. Y. Li, M. Grandadam, K. Kwok et al., "KDEL receptors assist dengue virus exit from the endoplasmic reticulum," *Cell Reports*, vol. 10, no. 9, pp. 1496–1507, 2015.

[14] M. Sanson, N. Augé, C. Vindis et al., "Oxidized low-density lipoproteins trigger endoplasmic reticulum stress in vascular cells: prevention by oxygen-regulated protein 150 expression," *Circulation Research*, vol. 104, no. 3, pp. 328–336, 2009.

[15] Z. Xu, L. Xu, L. Liu et al., "A glycolysis-related five-gene signature predicts biochemical recurrence-free survival in patients with prostate adenocarcinoma," *Frontiers in Oncology*, vol. 11, article 625452, 2021.

[16] Y. Bai, W. Qi, L. Liu et al., "Identification of seven-gene hypoxia signature for predicting overall survival of hepatocellular carcinoma," *Frontiers in Genetics*, vol. 12, article 637418, 2021.

[17] J. Parkin and B. Cohen, "An overview of the immune system," *Lancet*, vol. 357, no. 9270, pp. 1777–1789, 2001.

[18] M. Huse, "Mechanical forces in the immune system," *Nature Reviews. Immunology*, vol. 17, no. 11, pp. 679–690, 2017.

[19] D. P. Huston, "The biology of the immune system," *JAMA*, vol. 278, no. 22, pp. 1804–1814, 1997.

[20] M. Calvo, J. M. Dawes, and D. L. Bennett, "The role of the immune system in the generation of neuropathic pain," *Lancet Neurology*, vol. 11, no. 7, pp. 629–642, 2012.

[21] A. Sáez-Cirión and N. Manel, "Immune responses to retroviruses," *Annual Review of Immunology*, vol. 36, no. 1, pp. 193–220, 2018.

[22] L. Tagliaferri, V. Lancellotta, B. Fionda et al., "Immunotherapy and radiotherapy in melanoma: a multidisciplinary comprehensive review," *Human Vaccines & Immunotherapeutics*, vol. 18, no. 3, p. 1903827, 2022.

[23] M. E. Ritchie, B. Phipson, D. Wu et al., "limma powers differential expression analyses for RNA-sequencing and microarray studies," *Nucleic Acids Research*, vol. 43, no. 7, article e47, 2015.

[24] A. M. Newman, C. L. Liu, M. R. Green et al., "Robust enumeration of cell subsets from tissue expression profiles," *Nature Methods*, vol. 12, no. 5, pp. 453–457, 2015.

[25] A. Byrne, P. Savas, S. Sant et al., "Tissue-resident memory T cells in breast cancer control and immunotherapy responses," *Nature Reviews. Clinical Oncology*, vol. 17, no. 6, pp. 341–348, 2020.

[26] E. Kolaczkowska and P. Kubes, "Neutrophil recruitment and function in health and inflammation," *Nature Reviews. Immunology*, vol. 13, no. 3, pp. 159–175, 2013.

[27] R. Roy, M. Tiwari, G. Donelli, and V. Tiwari, "Strategies for combating bacterial biofilms: a focus on anti-biofilm agents and their mechanisms of action," *Virulence*, vol. 9, no. 1, pp. 522–554, 2018.

[28] S. M. Clemente, O. H. Martínez-Costa, M. Monsalve, and A. K. Samhan-Arias, "Targeting lipid peroxidation for cancer treatment," *Molecules*, vol. 25, no. 21, p. 5144, 2020.

[29] C. Chattopadhyay, D. W. Kim, D. S. Gombos et al., "Uveal melanoma: from diagnosis to treatment and the science in between," *Cancer*, vol. 122, no. 15, pp. 2299–2312, 2016.

[30] K. K. Tsai, K. B. Bollin, and S. P. Patel, "Obstacles to improving outcomes in the treatment of uveal melanoma," *Cancer*, vol. 124, no. 13, pp. 2693–2703, 2018.

[31] S. Khan and R. D. Carvajal, "Novel approaches to the systemic management of uveal melanoma," *Current Oncology Reports*, vol. 22, no. 10, p. 104, 2020.

[32] K. L. Marie, A. Sassano, H. H. Yang et al., "Melanoblast transcriptome analysis reveals pathways promoting melanoma metastasis," *Nature Communications*, vol. 11, no. 1, p. 333, 2020.

[33] S. Gampala and J. Y. Yang, "Hedgehog Pathway Inhibitors against Tumor Microenvironment," *Cell*, vol. 10, no. 11, p. 3135, 2021.

[34] X. Li and J. Wang, "Mechanical tumor microenvironment and transduction: cytoskeleton mediates cancer cell invasion and metastasis," *International Journal of Biological Sciences*, vol. 16, no. 12, pp. 2014–2028, 2020.

[35] X. Fu, Y. He, M. Li, Z. Huang, and M. Najafi, "Targeting of the tumor microenvironment by curcumin," *BioFactors*, vol. 47, no. 6, pp. 914–932, 2021.

[36] M. Kienzl, J. Kargl, and R. Schicho, "The immune endocannabinoid system of the tumor microenvironment," *International Journal of Molecular Sciences*, vol. 21, no. 23, p. 8929, 2020.

[37] H. Jang, E. H. Kim, S. G. Chi, S. H. Kim, and Y. Yang, "Nanoparticles targeting innate immune cells in tumor microenvironment," *International Journal of Molecular Sciences*, vol. 22, no. 18, p. 10009, 2021.

[38] M. G. Netea, L. A. Joosten, E. Latz et al., "Trained immunity: a program of innate immune memory in health and disease," *Science*, vol. 352, no. 6284, p. aaf1098, 2016.

[39] A. Hosseini, V. Hashemi, N. Shomali et al., "Innate and adaptive immune responses against coronavirus," *Biomedicine & Pharmacotherapy*, vol. 132, article 110859, 2020.

Hindawi
Disease Markers
Volume 2022, Article ID 6408879, 8 pages
https://doi.org/10.1155/2022/6408879

Research Article

Downregulation of LEMD1-AS1 and Its Influences on the Diagnosis, Prognosis, and Immune Infiltrates of Epithelial Ovarian Cancer

Xiaoju Yang,[1] Shen Zhou,[2] Chunlin Li,[3] Li Huang,[4] Chuanqi Chen,[1] Xiao Tang,[1] Xingyan Su,[5] and Hongcheng Zhu[1]

[1]*Department of Obstetrics and Gynaecology, The Central Hospital of Enshi Tujia and Miao Autonomous Prefecture, Enshi, 445000 Hubei Province, China*
[2]*Clinical Laboratory Center, The Central Hospital of Enshi Tujia and Miao Autonomous Prefecture, No. 158 Wuyang Avenue, Enshi City, 445000 Hubei Province, China*
[3]*Department of Radiology, The Central Hospital of Enshi Tujia and Miao Autonomous Prefecture, No. 158 Wuyang Avenue, Enshi City, 445000 Hubei Province, China*
[4]*Department of Infection, Enshi Tujia and Miao Autonomous Prefecture Center for Disease Control and Prevention, Hubei Province, China*
[5]*Department of Anesthesiology, The Central Hospital of Enshi Tujia and Miao Autonomous Prefecture, Enshi City, 445000 Hubei Province, China*

Correspondence should be addressed to Xingyan Su; sxy46470916@163.com
and Hongcheng Zhu; zhuhongcheng198266@163.com

Received 15 June 2022; Revised 21 July 2022; Accepted 23 July 2022; Published 3 August 2022

Academic Editor: Fu Wang

Previous studies have confirmed long noncoding RNA LEMD1-AS1 (LEMD1-AS1) as a functional factor in several tumors. The present work is aimed at exploring the prognostic and diagnostic values of LEMD1-AS1 in patients with epithelial ovarian cancer (EOC). We examined the expressions of LEMD1-AS1 in pan-cancer from TCGA microarray datasets and GTEx Project. The expressions of LEMD1-AS1 were detected by qRT-PCR in EOC specimens and normal ovarian specimens from 30 EOC patients. The χ^2 test was applied to compare the clinicopathological characteristics of different groups. ROC curves were established to determine the diagnostic values of LEMD1-AS1 in screening EOC tissues. The association of LEMD1-AS1 expression with clinical outcome was determined by the Kaplan-Meier methods and COX assays. A decreased expression of LEMD1-AS1 was observed in EOC tissues compared to matched normal specimens ($p < 0.01$). Low LEMD1-AS1 expression could be used to distinguish EOC from adjacent normal specimens. A clinical study revealed that patients with low LEMD1-AS1 expression have a shorter overall survival ($p = 0.035$) and progress-free interval ($p = 0.041$) than those with high LEMD1-AS1 expression. The Spearman correlation test revealed that LEMD1-AS1 expressions were negatively associated with the expressions of neutrophil and myeloid dendritic cell. Overall, our finding suggested that LEMD1-AS1 may have potential roles as a potential biomarker and/or a therapeutic target in EOC.

1. Introduction

Epithelial ovarian cancer (EOC) is one of the three most common gynecological malignant neoplasms and the third most common cancer in females worldwide [1]. It is anticipated that more than 255,000 women will be diagnosed with EOC each year, which would result in at least 120,000 fatalities per year throughout the world [2]. EOC is characterized by multiple distant metastases in other organisms, advanced-stage appearances, and refractory ascites when firstly diagnosed [3, 4]. Despite various improvements in surgical technology, radiotherapy, or chemotherapy for

EOC treatments, the 5-year overall survivals of many EOC patients are still dissatisfied [5, 6]. The major obstacles in the treatments of EOC are the metastasis and multidrug resistance [7]. Therefore, it is necessary to develop a novel and reliable biomarker to evaluate the prognosis and efficacy of therapeutic strategies for EOC.

Numerous studies have demonstrated, as a result of significant developments in high-throughput RNA sequencing technology, that the majority of the human transcriptome may be categorized as long noncoding RNAs (lncRNAs) [8]. lncRNAs are noncoding RNAs over 200 nucleotides in length [9]. Growing studies have confirmed that this class of RNAs shows a regulator effect on the modulation of gene expressions at both transcriptional and posttranscriptional levels [10]. A large number of studies on the basic and clinical assays have revealed that lncRNAs are involved in various biological processes and are distinctly dysregulated in various types of diseases, especially in neoplasms [11, 12]. For instance, lncRNA HAS2-AS1 was significantly expressed in EOC, and it regulated the miRNA-466/RUNX2 axis in a way that made EOC cells more likely to proliferate and metastasize [13]. Upregulation of lncRNA NORAD was shown to promote EOC cell proliferation and decrease bufalin chemoresistance via sponging miR-155-5p [14]. Over the course of the past few years, an increasing number of research have shed light on the possibility that lncRNAs could be utilized as novel biomarkers in the diagnosis of a wide variety of tumor patients. Several biomarker-related lncRNAs have been clinically identified, such as lncRNA SNHG1, lncRNA HOTAIR, and lncRNA MEG3 [15–17]. However, many functional lncRNAs remained unknown.

Long noncoding RNA LEMD1 antisense RNA 1 (LEMD1-AS1) is a recently identified lncRNA. So far, its roles in tumors were rarely reported. In this study, we focused on LEMD1-AS1 and explored its expression and clinical significance in EOC.

2. Patients and Methods

2.1. Expression Analysis of LEMD1-AS1 and Sample Data across Cancers. The pan-cancer RNA sequencing data relating to 33 different forms of cancer were obtained by downloading them from the Internet database UCEC, which came from TCGA database. In addition, the sequencing information for LEMD1-AS1 was obtained from the GTEx Project. All of the expression data were normalized by converting them to $\log_2$ format. Evaluation of LEMD1-AS1 expression was performed with the help of the edgeR package in R. 427 EOC samples and 88 normal samples were included for further assays. Clinicopathological features of all patients from TCGA datasets are shown in Table 1.

2.2. Patients and Specimens. From 2020 to 2021, 30 EOC patients who underwent complete resection of the tumor in the Central Hospital of Enshi Tujia and Miao Autonomous Prefecture were subsequently enrolled in our study. A total of 30 EOC specimens and nontumor samples were collected from all cases and were flash frozen in liquid nitrogen following surgery. The inclusion criteria are as follows. All patients were diagnosed as EOC by pathological findings; none of the patients had a history of other tumor or received preoperative treatment. Written informed consent was obtained from all cases. Our experiments were approved by the Research Ethics Committee of the Central Hospital of Enshi Tujia and Miao Autonomous Prefecture.

2.3. Real-Time PCR. Total RNA was extracted from all specimens with TRIzol reagent (Invitrogen, Xuhui, Shanghai, China). RNA concentration was examined by the use of a spectrometer under a wavelength of 260 nm. cDNA was reverse transcribed using the Quantitect Reverse Transcription Kit (Qiagen, Kunming, Yunnan, China). Then, qRT-PCR was performed to quantify relative LEMD1-AS1 expression using the SYBR Premix Ex Taq kit (TaKaRa, Kunming, Yunnan, China) on CFX99 Real-Time PCR Detection System (Bio-Rad, Hangzhou, Zhejiang, China). GAPDH was used as endogenous control with the $2^{-\Delta\Delta Ct}$ methods applied for the calculation of the relative expressions of LEMD1-AS1. The sequences of the primers were listed as follows: LEMD1-AS1 forward (5′-3′): AATGACCGCAATCCCAAGGT, LEMD1-AS1 forward (5′-3′): GGTGACTAGCAGTGCGTGAT, GAPDH forward (5′-3′): GGAGCGAGATCCCTCCAAAAT, and GAPDH reverse (5′-3′): GGCTGTTGTCATACTTCTCATGG.

2.4. TIMER Database Analysis. TIMER, which can be found at https://cistrome.shinyapps.io/timer/, is a database that was created for the purpose of analyzing immune cell infiltrates in a variety of malignancies. This database used a statistical methodology that has been validated by a pathological investigation in order to estimate the amount of immune infiltration that a tumor has, including neutrophils, macrophages, dendritic cells, B cells, and CD4/CD8 T cells. Using the TIMER database, we first investigated the differences in LEMD1-AS1 expression levels between the various types of tumors. Next, we investigated the association between LEMD1-AS1 expression and the degree of infiltration by the various immune cell subsets. Finally, we drew conclusions about the significance of these findings.

2.5. Statistical Analysis. SPSS software (version 16.0; Chicago, IL, USA) and R (version 3.6.0) were applied to perform statistical analyses. Differences between measured groups were assessed using Student's *t*-test or chi-square test. The Kaplan-Meier method was used to calculate survival, and significance was determined by the log-rank test. Receiver-operating characteristic (ROC) curves were used to assess the feasibility of the application of LEMD1-AS1 expression used as a diagnostic tool for detecting EOC. Multivariate analysis was performed to investigate the prognostic factors. $p < 0.05$ was regarded as statistically significant.

3. Results

3.1. Pan-Cancer Analysis of LEMD1-AS1 Expression. Using the LEMD1-AS1 expression data for 33 cancers retrieved from TCGA database and GTEx Project, our group observed that LEMD1-AS1 expression was decreased in several types of tumors, including ACC, BRCA, LGG, LIHC, OV, PCPG,

Table 1: Association between LEMD1-AS1 expression and clinicopathological characteristics of EOC.

Characteristic	Low expression of LEMD1-AS1	High expression of LEMD1-AS1	p
n	189	190	
FIGO stage, n (%)			0.151
Stage I	0 (0%)	1 (0.3%)	
Stage II	7 (1.9%)	16 (4.3%)	
Stage III	152 (40.4%)	143 (38%)	
Stage IV	29 (7.7%)	28 (7.4%)	
Primary therapy outcome, n (%)			0.109
PD	18 (5.8%)	9 (2.9%)	
SD	11 (3.6%)	11 (3.6%)	
PR	26 (8.4%)	17 (5.5%)	
CR	100 (32.5%)	116 (37.7%)	
Race, n (%)			0.501
Asian	4 (1.1%)	8 (2.2%)	
Black or African American	13 (3.6%)	12 (3.3%)	
White	165 (45.2%)	163 (44.7%)	
Age, n (%)			0.646
≤60	101 (26.6%)	107 (28.2%)	
>60	88 (23.2%)	83 (21.9%)	
Histologic grade, n (%)			0.874
G1	0 (0%)	1 (0.3%)	
G2	23 (6.2%)	22 (6%)	
G3	163 (44.2%)	159 (43.1%)	
G4	0 (0%)	1 (0.3%)	
Age, median (IQR)	60 (52, 70)	58 (50.25, 66.75)	0.161

PRAD, SKCM, TGCT, UCEC, and UCS tissues compared to their corresponding normal tissues. However, increased LEMD1-AS1 expression was found in BLCA, CHOL, COAD, DLBC, ESCA, HNSC, KIRC, LUAD, LUSC, PAAD, READ, STAD, THCA, and THYM (Figure 1). Our findings suggested that LEMD1-AS1 may display a different role in tumor progression based on the specific types of tumors.

3.2. LEMD1-AS1 Was Lowly Expressed in EOC Tissues. Based on the data of TCGA database and GTEx Project, we found that LEMD1-AS1 expression was distinctly decreased in EOC samples compared with normal samples (Figure 2(a)). The diagnostic value of lncRNAs in EOC patients had been frequently reported in several studies. Thus, we further explored the diagnostic value of LEMD1-AS1. As shown in Figure 2(b), the results of ROC assays suggested that LEMD1-AS1 effectively differentiated EOC specimens from normal specimens with an area under the ROC curves (AUC) of 0.965 (95% CI: 0.936 to 0.995). Moreover, we further determined whether LEMD1-AS1 expression was dysregulated in EOC in our cohort. As shown in Figure 2(c), RT-PCR results showed that LEMD1-AS1 expressions were distinctly decreased in EOC samples compared with the noncancerous specimens ($p < 0.01$), implying that deregulated expression of LEMD1-AS1 could play a role in the developments of EOC. Moreover, the results of ROC assays suggested that LEMD1-AS1 effectively differentiated EOC specimens from normal specimens with an area under the ROC curves (AUC) of 0.8111 (95% CI: 0.6922 to 0.9300) (Figure 2(d)).

3.3. Association of LEMD1-AS1 Expressions with Clinicopathological Features of EOC. We split all 379 EOC patients into a high expression group ($n = 190$) and a low expression group ($n = 189$) based on the mean expression of LEMD1-AS1 in the 379 EOC specimens. This was done so that we could gain a better knowledge of the clinical significance of LEMD1-AS1 expressions in EOC. Then, the chi-square test was performed for the statistics assays. As presented in Table 1, there were no distinct connections between the dysregulated expressions of LEMD1-AS1 and any other clinical characteristics (all $p > 0.05$).

3.4. High Levels of LEMD1-AS1 Were Correlated with Unfavorable Survivals in EOC. To study whether the abnormal expression of LEMD1-AS1 influences the clinical outcome of EOC patients, we performed Kaplan-Meier analysis for the statistical assays, finding that patients with low LEMD1-AS1 expression have a shorter overall survival ($p = 0.035$, Figure 3(a)) and progress-free interval ($p = 0.041$, Figure 3(b)) than those with high LEMD1-AS1 expression. For further

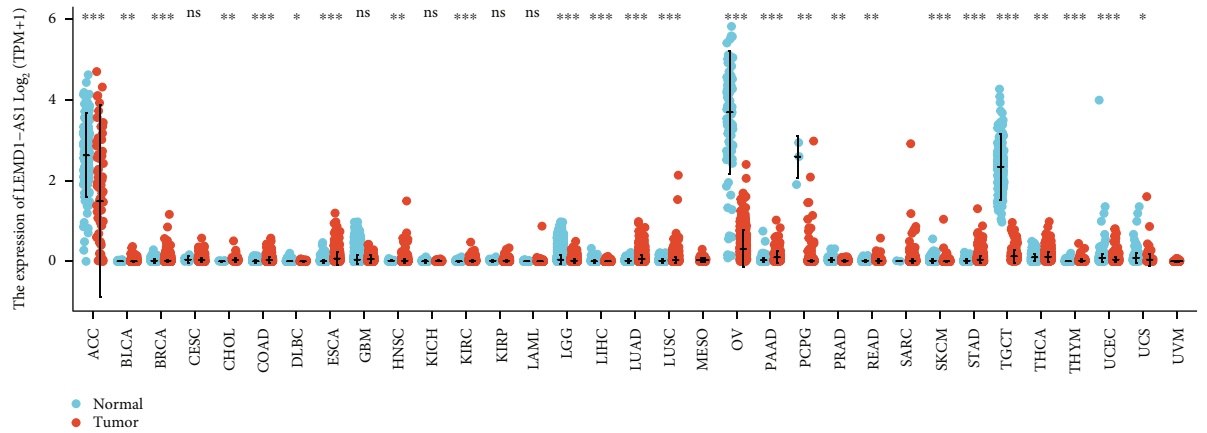

Figure 1: Expression level of LEMD1-AS1 in different cancer types from TCGA and GTEx data. $^{*}p < 0.05$, $^{**}p < 0.01$, and $^{***}p < 0.001$.

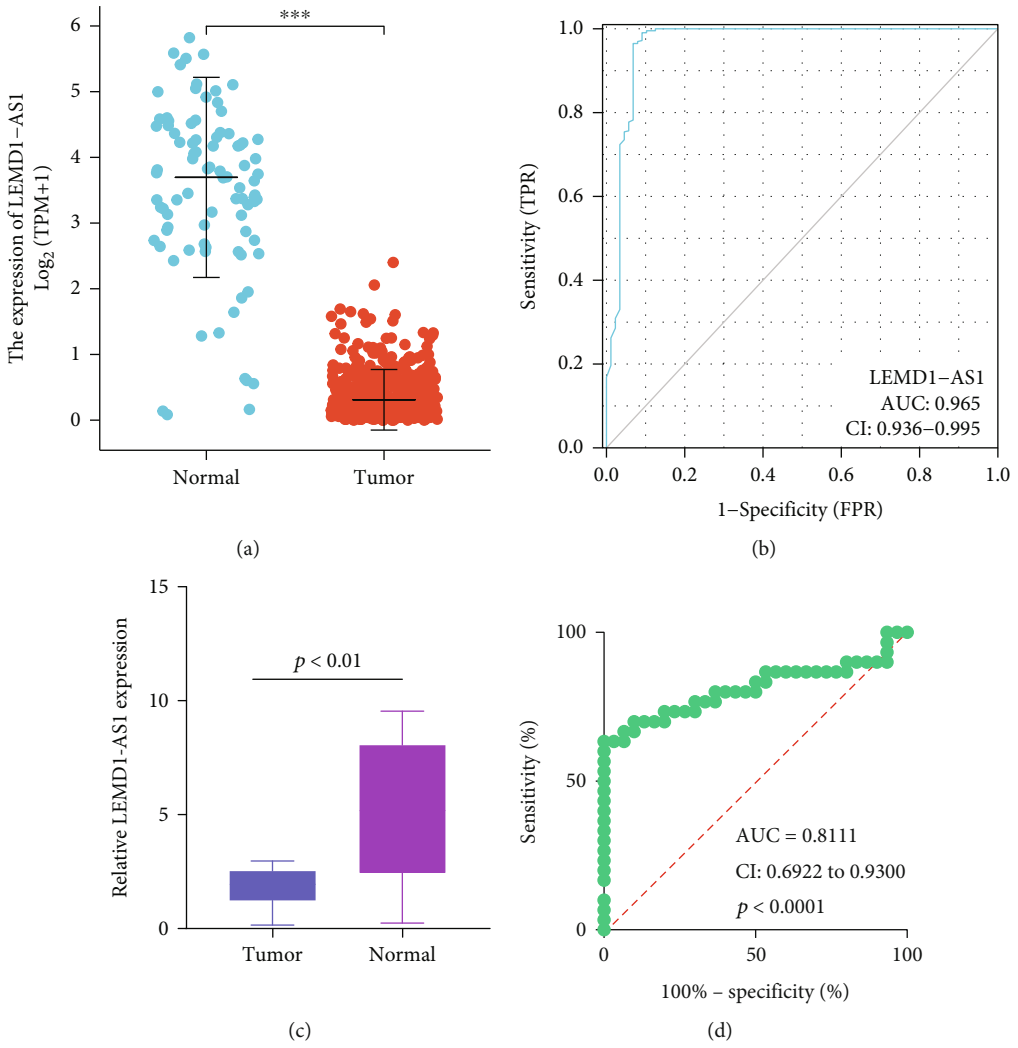

Figure 2: The distinct upregulation of LEMD1-AS1 in EOC patients. (a) The expression of LEMD1-AS1 in EOC specimens and nontumor samples based on TCGA and GTEx data. (b) ROC curve analysis of the diagnostic performance of LEMD1-AS1 expression using TCGA and GTEx data. (c) LEMD1-AS1 was analyzed by RT-PCR assays in 30 EOC tissues and adjacent nontumor specimens from 30 patients. (d) The diagnostic value of LEMD1-AS1 was demonstrated in our cohort. $^{***}p < 0.001$.

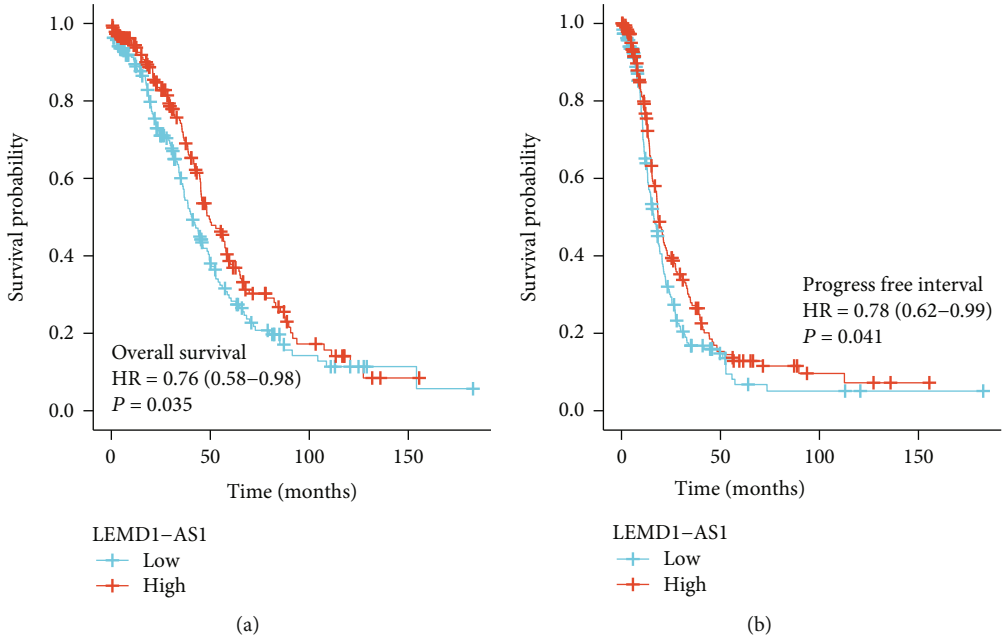

Figure 3: Kaplan-Meier curves estimating the (a) overall survival and (b) progression-free interval rates according to the expression of LEMD1-AS1 in patients with EOC.

Table 2: Univariate and multivariate analyses of prognostic factors in EOC patients.

Characteristics	Total (*N*)	Univariate analysis		Multivariate analysis	
		Hazard ratio (95% CI)	*p* value	Hazard ratio (95% CI)	*p* value
FIGO stage	374				
Stage I & stage II	24	Reference			
Stage III	293	2.045 (0.905-4.621)	0.085	2.255 (0.815-6.241)	0.118
Stage IV	57	2.495 (1.057-5.889)	**0.037**	2.441 (0.839-7.100)	0.101
Primary therapy outcome	307				
PD	27	Reference			
SD	22	0.441 (0.217-0.895)	**0.023**	0.443 (0.213-0.918)	**0.029**
PR	42	0.652 (0.384-1.107)	0.113	0.598 (0.341-1.049)	0.073
CR	216	0.152 (0.093-0.247)	**<0.001**	0.150 (0.090-0.251)	**<0.001**
Race	364				
Asian & Black or African American	37	Reference			
White	327	0.637 (0.405-1.004)	0.052	0.711 (0.419-1.206)	0.206
LEMD1-AS1	377				
Low	188	Reference			
High	189	0.757 (0.585-0.981)	**0.035**	0.866 (0.640-1.170)	0.348
Age	377				
≤60	206	Reference			
>60	171	1.355 (1.046-1.754)	**0.021**	1.421 (1.049-1.925)	**0.023**

exploration of the prognostic value of LEMD1-AS1 levels in EOC patients, we performed univariate analysis which revealed that primary therapy outcome, stage, age, and LEMD1-AS1 expression were related to the clinical outcome of EOC patients (Table 2). However, in multivariate analysis, we just observed that age and primary therapy outcome were an independent prognostic factor for overall survival of EOC patients (Table 2).

3.5. The Association between LEMD1-AS1 Expression and Immune Infiltration. The Spearman correlation test was applied to explore the relationships between LEMD1-AS1 expressions and immune cell infiltration by the use of TIMER. We observed that LEMD1-AS1 expression was negatively associated with the levels of neutrophil and myeloid dendritic cell (Figure 4).

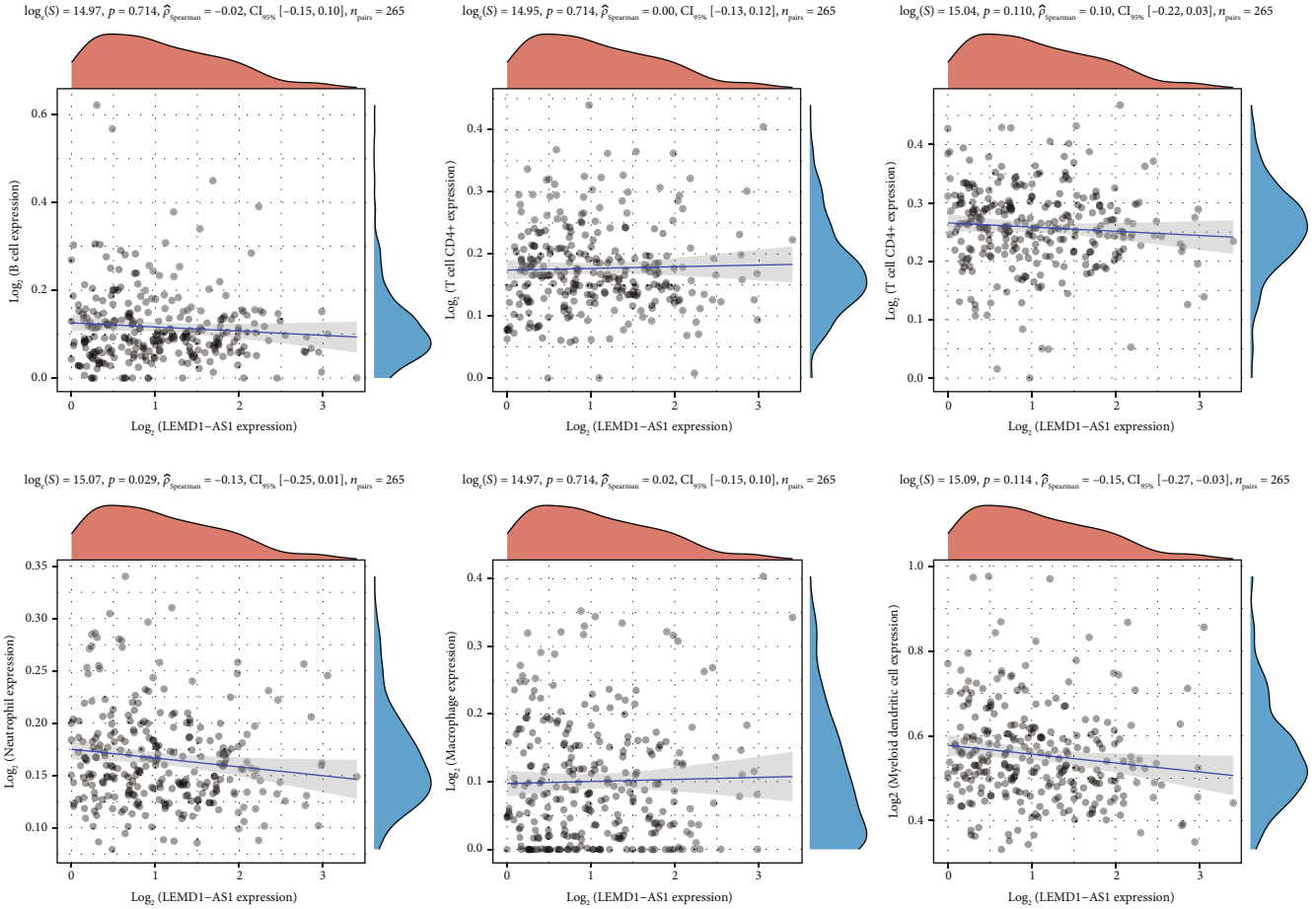

Figure 4: Correlation of LEMD1-AS1 expression with immune infiltration level in EOC.

4. Discussion

EOC is the eighth most common cause of death from cancer in women. The clinical prognosis of EOC patients remained poor after the comprehensive treatments, including surgery, chemotherapy, and radiotherapy [18, 19]. The early diagnosis contributed to a favorable long-term survival of EOC patients, and the early prediction of clinical outcome could guide the targeted therapies and optimize therapeutic schedules [20]. However, up to date, the sensitive and specific biomarkers are limited in clinical practice. In recent years, an increasing number of studies have suggested that lncRNAs have the potential to be employed as novel biomarkers due to the specific dysregulation of lncRNAs and their capacity to behave as tumor promoters or oncogenes [21, 22].

Recently, more and more studies have demonstrated that the expression abnormalities of lncRNAs were associated with the progression of many cancers. For instance, Wang et al. firstly indicated that lncRNA B3GALT5-AS1 expression was distinctly decreased in colon cancer and promoted suppressed colon cancer liver metastasis via the miRNA-203/EMT axis, suggesting that LEMD1-AS1 served as an oncogenic lncRNA in this tumor [23]. Qian et al. reported that lncRNA MIR4435-2HG expressions were distinctly increased in lung cancer and predicted an advanced stage and distant metastasis. Functional experiments revealed that MIR4435-2HG silence suppressed the proliferation and metastasis of lung cancer cells via by activating β-catenin signalling. To date, only a study by Guo et al. reported that there was a downregulation of LEMD1-AS1 expression in both the OC tissues and the OC cell lines. In addition, the regulation of miR-183-5p and TP53 by forced upregulation of LEMD1-AS1 decreased the proliferation and metastasis of ovarian cancer cells. However, the expression and function of LEMD1-AS1 in other tumors have not been investigated.

In this research, LEMD1-AS1 was demonstrated to be lowly expressed in EOC specimens based on TCGA datasets and our cohort. Then, ROC assays revealed LEMD1-AS1 as a useful tool to distinguish EOC specimens from normal ovarian tissues. A clinical study indicated that patients with low LEMD1-AS1 expression have a shorter OS and PFI than those with high LEMD1-AS1 expression. We performed univariate analysis which revealed that primary therapy outcome, stage, age, and LEMD1-AS1 expression were associated with the clinical outcome of EOC patients. However, in multivariate analysis, we just observed that age and primary therapy outcome were an independent prognostic factor for overall survival of EOC patients. In addition, we offered evidences that LEMD1-AS1 may be exploited as an innovative diagnostic and prognostic biomarker for EOC patients.

There is a correlation between immune infiltration of tumor cells and the spread of EOC to lymph nodes, as well as the patient's prognosis [24, 25]. An examination of the TIMER database revealed that the expression of LEMD1-AS1 was inversely linked with the expression of both neutrophil and myeloid dendritic cell. It is essential for antitumor immunity for T cells to get activated and expand while they are in the tumor microenvironment [26]. As a result of complement-dependent T cell suppression, neutrophils in the TME become unique from myeloid-derived suppressor cells in their ability to block T cell proliferation and activity. Based on these findings, it appeared that LEMD1-AS1 may play a role in the immunological response of EOC tumors to their surrounding microenvironment.

5. Conclusions

We identified LEMD1-AS1 as a novel EOC-related lncRNA which was lowly expressed in EOC specimens and predicted a poor prognosis. We found the correlation of LEMD1-AS1 with neutrophil and myeloid dendritic cell. Overall, we confirmed that LEMD1-AS1 could be applied as a potential biomarker of EOC diagnosis and prognosis. However, the specific function and exact molecular mechanisms of LEMD1-AS1 in EOC remain unclear and require further investigation.

Data Availability

The datasets used and/or analyzed during the current study are available from the corresponding author upon reasonable request.

Conflicts of Interest

The authors declare that they have no conflict of interests.

Authors' Contributions

Xiaoju Yang and Shen Zhou contributed equally to this work.

Acknowledgments

This work is supported by grants of the Precision Medicine Special Project (Special Nursing Project) of Hubei Province (No. ZLJZ2020HLYB007).

References

[1] R. L. Siegel, K. D. Miller, H. E. Fuchs, and A. Jemal, "Cancer statistics, 2021," *CA: a Cancer Journal for Clinicians*, vol. 71, no. 1, pp. 7–33, 2021.

[2] F. Bray, J. Ferlay, I. Soerjomataram, R. L. Siegel, L. A. Torre, and A. Jemal, "Global cancer statistics 2018: GLOBOCAN estimates of incidence and mortality worldwide for 36 cancers in 185 countries," *CA: a Cancer Journal for Clinicians*, vol. 68, no. 6, pp. 394–424, 2018.

[3] S. Lheureux, M. Braunstein, and A. M. Oza, "Epithelial ovarian cancer: evolution of management in the era of precision medicine," *CA: a Cancer Journal for Clinicians*, vol. 69, no. 4, pp. 280–304, 2019.

[4] B. Orr and R. P. Edwards, "Diagnosis and treatment of ovarian cancer," *Hematology/Oncology Clinics of North America*, vol. 32, no. 6, pp. 943–964, 2018.

[5] D. M. Gershenson, "Management of rare epithelial ovarian cancers," *Clinical advances in hematology & oncology: H & O*, vol. 17, no. 8, pp. 444–446, 2019.

[6] C. Nero, A. Fagotti, G. F. Zannoni, E. Palluzzi, G. Scambia, and M. Petrillo, "Pathologic response to neoadjuvant chemotherapy in advanced ovarian cancer: utility of a scoring system to predict outcomes," *International journal of gynecological cancer: official journal of the International Gynecological Cancer Society*, vol. 29, no. 6, pp. 1064–1071, 2019.

[7] T. Manchana, N. Phoolcharoen, and P. Tantbirojn, "_BRCA_ mutation in high grade epithelial ovarian cancers," *Gynecologic oncology reports*, vol. 29, pp. 102–105, 2019.

[8] M. Winkle, S. M. El-Daly, M. Fabbri, and G. A. Calin, "Noncoding RNA therapeutics – challenges and potential solutions," *Nature Reviews. Drug Discovery*, vol. 20, no. 8, pp. 629–651, 2021.

[9] S. Jathar, V. Kumar, J. Srivastava, and V. Tripathi, "Technological developments in lncRNA biology," *Advances in Experimental Medicine and Biology*, vol. 1008, pp. 283–323, 2017.

[10] L. Ma, V. B. Bajic, and Z. Zhang, "On the classification of long non-coding RNAs," *RNA Biology*, vol. 10, no. 6, pp. 925–933, 2013.

[11] R. O. Niederer, E. P. Hass, and D. C. Zappulla, "Long noncoding RNAs in the yeast S. cerevisiae," *Advances in Experimental Medicine and Biology*, vol. 1008, pp. 119–132, 2017.

[12] W. X. Peng, P. Koirala, and Y. Y. Mo, "LncRNA-mediated regulation of cell signaling in cancer," *Oncogene*, vol. 36, no. 41, pp. 5661–5667, 2017.

[13] L. Tong, Y. Wang, Y. Ao, and X. Sun, "CREB1 induced lncRNA HAS2-AS1 promotes epithelial ovarian cancer proliferation and invasion via the miR-466/RUNX2 axis," *Biomedicine & Pharmacotherapy*, vol. 115, p. 108891, 2019.

[14] L. Tong, Y. Ao, H. Zhang, K. Wang, Y. Wang, and Q. Ma, "Long noncoding RNA NORAD is upregulated in epithelial ovarian cancer and its downregulation suppressed cancer cell functions by competing with miR-155-5p," *Cancer Medicine*, vol. 8, no. 10, pp. 4782–4791, 2019.

[15] A. Al-Rugeebah, M. Alanazi, and N. R. Parine, "MEG3: an oncogenic long non-coding RNA in different cancers," *Pathology oncology research: POR*, vol. 25, no. 3, pp. 859–874, 2019.

[16] Q. Tang and S. S. Hann, "HOTAIR: an oncogenic long noncoding RNA in human cancer," *Cellular Physiology and Biochemistry: International Journal of Experimental Cellular Physiology, Biochemistry, and Pharmacology*, vol. 47, no. 3, pp. 893–913, 2018.

[17] K. Z. Thin, J. C. Tu, and S. Raveendran, "Long non-coding SNHG1 in cancer," *Clinica chimica acta; international journal of clinical chemistry*, vol. 494, pp. 38–47, 2019.

[18] Y. Kobayashi, K. Banno, H. Kunitomi, E. Tominaga, and D. Aoki, "Current state and outlook for drug repositioning anticipated in the field of ovarian cancer," *Journal of Gynecologic Oncology*, vol. 30, no. 1, article e10, 2019.

[19] M. Markman, "Pharmaceutical management of ovarian cancer: current status," *Drugs*, vol. 79, no. 11, pp. 1231–1239, 2019.

[20] M. A. Lisio, L. Fu, A. Goyeneche, Z. H. Gao, and C. Telleria, "High-grade serous ovarian cancer: basic sciences, clinical and therapeutic standpoints," *International Journal of Molecular Sciences*, vol. 20, no. 4, p. 952, 2019.

[21] Y. Xie, W. Dang, S. Zhang et al., "The role of exosomal noncoding RNAs in cancer," *Molecular Cancer*, vol. 18, no. 1, p. 37, 2019.

[22] S. R. Khan, A. G. Rockall, and T. D. Barwick, "Molecular imaging in cervical cancer," *The Quarterly Journal of Nuclear Medicine and Molecular Imaging: Official Publication of the Italian Association of Nuclear Medicine (AIMN)[and] the International Association of Radiopharmacology (IAR),[and] Section of the Society of*, vol. 60, no. 2, pp. 77–92, 2016.

[23] L. Wang, Z. Wei, K. Wu et al., "Long noncoding RNA B3GALT5-AS1 suppresses colon cancer liver metastasis via repressing microRNA-203," *Aging*, vol. 10, no. 12, pp. 3662–3682, 2018.

[24] Y. Huang, B. Y. S. Kim, C. K. Chan, S. M. Hahn, I. L. Weissman, and W. Jiang, "Improving immune-vascular crosstalk for cancer immunotherapy," *Nature Reviews. Immunology*, vol. 18, no. 3, pp. 195–203, 2018.

[25] A. Jiménez-Sánchez, P. Cybulska, K. L. Mager et al., "Unraveling tumor-immune heterogeneity in advanced ovarian cancer uncovers immunogenic effect of chemotherapy," *Nature Genetics*, vol. 52, no. 6, pp. 582–593, 2020.

[26] O. M. T. Pearce, R. M. Delaine-Smith, E. Maniati et al., "Deconstruction of a metastatic tumor microenvironment reveals a common matrix response in human cancers," *Cancer Discovery*, vol. 8, no. 3, pp. 304–319, 2018.